

Integrated Lithostratigraphic, Formation and Structural Evaluation  
of the Migrant Structure, Sable Subbasin, Offshore Nova Scotia.

By

Kenneth T. Martyns-Yellowe

Submitted in partial fulfilment of the requirements  
For the degree of Master of Science.

at

Dalhousie University  
Halifax, Nova Scotia

April 2021

© Copyright by Kenneth Martyns-Yellowe, April 2021

DALHOUSIE UNIVERSITY

## Dedication

I dedicate this thesis to my Mother Emilia Alaputa for you are my first teacher. Also, to my late father Senator I.S. Martyns-Yellowe for making me see the value of education at every stage of my life. My late grandmother (Charity Alaputa) for having faith in me to succeed in my educational endeavors. I pray that you both continue to rest easy. Amen. To the good people of Rivers State and the Niger Delta Region of Nigeria.

I thank the Dalhousie University community, the Government of Nova Scotia, and Government of Canada for accommodating me in my endeavour to study and learn in a forward-thinking environment. You gave a Rivers boy from the South of Nigeria a reason to be inspired.

## Table of Contents

List of Tables .....	viii
List of Figures .....	xii
Abstract.....	xxi
List of Abbreviations Used.....	xxii
Glossary .....	xxiii
CHAPTER 1: INTRODUCTION.....	1
1.1. Project Overview .....	1
1.2. Problem.....	2
1.3. Study Area .....	4
1.4. Project Objectives.....	6
1.5. Hypotheses.....	6
1.6. Thesis Outline.....	7
1.7. Project Workflow.....	8
CHAPTER 2: BACKGROUND.....	9
2.1. Regional Structural Setting.....	9
2.2. Stratigraphy of the Sable Subbasin.....	10
2.3. Petroleum Systems in the Sable Subbasin.....	14
2.4. Exploration History of the Scotian Basin (Modified after CNSOPB 2018).....	14
CHAPTER 3: STRATIGRAPHIC WELL CORRELATION AND SEDIMENTARY CORE ANALYSIS OF THE MIGRANT EXPANSION TREND .....	19
3.1. Introduction.....	19
3.2. Data and Methods .....	20
3.2.1. Well Data .....	20
3.2.2. Stratigraphic Analysis and Core Description .....	20
3.2.3. Well Stratigraphic Correlation .....	23
3.2.4. XRF Core Analyses .....	23
3.3. Results.....	24

3.3.1. Core Lithofacies Description.....	24
3.3.2. XRF Analyses Results.....	30
3.3.3. Well Stratigraphy.....	35
3.4. Discussions from Sedimentary Core Obserations .....	36
3.4.1. Depositional Relationship - F3 and H2 Sand Intervals .....	36
3.4.2. Depositional Relationship- I-93 Core #1 Interval.....	39
3.4.3. Depositional Facies at Migrant.....	42
3.4.4. Reservoir Stratigraphic Framework .....	44
3.4.5. Well Correlation .....	52
<b>CHAPTER 4: PETROPHYSICAL WELL LOG AND PRESSURE ANALYSIS OF THE MIGRANT EXPANSION TREND.....</b>	
4.1. Introduction.....	55
4.2. Data and Methods .....	57
4.2.1. Standardized Petrophysical Analysis Workflow .....	57
4.2.2. Pressure Analyses Workflow.....	57
4.3. Results.....	58
4.3.1. Petrophysical Analyses Results .....	58
4.3.2. Pressure Analyses Results .....	62
4.4. Discussion.....	65
4.4.1. Porosity and Permeability Relations from Core Data .....	65
4.4.2. Porosity and Permeability Relations from Log Analyses .....	67
4.4.3. Reservoir Fluid and Water Saturation Relations .....	69
4.4.3.1. Reservoir Fluid Relations .....	69
4.4.4. Net Pay Criteria .....	78
4.4.5. Petrophysical Signature of Fault Contact in the Migrant N-20 Well..	82
4.4.6. Pressure vs Elevation (Depth) Characterization.....	84
<b>CHAPTER 5: 3D SEISMIC INTERPRETATION AND FAULT SEAL ANALYSIS OF THE MIGRANT STRUCTURE .....</b>	
5.1. Introduction.....	87



5.2. Data and Methods .....	87
5.2.1. Seismic Data .....	87
5.2.2. Database Construction .....	89
5.2.3. Methods .....	89
5.2.3.1. Seismic Stratigraphy .....	89
5.2.3.2. Static Model Building Workflow Overview (Petrel™) .....	90
5.2.3.3. Seismic Horizon and Fault Interpretation .....	90
5.2.3.4. Geocellular TWT Modelling .....	91
5.2.3.5. Fault Modelling .....	92
5.2.3.6. Pillar Gridding .....	93
5.2.3.7. Horizon Modelling .....	94
5.2.3.8. Time-to-Depth Conversion .....	94
5.2.3.9 Zone Index .....	96
5.2.3.10. Layering and Scale Up of Well Logs .....	97
5.2.3.11. Petrophysical Modelling .....	98
5.2.3.12. Construction of Fault Plane Profiles .....	100
5.3. Results .....	100
5.3.1. Seismic Interpretation: Horizons .....	100
5.3.2. Seismic Interpretation: Seismic Facies .....	102
5.3.3. Geocellular TWT Model with Pillar Grids .....	107
5.3.4. Faults, Zones and Horizon Model .....	107
5.3.5. Time-Depth Model .....	109
5.3.6. Petrophysical Modelling .....	111
5.4. Discussion .....	114
5.4.1. Migrant Structure .....	114
5.4.2. Fault Seal Analyses of the Migrant Structure .....	117
5.4.3. Fault Seal in Analogous Settings .....	123
CHAPTER 6: DISCUSSION .....	126
6.1. Trapping Mechanisms of the Migrant Structure .....	126

6.1.1. Sediment Interactions in Structural Rollover .....	126
6.1.2. Structural Analogs and Velocity Discussion.....	134
6.1.2.1. Structural Analog.....	134
6.1.2.2. Potential Uncertainties from Time-to-Depth Relationship .....	136
6.1.3. Depositional Relations.....	139
6.1.3.1. The Mixed Clastic and Carbonate Transition.....	139
6.1.3.2. Mixed Siliciclastic-Carbonate Transitions .....	144
6.2. Discussion of Overpressure at the Migrant Structure .....	148
6.3. Reservoir Discussion .....	151
6.3.1. Reservoir Analyses Including Mud Gas Relationship .....	151
6.3.2. Permeability and Pressure Discussion.....	155
6.3.2.1. Permeability.....	155
6.3.2.2. Dynamic Fluid Simulation Discussion.....	156
6.3.3. Fault and Seal Discussion.....	158
6.3.3.1. Trapping Scenarios of Rollover Structures in the Sable Subbasin.. .....	158
6.3.3.2. Trapping Conditions in the Migrant Structure .....	163
6.3.3.3. Hydrocarbon Trapping in Rollover Structures on the Scotian Shelf.....	166
6.3.3.4. Risks and Opportunities in Rollover Structures on the Scotian Shelf.....	170
6.4. Uncertainties .....	176
6.4.1. Seismic Uncertainties .....	176
6.4.2. Uncertainties from Well Data.....	177
6.4.3. Uncertainties from Modelling .....	177
CHAPTER 7: CONCLUSIONS AND RECOMMENDATIONS .....	179
7.1. Conclusions.....	179
7.1.1. Stratigraphy and Sediment Deposition.....	179
7.1.2. Pressure Connectivity and Petrophysical Log Analysis.....	179

7.1.3. Seismic Interpretation and Depth Conversion.....	180
7.1.4. Fault Seal Analysis .....	181
7.1.5. New Findings and Risk Mitigation in Other Basins. ....	182
7.2. Additional Recommendations. ....	182
REFERENCES .....	187
APPENDIX A.....	201
A.1. Sediment Core Description.....	201
A.2. XRF analysis.....	206
A.2.1. Sampling, Elemental Conversions and Resulting Tables.....	206
APPENDIX B.....	220
B.1. Wireline Logs.....	220
B.1.1. Gamma-Ray Log.....	220
B.1.2. Density Log.....	221
B.1.3. Resistivity Log .....	221
B.1.4. Sonic Log .....	222
B.1.5. Lithology .....	223
B.2. Calculations Involving Wireline Logs.....	224
B.2.1. Lithology and Shale Volume (Vsh) Prediction from Wireline Gamma-Ray Log.....	224
B.2.2. Porosity Estimation .....	226
B.2.3. Water and Hydrocarbon Saturation Estimation .....	229
B.2.4. Permeability Estimation.....	232
APPENDIX C.....	233
C.1. Pressure Relations from Flow Test – Migrant N-20.....	233
C.2. Horner Plot Relations from Flow Test – Migrant N-20 .....	236
C.3. Pressure Relations from Flow Test – Adamant N-97 .....	237
APPENDIX D.....	244
APPENDIX E. ....	247
E.1. Core Reservoir Estimate Tables.....	247

E.2. Well Log Reservoir Estimate Tables .....	255
E.3. Risking .....	278
SIGNATURE PAGE .....	282

## List of Tables

Table 1.1: The Migrant N-20 well DST test intervals (Tetco, 1978). .....	4
Table 3.1: Well information of the four wells used in this study.. .....	20
Table 3.2: Core data incorporated in this study.. .....	21
Table 3.3: Physical rock data availability in the project area. ....	24
Table 3.4: Summary of lithofacies examined from core in the Thebaud I-93 well. ....	25
Table 4.1: Net pay estimates from well log analysis of the Migrant N-20 well. ....	79
Table 4.2: Net reservoir estimates from well log analysis of the Migrant N-20 well. ....	80
Table 4.3: Net clean rock estimates from well log analysis of the Migrant N-20 well. ...	81
Table 5.1: Summary of the five key seismic facies used for interpreting the seismic structural and stratigraphic framework. ....	103
Table 6. 1: Interpreted horizons in TWT and their equivalent depth and estimated thicknesses. ....	139
Table 6. 2: A summary of failed wells in the Scotian Shelf (CNSOPB, 2013). ....	167
Table 6. 3: The three structures analysed in this study. ....	168
Table 6.4: Significant and commercial discoveries of the Scotian Margin.. .....	168
Table 6.5: Unrisked in place hydrocarbon volumes.. .....	171
Table 7.1: Net pay thickness and attribute estimates based on wireline derived interval depths. ....	184
Table 7.2: Net reservoir and attribute estimates based on wireline derived interval depths.. .....	184
Table 7.3: Net clean rock thickness and attribute estimates based on wireline derived interval depths when only the Vsh has been used as the cutoff criteria. ....	186
Table A.2.1: Conversion of elements to oxides after Korotev (2009). ....	208
Table A.2.2: Calculated results from geochemical analysis of the sandstones in the Migrant N-20 cuttings samples. ....	209
Table A.2.3: Calculated results from geochemical analysis of the sandstones in the Adamant N-97 sidewall cores. ....	210

Table A.2.4: Calculated results from geochemical analysis of the sandstones in the Thebaud I-93 full diameter cores.....	211
Table A.2.5: Calculated results from geochemical analysis of the sandstones in the Thebaud E-74 (T5) F3 full diameter cores. ....	212
Table A.2.6: Calculated results from geochemical analysis of the sandstones in the Thebaud E-74 (T5) H2 full diameter cores.....	214
Table A.2.7: Log-ratio estimates from corresponding oxide ratios from the Migrant N-20 well.....	215
Table A.2.8: Log-ratio estimates from corresponding oxide ratios from the Adamant N-97 well.....	216
Table A.2.9: Log-ratio estimates from corresponding oxide ratios from the H2 interval of the Thebaud E-74-T5 well.....	217
Table A.2.10: Log-ratio estimates from corresponding oxide ratios from the F3 interval of the Thebaud E-74-T5 well. ....	218
Table D.1: Checkshot values from the Migrant N-20 well.....	246
Table E.1.1: A summary table of core data estimates for the I-93 Sand in the Thebaud Field. ....	247
Table E.1.2: A cumulative of interval porosity and permeability estimates for the I-93 sand interval. ....	248
Table E.1.3: A summary table of core data estimates for the H2 Sand in the Thebaud Field. ....	249
Table E.1.4: A cumulative of interval porosity and permeability estimates for the H2 sand interval. ....	250
Table E.1.5: A summary table of core data estimates for the F3 Sand in the Thebaud Field. ....	253
Table E.1.6: A cumulative of interval porosity and permeability estimates for the F3 sand interval.....	254
Table E.2.1: Summation table of intervals that meet contribution criteria when only Vsh, is applied to the open hole DST 2 interval. ....	255
Table E.2.2: Summation table of intervals that meet contribution criteria when the Vsh and Effective porosity are applied to the open hole DST 2 interval. ....	256

Table E.2.3: Summation table of intervals that meet contribution criteria when the Vsh, Effective porosity, and Water Saturation parameters (which incorporates flowable amounts of hydrocarbons) are applied to the open hole DST 2 interval. ....	257
Table E.2.4: Summation table of intervals that meet cutoff criteria when only Vsh is applied to the casing depth derived DST 5 interval. ....	258
Table E.2.5: Summation table of intervals that meet cutoff criteria when Vsh and Effective porosity are applied to the casing depth derived DST 5 interval. ....	259
Table E.2.6: Summation table of intervals that meet cutoff criteria when Vsh, Effective porosity, and Water Saturation parameters (which incorporates flowable amounts of hydrocarbons) are applied to the casing depth derived DST 5 interval. ....	260
Table E.2.7: Summation table of intervals that meet cutoff criteria when only Vsh, is applied to the casing depth derived DST 8 interval. ....	261
Table E.2.8: Summation table of intervals that meet cutoff criteria when Vsh and Effective porosity are applied to the casing depth derived DST 8 interval. ....	262
Table E.2.9: Summation table of intervals that meet cutoff criteria when the Vsh, Effective porosity, and Water Saturation parameters are applied to the casing depth derived DST 8 interval. ....	263
Table E.2.10: Summation table of intervals that meet contribution criteria when only Vsh is applied to the Bottom Sand open hole Interval. ....	264
Table E.2.11: Summation table of intervals that meet contribution criteria when Vsh and Effective porosity are applied to the Bottom Sand open hole Interval. ....	266
Table E.2.12: Summation table of intervals that meet contribution criteria when Vsh, Effective porosity and Water Saturation parameters are applied in the Bottom Sand open hole Interval Below DST 2. ....	268
Table E.2.13: Summation table of intervals that meet cutoff criteria when only Vsh is applied to the wireline derived DST 5 interval. ....	270
Table E.2.14: Summation table of intervals that meet cutoff criteria when Vsh and Effective porosity are applied to the wireline dericed DST 5 interval. ....	271
Table E.2.15: Summation table of intervals that meet cutoff criteria when Vsh, Effective porosity, and Water Saturation parameters are applied to the wireline derived DST 5 interval. ....	272
Table E.2.16: Summation table of intervals that meet cutoff criteria when only Vsh is applied to the open hole DST 2 interval. ....	273

Table E.2.17: Summation table of intervals meeting cutoff when the Vsh and Effective porosity are applied in the open hole DST 2 interval.....	275
Table E.2.18: Summation table of intervals that meet contribution criteria when the Vsh, Effective porosity, and Water Saturation are applied to the DST 2 interval..	277
Table E.3.1: Relative probability scale for the probability of structural closure (Milkov, 2015).	278
Table E.3.2: Probability scheme for the probability of effective migration (CCOP, 2000).	279
Table E.3. 3: Probability scheme for the probability of effective trapping/ retention (CCOP, 2000).	279
Table E.3.4: Probability schemes for the probability of effective reservoir facies (CCOP, 2000).	280
Table E.3.5: General relative probability scale for the probability (CCOP, 2000).	281



## List of Figures

Figure 1.1: A location map of the Sable Subbasin, offshore Nova Scotia.....	1
Figure 1.2: A pie chart showing the different play types tested by drilling offshore Nova Scotia.....	2
Figure 1.3: A seismic section of the Migrant Structure and N-20 well penetration shows evidence of extensional-related crestal faulting represented by the light blue line.	3
Figure 1.4: A structural map of growth fault networks and associated rollover structures with well penetrations around Sable Island (Wach and Hirschmiller, 2012).....	5
Figure 1.5: A seismic stratigraphic section showing growth faults in the Sable Subbasin including the Migrant, Adamant, and Thebaud rollover anticlines (SOEP, 1997).....	5
Figure 1.6: Complete workflow used in this project.....	8
Figure 2.1: A block diagram showing the Geology of the Scotian Shelf from Williams et al., (1997), later modified by CNSOPB (2009).....	9
Figure 2.2: A stratigraphic chart of the Scotian Basin by Campbell (2018).....	10
Figure 2.3: A paleogeographic map of the Scotian Basin showing the early lakes and shallow seas with associated salt deposited during the Late Triassic (CNSOPB 2012)...	11
Figure 2.4: A Late Jurassic paleogeographic illustration of the Scotian Basin depicting the Abenaki carbonate platform and the advancing deltaic clastics of the Mic Mac Formation that inundated the carbonate system (CNSOPB 2012).....	12
Figure 2.5: Recent and previous stratigraphic columns of the zones of interest comprising the Migrant expansion trend revised by Campbell (2018).....	13
Figure 2.6: A chart showing the significant rollover discoveries (brown) with those that became commercial fields (green) in the Scotia Basin, offshore Nova Scotia (SOEP, 1997).....	15
Figure 2.7: A bar graph of all wells drilled offshore Nova Scotia to date.....	16
Figure 2.8: A bar graph of the associated seismic data (2D or 3D) with which the various exploration cycles have been based off (CNSOPB, 2019). .....	17
Figure 2.9: A map of the offshore sedimentary basin with the fields, closures, wells, and pipelines linking various hydrocarbon structures from the Sable Subbasin.....	18
Figure 3.1: A plan view of the study area comprising the four project wells and their relative spacing from Petrel. ....	22

Figure 3.2: The well correlation workflow used for building a stratigraphic cross-section.....	23
Figure 3.3: A figure of the log facies described in the Thebaud I-93 well. ....	29
Figure 3.4: Histogram of data distributed on a sandclass plot for the respective fields in the analyzed wells and intervals of interest including the Mic Mac and Missisauga formation reservoirs. ....	31
Figure 3.5: A series of sandstone classification plots of samples from the cores for the project wells. ....	32
Figure 3.6: A cross-section of the key wells used in this project. ....	35
Figure 3.7: A well composite for three of the four project wells.....	36
Figure 3.8: A figure of the F3 Sand interval in the Thebaud Structure showing the Gamma-Ray log (second track) with cleaning up signature right of the depth track. ....	37
Figure 3.9: A figure of the H2 Sand interval in the Thebaud Structure showing the Gamma-Ray log (second track) with a blocky log signature right of the depth track. ....	39
Figure 3.10: Sedimentological characteristics of the I-93 cored section from the Lower Missisauga Formation showing the facies and their sedimentary characters. ....	41
Figure 3.11: A figure showing the basinward progradation of deltaic sediments modified from (Scruton, 1960). ....	42
Figure 3.12: A figure of the Thebaud T5 well composite showing the alphabetic-numeric nomenclature used in the deeper overpressure interval below the Thebaud Shale.....	45
Figure 3.13: A figure of the Thebaud I-93 well composite showing the numeric-alphabetic nomenclature used in the shallow, hydro-pressure interval above the Thebaud Shale.....	46
Figure 3.14: A figure of the Adamant N-97 well composite showing the Cretaceous nomenclature used for identifying the sands in the well.....	48
Figure 3.15: A figure of the Adamant N-97 well composite showing the next Cretaceous sand sequence (C5 to C1A) overlying the top of the Cretaceous C1A to C1 sand interval.....	49
Figure 3.16: A figure of the Adamant N-97 well composite showing the next Cretaceous sand sequence overlying the top of the Cretaceous C6 to C5 interval. ....	50
Figure 3.17: A figure of the Migrant N-20 well showing the tested zones below the well.....	51

Figure 3.18: A well composite for three of the four project wells.....	52
Figure 3.19: A figure showing the stratigraphic relationship between the Migrant, Adamant, and the Thebaud Field sands..	54
Figure 4.1: A pressure elevation plot (Modified from Schlumberger, 2020). .....	56
Figure 4.2: A flow chart of the analysis steps for the petrophysical deliverable for this project. ....	57
Figure 4.3: Pressure workflow used in this project modified after Skinner (2016).....	58
Figure 4.4: A formation evaluation composite plot Migrant N-20 with input curves in the first five tracks and output curves in the last four tracks..	59
Figure 4.5: A formation evaluation composite from the Migrant N-20 well with input curves in the first four tracks on the left and output curves in the last four tracks on the right..	61
Figure 4.6: A pressure elevation plot of the Migrant N-20 well RFT data points (black) with DST point data in red..	62
Figure 4.7: A pressure elevation plot of three of the four project wells. ....	63
Figure 4.8: A pressure elevation plot of the pressure elevation data for four project wells..	64
Figure 4.9: A cross plot showing the clusters and regression relationship through the project wells. ....	68
Figure 4.10: A well composite for Migrant N-20 showing the Gamma-Ray and resistivity tracks..	70
Figure 4.11: A Pickett plot of the Migrant well showing the plotted points from the Upper Mic Mac Formation (3935 – 4035m).....	73
Figure 4.12: A Pickett plot of the Migrant well showing the plotted points from the Lower Mic Mac Formation (4100 – 4350 m).....	74
Figure 4.13: A chart is used for establishing the resistivity of an equivalent NaCl concentration at a specific temperature.....	76
Figure 4.14: A well composite from Migrant N-20 showing the Gamma-Ray, water saturation (gas implied), porosity/BVW, and Permeability tracks..	78
Figure 4.15: A log composite of the general area thought to be intersected by the fault in the well 3780 m – 3910 m. ....	83

Figure 4.16: A mud gas log of the area of the well thought to be intersected by the fault showing 12,400 ft – 12,850 ft (3779 – 3916 m). .....	84
Figure 5.1: A juxtaposition triangle diagram (right) illustrating the displacement of a fault in 3D varying along strike (Knipe, 1997). .....	87
Figure 5.2: A figure of the area covered by the Sable MegaMerge 3D seismic volume (thick white outline) with Sable Island (yellow) shapefile in the 3D area.....	88
Figure 5.3: An illustration of the various seismic reflection termination patterns. ....	89
Figure 5.4: A figure showing the interpretation tool palette in Petrel™ used for completing the 3D seismic interpretation for this study.. .....	90
Figure 5.5: A seismic section of the Migrant area showing the interpreted horizons. ....	91
Figure 5. 6: A figure showing the corner point gridding workflow in Petrel™ used for setting up a structural model. ....	92
Figure 5.7: A screen capture of the model area defined by a boundary polygon (blue line) and the imported faults (white lines). .....	93
Figure 5.8: Screen capture of the model area and faults displayed on the 3D window in Petrel™. ....	93
Figure 5.9: A figure showing the horizon modelling step in Petrel™. .....	94
Figure 5.10: A figure of the advanced velocity modelling step in the geophysics workflow in Petrel™. .....	95
Figure 5.11: A figure of the advanced velocity modelling step in Petrel™. ..	95
Figure 5.12: A figure of the depth convert 3D grid dialog box, which was used for depth converting the time grid (brown) in Petrel™. .....	96
Figure 5.13: A figure of a dialog box that enables zones and segments to be assigned numerical indices in Petrel™. .....	97
Figure 5.14: A figure of the scale-up well log step highlighted in the property modelling workflow in Petrel™ used for scaling petrophysical logs.....	98
Figure 5.15: A figure of the petrophysical modelling dialog box in Petrel™. ....	99
Figure 5.16: A figure of the five alphanumeric horizons (MK1 to MK 5) from top to bottom (a-e). .....	101
Figure 5.17: A seismic section across the Migrant Structure to illustrate the seismic facies characterised in Table 5.1. ....	105

Figure 5.18: A detailed seismic image from the area of interest of the Migrant Structure.....	106
Figure 5.19: A figure of the model and gridding pattern made in Petrel™.....	107
Figure 5.20: A 3D model of the Migrant Structure at the N-20 well showing the three fault-defined segments. ....	108
Figure 5.21: A 3D model of the Migrant Structure at the N-20 well.....	109
Figure 5.22: A reservoir time map for the top of the uppermost reservoir Mk-2. ....	110
Figure 5.23: A reservoir depth map for the top of the uppermost reservoir Mk-2. ....	110
Figure 5.24: Depth converted structural maps of each interpreted reservoir top in the Migrant Structure (MK-1 to MK-5) concerning the crestal fault. ....	111
Figure 5.25: A figure of the scaled-up porosity log on the top left (A) and the intersecting I and J planes of the depth converted Migrant Structure depicting the distribution of the porosity (B) and permeability (C) derived from the porosity log in the property calculator through the structure.....	112
Figure 5.26: A figure of the intersecting I and J planes of the depth converted Migrant Structure depicting the distribution of shale volume (Vsh).. ....	112
Figure 5.27: A figure of the porosity (left) and permeability (right) of the top of each of the five interpreted zones (Mk 1 to Mk 5) from top to bottom (A-E).. ....	113
Figure 5.28: A simple structural closure showing various components of the structure and the relationship between fluids (gas and water) contained within. ....	115
Figure 5.29: A figure showing seismic interpretation comprising key horizons and the crestal fault (faint black line) with structural maps of (a) Marker 4-Aqua, (b) Marker 5- Brown & (c) Marker Base-Green.....	116
Figure 5.30: A diagram depicting reservoir relationship at the fault (Move, 2016). ....	117
Figure 5.31: A figure of the Migrant N-20 well showing the intermediate reservoirs between Mk 3 and Mk 4 indicated in Figure 5.32 and Figure 5.33 below approximately 3770 m – 3904 m. ....	119
Figure 5.32: A fault plane profile (FPP) of the crestal fault in the Migrant Structure looking northwest.....	119
Figure 5.33: A modelled cross-section of the Migrant Structure populated with sand and shale properties from well log value reveals the magnitude of crestal faulting through the offset of sand-shale pairs. ....	120

Figure 5.34: A figure of the Migrant N-20 well showing the bottom tight reservoirs between 4178 m – total depth TD.....	121
Figure 5.35: A diagram of the modes of hydrocarbon migration at various depths (Downey, 1994).. .....	122
Figure 5.36: Diagram showing an upward and outward migration scenario through juxtaposed leak points.....	123
Figure 6.1: An illustration of the stages of growth fault development in a sedimentary basin (Modified after SOEP 1997).. .....	127
Figure 6.2: A seismic section and annotation of the Miocene Queen Bess Field in Louisiana from Wach et al. (2000). .....	129
Figure 6.3: An unannotated seismic image of the Migrant, Adamant, and Thebaud structures.....	132
Figure 6.4: An annotated seismic image of the Migrant, Adamant, and Thebaud Structures depicting their various structural and depositional relationships.. .....	133
Figure 6.5: A figure of the McAllan Ranch field showing the stratigraphic variation across the major faults (Wach et al., 2002a). .....	135
Figure 6.6: A schematic cross section of the Funiwa area of the North Apoi-Funiwa field (from Wach et al., 1997).....	136
Figure 6.7: A schematic showing the sediment thickness variation between a footwall and hangingwall of a fault.. .....	137
Figure 6.8: A seismic line showing two well tops corresponding to the top and base expansion trend at the Migrant N-20 well. ....	138
Figure 6.9: A Northwest-Southeast dipping interpreted seismic cross-section across the shelf margin areas of the Sable Subbasin that includes the Migrant to Thebaud Expansion trends (Kidston et al., 2007).....	140
Figure 6.10: A figure showing the seismic interpretation from continental shelf margin to slope and distal fore slope area of the Sable Subbasin from Campbell (2018). .....	141
Figure 6.11: An annotated seismic image of the Migrant, Adamant, and Thebaud structures depicting their various depositional relationships to one another. ....	143
Figure 6.12: An example of expansion trend interpreted at McAllan Ranch Field (modified from Bain, 2015). .....	144
Figure 6.13: A geographical map showing the Eastern Red Sea Margin.. .....	145

Figure 6.14: A lithostratigraphic chart of the Scotian and Moroccan Conjugate margins.....	147
Figure 6.15: An annotated figure of the McAllan ranch field. Each group of sands is likely a “closed” system: connection to the system above is via episodic opening and closing of fractures – in the topseal and/or at faults..	150
Figure 6.16: A composite showing the key DST intervals (especially DST #2) and the next higher sand zone interpreted as being wet. ....	151
Figure 6.17: A figure representing the zones of hydrocarbon saturation from log analyses compared to the mud log (Tetco, 1978). ....	152
Figure 6.18: A composite from the Migrant N-20 well showing zones of decreased water saturation and increased hydrocarbon saturation (likely free gas) and water-filled sand interval (water overlain by gas)..	153
Figure 6.19: A mud gas log from the Migrant N-20 well showing the intervals 11,600 to 12,000 (Tetco, 1978).....	154
Figure 6.20: A cross plot of the Thebauds I-93, E-74 (T5), Adamant N-97, and Migrant N-20 showing the clusters and an average regression relationship for the project wells available that have core data..	155
Figure 6.21: A figure showing the migration of injected methane CH <sub>4</sub> in the Migrant Structure by O’Connor et al., 2019.....	157
Figure 6.22: A figure of a seismic line showing the inflection of bright amplitudes representing the crestal fault trace around the Migrant structure. ....	158
Figure 6.23: A structural map of the Top Sand 2 in the South Venture Field (SOEP, 1997).....	159
Figure 6.24: A schematic cross-section of the South Venture Structure showing the major bounding fault and inferred top of overpressure (SOEP, 1997). ....	160
Figure 6.25: A structural map of the top A sand in the Thebaud Structure (SOEP, 1997).....	161
Figure 6.26: A schematic cross-section of the Thebaud Structure showing the faults and crestal faults (SOEP, 1997).....	162
Figure 6.27: A figure showing the options for spilling in a faulted structural trap, modified after Sales (1997).....	164
Figure 6.28: A diagram of the three different classes of traps according to Sales (1997) .....	165

Figure 6.29: A figure of the stratigraphic distribution of discoveries in the Scotian Basin (OETR, 2011)..	170
Figure 6.30: The Scotian Margin showing the division of the margin into six zones (OETR, 2011)..	172
Figure 6.31: A map of the offshore sedimentary basin with the fields, closures, wells, and pipelines linking various hydrocarbon structures from the Sable Subbasin..	173
Figure 6.32: A probability matrix showing the confidence (degree of how much is known) on the Y-axis and the chance of success on the X-axis (Rose, 2001).	175
Figure 6.33: A seismic image from the Migrant rollover (A) showing a fault zone comprising cumulatively offset.....	176
Figure 7. 1: A formation evaluation composite from the Migrant N-20 well.....	185
Figure A.1.1: A figure of the Lower Missisauga Formation Sedimentary Cores Described for this Study from the Thebaud I-93 Well.	204
Figure A.1.2: Photo compilation of slabbed core from the Thebaud I-93 well's core No. 1 (3065.68-3081.27 mRT MD).....	205
Figure A.2.1: A QtFL classification of Folk (1968).	206
Figure A.2.2: A QtFL provenance indicator plot after Ingersoll and Suczek (1979) and Dickinson (1985).....	207
Table A.2.6: Calculated results from geochemical analysis of the sandstones in the Thebaud E-74 (T5) H2 full diameter cores.....	214
Figure B.2.1: A cross plot of Density against Gamma-Ray curves made in Techlog™.	225
Figure B.2.2: A cross plot of sonic and shale volume logs used for determining the slowness (shale velocity) to be used for porosity correction.	227
Figure B.2.3: A cross plot of sonic and shale volume logs used for determining the slowness (shale velocity) to be used for porosity correction..	228
Figure B.2.4: A temperature, salinity, and Rw conversion calculator online version. ...	230
Figure B.2.5: A Pickett plot of resistivity presented on a logarithmic scale on the x-axis against porosity on a double-decade logarithmic scale on the y-axis (Watson, 2017).	231
Figure C.1.1: A diagram of a Drill Stem Test application in a borehole (Glover, 2012a).	233



Figure C.1.2: A DST pressure response from test #2 done in the Migrant Structure (Tetco, 1978).....	234
Figure C.1.3: A figure of traditional pressure analysis based on a DST chart of DST test #5 done in the Migrant Structure (Tetco, 1978).....	235
Figure C.1.4: A DST chart from test #8 done in the Migrant Structure (Tetco, 1978)..	236
Figure C.2.1: A Horner plot of the Migrant N-20 DSTs based on the log of time + change in time/ change in time and pressure at each of those times (Tetco, 1978). .....	237
Figure C.3.1: A figure of the RFT tool showing the key components involved in the positioning and testing with the tool (Quora, 2019). .....	238
Figure C.3.2: A figure of the MDT tool showing the key components involved in the positioning and testing with the tool (IODP, 2010).....	239
Figure C.3.3: An MDT chart from the Adamant N-97 well test depth at 4222 m showing the various acquired measurements during testing (Mobil et al., 2000).. .....	240
Figure C.3.4: An MDT chart from the Adamant N-97 well test depth 3634 m showing the various measured components during testing (Mobil et al., 2000).. .....	241
Figure C.3.5: An MDT chart from the Adamant N-97 well test depth 4120 m showing the various measurements during testing (Mobil et al., 2000). .....	242
Figure C.3.6: An MDT chart from the Adamant N-97 well test depth 3978 m showing the various measured components during testing (Mobil et al., 2000). .....	242
Figure D.1: A schematic of a borehole checkshot data (Schroeder, 2006).....	244
Figure D.2: An example of a typical time-depth velocity relationship extracted from a well's checkshot survey (ODP, 2007).....	245

## Abstract

On the Scotian Shelf, rollover anticlines host majority of the significant and commercial hydrocarbon discoveries. The Upper Jurassic to Lower Cretaceous age reservoirs analyzed in this study are contained in a rollover structure explored by the Migrant N-20 well. This structure is located up-dip from the Adamant rollover explored by the Adamant N-97 well and the Thebaud Structure, which contains economically developed reservoirs. Despite initially flowing gas at a considerable rate during drill stem testing, pressure depletion was encountered in the structure. This led to a preliminary conclusion of the presence of an a volumetrically limited reservoir, similar to deep diagenetically altered reservoirs in other related structures that failed to encounter commercial volumes of hydrocarbons.

This research integrates well data and 3D seismic data to investigate the impact of sand-on-sand juxtaposition across the crestal fault in the Migrant Structure previously missed in 2D seismic. Additionally, we include well pressure analysis, petrophysical analysis, and seismic mapping of siliciclastic reservoirs in the Migrant rollover anticline, a part of the Migrant-Adamant-Thebaud expansion trend (a group of elongate depocentres with sediment fill). Overall, changes in seismic character and isochron thicknesses in the Jurassic to Lower Cretaceous section observed between the Migrant and Thebaud fault blocks characterizes the timing of fault activity. As a result, between 500 and 1000 m (750 m based on chosen average velocity) of clastic sediment deposits in the Thebaud area have no equivalent (likely from non-deposition) on the north side of the boundary fault.

To demonstrate the failure mechanism associated with the crestally faulted Migrant rollover, 3D geocellular models populated with petrophysical parameters from the N-20 well were used to carry out a trap analysis of the structure. As part of the trap analysis, depth conversion of TWT seismic picks in the Migrant Structure was done to ensure that the structure is enclosed in depth. Results show that there is increased displacement along the crestal fault in the shallow and intermediate sections where the intraformational shales are relatively thin.

Residual gas shows at different levels of the structure from petrophysical analysis suggest hydrocarbon migration through the system. Also, structural closure and reservoir quality diminish with depth in the structure with a termination of the crestal fault in areas of low net sand to gross interval thickness deep in the Migrant Structure. The presence of localized gas trapped below the crestal fault termination represents a different trapping mechanism from the hangingwall dip-closed shallow to intermediate reservoirs above the crestal fault.

## List of Abbreviations Used

**API** -- American Petroleum Institute

**BVH** -- Bulk volume of Hydrocarbon

**BVW** -- Bulk Volume of Water

**CNSOPB** -- Canada-Nova Scotia Offshore Petroleum Board

**DHI** -- Direct Hydrocarbon Indicators

**DST** -- Drill Stem Test

**Kh** -- Permeability Thickness

**Km** -- Kilometre

**m** -- Metre

**MD** -- Measured depth

**MDT** -- Modular Dynamic Tester

**MMscf** -- Million Standard Cubic Feet

**mRT** -- Mean Rotary Table

**ms** -- Millisecond

**mSS** -- Mean SubSea.

**NTG** -- Net-to-Gross

**OERA** -- Offshore Energy Research Association

**PFA** -- Petroleum Fairway Analyses

**RFT** -- Repeat formation Tester

**Rw** -- Formation Water Resistivity

**SOEP/ SOEI** -- Sable Offshore Energy Project /Sable Offshore Energy Inc.

**Sw** -- Water Saturation

**TCF** -- Trillion Cubic Feet

**TD** -- Total Depth

**TVD** -- True Vertical Depth

**TVDSS** -- True Vertical Depth Subsea

**TWT** -- Two-way-time

**Vsh** -- Shale Volume

## Glossary

**American Petroleum Institute:** A classification system developed by the American Petroleum Institute to describe the gravity/viscosity of gas-free crude oils expressed as °API. Gravities can vary from low ( $>31.1^{\circ}\text{API}$ ), medium  $31.1\text{-}22.3^{\circ}\text{API}$ ), heavy ( $22.3\text{-}10.0^{\circ}\text{API}$ ) to extra-heavy ( $<10^{\circ}\text{API}$ ) crude oils and extend to tars and solid forms.

**Commercial Discovery:** A discovery of petroleum that has been demonstrated to contain petroleum reserves that justify the investment of capital and effort to bring the discovery to production.

**Development well:** A well drilled for natural gas (or crude oil) within a proven field or area for the purpose of completing the desired pattern for production.

**Drill Stem Test (DST):** A method for isolating and testing the pressure, permeability, and productive capacity of a geological formation during the drilling of a well; provides important measurements of pressure behaviour and information on fluid type with sample collection.

**Dry hole:** A well that does not yield sufficient volumes of gas or oil to support commercial production.

**Excess Pressure:** Subsurface pressure that is abnormally high, exceeding hydrostatic pressure at a given depth.

**Exploratory well** A well in an area where petroleum has not been previously found, or a well targeting formations above or below known reservoirs.

**Hydrocarbon:** Any one of hundreds of organic compounds (gas, liquid, or solid) containing only hydrogen and carbon.

**Hydrostatic Pressure:** The pressure on any rock at a given depth based on a hydrostatic head.

**Lithostatic Pressure:** Pressure of the weight of overburden on a formation at a given depth.

**Mcf (thousand cubic feet):** A unit of volume most used in the low-volume sectors of the natural gas industry (such as residential distribution).

**Mud Gas Log:** A catalog of data from hydrocarbon gas detectors to determine the level of gas recovered from the drilling mud.

**Net Reservoir Thickness:** Refers to the sum of the productive intervals of a reservoir and is determined by the application of cutoffs.

**Overpressure:** Formation pressure more than hydropressure.

**Pay Zone:** The producing part of a formation.

**Play:** A conceptual model to describe hydrocarbon accumulation in prospective basins or regions.

**Pressure Gradient:** Change in pressure per unit of depth

**Repeat Formation Tester (RFT):** A wireline method for testing pressure of a geological formation during drilling quickly; provides important measurements of pressure behavior and information on fluid type with sample collection

**Reserves:** Quantity of hydrocarbons, coal, or minerals considered to be economically recoverable using current technology.

**Seismic:** Pertaining to or characteristic of sound waves in the earth; used in the oil and gas and coal industry via seismic surveys to determine underground rock structure. S (sound waves produced by small, controlled explosions are focused into the ground, and the reflections from various layers in the earth are recorded; – the sound waves travel at different speeds in rock layers having different densities, thereby allowing determination of structure based on the makeup of rock types).

**Significant Discovery:** A discovery indicated by the first well on the geological feature that demonstrates by flow testing the existence of hydrocarbons in that feature and, having regard to geological and engineering factors, suggests the existence of an accumulation of hydrocarbons that has potential for sustained production.

**Tcf (Trillion cubic feet):** A measurement of high-volume for natural gas.

**Unrisked Gas:** A volume of gas discussed, not multiplied by the risk factors associated with being able to produce it.

**Key Words:** Sable MegaMerge, Nova Scotia, Offshore, Migrant Structure; Petroleum systems, Rollover anticline; Hydrocarbon; Crestal fault.

## Acknowledgements

The journey to the completion of this thesis could not have been possible without the guidance and support of many. Essentially it took a whole village, and I am very thankful for this. First and foremost, I thank God for life and my siblings (Lizzy, and Tonye). I am thankful to my supervisor Grant Wach, for all your support and patience throughout my development under your tutelage. Furthermore, I acknowledge ExxonMobil Canada and the operators of the Sable Offshore Energy Project (SOEP), for providing me with the data to work with. Also, the kind support of Canadian Stratigraphic Services Ltd (CanStrat) and Anne Hargreaves for the data donations. I will not forget the support of the Offshore Energy Research Association (OERA) for their kindness in supporting my graduate studies. Thanks to Trudy Lewis, Chloe Younger, Dr. Kettanah, and Kristie Mcvicar for the help through the years.

Importantly, I would like to acknowledge members of my committee including Bill Richards (you have been a great coaching me on how to use the Schlumberger Petrel™ software throughout this work), Owen Sherwood for your insightful contribution on improving my research, and the continual support of Mr. Neil (who was the wellsite geologist that sat the Migrant N-20 well), and his wife Elen Watson. The team at the CNSOPB Geo Science Research Centre including Mr. Mike, Les Eliuk, Debra Wheeler, the late Mary Jean Verrall (may you rest in peace), Mr. Dave Brown (recently retired) and the rest of the staff. Many thanks to Carl Makrides and Shaun Rhino of the Canada Nova Scotia Offshore Petroleum Board (CNSOPB) for supporting me in this project. It has been a privilege to contribute to research on the Sable Subbasin facilitated by their support.

I also thank Dr. Ricardo Silva and Darragh O'Connor for offering their technical views on writing the thesis as well as Mladen and Isabel at the beginning. How can I forget Mike Young and members of the administrative and technical staff of the Earth and Environmental Science Department including Norma Keeping, Darlene Van de Rijt, John Thibodeau, and Shaun Hartwell. Also, I acknowledge colleagues in the Department of Earth Science Anna, Masoud, Bryan, Harold, Gonzalo and those at the Basin and Reservoir Lab including Carla, Taylor, Carlos, Trevor, Charlie, Max, Ryan, Lauren, Emma, Kallen, Natasha, Lauren, Cambria and more to mention. You guys were awesome to be around and thank you so much for your help and support. I would also like to acknowledge some of my friends that started the academic journey here in Canada including Yako, Frances, Lisa, Frank, and Alpha. Thank you for the great memories. During this pandemic, I could not forget the communicative support from friends from AFCS Enugu and Halifax friends including YT, Tony, Josh, Samir, Mo, Matt, Aaron, Joe, Kathleen, and especially Kyanna. Special thanks to Mitch Grace and Colin Price. Also, thanks to my property managers Peter, Connie, and Debbie.

# CHAPTER 1

## INTRODUCTION

### 1.1. Project Overview

Rollover anticlines are syn-depositional structures that develop in the downthrown side (hangingwall) of deltaic growth faults (listric normal) in sedimentary basins (Vendeville, 1991; Cummings & Arnott, 2005; Adam et al., 2006). Their formation is attributed to the interaction between gravity-driven extension, syn-sedimentary deposition, and the movement of a mobile substrate (Vendeville, 1991). These structures may contain stacked sedimentary units with porous rock (reservoir) and an impermeable rock (seal) capable of containing hydrocarbons (Vendeville, 1991; Adam et al., 2006). Globally, they are targets in hydrocarbon basins such as the Nile Delta (Sestini, 1989; Beach & Trayner, 1991), Amazon Delta (Cobbold & Szatmari, 1991), Gulf of Mexico (Diegel et al., 1995), Niger Delta (Doust & Omatsola, 1989; Wach et al., 1998a, 1998b, 1998c) and the ancient Sable Delta (Cummings & Arnott, 2005).

On the Scotian Shelf, most of the wells drilled to date occur in the Sable Subbasin (OERA, 2011; Figure 1.1). Among the tested play types, growth fault-controlled rollover anticlines account for most of the significant and commercial hydrocarbon discoveries made to date of which about 74% occurs mainly in Cretaceous sands (OERA, 2011). Other discoveries are related to salt diapirs, carbonate banks, and drape structures (Figure 1.2).

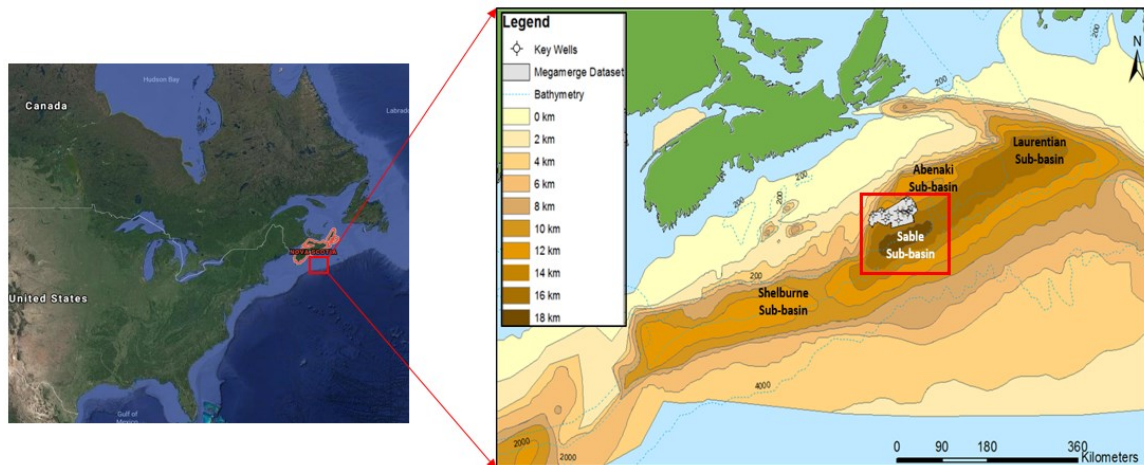


*Figure 1.1: A location map of the Sable Subbasin, offshore Nova Scotia. The sediment thickness map on the right (after Wade, 2000) including labels of the subbasins and the area of the Sable MegaMerge 3D seismic volume is contained in the area within the red box.*

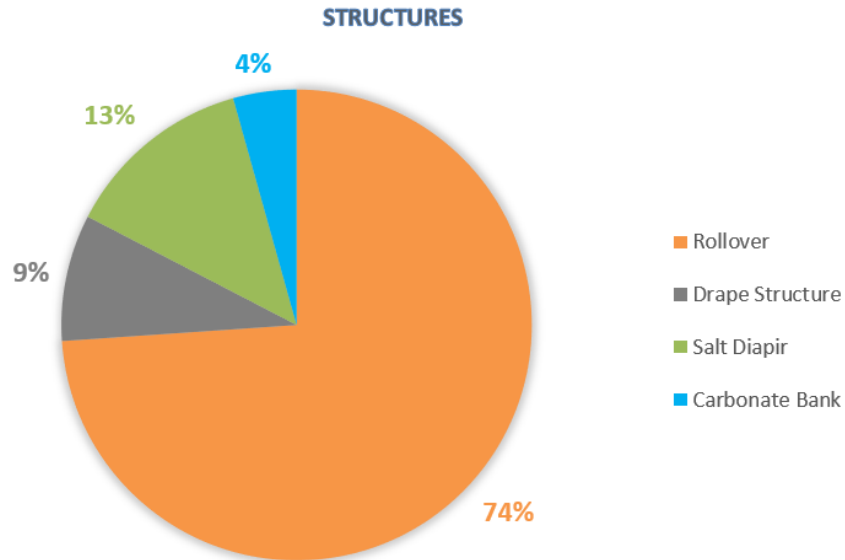


*Figure 1.2: A pie chart showing the different play types tested by drilling offshore Nova Scotia. Note that rollover plays appear to be the most successful of the tested play types (OETR, 2011).*

Hydrocarbon drilling results from around the world highlight trap and seal failure as the reason most exploration wells fail to encounter producible hydrocarbons (Almon & Dawson, 2004; Dawson & Almon, 2002 and 2006; Rudolph & Goulding, 2017). An investigation of wells on the Scotian Shelf was found to contain no commercial amounts of hydrocarbons. Furthermore, published data by the CNSOPB reported “no fault-seal” as the primary cause of failure for most wells targeting rollover structures offshore Nova Scotia (CNSOPB, 2013). In rollover structures, the sealing potential of a fault depends on the relationship between the amount of displacement on the fault, and the thickness of the reservoir overlain by an impermeable lithology (a seal) overlying each reservoir (Allan, 1989; James et al., 2004; Richards et al., 2008, 2010). The juxtaposition of porous and permeable lithologies containing hydrocarbon fluids on one side of a fault with porous and permeable lithologies on the other side of the fault may lead to cross-fault leakage of hydrocarbons.

## 1.2. Problem

The acquisition of high-resolution 3D seismic data between 1996 and 2006 has had little effect on the exploration success along the margin. This has encouraged the need to understand the relative distribution of good quality reservoirs and competent seals as key for future exploration. Positioned west of Sable Island, the Migrant Structure (Figure 1.3)



is a low relief rollover anticline drilled by Mobil in 1977 to test for hydrocarbons trapped in Upper Jurassic Mic Mac Formation sandstone reservoirs. Drill stem test results from the Migrant N-20 well indicated that it encountered a reservoir that contained free hydrocarbons (gas) that flowed to the surface (CNSOPB, 2009).

Despite its proximal position to the downdip Thebaud gas field (a commercial discovery), the hydrocarbons discovered in the Migrant Structure were deemed to be non-commercial by the operator (SOEP) with drill stem test (DST) results indicating limited hydrocarbon volumes in the reservoir. Mapping the closure was aided by the presence of check shot data (well velocity data), to discern velocity variations resulting from differences in sedimentary thickness on either side of a fault (Bain, 2015). Such velocity variations may affect the the interpretations of closure extent in true vertical depth (TVD).

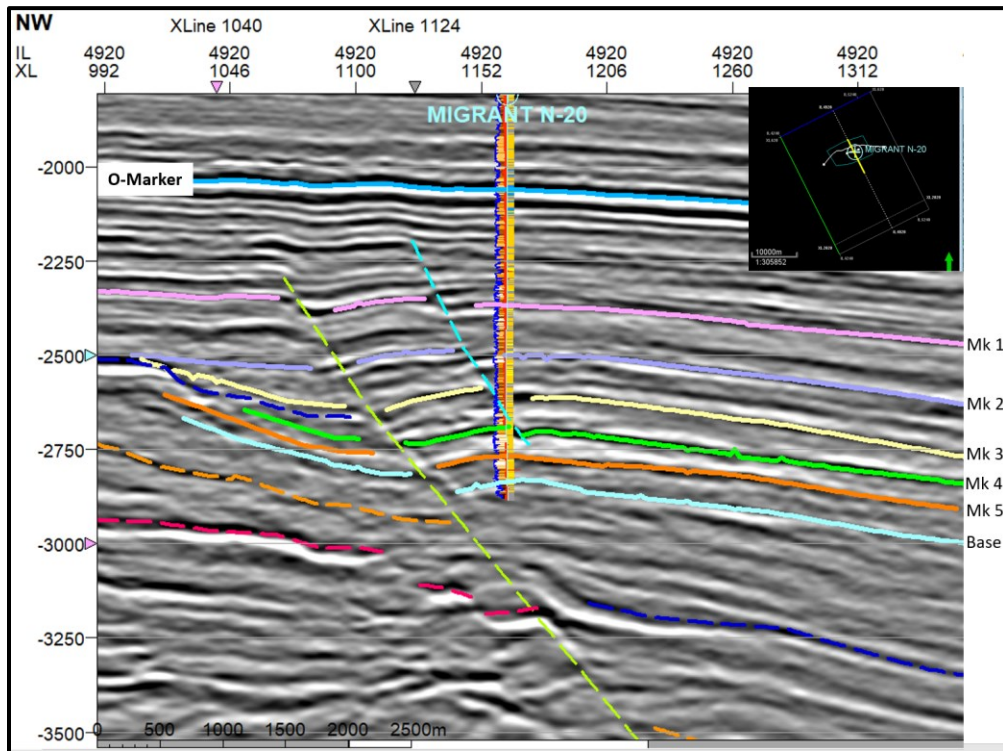


Figure 1.3: A seismic section of the Migrant Structure and N-20 well penetration shows evidence of extensional-related crestal faulting represented by the light blue line. The main listric fault (light green dashed lines) extends below the structure (in the full view). The crestal fault terminates with depth. An average constant velocity of 2900 m/s derived from checkshot survey was used for depth conversion of the seismic time interpretations.

The Migrant N-20 exploration well (Figure 1.3) reached a total depth of 4669 m in the Mic Mac Formation (Tetco, 1978). Eight drill stem tests (DSTs) were attempted in

three upper Mic Mac Formation sands (Table 1.1). The preliminary well history report concluded that the cause of depletion in pressure was either insufficient structural closure in the zone or the presence of a geologic boundary such as a fault near the wellbore (Tetco, 1978). The two other Mic Mac Formation sands that were tested also appeared to be gas-bearing on petrophysical logs but did not flow gas at measurable flow rates possibly due to low calculated effective porosities of ~7% and possibly inadequate “permeability thickness” in the test interval (CNSOPB, 2009). From wireline log analysis, the fluvio-deltaic succession is represented by numerous blocky and fining up sands on well logs (Chapter 4). Hence, with the fault influence, the concept of stair-stepping of hydrocarbons laterally between reservoirs will be tested (as outlined in Section 1.5). The high net-to-gross (NTG) of the Missisauga Formation section higher up the Migrant Structure suggests that hydrocarbon leakage likely occurred around the crest of the structure from syndepositional faulting of the shallow sediments (Smith, 1980; Downey, 1994; Richards et al., 2008, 2010).

*Table 1.1: The Migrant N-20 well DST test intervals (Tetco, 1978).*

<b>Test Type</b>	<b>Top</b>	<b>Bottom</b>	<b>Units</b>	<b>Notes</b>	<b>Formation Tested</b>
DST #1	4333.09	4361.74	M	Misrun	Mic Mac Fm.
DST #2	4333.09	4361.74	M	Flowed gas	Mic Mac Fm.
DST #3	4270.3	4273.35	M	Misrun	Mic Mac Fm.
DST #4	4270.3	4273.35	M	Misrun	Mic Mac Fm.
DST #5	4270.3	4273.35	M	No recovery	Mic Mac Fm.
DST #6	4205.7	4213	M	Misrun	Mic Mac Fm.
DST #7	4205.7	4213	M	Misrun	Mic Mac Fm.
DST #8	4205.7	4213	M	No recovery	Mic Mac Fm.

### 1.3. Study Area

The study area comprises the Migrant-Adamant-Thebaud expansion trends associated with large-scale listric growth-faulting on the Scotian Margin. The sedimentary succession can be tied and correlated to the 3D Sable MegaMerge seismic survey at the Migrant, Adamant and Thebaud wells and correlated between the fault blocks (Figure 1.4; Figure 1.5). The absence of core data in the Migrant N-20 well, and limited sidewall cores in the Adamant N-97 well core data from wells that penetrate similar-aged fluvio-deltaic

sediments in the down dip Thebaud rollover were studied (Figure 1.4; Figure 1.5). Variations in depositional energy and facies distribution between the Migrant Structure and the distal Thebaud Structure ~15 km apart may introduce some uncertainties where core data have been supplemented in the Migrant area.

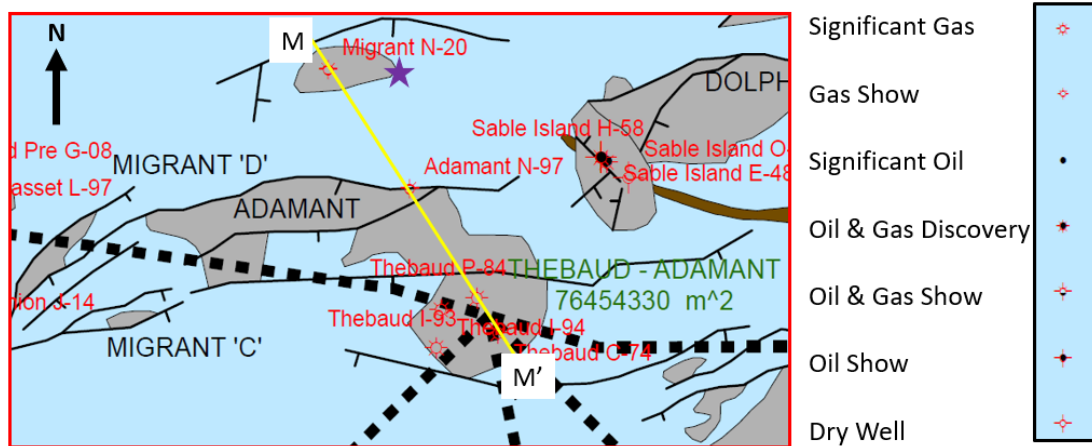


Figure 1.4: A structural map of growth fault networks and associated rollover structures with well penetrations around Sable Island (Wach and Hirschmiller, 2012). The Migrant Structure is represented by the purple star. The black dashed lines are pipelines connecting other producing fields to the commercial gas field in the Thebaud Structure. The yellow line from M and M' represents the cross-section (Figure 1.5) with the Adamant penetration in the center of the line.

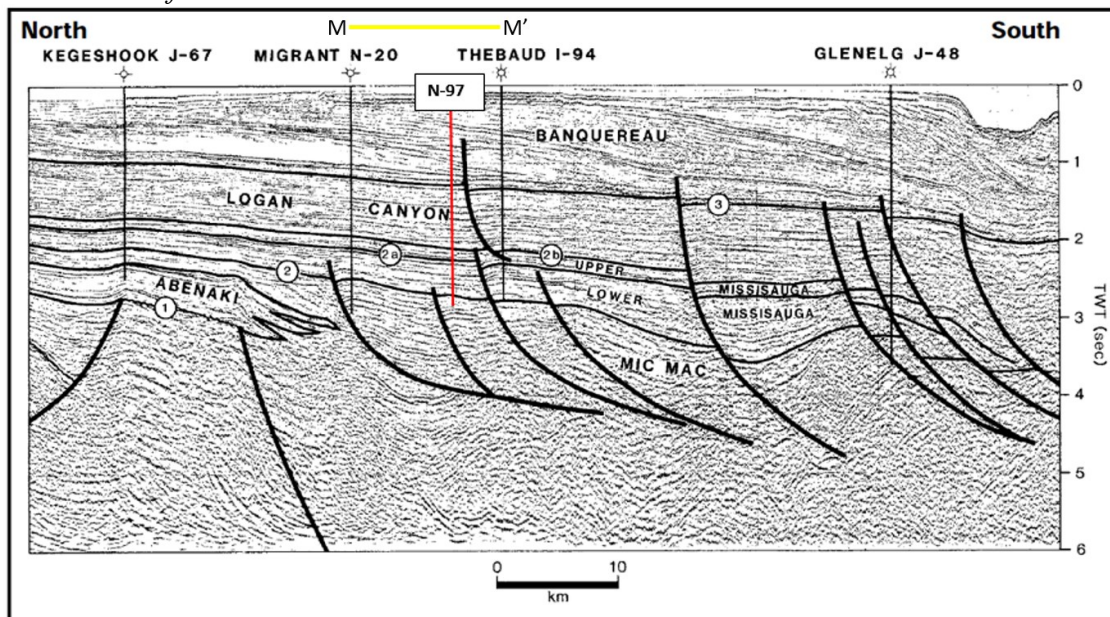


Figure 1.5: A seismic stratigraphic section showing growth faults in the Sable Subbasin including the Migrant, Adamant, and Thebaud rollover anticlines (SOEP, 1997). The wells penetrating the structures are indicated on the section with the Adamant N-97 well indicated in red. Notice the curvature of the main listric faults (dense black lines) as they sole-out in the deeper sections.

#### 1.4. Project Objectives

- (a) Establish a **consistent stratigraphic template** between the newer Thebaud T5 E-74 and Adamant N-97 wells with the older Thebaud I-93 and Migrant N-20 wells showing the succession of key zones from the proximal to distal positions. The stratigraphic work done in newer and older wells are revised in this study to produce a template that integrates work done in both the older and newer wells.
- (b) Evaluate the change in the **pressure-depth** relationship between reservoir intervals. This will aid in confirming if there is a stratigraphic control on the overpressure from Migrant through the Thebaud structures.
- (c) Determine **porosity, permeability, and fluid saturation** distribution within reservoir intervals.
- (d) Use an **average velocity** to generate time structure, and **depth maps** from the 3D seismic data, which offers improved resolution from which the crestal fault previously missed in 2D data has been identified.
- (e) Assess hydrocarbon **trapping** through **fault-seal analysis** at Migrant. The presence of sand traps indicated by the bright amplitudes on the hanging wall of the structure are an added benefit to using the much-improved 3D seismic.

#### 1.5. Hypotheses

At Migrant four hypotheses were considered to explain only minor hydrocarbons in stacked four-way dip-closed reservoirs. The first two hypotheses were explored with the latter two hypotheses investigated further in this study.

**Top seal failure at Migrant:** Mechanical and capillary breaching of seals occurs due high pressure and may explain why the Migrant structure failed. However, pressure elevation plot of the Migrant N-20 well shows that only the bottom reservoir at Migrant is overpressured with most of the reservoirs above the overpressured reservoir being hydrostatically pressured. The hydropressured reservoirs occur within the section influenced by the crestal fault.

**Fluid migration shadow at Migrant:** The location of Migrant in a fluid migration shadow was thought to be a potential source of failure. However, a daily gas flow rate of 10 MMscf /day in one reservoir interval with pressure depletion suggests that there was hydrocarbon

accumulation. This allowed for much of the research efforts to be concentrated on the more probable hypotheses.

**Depth conversion issue:** Uncertainties with the conversion from time to depth. In cross section view, Migrant looks like a 2-way dip closure (as seen on seismic) and 4-way dip closure when mapped in 2-way time. Structure may not be enclosed as it appears. Though it looks enclosed in time it may not be in depth (**Will be investigated**).

**Possible cross fault leaks:** If shale units are thinner than the fault offset, the sand beneath the shale may be juxtaposed with another sand interval above the shale on the other side of the fault. This will allow hydrocarbons to migrate between sands of different ages across the fault upwards and outwards resulting to a stair stepping of hydrocarbons stratigraphically up structure until a level above closure. **This will be tested through 3D seismic mapping and Allen diagrams.**

## 1.6. Thesis Outline

The thesis is made up of seven chapters and supporting appendices.

Chapter 1: INTRODUCTION This chapter introduces the project, including the background statement of the location of the study area, hypothesis, project objectives, and thesis outline.

Chapter 2: BACKGROUND This chapter presents the regional geology, petroleum systems elements, and past exploration of the Scotian Basin.

Chapter 3: STRATIGRAPHIC WELL CORRELATION AND SEDIMENTARY CORE ANALYSIS OF THE MIGRANT EXPANSION TREND This chapter presents the well correlation and pressure data analysis for the four project wells. The results from the pressure data analyses are presented in this chapter.

Chapter 4: PETROPHYSICAL WELL LOG AND PRESSURE ANALYSIS OF THE MIGRANT EXPANSION TREND In this chapter, the results from petrophysical analyses in the project are presented.

Chapter 5: 3D SEISMIC INTERPRETATION AND FAULT SEAL ANALYSIS OF THE MIGRANT STRUCTURE This chapter presents the seismic datasets and fault-seal analysis at Migrant.



Chapter 6: DISCUSSION This chapter includes discussions on the structural and depositional patterns observed across the expansion trends. It also addresses fluid and pressure distribution within the Migrant, Adamant and Thebaud structures as well as strata correlation and the role of crestal faulting on trap integrity and gas migration in rollover structures.

Chapter 7: CONCLUSIONS AND RECOMMENDATIONS This chapter comprises the conclusion, applications of this study, and recommendations.

### 1.7. Project Workflow

Figure 1.6 outlines the workflow used in this study. Schlumberger Petrel™ software (donated to the Dalhousie Basin and Reservoir Lab; Professor Grant Wach P.I) was used for most of the work in this project including log correlations, petrophysical analysis, geocellular modelling, and time to depth conversion.

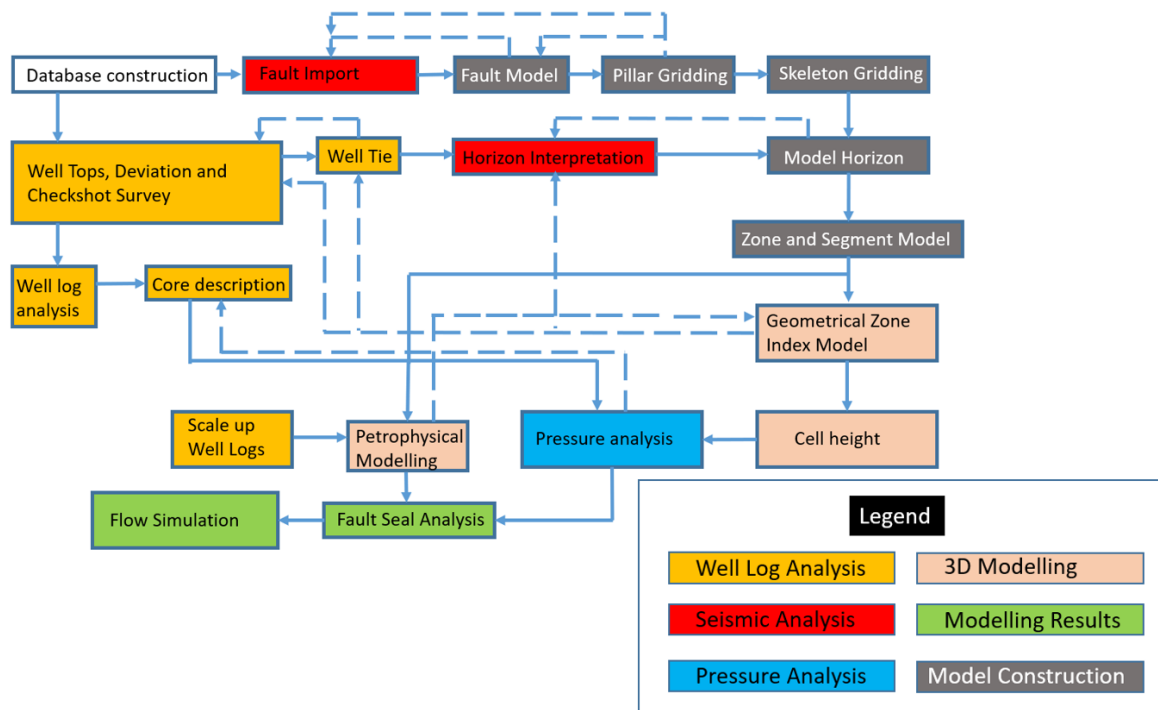


Figure 1.6: Complete workflow used in this project. The workflow integrates the well data (including core, pressure, and well log analysis) and seismic data (used for seismic analysis and 3D modelling). The yellow boxes indicate the aspects of the well data used. Blue relates to pressure data used in the study. The red boxes indicate the seismic data before being transferred over to the model building (grey boxes) and finally used in modelling (brown boxes). The solid lines indicate the parts of the workflow that were required before the next steps, whereas the broken lines represent those used iteratively between steps (not strongly required for the next step).

## CHAPTER 2

### BACKGROUND

#### 2.1. Regional Structural Setting

Offshore Nova Scotia, the Scotian Basin extends from the Yarmouth Arch in the Southwest to the Grand Banks in the Northeast, covering an area of  $\sim 400,000 \text{ km}^2$  (Wade & MacLean, 1990; Hansen et al., 2004; Kidston et al., 2005; Figure 2.1). The basin evolution begins with continental extension and rifting as well as the opening of the North Atlantic Ocean from the break-up of Pangea that began in the Early Mesozoic ( $\sim 200 \text{ Ma}$ ). Episodes of rifting between the African and North American plates resulted in the formation of the Atlantic Ocean (Schlische, 1993; Withjack, Schlische, & Olsen, 1998).

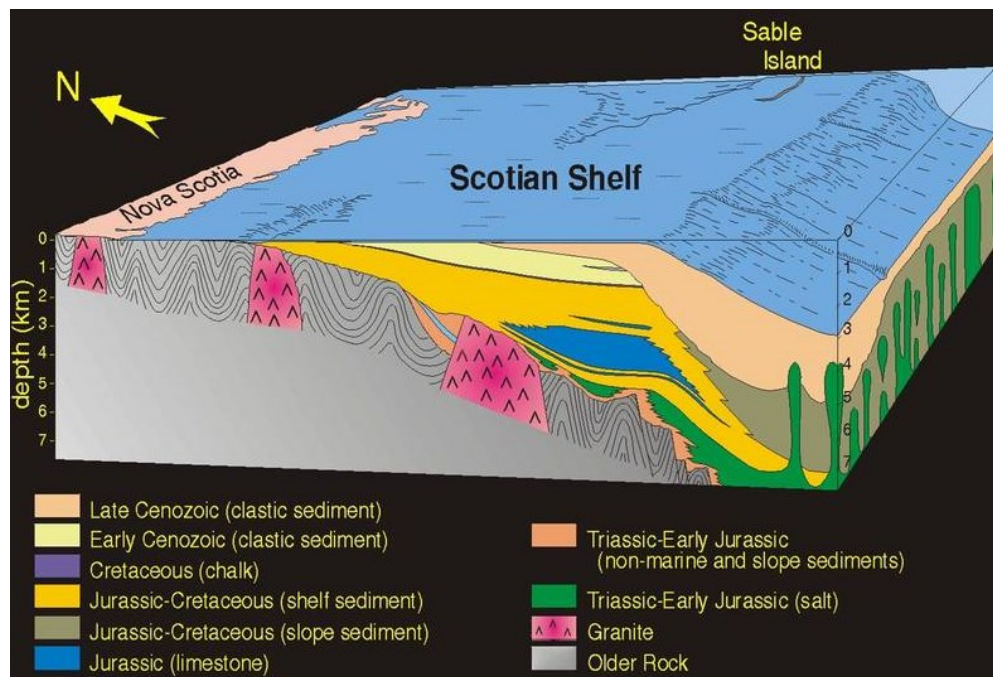


Figure 2.1: A block diagram showing the Geology of the Scotian Shelf from Williams et al., (1997), and later modified by CNSOPB (2009).

According to Welsink et al., (1989), extension began in the Late Triassic and terminated in the Early Jurassic, producing NE-SW oriented horst and graben systems on the Scotian Margin. These controlled the formation of the Mesozoic Subbasins and the deposition of sediments. The Sable Subbasin is a portion of the Scotian Basin that formed from extensional-related tectonism (Williams et al., 1998; Figure 1.1). The basin represents a significant sediment trap on the passive Scotian Margin, which comprises the continental shelf and slope, accumulating up to 16 km of Mesozoic-Cenozoic sediments (Wade et al.,

2000). With a sedimentary sequence commenced by Triassic evaporites (i.e. salt) and Mesozoic-Cenozoic siliciclastic (Weston et al., 2012) sit on structural basement comprising complex Cambro-Ordovician meta-sediments and Devonian granites.

## 2.2. Stratigraphy of the Sable Subbasin

Following the formation of the NE-SW trending grabens and half grabens from rifting in the Mesozoic, the Early-Middle Triassic is characterized by an arid-semiarid dominated climate. These conditions led to the deposition of continental red beds and thick salt layers (Figure 2.2).

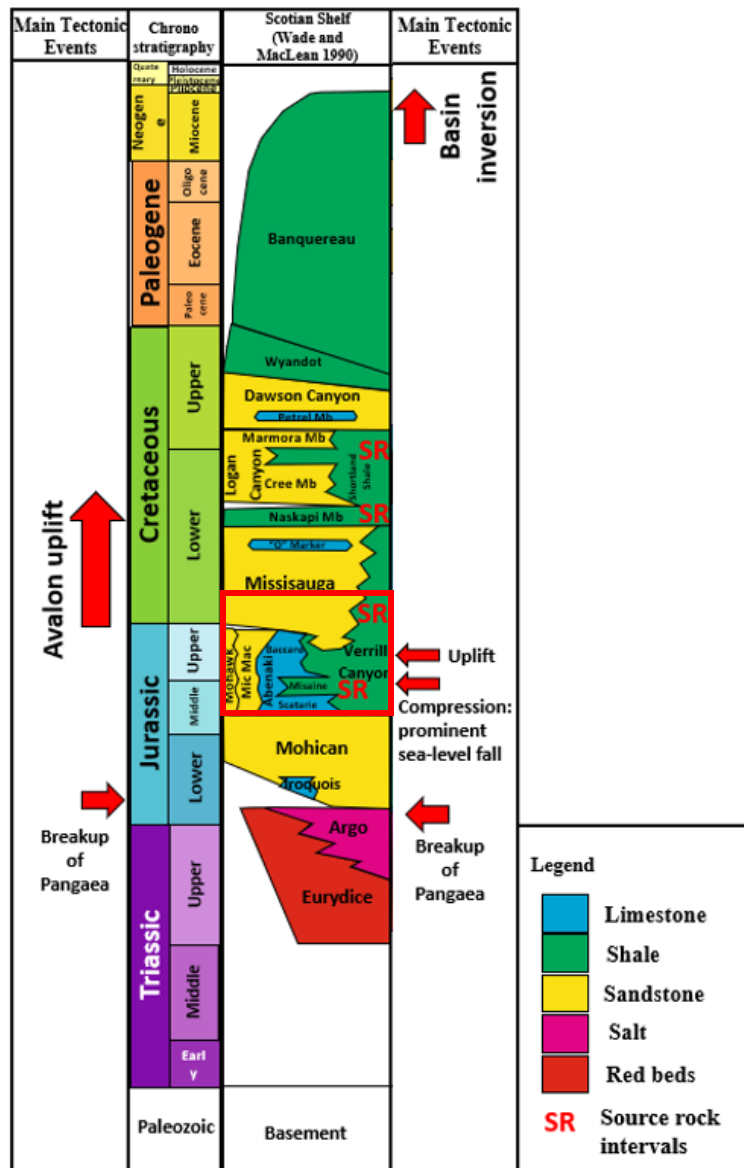


Figure 2.2: A stratigraphic chart of the Scotian Basin by Campbell (2018). The red box in the middle of the chart shows the target Lower Missisauga and Mic Mac formations.



The deposition of these sediments represented by the Eurydice and Argo formations occurred during early rifting (Weston et al., 2012) as shown in Figure 2.3. Most of the Argo Salt accumulated in the earliest post-rift in the Early Jurassic (Ings & Shimeld, 2006; Deptuck et al., 2014; Deptuck & Kendell, 2017).

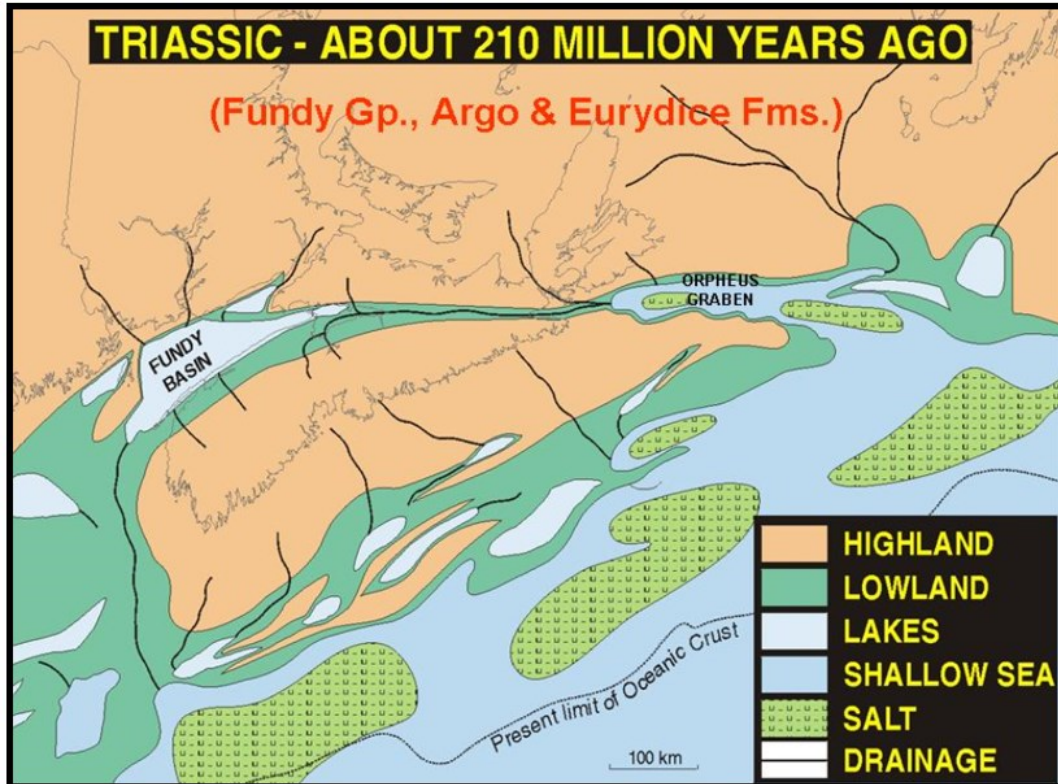


Figure 2.3: A paleogeographic map of the Scotian Basin showing the early lakes and shallow seas with associated salt deposited during the Late Triassic (CNSOPB 2012).

After Late Triassic-Early Jurassic time, widening of the basin and expansion of the Atlantic seaway began in the Middle Jurassic with marine incursion (O'Connor et al., 2018). This led to the deposition of the Iroquois Formation dolomites (Figure 2.4). The dolomite passes laterally westward into post-rift fluvial clastic sediments of the Mohican Formation, which is thickest on the northwest and southeastern parts of the margin (Steele et al., 2011). With increased sea level and regional subsidence, the Abenaki Formation, a platform carbonate with three members (Scatarie, Misane, and Baccaro) was deposited (Kidston et al., 2005). Marine conditions with widespread carbonate banks developed on the western edge of the margin with a mixed clastic-carbonate system developing along the eastern part of the margin comprising the Scatarie Member in the Middle Jurassic (Campbell, 2018).

A rapid change in slope gave way to a deepwater environment seaward of the carbonate platform, characterized by the deposition of marine shales including the Lower Verrill Canyon Formations (Figure 2.4). The landward equivalent comprises calcareous sands, shales, and carbonate muds of the Mic Mac Formation, as well as the terrigenous Missisauga Formation (Jansa & Wade, 1975; SOEP, 1997). The Late Jurassic-Early Cretaceous period saw an increase in the deposition of clastic sediments generated by largescale continental drainage systems that resulted in the formation of the Sable Delta complex (Figure 2.4). The vast clastic influx is thought to have been tectonically influenced (Jansa et al., 1975).

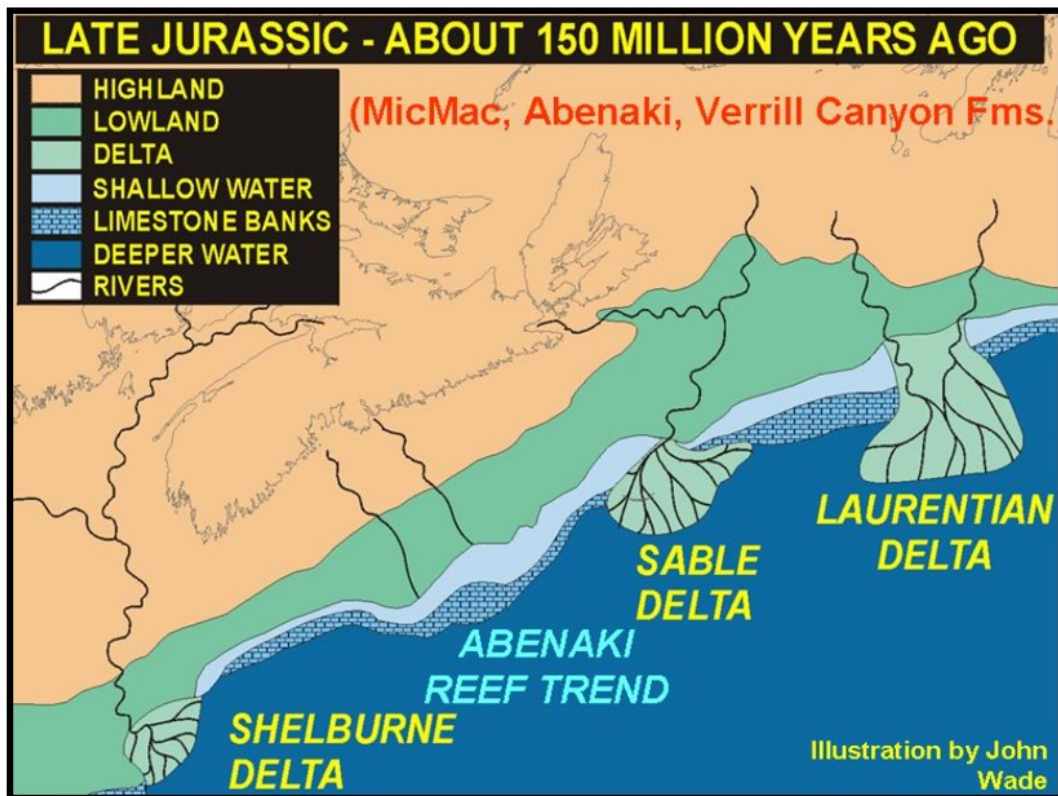


Figure 2.4: A Late Jurassic paleogeographic illustration of the Scotian Basin depicting the Abenaki carbonate platform and the advancing deltaic clastics of the Mic Mac Formation that inundated the carbonate system (CNSOPB 2012).

Continued progradation of the Sable Delta was accompanied by the deposition of delta front and delta plain clastics of the Missisauga Formation in the center of the delta, which transitions to a basal prodeltaic equivalent, the Verrill Canyon shales (Wade & MacLean, 1990). Alternating sandstone, and shale successions from progradation and retrogradation of deltaic succession in the Early Cretaceous produced reservoir seal pairs.

These grade laterally into the shaley basal member of the Logan Canyon Formation, defined only on the shelf and transitions to the Shortland Shale at the shelf margin.

This study focuses on deltaic complex of the Mic Mac and Lower Missisauga formations indicated by the red arrow in Figure 2.5 below. The Oxfordian-Tithonian aged Mic Mac Formation records the earliest phase of delta progradation into the Sable Subbasin. The formation comprises cyclic interfingering of distributary channels and delta front fluvial sands, with prodeltaic and shelf marine shales of the Verrill Canyon Formation (Weston et al., 2012; Campbell, 2018; Figure 2.5). The Tithonian-Aptian aged Missisauga Formation comprises fluvial to slope siliciclastics interval that forms a seaward-thickening then thinning wedge in the Sable Subbasin (Weston et al., 2012). The formation reaches an estimated maximum thickness of ~3.5 km below the modern shelf edge (Wade & MacLean, 1990). In the central parts of the Sable Subbasin, the formation overlies the mudstone and carbonate-rich Mic Mac Formation and is overlain by mudstones of the Naskapi Member of the Logan Canyon Formation (Figure 2.5). The Missisauga Formation is further divided into three members, with the lower member downlapping Jurassic carbonates of the Abenaki Formation in the western edge of the Sable Subbasin (MacLean & Wade, 1993).

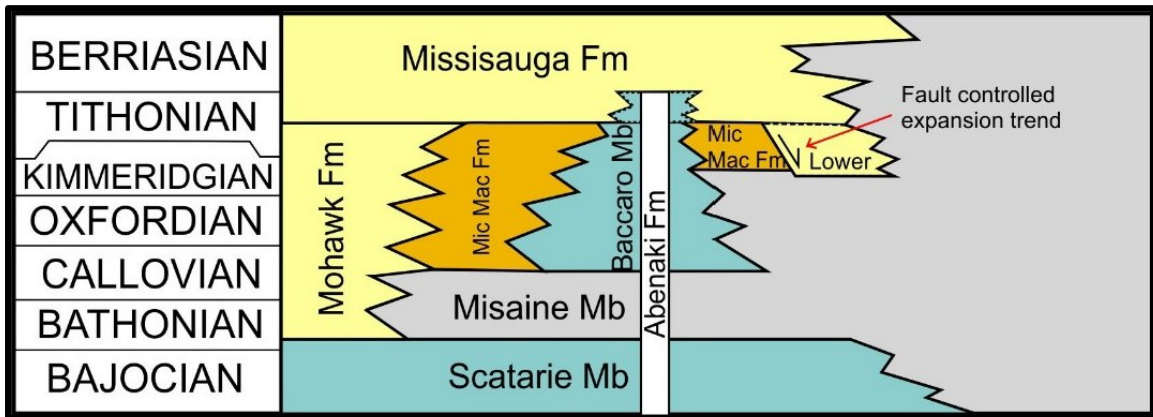


Figure 2.5: Recent and previous stratigraphic columns of the zones of interest comprising the Migrant expansion trend revised by Campbell (2018). The chart focuses mainly on the Mic Mac and Lower Missisauga formations. In the revised stratigraphic chart created by Campbell (2018) represented in C, the siliciclastics appear to be interfingering with carbonates, which are juxtaposed against siliciclastics of the Missisauga Formation by faulting. The siliciclastics are thought to be from the Mic Mac Formation.

### 2.3. Petroleum Systems in the Sable Subbasin

The onset of rifting and the opening of the Atlantic during the Late Triassic-Early Jurassic was accompanied by the deposition of salts of the Argo Formation in a dominantly arid to the semi-arid environment (Jansa et al., 1975; Wade & MacLean, 1990; Kendell, 2012; O'Connor et al., 2018). The evolving rift architecture impacted the thickness and distribution of these salts, which influenced the overlying strata with the development of post-rift structure in Middle Jurassic to Early Cretaceous age sediments (Deptuck, 2011; Deptuck et al., 2014; Deptuck & Kendell, 2017). As extension occurred, variable rates of sediment loading and salt withdrawal aided the evolution of seaward dipping growth faults with associated rollover formation (Cummings & Arnott, 2005; Adam et al., 2006; Deptuck et al., 2014).

Increased sedimentation with corresponding near-horizontal movement along these listric faults in contact with the underlying decollement surface (usually a shale or salt) results in the juxtaposition of strata of different ages at the fault plane as the hangingwall fault block rotates downwards (Oomkens, 1970; Vendeville, 1991; Porębski & Steel, 2003). Localized extension occurs on top of the rollover anticline in response to the downward bending and results in faulting (synthetic or antithetic) across the crest of the structure (i.e. crestal faulting). Crestal faults have been identified in rollover anticlines in the Sable Subbasin (e.g. Migrant) and are thought to pose a potential risk to hydrocarbon trap integrity in these structures (Richards et al., 2008, 2010).

### 2.4. Exploration History of the Scotian Basin (Modified after CNSOPB 2018)

Since the award of the first license near Sable Island in 1959, a reported total discoverable resource estimate of 6.5 TCF /381 MMBOE (Million Barrels of Oil Equivalent) (P50) has been reported from drilling 210 wells to date on the Scotian Shelf (CNSOPB, 2019). Figure 2.6 shows the gas-in-place estimate for significant discoveries in rollover anticlines with those that became commercial fields in the Scotia Basin, offshore Nova Scotia.

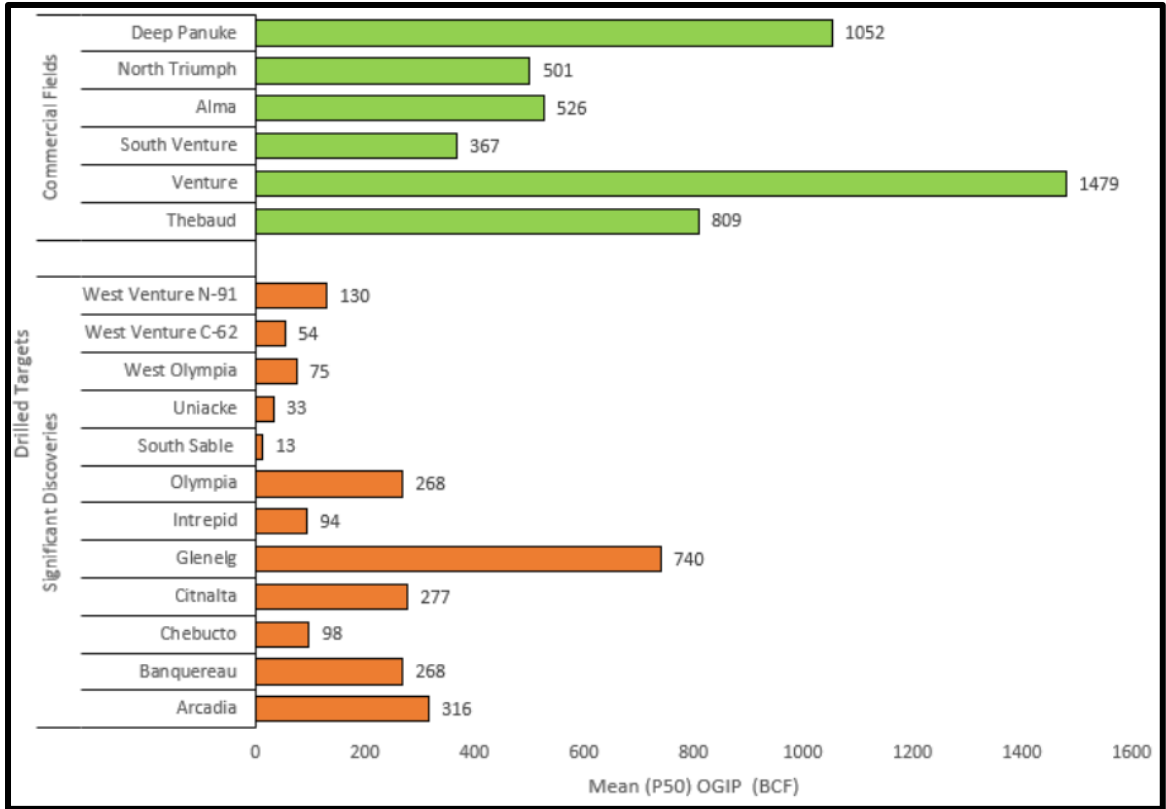


Figure 2.6: A chart showing the significant rollover discoveries (brown) with those that became commercial fields (green) in the Scotia Basin, offshore Nova Scotia (SOEP, 1997). The net present value (NPV) will vary with reserve size (Rose, 1992).

Figure 2.7 demonstrates most of the wells offshore drilled before 1986 (OETR, 2011). Since 2005, seven wells comprising one injector well, three gas development wells, and three exploration wells have been drilled (CNSOPB, 2018). Two of the exploration wells drilled as part of the Shelburne Basin Venture Exploration Drilling Project operated by Shell Canada Ltd. (Cheshire L-97 and Monterey Jack E-43) show a plugged and abandoned status (CNSOPB, 2018). After the third exploration well (Aspy D-11) drilled by BP Canada, and devoid of commercial hydrocarbons (CBC, 2018), no exploratory drilling projects offshore Nova Scotia have been done.



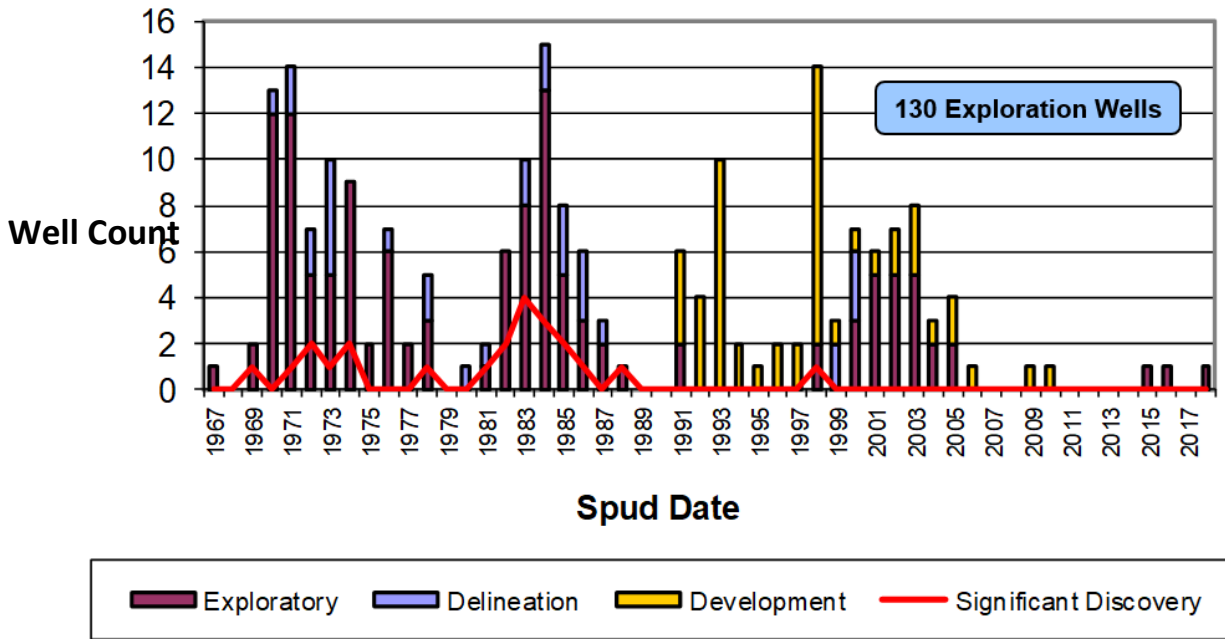


Figure 2.7: A bar graph of all wells drilled offshore Nova Scotia to date. An underlying curve distinguishes the exploration periods and degree of success in the Scotian Basin (CNSOPB, 2019).

Before the year 2000, a 1:5 exploration success rate on the Scotian Margin was achieved using relatively poor quality 2D seismic data (Figure 2.8). Following the successes with analogous salt plays in the Gulf of Mexico, the first exploration cycle in offshore Nova Scotia resulted in three significant discoveries made from 28 wells targeting salt plays including Onondaga E-84, Primrose A-41, and on the western end of Sable Island at Sable 1H-58 (CNSOPB, 2007). During this exploration cycle, the first hydrocarbon discovery in rollover anticlines was made by Mobil (now ExxonMobil) in 1972 when the Thebaud P-84 well found gas in the Missisauga and Mic Mac formations. The following year, the Mobil team discovered light oil in structures draped subtly over Jurassic age Abenaki Formation carbonates when the Cohasset D-42 well tested the new play type (CNSOPB, 2007). Additional significant gas discoveries made in Mic Mac and Missisauga formation sediments in rollover anticlines at Citnalta and Intrepid marked the end of an 11-year exploration cycle that began in 1967 and included the unsuccessful Migrant N-20 well drilled in 1977.

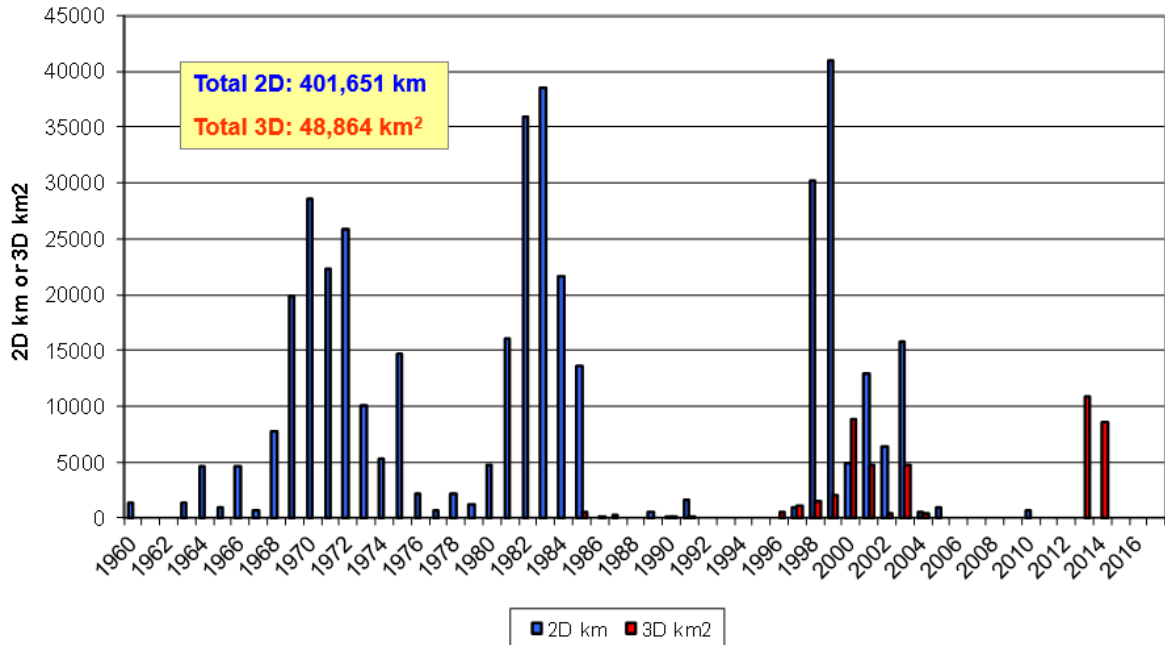


Figure 2.8: A bar graph of the associated seismic data (2D or 3D) with which the various exploration cycles have been based off (CNSOPB, 2019). Earlier exploration successes were based on 2D seismic data. The acquisition of 3D seismic data between 2000 and 2006 has had little effect on the recent exploration efforts along the margin.

The second exploration cycle spanned 10 years from 1979 to 1989. The cycle was initiated by the major gas discovery in the Venture field rollover anticline targeted by the Venture D-23 well operated east of Sable Island by Mobil and Petro-Canada. Currently, this remains the most successful exploration cycle with 15 significant discoveries made from 54 wells drilled. The third exploration cycle saw shared exploration focus in both the shelf and deep-water regions (CNSOPB, 2007). With improved seismic quality associated with 3D data, this would contribute to meaningful interpretation of siliciclastic and carbonate prospects offshore. However, the acquisition of large 2D and 3D seismic volumes during the third exploration cycle has had minimal influence on the success rate to date with exploration of rollover anticlines notably the Adamant structure and Cree structure resulting to non-commercial gas discoveries.

To date, 23 significant discovery licenses have been awarded, eight of which were declared as commercial discoveries (two oil fields & six gas fields) by the Canada Nova Scotia Offshore Petroleum Board CNSOPB (Smith et al., 2014; Figure 2.9). According to part II, section 49 of the Canada-Nova Scotia Offshore Petroleum Resource Accord

Implementation Act (July 21, 1988), “a significant discovery is defined by the first well on a geologic feature that demonstrates the existence of hydrocarbon in the feature by flow testing and suggests the existence of an accumulation of hydrocarbons that has potential for sustained production”. Further, the resource act defines a commercial discovery as “a significant discovery that has been demonstrated to contain quantities of petroleum that justifies the investment of capital and effort to bring into production (Lee, 2009; Smith et al., 2014). This study will help to evaluate the risks associated with drilling on the Scotian Margin.

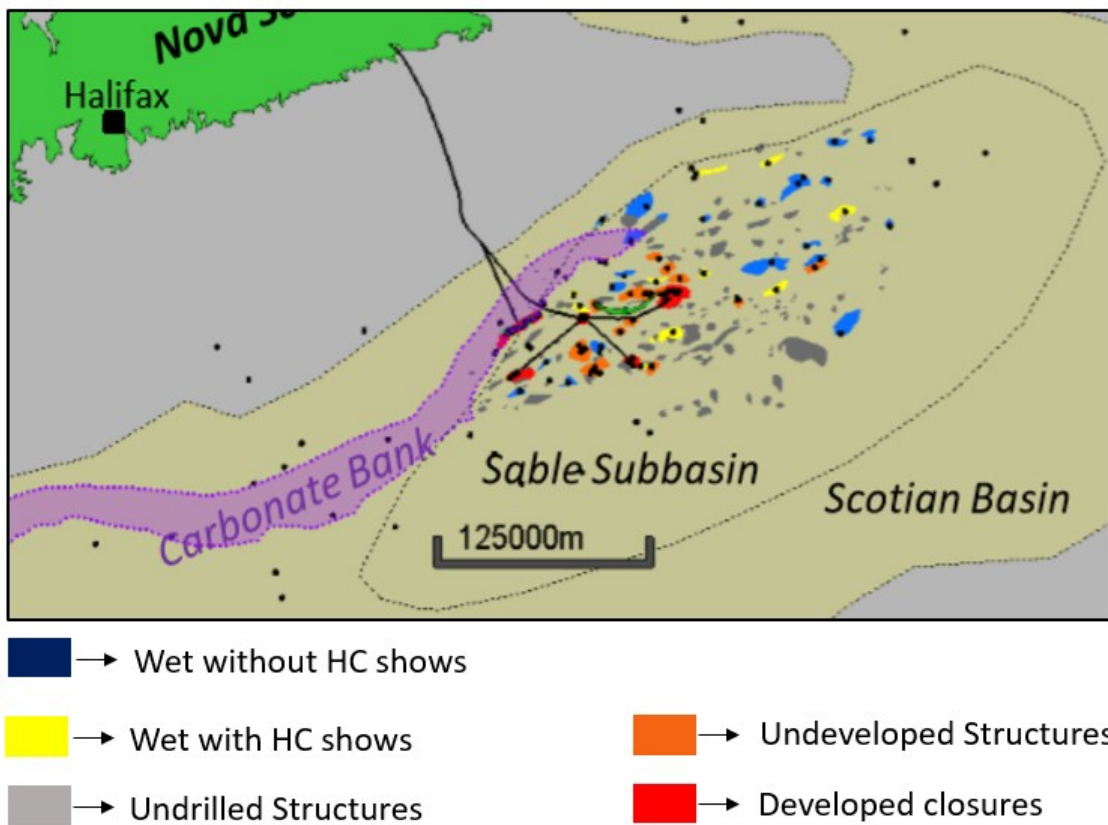


Figure 2.9: A map of the offshore sedimentary basin with the fields, closures, wells, and pipelines linking various hydrocarbon structures from the Sable Subbasin (Modified by O'Connor et al. (2018) after Williams & Keen, 1990; and NSPD, 1999). The extensive Abenaki carbonate platform is represented by purple and Sable Island in green.



## CHAPTER 3

### STRATIGRAPHIC WELL CORRELATION AND SEDIMENTARY CORE ANALYSIS OF THE MIGRANT EXPANSION TREND

#### 3.1. Introduction

Well correlation of the four project wells in this study comprises new contributions in this study. This was accomplished by synthesizing the work done by previous worker and integrating them into our current contributions. Using formation tops downloaded from the Natural Resources Canada's online BASIN database, the various stratigraphic names used for the different wells in this study were reconciled in this chapter. Their stratigraphic well tops were imported into Petrel™ for correlation purposes. The newer wells have better well logs, and tops that are defined within a consistent chronostratigraphic scheme that is seismically consistent. Marine shales and carbonates are ideal for making key stratigraphic correlations due to their easily identifiable well log and seismic characteristics and widespread distribution as marine flooding surfaces.

The integration of Gamma-Ray logs and gamma normalized Vsh logs with Canstrat lithology logs was used to improve the well correlation. Where available, the sonic and density logs were used in combination with the Gamma-Ray logs in cases where it was difficult to distinguish between lithologies and their lateral extent during correlation. Also, with the overpressure marking the effective top for the trapping of hydrocarbons in the Thebaud Field, the absence of Gamma-Ray log in the Migrant N-20 well between depths of 4025 to 4099 m made it difficult to determine the presence of a significant shale unit.

As a result, the absence of core data at Migrant and the failure of sidewall cores from Adamant to capture the transitions between depositional sequences raised the need to look for core information from neighboring wells. In this study, rocks from core #1 of the Thebaud I-93 well seemed most similar in age to the sediments studied at Migrant. This core was described for this study with the sedimentological and geochemical characteristics used in matching results from the geochemical analysis of cuttings. The sedimentological, stratigraphic, and geochemical results were used to better understand the paleo-depositional environment key zones (including the DST intervals and missing section of the Gamma-Ray log). A consistent stratigraphic template of the newer Thebaud T5 E-74 and Adamant N-97 wells with the older Thebaud I-93 and Migrant N-20 wells showed the

succession of key zones from the proximal to distal positions as well as confirming if there is a stratigraphic control on the overpressure between the Migrant and Thebaud structures.

## 3.2. Data and Methods

### 3.2.1. Well Data

The well datasets used in this research comprising wireline logs, lithology logs, deviation and velocity surveys, and pressure data are courtesy of the Canada Nova Scotia Offshore Petroleum Board CNSOPB, Natural Resource Canada online BASIN Database, Divestco, and Canadian Stratigraphy (CanStrat). The four wells summarised in Table 3.1, were used in this study. The data from the wells were used for well correlation, petrophysical analysis, and integration with 3D seismic data. Of the four wells, one well (Thebaud I-93) was used for core description.

*Table 3.1: Well information of the four wells used in this study. This information was extracted from the BASIN database of Natural Resources Canada.*

<b>Well Name</b>	<b>Formations</b>	<b>GSC #</b>	<b>UWI Coordinates</b>	<b>Spud Date</b>	<b>Operator</b>	<b>TD (mRT)</b>
Migrant N-20	L. Missisauga Mb., Mic Mac Fm.	D170	300 N20 44000 60000	28/07/1977	Mobil et al.	4468.7
Adamant N-97	L. Missisauga Mb., Mic Mac Fm.	D369	300 N97 44000 60000	05/11/2000	ExxonMobil	4708
Thebaud E-74 (T5)	L. Missisauga Mb., Mic Mac Fm.	D359	305 E74 44000 60000	25/11/1998	Sable et al.	5015
Thebaud I-93	L. Missisauga Mb., Mic Mac Fm.	D271	300 I93 44000 60000	27/03/1985	Mobil et al.	5166

### 3.2.2. Stratigraphic Analysis and Core Description

Characterization of stratigraphy was refined by detailed core analysis and the depositional facies were linked to well log response to produce depositional facies interpretations. In the absence of core at Migrant, the similarities, and differences between the Thebaud and Migrant clastic depositional facies through core analysis of the Thebaud I-93 core 1 interval were identified at the Canada-Nova Scotia Offshore Petroleum Board's Geoscience Research Centre (CNSOPB GRC) in Dartmouth, Nova Scotia. The calibration of the cores with the petrophysical logs allows for seismic ties. Making comparisons against existing core descriptions and interpretations from the deeper overpressured

sections allows for a closer look at the stratigraphic implications on a well-by-well basis. The Thebaud I-93 core 1 interval was most closely related to the clastic deposition at Migrant based on well stratigraphic correlation and 3D seismic facies. Given the deltaic depositional system distribution across the Migrant expansion trend, there is likely to be variations in facies distribution and depositional energy between sediments deposited in the Migrant and the distal Thebaud depocenters ~15 km apart. A list of core data available in the four wells in this study are presented in Table 3.2 below.

*Table 3.2: Core data incorporated in this study. Of the four cores, three of the physical rock data (Thebaud I-93 and Thebaud E-74 (T5) as well as Adamant N-97 were described by the operators. Only the Core #1 was described in this study.*

<b>Well</b>	<b>Top</b>	<b>Bottom</b>	<b>Sample Location</b>	<b>Core Analyses</b>	<b>Formation Cored</b>	<b>Recovered</b>
I-93 (FDC)	3065.68	3081.3	CNSOPB	Y	Missisauga Fm.	15.99 m
T 5 Core 1 (FDC)	4621	4639.5	CNSOPB	Y	Missisauga Fm.	18.5 m
T5 Core 2 (FDC)	4922	4948.5	CNSOPB	Y	Missisauga Fm.	26.5 m
N-97 (SWC)	3542	4146	CNSOPB	Y	Missisauga Fm. Mic Mic Fm.	48 cores

The Thebaud I-93 well was drilled on the Central western block of the Thebaud Structure within the Sable MegaMerge (Figure 3.1), reaching a total depth of 5166 m TDSS on the flank of the structure. The core #1 described in this work was taken from a dominantly mudstone with occasional sandstones and siltstones interval, which dominates the 3158 m – 4768 m depth range at Migrant based on work by (Campbell, 2018). Approximately 15.8 m of the core was recovered of the Lower Cretaceous from a depth of 3081-3097 m in the Thebaud Structure. Core description of key intervals in the T5 well found in the supplementary files at the end of the well report suggests an older age limit for the Missisauga Formation Sandstone from the deeper H2 and F3 Sands compared to the contiguous sandstone section of the I-93 core (Section 3.4.).

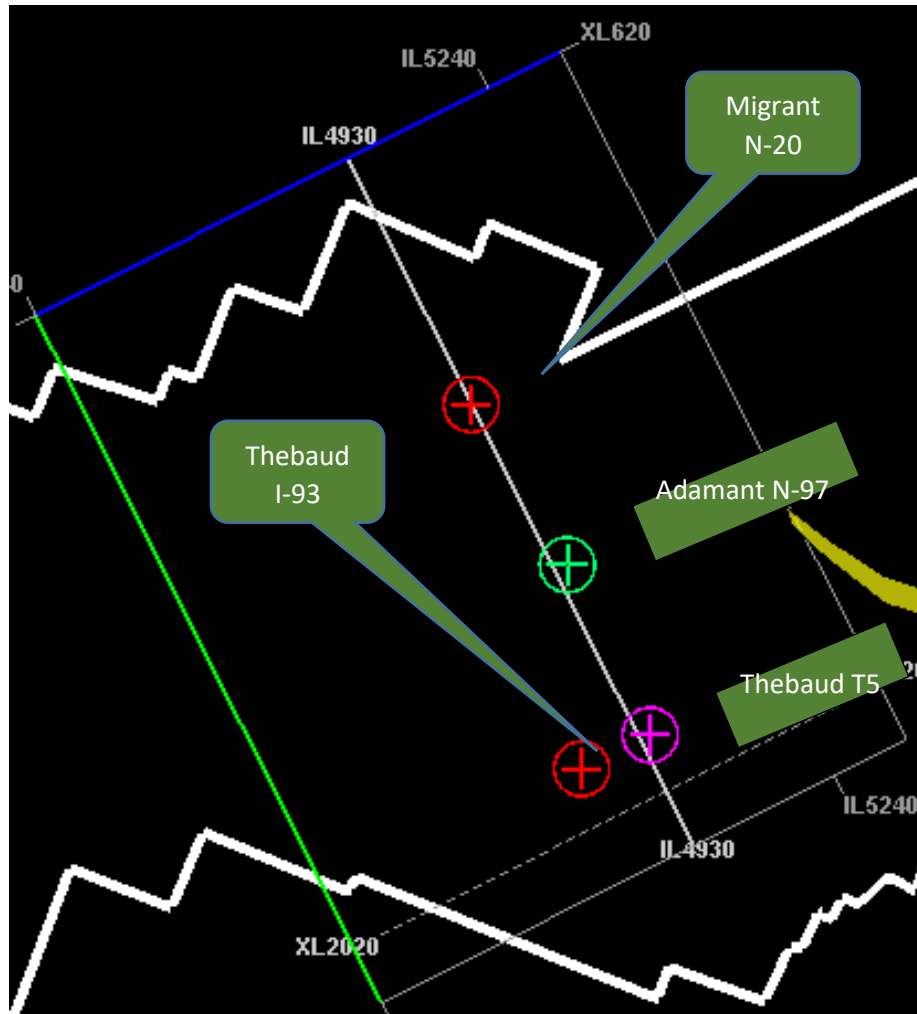


*Figure 3.1: A plan view of the study area comprising the four project wells and their relative spacing from Petrel.*

The full diameter core from the Thebaud I-93 was useful for investigating the transition between non-reservoir rocks (shales) to reservoir rocks (sandstone) and back to non-reservoir rocks in areas that are stratigraphically similar in age to the Migrant Rollover. This cored interval is correlatable to the normally pressured zone of interest in the Migrant Structure, which allows for comparing the depositional facies as well as their associated energy levels at the time of their deposition. The Thebaud I-93 well comprises five cored intervals making up approximately 53 m of core all from the Missisauga Formation. For this study, only Core 1 (the well's top core) was described (APPENDIX A.1.; Section 3.3.1.).

### 3.2.3. Well Stratigraphic Correlation

The construction of a stratigraphic cross-section of the four project wells was completed by correlating stratigraphic tops with easily distinguishable, seismically identifiable markers using the Petrel™ stratigraphic well top correlation workflow (Figure 3.2). Given the observed lithostratigraphic discrepancies between newer wells (e.g. Thebaud T5 and Adamant N-97) and older wells (e.g. Migrant N-20), the operators (SOEP) adopted the same lithostratigraphic framework for the Thebaud and Adamant structures. For consistency, the formation top picks were first correlated before the hydro pressured sands #2, #4 and #6 were correlated from the newer Thebaud T5 well to the Migrant Structure and N-20 well. The Cretaceous C sands in the Adamant well was correlated to the key hydro-pressure section in the Thebaud Structure comprising Sands #2, Sand #4 and, Sand #6 before being correlated to the Migrant N-20 well.

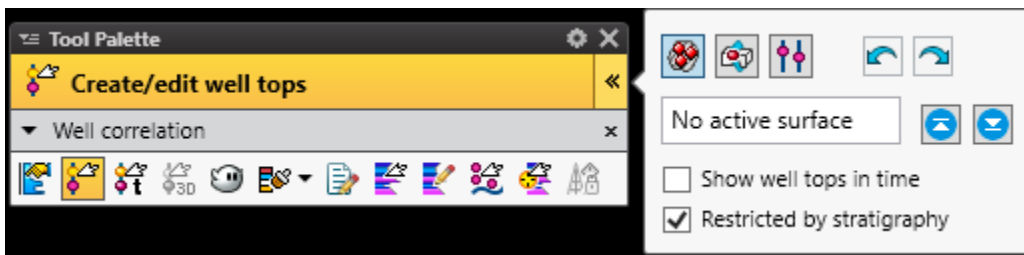


Figure 3.2: The well correlation workflow used for building a stratigraphic cross-section.

### 3.2.4. XRF Core Analyses

A calibrated Thermo Fisher Scientific handheld XRF (X-ray fluorescence) analyzer was used to analyze whole-rock samples to map the geochemical concentration in the available cores, sidewall cores, and cuttings. While these XRF measurements are useful for providing quick, onsite chemical rock analysis data from cuttings, and cores, they can be used to identify the mineral composition of a rocks. This technique may be enhanced if there are good sample preparation practices (e.g pulverization), which creates better consistency of the rock sample than whole rock measurements (including full diameter cores, sidewall cores, and cuttings) done in this study. The instrument detects the concentration of a range of elements after exciting a rock with X-rays (Ryan et al., 2017). Each sample point was analyzed by the device for a total of 180 seconds. Three physical rock data analyzed through this method are listed in Table 3.3.

*Table 3.3: Physical rock data availability in the project area analyzed either for their sedimentary features, grain size, or geochemically classified after (Herron, 1988).*

<b>Well</b>	<b>Sample.</b>	<b>No. of XRF Readings</b>
Thebaud I-93	Core #1	46
Thebaud T5 E-74	F3 Core H2 Core	84 58
Adamant N-97	48 Side wall Cores (Including a disintegrated sandy sample)	47
Migrant N-20	35 Vials of Well cuttings	35

### 3.3. Results

#### 3.3.1. Core Lithofacies Description

Five lithofacies were identified in this study from the core description of the Thebaud I-93 well. When compared to core photographs from the predominantly siliciclastics overpressured F3 and H2 sands described by Welner et al., (2000), physical rock characteristics indicate a slightly different depositional influence in the region of the Thebaud I-93 core 1 interval. Comparing this to petrophysical well logs at Migrant will introduce some uncertainty due to lateral facies variation when core data is used for supplementary purposes in the absence of core at Migrant. The considerable spacing between the wells with no closely spaced substitute meant that this uncertainty could not have been avoided.

Table 3.4: Summary of lithofacies examined from core in the Thebaud I-93 well.

Lithofacies	Cored interval (m)	Texture and color	Trace Fossils and constituents	Sedimentary Structures	Interpretation
Medium to Coarse Laminated Sandstone (F1)	3065.68-3066.28, 3066.46-3067.02, 3077.73-3080.18, 3080.7 - 3081.15	Coarse grained and whitish grey	None	Rip-up of mud, shales, and coal	Lower intertidal to subtidal, Sand flat, Beach/Marginal
Mudstone/ Shale (F2)	3066.43- 3066.46 3070.91- 3072.28	Fine grained, Dark to limey grey	Siderite Nodules	Erosional scours, low angle cross-lamina, asymmetric ripples, rip-up clasts	Intertidal flat Coastal Plain, Lagoon/Back reef Offshore shelf
Dark Massive Sandstone (F3)	3068.95 – 3069.4	Coarse grained and black	None	None	Fluvial/Tidal channel in the intertidal zone
Poorly Sorted Lithic Sandstone (F4)	3067.02 – 3068.95, 3080.18 -3080.7, 3081,15 – 3081.27	Coarse grained and grey with dark fragments	None	Planar horizontal lamination, mottling	Subtidal to lower intertidal environment
Lenticular-bedded mixed Sandstone and Mud stones (F5)	3072.28 – 3077	Fine to Coarse grained, Grey White	Shell patch, Burrow marks ( <i>Teichichmus</i> , <i>Zoophycos</i> or <i>Rhizocorallium</i> )	Bioturbations, ripples, lens/lenticular bedding	Subtidal

We identified five lithofacies in this study from the core description of the Thebaud I-93 well. When compared to core photographs from the predominantly siliciclastics overpressured F3 and H2 sands described by Welner et al., (2000), physical rock characteristics indicate a slightly different depositional influence in the region of the Thebaud I-93 core 1 interval.

## Lithofacies 1: Poorly Sorted Lithic Sandstone

**Description:** Lithofacies 1 (Table 3.4) is mainly a grey, coarse medium to lower coarse-grained sand with poor sorting. It occupies the bottom of the core and is also present in the top where it is seen interfacing with lithofacies 2. The section is mainly white, with some calcite and changes to grey when sprayed with water, which percolates through the grains rapidly (Figure 3.3A). The lithofacies is characterized by the presence rip-up of mud, shale and coal fragments with sulphuric smell (at the bottom) of the section. Wetting further reveals sedimentary lithic fragments with some oolitic presence in the section found at the top of the core (APPENDIX A.1).

**Interpretation:** F1 represents deposits typical of a subtidal to lower intertidal environment (Siddiqui et al., 2017). In addition to the poor sorting, the occurrence of shale and mudstone (or possible coal fragments) rip-up clasts suggests scouring of channel base/ banks that typically runs along the length of an intertidal regime in the estuary (Darlymple et al. 1992).

## Lithofacies 2: Cross Laminated Sandstone

**Description:** Lithofacies 2 (Table 3.4) is comprised of medium to coarse grained micaceous sand, showing some burrowing with fossils and mud drapes (Figure 3.3). There is low-angle cross lamina with reactivation surface, grading from fine to medium-grained sands. Scouring and asymmetric ripples, with lamina dipping at ~ 10 degrees are present in addition to mud rip-up clasts. In these two intervals of core within box 19 - box 21 and box 4 and box 5 (APPENDIX A.1). This section of the core is mainly white and changes to grey when sprayed with water which percolates through the grains in a short period.

**Interpretation:** F2 represents deposition within a lower intertidal to a subtidal domain (Siddiqui et al, 2017). There are low-angle cross lamina and asymmetric ripples with reactivation surfaces identified in this core which suggests a mild degree of energy likely related to changing tidal currents during retreating tide levels towards a slack water regime (Reineck & Wunderlich, 1968). The reactivation surface indicates changes in energy level (likely increasing) with mild burrows and fossil presence a further indication of intertidal influences.



### Lithofacies 3: Dark Massive Sandstone

**Description:** Lithofacies 3 (Table 3.4) is mainly medium to coarse-grained massive sands with some dark minerals that give a dark appearance to the sandstone (Figure 3.3C). The section interfaces with a reactivation surface that mark the beginning of the next unit where some asymmetric ripples with lamina dipping at  $\sim 10$  degrees. In the main area of its distribution higher up in the cored section, there are no obvious sedimentary features in this facies as seen in box 6 (APPENDIX A.1). When sprayed with water, it percolates through the grains in a short period and is dispersed through the cored section. A sparse section of the facies can be seen at the bottom of the core with some coal fragments.

**Interpretation:** F3 represents deposits of a tidal channel in the intertidal zone (Siddiqui et al., 2017). The dark sands we documented in core were likely sourced from a supratidal coastal plain/marsh environment with the dark coloration related to the accumulation of salt or freshwater peat (Siddiqui et al., 2017). Thus, there is a slight change in provenance. The interfacing reactivation surface in our observation is a characteristic structure of the subtidal and lower intertidal zone (Van Wagoner et al., 1990). Here, the currents are slightly higher with a slightly higher sediment supply (Webb et al., 2015).

### Lithofacies 4: Mudstone/Shale

**Description:** Lithofacies 4 (Table 3.4) is comprised of featureless gray to dark mudstone with some mottling. The facies comprised planar horizontal laminations (Figure 3.3D). Mild siderite nodule ( $\sim 1$  cm) components can be seen in this facies. It makes up for lesser amounts of the core found in box 7 and box 10. A small section of this facies exists in box 2 (APPENDIX A.1). The facies changes to limey grey when sprayed with water. The water percolates through the grains slowly with some ponding observed on some core cutouts.

**Interpretation:** F4 represents intertidal mudflat deposits (upper to the middle intertidal regime). The mudstone section we see in this core was deposited after the flocculation and settling of lagoon mud/clays suspended in flood water through distributary channels and resulting in laterally extensive laminations distributed across the mudflat. This is aided by the low surface gradients of the tidal flat (Webb et al., 2015). Thus, allowing for less rapid drainage of a fluvial inflow. The nodular presence we observe in core is related to poorly

drained, low energy, the non-marine influence of dissolved iron that precipitated into siderite likely derived from fluvial input (Cecil, 2003; Cecil, 2013).

### **Lithofacies 5: Lenticular-Bedded Sandstone and Bioturbated Mudstone**

**Description:** Lithofacies 5 (Table 3.4) is comprised of grey to dark shaly and white fine to medium-grained sandstone mixture. The section is of heavy to mild bioturbation in the mudstone with some burrowing and occasional fossils in the sand patches with siderite nodules (Figure 3.3E). In zones of abundant sands, lenses/lenticular beds are common with mild current ripples. There is increased bioturbation as it grades towards abundant mud. Also, fossils and burrowing (both vertical and round/horizontal) are observed in the section with 1-6% bioturbation. In total, the facies make up about 50% of the core occupying mainly the middle sections) box 8 and box 9 as well as mainly box 11 - box 18 (APPENDIX A.1). The section is mainly white in color and changes to limey grey when sprayed with water, which percolates through the grains slowly with some ponding observed on some core cutouts.

**Interpretation:** F5 represents deposits of a subtidal environment. (Siddiqui et al., 2017). The sandstone and mudstone mixture with lenticular bedding observed in this core description suggests a change in depositional energy. According to work by Reineck and Wunderlich (1968), current ripples may occur in a mud-rich environment that experienced alternating periods of tidal current and tidal slack water. Diagnostic of subtidal conditions, bioturbation in this core is likely from *Planolites* and *Teichichnus* ichno fossils suggesting a brackish water environment. The nodular presence indicates low energy, non-marine influence where dissolved iron precipitated into siderite (Cecil, 2003; Cecil, 2013).

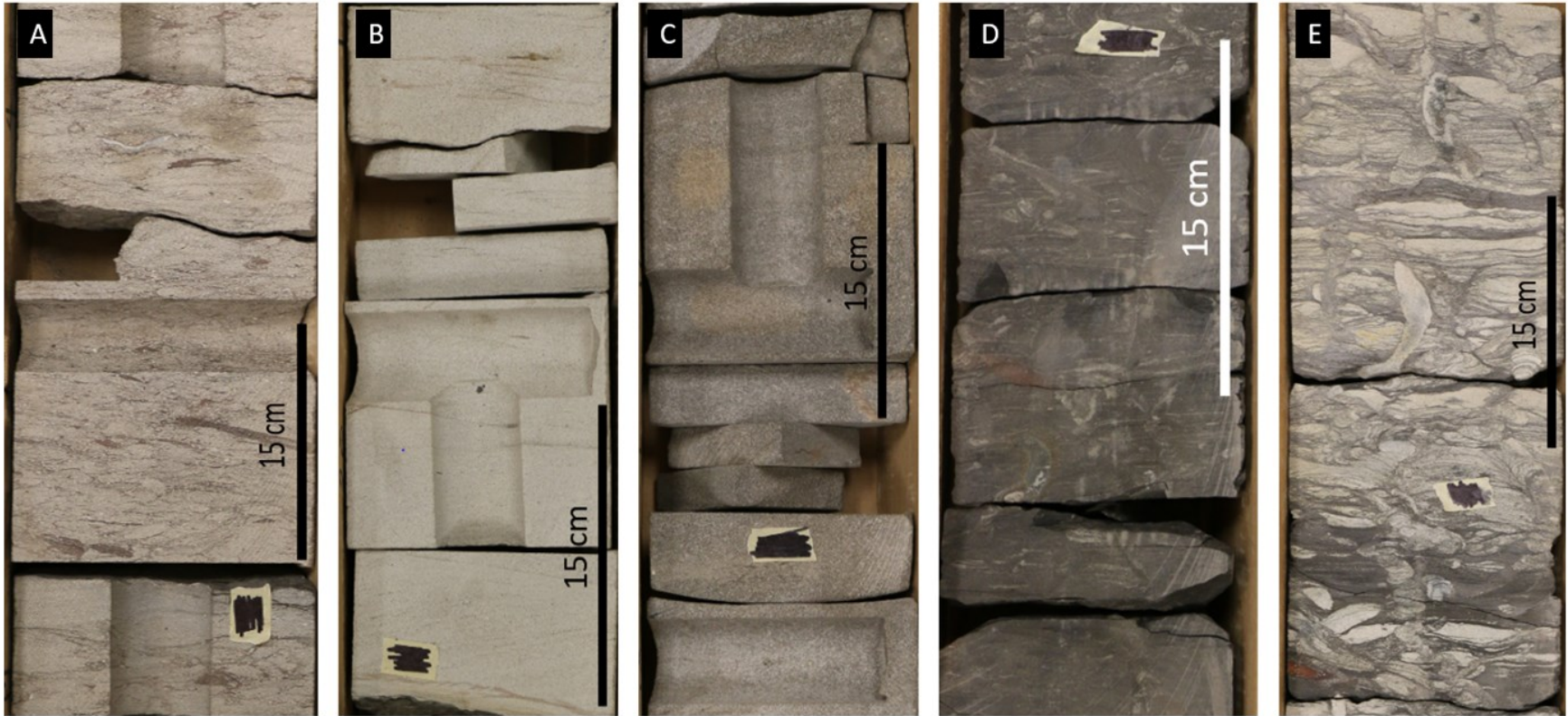


Figure 3.3: A figure of the log facies described in the Thebaud I-93 well.

### 3.3.2. XRF Analyses Results

Figure 3.4 and Figure 3.5 show the results of geochemical concentration of major elements compared on a sandclass plot after Herron (1988). The sidewall cores from the Adamant N-97 well appear to be spread-out represented by the red diamonds (Figure 3.5). The data is present in all fields on the sandclass plot except Arkose (Figure 3.5). The ferruginous fields (upper section of the plot including Fe-Shale and Fe-Sand) contained fewer points than the non-ferruginous section (lower section containing Shale, Wacke, Litharenite, Arkose, Sublitharenite, Subarkose). Most of the points plot within the Sublitharenite field, which contains the average plot value (Figure 3.5). The Fe-Shale facies occur in the silica poor, an iron-rich area of the sandclass plot (Figure 3.5). Data points in this field are present in all the analyzed intervals except the Thebaud I-93 top core #1 and the Thebaud E-74 (T5) H2 Sand cored interval (Figure 3.4). In the Adamant N-97 well one of the 44 data points plot in this field (Figure 3.5). The Thebaud E-74 (T5) F3 Sand cored interval shows that five of the 85 points plot in this field (Figure 3.4).

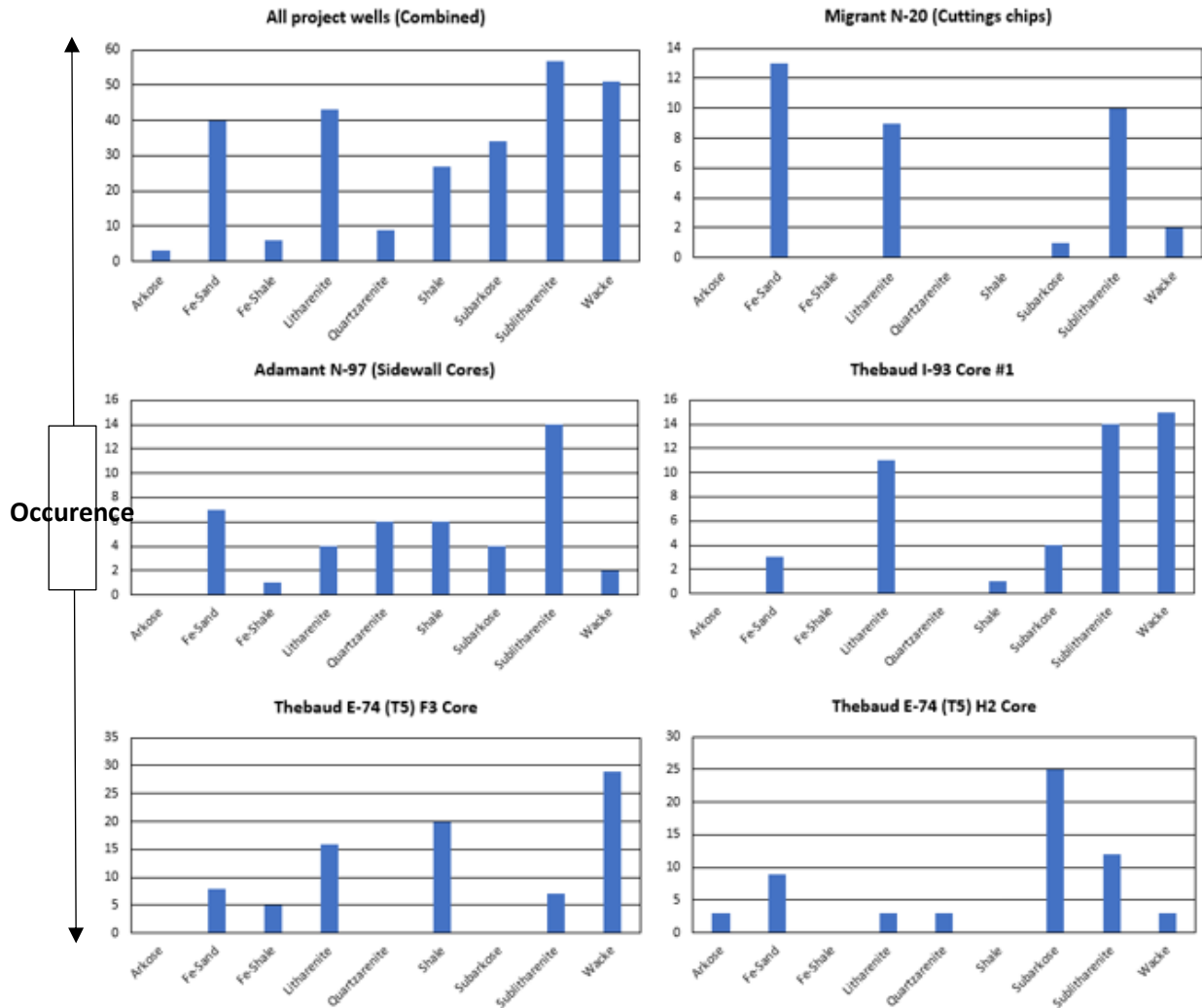


Figure 3.4: Histogram of data distributed on a sandclass plot for the respective fields in the analyzed wells and intervals of interest including the Mic Mac and Missisauga formation reservoirs. The vertical axis represents the occurrence with the horizontal axis representing lithological facies. The Adamant N-97 well shows increased amounts of sublitharenite and Fe-Sand composition. The Thebaud I-93 Top Core #1 shows a higher concentration of Wacke, Sublitharenite, and Litharenite compositions. The Thebaud E-74 T5 F3 core shows an increase in Wacke and Shale content with some Litharenite, Sublitharenite, and Fe Sand and Shale. The H2 interval shows an increase in the amount of Subarkose with some Sublitharenite.

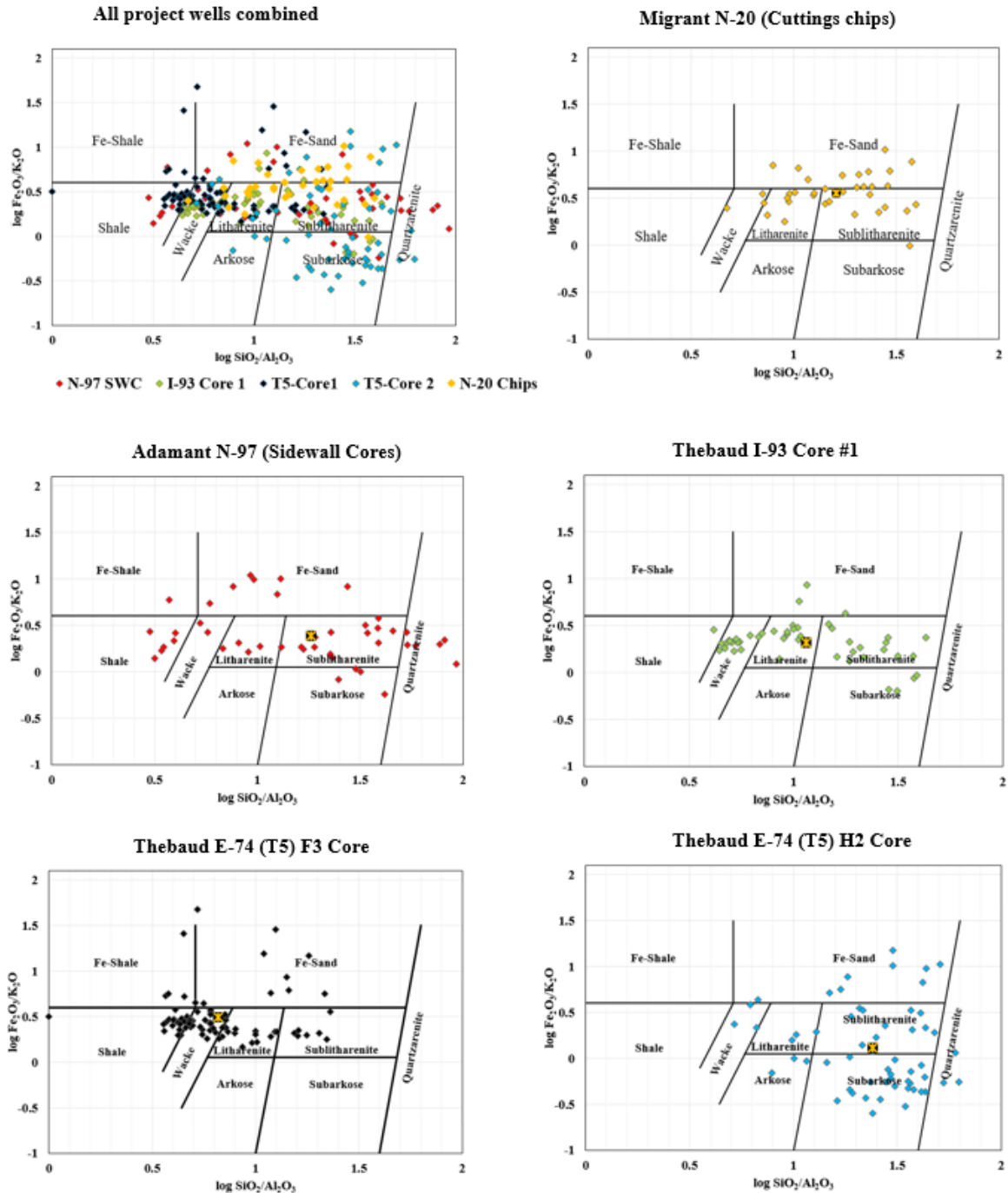


Figure 3.5: A series of sandstone classification plots of samples from the cores for the project wells. Each plot takes into comparison the concentration of the  $\log \text{SiO}_2/\text{Al}_2\text{O}_3$  on the x-axis against that of  $\log \text{Fe}_2\text{O}_3/\text{Al}_2\text{O}_3$  on the y-axis.

Most of the values in the sand class plot for Thebaud I-93 top core #1 occur in the Wacke field (Figure 3.5). In this well, three fields without any data points include the ferruginous Fe-Shale, non-ferruginous Arkose, and Quartzarenite (Figure 3.4 & Figure

3.5). The plot average value for this plot is contained in the Litharenite field (Figure 3.5). The data points for the Thebaud E-74 (T5) core from the F3 sand interval shows some clustering in the shale and Wacke fields (Figure 3.5). The data points plot in all fields except the Arkose, Subarkose, and Quartzarenite (Figure 3.4 & Figure 3.5). The average value plots in the Wacke field (Figure 3.5). In the H2 core interval of the same well, the data points are spread out in all fields except the Fe-Shale and Shale fields (Figure 3.4 & Figure 3.5). Most of the data points plot in the Subarkose field with the average plotted in the Sublitharenite field (Figure 3.5).

The Arkose facies occupies the intermediate silica, low iron field on the sandclass plot and is not as common in our classification of the various wells and intervals (Figure 3.4). This facies is present only in the Thebaud E-74 (T5) well where only three data points plot on the sandclass plot (Figure 3.4 & Figure 3.5). The Subarkose facies occurs in all the analyzed intervals except the Thebaud E-74 (T5) F3 Sand cored interval (Figure 3.4 & Figure 3.5). This facies occupies high silica, low iron portion of the sandclass plot between the Arkose and Quartzarenite fields (Figure 3.5). Four of the 44 data points in the Adamant N-97 well as well as four of the 48 data points in the Thebaud I-93 well plot in this facies (Figure 3.4). In the Thebaud E-74 (T5) well, 24 of the 58 data points in the H2 Sand core plot in this facies (Figure 3.4). Occupying the silica and iron-rich area of the plot, the Fe-Sand facies are present in all the analyzed intervals (Figure 3.5). In the Adamant N-97 sandclass plot, seven of the 44 data points plot in this field (Figure 3.4 & Figure 3.5). The Thebaud I-93 top core sees three of the 48 data points plot in this field (Figure 3.4). The sandclass plot for the Thebaud E-74 (T5) well shows that eight of the 85 data points in the F3 Sand interval plot in this field with nine of the 58 data points for the H2 Sand interval plotting in this field (Figure 3.5).

Litharenites facies are one of the more pronounced of the nine classification fields occurring in all analyzed intervals (Figure 3.5). Occupying the area above the Arkose field but just under the ferruginous demarcation, this facies is most common in the Thebaud E-74 (T5) F3 Sand cored interval where 16 of the 85 points plot in this facies. This is followed by the Thebaud I-93 top core #1, which has 11 of the 85 points in this facies (Figure 3.4). The Adamant N-97 sidewall cores had four of the 44 points in this facies with the Thebaud E-74 (T5) H2 Sand cored interval having the least number of points in this field with four



out of its 58 data points (Figure 3.4 & Figure 3.5). The Sublitharenite facies occupies an area in the high silica, intermediate (just below the demarcation of the ferruginous and non-ferruginous fields) and just above the Subarkose field (Figure 3.5). It is the most dominant facies present in all the analyzed plots. Both the Adamant N-97 and Thebaud I-93 well showed the highest concentrations both with 14 out of 44 and 48 data points respectively (Figure 3.4). The Thebaud E-74 (T5) H2 Sand core had 12 of its 58 datapoints plot in this field of the sandclass plot (Figure 3.5). The F3 Sand cored interval had seven of its 85 datapoint plot in this facies (Figure 3.4).

Quartzarenite facies occupies the highest silica and iron extreme of the sandclass plot (Figure 3.5). This facies occurs only in the Adamant N-97 sidewall core and the Thebaud E-74 (T5) H2 Sand cored interval (Figure 3.5). In the N-97 well, six of the 44 data points plot in this facies (Figure 3.4). The E-74 well has three of its 58 data points plot in this facies (Figure 3.4). Shale facies occur in the low silica, low iron end of the sandclass plot (Figure 3.5). In the Adamant N-97 well, six of the 44 data points plot in the shale facies with the Thebaud E-74 (T5) H2 Sand cored interval having the highest occurrence with 20 of the 58 datapoints plotting in this facies (Figure 3.5). This allows for the mapping of geochemical elements in the various lithofacies to discern the variability in elements related to the lithofacies and depositional environment.

The Thebaud I-93 has the least number of data points in this facies with only one of the 48 datapoints plotting in this field (Figure 3.4 & Figure 3.5). Wacke is present in all the analyzed intervals (Figure 3.5). Occupying an area between the non-ferruginous Shale and Arkose/Litharenite fields, the Thebaud E-74 (T5) F3 Sand cored interval appeared to show the highest proportions of this facies with 29 of the 85 data points plotting in this field (Figure 3.4 & Figure 3.5). In the Thebaud I-93 top core #1, 15 of the 48 points plot in this field with the Thebaud E-74 (T5) F3 Sand cored interval and Adamant N-97 sidewall cores showing lower proportions of points in this facies with three of the 85 and two of the 44 data points respectively for both wells (Figure 3.4 & Figure 3.5). While the results from analyzing geochemical data (from cuttings or core) integrated into this study was aimed at increasing the confidence of depositional environment interpretation, matching the elemental variability of the XRF result to textural and composition properties associated with various depositional environment may present some limitations.



### 3.3.3. Well Stratigraphy

A well correlation panel was created to delineate the Mic Mac to Missisauga formation reservoirs in the Migrant expansion trend as well as the top of overpressure in the project wells (Figure 3.6). Differences between the lithostratigraphic framework used by the GSC and the operator (SOEP) in the online BASIN Database were accounted for during a preliminary correlation exercise of three of the four project wells (Figure 3.7). This was done to enable further correlation towards the Migrant N-20 well.

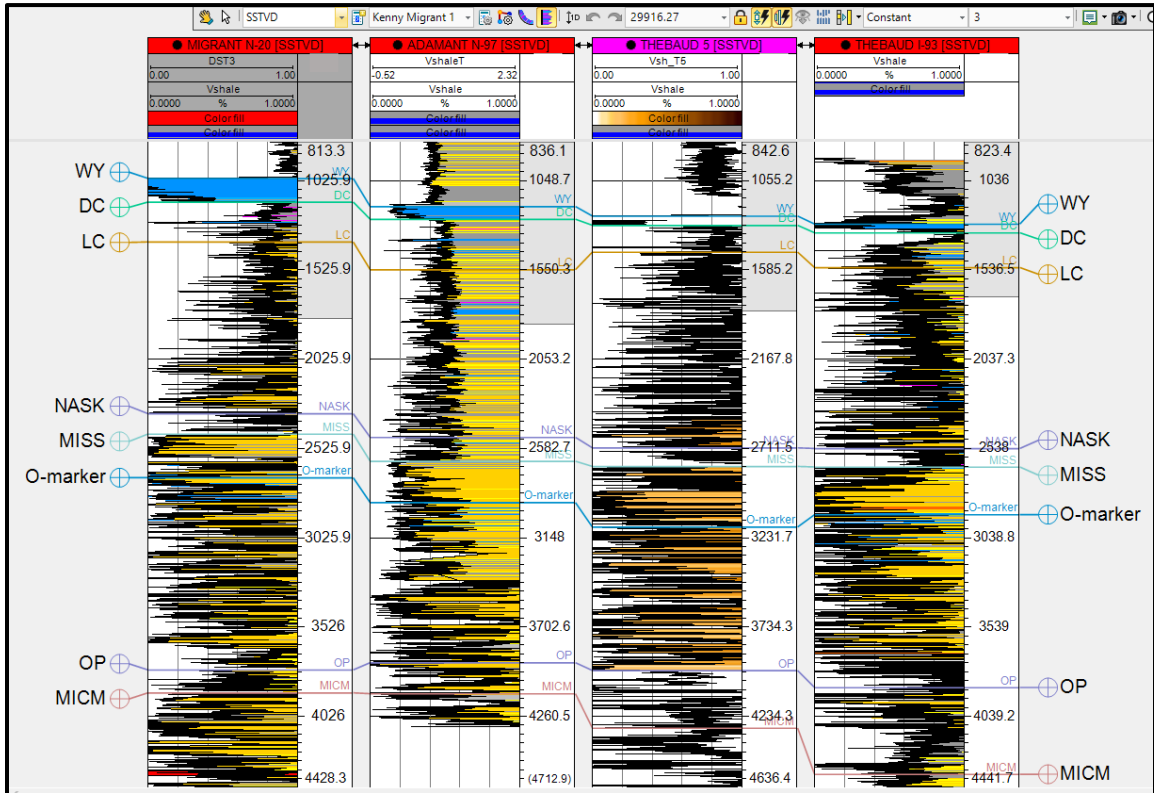


Figure 3.6: A cross-section of the key wells used in this project. Given the high net to gross nature of the system, log-based correlations across the four wells proved challenging. The absence of a Canstrat lithology log for T5 meant that the Gamma-Ray derived shale volume log was relied on for correlation purposes with the rightward kicks commonly shale zones. The Wyandott Marker was flattened as the datum before the subsequent markers were flattened on to aid the correlation of the following marker. The current display is based on true vertical subsea depth (TVDss). To demonstrate the sequence stratigraphic relationship the horizontal distances have not been displayed to scale.

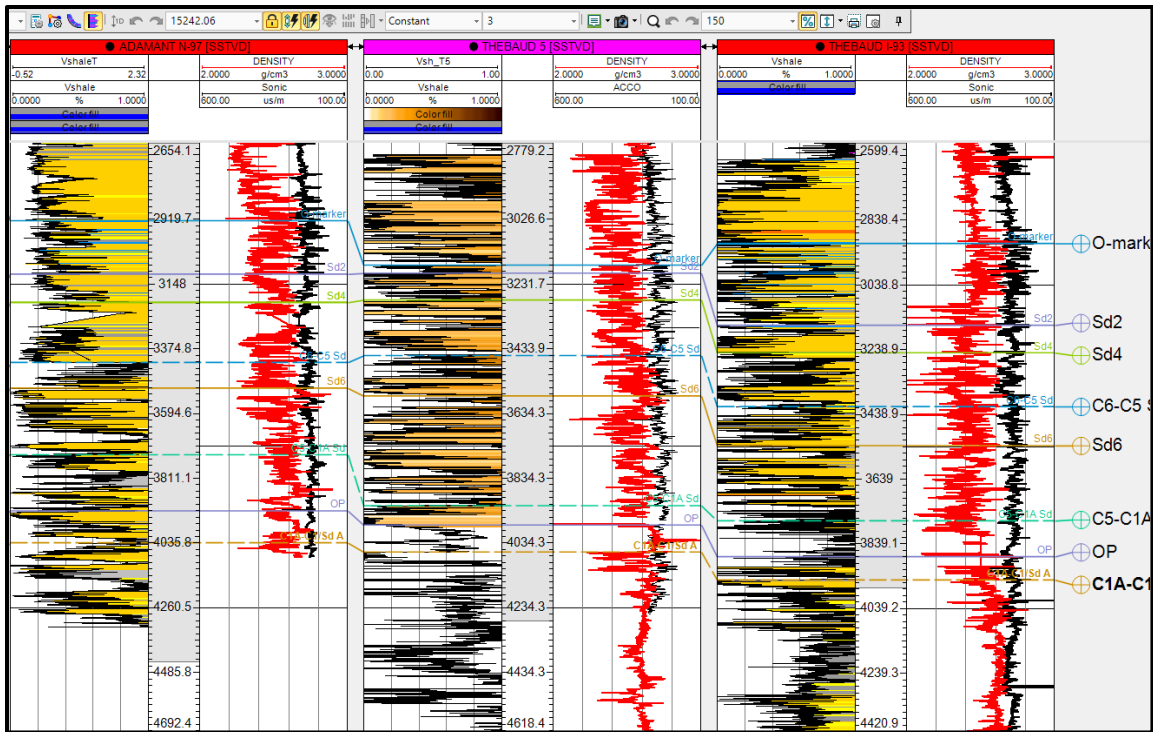


Figure 3.7: A well composite for three of the four project wells. For consistency, a combination of Gamma-Ray derived shale volume log (first track) and combined sonic and density logs (second track) were used for correlating key reservoir tops from the older and newer Thebaud wells through to Adamant. The Wyandott Marker was flattened as the datum before the subsequent markers were flattened on to aid the correlation of the following marker. Given the impact of MD in skewing the apparent thickness relationships for a deviated well, the current display is based true vertical subsea depth (TVDSS).

Considering the new stratigraphic scheme adopted in wells drilled after the time of the Thebaud I-93 and Migrant N-20 wells, there was a need to reconcile the noticeable differences in the naming convention in both old and new wells. This involved adjusting the various naming systems established by various workers through the correlation panel in this project to create a consistent framework. This was integrated into Despite the age difference between the two Thebaud wells, the nomenclature used in the normally pressured section was similar for both wells. The reservoirs in this section of the well were named using a numeric naming convention going from 1 to 7, which changes to an alpha-numeric nomenclature deep in the structure below the Thebaud Shale.

### 3.4. Discussions from Sedimentary Core Observations

#### 3.4.1. Depositional Relationship - F3 and H2 Sand Intervals

Sedimentary core analysis in this study involved three cored intervals from the Missisauga Formation in two wells Thebaud I-93 and Thebaud E-74 (T5). Two cored

intervals from the Thebaud E-74 (T5) well were mainly studied based on work by previous workers (e.g. Welner et al., 2000). A review of the top core (the F3 sand interval) from the Thebaud E-74 well gives a Gamma-Ray log motif with an overall cleaning upward signature (Figure 3.8). Also, syndepositional slumping/ micro faulting observed in the F3 cored interval as well as the presence of bioturbation (burrows) and ripples, suggests a sporadic change in depositional influence as observed from the grain size variation, which ranges from coarse to very fine grained. These characteristics are consistent with deltaic depositional environment (Bhattacharya & Willis, 2001). The bioturbation comprises horizontal burrows that are 1- 5 mm long likely *Planolites*.

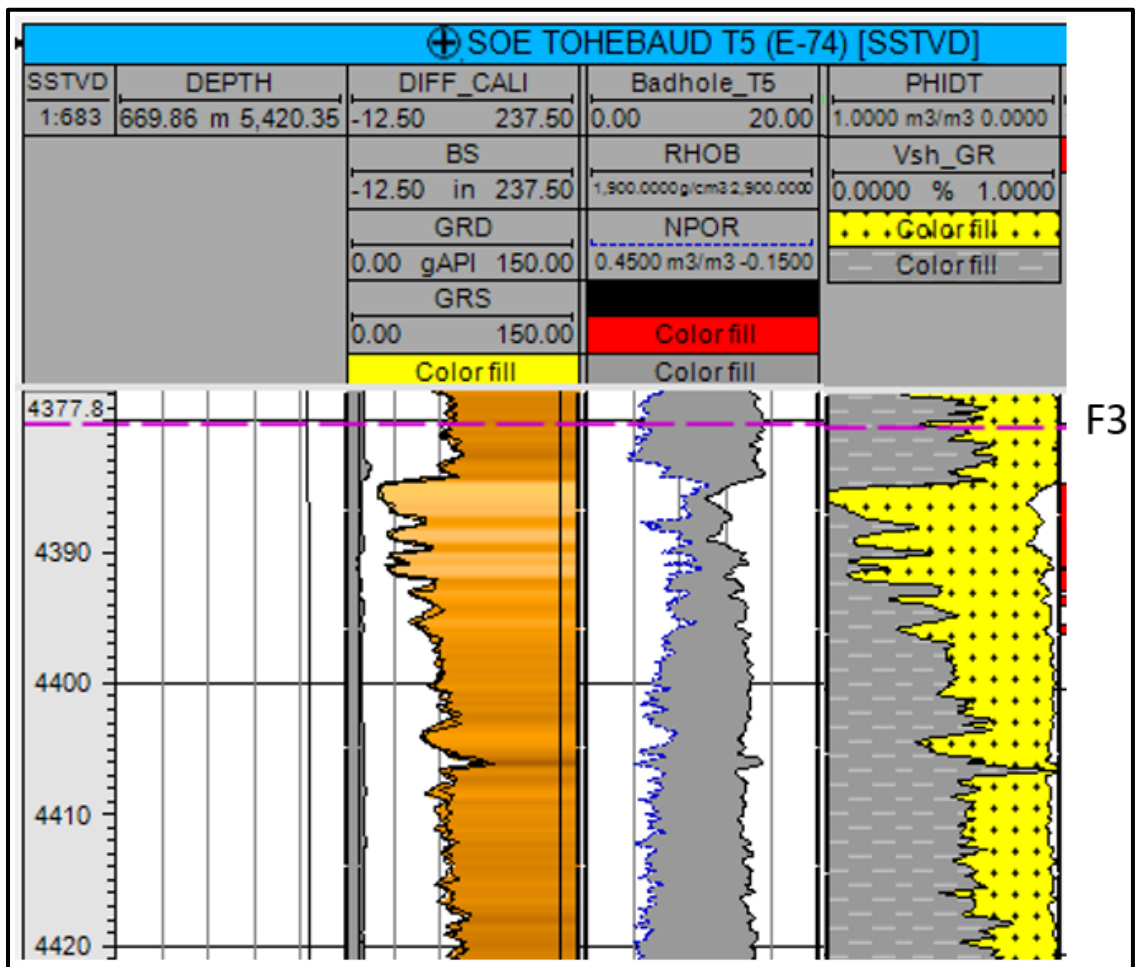


Figure 3.8: A figure of the F3 Sand interval in the Thebaud Structure showing the Gamma-Ray log (second track) with cleaning up signature right of the depth track. The absence of gas in the sand is indicated by the absence of cross over of Neutron and Density logs in the third track with the separation between both logs is an indication of shaliness (high shaliness). The increased shale volume (grey) and decreased porosity (yellow) combinations on the fourth track support variable sand content in the interval

The bottom of the H2 core, is characterised by laminated sands thought to indicate unidirectional high energy deposits. There is a change in character indicating more sign of biological activity. This may indicate a resumption of fair-weather wave base conditions allowing for the biological activities observed from the bioturbation. Also, evidence of wave agitation supported by the deposition of thick fine-grained, hummocky cross stratified sand packages followed by tidal influence on top of this section suggests a return to tidal conditions known to interface with periods of fluvial dominance close to shore (Siddiqui et al., 2017). Upwards in the H2 cored interval the deposits share similar characteristics with middle shoreface deposits and suggests a transition from offshore facies to middle shoreface facies. Facies further up give hint of an estuary mouth followed by characteristics in the top that indicate barrier bar environment in front of the estuary or to some degree right up to where there is wave action. Alternatively, this could possibly be a channel with a stark change in reservoir characteristics that appear to be well sorted and much cleaner.

Based on the similar grain size (not observable in log data) amongst the reservoir at the top F3 (Figure 3.8) and bottom test H2 intervals (Figure 3.9), it is likely that the sediments were derived from the same source location. This is supported by geochemical data results in Section 3.3.2. However, their porosity/permeability relationship in a cross plot (Section 4.4.2) suggests some variation, which may be linked to their deposition. Judging by the overall, Gamma-Ray log response and physical characteristics of the cored interval combined with the indicated shale distribution, this suggests a transition interpreted as a retrogradational event likely from estuarine to shoreface environment (Angela et al., 2003). Besides, regular occurrence of clay and fine parallel laminated sand throughout the core with re-established shaliness of top the core is typical of storm deposits with associated hummocky cross-stratification interpreted by Welner et al., (2000).

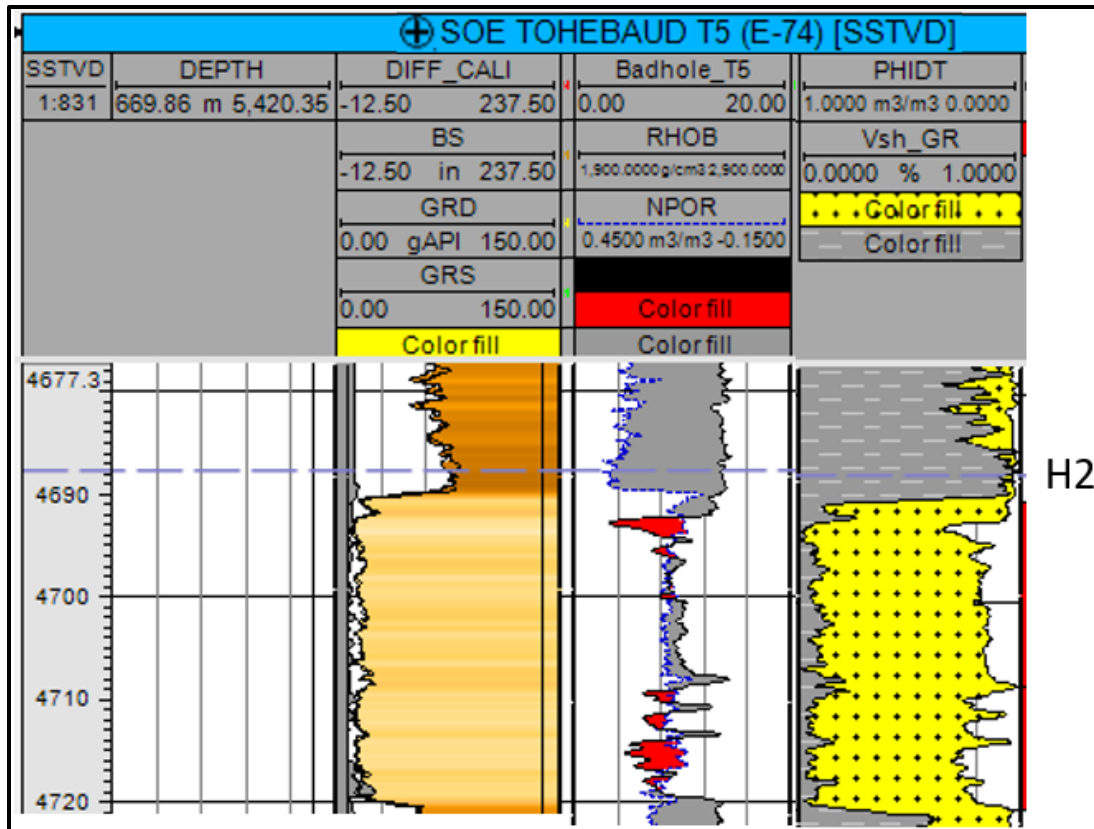


Figure 3.9: A figure of the H2 Sand interval in the Thebaud Structure showing the Gamma-Ray log (second track) with a blocky log signature right of the depth track. The presence of gas in the sand is indicated by the cross over of Neutron and Density logs (colored in red) in the third track. Separation between both logs is an indication of shaliness (low shaliness). The reduced shale volume (grey) and increased porosity (yellow) combinations on the fourth track support the rich sand content in the interval.

### 3.4.2. Depositional Relationship- I-93 Core #1 Interval

The top core (Core #1) from the Thebaud I-93 well was the only one described in this study given its direct relevance to the normally pressured interval studied in the Migrant Structure. The core description (Figure 3.10) compared favourably against the Gamma-Ray log signatures in the core analysis report. The presence of a solid shale interval in the core section resembles a lagoon or distal offshore shale from its dark featureless character. The parallel lamination of the shales suggests a straight core to TVD cut out with a lack of deviation (Section 3.3.1.). Going by observations, the core was deposited in a likely marginal marine environment based on the combination of bioturbated shaly and sandy units. Also, observed reactivation surfaces with rip-up clasts, siderite mud, and down-going burrows perhaps from *Teichichmus* are like features observed in a typical channel base environment with some channel sands and clay intermix.

While worm trace fossils in muds tend to be characteristic of a low energy environment, the frequency of their occurrence in this log is typical of sedimentation pattern found in a drainage area where avulsion is common (e.g tidal flat). Alternatively, supported by log signatures, this may hint at a pulse of deltaic sedimentation with a slowly transgressing sequence above it. While work by Kidston et al. (2005) referred to the target of the I-93 well as back reef, located slightly away from the margin, this supports the mudstone composition. However, the shale interval represents a sequence boundary, which may be associated with the top of an interfluvial deposit above a middle shoreface or estuarine succession where there are minimal storm events (Angela et al., 2003). The siderite nodules in the core suggest a combination of fluvial influence with some tidal contributions.

Thebaud I-93 Core	Facies	Core Photo	Interpretation
	F2		Lower intertidal to subtidal, Sand flat, Beach/ Marginal
	F3		Fluvial / Tidal channel in the intertidal zone
	F4		Intertidal flat, Coastal plain, Lagoon/ Back reef, Offshore shelf
	F1		Subtidal Environment
			Subtidal to lower intertidal environment
			Intertidal flat, Coastal plain, Lagoon/ Back reef, Offshore shelf
	F5		Intertidal flat, Coastal plain, Lagoon/ Back reef, Offshore shelf
			Subtidal Environment

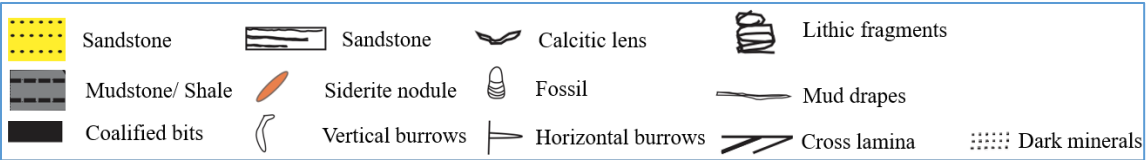
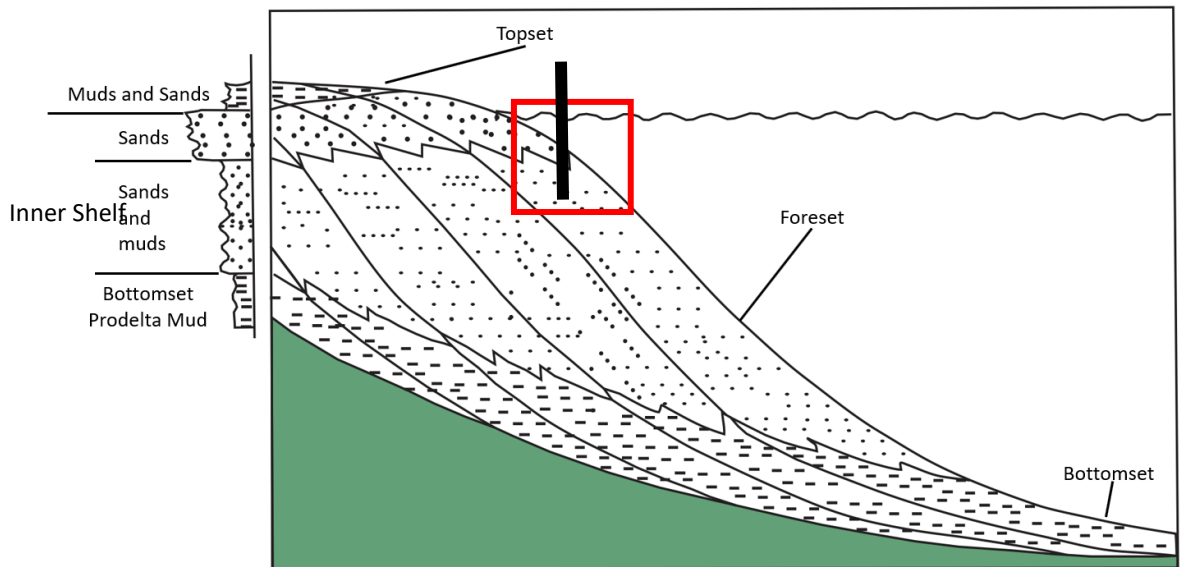


Figure 3.10: Sedimentological characteristics of the I-93 cored section from the Lower Mississauga Formation showing the facies and their sedimentary characters.



### 3.4.3. Depositional Facies at Migrant

The data acquired from the rocks discussed in the previous section (Section 3.4.2) plots in the sublitharenite field, which may suggest that the sands are texturally and compositionally immature based on the characteristics of this field by Folk (1968). Based on the results from section 3.3.2, a progressively decreasing quartz content in the sand class plot from the Thebaud to Adamant and the Migrant structure suggests that the sands in the Migrant area had moderate textural and compositional maturity. Thus, the sands were subjected to a short travel distance with a mild degree of reworking. Comparative observation in Figure 3.11 supports the conclusion on the Mic Mac Formation sands (inset) encountered in the zone of interest in the Migrant Structure (below 4,100).



*Figure 3.11: A figure showing the basinward progradation of deltaic sediments modified from (Scruton, 1960). The figure shows a cleaning upward pseudo log on the left of the diagram that transitions from non-marine siliciclastic topset deposits to offshore marine shales. This cleaning up signature is characteristic of the Gamma Ray log pattern of the lower section. Based on the overall cleaning up trend in the section of the well where the DST test intervals occur in the Mic Mac Formation Section 3.4.4 (Figure 3.17), which hints suggests a delta front environment (indicated by the red box), the black vertical bar represents the hypothetical position of the Migrant N-20 well in this environment.*

Plotting in the higher end of the litharenite field (Section 3.3.2), the average from the Thebaud I-93 shares a close relationship to the Migrant N-20 well. Their corresponding fields on the Folk classification plot suggests that the composition and texture of these sands hints at their deposition within a supralittoral to littoral regime comprising a mixture of sand and clay clasts. These characteristics are typical of fluvial, beach, and sometimes



marshy environments. Hence, this confirms the deposition of the interval of interest in the Migrant N-20 well in a proximal shelf location. In comparison, the good sorting from core observation that characterizes the F3 sands in the Thebaud T5 well is typical of deposition below wave base conditions with occasional storm events.

Similar to the F3 sand, the H2 core facies is typical of a wave-dominated shoreface assemblage (likely upper shoreface) with some degree of incised valley fill assemblage. The mixture of sand and mud in the analyzed I-93 core section described in this study is characteristic of estuarine influence (Siddiqui et al., 2017). This may impact the estimation of net reservoir thickness depending on the presence/absence of conductive minerals or kaolinites (Kaldi, 2019). However, in the absence of full diameter cores at Migrant, the cleaning up signature from Gamma-Ray log from well FTD to 4225 mRT suggests that the tested zones were likely deposited in an inner shelf environment known to be dominated by rivers (Siddiqui et al., 2017). Generally, the environment of deposition (EOD) from Migrant to Thebaud is a combination of fluvio-deltaic to shallow water marine wave, and tide (estuarine) influence.

Overall, the results from geochemical analysis of rock samples (cuttings or core) integrated into this study may be useful for increasing the confidence of depositional environment interpretation. However, matching the elemental variability of the XRF result to textural and composition properties associated with various depositional environment may present some limitations on integrating the XRF results. Given that rock chemistry is not a property of texture, this may introduce some uncertainties when plotting the sandclass facies averages on the various ternary diagrams (APPENDIX A.2.1.) after Folk (1960), Dickinson (1985) and Ingersol & Suczek (1979). Also, key elemental readings acquired from XRF data converted to their corresponding oxides by multiplying the data by the appropriate conversion constant (APPENDIX A.2.1.) was used to map geochemical content in the physical rock data in this study, which may be matched to well logs (Ruppel et al, 2017). However, the inability of the portable XRF device to pick up Sodium (Na) concentrations from rocks due to its low detection limit may present further limitations to integrating the XRF results in our interpretation.

#### 3.4.4. Reservoir Stratigraphic Framework

In the project wells, the naming convention of formation tops used by the regulators (CNSOPB) varied between a regional naming framework initially adopted for the earlier wells (e.g. Migrant N-20, Thebaud I-93) and a sequence stratigraphic naming convention used in the newer wells in this study (e.g. Adamant N-97, Thebaud E-74 (T5)). The regulators (CNSOPB) have commented that older Jurassic and Cretaceous naming conventions applied in the Venture field to the Northeast were used for the Thebaud development wells. As a result, the naming convention used in the overpressured reservoirs at Thebaud comprising the A-H naming system formulated during the development of the Thebaud field differed from the numerical naming style that was adopted when the older Thebaud I-93 well was drilled. This study integrates the different naming styles at Thebaud with increasing depth in the hydro-pressure and overpressured regimes from 1- 7 and A to H respectively used for field development (Figure 3.12 & Figure 3.13) with the Cretaceous stratigraphic naming convention (C) used at Adamant.

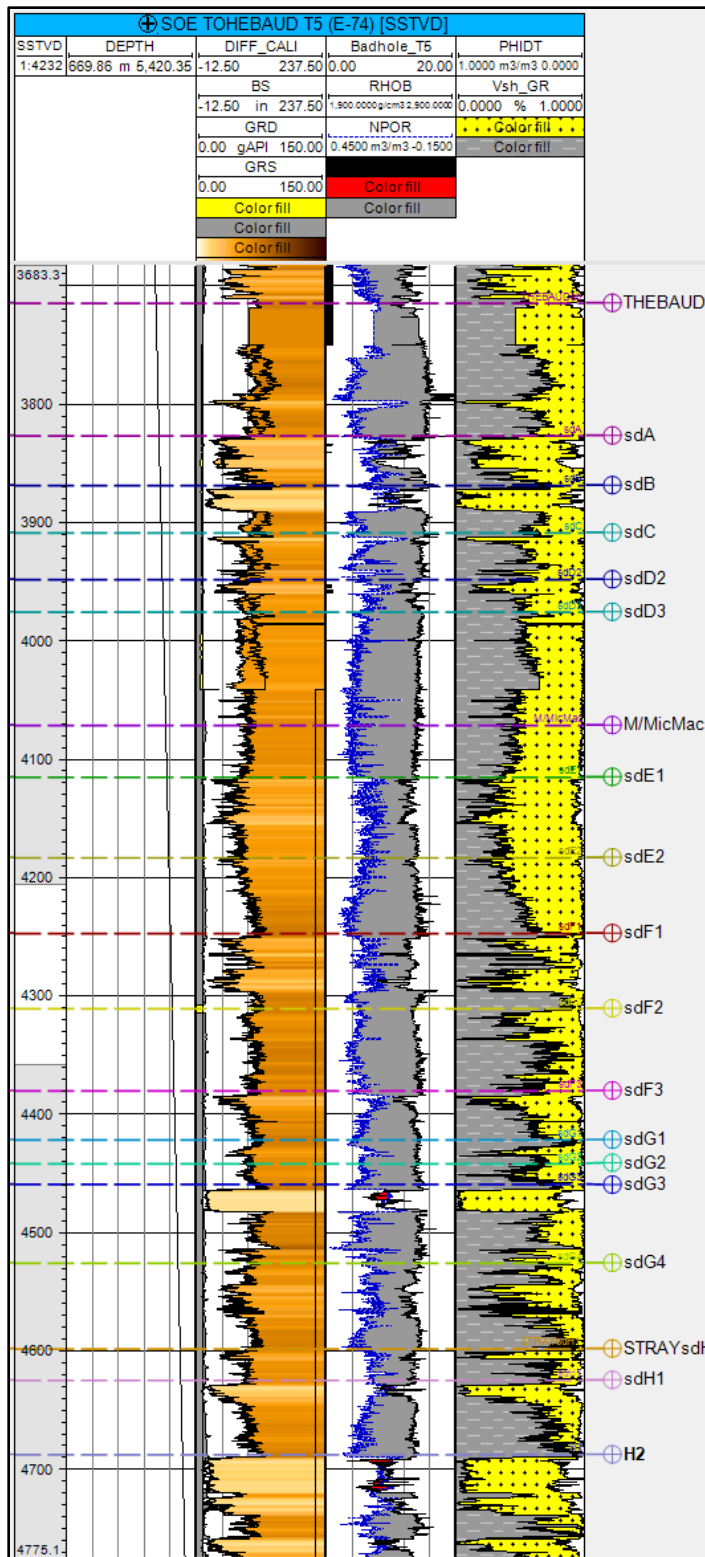


Figure 3.12: A figure of the Thebaud T5 well composite showing the alphabetic-numeric nomenclature used in the deeper overpressure interval below the Thebaud Shale. Sd = Sand.

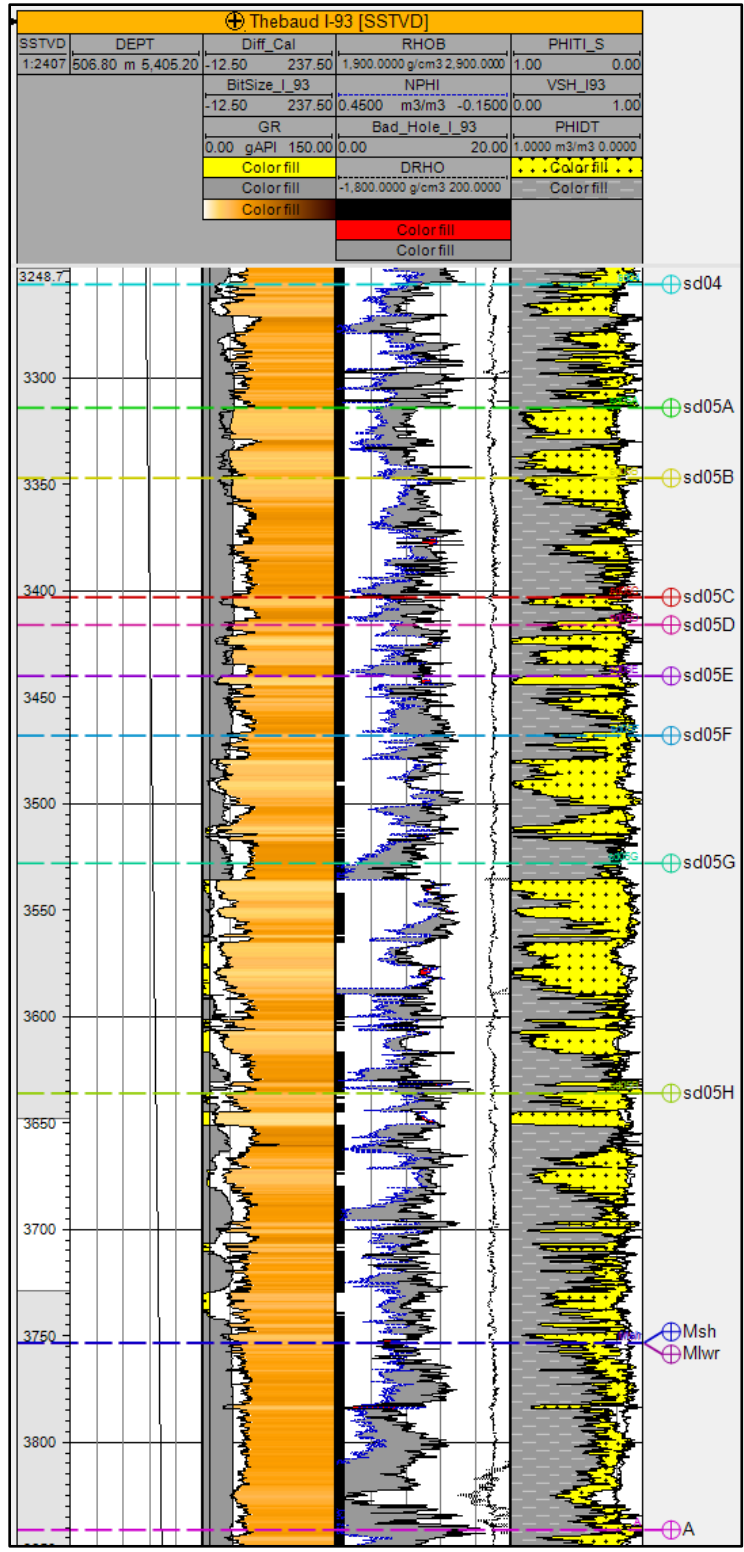


Figure 3.13: A figure of the Thebaud I-93 well composite showing the numeric-alphabetic nomenclature used in the shallow, hydro-pressure interval above the Thebaud Shale. Sd = Sand.

In the Adamant N-97 well, a different naming style was adopted by the previous workers (Figure 3.14, Figure 3.15 & Figure 3.16). Drilled two years after Thebaud E-74 (T5) well, the stratigraphic nomenclature adopted in the Adamant well showed an organized systematic naming convention. This style was adopted to match the age of the sands as indicated by their Cretaceous (C) nomenclature. During the regional study done by the operators (SOEP) in the early 2000s, the Cretaceous (C) nomenclature comprising the C1-C6 established after the ExxonMobil merger was assigned to the clastic reservoirs at Adamant. This naming style was a continuation of the stratigraphic convention adopted for the Jurassic where the (J) nomenclature was adopted. Based on this naming style, the J210 marker that preceded the C1 (deepest Cretaceous horizon at Adamant) was the last of the Jurassic markers.

The sequence stratigraphic naming convention used in Adamant N-97 comprised sand names C1– C6 used for the non-overpressured, Cretaceous aged sands with C1 being the oldest sand in the sequence. Interestingly, C1 marks the beginning of cleaning up sand sequence, from which Gamma-Ray log characteristics are different from the mainly blocky log signature of the underlying sequence that started from the J210 marker. Hence, the C1 marker is a significant stratigraphic marker (sequence boundary) that shows the transition from a dominantly regressive to a lowstand system. This character may be associated with a switch from a dominantly lower shoreface to an upper shoreface (fluvial, beach/estuary) type environment. Furthermore, intervals of hydrocarbon presence have been identified in logs just below the C1 marker and midway between the C1 and overlying C1A marker, which suggests some degree of trapping likely from the presence of a competent seal as seen in the Vsh log (Figure 3.14).

In the next sequence comprising the C5 to C1A sands, a combination of blocky and small order cleaning up log signatures, which suggests a transition from a lowstand to a transgressive/retrogradational system (Van Wagoner, 1991). The stratigraphic characteristics from logs between the C1 to C1A sequence show a different log signature from the overlying sand sequence between the C6 to C5 sequence. The C6 to C5 sequence is characterized by numerous blocky Gamma-Ray signatures separated by progressively small scale, cleaning upwards (highstand) systems.

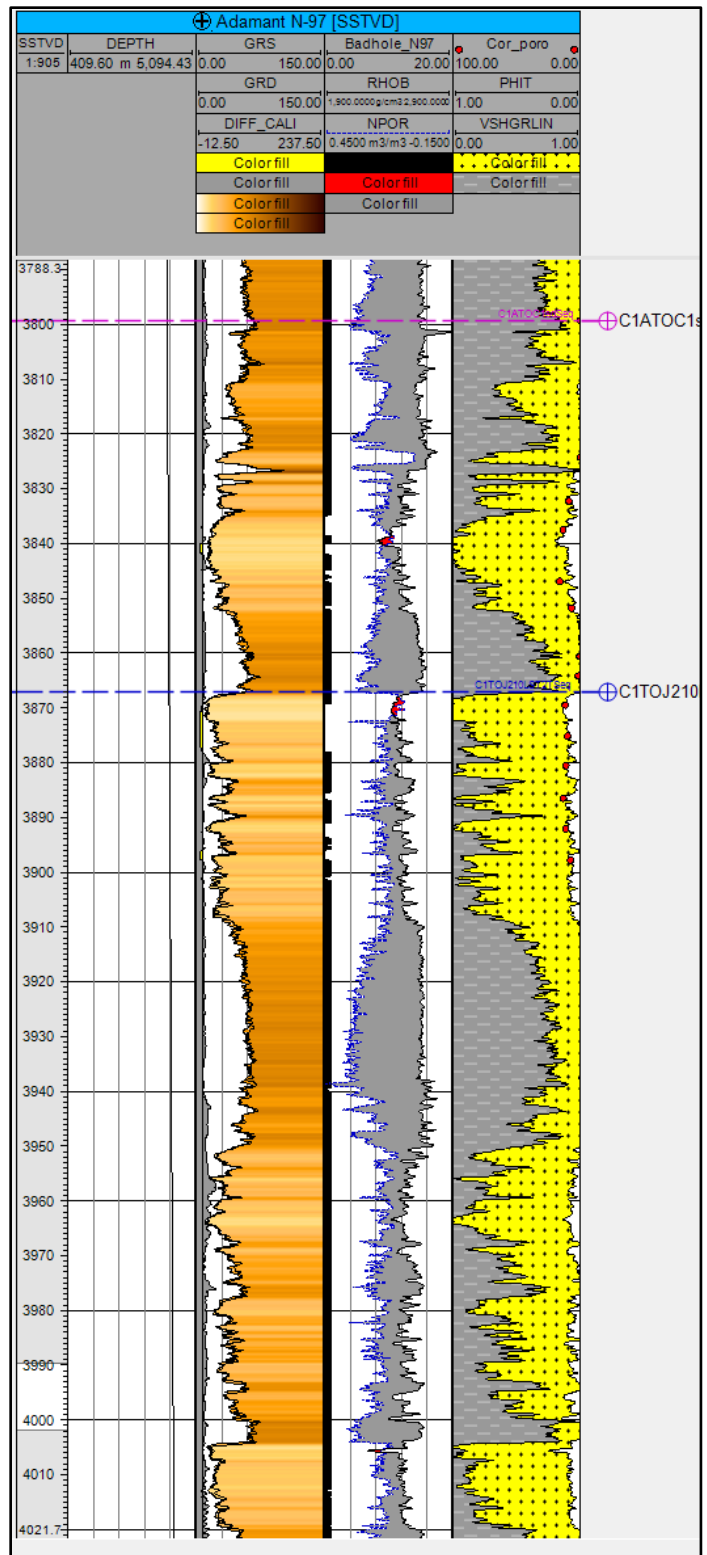


Figure 3.14: A figure of the Adamant N-97 well composite showing the Cretaceous nomenclature used for identifying the sands in the well. It shows the lowermost of the Cretaceous sands overlying the top of the Jurassic section marked by the J210 marker.

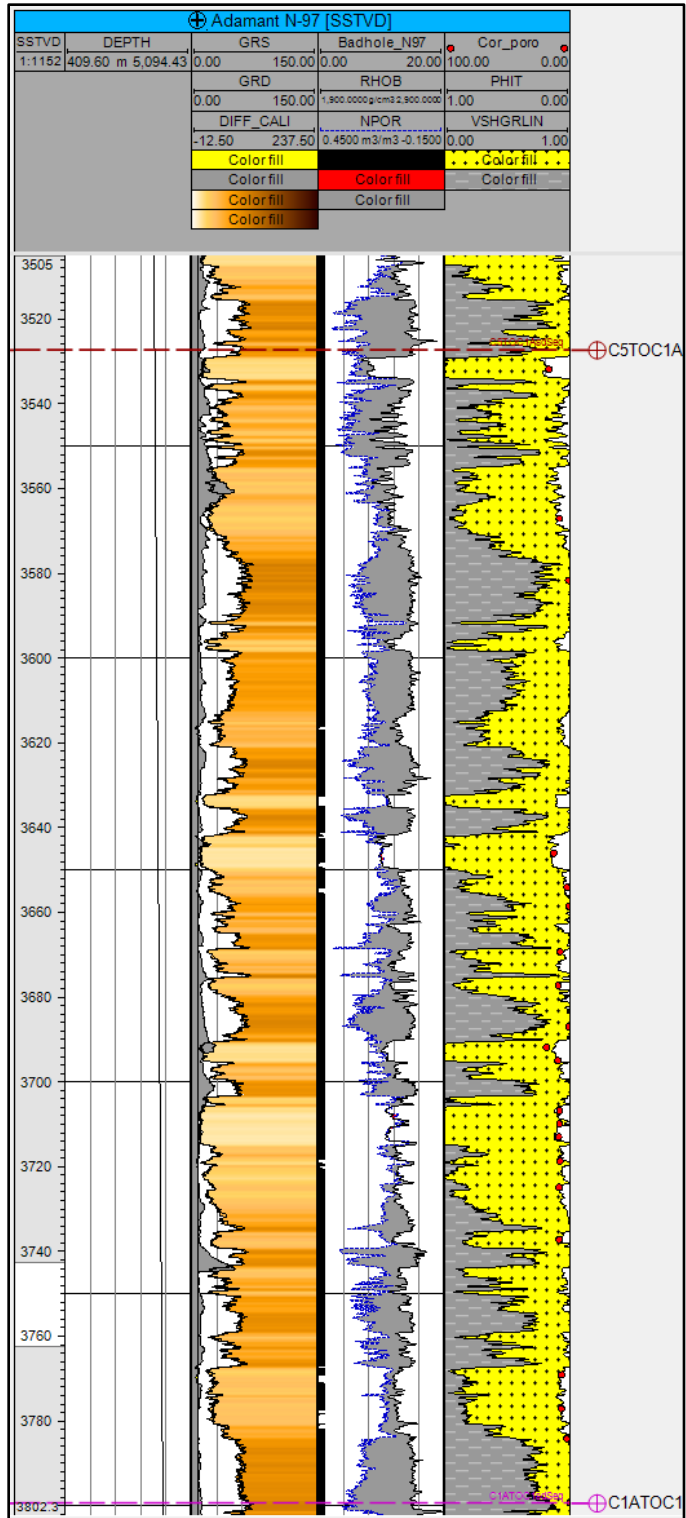


Figure 3.15: A figure of the Adamant N-97 well composite showing the next Cretaceous sand sequence (C5 to C1A) overlying the top of the Cretaceous C1A to C1 sand interval.

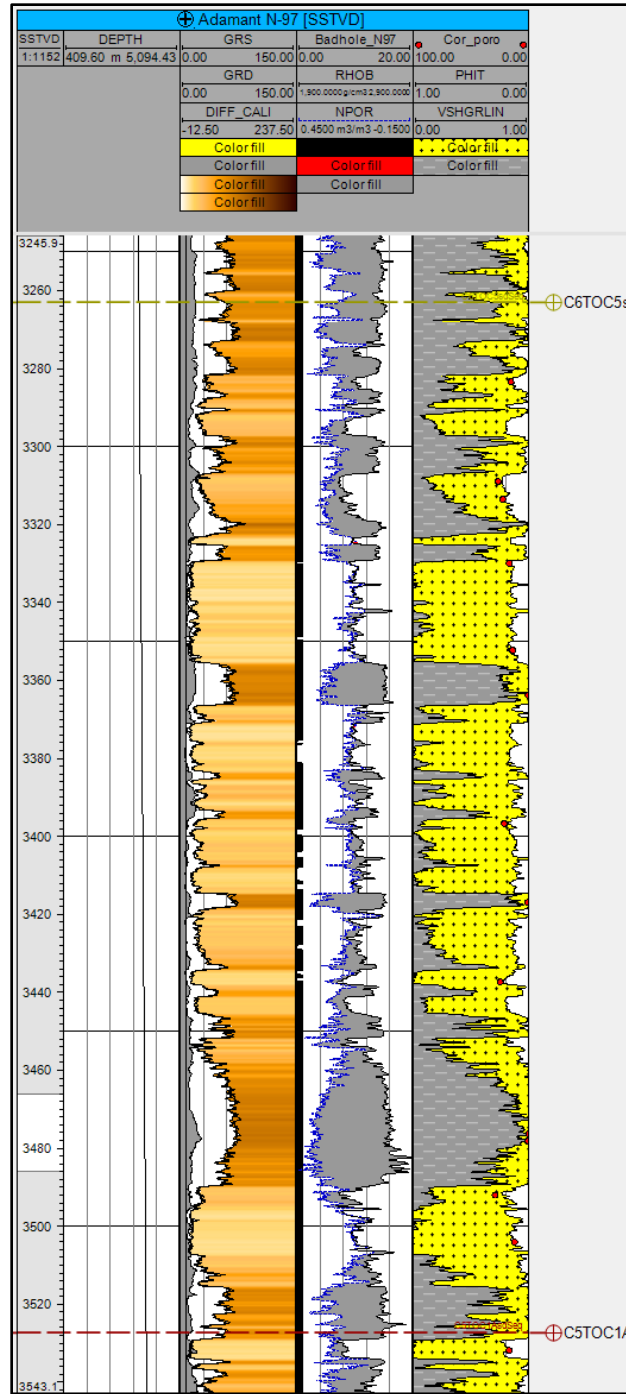


Figure 3.16: A figure of the Adamant N-97 well composite showing the next Cretaceous sand sequence overlying the top of the Cretaceous C6 to C5 sand interval.

In this study, the log characteristics in the Migrant N-20 well show a cleaning uptrend from the bottom of the well. Similar to the C6 to C5 sequence in the Adamant N-97 well the basal section is characterized by numerous blocky signatures separated by thin shale units (Figure 3.17). Building upon reservoir nomenclature from the Adamant and



Thebaud wells, the MK naming from seismic interpretation in this study was transferred over to the Migrant N-20 well. This contribution forms a basis of comparing the succession of key zones at Migrant and establishing a consistent reservoir stratigraphic template between the newer and older wells in Section 3.4.5.

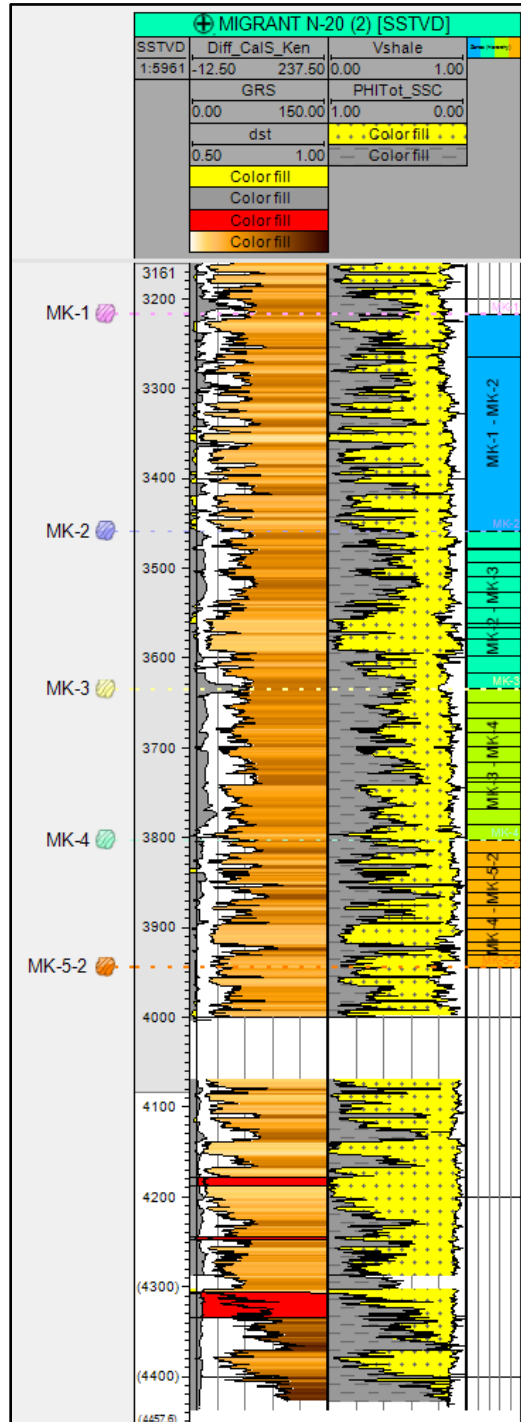


Figure 3.17: A figure of the Migrant N-20 well showing the tested zones below the well. The log pattern shows a generally cleaning uptrend around the base.

### 3.4.5. Well Correlation

Correlation of the reservoir tops and top of overpressure between the Thebaud, Adamant and Migrant structures reveal the overall stratigraphic character in each of the fault blocks (Chapter 3). Out of the seven hydro-pressured reservoirs, Sand 6 and Sand 5 (including 5a and b) belong to the Lower-Middle Missisauga Formation in the Thebaud fault block. In this study, a correlation of the normally pressured reservoirs 2, 4, and 6 to Migrant, first through Adamant where sand 2 and sand 4 are seen to overlie the uppermost Cretaceous sand marker (C6 – C5) while sand 6 is overlain by the marker (Figure 3.18).

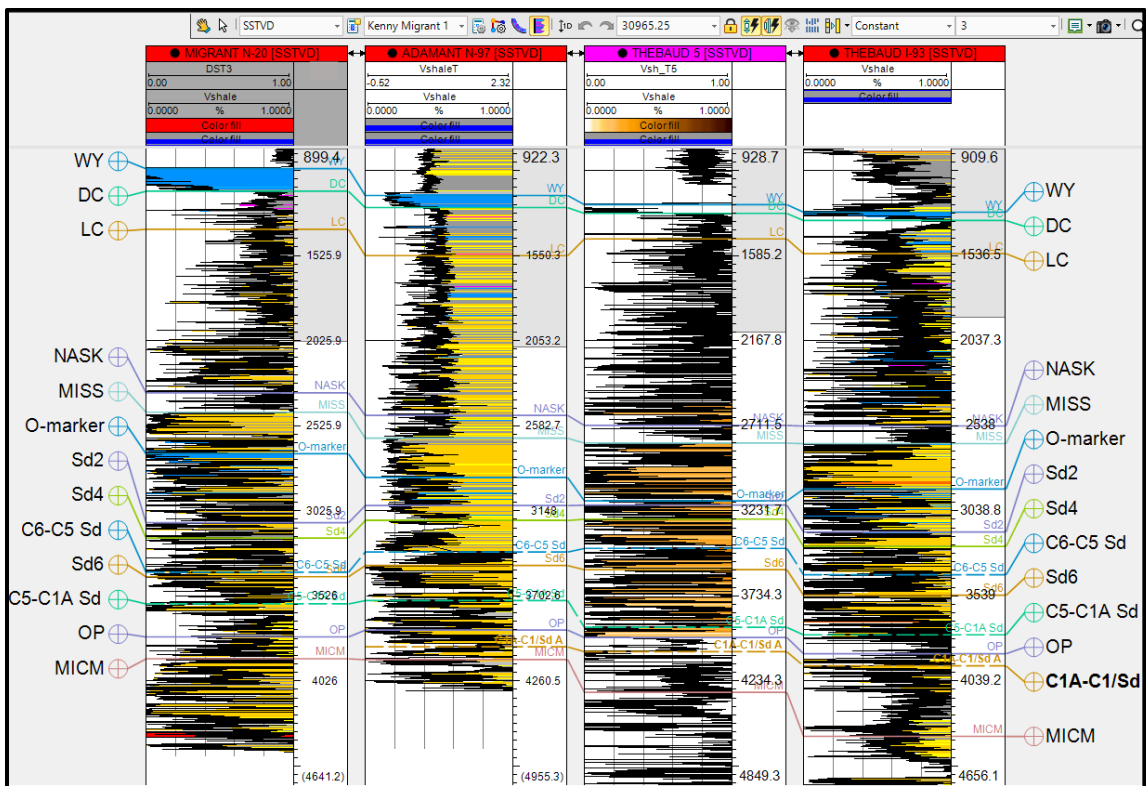


Figure 3.18: A well composite for three of the four project wells. For consistency, key reservoirs from the newer Thebaud wells were correlated through Adamant. The current display is based on measured depth (TVDSS). The Wyandott Marker was flattened as the datum before the subsequent markers were flattened on to aid the correlation of the following marker. In the figure, WY = Wyandot Formation, DC= Dawson Canyon Formation, LC=Logan Canyon Formation, NASK=Naskapi Shale, MISS=Missisauga Formation, Sd2=Sand 2, Sd4=Sand 4, Sd 6=Sand 6, C5-C1 Sd = Cretaceous Sand 5 to Sand 1A, C1A-C1 Sd= Cretaceous Sand 1A to Sand 1, OP=Overpressure, MICM=Mic Mac Formation.

From Migrant, the well correlation suggests that the deposition above the top of overpressure changes gently basinward within the overall stratigraphic sequence (Figure 3.19). Also, the absence of any equivalents to the top two overpressured Thebaud A and B sands supports the limited stratigraphic control in the area. In the Thebaud Structure, the top of overpressure occurs at a depth of 3800 TVD mSS in the Thebaud I-93 well marked by the Missisauga Formation Shale, which corresponds to the Thebaud Shale around a similar depth in the Thebaud E-74 (T5) well. Therefore, while the Thebaud Shale marks the onset of overpressure in the Thebaud rollover, and partly at Adamant N-97 well, it will be speculative to assume that an equivalent exists at Migrant that may have been missed by previous workers.

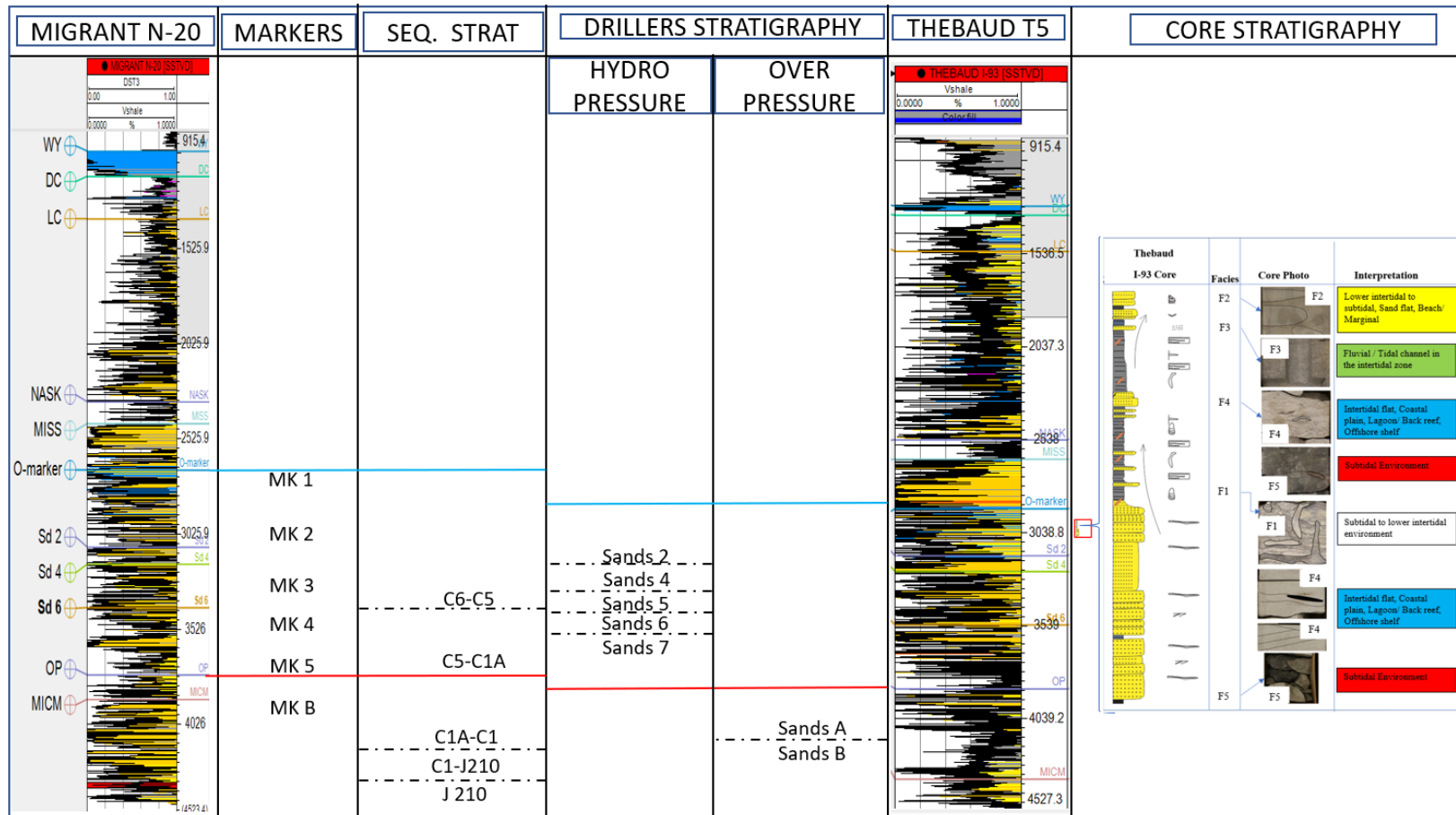


Figure 3.19: A figure showing the stratigraphic relationship between the Migrant, Adamant, and the Thebaud Field sands. Some of the names were adopted by Mobil Oil Canada up to the time of drilling of the development wells, which saw the switch to legacy Mobil sand names A-I used in the Thebaud T5 well. This nomenclature was also used in wells such as Olympia and West Olympia, all on-trend with the Venture Field. However, fields like South Venture show a return to sequence stratigraphic names used for the Cretaceous lowstand sands. Unlike South Venture, reservoirs at Thebaud were identified according to the legacy framework in which some of the legacy names have been split, based on cleaning uptrend, or their highstand/lowstand relationship.

## CHAPTER 4

### PETROPHYSICAL WELL LOG AND PRESSURE ANALYSIS OF THE MIGRANT EXPANSION TREND

#### 4.1. Introduction

This chapter introduces the workflow, datasets (mainly wells), and methods used to analyze well data in this project. Files for the key project wells available through the Data Management Centre of the Canada-Nova Scotia Offshore Petroleum Board CNSOPB were reviewed for suitable routine core analysis datasets.

Preliminary observations at Migrant from Gamma-Ray log show a very high net to gross section with very low Gamma-Ray responses, representing either sandstone or limestones. Detailed petrophysical analyses done on the Migrant N-20 well in key reservoir intervals are compared with DST results discussed further in this chapter. Well log analysis of the zone that yielded 10 million standard cubic feet a day (mmscf/d) indicates a similar porosity and water saturation to those in the two overlying tested intervals that encountered no flow. As a result, understanding the difference in reservoir characteristics between the three intervals is key. While the influence of an additional factor is likely, investigating differences in matrix porosity and permeability constitutes a principal focus of this chapter. From the investigation, an additional possible influence on permeability such as fracture permeability will be revealed by the calculated zone permeability thickness number from selected cut-offs. In doing this, the calculated permeability can be checked against results from flow testing.

Besides, pressure data from the four wells [(N-20, N-97, I-93, E-74 (T5))] were used in this study to guide the reservoir correlation as well as determining the connectivity of reservoirs across faults. This was done by plotting the pressure data against an elevation depth in TVDss (True Vertical subsea depth). A hydrostatic trend line was added to the data points to provide information on the fluids contained in a reservoir since different reservoir fluids are characterized by different gradient values. While the point of intersection between the different gradients marks the contacts of the fluids contained in a reservoir (Figure 4.1), pressure plots in this study was used to investigate the discontinuities in reservoir pressure resulting from a combination of the overburden sediment and the fluids contained in their pore spaces. This provides insight into similarities and differences

in stratigraphy between the newer Thebaud T5 E-74 and Adamant N-97 wells and the older Thebaud I-93 and Migrant N-20 wells. The use of these gradients will be used to demonstrate the succession of key zones (particularly the top of overpressure) from the distal to proximal shelf based on their associated pressure changes with depth as well as investigating if there is a stratigraphic control on the overpressure from the Migrant to Thebaud.

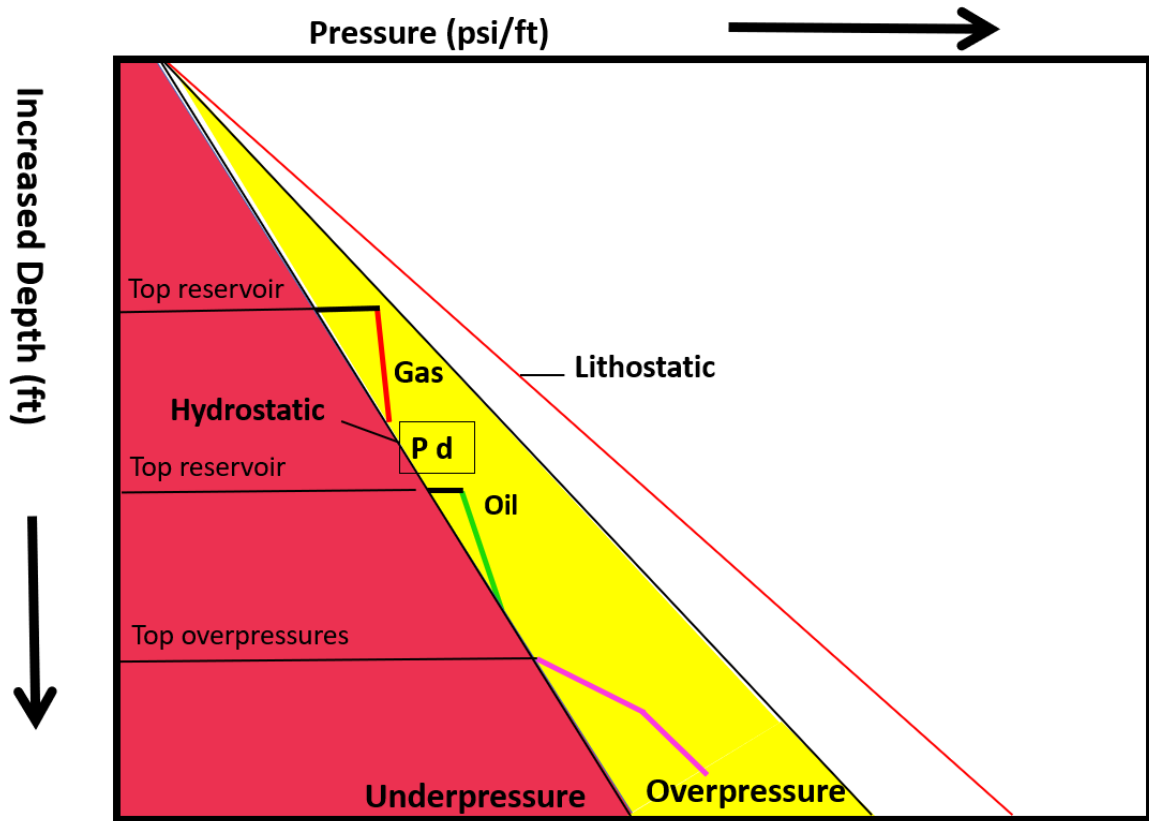


Figure 4.1: A pressure elevation plot (Modified from Schlumberger, 2020).

Based on the plot above (Figure 4.1), data that plot on or near the hydrostatic pressure gradient that increases at a rate of 0.433 psi/ft from sea level are indicative of connectivity referred to as “hydro pressured” reservoirs. Alternatively, pressures in reservoirs that plot at a lower pressure than a hydrostatic pressure line are said to be “under pressured”. While abnormally high pressures are “overpressured” and may signify differential sediment compaction, in some circumstances they are also indicators of a hydrocarbon charged system. The plot may be used to estimate fluid densities, determine fluid contacts, and identify fluid types in a reservoir. Graphically, water gives the highest gradient  $\sim 10.1$  kPa/m (0.44 psi/ft) followed by intermediate gradient of oil  $\sim 7.46$  kPa/m

(0.33 psi/ft). For gases, the pressure does not decrease per unit change in depth as quickly. Hence, the gas gradient in a gas-charged reservoir is characterized by a gradient of  $\sim 2.26$  kPa/m (0.1 psi/ft). While specific values of gradients are noted above, formation water gradients will vary according to the salt concentration in them, while oil, condensate, and gas gradients will vary accordingly to the concentrations of lighter and heavier hydrocarbon components. The intersection of trends such as water and gas gradients from formation pressure test values indicates the gas/free water contact. Under overburden conditions, a lithostatic gradient can be estimated by multiplying the hydrostatic gradient by 2.2-2.3, accounting for the overlying weight of the rock and fluid mass.

## 4.2. Data and Methods

### 4.2.1. Standardized Petrophysical Analysis Workflow

In this study, the petrophysical analysis was completed in a series of steps (Figure 4.2). Quality checks (QC) on digital wireline log curves used in this project. Renaming, re-splicing, and digitizing of wireline logs (in the absence of key curves) was possible through the assistance of Mr. Neil Watson of Atlantic Petrophysics Limited. We used screened, verified, and optimized raw curves of the project wells, and calibrated calculated reservoir parameters with core data beginning the analysis with shale volume (Vsh) calculation (APPENDIX B.2.1.). We used index values to numerically distinguish the sand and shale beds by comparing the Gamma-Ray log value at each depth to those of clean sand and shale endpoints selected for the various zones. The workflow was completed with a permeability (permeability index) computation.

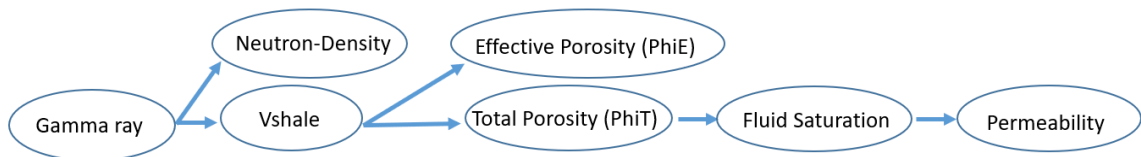
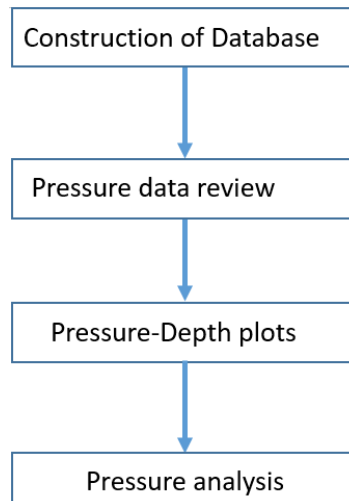


Figure 4.2: A flow chart of the analysis steps for the petrophysical deliverable for this project.

### 4.2.2. Pressure Analyses Workflow

For this study, the pressure analysis workflow (Figure 4.3) began with downloading the default pressure dataset for each well from the online BASIN database. The data were merged into an Excel spreadsheet containing repeat formation test RFT, MDT, and DST formation pressures.



*Figure 4.3: Pressure workflow used in this project modified after Skinner (2016). This was further integrated with the geocellular modelling workflow.*

After loading the pressure data in Excel, the data points were filtered by removing the ones interpreted to be invalid. The invalid data points were identified based on the operators reported flow instabilities including dry test results due to slow build or supercharging. Such conclusions were reached by examination of DST pressure buildup charts and MDT advisory reports. In a few cases, this interpretation could be reached only after a “normal” trend could be established in the data, and the actual pressure data buildup for suspect points examined in detail. The valid RFT reservoir pressures in the Migrant N-20 well, and reservoir MDT pressures in the Adamant N-97 well, and two additional wells that penetrate the Thebaud field were exported from Excel as .csv files and imported as a well point data set into Techlog™. These data points were then plotted on the x-axis against depth on the y-axis. The correct pressure-elevation reading in kPa/m was obtained by changing the regression format in Techlog™ to pressure as a function of depth.

## 4.3. Results

### 4.3.1. Petrophysical Analyses Results

Formation tops or bit size interval provided through BASIN database and final well reports respectively are a good way of dividing the well data into sections, which allows for more focus into the intervals of interest. Additional information used for selecting reservoir intervals was provided by the caliper log laid in the same track as the Gamma-Ray log (first track, Figure 4.4 below). The filter-cake buildup in yellow is an indication of a permeable zone and the grey areas may hint at areas of washout from caving of the



lithology and unreliability of porosity log readings. The first analysis step of the petrophysical workflow involved cross plotting the log data used to determine the volume of shale. In the composite (Figure 4.4), the Gamma-Ray log acquired with the sonic log (GRS) was used to compute the volume of shale (Vsh) in the Migrant N-20 well (sixth track from the left). The Vsh computation normalizes the Gamma-Ray log by comparison to sand and shale end points derived from a cross-plot of the Gamma-Ray and density logs. The computation is based on using a series of conditional statements in Petrel™.

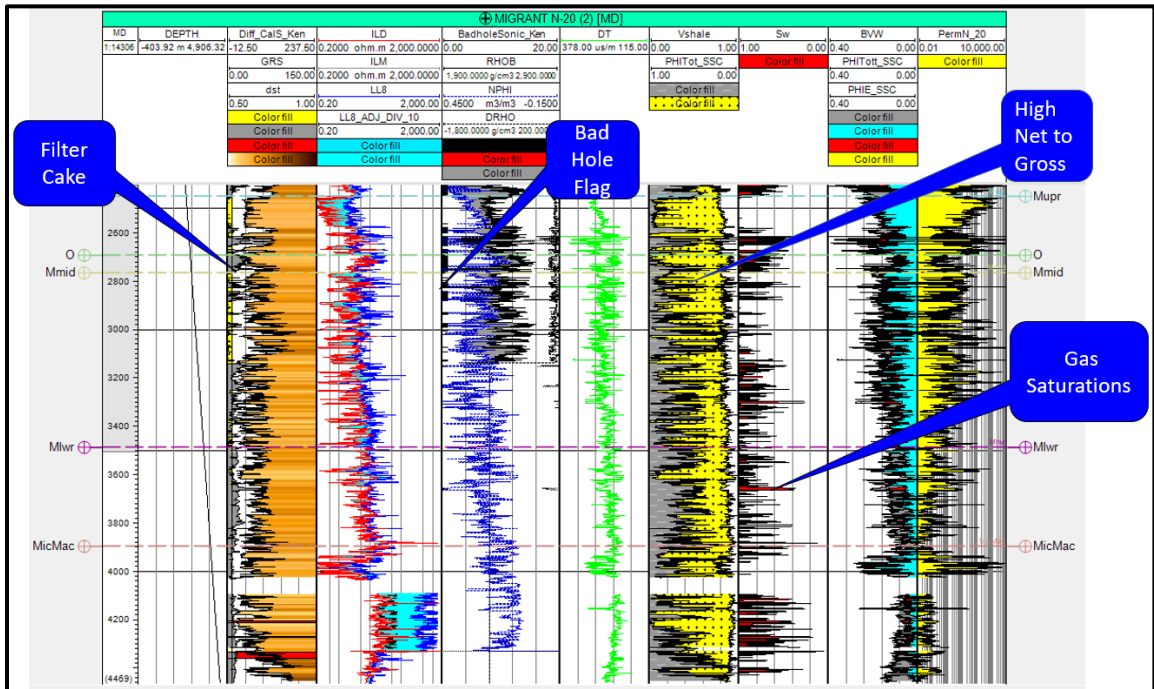


Figure 4.4: A formation evaluation composite plot Migrant N-20 with input curves in the first five tracks and output curves in the last four tracks. The density log has been scaled in density values (fourth track from the left) and the sonic log in sonic values (fifth track). The analysis curves, left to right are Vsh, water saturation, porosity, and permeability.

In the resistivity track (third tracks from the left), a separation between deep and shallow resistivity logs (highlighted in pale blue) with an increase in resistivity (rightward in track) from the shallow to deep resistivity curve can point to the presence of oil or gas, particularly when a conductive water-based drilling fluid has been used. While the separation between the deep and shallow resistivity logs can also be used as an indication of permeable zones, the continuous separation of these curves in the interval below 4000 m and above 4250 m MD is an anomaly likely related to tool error in the shallow resistivity tool and is discussed further in Section 4.4.3.1. Where available, bad hole flags may be

used in deciding if porosity logs having quality issues and should not be used. For intervals where the caliper log indicates borehole wash out “bad hole” flag is created (black bars on the left side of the neutron/density track). This alerts the viewer to the possibility that the total porosity curve created from the density log is often erroneously high. Given the incomplete density log coverage in the well, the bad hole flag was hardly used for this reason. With the absence of density logs from about 3137 m to total depth (TD), continuous porosity calculation was completed using the available sonic log. The sonic log can also be adversely influenced by the hole washout intervals indicated by the caliper log (3600- 3700 m MD), but to a much lesser extent than for the density log.

With increased overburden compaction down the well, the sands get tighter (have lower porosity) down the well and there is likely a substantial contribution of water from the surrounding shales that is in proportion to the percentage of shale present (Figure 4.5). Hence, by subtracting the shale porosity (the shale water component) from the total porosity an effective porosity is the result. From the basic porosity equation, the DT sonic value equivalent to the conventional porosity scaling of 0.40 to 0.00v/v was determined through estimating the total sonic porosity using the Wyllie equations. This considered the matrix value (180 us/m in the case of sandstones) and 620 us/m for water in the porosity. From this, the shale contribution/shale water component was subtracted from the total porosity (PHIT), resulting in an effective porosity (PHIE). Typical of deltaic environments, the decreasing net sand to gross interval thickness with increasing depth means that the DT value of shales will vary from the top to bottom of the well.

As a result, varying DT shale values were used for the shale correction based on bit run intervals in the Migrant well (including 311 mm = 260 us/m, 216 mm = 240 us/m, and 152 mm = 225 us/m). From the Wyllie equation (APPENDIX B.2.2.), applying a shale DT of 260 us/m, 250 us/m and 225 us/m for hole intervals of 311 mm, 216 mm and 152 mm, results to values of 0.178, 0.132 and 0.07 respectively. This suggests that the variation in shale porosity within the intervals compared to differences between them will depend on their shale volume (which they are multiplied by) given that larger values of shale volume will result to a reduced matrix porosity.

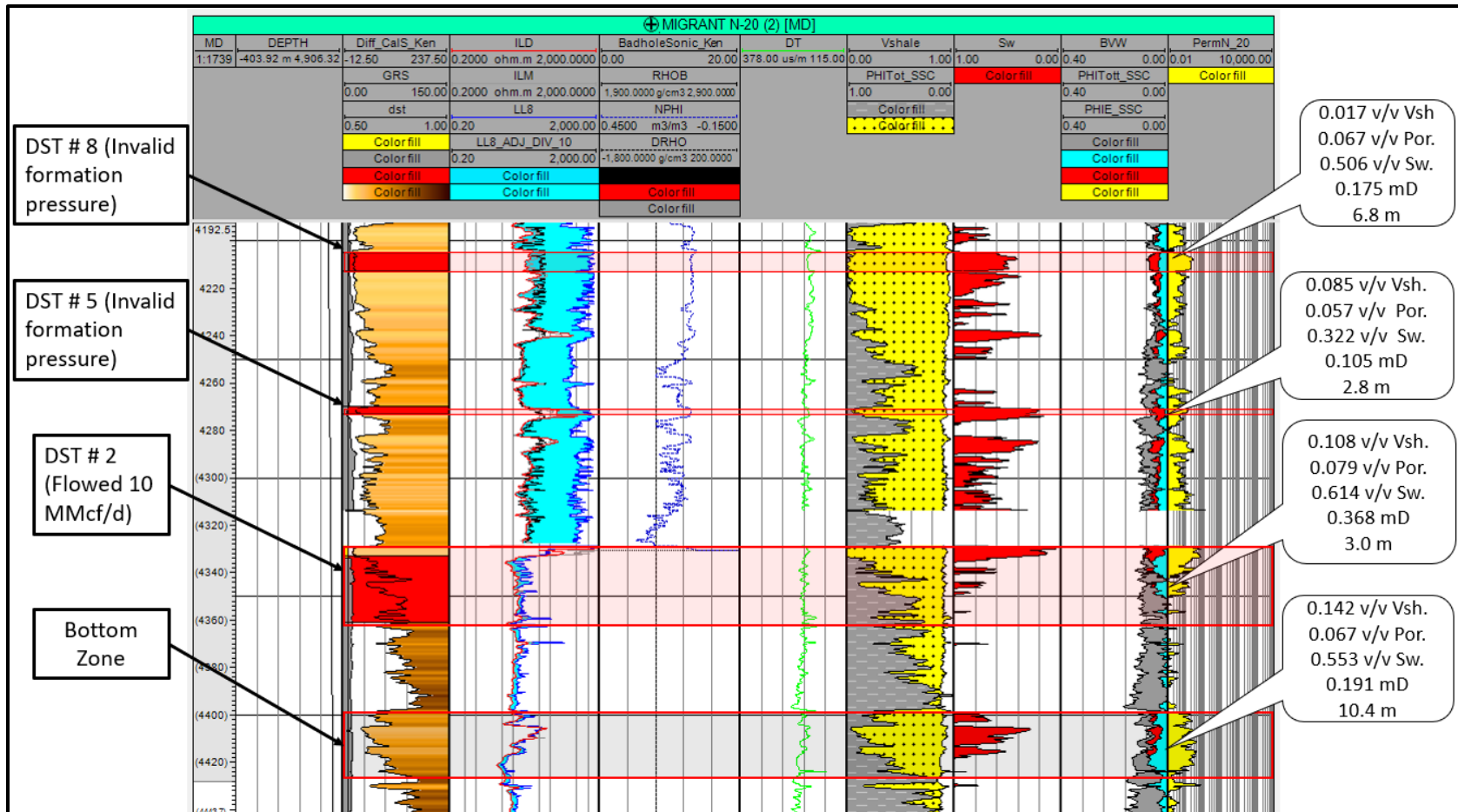


Figure 4.5: A formation evaluation composite from the Migrant N-20 well with input curves in the first four tracks on the left and output curves in the last four tracks on the right. The DST test intervals (test 2, 5, and 8) are indicated on the composites by the red bar in the Gamma-Ray track. The estimate in the labels averages interval values that satisfied the applied cut-offs. The thicknesses are DST test thicknesses. (As indicated in Section 4.4.4. the cut-off criteria used in establishing the values displayed in the labels in the above composite include  $Vsh \leq 0.25$ ,  $Porosity \geq 0.05$ , and  $Sw \leq 0.70$ ).

### 4.3.2. Pressure Analyses Results

Pressure analysis of reservoir units within the Mic Mac and Missisauga formations was completed on the four wells used in this project. RFT measurements from the Migrant N-20 and Thebaud I-93 wells as well as MDT measurements from the Adamant N-97 and Thebaud E-74 (T5) wells were combined in this study for comparison purpose. These data were downloaded from Basin Database combined with additional sources of information such as the CNSOPB well files. The pressure measurements were cross plotted against their TVD mSS depths in Techlog™, first by importing the pressure data as a .csv file before the respective pressures and their corresponding true vertical depth in subsea (TVD mSS) were plotted (Figure 4.6, Figure 4.7 & Figure 4.8).

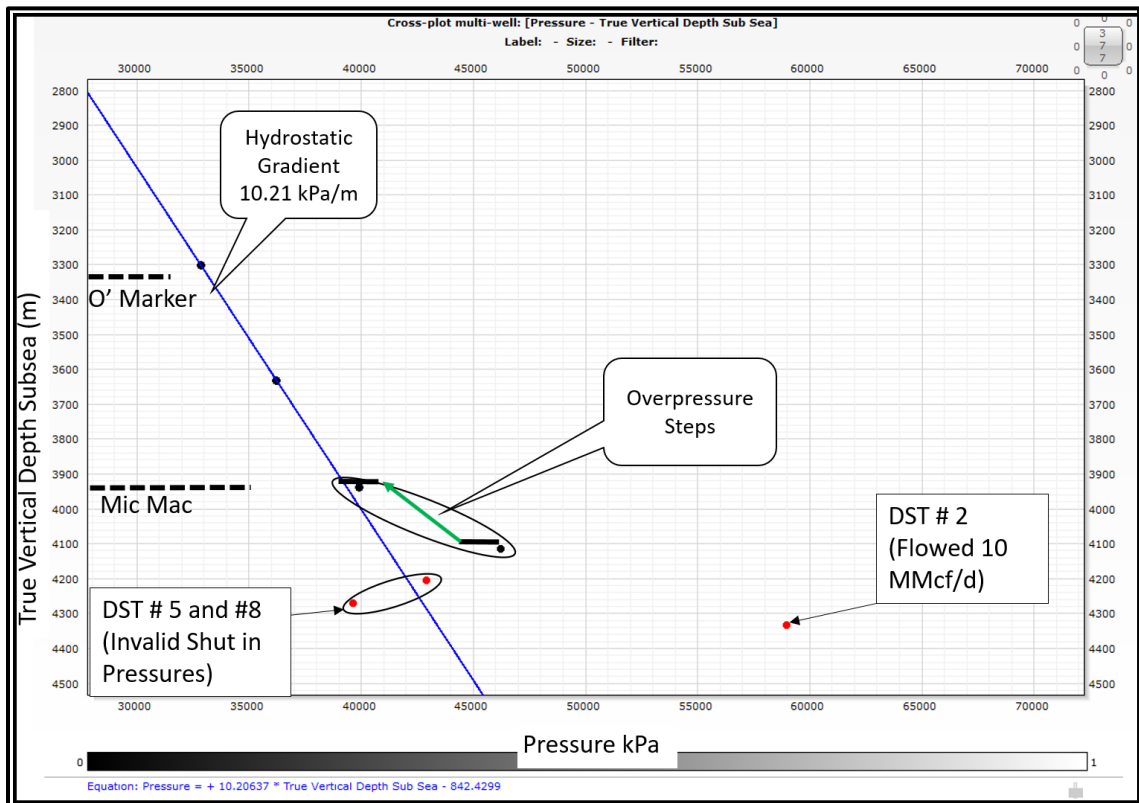


Figure 4.6: A pressure elevation plot of the Migrant N-20 well RFT data points (black) with DST point data in red. Based on an interpretation of the downhole pressure charts that showed pressure response versus elapsed time, two of the three test points posted in the BASIN database gave an invalid test result (apparent formation pressure believed not to be representative of the actual formation pressure) with the third, DST #2, being interpreted to be valid and indicating some reservoir fluid inflow. A shift in pressure trend is noticeable from the plot at about 3800 m where the pressure response increases significantly beyond that explainable by the hydrostatic gradient. Despite plotting observed test pressures on the figure, no true formation pressure was recorded for the DST #5 and DST #8 intervals.

In Figure 4.6 above, the blue line represents a hydrostatic pressure gradient with a value of 10.21 kPa/m, based on the top-most two RFT pressure points. There are four RFT points in the Migrant N-20 well. In the pressure elevation plot, anomalous pressure behavior from the hydrostatic trend can be seen for the points at around 4,000 m depth and greater. The two anomalous low-pressure values at greater depths on the plot characterize tight or low permeability sands in the test intervals, as obtained during DSTs #5 and #8. In Figure 4.7, steeper isolated clusters of Adamant N-97 (blue points) starting at 4,000 m depth may indicate tight, discontinuous reservoirs from that depth downward.

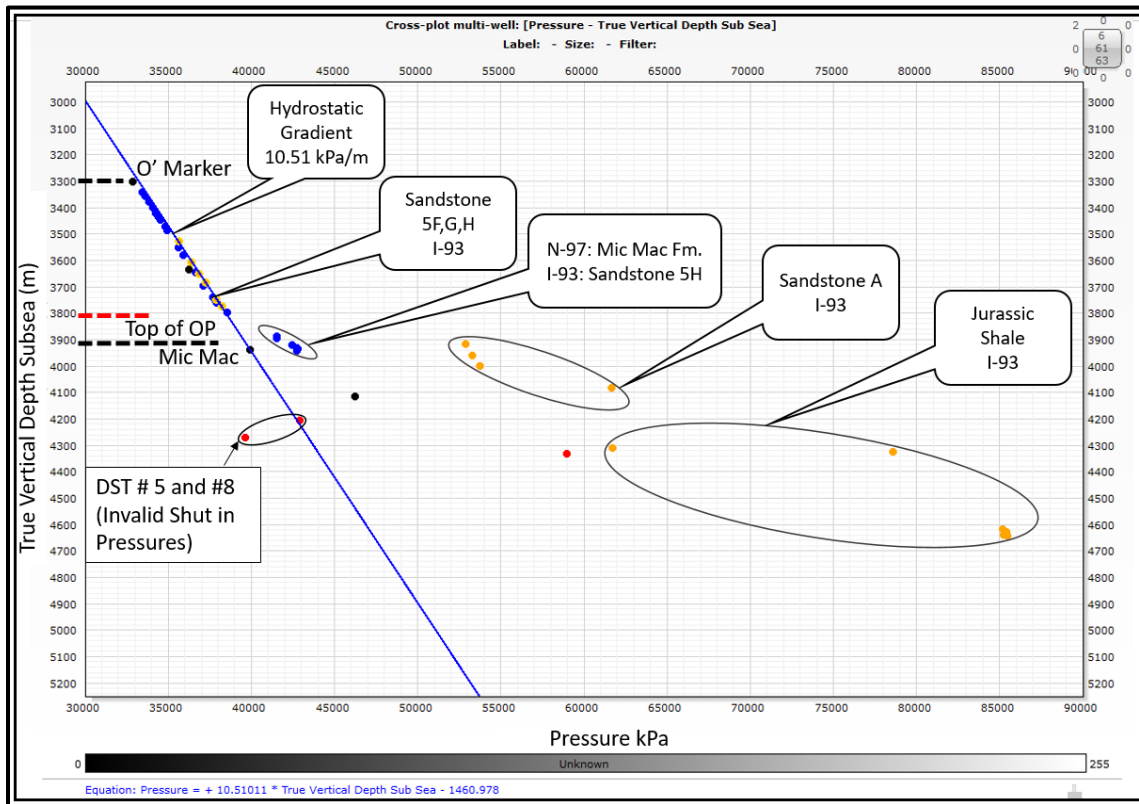


Figure 4.7: A pressure elevation plot of three of the four project wells. From the pressure-elevation plot, the Adamant N-97 points (blue points) and the Migrant N-20 points (black points) lie to the left of the blue gradient line and Thebaud I-93 pressure points to the right of it (yellow points). A new hydrostatic gradient was established for the I-93 points, which worked out to 10.51 kPa, higher than the gradients from the previous plot. Also, a second data point showing a significantly lower pressure for a similar depth may represent a possible slow build (invalid formation pressure) as seen in the case of I-93 pressure points around depths of 4300 TVD mSS.

Alternatively, they may provide gradients consistent with gas-filled reservoirs with the difficulty being that non-characteristic fluid gradients result when there is only one pressure point, or the pressure points are so close together that errors in gradient are

magnified. Adding a separate gradient will confirm the presence of gas with an expected gradient of 1-3 kPa/m. By default, the regression in Techlog™ is displayed in the form, “y in terms of x”. Setting the regression to the form “x as a function of y”, allows calculation of a pressure value for every depth in kPa/m. This was done to obtain an indicated hydrostatic gradient of 10.2 kPa/m in the case of Migrant N-20 in Figure 4.6, 10.51 kPa/m (for the three well average- N-20, N-97, and I-93) in Figure 4.7 and 10.3 kPa/m in Figure 4.8 (for the Thebaud E-74/T5).

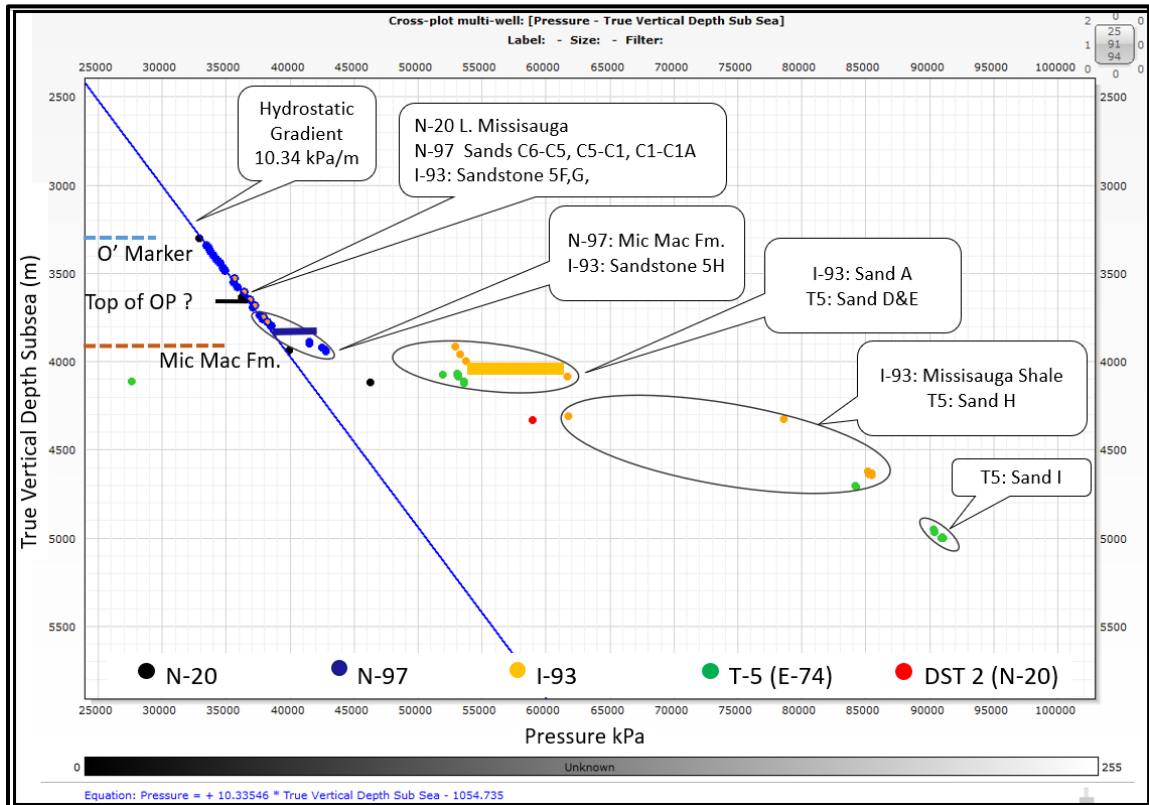


Figure 4.8: A pressure elevation plot of the pressure elevation data for four project wells. From the PE plot, there is a good indication of a normal (hydrostatic) pressure trend in the Adamant N-97 and Thebaud I-93 pressure data. The tops inferred on the left are based on the Migrant N-20 well. The black points are RFT pressure readings from the Migrant well. Showing where significant shales lie in the pressure plot helped in discerning the separation of reservoirs based on pressure changes with increasing depth. From the Adamant N-97 points plotted, it appears that the shifted gradients seem to indicate the presence of two different sand reservoirs at around 4000 m depth. This shift gives a likely indication of overpressure increases and pressure isolation between these two reservoir units. The green points (T-5/E-74) lie below the Thebaud Shale in that well and the pressure values at 4100 and 5000 TVDmss both confirm the presence of gas-charged reservoirs, and numerous semi-isolated, overpressure reservoir units.



Combining the TVD mSS depth of the lithostratigraphic well tops with the pressure plots allowed for a more accurate investigation of the inter-well flow zones. Also, DST data if available is useful in conjunction with the PE plot and well log analyses to increase the confidence of our interpretations. Comparing the individual pressure points against lithostratigraphic information helped to further improve the overall interpretation of the stratigraphic behavior with non-systematic increases in pressure with increasing depth. In Figure 4.8, there are significant increases in pressure with depth for the points from the Thebaud T5 and I-93 wells below 3950 TVDmss represented by the green and yellow points respectively, which is the depth at which the Thebaud Shale occurs. This may imply a downward decrease in the connectivity between reservoirs. Hence, it is likely that the formation pressures for the points between the onset of overpressure and well formation test data result from pressure releases (leakage) from deeper, discontinuous, and overpressured reservoirs. This leakage may be due to non-effective top seals in the reservoir units but may also be due to leakage between reservoir units juxtaposed across fault plane traces.

#### 4.4. Discussion

##### 4.4.1. Porosity and Permeability Relations from Core Data

For the wells used in this study, two routine core analyses reports containing porosity, permeability and fluid saturation estimates were reviewed to understand how the differences in physical rock characteristics (mainly grain size) impact influence the porosity-permeability relationship. Below, I summarise the project wells and extrapolate results to the Migrant N-20 well, which lacks core data.

**Thebaud I-93:** The top core #1 from the I-93 well is comprised of moderately to well-sorted, fine to medium-grained sandstones mainly sublitharenite and litharenite (Section 3.3.2.). The summary at the end of the core analysis report indicates a poor to fair intergranular weighted average porosity of 0.123 fracs (12.3 % equivalent) with an average grain density of 2673 kg/m<sup>3</sup> hinting at the presence of modest amounts of calcite cementation or accessory minerals (some pyrite). Besides, the core summary report reveals an average permeability of 242.566 mD recorded for this cored interval. Multiplying the porosity and permeability of each contributing core measurement by their respective core thicknesses and taking the cumulative of the product divided by the cumulative thickness

results in values of porosity and permeability that are very close to those results summarized in the core summary report (APPENDIX E.1.).

**Thebaud E-74 (T5):** Two main intervals were cored in the Thebaud E-74 (T5) well, an upper cored interval covering portions of the F3 core and a lower core covering portions of the H2 stratigraphic intervals. The **F3 sand** is comprised of moderately and poorly sorted, very fine to fine-grained sandstones mainly litharenite (Section 3.3.2.). The average porosity of 0.078 frac (7.8 % equivalent) and average grain density of 2701 kg/m<sup>3</sup> from the core summary report (APPENDIX E.1.) support the presence of some calcite cementation and accessory minerals (including siderite and pyrite). Based on the core summary report, the average recorded permeability of 0.44 mD reported for this interval was 0.23 mD higher than the cumulative interval estimates in this study (APPENDIX E.1.).

While the calculated porosity of the F3 interval in this study agrees with the core summary estimate (APPENDIX E), a noticeable difference exists in the cumulative permeability. On the other hand, the **H2 cored interval** comprises well-sorted, quartz-rich sands, mainly of subarkose and sublitharenite (Section 3.3.2.) with fewer accessory minerals. With an average grain density of 2658 kg/m<sup>3</sup>, the reported average porosity for the H2 sand is 0.157 frac (15.7 % equivalent), which agrees with the calculated porosity of the F3 interval in this study (APPENDIX E.1.). Similarly, an average recorded permeability of 146 mD in the core summary report for this interval agrees with cumulative interval estimates in this study (APPENDIX E.1.). Despite the average porosity and permeability reported for the I-93 Core 1, F3 and H2 sand cores, the cumulative porosity and permeability summations were done in this study for compare the apparent differences in how the values were arrived by the core lab and the approach taken in Appendix E.1. Interestingly, with the exception of the varying average recorded permeability of the F3 Sands and the cumulative estimate, there were no differences.

**Adamant N-97:** Considering the inadequacy of sidewall cores in the Adamant N-97 well to capture key depositional transitions, full diameter cores from the Thebaud wells were relied on for description and observation purposes. From a physical rock characteristic standpoint, the sidewall cores from the Adamant well are comprised of well to moderately sorted sandstones and silty sandstones mainly sublitharenite (Section 3.3.2.). With an average grain density of 2656 kg/m<sup>3</sup>, the grain size ranges from very fine to coarse-grained



(mainly very fine) with fair intergranular porosity occluded by cement (likely silica). The end of the core analysis report summarizes a porosity range of 1.9-27.2 % and a permeability range of 0.01-1660 mD for the cored range.

**Migrant N-20:** Given the absence of cores in the Migrant N-20 well, cuttings samples were relied on for physical rock characteristics. Cuttings from the Migrant N-20 well are comprised of moderately sorted, medium to coarse-grained sandstones. These are mainly Fe-sands, sublittarenite, and litharenite (Section 3.3.2.). Cuttings' analysis report suggests that the sands drilled in some sections are silty and argillaceous, with some coal. The presence of glauconite, calcite cement, kaolinite, and some silica overgrowths support the poor porosity measured for the sands in the well report. With average grain densities of 2650 kg/m<sup>3</sup> in the reservoirs that occur in the interval penetrated by the 146 mm drill pipe, the tested reservoirs at Migrant were more related in density to the 2658 kg/m<sup>3</sup> reported in the Thebaud H2 Sand and 2656 kg/m<sup>3</sup> at Adamant.

To avoid using the porosity/permeability values from just the overpressured reservoirs from the Thebaud field, all available core measurements for the project wells were compiled in one plot (Section 4.4.2.). The regression from the plot was applied to the Migrant and Adamant wells where there were no full diameter cores available. Compared to the linear function, a polynomial function would have been much suitable. This would have allowed for obtaining the best absolute values with regards maximums in the best quality reservoirs that plot on the higher end of the cross plot and minimums in the poor-quality reservoirs that plot on the lower end of the cross plot including core porosity and permeability measurements from the overpressured reservoirs.

#### 4.4.2. Porosity and Permeability Relations from Log Analyses

In this study, the porosity calculations from sonic log analyses were completed to produce an effective and total porosity in the Migrant N-20 well. The calculated effective porosity seemed to be better suited for a qualitative assessment of reservoir quality since it removes shale porosity contributions from the answer. In the seventh track of the composite in Section 4.3.1 comprising the total porosity, effective porosity, and BVW curve all on the same track, the shale water contribution is represented by the grey shaded area in the total porosity curve. This area is typically filled with shale-bound water, with the effective porosity components filled with various reservoir fluids and drilling fluid

filtrate. Furthermore, from the calculated sonic porosities, applying a 25% Vsh cut-off yields a porosity range of 5-10 % with a corresponding permeability range of 0.1– 1.0 mD- (based on regression of the core porosities and permeabilities).

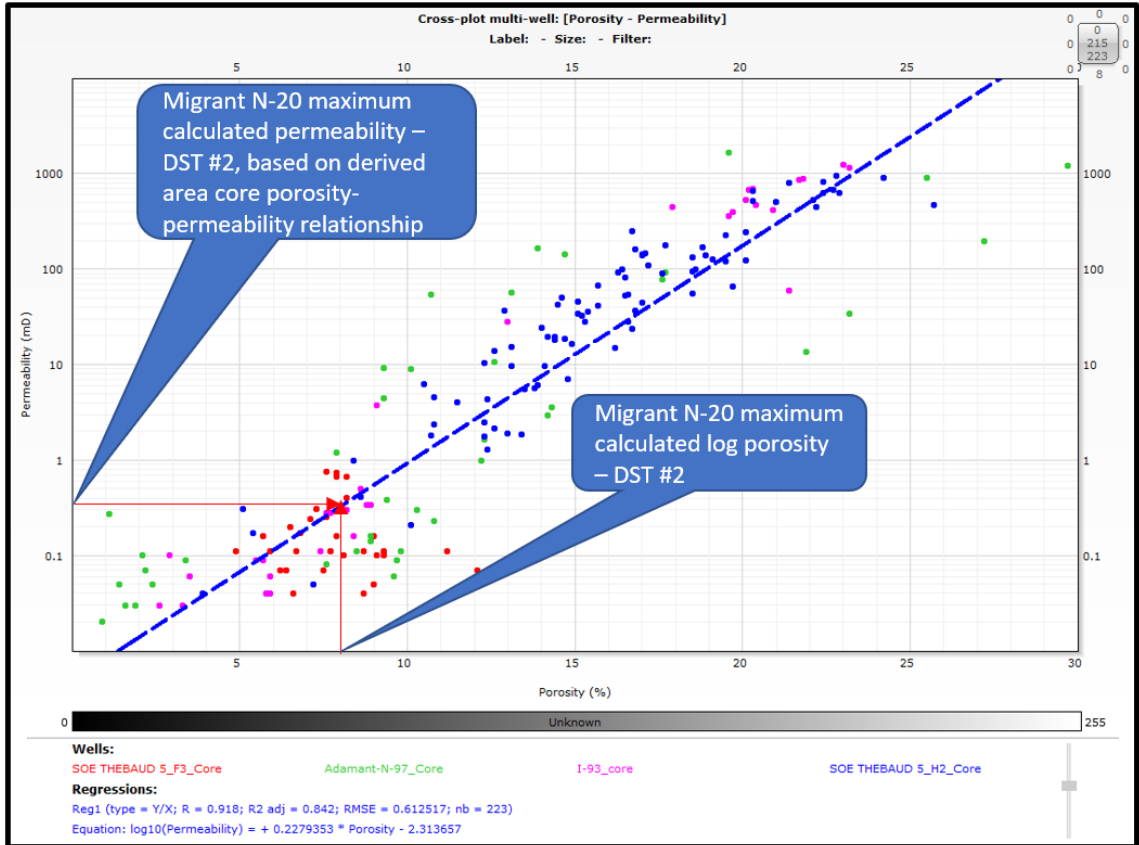


Figure 4.9: A cross plot showing the clusters and regression relationship through the project wells. The red lines indicate the equivalent permeabilities expected from the low apparent porosities calculated at the test level in the Migrant N-20 well.

The permeability estimation for the test intervals in the Migrant N-20 well was carried out using the area porosity-permeability regression equation. As observed from the cross plots of porosity and permeability above (Figure 4.9), core data acquired for the closest wells around the Migrant N-20 define the expected relationship between the magnitude of porosity and permeability. This is important since the magnitude of the averaged permeability over a reasonable reservoir thickness controls fluid rate. Considering that the test zones including the interval which flowed gas in Migrant N-20 lie on the low porosity-low permeability portion of the trendline, the high initial flow rate of gas occurring during DST #2 is likely a case of permeability enhancement through natural fracture from faulting (Section 5.4.2.). Especially, when the DST 32 net pay value of 8%

porosity extrapolated on the cross-plot results in an equivalent calculated matrix-based permeability of 0.3 - 0.4 mD, which seems low to support such high flow rates (10 mmscf/d).

### 4.4.3. Reservoir Fluid and Water Saturation Relations

#### 4.4.3.1. Reservoir Fluid Relations

Despite the importance of the resistivity log in determining the type of fluids contained in a reservoir, it also provided the added benefit of indicating a good quality reservoir. This is because the kind of fluid contained in an interval can be a function of its reservoir quality. A separation between shallow, intermediate, and deep resistivity logs can show intervals where drilling fluid filtrate has invaded into a reservoir, which indicates permeability (Davis 2010; Rider & Kennedy, 2011). This log signature may be attributed to the mixing and replacement of more conductive formation water in the near wellbore space by drilling fluid filtrate, which has a lower salinity. In recent times, water-based drilling fluid filtrates have been chosen to match or slightly exceed the salinity of the seawater in which the shales were originally deposited (Watson, pers comm. Oct. 2019). This ensures that the clays in the wellbore do not react to the drilling fluid, which may result in swelling into the wellbore initially, followed by dropping into the wellbore. Intervals, where this occurs, are indicated by caliper log values greater than the bit size used to drill that interval.

Additionally, it is possible that shale densities measured when logging with the density tool either measured reduced densities, or erroneous densities resulting from the swelling of shale and clay in intervals containing these constituents. In turn, this results in the density reading picking up the lower density drilling mud effect directly in front of the density tool as part of the total reading and indicating a value that is too low. As a result, care is taken when using a cross plot of the density and Gamma-Ray density logs to extract valid shale Gamma-Ray and density readings. As mentioned earlier, a separation of the resistivity logs can point to the location of porous, permeable intervals. However, with increasing depth, the amount of porosity is gradually reduced as observed from the Migrant N-20 well. This results in the overall resistivity baseline shifting to the right (towards high resistivity) since the resistivity reading is responding to both the conductivity of the amount of water-filled porosity and the porosity which is gradually reducing downward. While this

is true for most cases, this can not be said for the interval ranging from 4050-4300 m MD where the shallow resistivity curve has been displaced an order of magnitude (Figure 4.10).

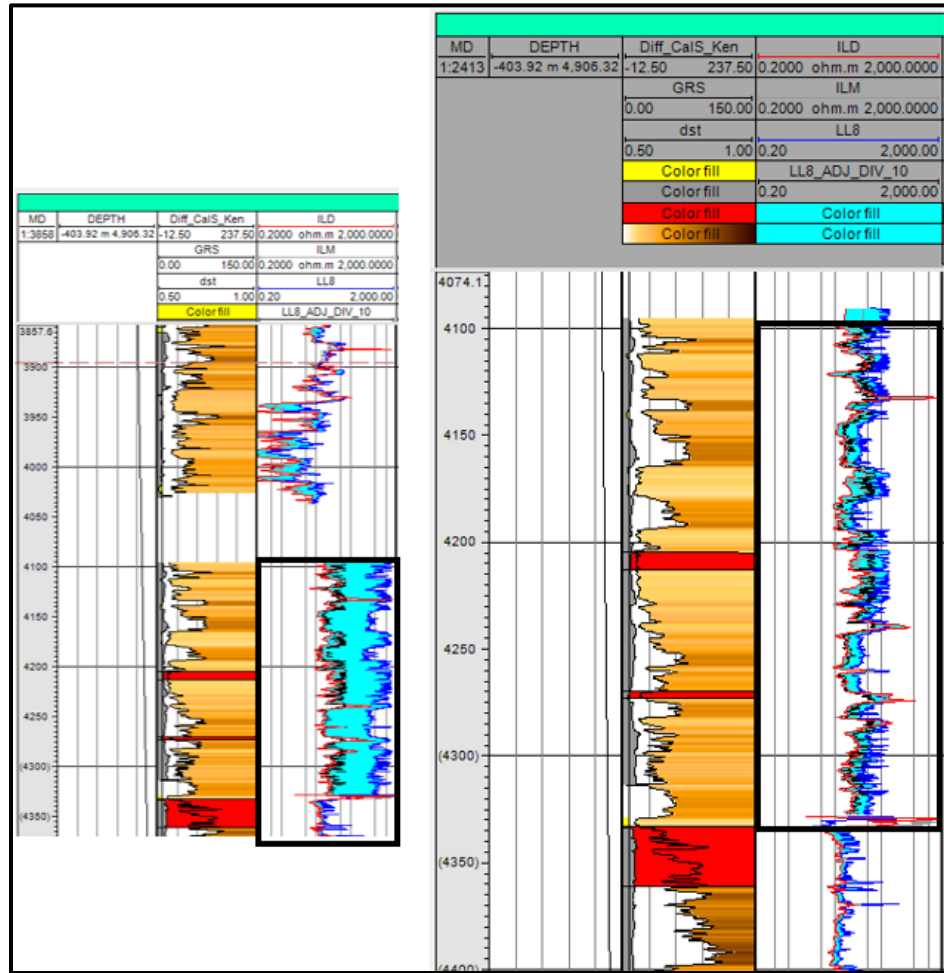


Figure 4.10: A well composite for Migrant N-20 showing the Gamma-Ray and resistivity tracks. The version on the left appears to show a continuous, highly porous and permeable interval from ~4100-4330 m MD, based on the separation of the shallow resistivity curve from the deep resistivity curve (interval in aqua). However, all other logs and rock indications point to the likelihood that the shallow resistivity tool was malfunctioning and reading a resistivity that is much too high. Comparisons with other data confirmed that permeable/non-permeable intervals were correctly identified and consistent with other data by dividing the logged shallow resistivity reading by an order of magnitude (x10).

This is likely related to a tool malfunction leading to an error in the shallow resistivity reading (Watson, pers comm. Oct. 2019). As drilling mud is pumped downhole during drilling, the resulting pressure within the column of drilling mud may both act to prevent the flow of formation fluids into the wellbore (Davis, 2010), and to push drilling fluid filtrate into the near-wellbore portion of encountered reservoirs. In such intervals, the

ILM (intermediate resistivity) becomes separated from the shallow resistivity log, which in turn is separated from the deep resistivity curve (having the lowest reading in this case) due to the invasion of the conductive water-based drilling fluid filtrate. By dividing the shallow resistivity log in the interval ranging from 4050-4300 m MD by 10, the shallow resistivity log appeared to return to the correct relative position from the medium and deep resistivity curves in Figure 4.10 above. This allowed for the three curves to again be used for a qualitative separation of porous and permeable intervals from the tight intervals.

#### 4.4.3.2. Water Saturation Relations

The resistivity of formation water ( $R_w$ ) is a function of two inputs - salinity and temperature (Davis, 2010). Of the various known ways of determining a formation water  $R_w$ , one of the most common approaches involves taking the formation water sample of known salinity and measuring its apparent resistivity under laboratory conditions (1 atmosphere of pressure and a temperature of 25°C). Once completed, this value can be converted to determine the lower  $R_w$  that this formation water will have as depth and temperature increase downward in a well. The Pickett plot (Section 4.4.3.2.; APPENDIX B.2.3.) proves to be a useful indirect method of determining the apparent formation water  $R_w$  in the observed reservoir interval in the well. This is because it uses the formation resistivities and porosities at reservoir conditions, which limits any possible error that may arise from converting a formation water salinity under laboratory conditions to  $R_w$  at downhole formation temperature. The common limitation is in the assumption that some portion of the reservoir interval under consideration in the well is truly 100 % water-saturated (mainly in shales). Additional simplifications include the use of default values for A, M, and N, which are key inputs in the Archie  $S_w$  equation.

In the presence of good quality logs, water saturation values in lower porosity intervals may become increasingly uncertain due to their porosities (comprising the main denominator in the Archie equation) being very low. As a result, the equation becomes unstable as low porosities are approached and may result in the resulting  $S_w$  achieving values greater than 1.0 (100%). When little is known of the reservoir rock type, assumptions may be made around the cementation exponent M, which is the slope of the selected 100% water wet points on the Pickett plot (Glover, 2012b). Most commonly, a default value of 2.0 is used. Given the limited amount of information available for the

reservoir types at Migrant N-20, this justified using a default A (intercept) and N (saturation exponent) of 1 and 2 while adjusting the 100% water wet line (Figure 4.11; Figure 4.12). Comparing the default value of N to the reported value of N from the hydro-pressured sand in the neighboring Thebaud I-93 SCAL report, a value of 2.25 from the Thebaud I-93 SCAL report (Mobil et al., 1987) was unusually higher. This suggests that the reservoir present in that core exhibited complex pore connectivity (Glover, 2009). This is likely related to increased silica or calcite cementation.

For water saturation  $S_w$  estimation using Archie's equation, and assuming 1, 2, and 2 as default values of A, M, and N respectively as conventionally used in Canada (APPENDIX B.2.3.), a formation water resistivity of  $R_w$  of 0.0275 was used the Migrant N-20 well in the Upper Mic Mac interval. This value was used since the resulting water saturation  $S_w$  was comparable to estimates from DST. This value can be compared to estimated Pickett plots values (Figure 4.11 & Figure 4.12). Based on the plots, the 100% water saturation line is extended to where it intercepts the 100% extrapolated porosity line and read off as an  $R_w$  value. Before this  $R_w$  value can be used in the Archie equation, it is converted to an equivalent value at formation temperature (@ 25°C). The Pickett plot data in this study have been divided between the Upper and Lower Mic Mac Formations to allow for a reasonable solution to  $S_w$  determinations that are consistent with other available data.

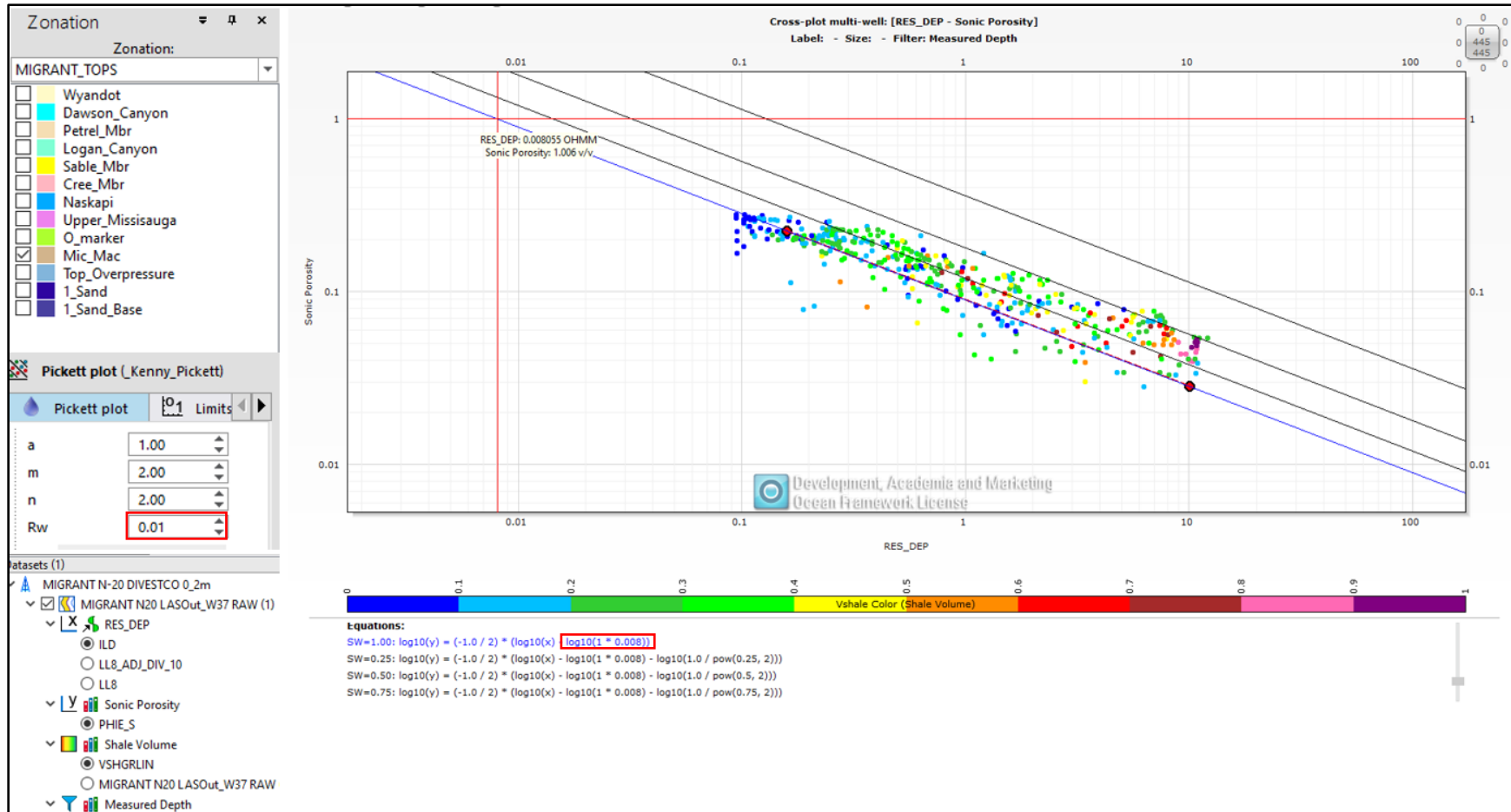


Figure 4.11: A Pickett plot of the Migrant well showing the plotted points from the Upper Mic Mac Formation (3935 – 4035m). The data points have been assigned a color scheme based on their relative shale volume contributions through which the 100% water line can be run through. Going with a 100 % water line through an average shale clean point cluster (blue data points), the  $R_w$  value results in about 0.01 (precisely 0.008). This value is much lower than the value obtained in the Lower Mic Mac in Figure 4.12.

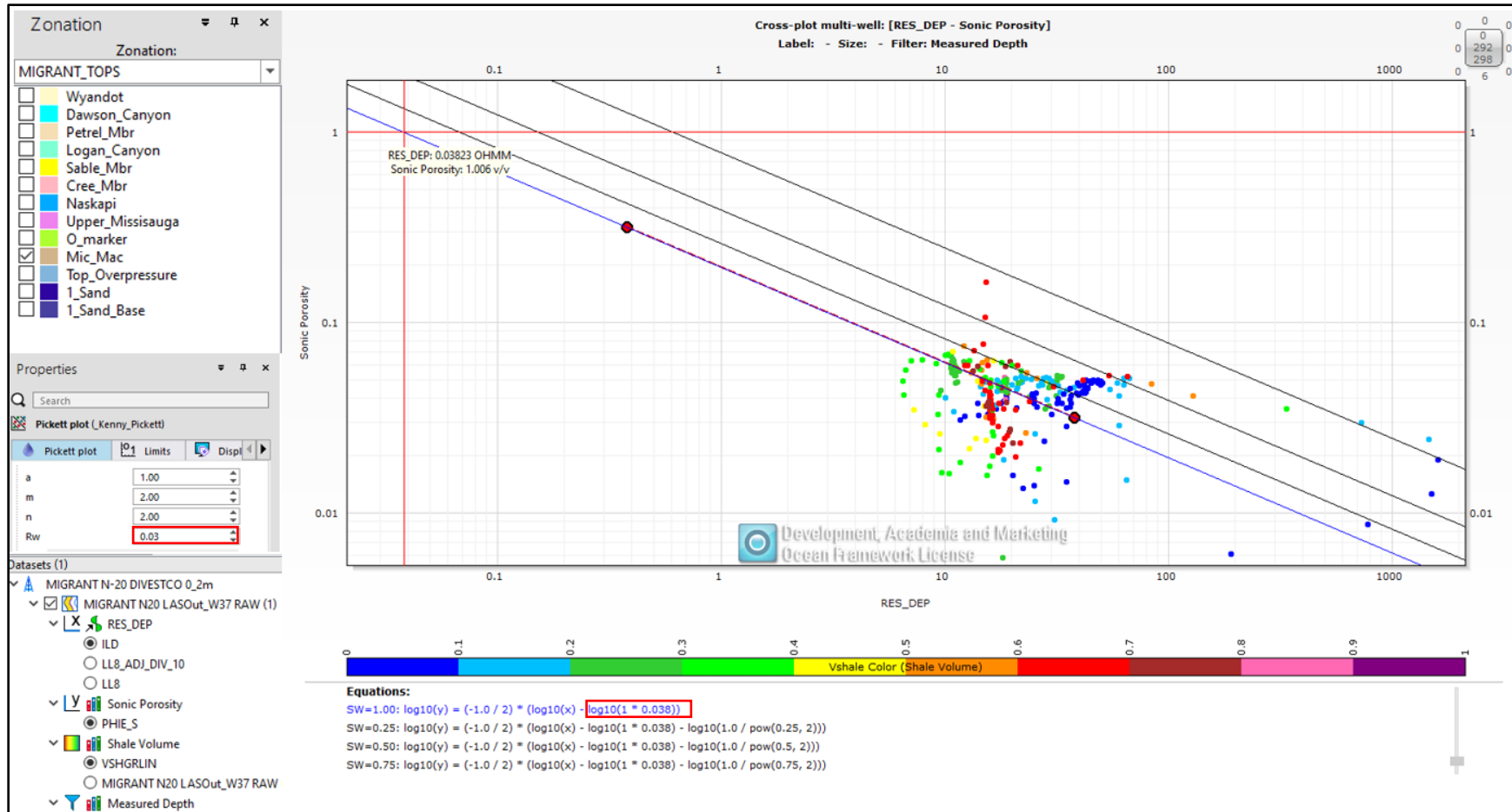


Figure 4.12: A Pickett plot of the Migrant well showing the plotted points from the Lower Mic Mac Formation (4100 – 4350 m). The data points have been assigned a color scheme based on their relative shale volume contributions through which the 100% water line is run. Placing the 100 % water line through the 100% water clusters (mainly blue), results in a formation  $R_w$  of around 0.03-ohm meter (precisely 0.038). It is speculated this higher  $R_w$ , relative to the Upper Mic Mac  $R_w$  is another confirmation of the isolation of the portion of the well below 4100mMD and the resulting over-pressure cells present.



In the area around the Migrant Structure, a formation  $R_w$  value of 0.064-ohm meter at 25° C was used by the operator in the hydro-pressured section of the downdip Thebaud Structure. This was derived from the water analysis tables in the Thebaud C-74 Special Core Analysis Report (Mobil et al., 1987) and corresponds to a water salinity of 140,000 ppm NaCl at 25° C formation temperature (Figure 4.13). A different value of 0.048-ohm meter at 25° C value was used by the operator in the overpressured sands below the Thebaud Shale as indicated in the SOEI (2000) Core Analysis Report. This corresponds to salinity of ~200,000 ppm NaCl at a formation temperature of 25° C (Figure 4.13). When compared to the Migrant Structure, the salinity values from both the hydro-pressured and overpressured intervals in the Thebaud Structures are more saline than the minimum case formation  $R_w$  of 0.03-ohm meter (at 113.8° C) obtained from the Pickett plot of the Lower Mic Mac Formation sands.

This formation  $R_w$  from Pickett plot considers the formation temperature measured at the corresponding logging depth in this case at 4100 – 4350 m in the Mic Mac Formation by the dual induction laterolog used in the Migrant N-20 well. A formation temperature of 113.8° C (from laterolog data published in the BASIN Database) combined with the formation  $R_w$  of 0.03-ohm meter obtained from the Pickett plot indicates a corresponding low salinity, high formation  $R_w$  (0.084 -ohm meter) estimate at a formation temperature of 25° C. This corresponds to a salinity value between 80,000 to 100,000 ppm NaCl. This resulting  $R_w$  is much greater than the values used by the operators in the Thebaud Structure (both hydro-pressured and overpressured). Possible reasons for the difference include actual changes in  $R_w$ /salinity across the area, errors in the selection of input parameters, or an apparent  $R_w$  for Migrant N-20 that is less than that observed in formation water analyses collected from fluid recoveries in wells in the area.

The latter is thought of as the most likely explanation. From an analysis point of view, while the apparent Pickett plot  $R_w$  likely represents a value between the actual formation water salinity and the drilling fluid filtrate salinity, it represents conditions in the near wellbore water filling portion of the reservoir at the time of logging. Consistent with this, a review of the operator well record indicates that the water cushion tested on the recovery of DST #2 had a salinity of ~38,000 ppm TDS. Also, analysis by operator appear

to have reached a similar conclusion, using a salinity of 90,000 ppm in their analyses that corresponds to an  $R_w$  of 0.18 -ohm meter @ 25° C reported in the Migrant Well report.

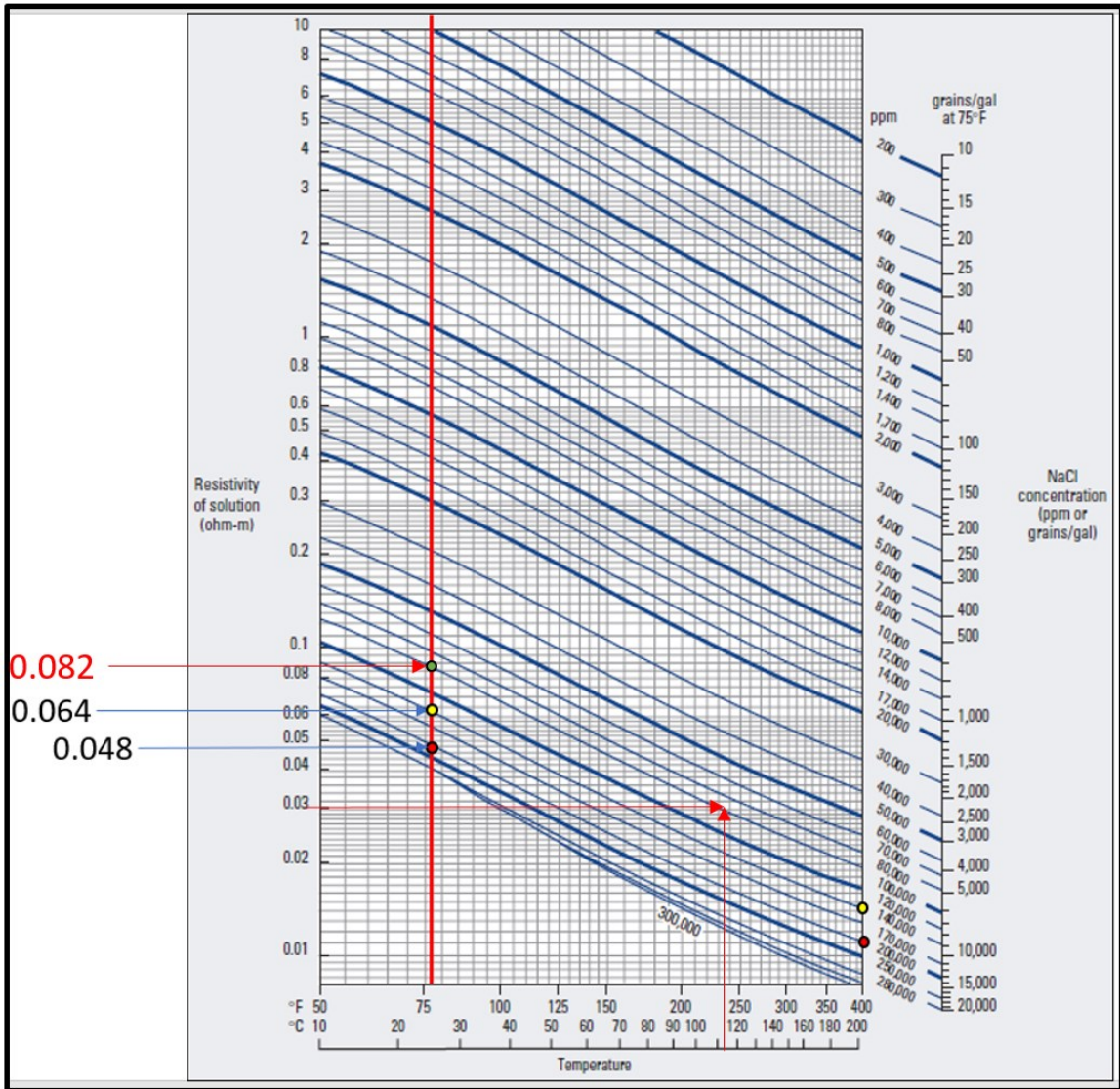


Figure 4.13: A chart is used for establishing the resistivity of an equivalent NaCl concentration at a specific temperature. There is a strong formation water ( $R_w$ ) dependency on both the salinity of the water and the temperature of the reservoir that it is found in (Schlumberger, 2009). In the hydro pressured Thebaud section that is contiguous with Migrant (yellow points), an average formation water resistivity of 0.065 was used by the operator with an estimated 0.048 derived for the over pressured zones (red points) according to their salinities at standard temperature (25 C).

Supporting this viewpoint is the suggestion of the water-based drilling fluid filtrate of lower salinity (higher resistivity) than the formation water in the area. Hence, large amounts are pushed into the formation in the process of maintaining a balanced mud

weight, which will prevent the inflow of formation fluids to the well during drilling. The addition of a conductive drilling fluid filtrate will act to reduce the resistivity recorded by the ILD curve used for the Pickett plot (and  $R_w$  selection) and subsequent Archie  $S_w$  calculations. The addition of higher resistivity water as a cushion during entry into the hole for DST #2 (reducing the possible effect of extreme pressure) around the open hole drill stem test interval, likely mixed with actual formation water before acquiring the resistivity logs later (Watson, pers comm. Oct. 2019). Also, the strong  $R_w$  dependency on salinity and temperature suggests that the reported 0.18 -ohm meter @ 25° C in the Migrant Well report result to about 0.071-ohm meter @ 100° C and roughly 0.06 @113.8° C.

While this value is close to that used by the operator in the Thebaud hydro-pressured reservoirs, it is less than the equivalent estimate of 0.084 @ 25° C from formation  $R_w$  of 0.03-ohm meter (at 113.8° C) obtained through Pickett plot. Thus, mixing has altered the true formation  $R_w$  in the reservoirs deep in the Migrant Structure. Given that water saturation estimates, the relationship between a calculated formation resistivity when/if a zone is saturated with formation water and that of the same formation having an observed greater formation water resistivity (e.g presence of hydrocarbons), the replacement of some of the water in the pore space through the invasion of water-based drilling fluid will alter the formation water resistivity.

Alternatively, it may be that the Lower Mic Mac section having a higher  $R_w$  indicates overpressure. Thus, a separate fault block may exist between this level and areas of significantly lower  $R_w$  values (with higher salinity) above 4035mRT where cross-fault communication permits a regional flow of highly saline formation water with no build-up of pressure. As observed in Figure 4.14, between 4100 - 4325 m, the portioning of the effective porosity curve by the BVW curve is similar to that seen between 4330 and 4400 m (including DST #2 producing gas) as well as in the reservoir below 4400 m. Lack of gas inflow in the intervals tested during DST #5 and DST #8 may point to a lack of the fracture porosity that likely resulted to flow in DST #2. Thus, this suggests the effective top of the hydrocarbon column is around 4100 m based on the fluid relations.

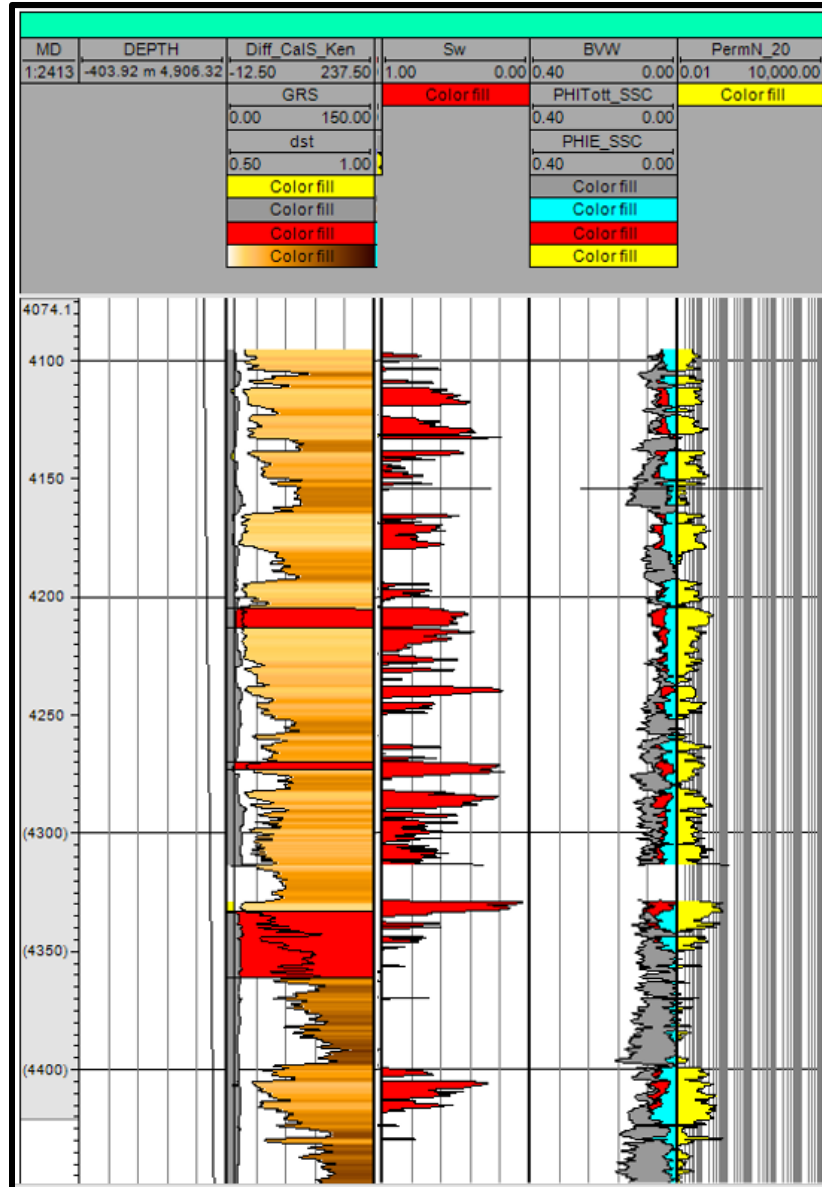


Figure 4.14: A well composite from Migrant N-20 showing the Gamma-Ray, water saturation (gas implied), porosity/BVW, and Permeability tracks. Given little apparent difference between the three indicated DST intervals (red shading in Gamma-Ray track), one explanation for the high gas flow rates over DST #2 (bottom test interval) is the presence of fracture porosity and permeability pointed to by DST pressure analysis, which shows a much higher  $kH$  product than indicated by the log analysis plot above.

#### 4.4.4. Net Pay Criteria

Net pay calculations determine the portion of an analyzed reservoir interval that is deemed capable of sustaining economic flow rates of contained fluid (hydrocarbons). A combination of  $V_{sh}$ , porosity, water saturation, and permeability may be used as criteria (APPENDIX E.2.) for establishing a net pay from the available reservoir intervals (Table

4.1; Table 4.2; Table 4.3). Generally, applying all four criteria reduces the net pay thickness, while increasing average porosity and permeability and reducing average Sw and Vsh, therefore resulting in a value that is much closer to those needed for a productive hydrocarbon zone. Results from this study show that where water saturation is not being used as a cut-off (Table 4.2 & Table 4.3), the elected cut-offs may result in a thicker reservoir segment that has attributes of porosity and permeability with low Vsh. A criteria involving Vsh alone results in an optimistic estimate in terms of thickness that meets the criteria (Table 4.3). In addition to obtaining a clean sand estimate from Vsh, portions of it might be of no use because of low Vsh or low porosity due to cementation. Therefore, it will be almost impossible to get an effective flow rate from such an interval since not all the portions of the indicated zones may be capable of delivering flow.

*Table 4.1: Net pay estimates from well log analysis of the Migrant N-20 well. The depths for the respective intervals are based on apparent drill pipe depth from which casing, perforations and openhole DST intervals were set. The Vsh, effective porosity and water saturation have been applied as the criteria for establishing the net pay thicknesses.*

<b>DST #</b>	<b>Depth of zone</b>	<b>Vsh. (v/v)</b>	<b>Total Porosity (v/v)</b>	<b>Effective Porosity (v/v)</b>	<b>Sw. (v/v)</b>	<b>Perm. index (mD)</b>	<b>Gross Interval (m)</b>	<b>Net. (m)</b>
DST 2	4333 – 4361 m	0.108	0.095	0.079	0.614	0.368	28	3.0
DST 5	4269 – 4273 m	0.085	0.071	0.057	0.322	0.105	4	2.8
DST 8	4205 – 4212 m	0.017	0.069	0.067	0.506	0.175	7	6.8
Bottom Zone	4400 - 4430 m	0.142	0.088	0.067	0.553	0.191	30	10.4
<b>Cutoffs</b>	_____	<b>&lt;= 0.25</b>	_____	<b>&gt;= 0.05</b>	<b>&lt;= 0.70</b>	_____	_____	_____

Table 4.2: Net reservoir estimates from well log analysis of the Migrant N-20 well. The depths for the respective intervals are based on apparent drill pipe depth from which casing, perforations and openhole DST intervals were set. The Vsh and effective porosity have been applied as the criteria for establishing the net reservoir thicknesses.

DST #	Depth of zone	Vsh. (v/v)	Total Porosity (v/v)	Effective Porosity (v/v)	Sw. (v/v)	Perm. index (mD)	Gross Interval (m)	Net. (m)
DST 2	4333 – 4361 m	0.135	0.090	0.070	0.739	0.251	28	7
DST 5	4269 – 4273 m	0.085	0.071	0.057	0.322	0.105	4	2.8
DST 8	4205 – 4212 m	0.017	0.069	0.067	0.506	0.175	7	6.8
Bottom Zone	4400 - 4430 m	0.145	0.088	0.066	0.597	0.196	30	12.4
<b>Cutoffs</b>	_____	$\leq$ <b>0.25</b>	_____	$\geq$ <b>0.05</b>	_____	_____	_____	_____

Progressing from a Vsh only criteria to a combination of Vsh and effective porosity, the average values stay fairly the same across the two tables (Table 4.2 & Table 4.3). Slight changes can be seen in the average Vsh and Permeability index of the DST 8 interval, which both increase with a fairly noticeable decrease in Sw from Table 4.3 to Table 4.2. Under the same criteria, the net pay estimated for DST 5 stayed the same with a slight decrease in the net pay values for the DST 2, 8, and bottom zones. Comparing the values between Table 4.2 (comprising Vsh and effective porosity) and Table 4.1 (comprising Vsh, effective porosity, and Sw), the average values for the DST 8 and DST 5 intervals remained unchanged in both tables. Also, the net thickness for both DST 8 and DST 5 intervals remained unchanged in both tables. However, the net thickness of the DST 2 and Bottom sand interval decreased. Also, while the Vsh and Sw in the DST 2 interval decreased, there was a noticeable increase in the porosities (especially effective) and permeability. In the bottom interval, except for average effective porosity and permeability which increases, the remainder is observed to decrease.

Table 4.3: Net clean rock estimates from well log analysis of the Migrant N-20 well. The depths for the respective intervals are based on apparent drill pipe depth from which casing, perforations and openhole DST intervals were set. The Vsh has been applied as the only criteria for establishing the net clean rock thicknesses.

DST #	Depth of zone	Vsh. (v/v)	Total Porosity (v/v)	Effective Porosity (v/v)	Sw. (v/v)	Perm. index (mD)	Gross Interval (m)	Net. (m)
DST 2	4333 – 4361 m	0.146	0.083	0.063	0.768	0.224	28	7.8
DST 5	4269 – 4273 m	0.085	0.071	0.057	0.322	0.105	4	2.8
DST 8	4205 – 4212 m	0.016	0.068	0.067	0.511	0.172	7	7
Bottom Zone	4400 - 4430 m	0.145	0.087	0.066	0.605	0.192	30	12.8
Cutoffs	_____	<= 0.25	_____	_____	_____	_____	_____	_____

Setting a porosity cut-off value of 0.05 or 5% (as in Table 4.1 & Table 4.2) results in a conservative result regarding net thickness in the DST 2 and bottom zones. With the total porosity being an indication of reservoir presence, the effective porosity determined the very best reservoirs that meet flow capacity especially with the addition of Sw in Table 4.1. As such, the apparent decrease in the total porosity with an associated increase in effective porosity between Table 4.2 and Table 4.1 is partly due to the absence of any cut-off applied to the total porosity. After adding a water saturation criterion, this resulted in a 4 m reduction of the net interval thickness from 7 m to 3 m as observed between Table 4.1 and Table 4.2 above. Hence, with each additional criterion applied, the result is a more conservative net thickness.

To achieve the flow of gas based on the log estimates, an uplift in permeability (possibly fracture related) in the tested zones was likely the case judging by the fault trace through the Migrant reservoirs in Section 5.4.2. This supports the elevated permeability thickness product of 301 mD-ft (91.75 mD-m) reported in the DST #2 pressure test report

from pressure buildup analysis. This value is higher than that obtained when the thickness from the net pay summation table for that interval is used. Considering the 3 m sand interval identified the net pay summations of the DST test interval #2 and the associated permeability of ~0.4 mD (Table 4.1), the resulting permeability thickness product of about 1.2 mD-m (3.6 mD-ft) is almost two orders of magnitude lower than the permeability thickness product in the well report. Additionally, this value is almost three times smaller than that derived for the same interval when the wireline depths were used to determine the reservoir interval in the summation table (Section 7.2.). This may be attributed to the fact that log analysis picks up the connected porosity and permeability whereas pressure analysis may include fracture contribution that would inflate the mD-ft/mD-m value (Watson, pers comm. Feb. 2021).

#### 4.4.5. Petrophysical Signature of Fault Contact in the Migrant N-20 Well

Considering the area where the fault crosses the wellbore, the petrophysical signature of the actual fault contact may prove to be speculative when petrophysical logs relied upon as the only supporting evidence. From a combining the depths of seismic markers mapped in this study with log composite, it appears that the fault crosses the well around marker 3 and marker 4, which corresponds to depths between 3780 - 3904 m. Generally, this is an area where the fault throw has reduced compared to the section higher up in the structure. Based on log configuration around these depths in the composite (3780 – 3904 m), there are thin gas zones with a decrease in permeability and separation in the resistivity log across a shale unit around 3835 m marked by a red line (Figure 4.15). This hints at the speculative nature of relying on petrophysical logs as the only supporting evidence.



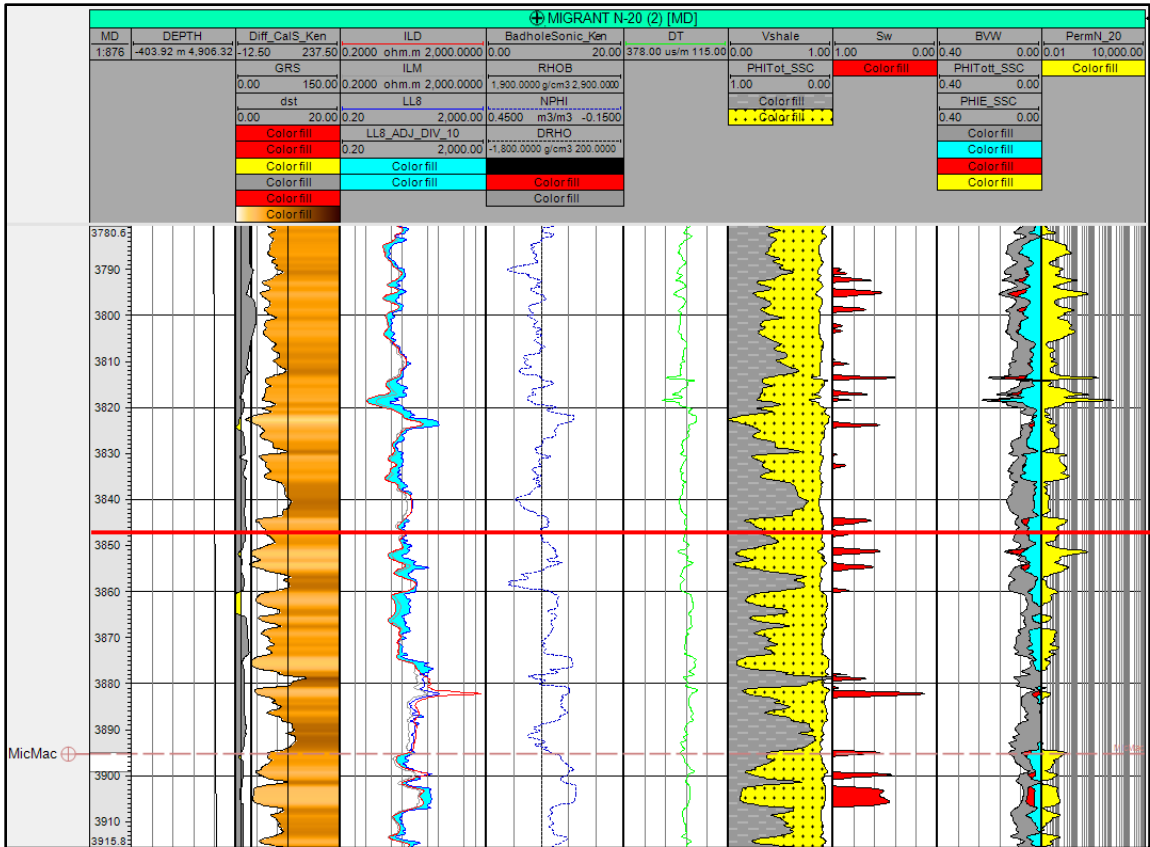


Figure 4.15: A log composite of the general area thought to be intersected by the fault in the well 3780 m – 3910 m.

Looking at all other sources of information to either support or refute the log characteristics of the area of the well intersected by the fault, other log signatures as well as mud gas indication may become useful. In the absence of other information, the fault crossing might be just above 3820 mRT (12583 ftRT) indicated by the blue line. This is supported by a downward spike to lower resistivities for both the shallow and deep resistivities and similar spiking on the sonic log. However, there is nothing to support this from mud log signatures (Figure 4.16). Whereby fractures associated with faulting may cause localized spiking of mud gas responses – there is no apparent evidence. Mud gas spike at ~12450 ftRT (~3795 mRT) as well as in the following 50 ft with notes of 4 different flow checks in areas where the drillers suspect an influx of fluids to the wellbore might be consistent with crossing open fractures or a fault containing formation fluids (red box).

The next deeper event on the mud gas log where a significant (though sustained) mud gas increase occurs is at ~12780 ftRT (~3895 mRT) indicated by the red line. In summary, there are log responses that might be consistent with crossing a fault trace at

around 3817 mRT, but there are mug gas responses that might be consistent with it at ~3795 mRT.

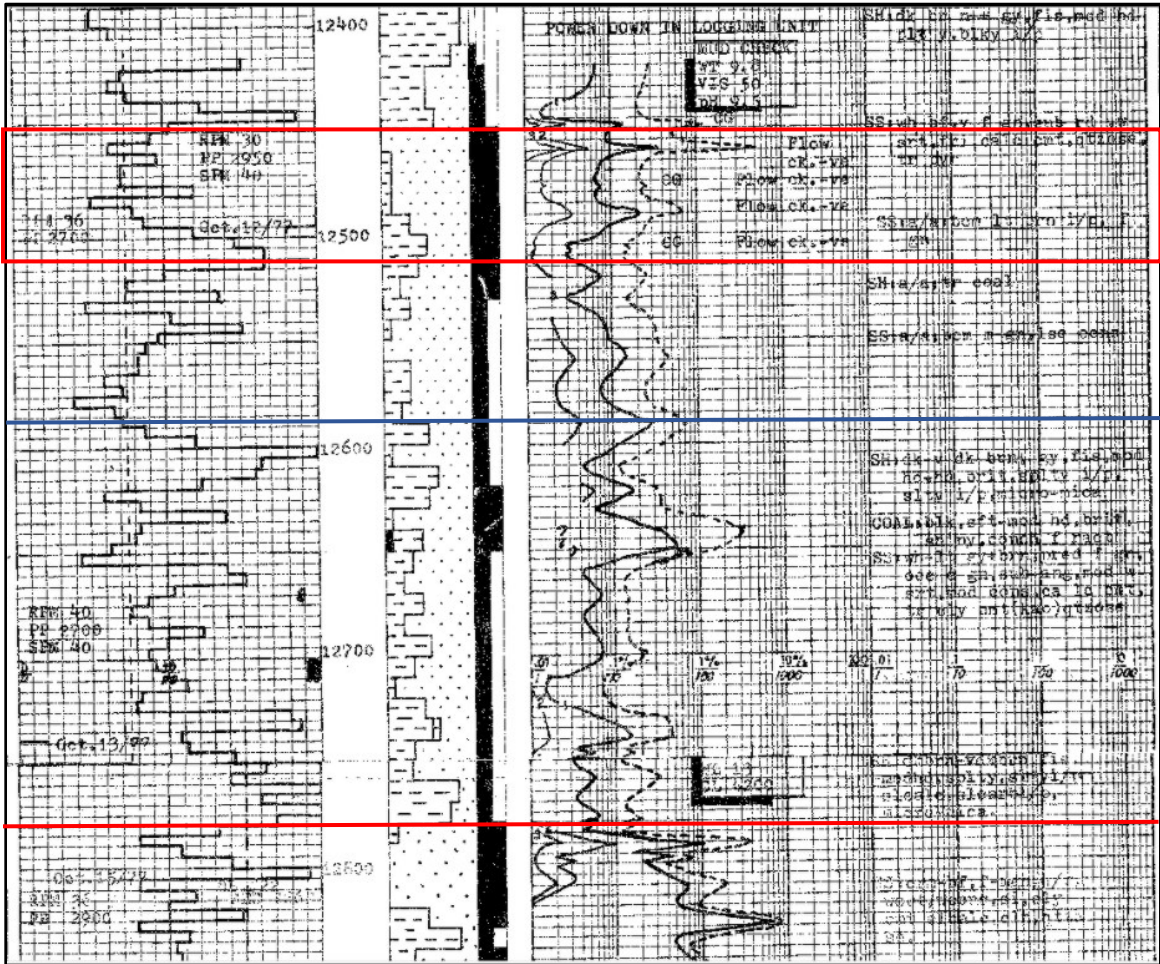


Figure 4.16: A mud gas log of the area of the well thought to be intersected by the fault showing 12,400 ft – 12,850 ft (3779 – 3916 m).

#### 4.4.6. Pressure vs Elevation (Depth) Characterization

For this study, the pressure data obtained through the BASIN database offered the advantage of being archived in a digital format. At the time of drilling the Migrant N-20 well in 1977, the RFT tool was available for measuring reservoir formation pressures. Drilled early in the exploration phase of the Sable Subbasin, open-hole pressure testing was done for the Migrant N-20 well for the interval tested by DST #2 (Watson, pers comm. Oct. 2019). For safety reasons, the flow testing was carried out through perforations in a cased hole interval for the uphole intervals tested in that well and in the more recent project wells (such as the Thebaud T5 production well). Where both RFT, and MDT data are available, preference is given to the MDT data over that of the RFT (Brown, 2003). This

is mainly due to the higher accuracy of the quartz gauge sensors used in the MDT tool, which stabilizes more quickly when subjected to the extreme (both high and low) pressures in the wellbore than the strain gauge used in the RFT tool (Rider & Kennedy, 2011).

Based on the small differences among the hydrostatic gradients of 10.2 kPa/m, 10.5 kPa/m, and 10.3 kPa/m, it is evident that a degree of hydrodynamic continuity exists between the same reservoirs in the different project wells. The estimated 10.5 kPa/m hydrostatic gradient from the combined pressure plot of the Migrant N-20 RFT data, Adamant N-97 MDT data and RFT data from the Thebaud I-93 well was established from a regression of Thebaud I-93, which is the only other well with RFT data (Figure 4.7). In addition to a 10.2 kPa/m gradient estimated for the Migrant RFT points, a new hydrostatic gradient of 10.3 kPa/m established from the newer Adamant N-97-data points in the plot comprising all four wells (Figure 4.8) is lower than the density of the water gradient published by the operators. The small variations in hydrodynamic gradient are likely a function of the different gauges and calibrations used in the respective tool at the time of drilling the wells. Therefore, with the newer “quartz gauges” used for pressure measurements in the MDT tool at Adamant known to be more reliable (Rider & Kennedy, 2011) the 10.3 kPa/m gradient is considered more reliable. To ensure accuracy, adjusting all pressure data to conform to the most accurate hydrodynamic gradient at Adamant is preferred (Chen, 2014). That being the scope of this, small differences in gradient between the wells in this study was ignored.

Additionally, intersections of gradients could not be determined due to insufficient data points at different depths in each fluid phase in the earlier generation wells like Thebaud I-93 and Migrant N-20 - with a minimum of two being required per phase and four for the resulting intersection of gradients. The result of the Migrant N-20 RFT plot earlier in this chapter (section 4.3.2.) shows a hydrostatic gradient based on the top two valid RFT points. Sitting slightly offset to the right, the lower two points indicate some level of increased pressure with the third point slightly right of the gradient and the fourth more so as overpressure increases with greater depth. A water/hydrostatic gradient (blue line) of 10.2 kPa/m obtained from the regression relationship of pressure data from the Migrant well is much less when compared to the 10.7 kPa/m water line published by the GSC Basin Database. While the 10.7 kPa/m gradient is heavily weighted and represents

the value used for the South Venture field, it is evident that this gradient was assumed to be the average for the basin. The application of this gradient will erroneously impact the overall results when used in the analysis. Thus, given the preferred gradient derived from the MDT data in the Adamant N-97 well that was drilled with a synthetic-based mud, this combination represents the best gradient for analyzing proximal fields anywhere around the Shelf.

## CHAPTER 5

### 3D SEISMIC INTERPRETATION AND FAULT SEAL ANALYSIS OF THE MIGRANT STRUCTURE

#### 5.1. Introduction

A fault-seal analysis is a method that integrates available well and seismic data related to the architecture of a fault zone, fault rock properties, and pressure data to determine if a fault is sealing (Cervený et al., 2004). The juxtaposition of stratigraphic units between a hanging wall and a footwall results from a change in fault displacement and varying lithological thickness between the footwall and hanging wall (Allan, 1989; Knipe, 1997). The potential for fault sealing can be assessed by identifying juxtaposed leak points through a fault plane profile. The three-dimensional capabilities of the Petrel™ software allow the investigation of leak points between permeable reservoirs in the hanging wall and footwall. From this, a diagram illustrating cross-fault juxtaposition (Knipe, 1997) such as in Figure 5.1 can be constructed to investigate potential leak points as outlined in Chapter 1 (Section 1.4 and Section 1.5.).

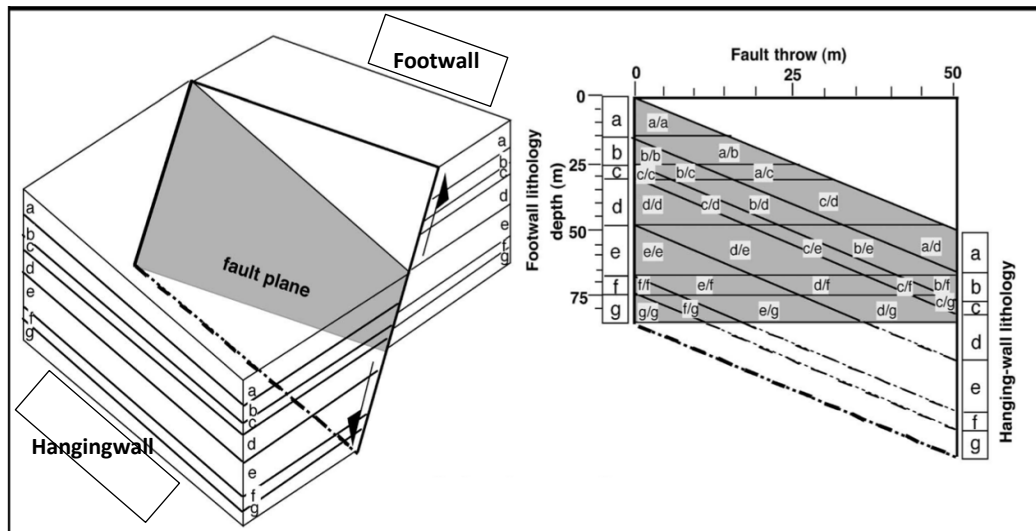


Figure 5.1: A juxtaposition triangle diagram (right) illustrating the displacement of a fault in 3D varying along strike (Knipe, 1997).

#### 5.2. Data and Methods

##### 5.2.1. Seismic Data

The 3D seismic dataset used for this study was made available by ExxonMobil Canada Limited and their Sable Offshore Energy Project partners to the Dalhousie

University Basin and Reservoir Lab (Professor Grant Wach, P.I). The Sable 3D MegaMerge seismic volume used for this study is a post-stack merge of six seismic surveys acquired off the coast of Nova Scotia between 1996 and 1999 by ExxonMobil. The 3D reprocessed volume (Figure 5.2) is characterized by a good signal-to-noise ratio, stable zero phases, and good seismic resolution (in meter vertical and lateral resolution). Overall, the 3D seismic volume exhibits the key architecture of the margin, such as rift architecture and rift-induced unconformity, salt tectonics, a high acoustic impedance Jurassic limestone bank, progressive deltaic listric faulting, and in the Tertiary, clinofolds and polygonal cracks.

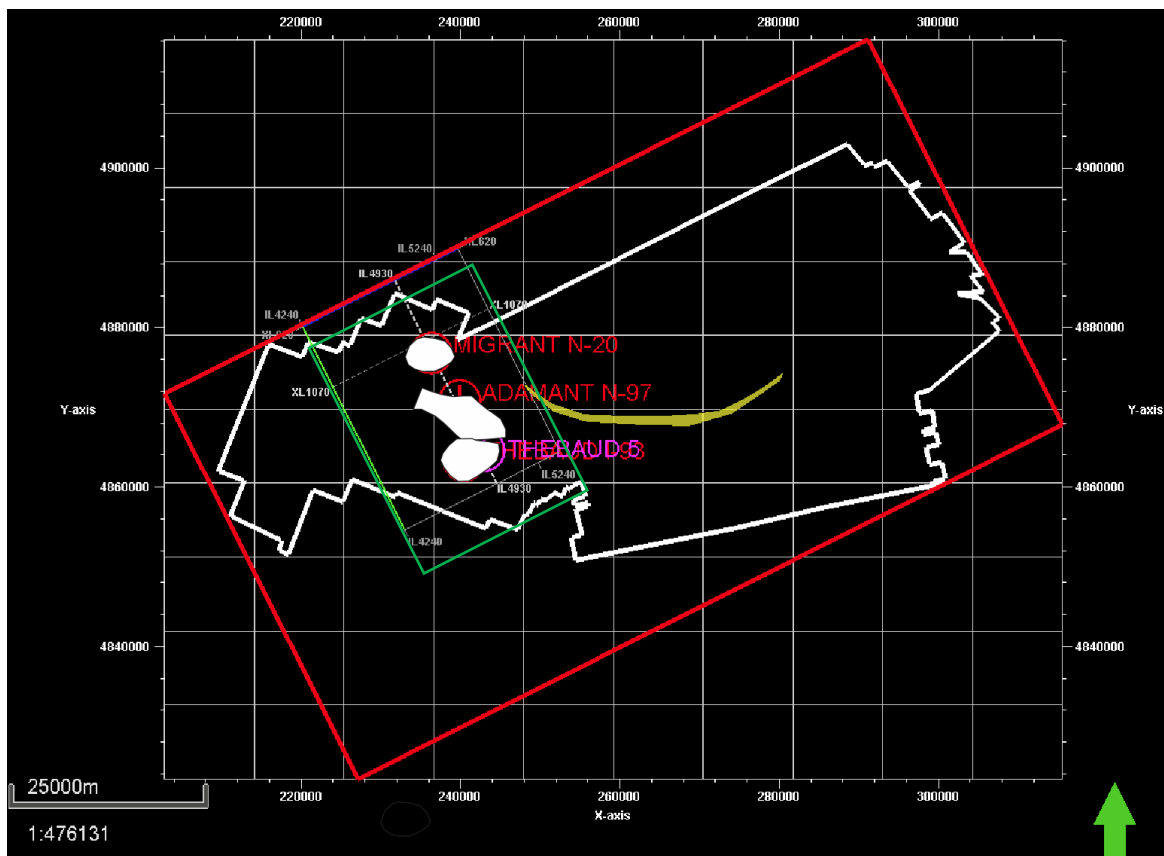


Figure 5.2: A figure of the area covered by the Sable MegaMerge 3D seismic volume (thick white outline) with Sable Island (yellow) shapefile in the 3D area. The green rectangular area left of the 3D survey represents the study area comprising the Migrant expansion trend with the Adamant and Thebaud rollover structures with the four project wells penetrating each structure. The red well head up-dip represents the Migrant N-20 well, the Adamant N-97 penetration is in the middle, just up-dip from the two Thebaud wells used in the project, Thebaud I-93 (red) and Thebaud E-74 T5 production well (purple). The extent of each structure separated by their respective boundary fault is represented by the white shape fills.



### 5.2.2. Database Construction

For this study, the integration of well and seismic data in Petrel™ was possible through the assistance of various members (both past and present) of the Dalhousie University Basin and Reservoir Lab. Well data including well logs, lithology and checkshots, and seismic survey (i.e. the Sable MegaMerge 3D seismic data) were imported into Petrel™ from previous projects.

### 5.2.3. Methods

#### 5.2.3.1. Seismic Stratigraphy

Correlating and differentiating between stratigraphic units in this study was possible through the integration of wireline logs, pressure data, core descriptions, and 3D seismic data. A seismic stratigraphic approach that combines sequence stratigraphic concepts (Vail, 1977; Van Wagoner, 1991; Catuneanu et al., 2009; Posamentier, 2009) with seismic geometry (Mitchum et al., 1977) was used. Reflection terminations such as onlap, downlap, toplap, and erosional truncation are key in defining the boundaries of seismically identifiable sequences (Mitchum et al., 1977) shown in Figure 5.3. The identification and interpretation of these reflection terminations in 3D seismic data, combined with lithology data, can prove useful in calibrating sedimentary facies determined from analysis of cores and their depositional environment interpretation.

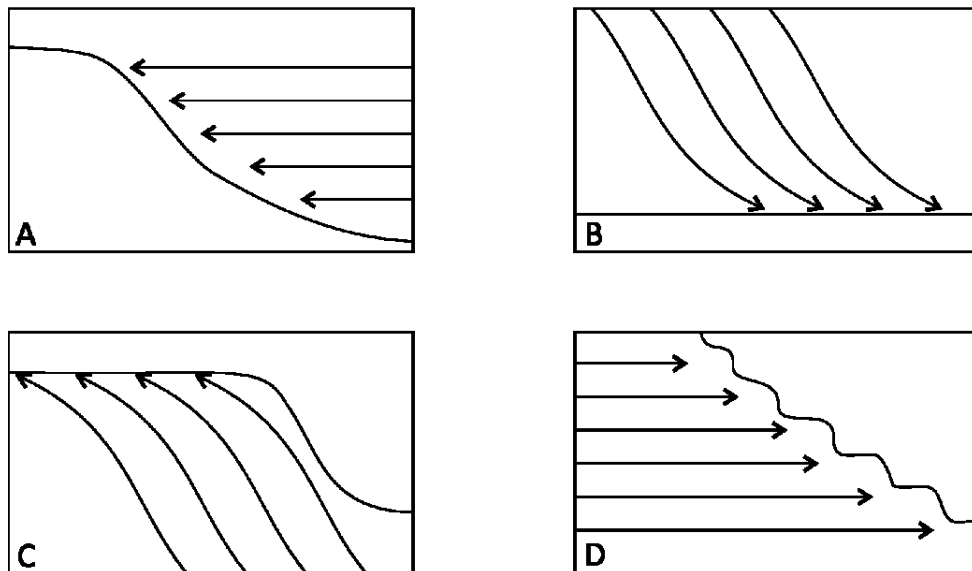


Figure 5.3: An illustration of the various seismic reflection termination patterns (A) onlap, (B) downlap, (C) toplap, (D) erosional truncation (Mitchum et al., 1977). The stratal terminations indicate key surfaces such as sequence boundary SB (a) and (d) while maximum flooding surface MFS (b) and (c) indicate downlapping.

### 5.2.3.2. Static Model Building Workflow Overview (Petrel™)

Stratigraphic interpretation, structural modelling, and analysis of the 3D seismic data for this study were completed using the Schlumberger Petrel™ software. Integrated lithology and petrophysical data were distributed throughout constructed 3D models of the study area, using pre-defined algorithms in Petrel™. The workflow is key for setting up zone and zone index functions in Section 5.2.3.9.

### 5.2.3.3. Seismic Horizon and Fault Interpretation

The seismic interpretation was done using Schlumberger's Petrel™ software with three fault picks imported from previous works including Richards et al. (2010), Skinner (2016), Morrison (2017), Campbell (2018) into the project. These faults were carefully inspected with half a dozen horizon picks ensuring a clean termination of the horizons at faults with no inconsistencies in fault throw. The horizons were interpreted in the 3D data using the “manual picking” tool in the Petrel™ seismic interpretation workflow (Figure 5.4).

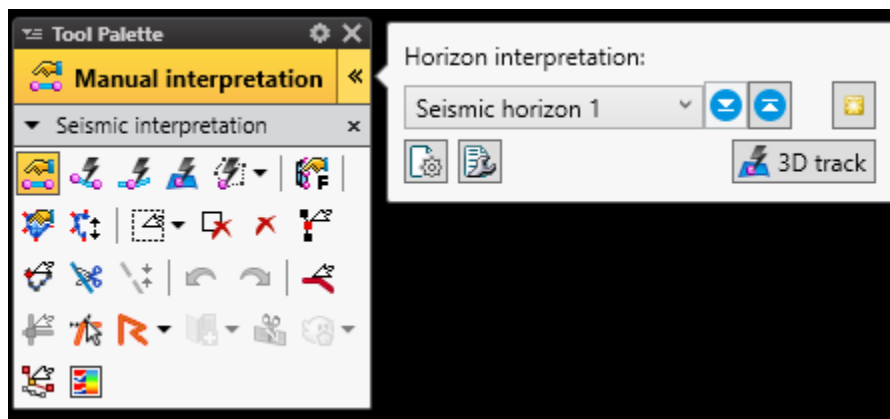


Figure 5.4: A figure showing the interpretation tool palette in Petrel™ used for completing the 3D seismic interpretation for this study. The manual picking approach highlighted in yellow in the top left corner of the box was used for the interpretation.

The interpretation of seismic in-lines and crosslines was done by setting the seismic intersection player in Petrel™ to increments of 100, then decreasing to 40, 20, and 10. Around the faults, increments of 5 were the most suitable. Six horizons, including a horizon depicting a base truncation surface, but incomplete due to poor seismic quality, were interpreted manually in the Upper Jurassic and Lower Cretaceous strata across the Migrant Structure (Figure 5.5).



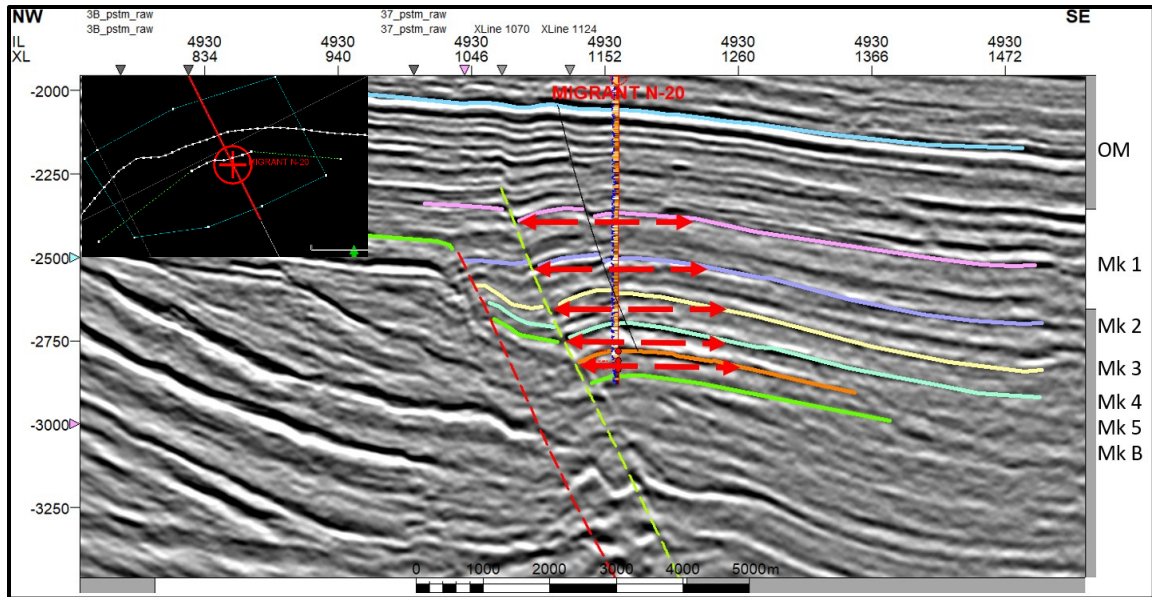
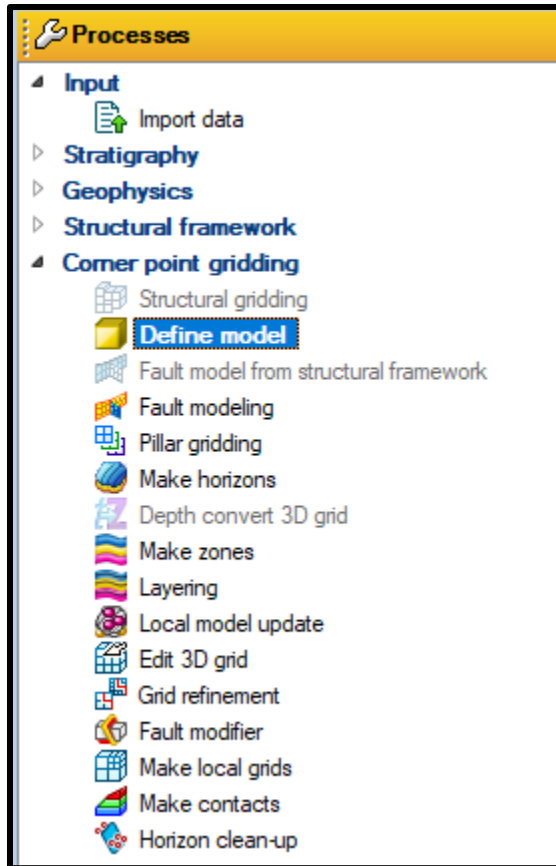


Figure 5.5: A seismic section of the Migrant area showing the interpreted horizons. The red arrows have been added to show the relationship between the various closure areas under each horizon. Zero vertical exaggeration applied

#### 5.2.3.4. Geocellular TWT Modelling

Geocellular modelling using generated surface maps and additional data (including well petrophysical data) was used in this work to model the sediment deposition related subsurface analyses. The absence of continuous analogous rocks onshore meant that data acquired from the area of interest offshore can be modelled to factor the subsurface reality of the rocks. A geocellular model was defined in space using the “corner point gridding” workflow in Figure 5. 6. The model is populated with properties such as shale volume and porosity (for this study) defined in each grid cells through a geostatistical approach (Sequential Gaussian Simulation). As a key step towards the building of the Migrant static models, a polygon was used to set the boundary of the static geocellular model. The model was defined (Figure 5. 6) before seismic horizons and fault traces were imported into the model and extended throughout the model (in the case of the fault trends).



*Figure 5. 6: A figure showing the corner point gridding workflow in Petrel™ used for setting up a structural model. The first step involved defining the model extent of the structure.*

### 5.2.3.5. Fault Modelling

After creating the model boundary and importing the fault sticks, the faults were inspected in the 3D window where irregularities (typical pillars at the end) were tidied up further before pillar gridding (the next step). The “fault modelling” workflow was used to extend the fault trace to the edge of the model area in the 2D window to further divide the model into segments (Figure 5.7).

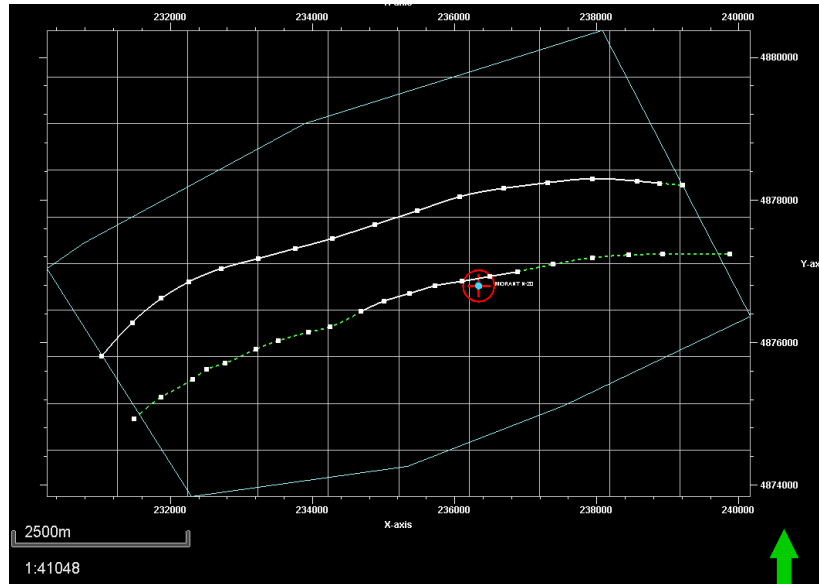


Figure 5.7: A screen capture of the model area defined by a boundary polygon (blue line) and the imported faults (white lines). The fault trends (green dashed lines) have been added using the fault modelling tool in Petrel™. The floating tool palette used to divide the model into segments can be seen embedded in the figure.

### 5.2.3.6. Pillar Gridding

In the previous step, pillar gridding was done after the faults imported into the model had been inspected. The “pillar gridding” step initiates a non-Cartesian, twisted ‘i,j,k’ 3D grid, which is much more efficient for flow calculations than the ‘xyz’ grid.

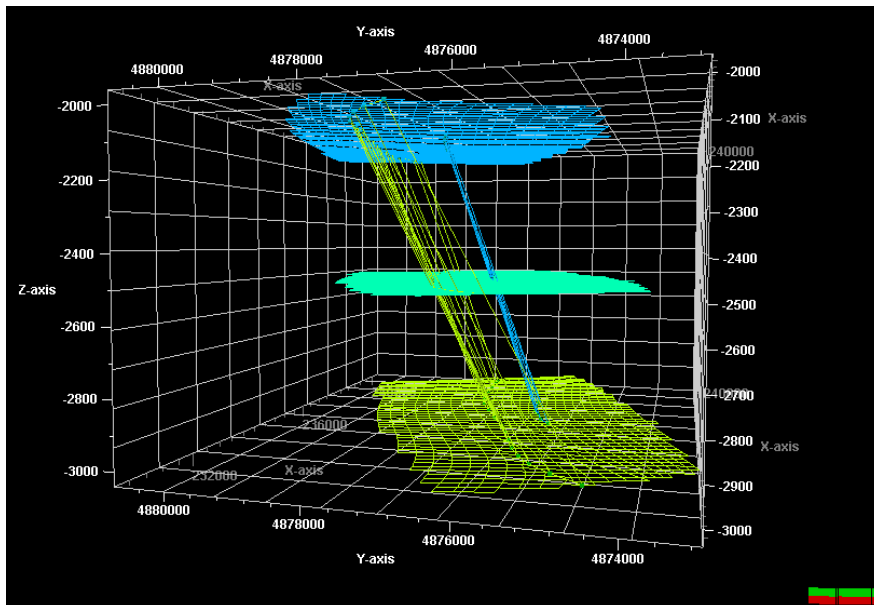


Figure 5.8: Screen capture of the model area and faults displayed on the 3D window in Petrel™. This was essential for inspecting the skeleton grids to ensure clean undistorted terminations at faults. 5X vertical exaggeration applied.

### 5.2.3.7. Horizon Modelling

The interpreted horizons were imported into the model through “make horizons” in Petrel™ processes. For this step, the horizons within the area of interest can be assigned either a conformable, erosional, discontinuous, or base strata relationship (Figure 5.9). The horizon modelling process ensured that each horizon was individually created to intersect faults accurately, which was carefully mapped. A 250 m allowance between the fault and the horizons was set to allow for consistency in case any of the horizons inadvertently extended across the fault, which would have skewed the model.

Index	Horizon name	Color	Calculate	Horizon type	Conform to another horizon	Status	Smooth iterations	Use horizon-fault lines	Well tops	Input #1
1	O ZX	Blue	<input checked="" type="checkbox"/> Yes	Conformable	No	1 Done	0	<input checked="" type="checkbox"/> Yes	+	+
2	MK-1	Pink	<input checked="" type="checkbox"/> Yes	Conformable	No	1 Done	0	<input checked="" type="checkbox"/> Yes	+	+
3	MK-2	Purple	<input checked="" type="checkbox"/> Yes	Conformable	No	1 Done	0	<input checked="" type="checkbox"/> Yes	+	+
4	MK-3	Yellow	<input checked="" type="checkbox"/> Yes	Conformable	No	1 Done	0	<input checked="" type="checkbox"/> Yes	+	+
5	MK-4	Light Green	<input checked="" type="checkbox"/> Yes	Conformable	No	1 Done	0	<input checked="" type="checkbox"/> Yes	+	+
6	MK-5-2	Orange	<input checked="" type="checkbox"/> Yes	Conformable	No	1 Done	0	<input checked="" type="checkbox"/> Yes	+	+

Figure 5.9: A figure showing the horizon modelling step in Petrel™. Interpreted seismic horizons converted to surfaces were rendered conformable to one another.

### 5.2.3.8. Time-to-Depth Conversion

A velocity-depth relationship derived from formation velocity data, plotted in Excel and imported into Petrel™, was used to depth convert the two-way time models. The “Advance Velocity Model” tool in the geophysics workflow in Petrel™ (Figure 5.10), was used to input velocity data obtained from checkshot surveys from well reports into the model.

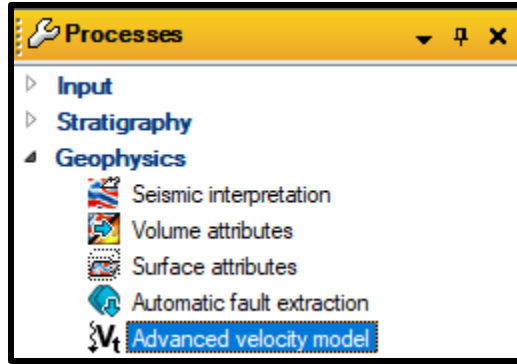


Figure 5.10: A figure of the advanced velocity modelling step in the geophysics workflow in Petrel™. This process was essential for depth converting the constructed two-way time models.

This step ensures that mapped structures in two-way time are depth converted to depict their true subsurface positions (Etris et al., 2001). For depth conversion, interval velocities for each layer were calculated from checkshot data.

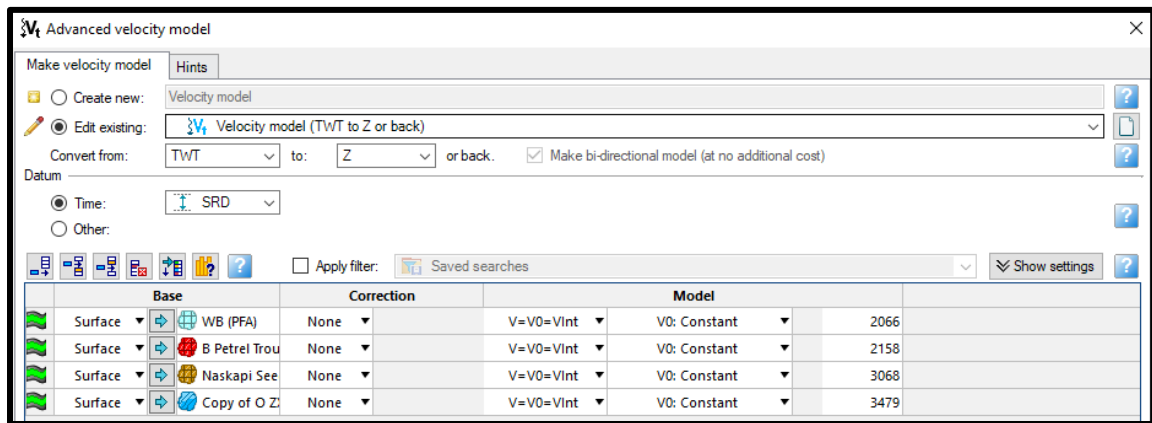


Figure 5.11: A figure of the advanced velocity modelling step in Petrel™. The time surfaces/horizons and an average velocity were used to output depth horizons/surfaces. The O-marker indicative of the highest stratigraphic unit with an average velocity of 2900 m/s was used for depth converting the seismic horizons below the O-marker relative to the checkshot velocities in Table D1.

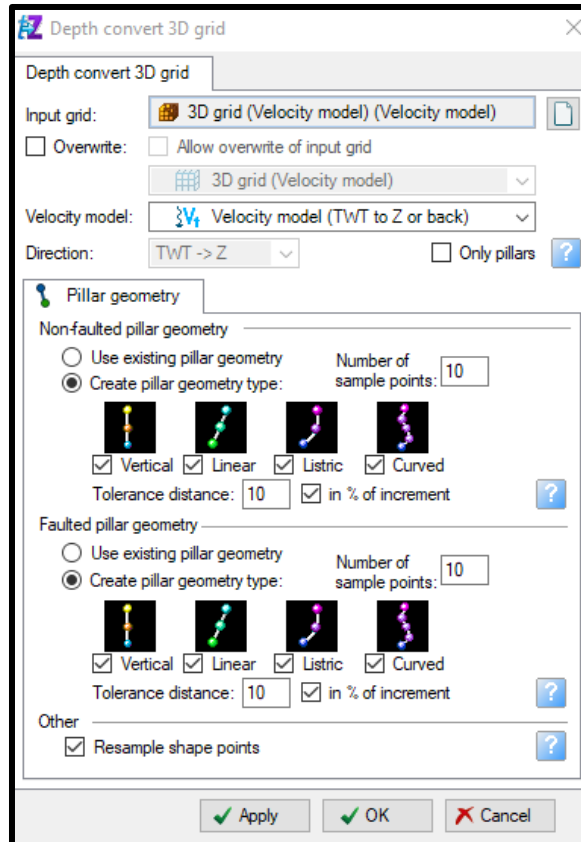


Figure 5.12: A figure of the depth convert 3D grid dialog box, which was used for depth converting the time grid (brown) in Petrel<sup>TM</sup>. The depthing was aided by the pre-established velocity model.

### 5.2.3.9 Zone Index

Between every pair of horizons is a zone. In Petrel<sup>TM</sup>, the “geometrical modelling” function in the property modelling workflow (Figure 5.13) was used to create discrete properties such as zone segments. The created zone index can be overlaid on the original seismic profile for further inspection and analysis.

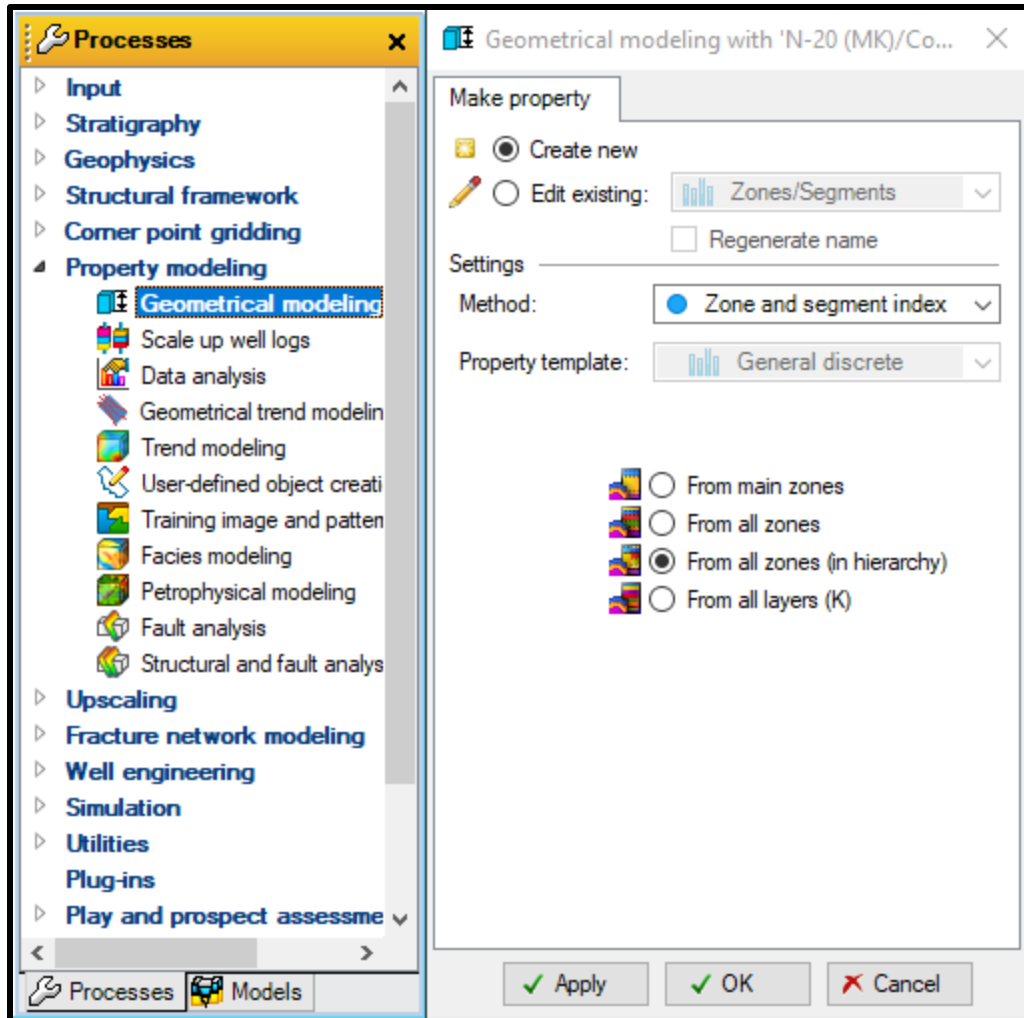


Figure 5.13: A figure of a dialog box that enables zones and segments to be assigned numerical indices in Petrel™.

#### 5.2.3.10. Layering and Scale Up of Well Logs

After inputting horizons, the subsequent zones are divided into layers, - and the petrophysical well logs are scaled up from the log sampling scale (every 6 inches) to the layering of the model (5 m) using an average algorithm. The scale-up well logs process was essential for distributing the petrophysical properties at a larger scale throughout the model. This was done for the calculated shale volume log (Vsh), porosity log. These logs were scaled up using the “scale up well logs” function in the property modelling workflow in Petrel™ (Figure 5.14).

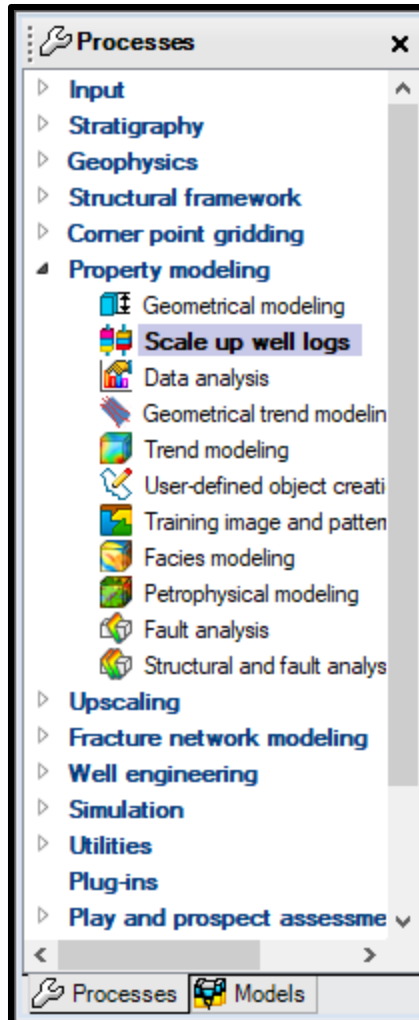


Figure 5.14: A figure of the scale-up well log step highlighted in the property modelling workflow in Petrel™ used for scaling petrophysical logs to fit the layering scheme of the cells applied to the model.

### 5.2.3.11. Petrophysical Modelling

The “petrophysical modelling” workflow was used to propagate continuous properties including porosity, and shale volume (Vsh) throughout the 3D grid by Sequential Gaussian Simulation (SGS). The SGS krigs the data and adds stochastic statistically valid variance. In this step, sample points that are close together have more similar properties than those separated by larger distances, based on a variogram (Figure 5.15). Additionally, the property distribution is dependent on the seismic. A variogram was used for kriging (grid interpolation between data points) to influence the orientation and length of continuity of properties. In kriging, a statistical algorithm employing the variogram – which plots the distance between known points relative to their similarity (variance) uses an available data



set. To populate the shale volume, porosity, and permeability through the model in this study, the trend of the variogram was changed from the default to match the depositional strike in the basin using a 46-degree azimuth (Figure 5.15).

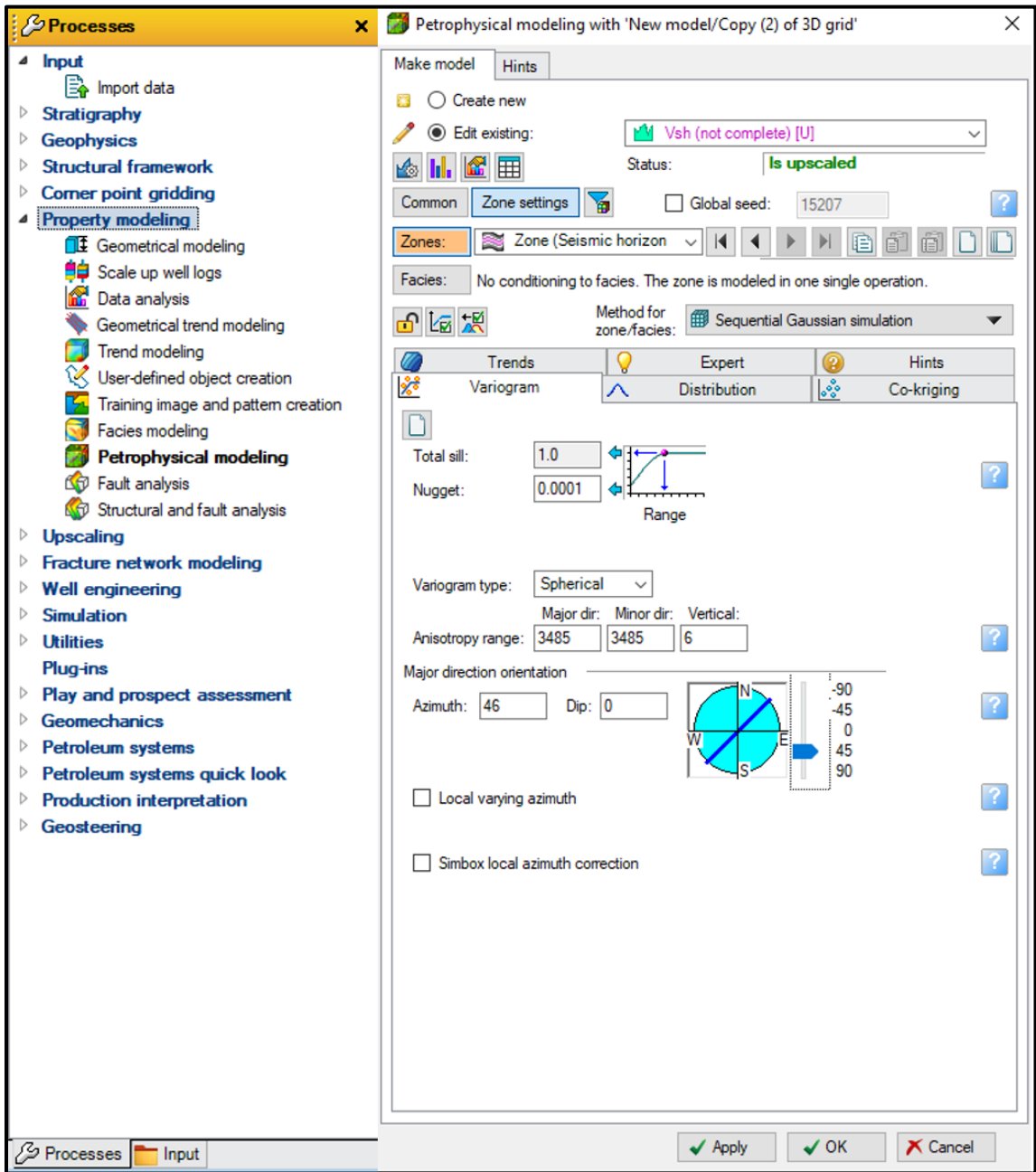


Figure 5.15: A figure of the petrophysical modelling dialog box in Petrel™. The upscaled petrophysical log properties were propagated throughout the model zone by zone through a method of Sequential Gaussian Simulation. With the knowledge of the dominantly NE trend of the faults in the basin and deposition perpendicular to the fault trend, the variogram was used to set major deponenter trend to the southeast.

#### 5.2.3.12. Construction of Fault Plane Profiles

After the scale-up of well logs using the Vsh for the Migrant N-20 well and petrophysical modelling, a fault index created in geometric modelling was used to display the cells next to the crestal fault. After this, a segment filter was used to display the cells adjacent to the fault plane, then a second copy of the constructed 3D grid was made to aid in the display of the hangingwall and footwall cells in yellow and orange respectively. A value filter in the model property settings was used to filter out the shales at the fault such that the crestal fault only displayed the areas that meet the cut-off for each of the models (the original and the copied).

### 5.3. Results

#### 5.3.1. Seismic Interpretation: Horizons

Five horizons (Figure 5.16) were interpreted based on strong persistent seismic reflections comprising peak-trough pairs in the clastic depositional sequence.

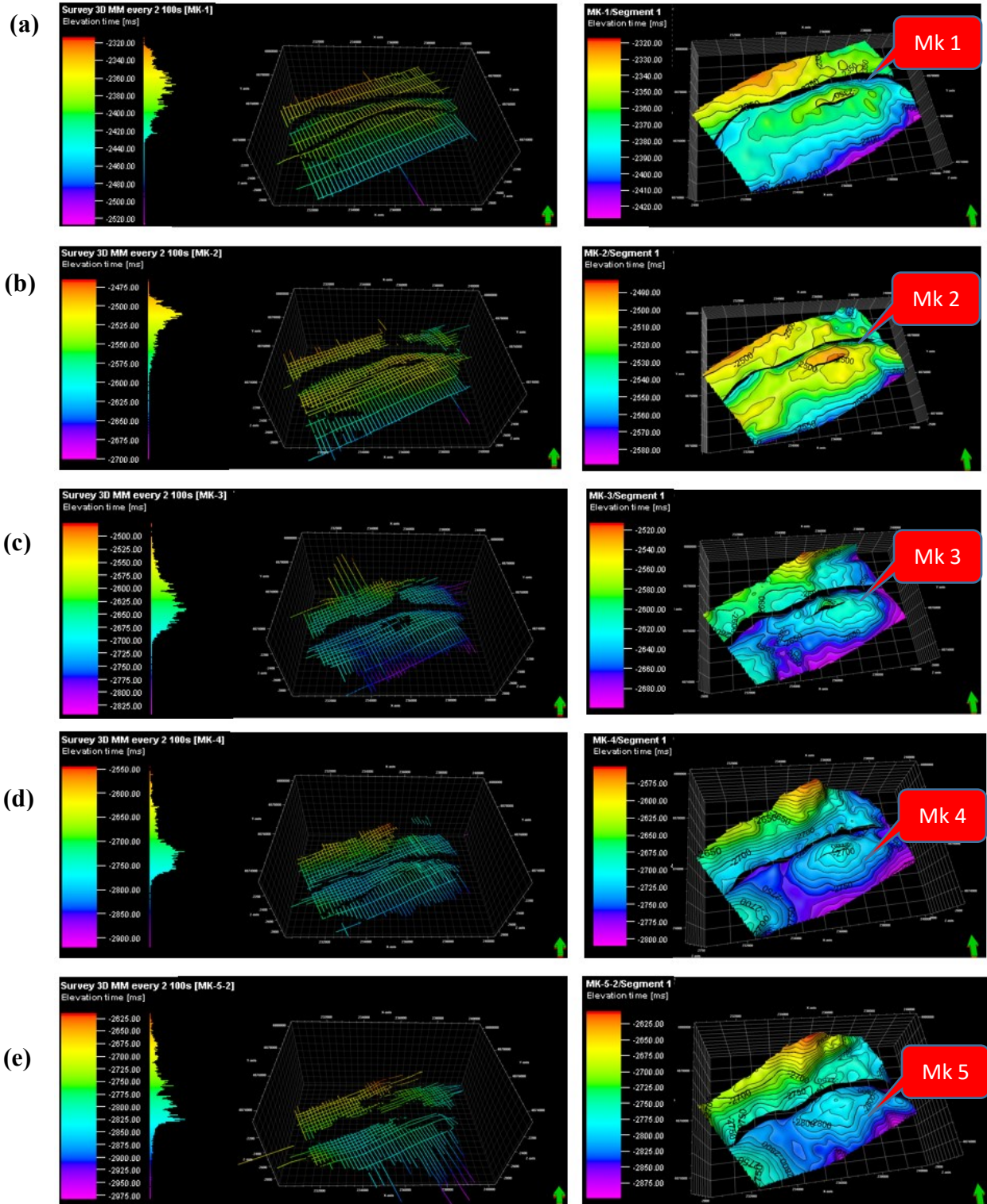
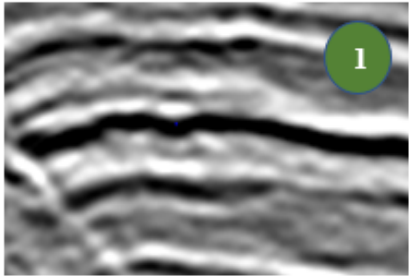
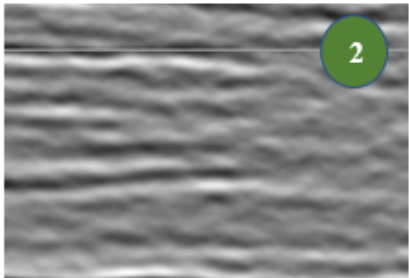
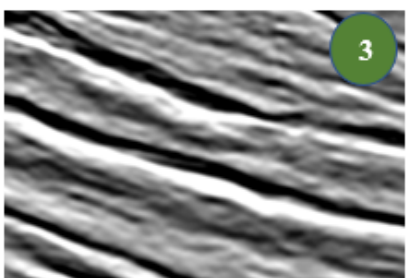
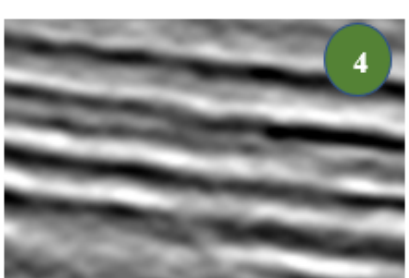


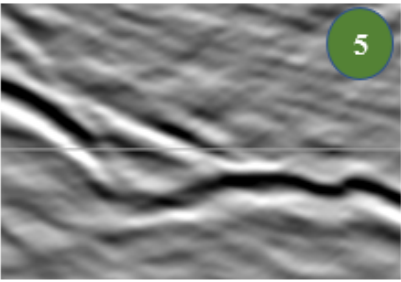
Figure 5.16: A figure of the five alphanumeric horizons (MK1 to MK 5) from top to bottom (a-e). On the left are the interpretation ribbons in TWT a 3D display and on the right, their corresponding Time contour maps in a 3D display. Fault offsets have been considered and correctly rendered throughout the interpretation. 10X vertical exaggeration applied.

### 5.3.2. Seismic Interpretation: Seismic Facies

A range of depositional characteristics has been interpreted from seismic facies calibrated to core observations. Sedimentation styles observed in 3D seismic around the Migrant Structure include high amplitude carbonates with overlying transparent weak intervals (likely shales) below the clastic section. There is a cleaning-up section that transitions into blocky and bright reflective deltaic sands. The combined log, and seismic characteristics are typical of progradational shelves characterized by decreasing net to gross with depth (Moss-Russell, 2009). From 3D seismic data, three distinguishable seismic facies were identified around the Migrant Structure supported by well logs. These are shown in the seismic cross-section in Figure 5.17, as well as are evidence of an angular unconformity in Figure 5.18. The facies, which are represented in the red arrows are characterized by their similar seismic configuration in relation to characteristics such as seismic reflectivity, seismic amplitude, and frequency, as well as structural similarities and progression (Campbell, 2018). Table 5.1 is a summary of the seismic facies observed around the Migrant Structure.

Table 5.1: Summary of the five key seismic facies used for interpreting the seismic structural and stratigraphic framework. They have been referenced by numbers according to their occurrence in Figure 5.17.

Seismic Facies	Seismic Facies Characteristics	Geologic Interpretation	Stratigraphic Interval
	Increase in amplitude in front of fault	Sand trap expansion in the hanging wall of the listric growth faults.	Missisauga Formation Expansion Trend
	Transparent weak intervals with some dip interbedded low to medium peak-trough seismic amplitudes.	Progradational shales that transition to carbonate mudstones within proximal to distal clinofolds.	Mic Mac Formation Expansion Trend/ Distal equivalents of the Abenaki carbonate (Abenaki 1 – Abenaki 7).
	High amplitude reflectors (Strong peak-trough pairs) with good continuity.	Carbonate platform dominated proximal regime with stable depositional conditions.	Abenaki 1-Abenaki 7
	High amplitude Reflective (Strong trough-peak pairs).	Prodelta siliciclastics that fills into the expansion trend.	Missisauga Formation/ Mic Mac Formation Expansion Trend

	Occasional discontinuous low amplitude reflectors.	Alloctonous salt movement into areas of least sediment resistance after episodic influx of siliciclastics from the Sable Delta.	Salt (Argo Formation)
---	--	---	-----------------------



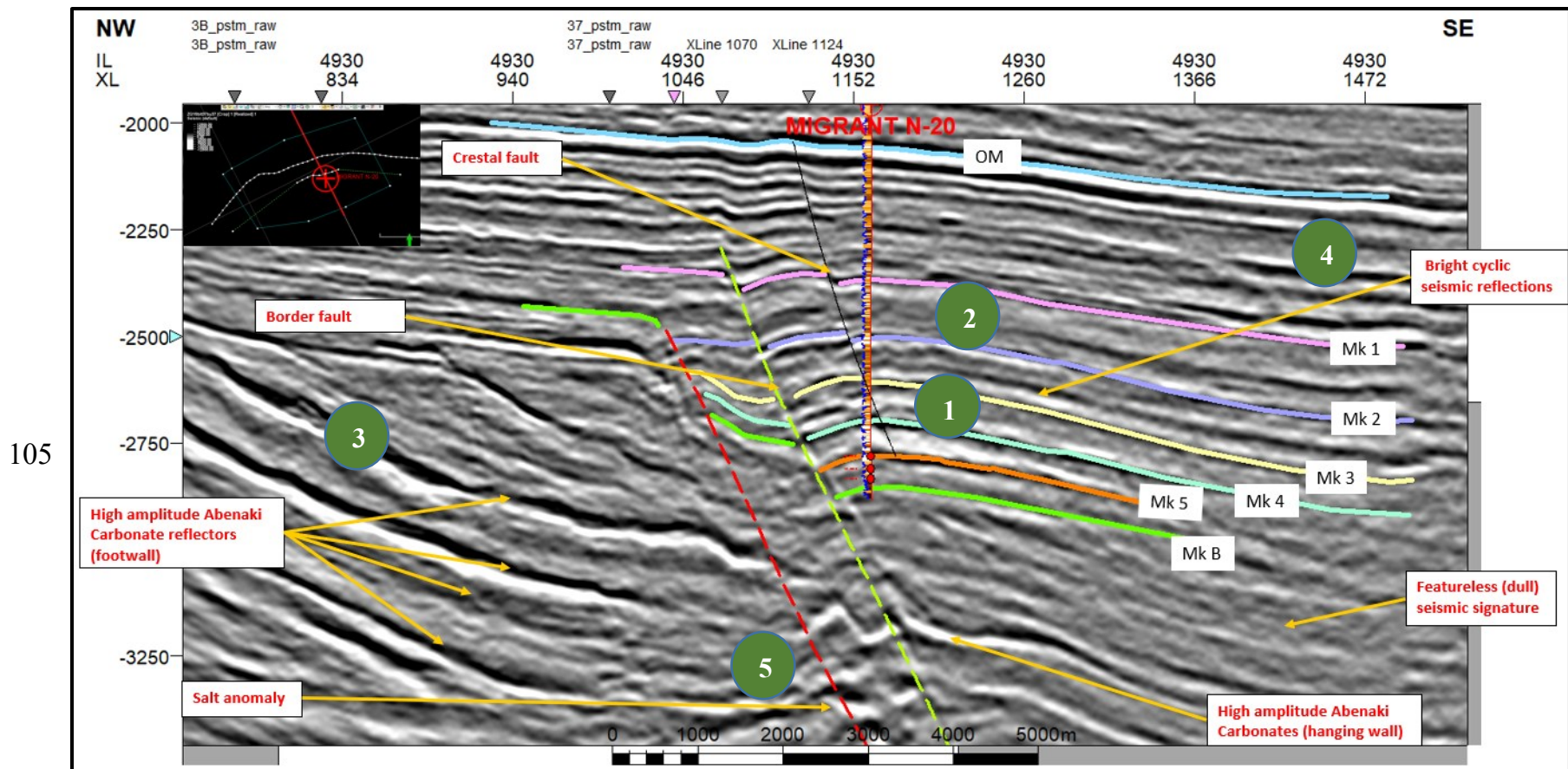


Figure 5.17: A seismic section across the Migrant Structure to illustrate the seismic facies characterised in Table 5.1. This seismic line was chosen to show most of the seismic character which aided in the interpretation of the Abenaki carbonate and the clastic reservoirs of the Migrant structure and its implication for growth faulting in marginal shelf deltaic sediments of the Sable Subbasin. There appears to be an expansion of the sedimentary package away from the fault (maybe related to sediment trapping). Judging from the degree of faulting, the fault appears to displace the carbonate reflector (high reflectivity units) and the older section. The numbers are referenced in Table 5.1 above. Zero vertical exaggeration applied.

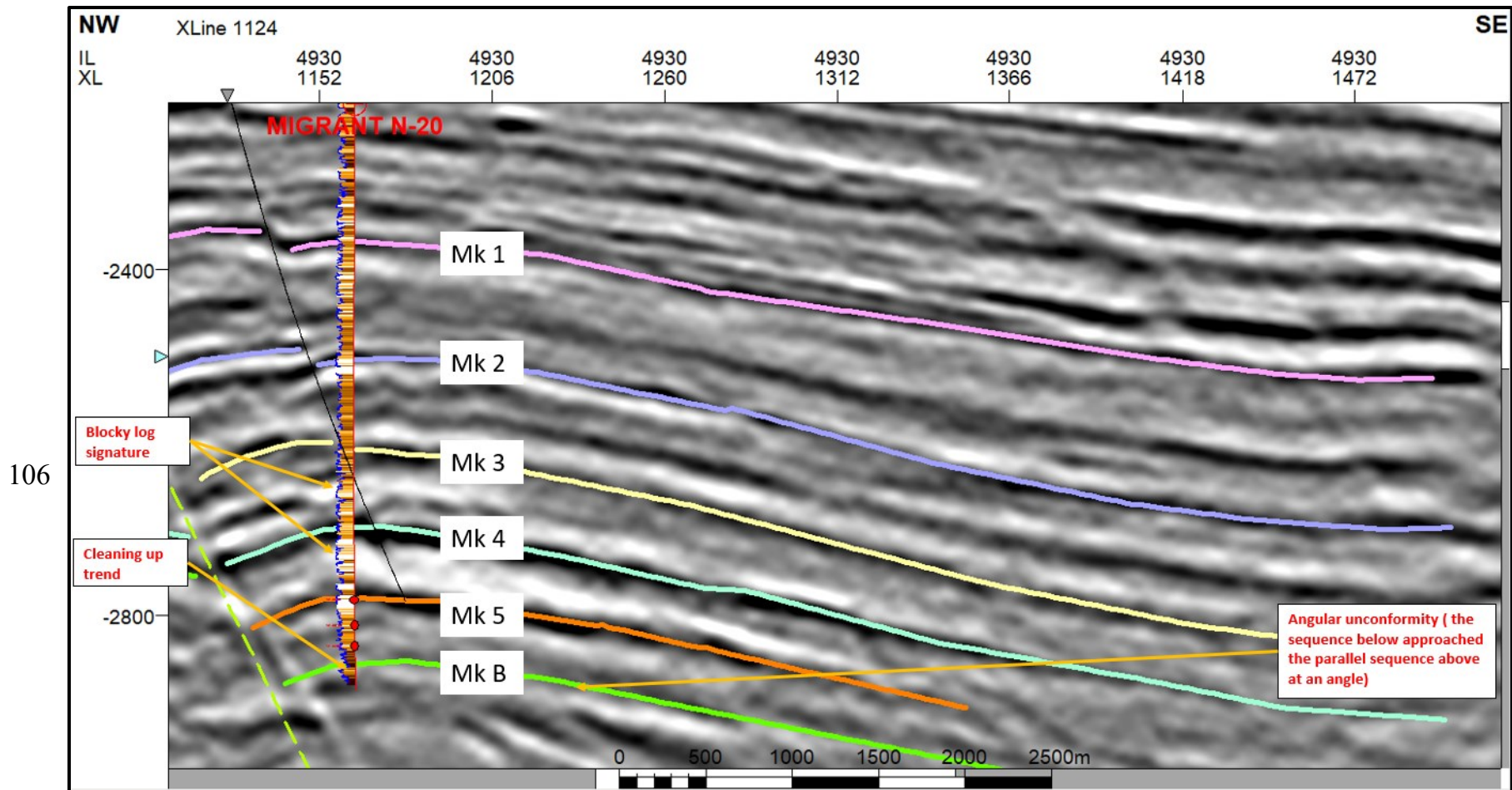


Figure 5.18: A detailed seismic image from the area of interest of the Migrant Structure. The green line is indicative of termination (a truncation surface in this case) that caps the low angle inclined stratifications underneath as mapped in the 3D seismic data and is a good example of a sequence boundary. Zero vertical exaggeration applied.



### 5.3.3. Geocellular TWT Model with Pillar Grids

For constructing the geocellular grid, the area of interest was defined by a polygon, which was then converted to the model boundary. The model area, comprising the Migrant N-20 well, was used to generate a 3D geocellular model with zones and segments defined from the interpreted seismic horizons and imported faults respectively. Given the tight reservoirs with low porosities at Migrant, a coarse grid (cell size 200 x 200) was constructed for this study (Figure 5.19). The model has 3 segments, 5 zones of 10 layers (1 m thick), applied to each zone after the thickness maps had been used as inputs.

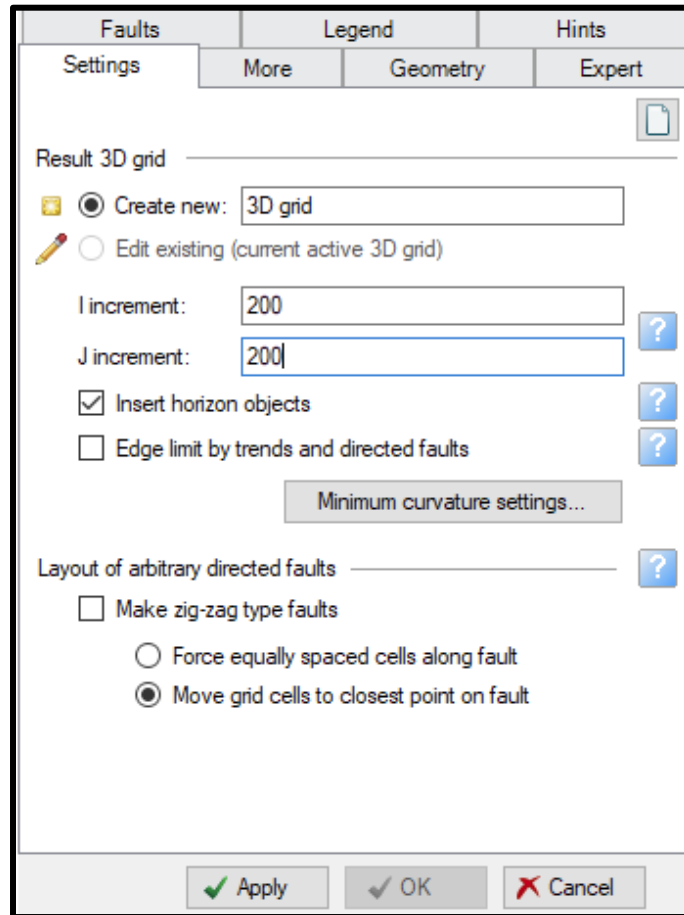
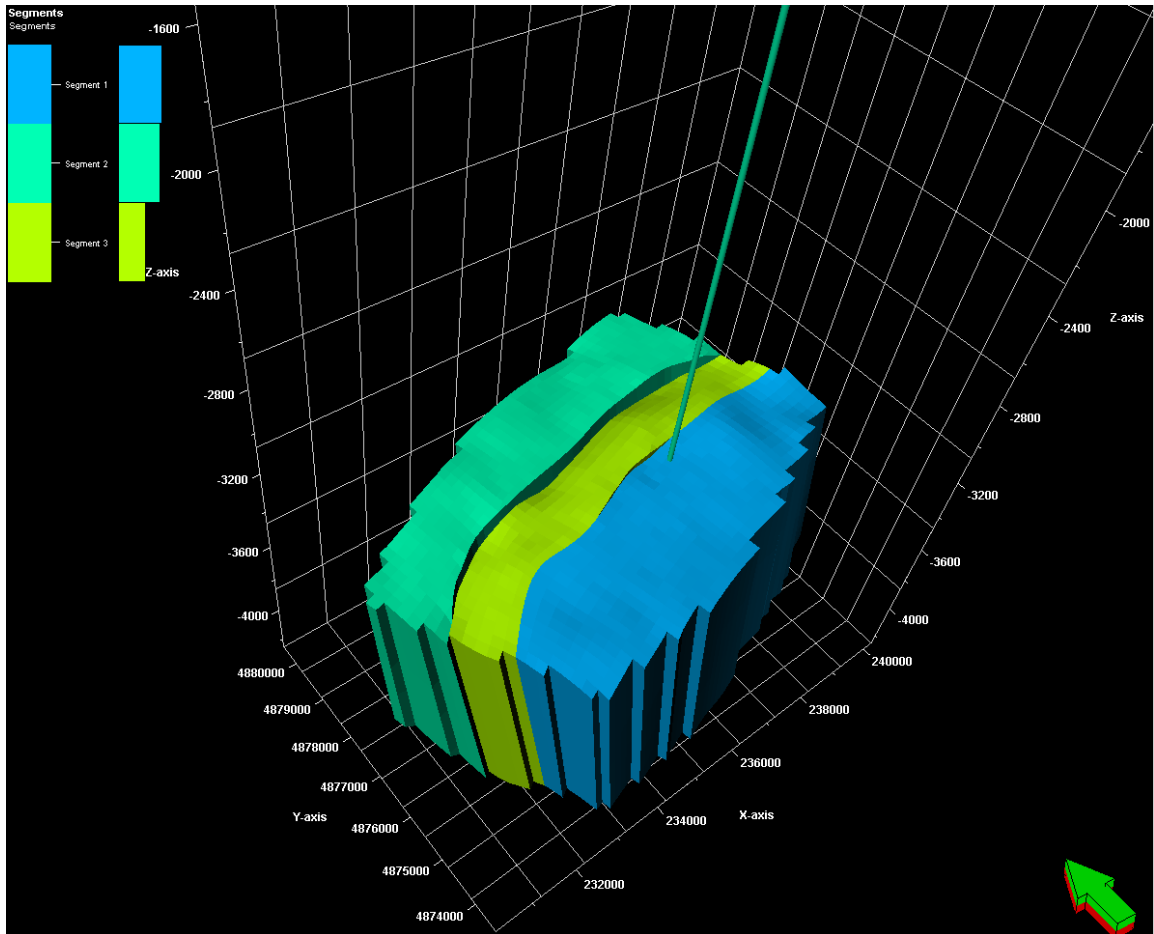


Figure 5.19: A figure of the model and gridding pattern made in Petrel™. The figure gives a summary of the grid layout, including the numbers of rows (“I” increments), the number of columns (“J” increments), geometries.

### 5.3.4. Faults, Zones and Horizon Model

The final 3D structural model is shown in Figure 5.20 and Figure 5.21. The Model has been displayed to show the three segments made from the imported faults. The boundary between the blue and yellow segments (segments 2 and 1 respectively) is

indicative of the Migrant crestal fault. The border fault of the expansion trend is marked by the boundary between the green and the yellow segments (Segments 3 and 1 respectively).



*Figure 5.20: A 3D model of the Migrant Structure at the N-20 well showing the three fault-defined segments. 5X vertical exaggeration applied.*

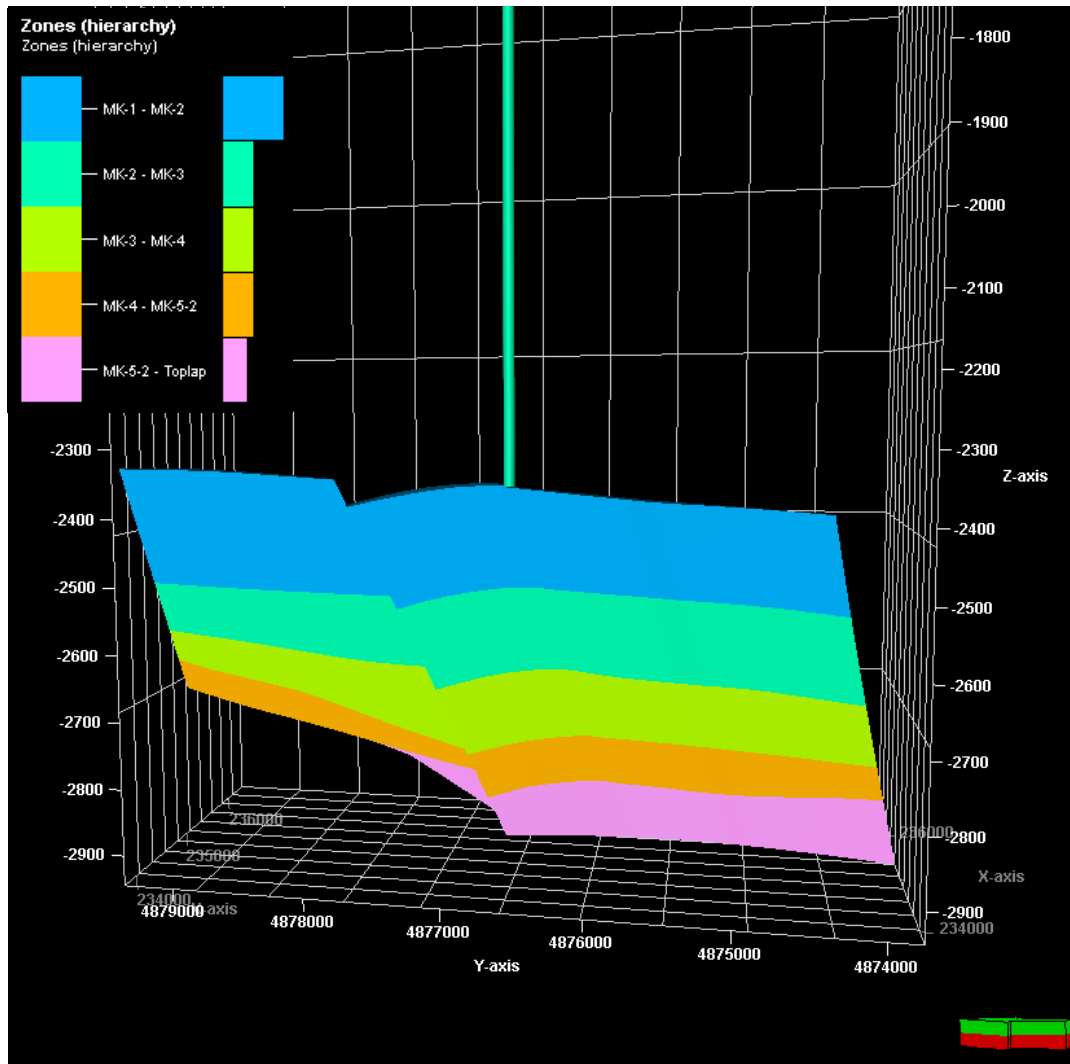


Figure 5.21: A 3D model of the Migrant Structure at the N-20 well. The model has been displayed to show the five key zones made from the O-marker and five alphanumeric horizons. 5x vertical exaggeration applied.

### 5.3.5. Time-Depth Model

For the conversion of the seismic two-way time model to depth, a simple layer cake velocity model using four stratigraphic markers were used. These include water bottom, lithostratigraphic tops of the Petrel limestone marker, Naskapi Shale, and O-marker. An average constant velocity extracted from calibrated well check shots in the Migrant N-20 well was used to convert maps of reservoir tops (in time) Figure 5.22 to depth illustrated in Figure 5.23. This was done by establishing a velocity model, which links the time and the depth information extrapolated from the check shot data. Applying the relationship  $\text{Velocity} = \text{distance}/\text{time}$ , ensures that a depth equivalent of the seismic data (in time) can be adequately derived.

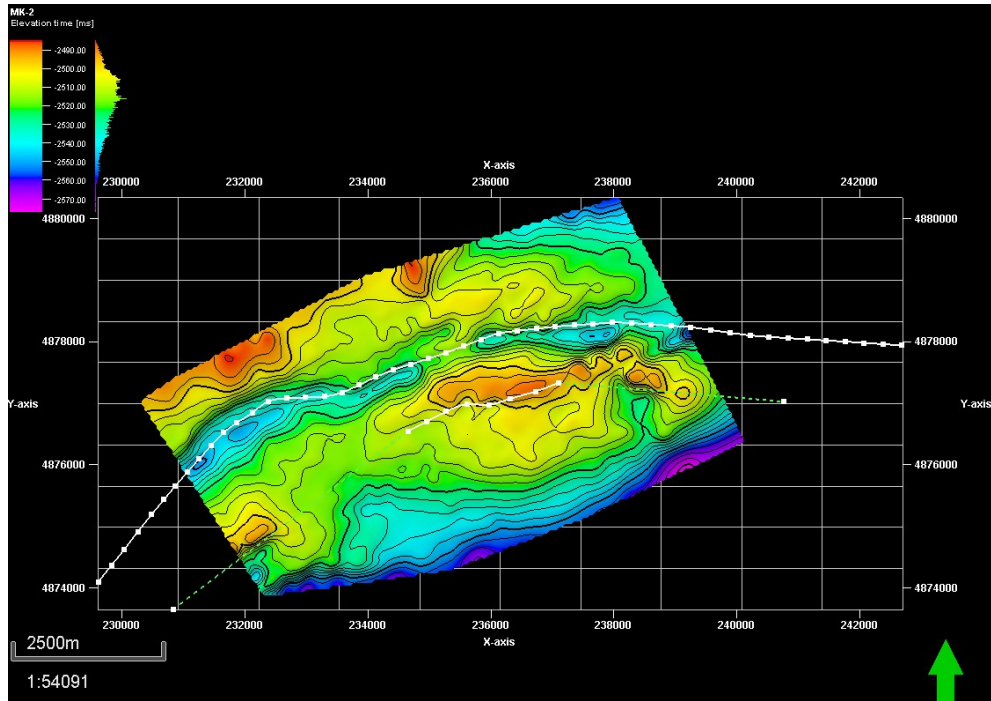


Figure 5.22: A reservoir time map for the top of the uppermost reservoir Mk-2. The Migrant N-20 well can be seen on the structure (red circle with cross) and the trend of the two Migrant faults extended outside the model boundary. 5X vertical exaggeration applied.

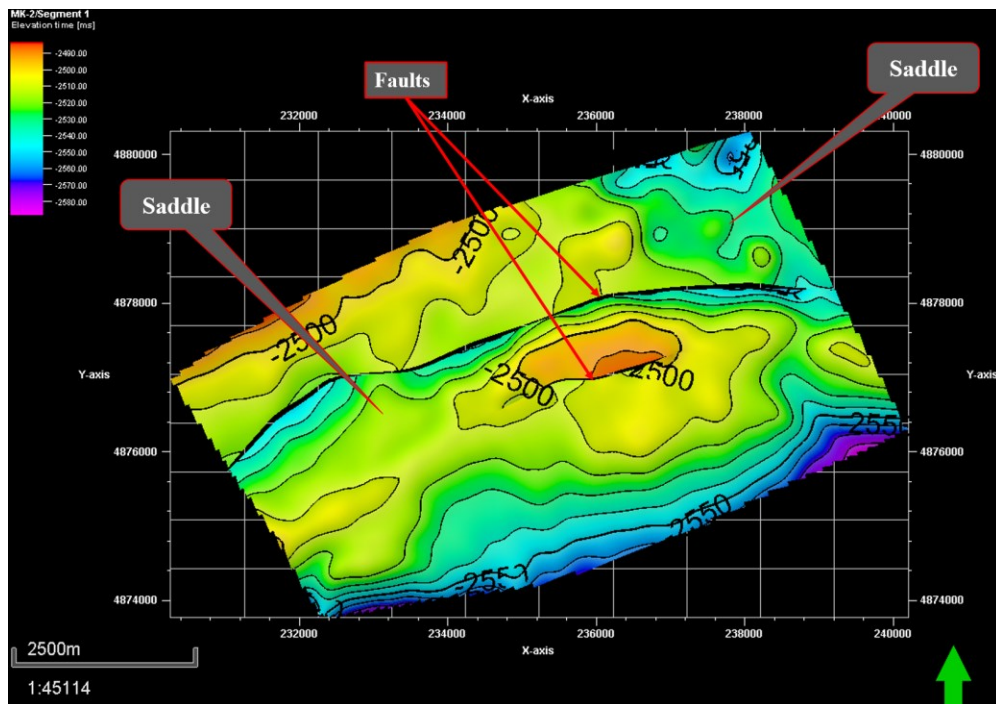


Figure 5.23: A reservoir depth map for the top of the uppermost reservoir Mk-2. The Migrant N-20 well can be seen passing through the crest of the structure (dark line) and the fault gaps for the two Migrant faults have been rendered (represented by the white area). The contour lines are in increments of 10 m. 5x vertical exaggeration applied. 5X vertical exaggeration applied.

Figure 5.24 shows five structural maps of the top of each reservoir in the Migrant Structure (MK-1 to MK-5) concerning the crestal fault. The maps with the crestal fault have been depth converted within the model area. Accurate interval thicknesses can be estimated based on the table of horizon intersection of the crestal fault and the well. As throw diminishes along the crestal fault plane with depth, there is a maximum throw of 40 m on the fault and zero throw on the bottom marker (Section 6.1.2.2.). With the fault intersecting the well through 2597 to 2635 ms, this corresponds to depths of 3765.65 to 3820.75 m using an average velocity of 2900 m/s.

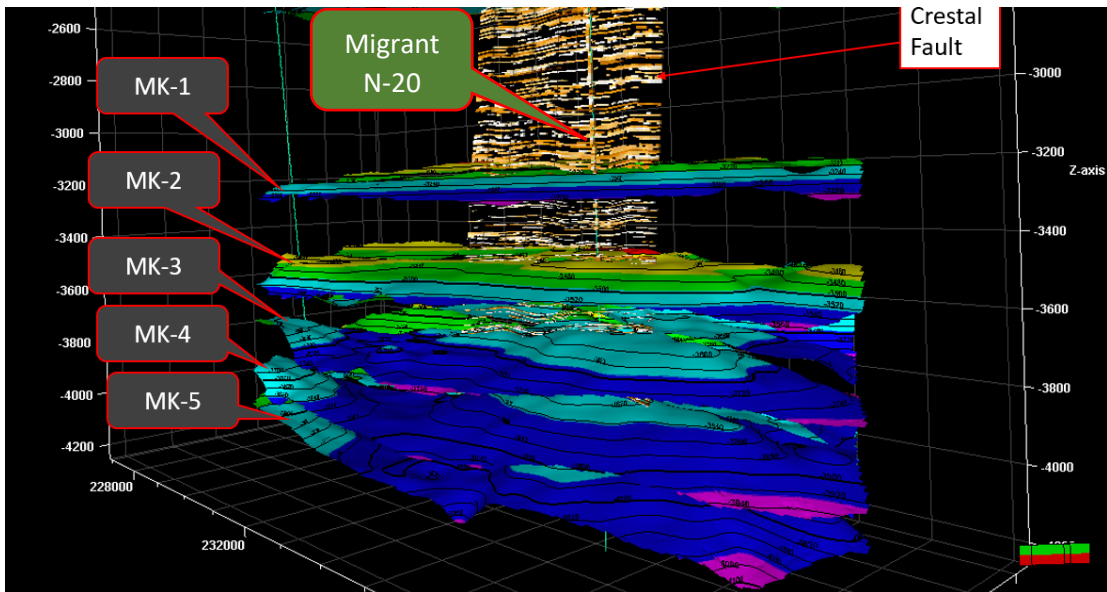


Figure 5.24: Depth converted structural maps of each interpreted reservoir top in the Migrant Structure (MK-1 to MK-5) concerning the crestal fault. In the figure, the Migrant N-20 well penetrates through all the available surfaces.

### 5.3.6. Petrophysical Modelling

In addition to the intersecting I and J planes of the depth converted Migrant Structure depicting the distribution of porosity, permeability and shale volume in the model Figure 5.25 and Figure 5.26, the distributed porosities and permeabilities as the various mapped horizons in the model are shown in Figure 5.27. As earlier stated in Section 5.2.3.11, the property distribution is dependent on the amplitude response of the seismic. For example, sand traps on the hanging wall were obvious in the structure given the bright seismic amplitudes that characterizes such zones of high porosity. This is obvious through the modelled intersecting I and J planes where good porosities are distributed shallow in the structure (Figure 5.25b and c).

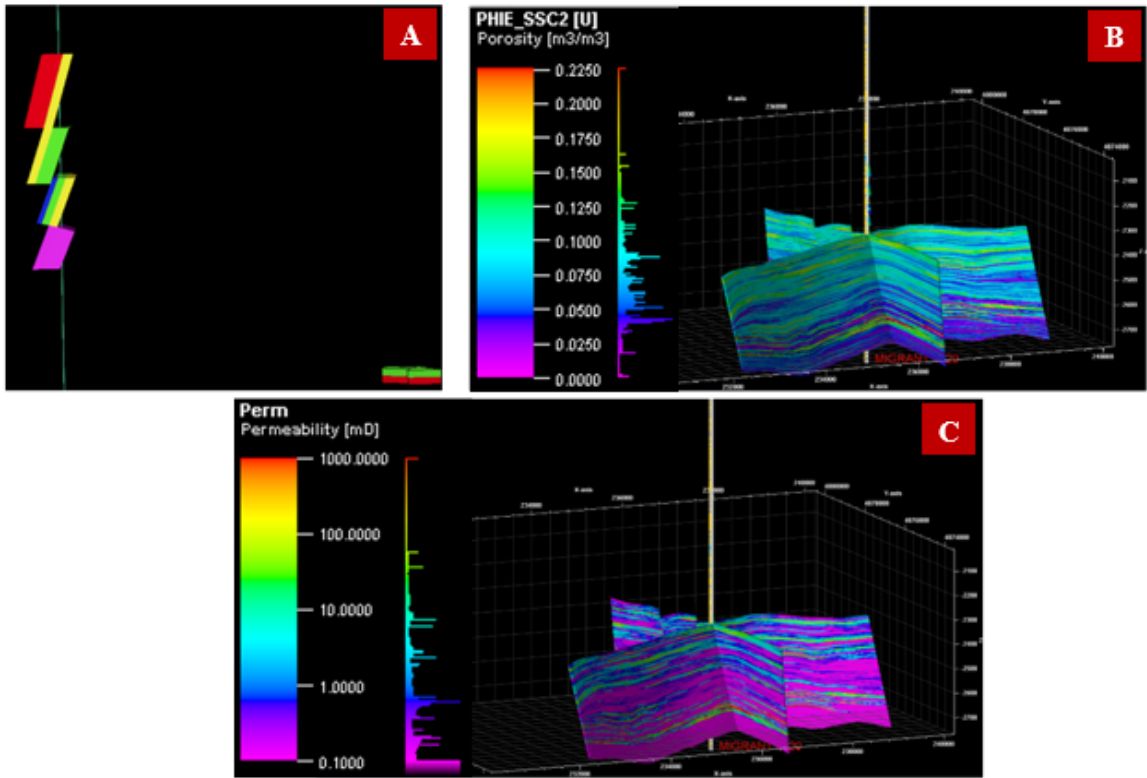


Figure 5.25: A figure of the scaled-up porosity log on the top left (A) and the intersecting I and J planes of the depth converted Migrant Structure depicting the distribution of the porosity (B) and permeability (C) derived from the porosity log in the property calculator through the structure. 5X vertical exaggeration applied.

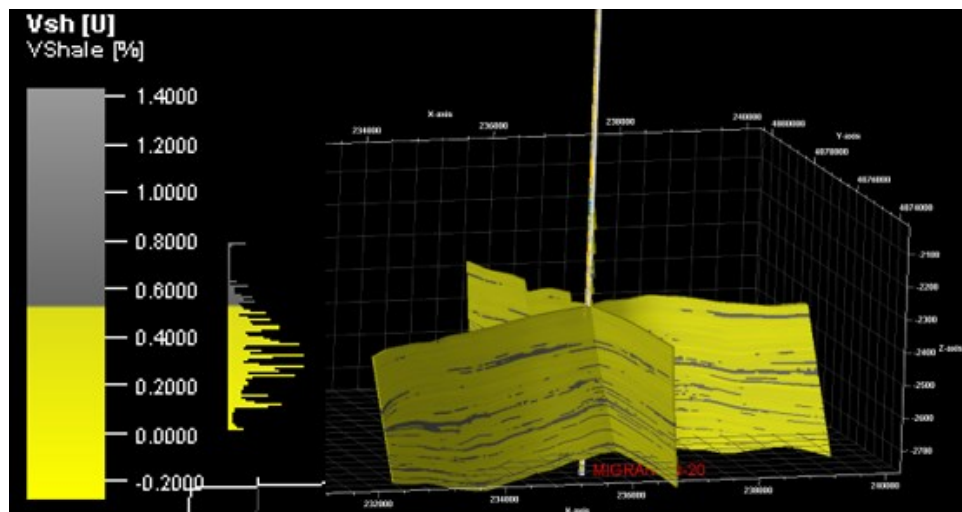


Figure 5.26: A figure of the intersecting I and J planes of the depth converted Migrant Structure depicting the distribution of shale volume (Vsh) derived from scaling up of the Vsh log through a step like the porosity log in Figure 5.25. This property makes up the key character distributed in Figure 5.32 and Figure 5.33 in Section 5.4.2. 5X vertical exaggeration applied.



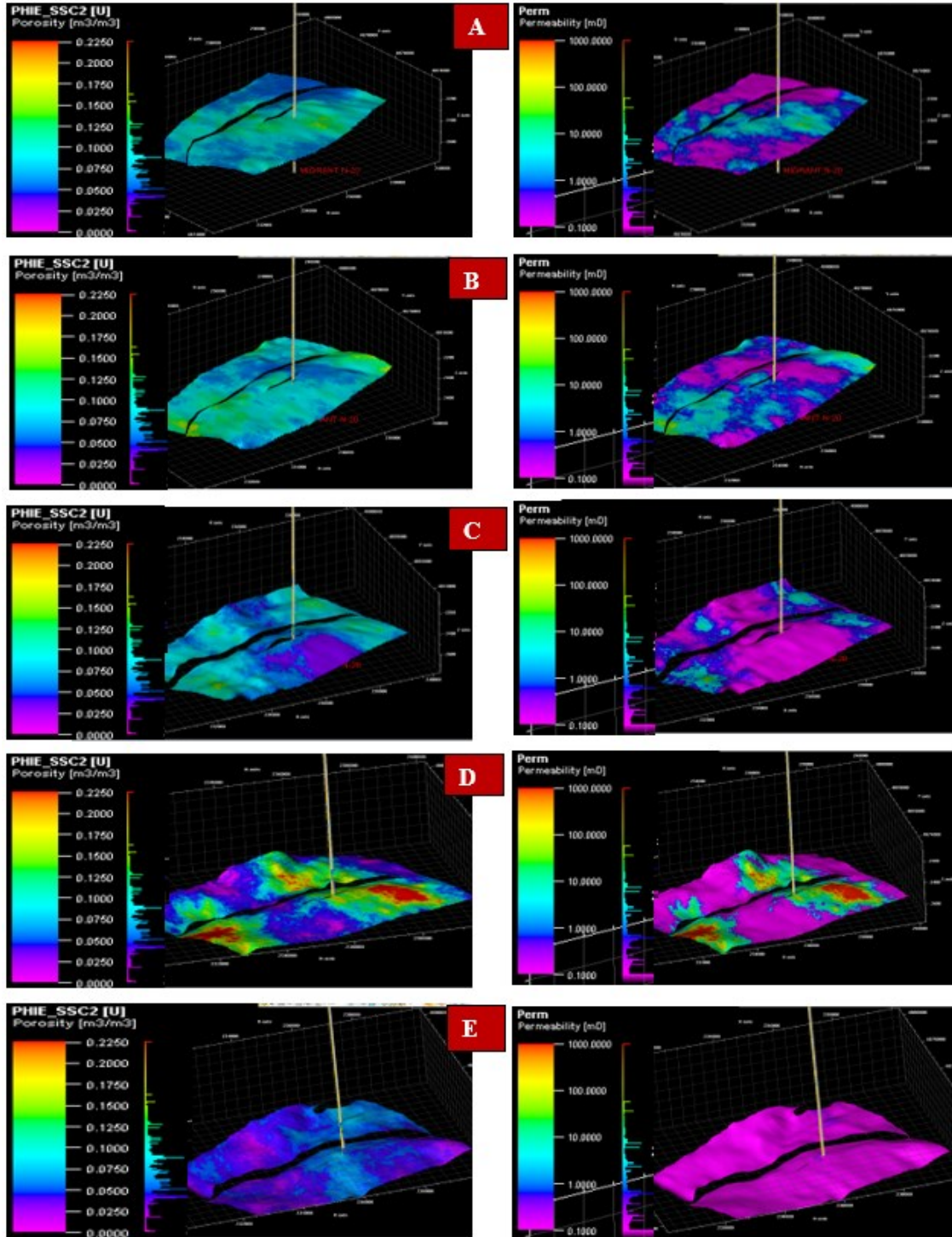


Figure 5.27: A figure of the porosity (left) and permeability (right) of the top of each of the five interpreted zones (Mk 1 to Mk 5) from top to bottom (A-E). The distribution of porosity and permeability for each of the horizons can be seen relative to the crestal fault which diminished down the structure. The best-connected porosity and permeability distributions can be seen in the top two horizons (A and B), and in patches in horizons C and D. The bottom horizon E shows diminished porosity and permeability distribution. 10X vertical exaggeration applied.

## 5.4. Discussion

### 5.4.1. Migrant Structure

The Migrant N-20 well was drilled to test for gas on a closure interpreted from 2D seismic data. The discovery of a small-scale, sub-seismic crestal fault, in the improved 3D Sable Megamerge seismic data was not apparent in previous interpretations of the 2D data. In shallower intervals intersected by the Migrant N-20 well, the penetration at the crest of the structure, there is crestal faulting with visible offset. This indicates a low likelihood for hydrocarbon trapping in the shallow to intermediate depths where the crestal fault has allowed cross-fault leakage within the 4-way dip closure of the structure, from approximately 3900 m upwards (Section 5.4.2.). Below this depth, the crestal fault appears to have moved off the apparent crest of the closure. As a result, there is an obvious change in the crestal fault plane down the Migrant Structure relative to the Migrant N-20 well penetration.

Without any crestal faulting, each flow unit would fill up with hydrocarbons to the structural saddle- a point of depression along with the axial trend of the rollover structure (Figure 5.28) At this point, contained hydrocarbons will spill out of the structure. With the limited influence of crestal fault in the Migrant Structure, below 3900 m the crestal fault has moved off the apparent crest and is characterized by the simple closure (Figure 5.29). As a result, it is reasonable to expect the reservoirs to contain hydrocarbons (gas). This is supported by the preliminary flow of gas trapped in thin, tight, sands within the closure, limited to the bottom of the Migrant Structure with minimal fault influence. Thus, in addition to the above-mentioned behavior of the crestal fault, which is absent in the zone of the successful test (DST #2), the poor reservoir quality also plays a role in the trapping of gas at the bottom of the Migrant Structure. Basically, where the reservoirs are of good quality at Migrant and of economic quality the trap fails due to cross-fault leak, and in areas deep in the structure where the crestal fault influence diminishes the trap is effective but the reservoirs are of poor quality.



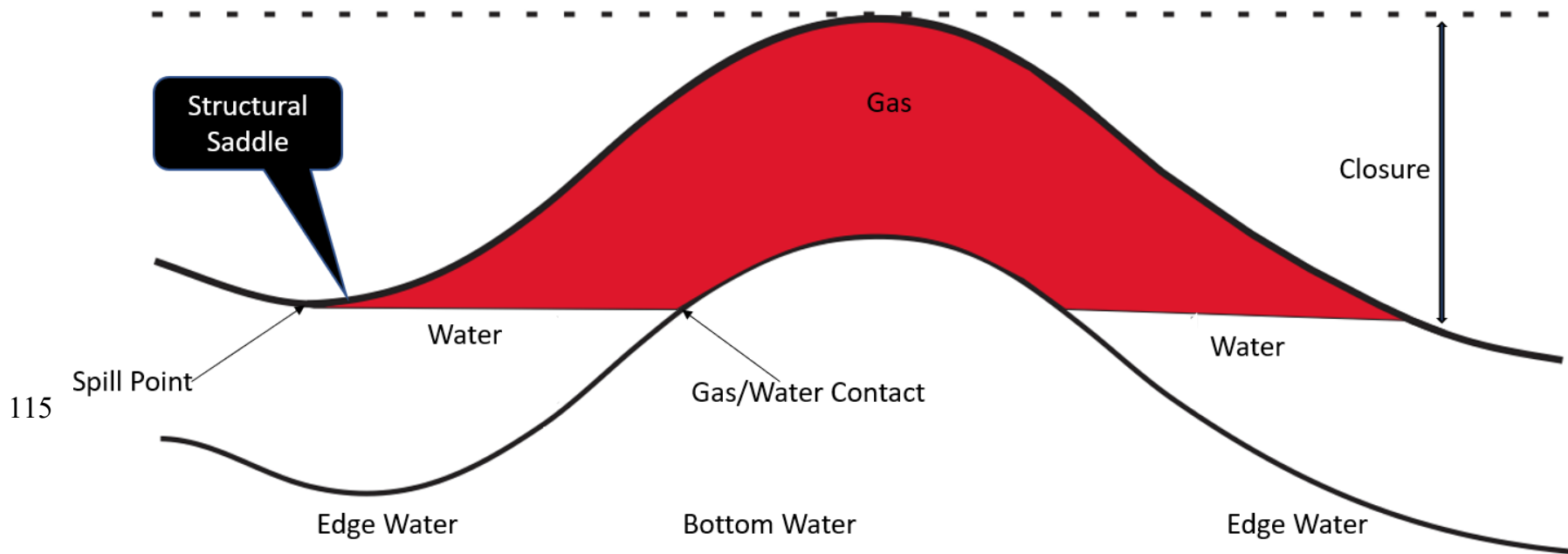


Figure 5.28: A simple structural closure showing various components of the structure and the relationship between fluids (gas and water) contained within. With enough hydrocarbon charge and in the absence of any faulting, there is a low tendency for leakage, which results in flow units filling up to their structural saddle point before spilling out in the structure.

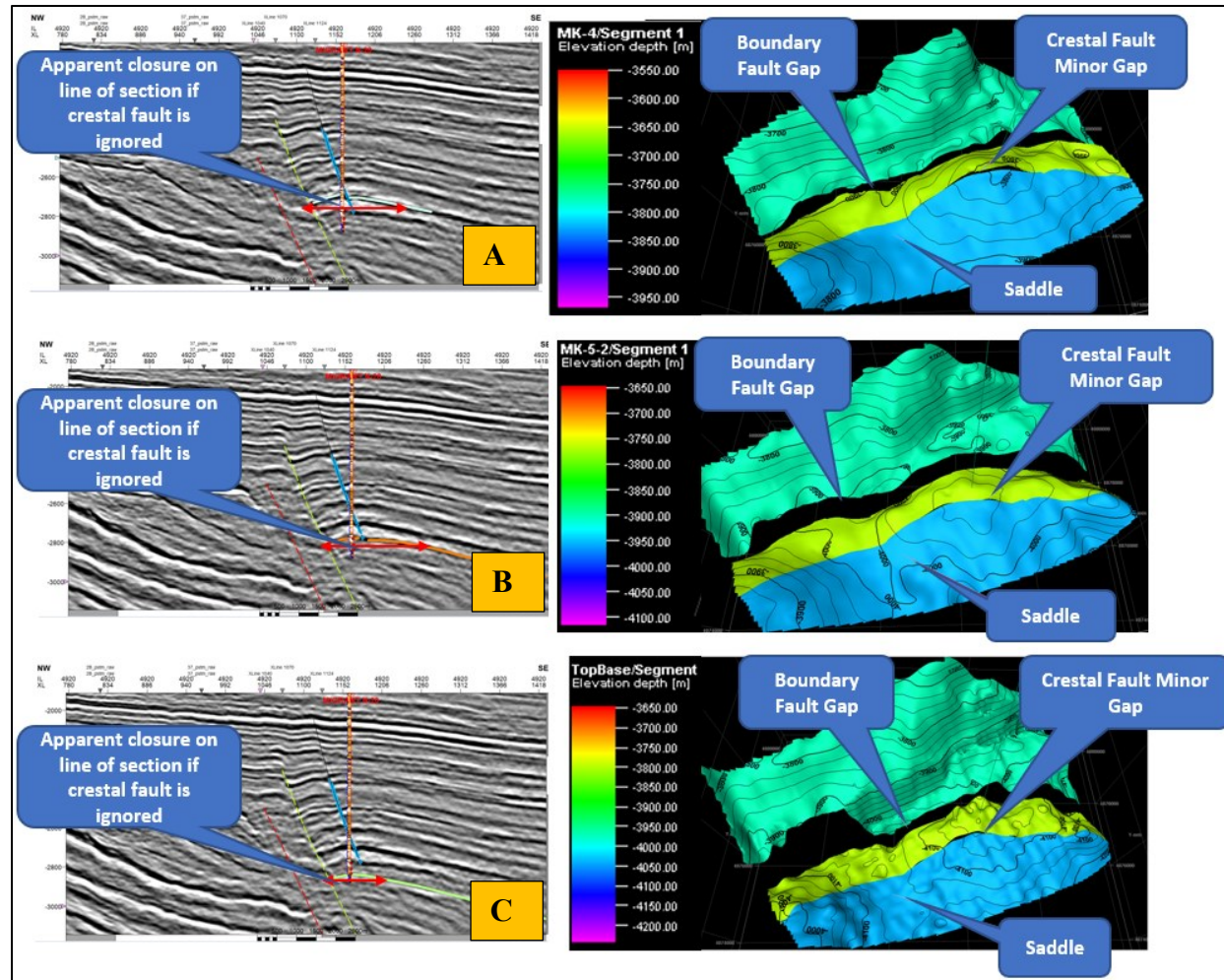
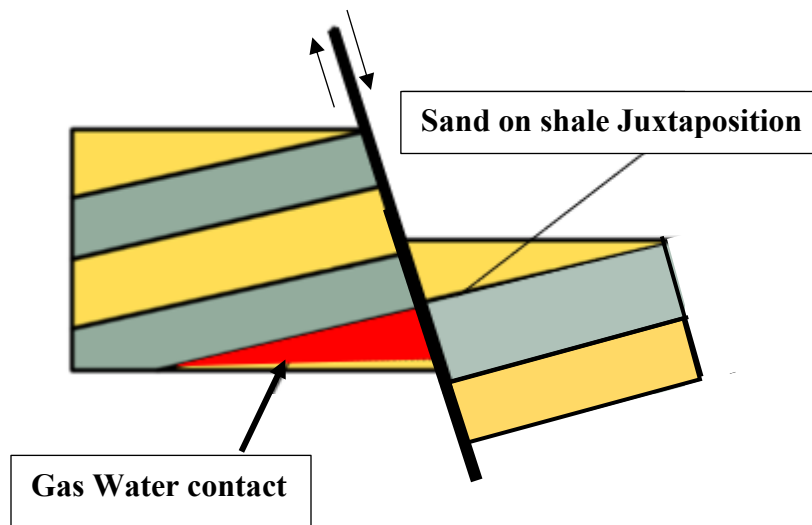


Figure 5.29: A figure showing seismic interpretation comprising key horizons and the crestal fault (faint black line) with structural maps of (a) Marker 4-Aqua, (b) Marker 5- Brown & (c) Marker Base-Green. Based on the maps, the boundary fault zone, the crestal fault, and the saddle point are indicated. These maps give the change in closure size and degree of crestal fault influence in the lower end of the Migrant Structure. 10X vertical exaggeration applied.

### 5.4.2. Fault Seal Analyses of the Migrant Structure

The principles of fault seal analysis and hydrocarbon trapping in rollover systems on the low side of listric growth-faults on the Scotian Shelf have been evaluated by past studies (Richards et al., 2008, 2010). The potential for a fault to lend itself as a barrier or conduit to fluid flow has been reviewed in the literature (Childs et al., 2002; Yielding et al., 2010) and commonly involves the interaction between controlling factors such as fault throw and the lithologies juxtaposed across a fault (Figure 5.30)



*Figure 5.30: A diagram depicting reservoir relationship at the fault (Move, 2016). The red line is a hypothetical fault trace, the grey represents shale seal, and the yellow represents reservoir sands. Red shows the accumulation of gas.*

At Migrant, hydrocarbons trapped deeper in the structure are attributed to the favorable combination of reservoirs and impermeable shale seals, combined with the downward termination/curvature of the crestal fault away from the crest of the structure. The close spacing of potential reservoir sands above the Missisauga section in the Migrant N-20 well observed in well logs (Section 4.3.1.), suggests that they are easily offset by fault displacement, which will impact potential hydrocarbon accumulation and production.

In the Sable subbasin, typical of a prograding shelf environment, net-to-gross ratios decrease with depth (Moss-Russell, 2009). This is accompanied by a diminishing closure size as observed in the Migrant Structure (Section 5.4.1.) and captured in the fault plane profile of the crestal fault at Migrant (Figure 5.32). The figure shows the sand distribution

in the footwall (orange) and the hangingwall (yellow) derived from the Vsh log propagated throughout the model with some porosity (10%). The black gap represents areas of the fault plane where the lithologies do not meet the cut-off criteria to permit fluid flow (mainly shales). The red arrows point to the areas where there is a juxtaposition of the sand between the footwall and the hangingwall.

As an important tool for prospect assessment, the fault plane profile shows the connectivity of permeable zones across the fault and the juxtaposition of sand units on the footwall and hangingwall of the fault. The high connectivity section at intermediate and shallow depths where there are well-juxtaposed reservoir permeabilities with one another in the footwall and hangingwall suggests that the wet reservoirs are at hydrostatic pressure. The increasing thickness observed in the sand and shale zone in the upward direction in the Migrant Structure, suggests an increase in net-to-gross along the fault plane upward in the structure. This fault disrupts the integrity of the trap, which is why the Migrant Structure is water wet.

From the fault plane profile, the reservoirs around the shallow and intermediate Missisauga Formation depths of the Migrant Structure have poor fault sealing evident from their numerous juxtaposed leak points. Hence, it is likely that hydrocarbons migrated through the system at multiple established leak points between reservoirs. The high degree of sand on- sand connectivity across the crestal fault at Migrant in Figure 5.31 and Figure 5.32, combined with petrophysical and well data corroboration in section 6.3.1, shows that the reservoirs at the shallow and intermediate depths of Missisauga interval of the Migrant Structure are predominantly wet (with some residual hydrocarbons). To ensure adequate trapping, the amount of displacement between the fault and shale thicknesses will have to be minimized to prevent upward migration of fluids (Almon & Dawson, 2004; Dawson & Almon, 2002, 2006).

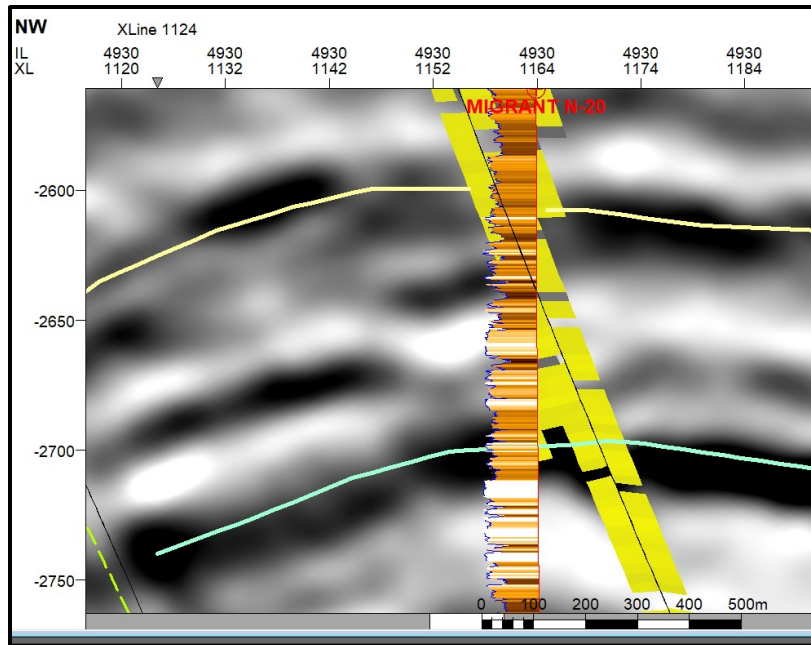


Figure 5.31: A figure of the Migrant N-20 well showing the intermediate reservoirs between Mk 3 and Mk 4 indicated in Figure 5.32 and Figure 5.33 below approximately 3770 m – 3904 m. This interval is intersected by the crestal fault at the wellbore and occurs much higher than the three DST test zones at the bottom of the well.

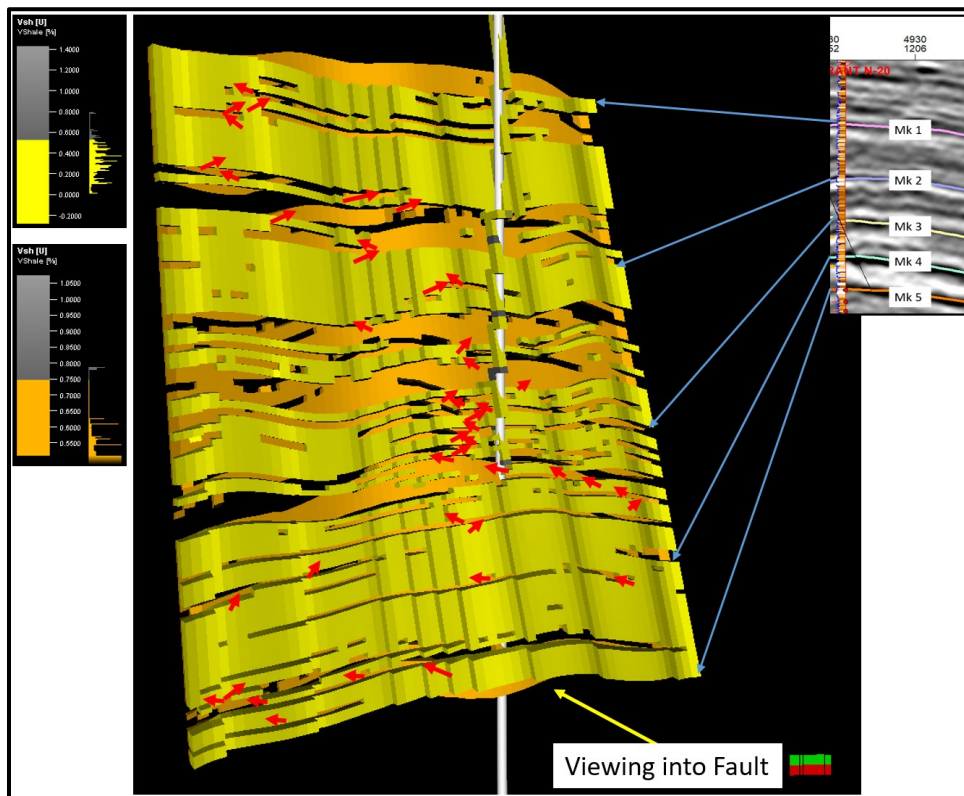


Figure 5.32: A fault plane profile (FPP) of the crestal fault in the Migrant Structure looking northwest. 7.5X vertical exaggeration applied.



Given that the three DST test intervals (Section 4.4.4.) have similar porosities and water saturation, the bottom-most DST interval #2 showed a much-uplifted permeability value of 200-300 mD-ft compared to the 3-25 md-ft range for the average calculated log matrix value. Irrespective of the well summary report indicating that the top two tested reservoirs above (DST #5 and DST #8 test intervals) were tight and unable to deliver any flow (Tetco, 1978), the bottom test interval that flowed gas was within four-way dip closure. This is further supported by the slight increase in pressure (Section 4.3.2.). The flow test result suggests an enhancement in permeability thickness (Kh) up to 301 mD-ft in the bottom test interval, which may be related to induced fracturing likely from activity along the boundary fault plane given that the test intervals fall below the extent of the crestal fault influence (Figure 5.33).

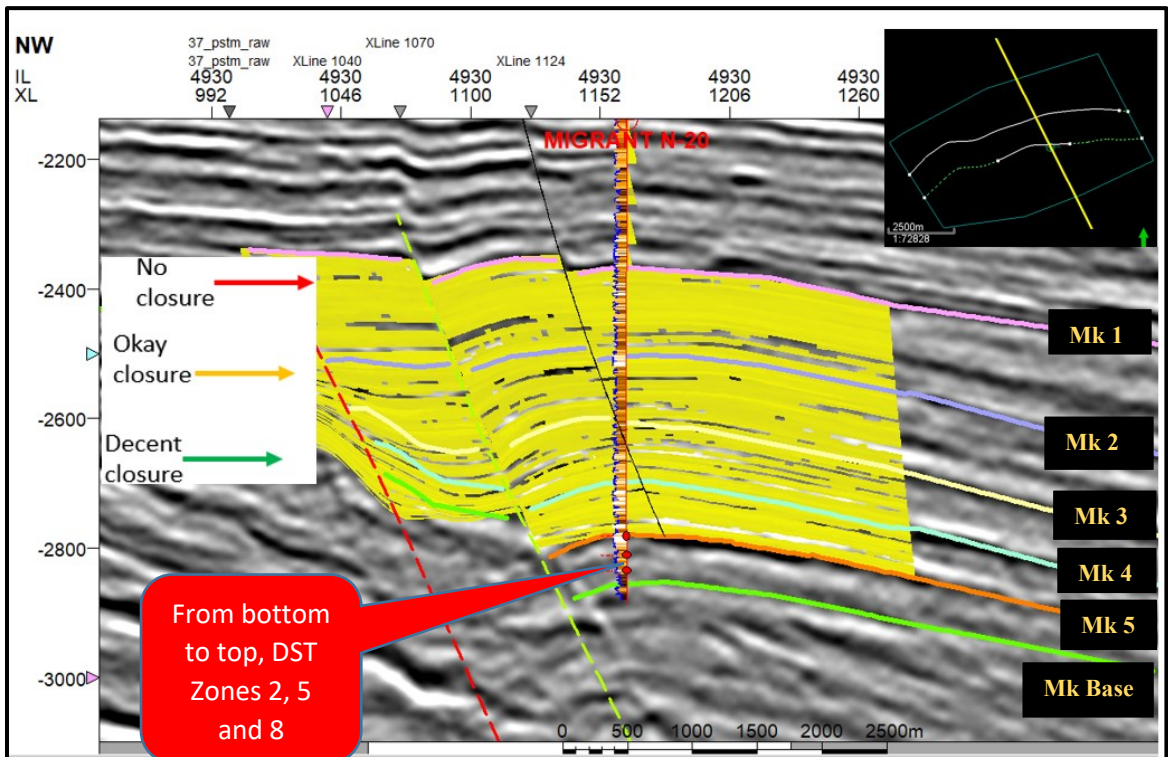


Figure 5.33: A modelled cross-section of the Migrant Structure populated with sand and shale properties from well log value reveals the magnitude of crestal faulting through the offset of sand-shale pairs. In shallow zones, faults with larger throws in a high net to gross section produce leakage of hydrocarbon. At the intermediate to deeper sections, the fault displacement is smaller as the fault soles out in more distal lower net to gross intervals. At greater depths, the reservoirs are cemented (tight) and are discontinuous. Following the fault trace, the fault terminates above the tested sand reservoirs that range from 4100 – 4205 m depths. Zero vertical exaggeration applied.

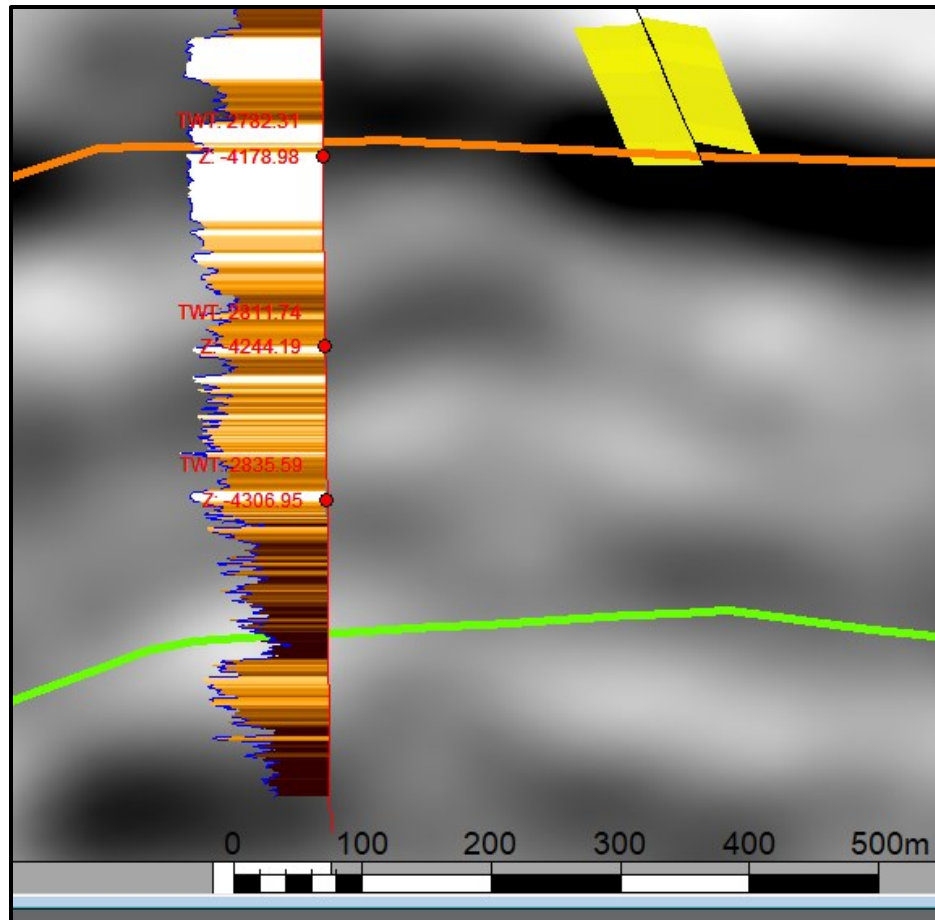
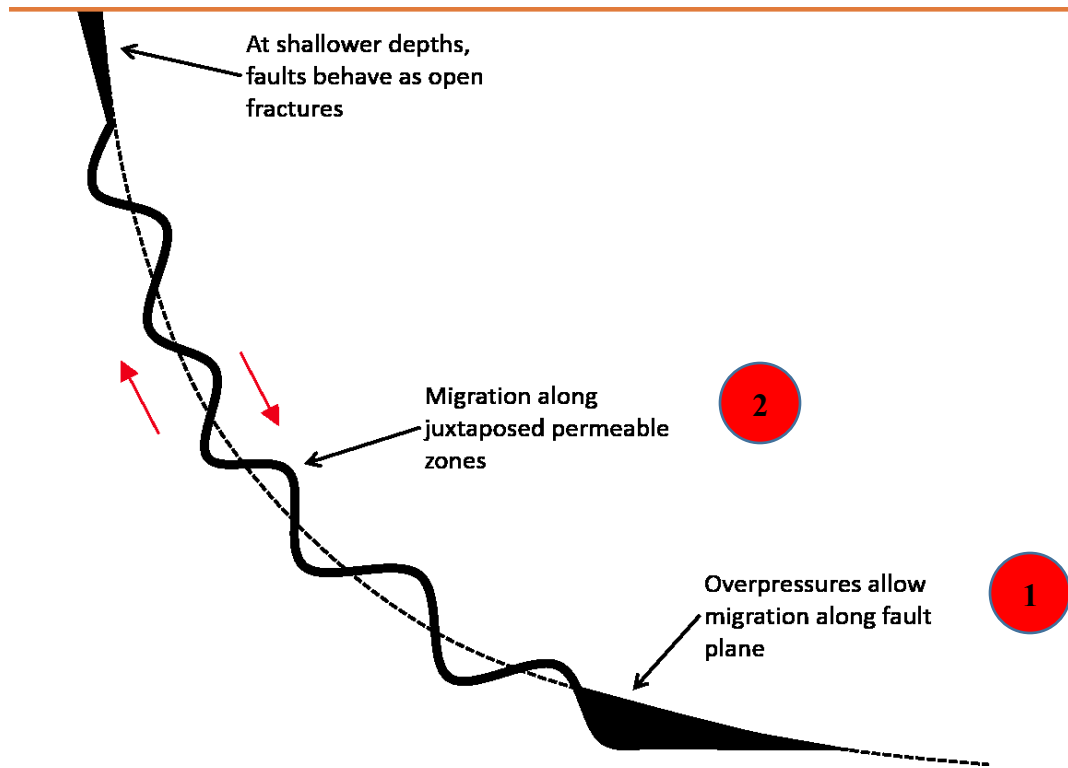


Figure 5.34: A figure of the Migrant N-20 well showing the bottom tight reservoirs between 4178 m – total depth TD. This interval contains the three DST test zones. Also, the crestal fault trace terminates just above the top tested sand reservoirs MK 5 in Figure 5.33 above.

For reservoirs at such great depths in the Migrant Structure, it will be difficult for fluids that would easily exit reservoirs in the shallow and middle sections to exit the zone given the low permeability. Work by Skinner et al., (2016) demonstrated that faults in the Sable Subbasin are characterized by two examples of three migration pathways, proposed by Downey (1994) in Figure 5.35. The first of these two involves the migration along a fault plane at greater depths where hydrocarbon accumulations have sufficient excess pressure to mechanically breach seals or open faults ( $>$  fracture closure pressure). This typically occurs above 2/3 of the lithostatic pressure. As the reservoir fills up, the pressure is relieved through leakage up and across a fault (likely the border fault) after which there is a corresponding build-up of pressure again as hydrocarbon is generated, and/or more compaction occurs. In the second pathway, hydrocarbons migrate across fault up



juxtaposed permeable units in a stair-stepping trend as expected in the intermediate and shallow depths.



*Figure 5.35: A diagram of the modes of hydrocarbon migration at various depths (Downey, 1994). Hydrocarbons can migrate along the fault plane at a shallow depth where they behave as open fractures (1) or juxtaposed permeable zones (2). The increased connectivity shown higher up in the chart is not seen at Sable. Such criteria are common in places where the faults become vertical and horizontal stress is low resulting to little separation between hydrostatic and lithostatic pressure lines like in the Rocky Mountains in the Western Canada Sedimentary Basin (WCSB). In addition to the build-up of pressure required before fluids may be released deep in the Migrant Structure, there is considerable downward stress acting to close the fault. As the overburden stress ( $\sigma_1$ ) almost completely acts normal to the fault, it progressively gets more listric deeper in the section as it overrides the substrate. In contrast, the stresses acting on the better reservoirs that show more juxtaposition and connectivity in the shallow and intermediate depths do not close the fault as much as they do deeper down the Migrant Section.*

Each time the capillary pressure of the top seals, or the fracture closure pressure of the fault is overcome, the reservoir may reach a critical pressure needed to exceed the capillary pressure of the seals or fault, which is capable of opening up the fault (Richards et al., 2008, 2010). In other words, for this to happen at the Migrant Structure, pressure equivalent to (if not higher than) the weight of all the overburden rock or pressures approaching lithostatic pressure, is required. This pressure is usually greater than the

hydrostatic pressure shallow up the system. Hence, for the crestal fault to act as a conduit for fluid flow, depending on the amount of critical stress it receives, there may be periodic reactivation following hydrocarbon charge (Move, 2016). Nevertheless, areas of sand juxtaposition are seen in Figure 5.31 and Figure 5.32 above at a crestal fault means that reservoirs in a structure may not fill to its saddle point. This was the case in the Migrant Structure where up to 10 m of fault offset is greater than the thickness of potential shale seals (especially where lateral sealing is needed). As a result, this was enough to pose a risk on the ability of the structure to effectively trap commercial hydrocarbons.

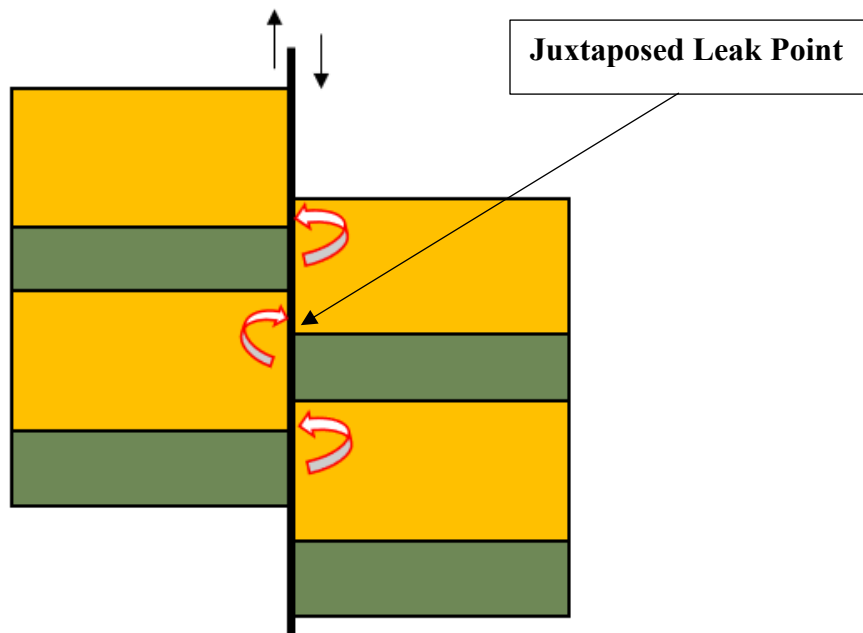


*Figure 5.36: Diagram showing an upward and outward migration scenario through juxtaposed leak points. The black line is a hypothetical fault trace, the grey represents shales, and the yellow represents reservoir sands. With increased fault movement, there is likely to be breaching of the trap, thus, facilitating the up-fault flow of hydrocarbons. This happens when the fault throw is greater than the thickness of the shale units present.*

#### 5.4.3. Fault Seal in Analogous Settings

The upwards and outward flow characteristics in Figure 5.36 is consistent with fluid migration pathway in a juvenile basin such as the inner trend subbasins of the shallow offshore areas in the Niger Delta. These basins are formed from a series of progressively younger prograding depocenters such that the younger depobelts are thought to have more juvenile characteristics than the older landward depobelts (Wach et al., 1997). Due to the younger age of the associated shallow offshore inner trend subbasins, the upward and

outward migration of fluid is expected (Wach et al., 1997; Figure 5.37). However, the presence shale diapirs against which seaward dipping parallel beds are truncated (Figure 5.37b) suggests that the upward and outward migration of fluids from the sediments adjacent to the shale diapir will be complicated. As a result, with increased fault displacement, there is increased tendency for lateral sealing provided by shale smearing, which acts to prevent upward fluid movement (Wach et al., 1997).

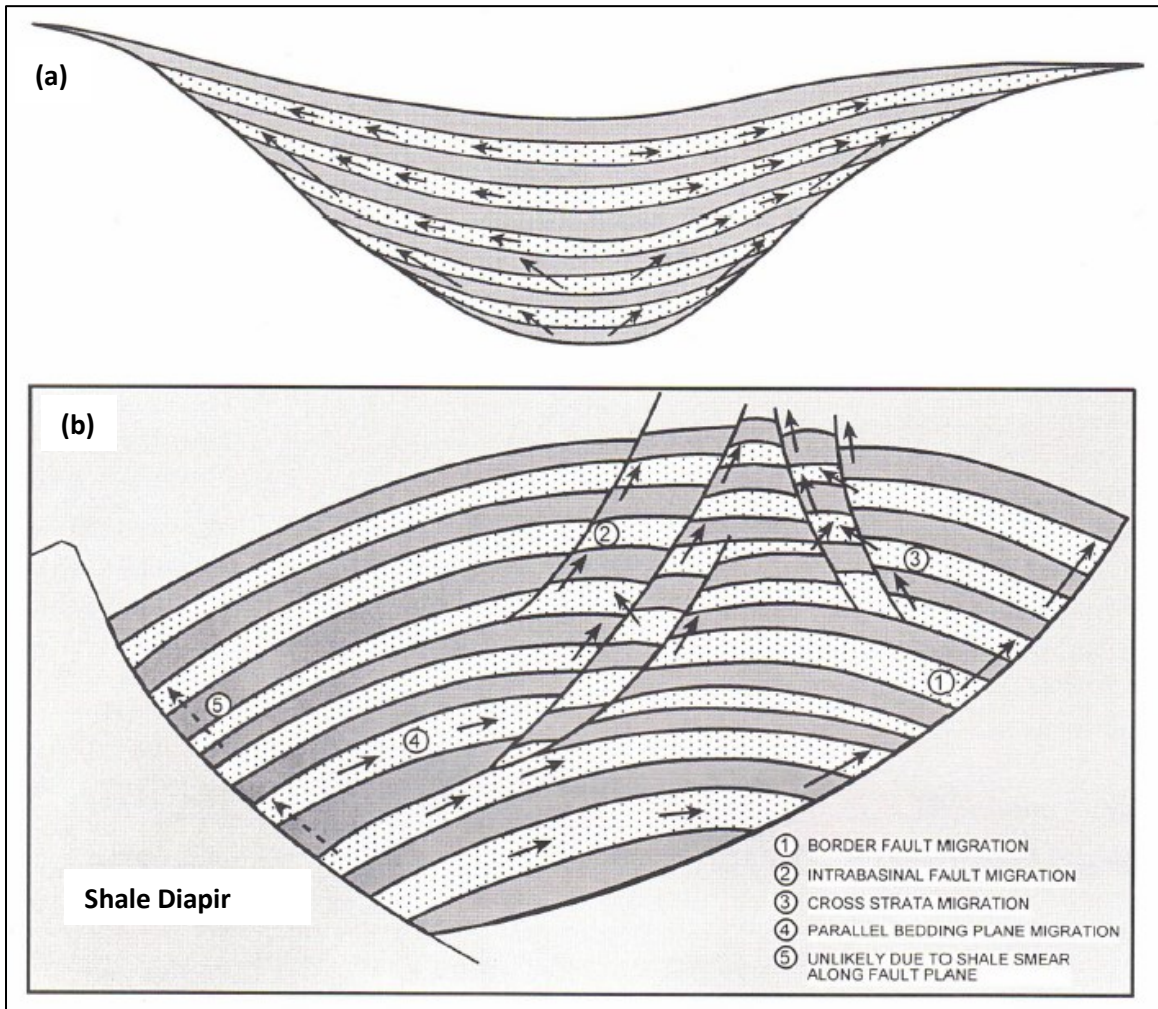


Figure 5.37: A schematic showing (a) the upward and outward fluid migration pathway within a juvenile basin from the basin depocenter, and (b) migration pathways for fluid flow within the inner trend subbasins (Wach et al., 1997).

Alternatively, depending on the fault displacement, the growth faults combined with complex collapse structure associated with antithetic faulting at the crestal areas of the North Apoi-Funiwa Field located in the inner trend of the Niger Delta (Section 6.1.2.1.) may or may not seal juxtaposed reservoirs (Wach et al., 1997). Originally thought to be

two separate fields offshore Nigeria, North Apoi-Funiwa are related by spill points governed by their gas drives (Wach, pers comm. Mar. 2021). This supports reports of their faults being conduits for reservoirs connectivity (Cathles et al., 2003), allowing for a net upward flow as observed in the middle of the Downey diagram in Section 5.4.2 (Richards, pers comm. Mar. 2021). Therefore, considering the likelihood of shale smearing to severely restrict upward fluid flow at the border fault, the internal cross-fault juxtapositions within the expansion trends (like the Migrant crestal fault) allows for net-upward cross-fault leak.

## CHAPTER 6

### DISCUSSION

This chapter discusses the Migrant Structure, including trapping mechanism in structural analogs, overpressure, depositional relations with analogs, reservoir aspects, trapping scenarios with conditions (including fault seal), and considerations for offshore Nova Scotia. This chapter builds on the results and discussions from previous chapters, including stratigraphic analyses, pressure analysis, petrophysical analysis, and geocellular modelling. In Chapter 5, a small crestal fault just above seismic resolution appeared to allow cross-fault juxtaposition of reservoirs in the footwall and hangingwall at Migrant. Allan diagrams have been used to characterize in the Migrant Structure to show areas of potential cross fault juxtaposition. Given the active petroleum system in the Sable Subbasin, reservoir and seal pairs produced as a result of the deltaic depositional setting and transgressive and regressive events produces effective sealing by marine shales. The distribution and intrafield migration of hydrocarbons may be attributed to high net-to-gross and increased faulting (Figure 6.1). The presence of residual gas saturation observed in the intermediate areas of the Migrant N-20 trap is proof of the migration and leakage.

#### 6.1. Trapping Mechanisms of the Migrant Structure

##### 6.1.1. Sediment Interactions in Structural Rollover

Rollover anticlines are ubiquitous geological features common in thick deltaic depositional environments (Cummings & Arnott, 2005). Literature review including Wach et al., (1997), Wach et al., (1998), Wach et al., (2000), and Wach et al., (2002) shows that rollover structures result from sediment compaction on an uneven topography with the formation and evolution of basin-ward normal growth faults due to sediment progradation. With an outward and upward depositional trend in each of the expansion trends (Pe-Piper & Piper, 2011), gliding and slumping of deposited sediments over any underlying substrate are common (Adam et al., 2006; Vendeville, 1991; Figure 6.1).

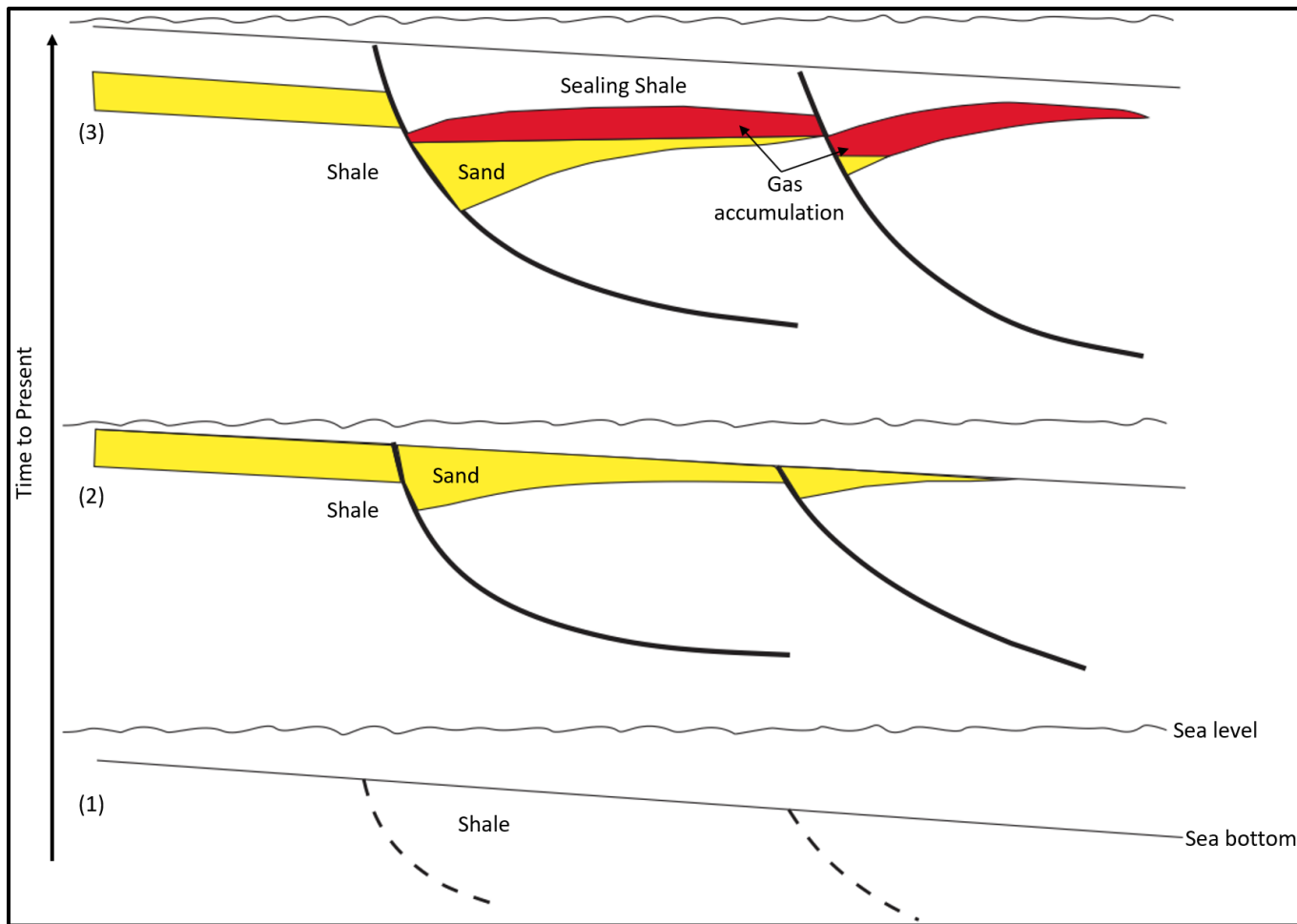


Figure 6.1: An illustration of the stages of growth fault development in a sedimentary basin (Modified after SOEP 1997). In the beginning stages, there is initiation of listric fault formation. During the intermediate stage, there is an onset of listric fault movement and associated clastic-rich sediment deposition. At the final stage, a rise in sea level or change in the direction of deltaic advance gives way to the deposition of shales that act as the top seals for reservoirs in the rollover. These transgressive and regressive cycles form excellent reservoir/seal pairs.

In Figure 6.1, the shape and size of rollover structures depends on their bounding listric fault, which progressively change becoming arcuate in shape with depth. Listric faults are often triggered by sediment loading in deltaic regimes such as the Orinoco (Sydow et al., 2003; Wood, 2000), Mississippi (Sydow & Roberts, 1994; Sydow et al., 1992) and Niger deltas (Mitchum & Wach, 2002). The additional loading coupled with a decollement surface of shale beneath the sediment creates a failure plane that the fault propagates on (Cohen & McClay, 1996). In the Gulf of Mexico, the basins formed in this manner are often called Mini-Basins (Mallarino et al., 2006). With increased depth, the once normal fault becomes curved and flattens after encountering the underlying substrate (e.g evaporites) (Deptuck, 2011; Vendeville, 1991).

Continued interaction with the underlying lithology (salt in the case of the Scotian Shelf) likely accentuated the basinward curvature of the faults, resulting in the rollover formation. Based on these interactions, sediment loading of the hangingwall was involved during normal growth faulting and rollover trap formation (Adam et al., 2006; Cummings & Arnott, 2005; Vendeville, 1991). Hence, episodes of basin-ward sedimentary influx aided in a downward displacement of the hangingwall at the fault accompanied by the creation of accommodation space. When the accommodation space is filled, sediments bypass the initial basin that is filled and spills over into the next basin, basinward as depicted in Figure 6.2 (Wach et al., 2000). This has been referred to as the fill and spill model in the Gulf of Mexico (Beaubouef et al., 2003; Beaubouef & Friedmann, 2000). This occurs when large-scale zones of listric faulting create an influx of sediments, often deltaic, which expanded into the additional accommodation space created in the basinward direction. This is evident offshore the Niger Delta (Wach et al., 2000; Figure 6.2) as well as in the Mesozoic Sable Delta (Richards et al., 2008; 2010).



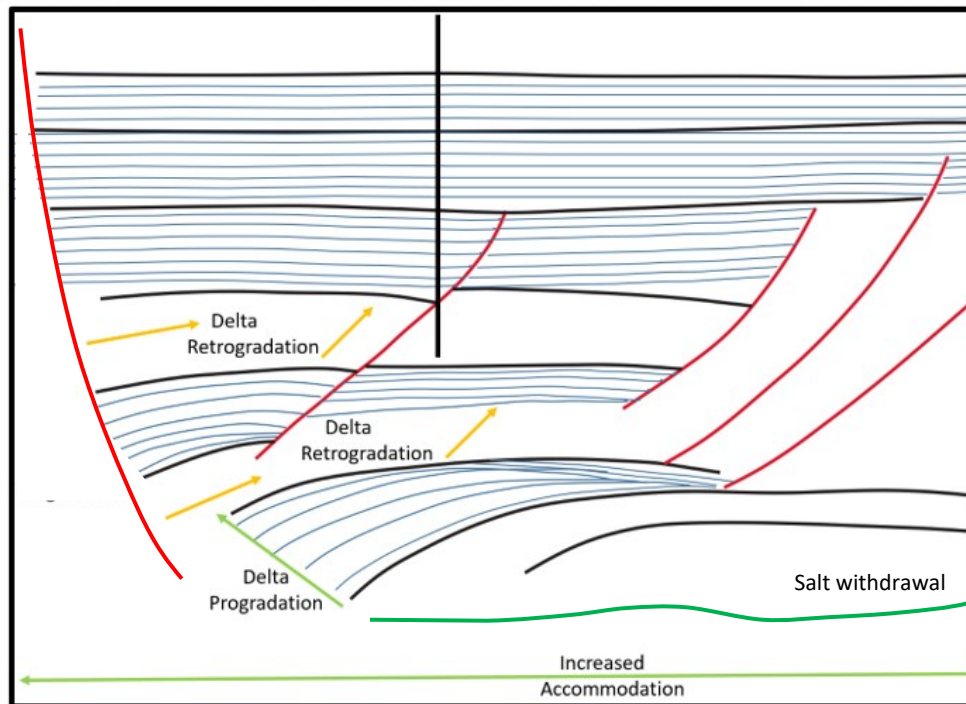
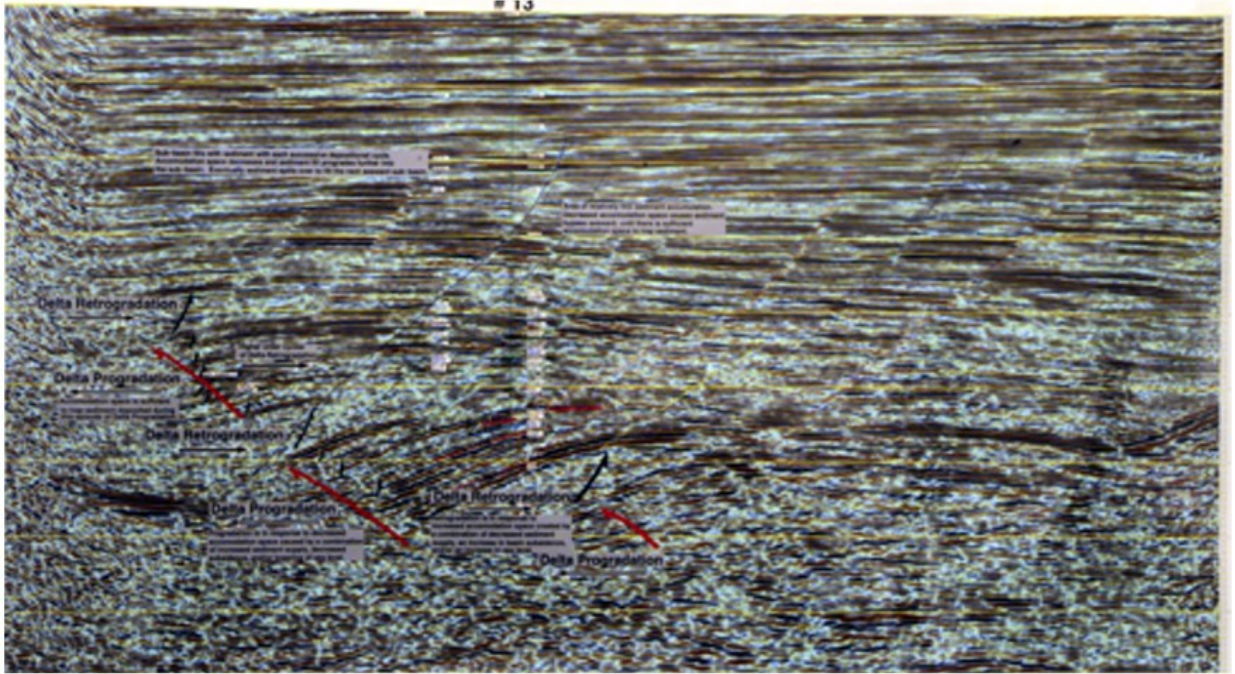


Figure 6.2: A seismic section and annotation of the Miocene Queen Bess Field in Louisiana from Wach et al. (2000). There is progradation (sand) packages represented by the downward dipping reflectors in seismic and retrogradation (shale) quiet seismic amplitudes. Decreased accommodation space is caused by a combination of increased sediment supply and decreased subsidence. With increased accommodation, from a combination of decreased sediment supply an increase in basin subsidence (salt withdrawal) and the increase in relative sea level caused a retrogradation of the delta. The chaotic seismic facies to the left and below the section is cognizant of counter regional faulting and salt withdrawal in the system.

The fill and spill process makes well log stratigraphic and biostratigraphic correlation difficult in basins with considerable listric faulting, for example, the East Coast Marine Area (ECMA) of offshore Trinidad (Wood, 2000). With increased slippage, more accommodation is created for new sediments (Vendeville, 1991; SOEP, 1997). The sediment loading and syndepositional fault dynamics that resulted in the bending of the fault blocks along with the depositional trend gave rise to reservoirs that are thickest at the fault. As suggested by Serck and Braathen (2019), a termination of the strata in the hanging wall block and absence in the footwall is an indication of continued folding. In Figure 6.3 and Figure 6.4 below, sand-rich deltaic siliciclastics in each expansion trend can be seen in front of the major bounding faults. The variation in sediment thickness between the deeper and shallower sections of each of the fault blocks may be used as a proxy for the timing of fault movement. As fault throw changes from the top to bottom in the Missisauga stratigraphic package at Migrant, the increased thickness between the basal carbonate marker (Abenaki 4) and the overlying clastic transgressive and regressive cycles (sandstones and shales) shows a considerable decrease in the thickness around the shallow sediments.

In each of the fault blocks in Figure 6.3 & Figure 6.4 below, changes in localized accommodation space have been influenced by changes in their counter regional dips. This affected the sedimentary deposition to the extent that some siliciclastic sections deposited right of the border fault (hangingwall) have little to no equivalents on the footwall. In the adjacent fault block, the sequence of thin interfingering clastics and carbonates around the vicinity of the Migrant N-20 well suggests the periodicity and the timing of fault displacement. Hence, the size of the reservoirs in the footwall block is controlled by the timing of formation and evolution of bounding faults. In advanced stages of deposition, some sedimentary sections in a succeeding fault block may not exist in the previous fault block, which may be attributed to a period of fault inactivity following complete infilling of the previous basin and subsequent sediment bypass to the next depocenter outward. In the shallow sections, there is a gradual drop in sediments further outwards through the bypass of the sediment across the earlier depocenters, where they are overlain by new sediments.

The strong reflectivity in the Missisauga Formation is indicative of high clastic activity, which interfingers with zones of low reflective and homogenous sediments (likely shales). Also, hydrocarbon shows in a reservoir can cause the occurrence of high amplitude signals or “bright spots” on the crestal fault at different levels of the Migrant Structure in 3D and highlight the hydrocarbon trapping mechanism. It appears that the listric fault and salt interaction are two key controls on timing of anticline trap formation in the Migrant, Adamant, and Thebaud structures based on their structural relationship. Therefore, the deposition of sediments into the hangingwall of a fault block with no equivalent on the Footwall as seen at Thebaud (Figure 6.4) may be a result of rapid influx of clastics from the north of the basin (Campbell, 2018).

Despite the productive Thebaud reservoirs that produced gas occurring at an absolute depth below the Migrant N-20 well (Figure 6.4), the reservoirs at Migrant are older than the deepest Thebaud reservoir. With the change in curvature of the bounding fault at Migrant, the optimum closure required for hydrocarbon trapping is limited to the base of the structure (below the depth at which the crestal fault appears to tip out or end). Hence, the idea that a different trapping style exists between the deep overpressured reservoirs at Thebaud and normally pressured reservoirs with hydrocarbon shows is reasonable. Also, as the extensional response of the rollover to the main listric fault, the formation of crestal fault that penetrates the normally pressured reservoirs at Thebaud, and the Migrant reservoirs have played a key control in their ability to work or fail as hydrocarbon traps. With the absence of any closure around the level of O-marker and continuity of that reflector from hanging wall to footwall side, its depositional period likely coincided with a period of tectonic quiescence. Thus, the timing of the trap formation occurred until the deposition of the blue horizon in all three fault blocks.

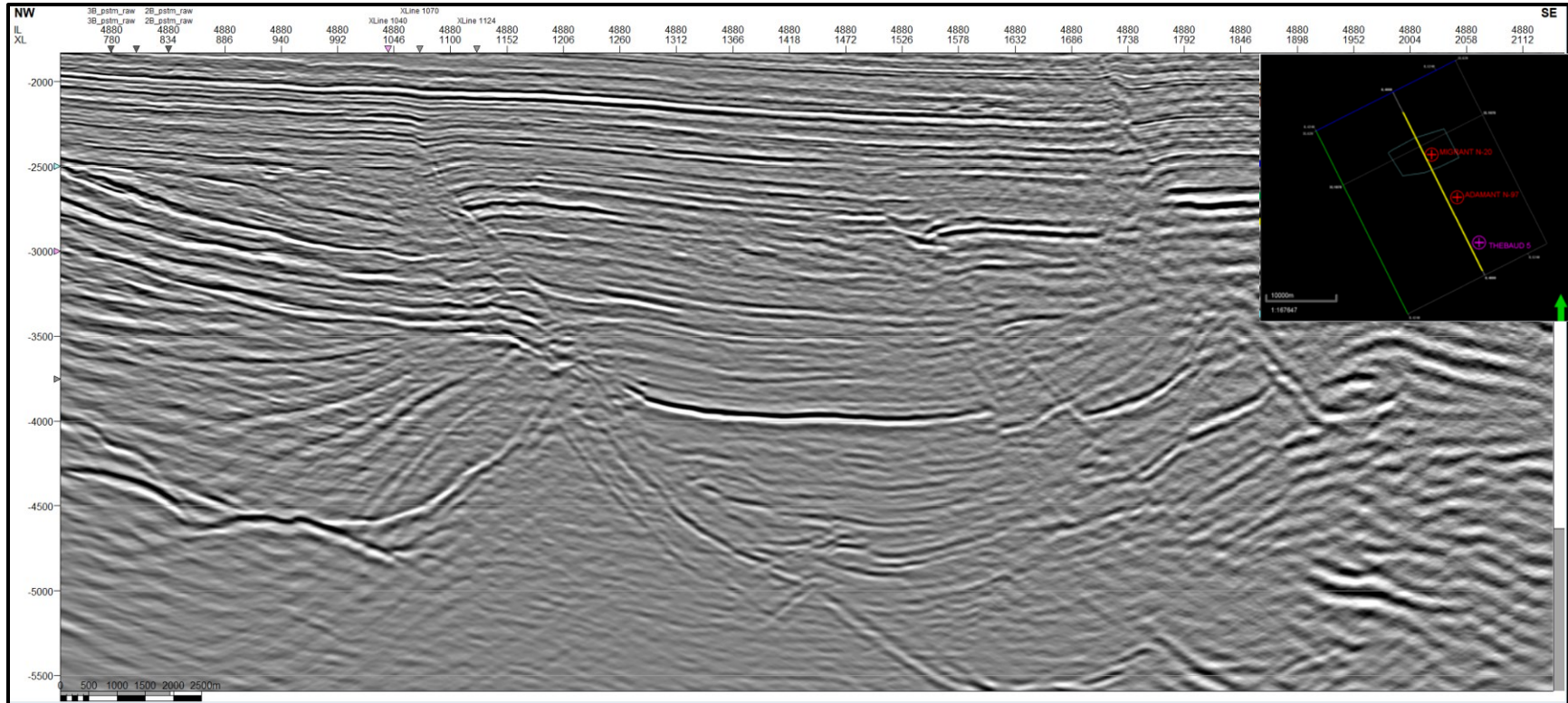


*Figure 6.3: An unannotated seismic image of the Migrant, Adamant, and Thebaud structures. The fault can be identified in the clastic section through the offset created between the cyclic reflectors around the proximal shelf areas. Distinguishable through their respective seismic polarity, some high amplitude signals are an indication of carbonate layers. Additionally, the varying dips between the overlying and underlying reflectors at the base of the clastic sequence at the Migrant Structure exhibit distinct seismic characters that resemble an angular unconformity.*



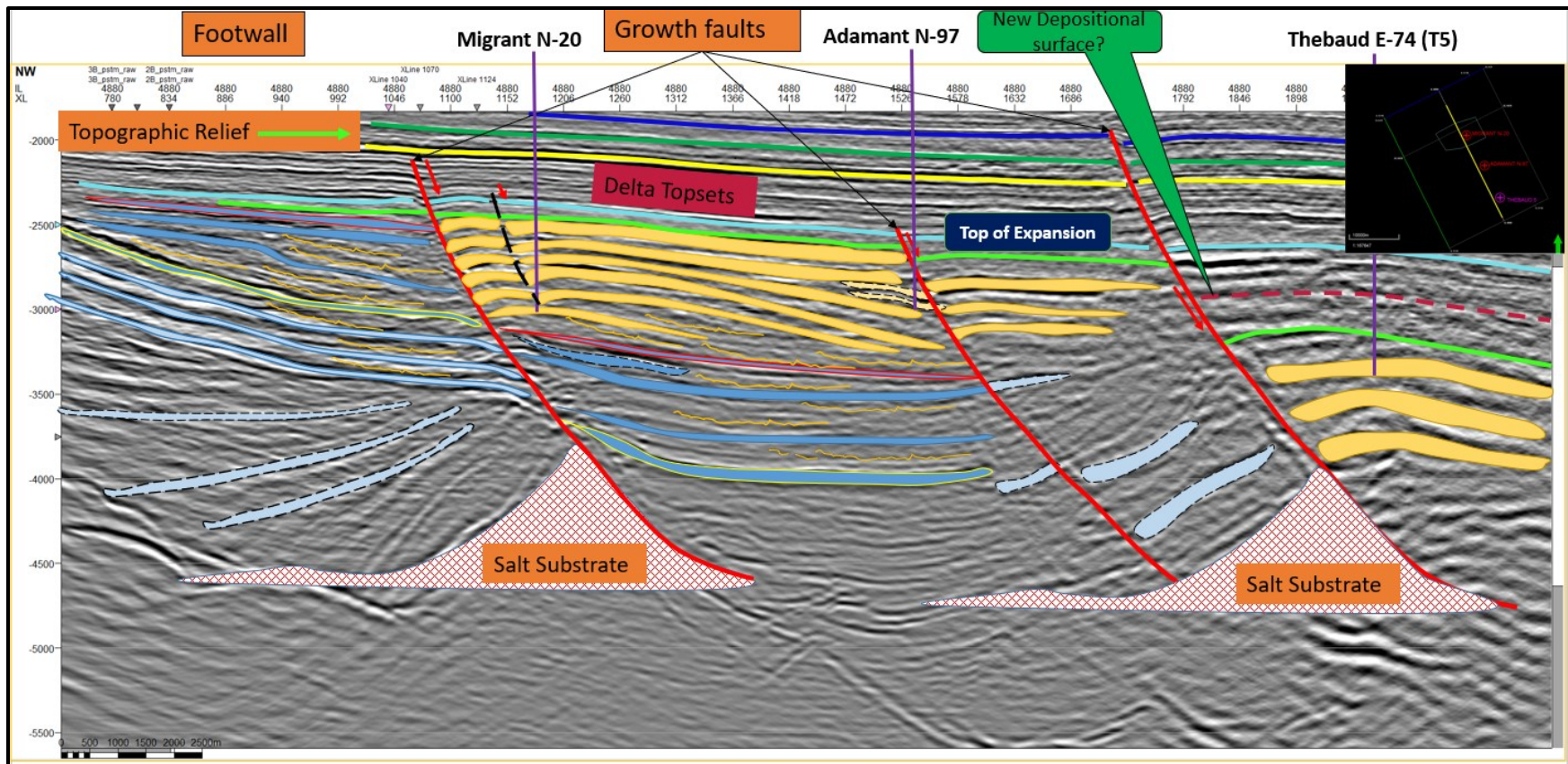


Figure 6.4: An annotated seismic image of the Migrant, Adamant, and Thebaud Structures depicting their various structural and depositional relationships. The series of depositional events post-dating the carbonates are important in explaining fluid trapping at Migrant given the basinward change in the deposition. The Thebaud reservoirs and shales do not exist in the proximal fault blocks. As a result, the main bounding faults offset the Abenaki 4 limestone sequence, which progressively drops outwards from the Migrant Structure, terminating where it encounters salt underneath the Thebaud Structure. Typical exploration strategy of such structures is to drill off the crest of the structure to test for a gas-water-contact.

## 6.1.2. Structural Analogs and Velocity Discussion

### 6.1.2.1. Structural Analog

The structural and trapping behavior documented on the Scotian Margin is not unique and can be seen in many places globally as mentioned in the previous section. Deltas often develop expansion trends, depocentres, and listric fault systems that override a mobile substrate be it shale ( Wu et al., 2000; Rowan et al., 2004; Vendeville, 2005) or salt diapirs (Vendeville, 1991; Morley, 2003; Ings & Shimeld, 2006; Deptuck, 2011). The Migrant growth section occurs above the carbonates, likely associated with gradual faulting and filling in of the prograding deltaic sediments into accommodation space created at the fault. Following deltaic progradation, the interaction between the overburden, fault, and substrate (Vendeville, 1991) resulted in the creation of accommodation space at the top of the Migrant rollover structure. In the Sable Subbasin, a periodic movement of the underlying Argo Salt likely triggered or induced by the prograding delta (Ings & Shimeld, 2006) led to the deposition of a chain of isolated, thick but narrow prodeltaic sandstone and shales in a series of expansion trends (Pe-Piper & Piper, 2011).

During the formation of each expansion trend, there is an introduction of new sediment. Depending on the degree of fault activity, the sediment fill may become confined to a fault block. The low relief nature of the Migrant structure reflects the amount of extensional growth faulting of the border fault (Serck & Braathen, 2019). Combined with possible instability at faults, this adds to the complexity of the structure, which may require a complex development and production strategy (should there be commercial volumes). As a result, the shelf margin deltaic succession in the Sable Subbasin exemplified by the Migrant expansion trend in this study is thought to be analogous to the younger (Oligocene aged) sediments of the McAllan Ranch, Texas (Wach et al., 2002a, 2002b; Wach et al., 2003), and Pliocene-Miocene age sediments of the North Apoi-Funiwa fields, of the “Inner Trend” offshore Niger River Delta, Nigeria (Wach et al., 1997, 1998a, 1998b, 1998c).

Similar to the NE trending rollover anticlines of the McAllan Ranch, there are sediments in the footwall that may exist in the hangingwall of the Migrant Structure (but thicker). McAllan Ranch is a shelf margin deltaic system with down to basin listric faults forming expansion trends (Wach et al., 2002a; Figure 6.5). The target in the field comprised cleaning upward reservoirs (Oligocene-aged) overlain by thick shales. The sands and

shales (reservoir and seal pairs) are much thicker than those observed at Migrant. Unlike the Migrant border fault which overrides Triassic-aged Argo salts, sands developed in the McAllan Ranch Field were offset by the Monte Christo Fault, a major bounding fault influenced by the underlying Jackson Shale (Bain, 2015). This structural and depositional relationship resulted in a localized thickening of clastic sediments on the hangingwall of the growth fault (Figure 6.5).

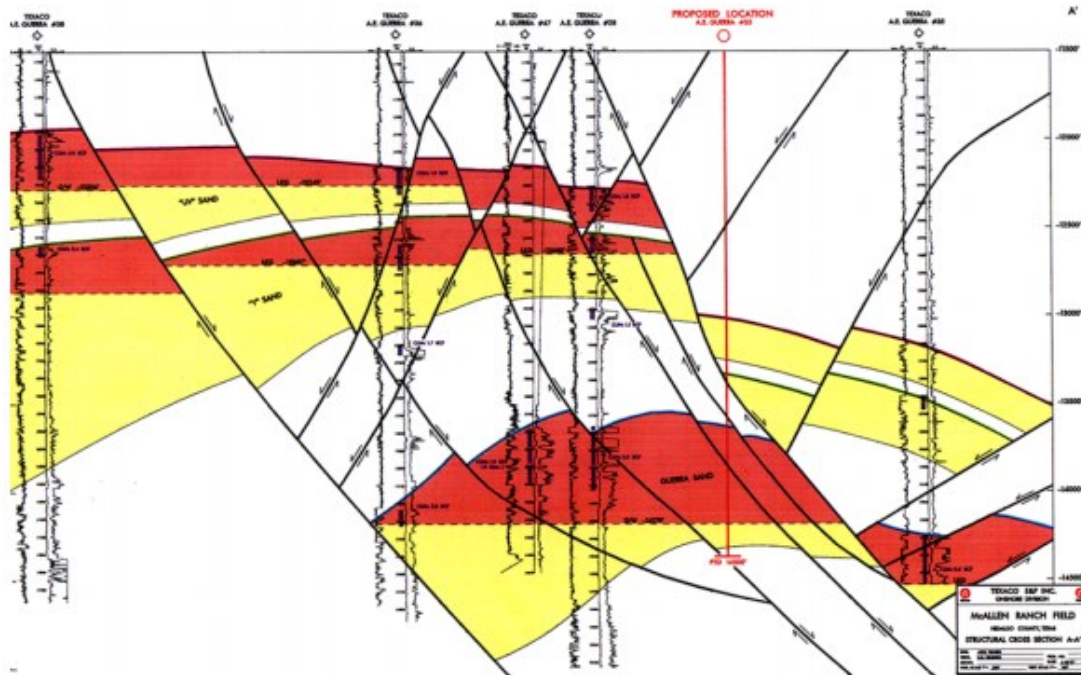


*Figure 6.5: A figure of the McAllan Ranch field showing the stratigraphic variation across the major faults (Wach et al., 2002a). Based on the dip-oriented structural cross-section, deposition along an unstable shelf margin delta has resulted in the large-scale listric faulting that has impacted the position of the Gas water contacts are represented by dashed lines. These dashed lines separate the gas-filled columns in red and the rest of the reservoir filled with water in yellow.*

In addition to the analogous rollover structure at McAllan Ranch, the complex collapsed crest structure with growth faults and antithetic faults of the North Apoi-Funiwa Field in the Niger Delta presents an interesting analogue with some differences to rollovers of the Sable Subbasin regarding their respective sediments. Key similarities can be seen in their similar shelf margin occurrences with listric faults and rotational trap. As shown in Figure 6.6, the complex faulted structure comprises of older growth faults to the northeast (related to the structural development in the subbasin along the basin bounding



fault), and younger growth faults to the southwest that offsets earlier antithetic faults with less throw (Wach et al., 1997).

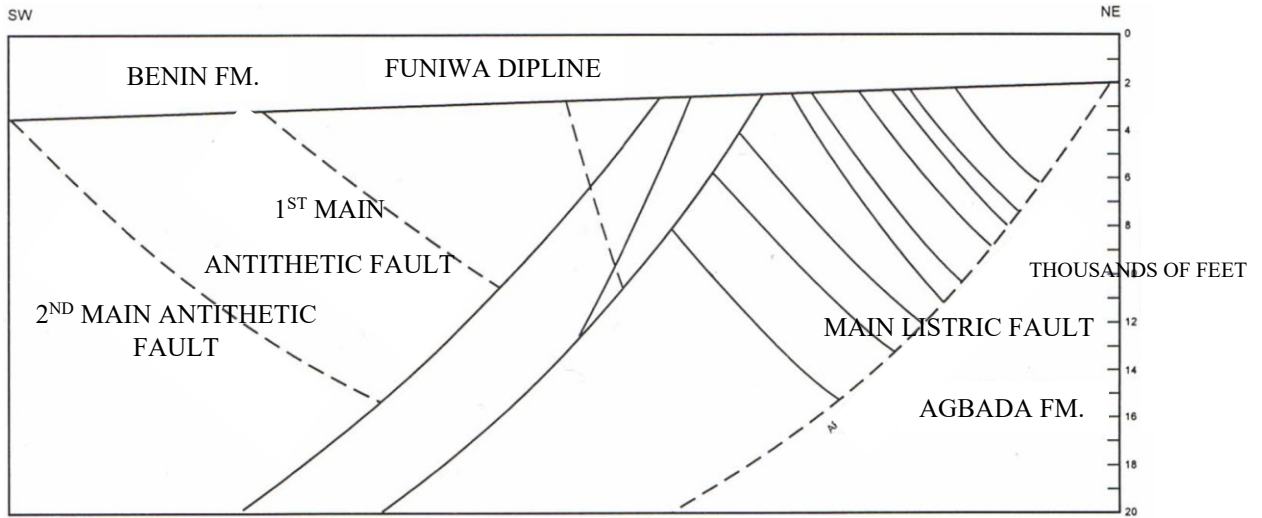
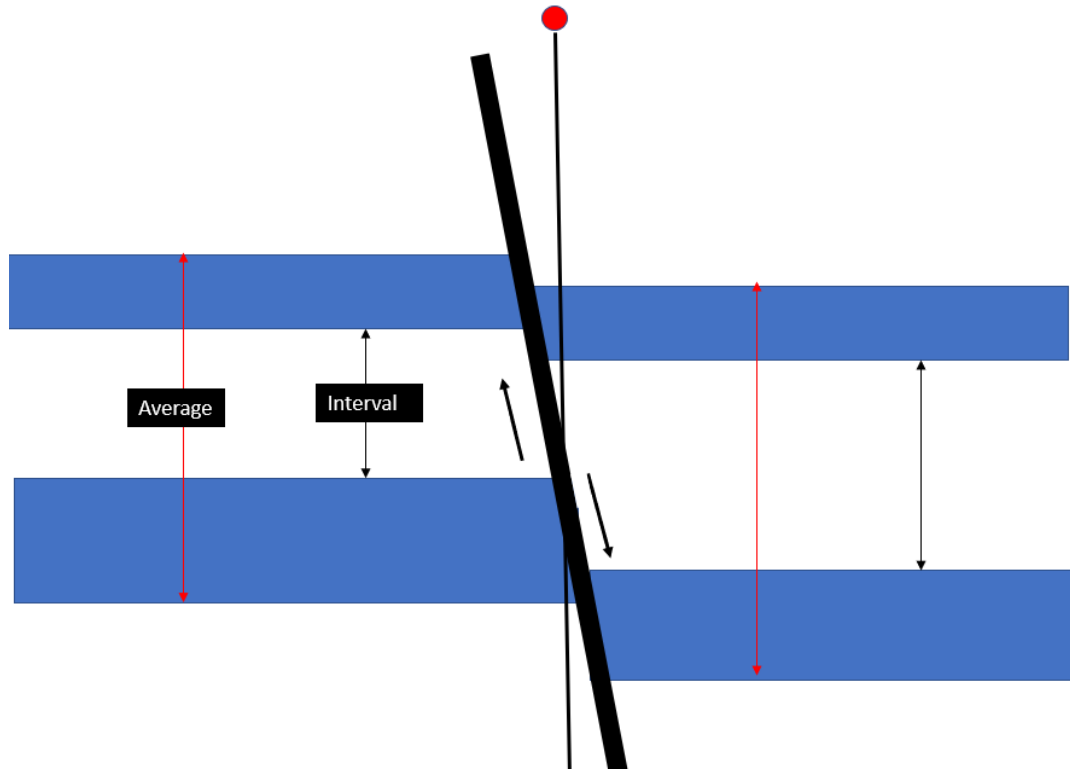


Figure 6.6: A schematic cross section of the Funiwa area of the North Apoi-Funiwa field (from Wach et al., 1997).

#### 6.1.2.2. Potential Uncertainties from Time-to-Depth Relationship

To ensure good depth conversion, the VOK method, a common velocity modelling method involving linear velocity functions was adopted to establish a simple velocity model from key layers. Based on the table associated with the Migrant N-20 checkshots in APPENDIX D, multiplying the one-way time OWT reading acquired from check shot by two results in a two-way time TWT equivalent for each depth. In addition to the average velocity to sea level, the interval velocity between the checkshot points can be compared to the relative depth and time at each well top. In this study, a set of average velocities to sea level for each point and interval velocity between points were established (APPENDIX D). The average velocity (Figure 6.7; Section 6.1.2.2.) is suitable for converting existing TWT below sea level to a depth for key markers on either side of the fault. These have been subtracted to result in an offset in meters in Table 6. 1. Alternatively, the interval velocity can be used to convert the fault offset from time thickness to depth thickness, which should result in the same answer as those derived using an average velocity. It is important to point out that synthetic seismograms built from the seismic data was built into the project master file from which previous work were complete. Therefore, the synthetic from these previous works were trustworthy and were not introduced here in our study.



*Figure 6.7: A schematic showing the sediment thickness variation between a footwall and hangingwall of a fault. The indicated well penetration passes through the areas of contrasting thicknesses, which will affect the velocity data depending on the gross sediment thickness as well as the composition of the layers.*

Considering the geologic complexities around the Migrant Structure (salt and mixed carbonate and siliciclastic relations), the lithological variation may be difficult to distinguish from any existing fault shadow. Fault shadows are caused by changes in lateral velocity across a fault (Bain, 2015). They are commonly associated with the lateral juxtaposition of lithologies with different velocities (Etris et al., 2001) and may result in significant ray-path distortions and errors in stacked, post-stack time migrated sections (Bain, 2015). They are known to mask the presence of structural accumulations of hydrocarbons in a trap, thus, making them appear in the wrong position relative to their true depth (Bain, 2015). Given the horizontal influence of the geology on the energy of travel (Hilterman, 2001), the apparent closure in TWT may not be closed in depth due to the velocity variation.

The simple layer-cake overburden relationship between the units in the hangingwall makes it unlikely to affect fault juxtaposition relations with no obvious velocity changes from amplitude loss from the Migrant bounding fault. In the absence of any associated

noise/distortions from fault shadows, the resolution is likely the key issue given the small fault offset and lateral velocity variations across the crestal fault around the area of interest. Also, sediment thickness behavior may result in a variation of the average interval velocity, which may influence the dip of seismic reflectors in the footwall as suggested by Bain (2015). While this is true for the major boundary fault where a variation in seismic velocity resulting from the expansion and thickening on either side of the fault (e.g. Figure 6.8) may contribute to a fault shadow effect, high reflectivity deltaic sands in the hangingwall with low reflectivity distal muds in the footwall are other contributors.

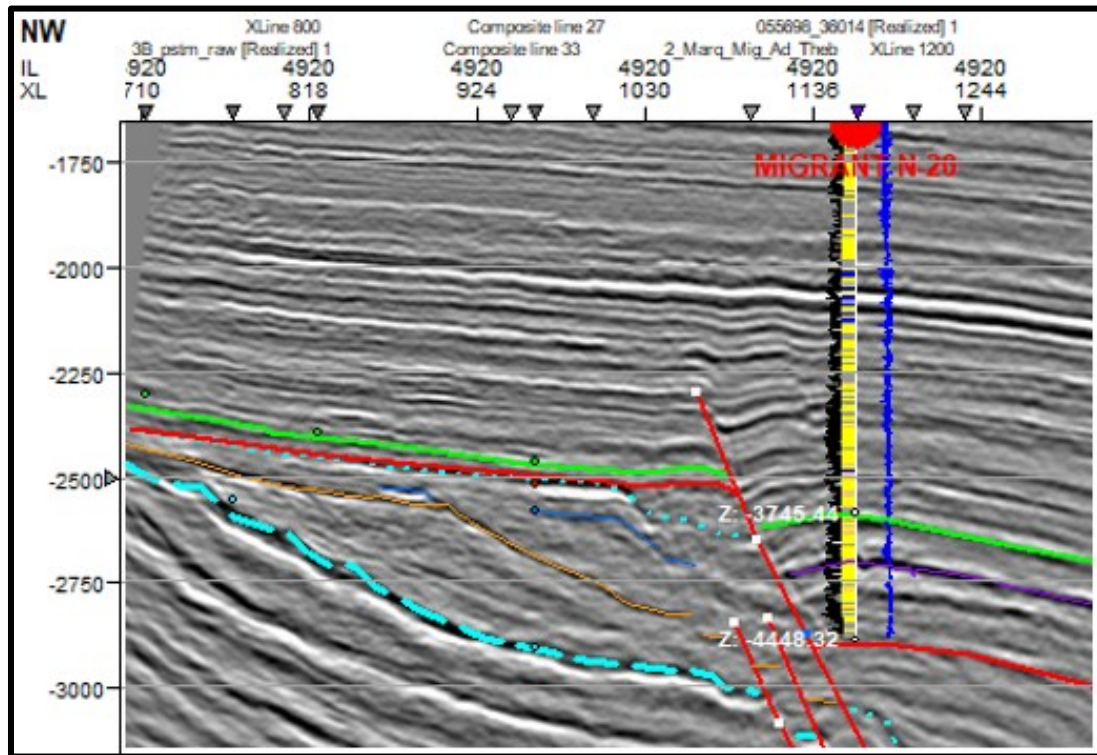


Figure 6.8: A seismic line showing two well tops corresponding to the top and base expansion trend at the Migrant N-20 well. Despite the dominant siliciclastic sediments with some carbonate above the dominantly carbonate-rich interval in the structure, the section in the hangingwall was treated as one gross unit. After applying the check shot velocity survey, some reasonable thicknesses were determined for each corresponding seismic time interval relative to the fault (Table 6. 1).

With depth conversion driven by simple interval velocities obtained from a single well (Migrant N-20) in this study (APPENDIX D.), this was used to arrive at a reasonable gross interval velocity for conversion. From the 4-layer input for depth conversion from checkshot data in Chapter 5, the velocity around the O-marker presents the closest accurate value to base any velocity for converting the interpreted seismic horizons below the O-

marker presented in table 6.1 below to true depth. Considering the offset between the footwall and hangingwall of the fault, a velocity within gross expansion between the green horizon with an offset of ~ 125 ms and the red horizon with up to 400 ms of offset was useful in getting an accurate depth for the markers in this study (Table 6. 1). Therefore, using an average velocity between the established top at the O-marker and an arbitrary greater depth at the bottom of the structure (~4450 m), an average velocity of ~2900 m/s was used for depth conversion. Based on the depth relationship of the well in the above figure (Figure 6.8), this average velocity is applied to the purple and red horizons.

*Table 6. 1: Interpreted horizons in TWT and their equivalent depth and estimated thicknesses. The fault trace spans through the well between 2597 to 2635 ms equivalent to depth range of 3765 – 3821 m. For the estimated depth of each marker, the isochron value (TWT ms) was divided by 2000, then multiplied by the average velocity to sea level. Their respective offset in metres obtained by subtracting the depth of the marker on the footwall from the hangingwall depth.*

<b>Marker</b>	<b>Left of CF TWT ms</b>	<b>Left of CF Depth m</b>	<b>Right of CF TWT ms</b>	<b>Right of CF Depth m</b>	<b>Marker offset Seismic TWT (ms)</b>	<b>Marker offset True Depth (m)</b>
MK 1	2347	3403.15	2374	3442.3	27	39.15
MK 2	2485	3603.25	2507	3635.15	22	31.9
MK 3	2600	3770	2607	3780.15	7	10.15
MK 4	2689	3899.05	2693	3904.85	4	5.8
MK 5	2776	4025.20	2776	4025.20	0	0

### 6.1.3. Depositional Relations

#### 6.1.3.1. The Mixed Clastic and Carbonate Transition

The transition between the carbonate and siliciclastic on the Scotian Shelf has been mapped by previous workers in 2D (e.g SOEP 1997; Smith et al., 2007; Eliuk & Wach, 2009; Eliuk, 2016) and 3D (Campbell & Wach, 2014; Campbell et al., 2015; Campbell, 2018) with some noticeable differences. These were mainly regarding strong mappable proximal reflectors representing the Abenaki 4, 5, 6, and 7 limestones. A version of the interpretation published by Smith et al. (2014) and the CNSOPB approaching from the Marquis Structure (Figure 6.9) shows some of the late stages of the Abenaki 6 and 7 carbonates isolated on the high side of the growth faults at the Migrant and Adamant structures.



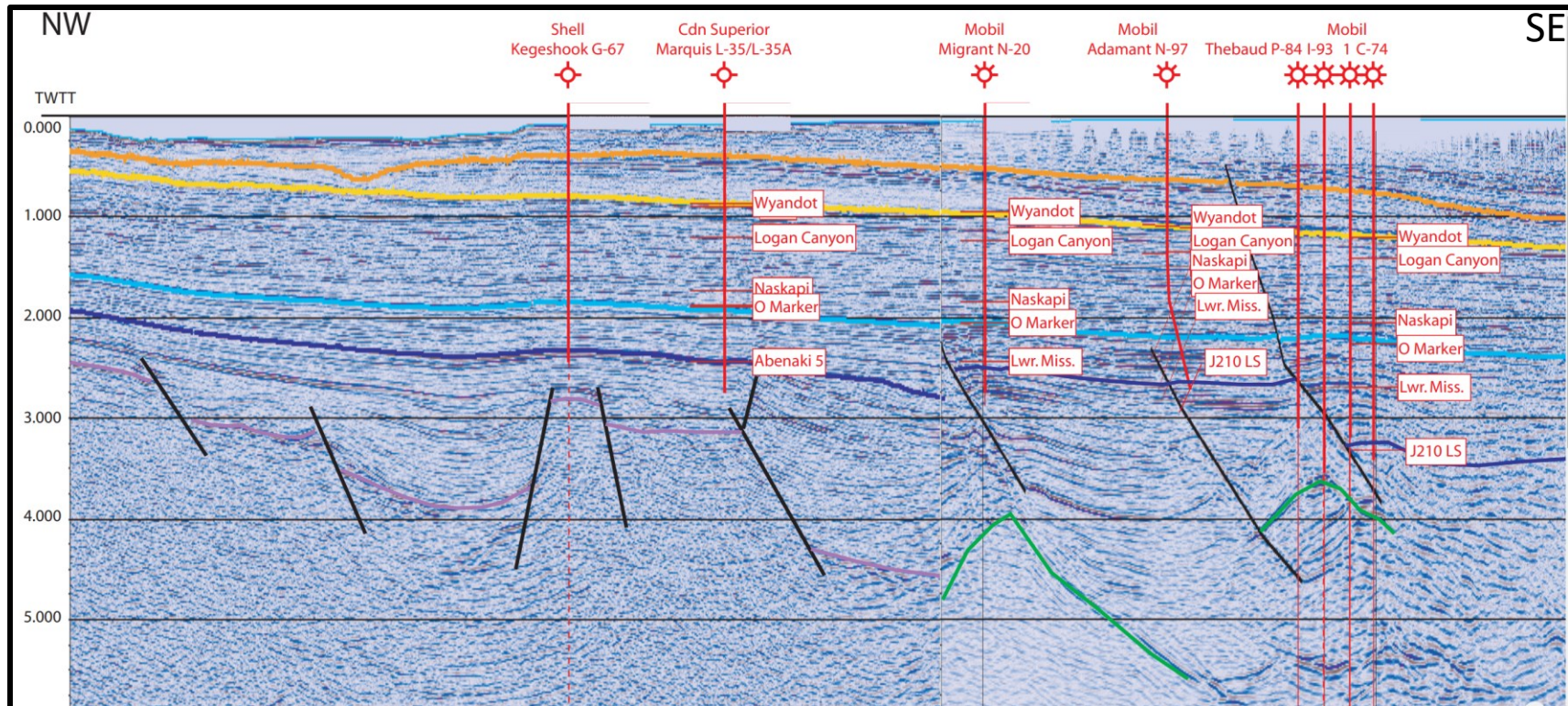


Figure 6.9: A Northwest- Southeast dipping interpreted seismic cross-section across the shelf margin areas of the Sable Subbasin that includes the Migrant to Thebaud Expansion trends (Kidston et al., 2007). The O-marker appears to represent the top of expansion in all three rollover regimes (Migrant, Adamant, and Thebaud). The almost 200 km of composite section spans from landward to seaward over the shelf to slope. The black lines are basement-induced faulting that resulted in horsts and grabens. The salt substrates represented by the green lines have lent themselves as a decollement surface for deep-reaching faults to glide over.

However, recent interpretations from Campbell (2018) supported by Figure 6.10 shows that the last of the strong carbonate seismic reflectors (Abenaki 7) can be correlated to underneath the Migrant well. Given the extent of the Abenaki 7 limestone seen progressively dropping down section basinward, this led to the conclusion by Campbell (2018) that the siliciclastic succession within the expansion trend does not interfinger with the carbonate bank and are separate and younger.

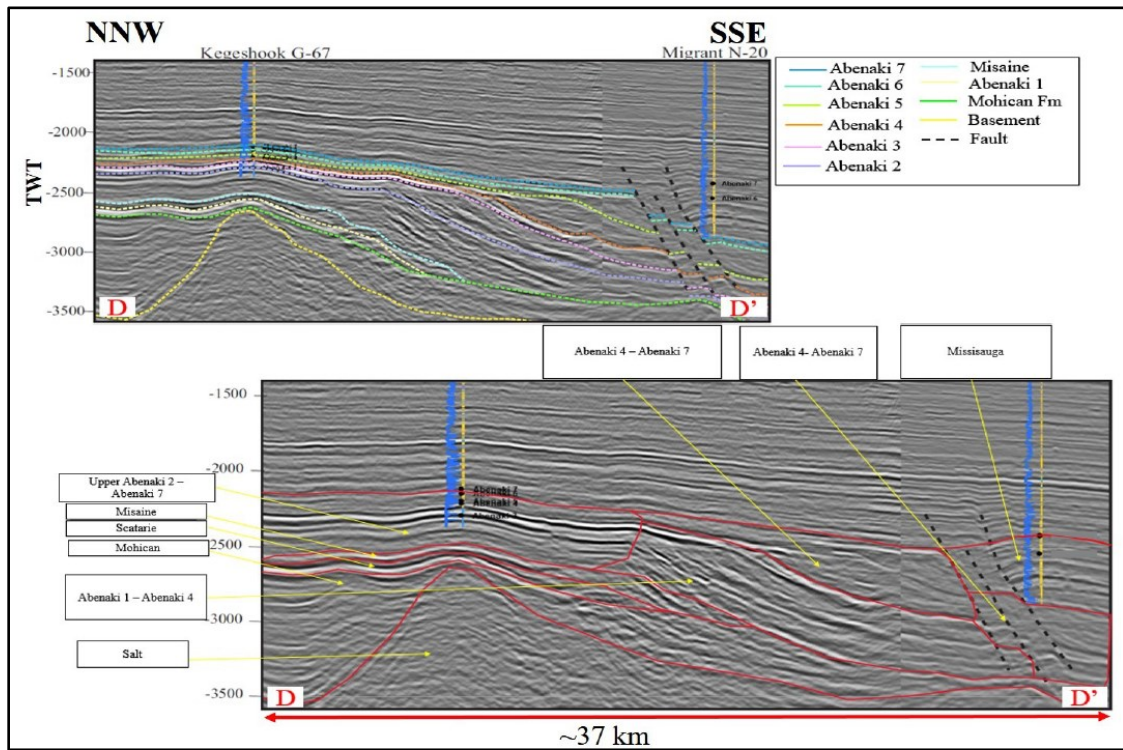


Figure 6.10: A figure showing the seismic interpretation from continental shelf margin to slope and distal fore slope area of the Sable Subbasin from Campbell (2018). The basinward growth and extent of the carbonates from Abenaki 5, 6, and 7 appear to be affected by the 1000 m of clastic influx from the north that began the expansion trend that gave rise to the movement of the underlying salt. From the figure, it appears that the carbonate only grew up to the Abenaki 4 cycle in the proximal interior. Then at the bank margin, the development of Abenaki 5, 6, and 7 cycles appear to develop.

From seismic section in Figure 6.11, the Abenaki 4-7 cycles comprise mainly of mixed carbonate and siliciclastic facies. Southwest of the Migrant N-20 well, Abenaki 5, 6, and 7 aggraded on the bank margin and prograded onto proximal fore slope, as observed in the Dominion J-14 well (Campbell, 2018). A thickening of clastics off bank margins in Cohasset L-97 offers further support for this observation. Northeast of the Migrant N-20 well, the Penobscot L-30 well demonstrates the Abenaki carbonate bank only grew until

the Mid Kimmeridgian (Abenaki 4), while Abenaki 5, 6, and 7 only grew on the fore slope of the platform. There is hint of more clastic influence further northeast with mudstone and shale at the base, prograding to carbonates at the top, seen in the I-93 core (APPENDIX A.1.) as well as penetration of basinal Jurassic sediments with high TOC in Desbarres O-76 well. The Abenaki 5-7 are siliciclastic dominated with little to no carbonate growth is seen at the stratigraphic interval it was encountered in the Arcadia J-16, Uniacke G-72, and Citnalta I-59 wells. This highlights the end of carbonate deposition through the transition from continental shelf with the carbonate platform, to slope/distal fore slope and basin.

The Abenaki 5 carbonate appear deeper as illustrated by Smith et al., (2007) in Figure 6.9 above with the Abenaki 7 dipping basinward from the proximal shelf positions in the figure by the SOEP 1997 (Chapter 1; Section 1.3.). These intervals likely occurred below the depth of well penetrations underneath the Thebaud Structure (if the carbonate layers made it that far). Besides, following the interpretations by SOEP (1997) in Chapter 1, the Abenaki 2 corresponds to the top of the expansion trend. However, as illustrated in Figure 6.11, the Abenaki 7 limestone coincides with the top of the Migrant expansion trend. Given the deposition of sediments that have equivalents on both the footwall and the hangingwall, this suggests an end to fault activity before the deposition. In viewing the expansion below the O-marker progressing from west to east, the idea of the expansion trend may be viewed as semantic. First, about this eastward expansion of the sediment depositional trend underneath the O-Marker and secondly in the obvious wedge-shaped form that contains key reservoir sections, which are thickest at the fault. This is similar to the expansion of younger-aged sediments in the analogous McAllan Ranch Field (Figure 6.12). For this study, the wedge-shaped deposition constitutes the focus of reference to the expansion.



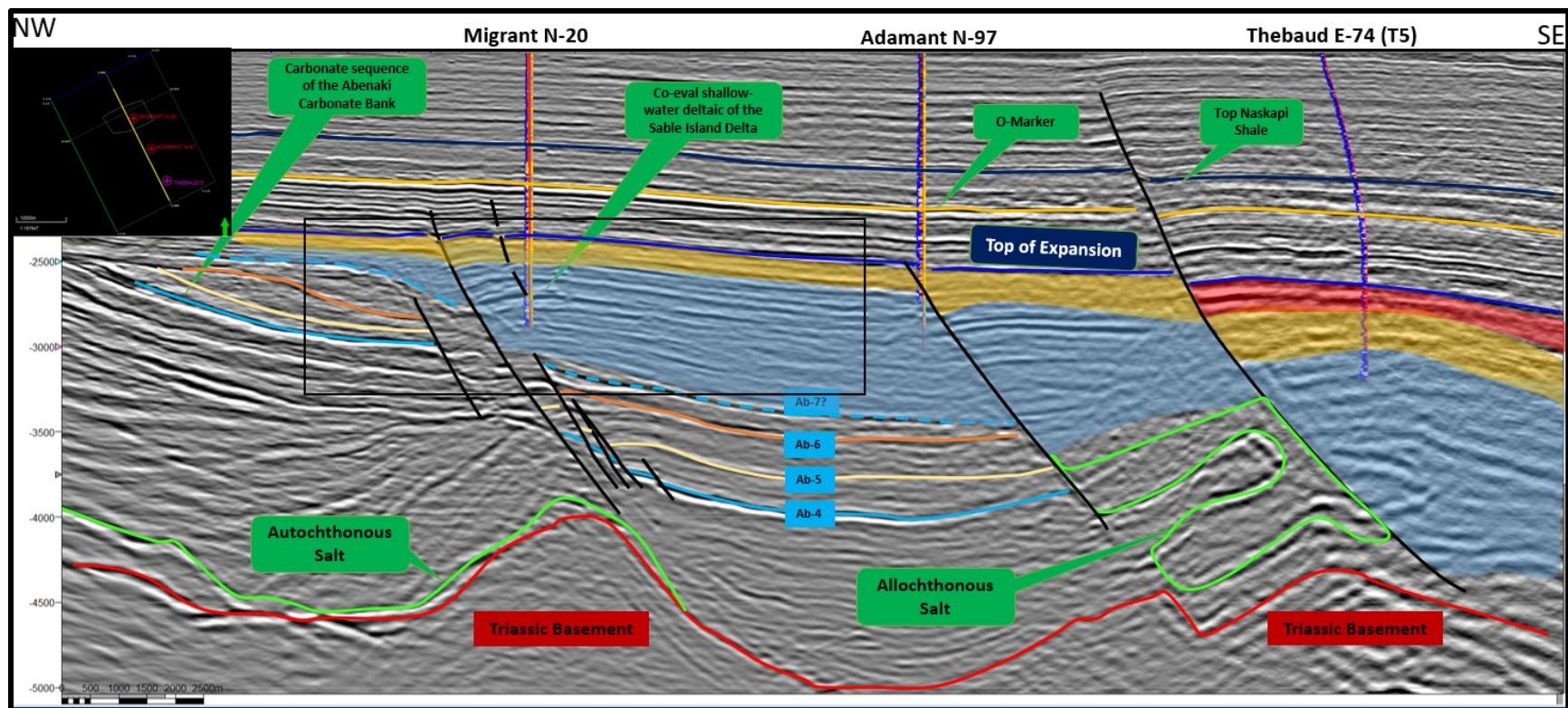


Figure 6.11: An annotated seismic image of the Migrant, Adamant, and Thebaud structures depicting their various depositional relationships to one another. The horizon interpretations in this study are such that the blue horizon picked to Thebaud serves two purposes. First, it represents the youngest level in the Migrant expansion trends based on our interpretation. Secondly, it highlights the top of closure at the Migrant Structure (incorporate into strat column).

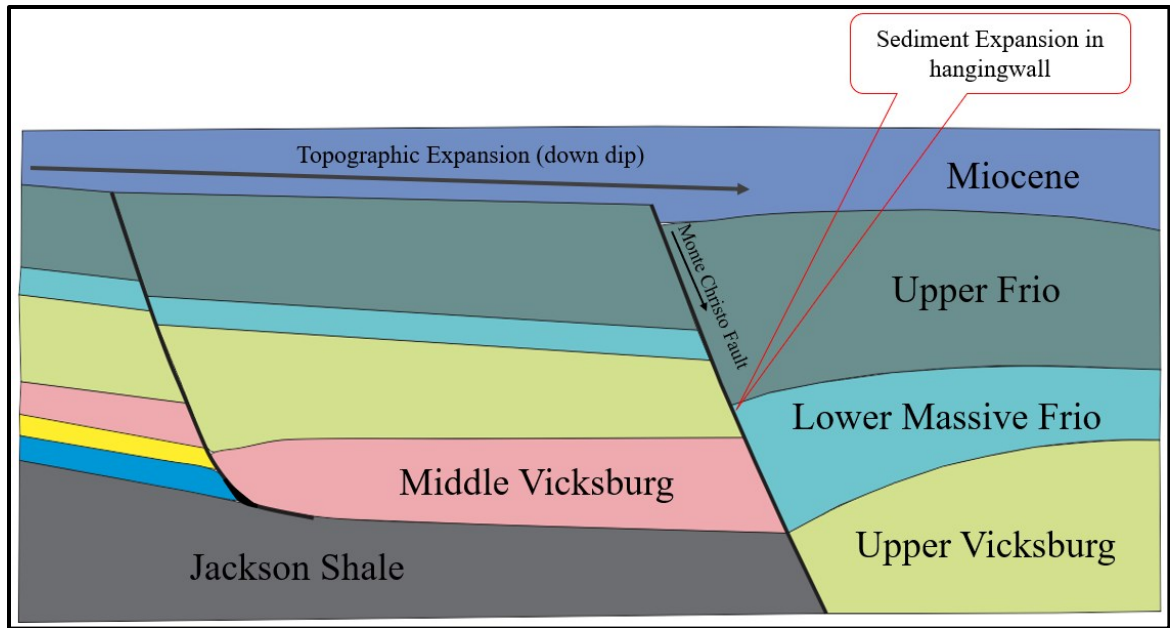


Figure 6.12: An example of expansion trend interpreted at McAllan Ranch Field (modified from Bain, 2015).

#### 6.1.3.2. Mixed Siliciclastic-Carbonate Transitions

On continental shelves globally, the carbonate to clastic transition is well documented with two of them known on the Western Atlantic Margin that includes the Iroquois to Mohican and the Abenaki Carbonate bank (Eliuk, 2016). Of the two, the Abenaki is a widespread carbonate system that occurs adjacent to thick clastics deposit observed at Migrant and Thebaud. The Eastern Atlantic Margins of Morocco and Spain (Braga et al., 2001; Lubeseder et al., 2009), as well as passive margins of NE of Australia (the Great Barrier Reef) and the Gulf of Papua are other analogs to the Abenaki Carbonate (Dickens et al., 2006; Tcherepanov, 2008; Tcherepanov et al., 2008; Campbell, 2018; O'Connor et al., 2018). As part of the early stages of rift formation in the Late Triassic to Early Jurassic, the Scotian Shelf was in a subtropical to a tropical environment. This is comparable to the Northern Australian Margin (Francis et al., 2007), mixed siliciclastic to carbonate systems of Papua New Guinea (Droxler et al., 1993; Tcherepanov, 2008; Tcherepanov et al., 2008), modern-day continental shelves of the East African Rift, particularly the margins east of the Red Sea (Koeshidayatullah et al., 2016) in Figure 6.13 and the Moroccan Margin (Sibuet et al., 2012; Campbell, 2018) in Figure 6.14.



*Figure 6.13: A geographical map showing the Eastern Red Sea Margin. The siliciclastic to carbonate interaction can be seen in the proximal offshore positions represented by the reflective character just offshore with regards to the carbonate. Inset photo with a red box indicating the geographical location.*

Shared similarities regarding the interfingering carbonates and siliciclastics depositional system on the Scotian Margin and the Eastern Red Sea Margin makes for a comparison between the carbonate deposition on the passive Scotian Margin and the active East African Margin ( Smalley et al., 1985; Koeshidayatullah et al., 2016). Hence, they present a case for comparing analogs from the ancient Scotian Margin and the modern East African Margin. The presence of distal carbonate deposits on the Scotian Shelf indicates that the carbonate deposition kept up with the sea level change judging by the continued carbonate platform growth (aggradation) of the margin. This is similar to mixed clastic and carbonate deposition along the Moroccan Margin (Sibuet et al., 2012) in Figure 6.14. The stratigraphic revision from Figure 6.14 by Campbell (2018) from the Scotian Margin shows the interfingering siliciclastics with carbonates juxtaposed against siliciclastics of the Missisauga Formation by normal faulting just outboard of the carbonate bank. However, the siliciclastic within the Migrant expansion trend appear to be younger and do not interfinger with the carbonate bank. This is supported by the absence of limestone of

considerable thickness around the lower sections (O-Marker and below) of the Migrant N-20 well seen earlier in Section 3.4.4.

With the expansion trend beginning around the Migrant N-20 well area comprising mixed siliciclastic and carbonate interactions (Section 6.1.3.1.), the siliciclastic influx from the northeast (Campbell, 2018) contributed to the periodic sediment loading with the initiation of normal faulting and accompanied the salt movement. Given that the carbonates and distal carbonate facies are correlated below the Migrant N-20 well (Campbell, 2018), this supports the idea of a sustained period of siliciclastic input of the Missisauga Formation, which is younger than the carbonate dominated depositional regime. Thus, the revised stratigraphic chart by Campbell (2018) suggests that faulting between siliciclastics of the Mic Mac Formation and the siliciclastics of the Missisauga Formation marks the beginning of the shelf expansion trend.



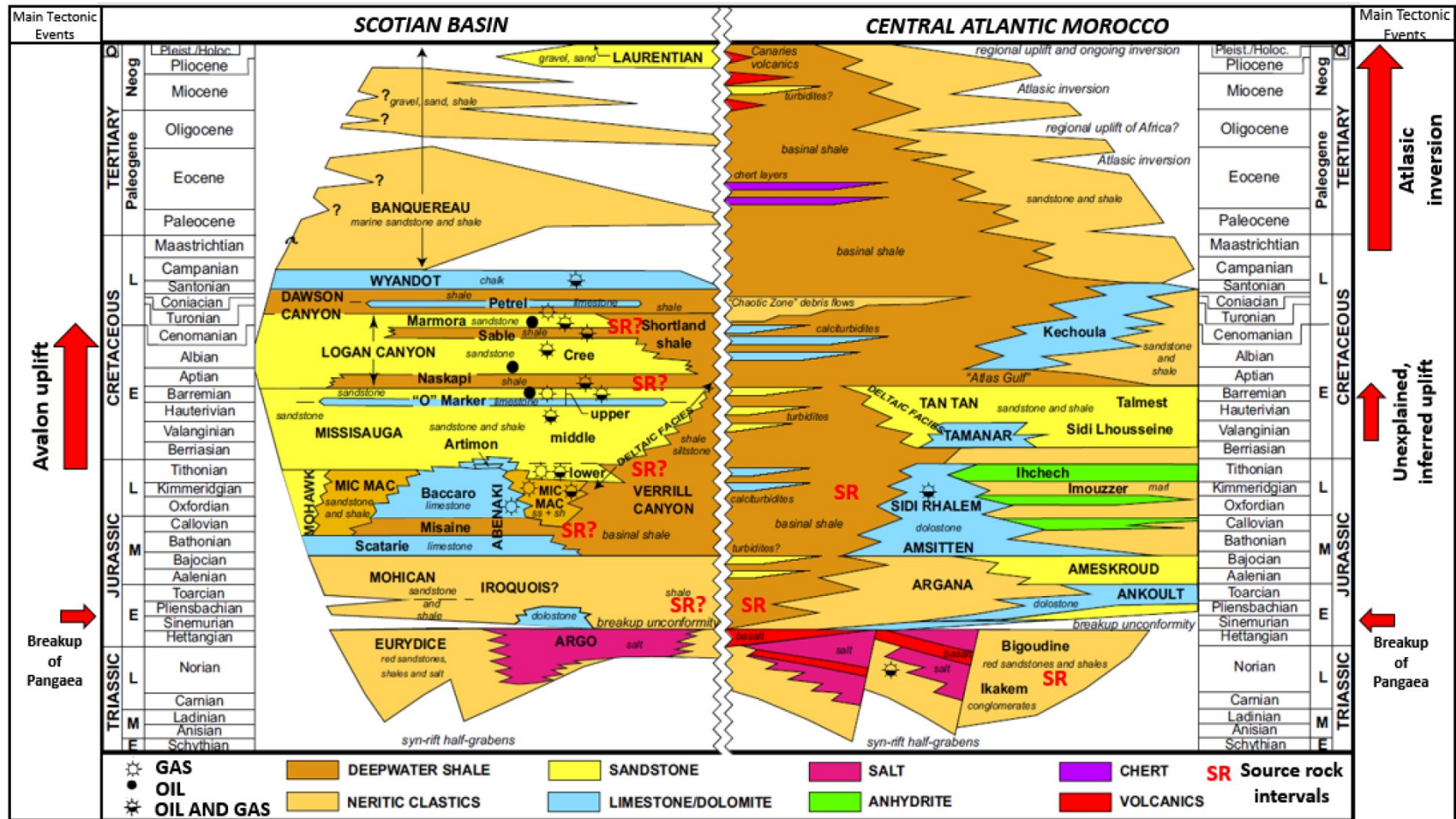


Figure 6.14: A lithostratigraphic chart of the Scotian and Moroccan Conjugate margins. The chart shows the Central Nova Scotian margin modified by Campbell (2018) from Hafid et al. (2012), after Wade and MacLean (1990).

## 6.2. Discussion of Overpressure at the Migrant Structure

The causes and controls on overpressure have been discussed by several authors and includes hydrocarbon generation and variable compaction of sediments (Osborne & Swarbrick, 1997; Swarbrick, et al., 2001; Hantschel & Kauerauf, 2009; Skinner, 2016). At Migrant, a hint of overpressure occurs at a shallower depth than the depth of the thick Thebaud Shale that likely extends into Adamant (Section 4.3.2.). Unlike the normally pressured system above the overpressure zone at Thebaud where there is hydrostatic continuity, there is a lack of pressure connectivity between the reservoirs below the top of the overpressure indicating the likely presence of a seal (baffle or barrier). As overpressure increases below the Thebaud Shale, the excess pressure occurs in a series of stepwise clusters between depths of 3900 m and 5000 m. Overall, incomplete sediment compaction in the basinward direction (Hantschel & Kauerauf, 2009) may have contributed to the depth-related increase in pressure below 4000 m depth, which is typical of isolated reservoirs (Vrolijk, 2005; Richards et al., 2008, 2010).

However, the relative sparseness of RFT pressure data at Migrant makes it unwise to link the stepwise change in overpressure with depth that occurs in the Thebaud I-93 and E-74 (T5) wells and part the Adamant N-97. The last hydro pressure point corresponds to a depth that is stratigraphically above the first overpressure point at both Adamant and Thebaud. Based on the gap between RFT measurements in the Migrant N-20 well and the top of the DST test intervals (Section 4.3.2.), it is possible that an unidentified shale unit or cemented calcite-rich interval that may provide the top seal (Almon & Dawson, 2004; S Bloch, 1991; Dawson & Almon, 2002, 2006; Summa, 1995; Vrolijk, 2005) was missed due to the relative sparseness of RFT data. Also, the ability to identify any link in overpressure at the Migrant Structure to a shale interval through stratigraphic correlation was made difficult in the absence of critical data (e.g. Gamma-Ray, Density, and Sonic log).

A well kick caused by a formation water influx to the wellbore around a depth of 4015 mRT coincides with an interval where cased hole Gamma-Ray was the only available data. Thus, it was difficult to identify the top of overpressure in the Migrant Structure with formation pressure reading around 4015 mRT appearing to be higher than shallow formation pressures. As a result, the effective top of overpressure may occur where the

well kick was taken. With little or no evidence of an equivalent to the Thebaud Shale, or any significant shale unit in this stratigraphic interval at the Migrant well, it is possible that the increase in pressure at Migrant below this depth resulted from a different mechanism and may not be compaction driven. Given the presence of several relatively low porosity intervals at Migrant, each unit may be separated by thin localized impervious units.

Overall, a combination of reduced pore volume from chemical compaction in the well-cemented gas-filled reservoirs and hydrocarbon generation from the tested interval at Migrant likely contributed to the increased pressure (Hantschel & Kauerauf, 2009). This is supported by the very high resistivities in tight sands with gas from preliminary log analysis (Chapter 4; Section 4.3.1.). With the tested zones in the Migrant Structure occurring at depths greater than 4000 m, the temperature and pressure conditions below this depth are consistent with those responsible for the onset of chemical cementation including silica and calcite cement formation (Bjørlykke et al., 1989; Bloch, 1991; Summa, 1995; Bloch et al., 2002; Thyberg et al., 2010), assuming a normal geothermal gradient. Additionally, a report of two potential source rock intervals by Campbell (2018) around Migrant below a depth of 4015 mRT may have generated hydrocarbons from these intervals. Thus, contributing to the increased pressure.

Compared to the analogous structure at McAllan Ranch in Section 6.1.2.1., the entire system at McAllan Ranch appears to be at fracture closure pressure, with fill and spill within pressure cells, but topseal failure between them (Figure 6.15). The presence of leak of test data or formation integrity test data would have confirmed the sediments to be at fracture closure pressure. Besides the minimal integration of pressure data in the work by Wach et al., (2002), a report of reservoir depth range from 11,500-14,500 feet and bottom hole pressures from 11,000-12,500 psi as the only quantitative information suggests that the pressure gradient lies somewhere in the range 0.956 to 0.862 psi/ft. This range in pressure almost double of the typical hydrostatic gradient of .450 psi/ft in the Gulf of Mexico and close to a lithostatic gradient of 1 psi/ft (assuming average overburden density of 2.2). Therefore, given the critical stress in such a system, the report of casing failure can be related to fault and bedding plane slip from pressure differentials as highly overpressured reservoirs got depleted.



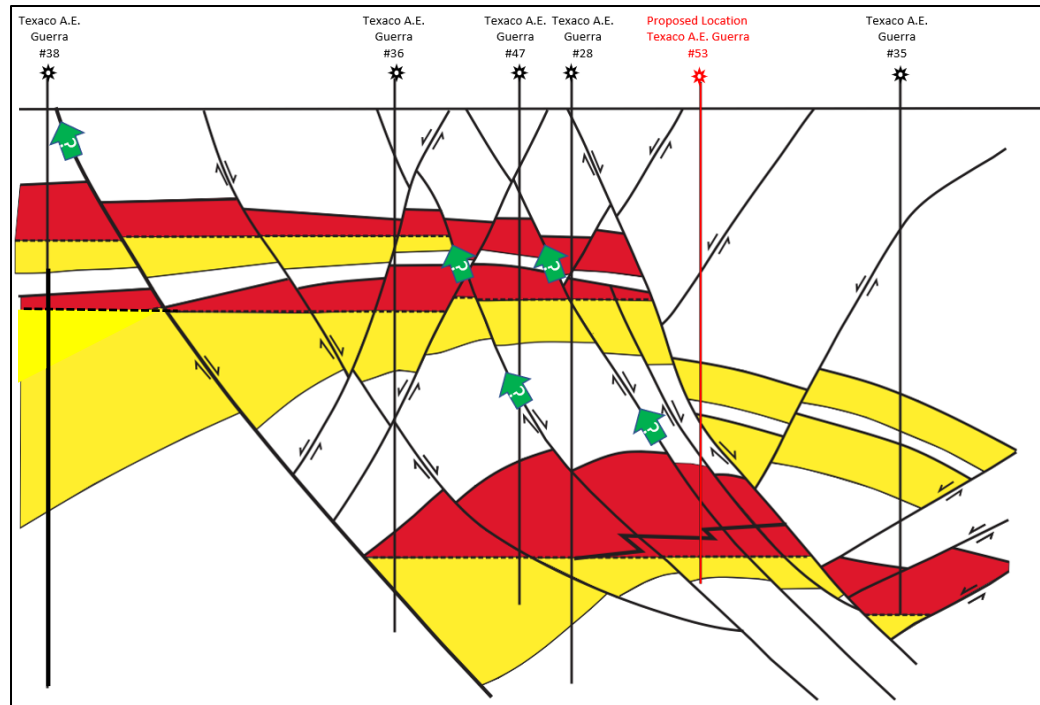


Figure 6.15: An annotated figure of the McAllan ranch field. Each group of sands is likely a “closed” system: connection to the system above is via episodic opening and closing of fractures – in the topseal and/or at faults. The individual closures within each major pressure compartment could be controlled individually by topseal failure – underfilled because of capillary or hydraulic leak. However, given how high the pressures already are and the column heights, they might be “protected traps” – with some updip leak-point (green arrows) in each pressure compartment that releases pressure. This allows each individual closure within each compartment to fill and spill at saddles and cross-fault juxtaposed leak point. Hence, fill and spill can still operate within each major compartment, but the simplest view is that the major compartments are likely not connected by cross-fault juxtapositions. If they were, there would be incremental pressure steps between major compartments - from fracture pressure to hydrostatic pressure - like those observed in Sable Fields such as Venture and Thebaud (Richards, pers comm. Mar 2021). Overall, the system is in the bottom third of the Downey model and the primary control on gas water contacts is topseal capacity. However, within each pressure compartment it’s in the middle third of the Downey model so the secondary control on GWCs is likely cross-fault spill. The difference from Migrant is you don’t have decent reservoir at the bottom of Migrant.

### 6.3. Reservoir Discussion

#### 6.3.1. Reservoir Analyses Including Mud Gas Relationship

Previous work by Campbell (2018) reported two potential source rock intervals around the Migrant expansion trend with the interval containing TOC values of 3.5% - 4% (4200 m MD – 4500 m MD) most pertinent to this study. Interestingly, the three DST tests were within this overall depth interval (Figure 6.16).

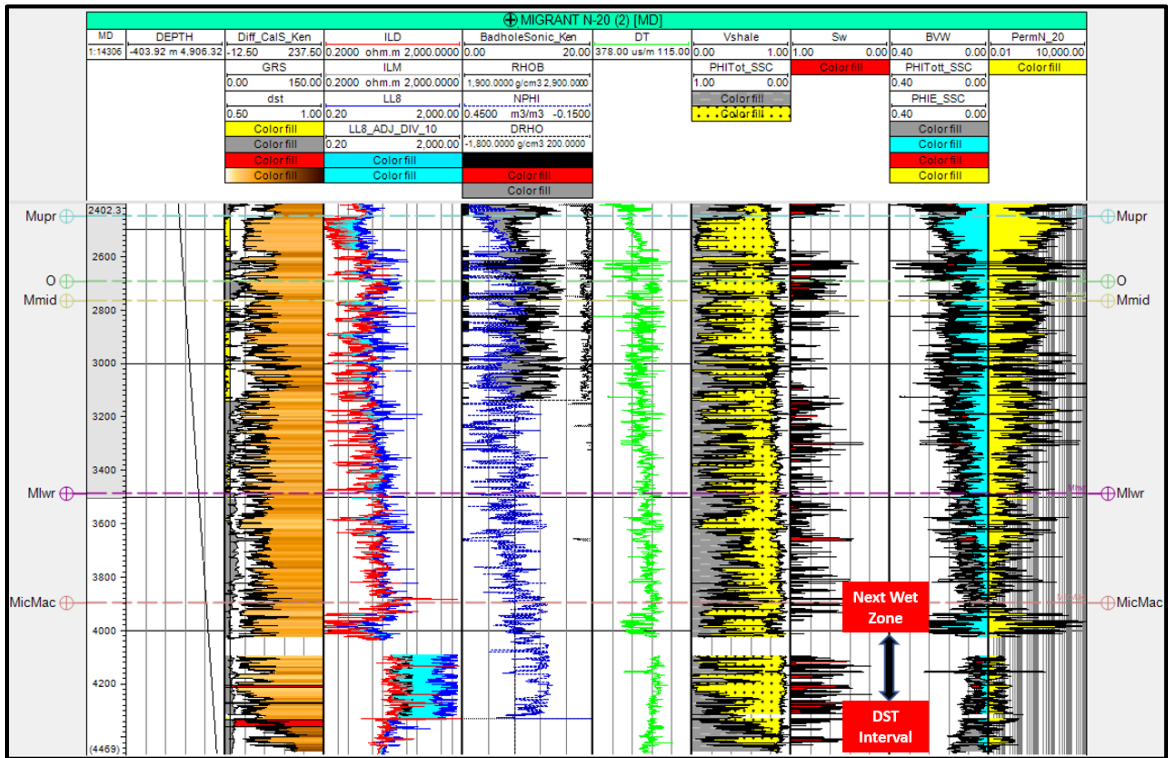


Figure 6.16: A composite showing the key DST intervals (especially DST #2) and the next higher sand zone interpreted as being wet. An approximate distance of 200 m exists between the two intervals.

Petrophysical analysis of the Migrant N-20 well in this study was combined with seismic interpretation of the Migrant Structure to determine the height of gas entrapment in the reservoirs above the DST where the significant flow was encountered (DST #2). The presence of “bright spots” in the region of the crestal fault above the DST #2 interval at Migrant may suggest the presence of free gas. This supports the idea of gas migration upward through the Migrant Structure. When looking at the seismic interpretation of key zones, the fault appeared to have moved off the crestal positions of the structure and to have terminated above the intervals where DST 2 encountered flowable gas (possibly from fault-induced fracture enhancement). Thus, despite water saturation analysis indicating

otherwise, changes in mud gas magnitude suggest that gas entrainment through the Migrant Structure reached at least a height just above 13450 ft (likely 13330 ft) in Figure 6.16 and possibly to the top of the crestal fault.

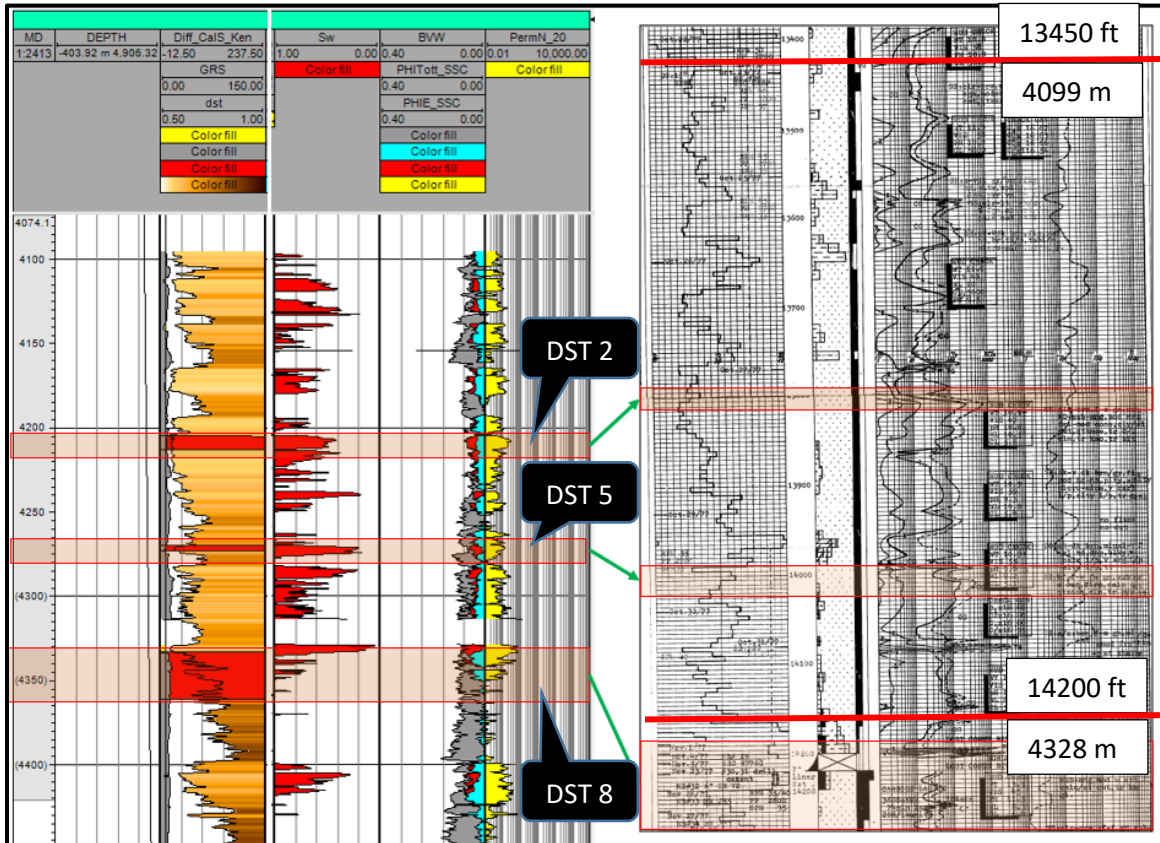


Figure 6.17: A figure representing the zones of hydrocarbon saturation from log analyses compared to the mud log (Tetco, 1978). Unlike the wireline depth in the log composite, the depth on the mud log is based on apparent drill pipe instead of wireline log depth. Further uncertainty is assigned lithology depths and associated mud gas readings on the log using drill pipe depth is that the samples and mud gas as they are described from ascending the annulus during drilling, and errors in estimating the speed at which they reach the surface will show up as errors in the apparent depth of those lithologies and mud gas readings.

The distance between the successful DST 2 interval and the next porous sand interval that appears to be water wet above this DST was useful in determining juxtapositional relationship and sealing potential between the intervals – or at least the intervals that might have contained gas accumulations before the breaching of top seals by the crestal fault (Section 5.4.2). Considering the low range of porosity (0.05v/v – 0.08 v/v) with increased gas saturations amongst the tested intervals, the trapping of residual gas may be attributed to the reduced porosity at greater depths (Bloch, 1991; Summa, 1995; Vrolijk, 2005). In areas devoid of any log data between 4020 m – 4100 m in the Migrant

N-20 well, mud log signature above 4099 m suggests the presence of continued low background gas in the reservoirs (Figure 6.17). Therefore, combining the mud logs with the wireline-derived water saturation logs for the three DST intervals in the Migrant Structure suggests that there has been containment in the tested horizons.

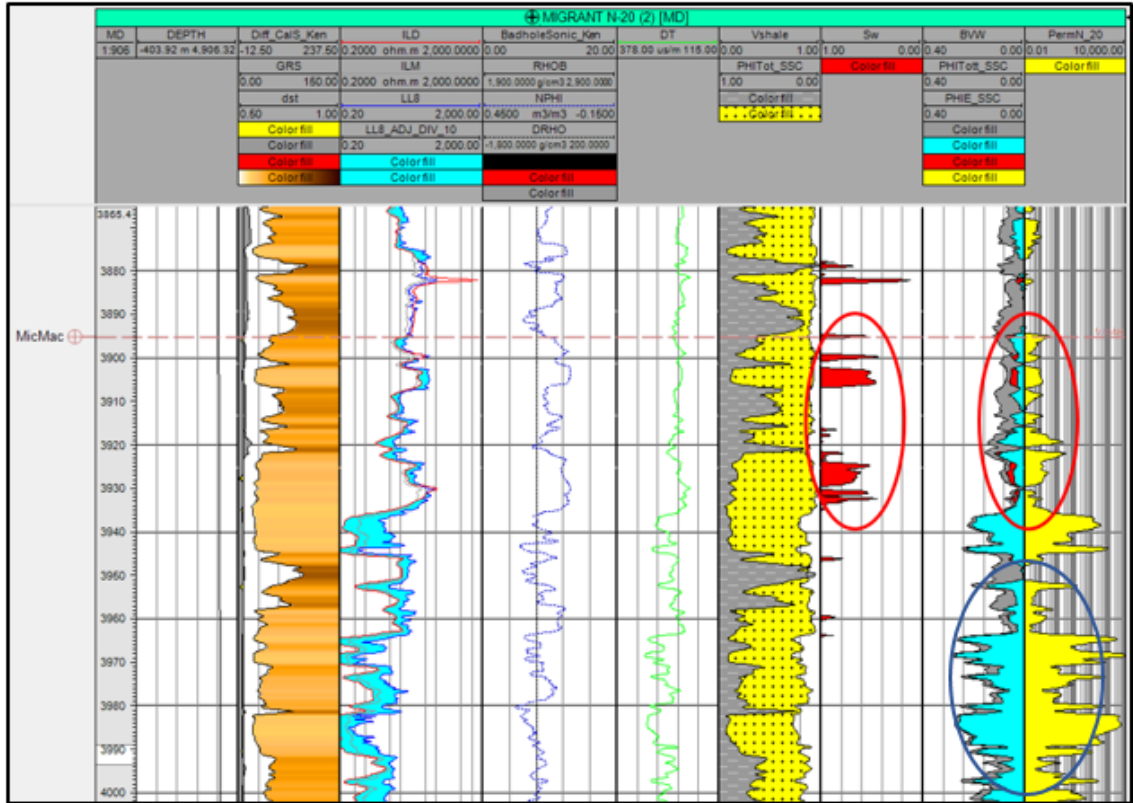


Figure 6.18: A composite from the Migrant N-20 well showing zones of decreased water saturation and increased hydrocarbon saturation (likely free gas) and water-filled sand interval (water overlain by gas) as indicated by reduced water saturation and increased bulk volume hydrocarbon between the calculated sonic porosity and BVW curves. With increased gas entrainment, the formation water may contain free gas bubbles, which moves upward because of buoyancy. In intervals containing reservoirs (sand) and seals (shales) that are calculated to be largely water-wet, intervals of bulk volume hydrocarbon and reduced water saturation immediately underneath seals can point to the migration of gas upward over considerable distances.

Despite the resistivity log indicating the presence of wet reservoirs throughout the porous sections above DST 2, in the mud gas log in Figure 6.17 above, significant gas accumulations below drill pipe depth of 13450ftRT (4100mRT) are likely due to the presence of a sealing shale (Dawson & Almon, 2002, 2006; Almon & Dawson, 2004). Alternatively, it may be a result of the interval previously containing gas before being breached by the crestal faulting. As shown in Figure 6.18, gas accumulation indicated by



reduced apparent water saturation and an increased bulk volume of hydrocarbon under the porosity curve offers support of this scenario (between depths 3895 - 3930). However, the moderately elevated mud gas levels between 3930 - 4025 appear to be almost entirely wet with an indicated  $S_w$  of 100% in the log composite (Figure 6.18 & Figure 6.19). There was likely gas migration through the shallower horizons that appear to be water wet. These responses are consistent with water-saturated intervals that contain dissolved gas that likely extends up to the level of closure that existed before being breached by the crestal fault (Watson pers com, 2020).

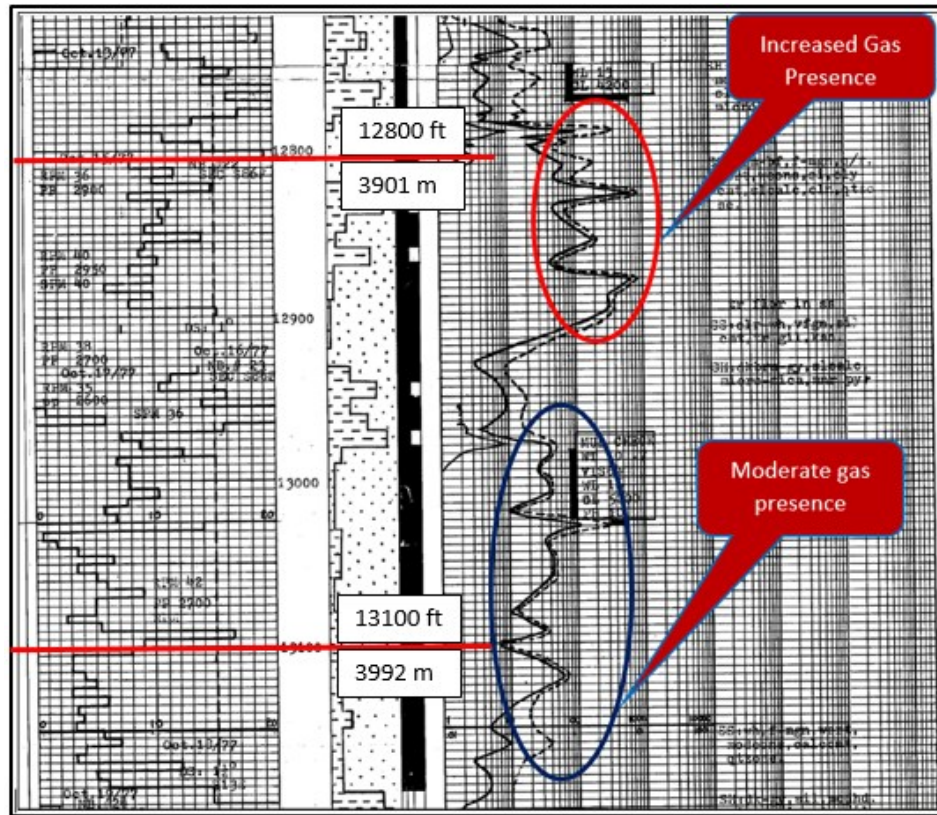


Figure 6.19: A mud gas log from the Migrant N-20 well showing the intervals 11,600 to 12,000 (Tetco, 1978).

When projected onto the reference seismic section showing the main faults and levels of closure (after depth conversion), the zones of indicated dissolved gas occur at a depth above the areas of simple closure where the crestal fault influence exists (Section 5.4.1.). Therefore, areas of localized gas presence above a drillers' depth of 4100 mRT in the mud gas log support the idea of gas entrainment across the crestal fault likely encouraged by the connectivity of reservoirs where the sealing shales are of lesser

thicknesses (Section 5.4.2). Also, the elevated mud gas readings above DST #2, indicate the likelihood of initial trapping of gas within the shallow areas of the closure before leakage across the crestal fault. Furthermore, it is speculated the higher  $R_w$  relative to the Upper Mic Mac  $R_w$  could be another confirmation of the isolation of the zones below 4100mMD and the resulting over-pressure cells present (Watson pers com, 2020).

### 6.3.2. Permeability and Pressure Discussion

#### 6.3.2.1. Permeability

A linear regression including the Thebaud I-93 #Core 1 was used to determine the equivalent permeability from porosity estimated at Migrant. The selection of this linear trend is known to impact dynamic flow modelling of reservoirs where permeability estimates are inaccurate (Delfiner, 2007).

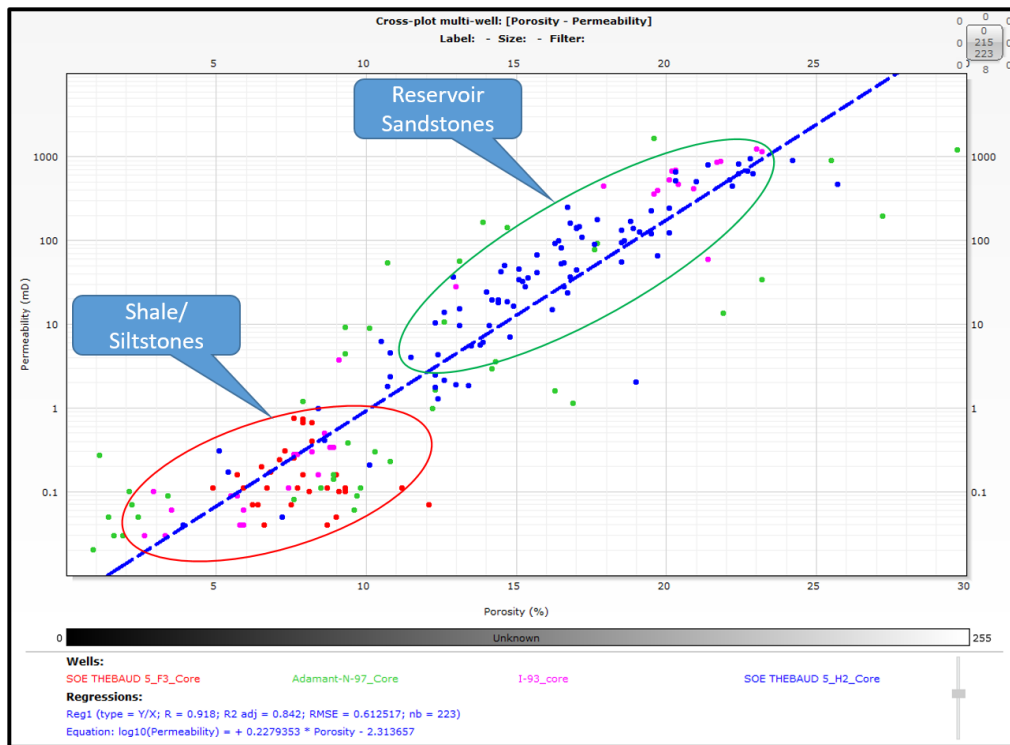


Figure 6.20: A cross plot of the Thebauds I-93, E-74 (T5), Adamant N-97, and Migrant N-20 showing the clusters and an average regression relationship for the project wells available that have core data. The sidewall core plugs showed the greatest scatter, while the plugs cut from full diameter cores collected in the overpressured interval in the Thebaud E-74 T5 showed the best porosity/permeability relationship. The core measurements for the F3 sands plot mainly in the lower-left corner of the cross plot and are an indication of a poor-quality reservoir compared to the cleaner H2 sands. The core plugs from the H2 zone in the Thebaud E-74 T5 well showed a good porosity/permeability relationship that was extended to Adamant while those for Migrant likely are most similar to those of the Thebaud T5 F3 core.

Using a curvilinear (polynomial) transform that might closely follow the entire dataset may result in lower permeabilities. Overall, newer wells (e.g Thebaud E-74 (T5)) showed a higher permeability reading for a given porosity than their older counterpart (e.g Migrant N-20, Thebaud I-93). This is likely a function of core samples that represent different lithofacies. Alternatively, as suggested by a study from the Hibernia field (Watson et al., 2000; Sinclair 2013), the applied coring technique may have affected the porosity/permeability relationship. The greater accuracy provided through low-invasion coring and lab analysis methods introduced in the mid-1990s played a key role with cores taken from wells drilled and cored before 1995 appearing to fall off at the high end of the permeability curve whereas core after 1995 plot reasonably close to the established trend. In summary, the work by Sinclair (2013) suggests that permeabilities for equivalent facies and porosities are higher in the newer Hibernia wells.

#### 6.3.2.2. Dynamic Fluid Simulation Discussion

Dynamic fluid simulation was done by O'Connor et al., 2019 to predict reservoir performance and demonstrate the failure of the Migrant Structure due to crestal faulting and lack of closure. The dynamic modeling (Figure 6.21) was carried out based on the static model of trap failure with resulting residual gas qualitatively matching the well log (Section 6.3.1). As seen in well logs, given that the lower quality reservoirs in the Migrant Structure occurs at a greater depth, a combination of compaction and cementation aided in creating an effective diagenetic trap. This contributed the decreased porosity, and permeability. These two estimated properties were obtained from well log analyses in this study and used to generate static reservoir models to assess preliminary observations from the Migrant N-20 well report. Also, the limited closure at the base of the structure, combined with the termination of the crestal fault with depth is different from the areas of fluid migration/leakage. The overall permeabilities do not exceed 1 mD. As a result, the outflow from the reservoir will take a long time to leak off in the lower intervals.

From the low porosity/permeability scenario in the Migrant Structure, dynamic modelling was used to show the migration of gas. The simulation by O'Connor et al., 2019 shows cross-fault leakage and residual gas, as expected, for the length of the simulation (~9000 years), which was the limit of the software. There was sustained flow before the simulation was discontinued. This was key in confirming the fault seal hypothesis.



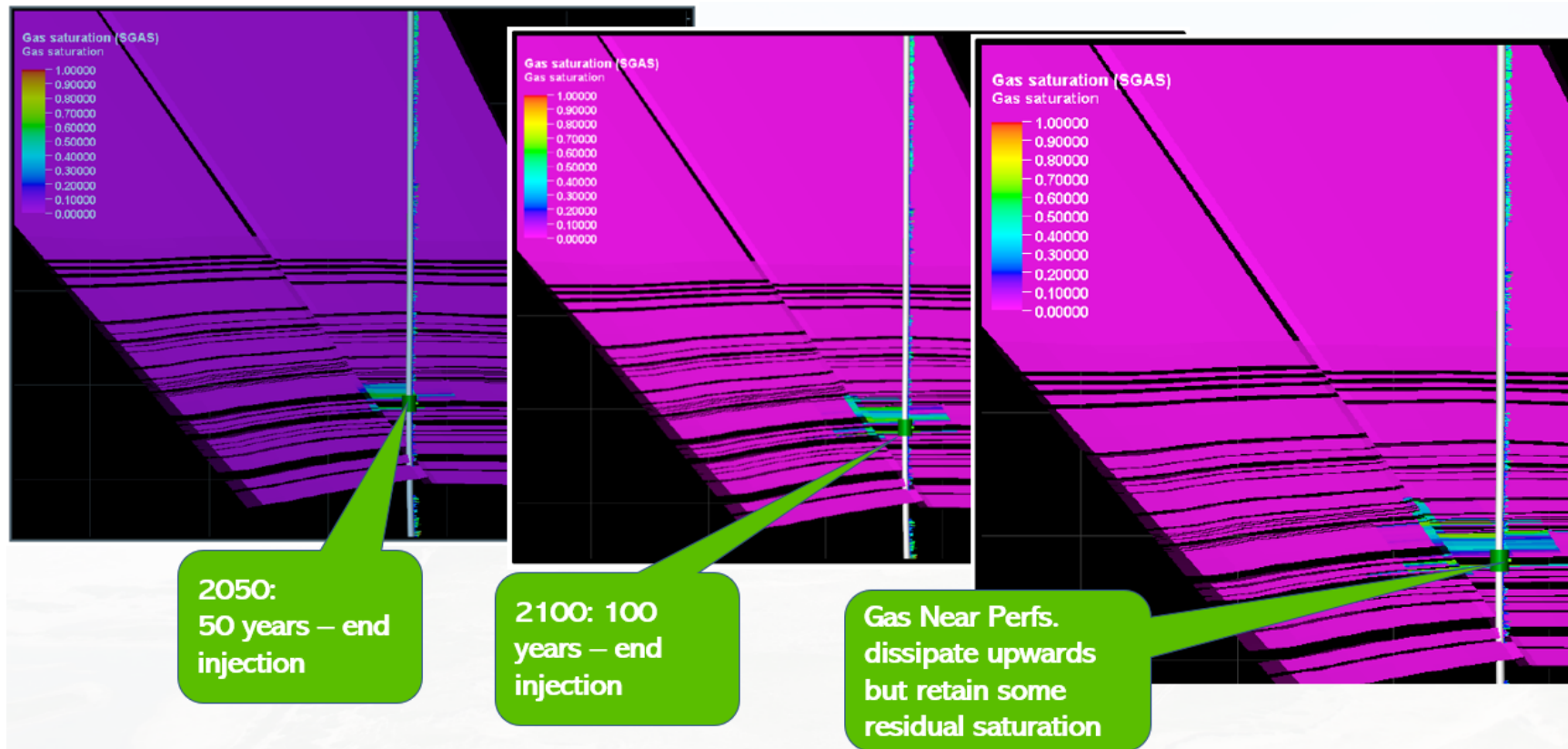


Figure 6.21: A figure showing the migration of injected methane  $CH_4$  in the Migrant Structure by O'Connor et al., 2019. The green bar on the wellbore represents the perforation with gas dissipating upwards after 50 years and then 100 years of injection. Some residual saturation is seen from the dynamic representation.

### 6.3.3. Fault and Seal Discussion

#### 6.3.3.1. Trapping Scenarios of Rollover Structures in the Sable Subbasin

In sedimentary basins around the world, the successful trapping of commercial hydrocarbons in rollover anticlines depends on having a significant gas and optimal column height in a structure (Gibson & Bentham, 2003). Together, a combination column height, charge efficiency, fault dependency (throw vs stratal thickness) that may establish leak points, and seal integrity (including lateral sealing) all play an important role in determining the commerciality of a given structure (Smith, 1980; Allan, 1989; Knipe, 1997; Knipe et al., 1998). In the Sable Subbasin, reservoir connectivity through cross-fault juxtaposition is known to exert significant control on pressure distribution and reservoir connectivity (Richards et al., 2008, 2010). As a result, the interplay between key controls including trapping mechanism (e.g. fault dependent or 4-way dip closure) and fault displacement to stratigraphic variation in thickness and spacing of units) are critical for hydrocarbon migration and trapping in rollover structures (Allan, 1989).

The juxtaposition of permeable units brought into contact on either side of a fault may allow for the migration of hydrocarbon and water upward from one reservoir to another in a rollover trap (Allan, 1989). For any undrilled rollover prospects, less fault dependency improves the trap effectiveness. In the Sable Subbasin, the South Venture Field presents evidence of this. Despite having high net-to-gross sand deposited in a deltaic depositional system like the Missisauga strata of the Migrant and Thebaud structures, South Venture is devoid of small-scale sub-seismic crestal faults (Richards et al., 2008, 2010) previously missed in 2D seismic at Migrant (Figure 6.22).

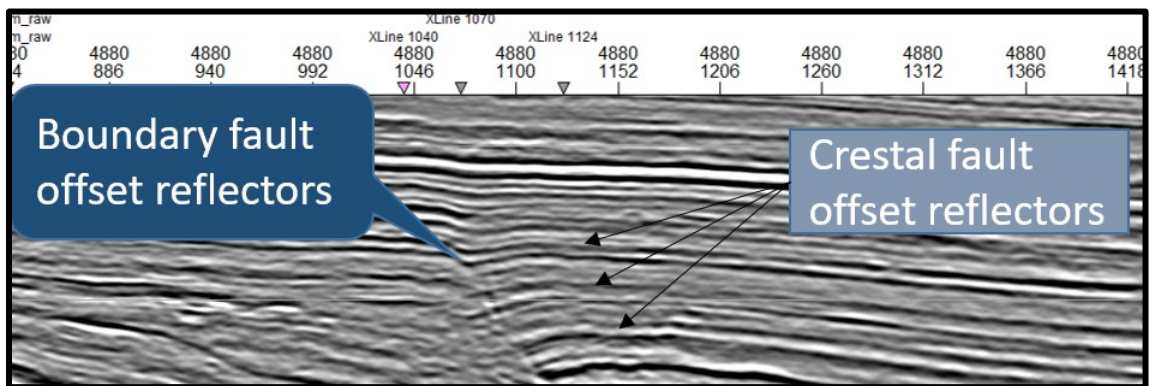
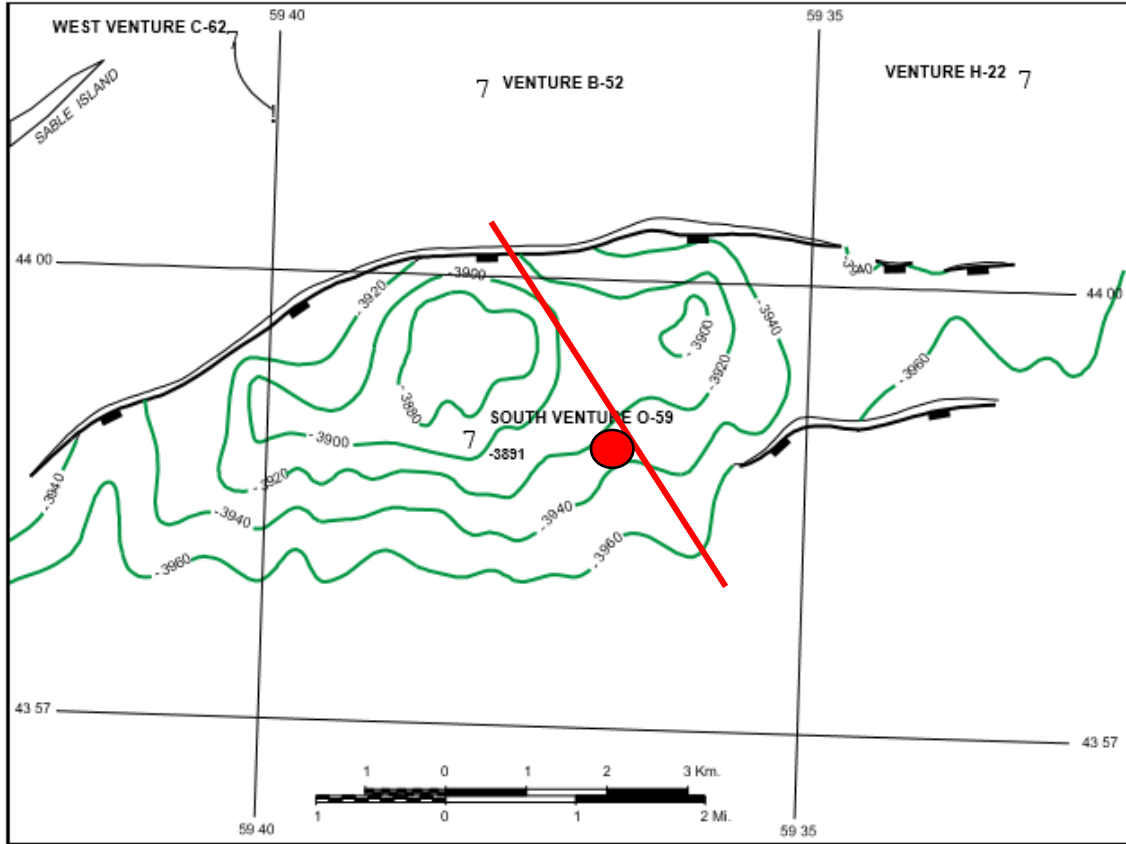


Figure 6.22: A figure of a seismic line showing the inflection of bright amplitudes representing the crestal fault trace around the Migrant structure.

Shale seals in the South Venture Field are continuous throughout the structure with no observable stratigraphic offsets on the crest of the structure (SOEP 1997; Figure 6.23). The absence of crestal faulting at South Venture (Figure 6.23) supports the idea that accumulations contained in any given reservoir in such structure will extend to the structural spill point. This relationship is illustrated in Figure 6.24 below.



*Figure 6.23: A structural map of the Top Sand 2 in the South Venture Field (SOEP, 1997). There is 4-way dip closure that the structure may succeed in trapping fluids. However, if the four-way dip structure is crestally faulted with a throw greater than the thickness of the top seal, this would impact trap effectiveness and integrity.*

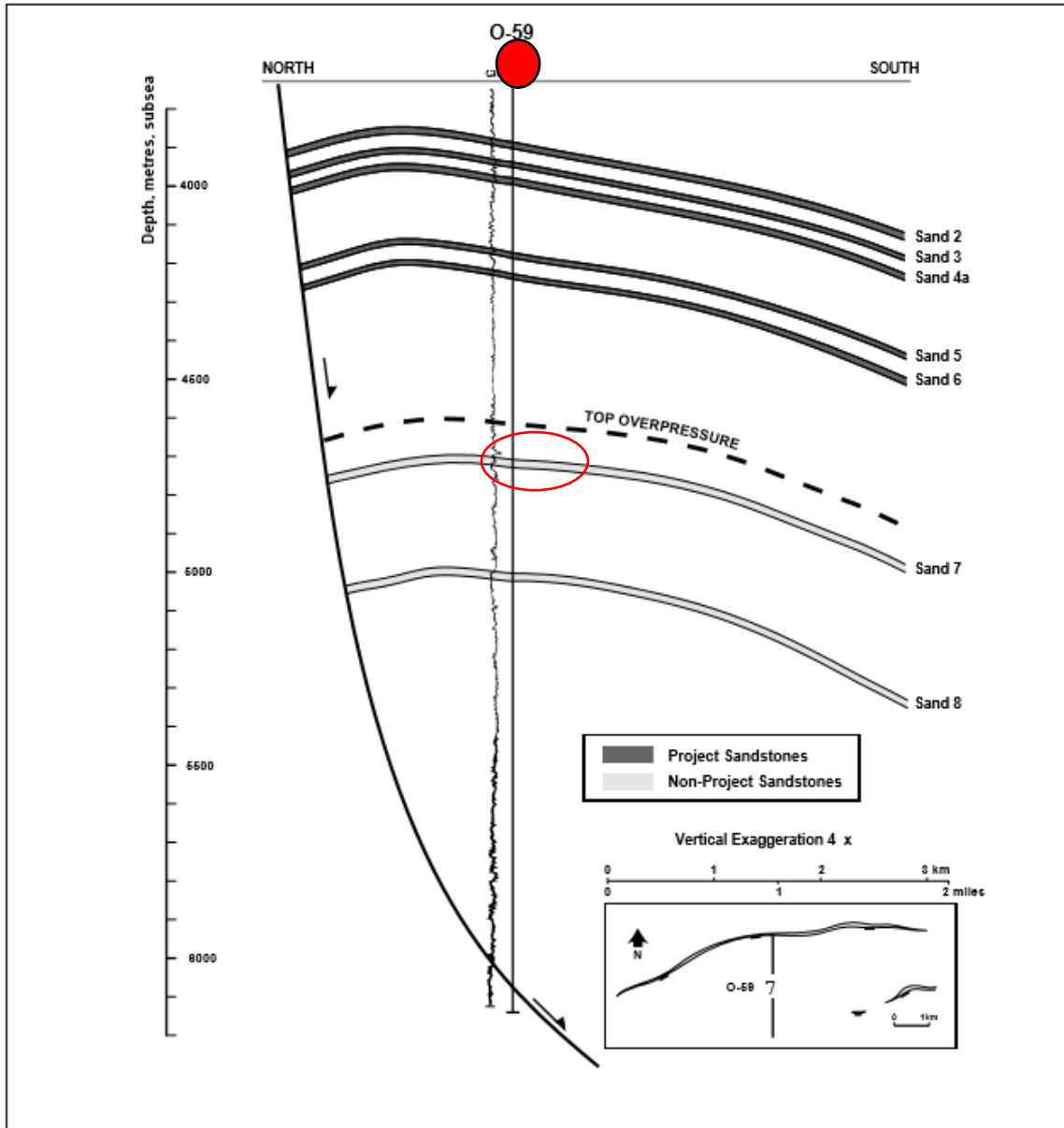


Figure 6.24: A schematic cross-section of the South Venture Structure showing the major bounding fault and inferred top of overpressure (SOEP, 1997).

The Thebaud Structure is like the Migrant Structure, except the crestal faulting runs deeper into the core of the rollover. At Thebaud, a different dynamic can be observed where two completely different systems are in play. The first one is controlled by crestal faults and the other by the structural spill point. In the absence of crestal faulting deep in the structure, the reservoir-filled accumulations are likely to fill down to their structural spill point provided there is enough hydrocarbon charge. The commercial reservoirs at Thebaud occur directly below the Thebaud Shale where Gamma-Ray and associated logs indicate a

low net to gross presence. It is also below the thick shale unit below which the productive Thebaud A and B sands were encountered (Figure 6.25; Figure 6.26). These reservoirs are limited to the deep overpressure section of the Thebaud Fault block. With an estimated vertical closure of ~ 160 m (Figure 6.25), gas trapped in the Thebaud A sand by simple closure is assisted by a fault sealing to the north through juxtaposition against thick shale layers in the structure.

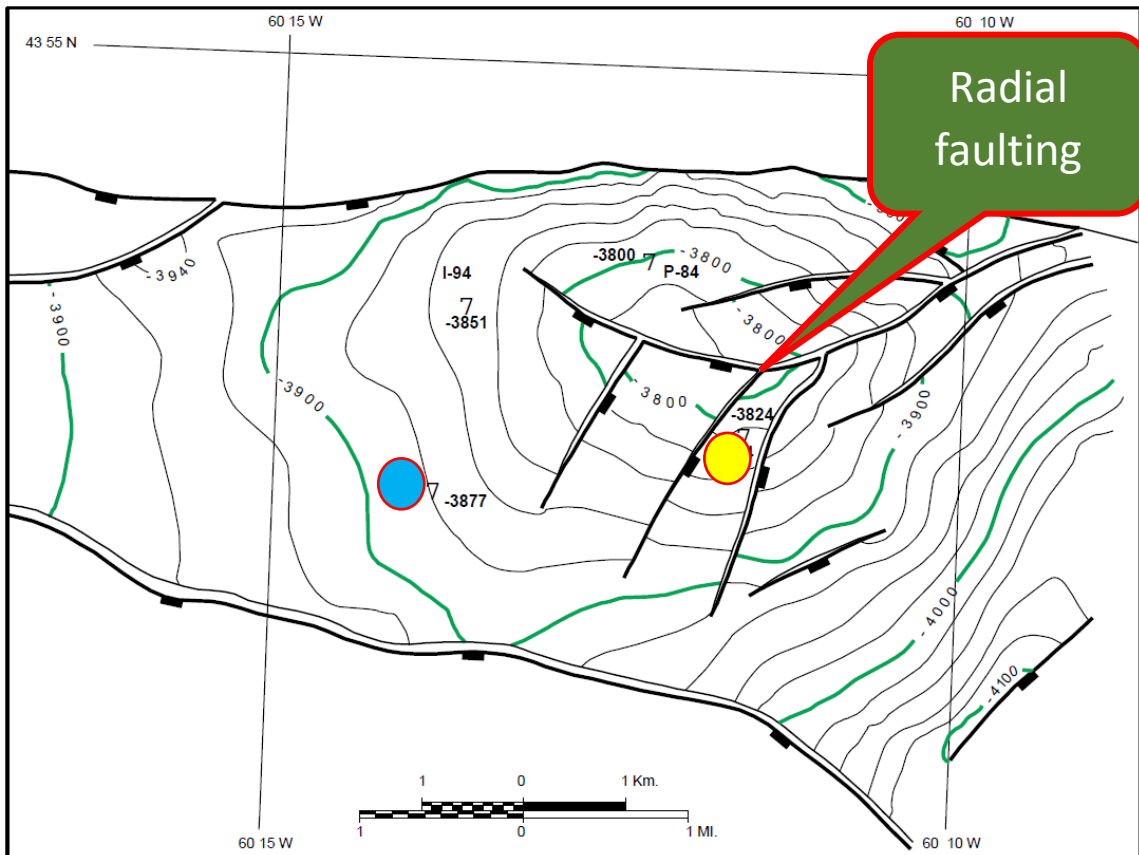


Figure 6.25: A structural map of the top A sand in the Thebaud Structure (SOEP, 1997). The location of the older Thebaud I-93 and C-74 wells have been indicated on the structure by the blue and yellow circles. In the cross-section view (Figure 6.26), the faults extend upwards through the structure. The faults likely resulted from salt piercing on the backside of the listric faults which resulted in the circular shape of the structure and radial faulting pattern (Caruthers et al., 2013).

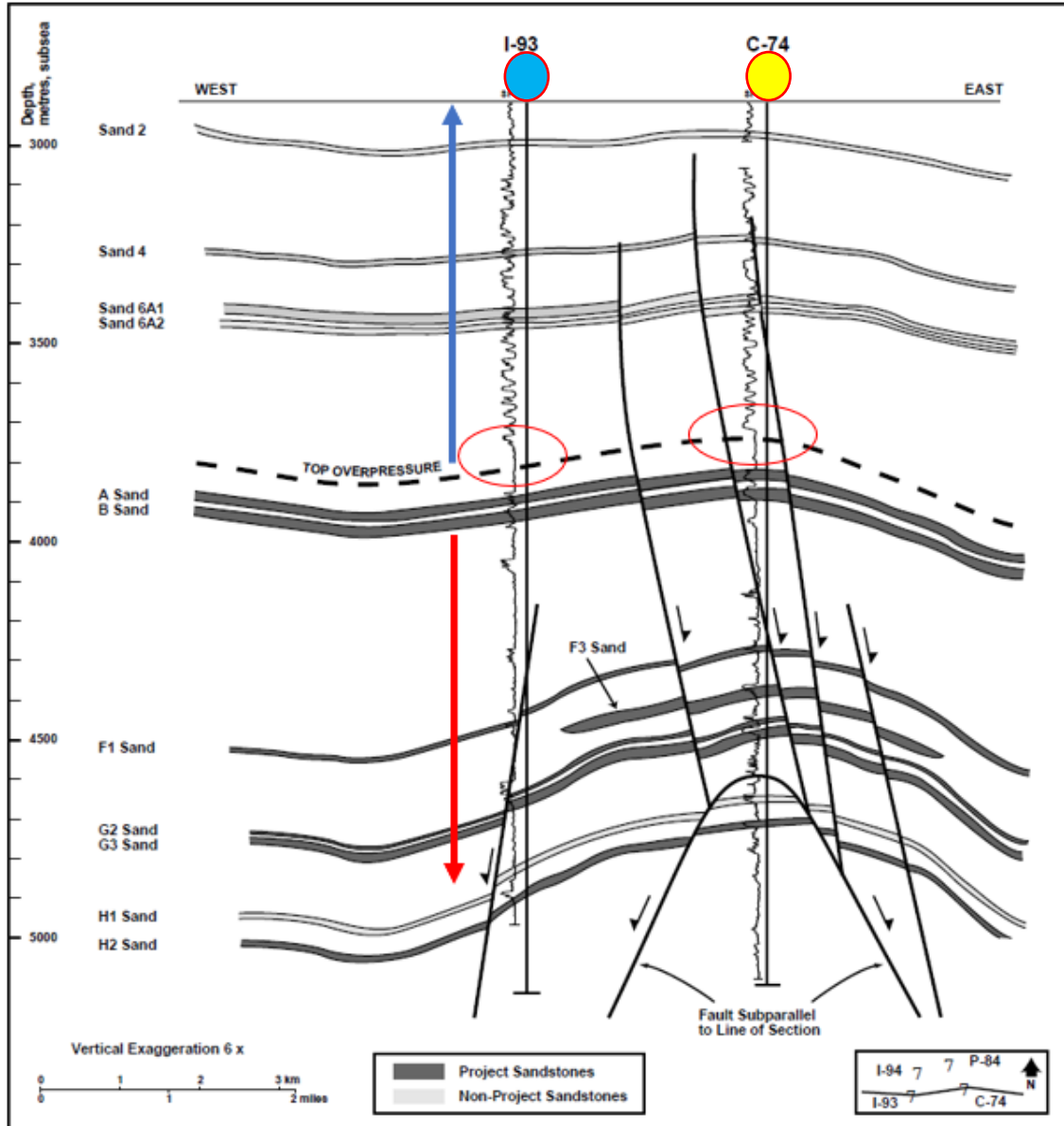


Figure 6.26: A schematic cross-section of the Thebaud Structure showing the faults and crestal faults (SOEP, 1997). The location of the older Thebaud I-93 and C-74 wells have been indicated on the cross section. The hydrostatic system at Thebaud has several gas legs that are very short because of the crestal faulting. Furthermore, these crestal faults pose a risk on hydrocarbon trapping when the throw on the fault is greater than the thickness of the shales typically in a high net-to-gross environment. In the absence of any faults and assuming the structure has a four-way dip closure each reservoir in the trap will be filled to its structural spill point.

On the other hand, the hydro-pressured reservoirs (Sands 2, 4, 6a, and 6b) occur above the Thebaud Shale as seen in Figure 6.26 above. The hydro-pressured sands show a lack of effective hydrocarbon trapping due to high net to gross and thin shales in the system



observed from well logs in Figure 6.26 above. This high net to gross section dominates the sections above the overpressure regime. As a result, there is a high tendency for an unfavorable juxtaposition of strata wherever the throw on the fault exceeds the thickness of shale seals as seen in Section 5.4.2 (Richards et al., 2008, 2010; Skinner, 2016). This allows for existing accumulations to leak through cross fault leakage (via stair-stepping) at the crestal fault (Richards et al., 2008, 2010). Alternatively, the presence of a competent top seal and favorable juxtaposition of reservoir rock with porosity against impermeable sediments across a fault (Section 5.4.2) would likely have been sealing (Allan, 1989; Knipe, 1997; Knipe et al., 1998).

#### 6.3.3.2. Trapping Conditions in the Migrant Structure

Offshore Nova Scotia, small extensional faults on the crest of 4-way dip closures on the hangingwall of rollover structures may present a risk to hydrocarbon trapping as demonstrated at the Migrant Structure in Chapters 5. The fault plane is the most important leakage pathway associated with rollover structures. This study investigated the most important controls (including fault throw and lithology thicknesses) at the fault plane (e.g., Figure 6.27). High net to gross packages with increased fault throw in the shallow sections at Migrant are more susceptible to leakage than the intermediate to deeper sections (3000 – 4455 m) where the fault throw diminishes. Also, these depths are characterized by increasing shale content/ lower Net-To-Gross NTG areas. The continuity of the thin shales shows the importance of a seal for fluid trapping. At the bottom of Migrant where there is no fault influence, simple closure in addition to the continuous shale with some diagenetic trapping has proven to be a useful combination in ensuring containment of gas. As a result, this made Migrant a technical success. Despite the capability of reservoir sequences in lower sections in trapping hydrocarbons, economic recovery and commerciality were not achieved due to the limited gas volume and associated depletion proven during DST #2.

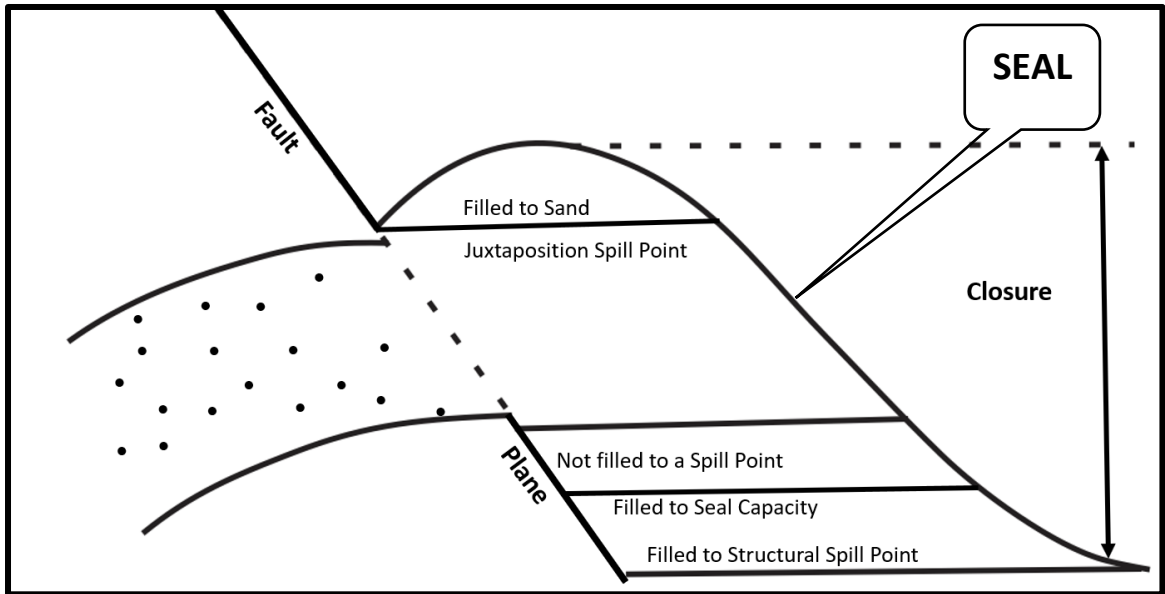


Figure 6.27: A figure showing the options for spilling in a faulted structural trap, modified after Sales (1997). The occurrence of leak points through a juxtaposition of permeable prevents any accumulation from extending to their structural spill points. Also, in the presence of a thin structural wet seal, there is a tendency for a capillary leak (represented by the bubble) to occur at the top of the structure if there is sufficient build-up of pressure from increased hydrocarbon charge with little or no leak points at an existing fault boundary.

Despite successfully testing for gas in reservoirs within the simple small closure that exists around the base of the Migrant Structure, the migration of fluids through the system at the fault up section would have occurred at any time following the juxtaposition of reservoir units on either sides of the crestal fault (Sales, 1997). Through reservoir connectivity at the existing crestal fault, it is possible that the inflow of hydrocarbons from a fault-dependent structure down-dip (in this case Adamant) would drain through the Migrant Structure. Besides, the main spilling mechanism (juxtaposed leak points) in the Migrant Structure (Section 5.4.2.) being limited to depths of 3765 – 3821 m, this acted to normalize any pressure differential that may lead to the forceful exit of hydrocarbons through a water wet seal especially if it is thin (Sales, 1997). In a high angle fault displacement profile, such thin seals will encourage the most exposure of cross-sectional reservoir area (Allan, 1989). As a result, there is a creation of numerous effective leak points between rocks of different ages. Thus, allowing for potential stair-stepping migration of hydrocarbons in and out of zones along an existing fault plane until the system has no hydrocarbons.

Given the fill and spill dependency of structural rollover traps at an established leak point in the structure, the presence of residual gas from log analysis that occurs in areas of crestal fault influence throughout the vertical section at Migrant offers proof of hydrocarbon. A dynamic fluid modelling would show migration through intervals of sand-on-sand juxtaposition at the fault. Coincidentally, the Vsh log distributed throughout the model of the Migrant Structure suggests that the entrained intervals are characterized by thin shales between the sand packages (Section 5.4.2.).

While it is uncertain if there was early migration of hydrocarbons into the Migrant Structure, the idea that entrained gas filled up the key reservoirs in the structure before leakage is open to debate. However, what is certain is that there was leakage, and this is proof of a functional petroleum system (CCOP, 2000). Also, the tight and discontinuous nature of the reservoirs at greater depth in the Migrant Structure represents a different system that is common in structures listed in the table of failed wells (Section 6.3.3.3.). Overall, the gas-dominated nature of the trap suggests that it is a typical class 1 trap with reduced closure area (Sales, 1997; Figure 6.28).

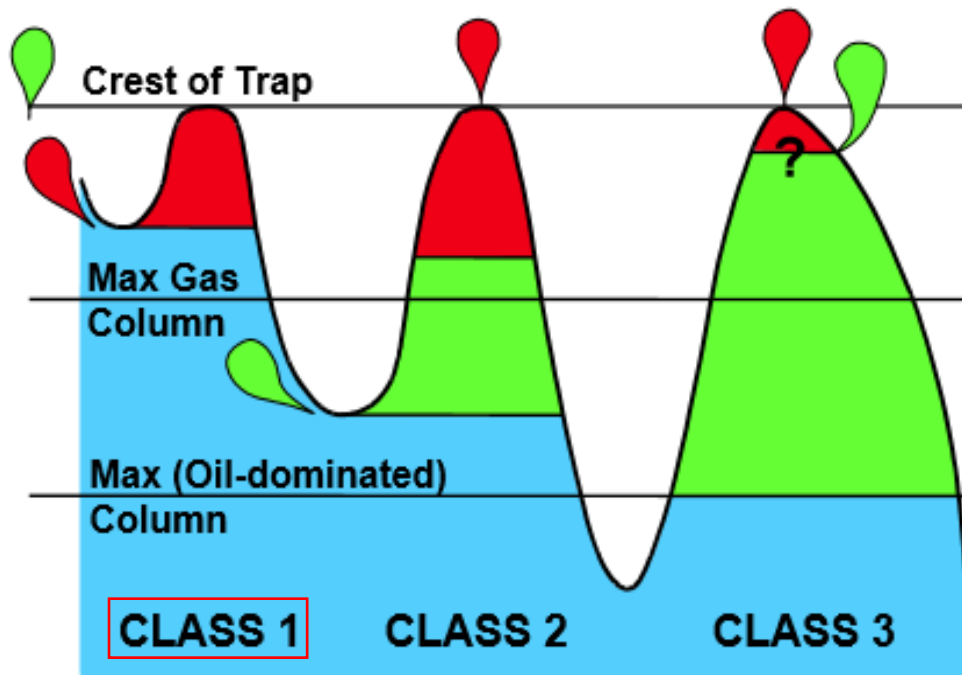


Figure 6.28: A diagram of the three different classes of traps according to Sales (1997). Limited areal extent (low relief structures) appears to be most affected in terms of fluid contacts, reservoir volume, and geologic controls on spillage. In the figure, the blue represents water, the green represents oil and red represents gas. The bubbles give an indication of potential leakage pathways in the various systems.

### 6.3.3.3. Hydrocarbon Trapping in Rollover Structures on the Scotian Shelf

In the Sable Subbasin, almost all faulted 4-way dip rollover anticlines have been tested (drilled) for hydrocarbons. Outside the core area of the productive area of the Sable Subbasin, there are some structures that are completely water wet/unsuccessful having no hydrocarbon shows. Reports indicate that a high proportion of the drilled structures contain hydrocarbons in their reservoirs, which are typically overlain by shales that act as seals (SOEP, 1997; Dawson & Almon, 2002, 2006; Almon & Dawson, 2004; Smith et al., 2014). Historically, trap and seal failure are known reasons why half of the drilled wells have failed to encounter producible hydrocarbons (Rudolph & Goulding, 2017). A summary of failed wells by the Canada Nova Scotia Offshore Petroleum Board (CNSOPB, 2013) indicates “no fault-seal” as the primary reason most wells targeting rollover structures offshore Nova Scotia fail to find producible volumes of hydrocarbons (Table 6. 2). These reasons may be compared to those reported in this study in Table 6. 3 and a summary of characteristics in the key significant and commercial discoveries offshore Nova Scotia (Table 6.4). While previous researchers have reported on the size of hydrocarbon accumulations in rollover structures based on drilling history (Cummings & Arnott, 2005; Smith et al., 2014), there are no studies that demonstrate the controls and mechanisms of failure.

Table 6. 2: A summary of failed wells in the Scotian Shelf (CNSOPB, 2013). Analyses completed by the CNSOPB indicates why the traps failed and adds to the overall understanding of trapping in rollover anticline on the Scotian Shelf. The CNSOPB concluded that most of the wells failed due to inadequate seal. Assessment by the PFA have not considered fault seal risk in their analyses.

Well	Parcel	Play Type	Target Formation(s)	Reservoir		Seal	Comments
				Net/Gross	Porosity		
Penobscot L-30	1	rollover anticline	Missisauga	High	Good	No Fault Seal	Oil bearing sands in Lower Missisauga trapped within simple closure
Emma N-03	1	rollover anticline	Missisauga	High	Good	No Fault Seal	Fault leaks due to high N/G; no simple closure at well location; sands wet
			Mic Mac	Fair	Fair	No Fault Seal	Small simple closure with thin gas pay
Mariner I-85	1	fault-bounded closure	Missisauga	High	Good	No Fault Seal	Fault leaks due to high N/G; no simple closure at well location; sands wet
			Mic Mac	Low	Low	Faults Seal	Tight limestones in Upper Mic Mac Fm. provide fault seal for gas sands
Mic Mac J-77	3	salt pillow	Logan Canyon	Fair	Good	No Fault Seal	No simple closure at well location; sands wet
			Missisauga	High	Good	No Fault Seal	Two sands with thin oil pay over water trapped in low relief simple closure
			Mic Mac	Fair	Fair	No Fault Seal	No simple closure at well location; sands wet
Mic Mac D-89*	3	salt pillow	Missisauga	High	Good	No Fault Seal	Oil zones in Dawson Canyon & Logan Canyon Fms. trapped in fault dependent closure
Wyandot E-53	3	basement high	Logan Canyon	Very High	Good	No Fault Seal	No simple closure at well location; sands wet
			Missisauga	Very High	Good	No Fault Seal	No simple closure at well location; sands wet
			Mic Mac	High	Good	No Fault Seal	One thin oil bearing sand trapped within simple closure in Mic Mac Fm.
Erie D-26	3	basement high	Logan Canyon	Very High	Good	No Fault Seal	No simple closure at well location; sands wet
			Missisauga	Very High	Good	No Fault Seal	No simple closure at well location; sands wet
			Mic Mac	High	Good	No Fault Seal	Two sands with thin oil pay trapped within simple closure in Mic Mac Fm.
N. Banquereau I-13	4	rollover anticline	Missisauga	High	Fair	No Fault Seal	Gas pay over water in Lr. Missisauga; sand trapped within simple closure
SW Banquereau F-34	4	rollover anticline	Missisauga	Fair	Low - Fair	No Fault Seal	Thin gas pay in Lr. Missisauga; sand trapped within simple closure
			Mic Mac	Not Penetrated	N/A	N/A	Last 1100 m of well has very low N/G (shale-dominated Verrill Canyon Fm.)
			Abenaki	Not Penetrated	N/A	N/A	
Louisbourg J-47**	5	rollover anticline	Missisauga	Fair - High	Fair - Good	No Fault Seal	Fault leaks due to high N/G; no simple closure at well location; sands wet
			Mic Mac	Low	Low	Fault Seals	Two sands with gas pay trapped within a fault dependent closure
			Abenaki	Not Penetrated	N/A	N/A	
* No oil zones were encountered in the target formation (Missisauga). Two sands with thin oil pay over water were encountered in the lower Dawson Canyon and upper Logan Canyon Formations. These sands are believed to be trapped in a small fault dependent closure. This section of the well has a high shale content which allows the fault to seal.							
** Two gas sands trapped within a fault dependent closure were encountered in the Mic Mac Formation. In Louisbourg, the Mic Mac has a very low sand/shale ratio and contains a significant number of tight limestones which allows the faults, at this level, to seal.							

Table 6. 3: The three structures analysed in this study.

Well	Parcel	Play Type	Target Formation	Reservoir		Seal	Comments
				Net/Gross	Porosity		
Migrant N-20	1	Rollover Anticline	Mic Mac Formation	Low	Low	No Fault Seal	Low relief rollover, with small simple closure with thin gas pay at base with fault leak due to high net-to-gross above (Missisauga) where sands are mainly wet with hydrocarbon shows
Adamant N-97	1	Fault Bounded Closure	Missisauga Formation	High	Fair	No Fault Seal	Low relief closure with thin gas zones, fault connectivity due to high net-to-gross above (Missisauga) where sand are mainly wet sands with hydrocarbon shows
Thebaud E-74 (T5)	1	Rollover Anticline	Missisauga Formation	High	Good	Fault Seal	Radial crestal faulted rollover with thick column, simple closure below the extensive Thebaud shale with thin gas pay. Isolated reservoirs with no fault leak at the base. High net-to-gross above (Missisauga) where sands are mainly wet with hydrocarbon shows.

168 Table 6.4: Significant and commercial discoveries of the Scotian Margin. The table lists their pressure relationships, structural relations, faulting relationship, seal category (inboard or outboard) and salt influence beneath the structures.

1	Discovery (Gas Fields)	Year	Reservoir	Formation	Status	Well OP	Res OP	Dip	Structure Relations	Faulting (Bounding, Crestal, Peripheral)	Seal (Outboard, Inboard)	Salt	
2	<b>Significant Discoveries</b>	Arcadia	Jul-83	Sandstone	Mic Mac	Undeveloped	OP	OP	3WD	Rollover above listric	Bounding (Bounded by 2), Peripheral	In	No
3		Banquereau	Jul-82	Sandstone	U. Missisauga	Undeveloped	OP	HP	4WD	Rollover above listric	Bounding, Peripheral	Out	No
4		Chebucto	Aug-84	Sandstone	U. Missisauga	Undeveloped	OP	2 HP, 1 OP	4WD	Rollover above listric	Bounding, Crestal and Peripheral	Out	No
5		Citnalta	Apr-74	Sandstone	Mic - Mac - L. Missisauga	Undeveloped	OP	HP	4WD	Rollover above listric	Bounding,	In	Yes
6		Glenelg	Nov-83	Sandstone	U. Missisauga	Undeveloped	OP	HP	4WD	Rollover above listric	Bounding, Crestal and En echelon	Out	Yes
7		Intrepid	Aug-79	Sandstone	M-U. Missisauga	Undeveloped	OP	HP	4WD	Rollover above listric	Bounding, Crestal	Out	Yes
8		Olympia	Jan-83	Sandstone	Mic Mac - L.Missisauga	Undeveloped	OP	OP	4WD	Rollover above listric	Bounding, Crestal	In	Yes
9		South Sable	Jul-88	Sandstone	L. Missisauga	Undeveloped	OP	No	4WD	Rollover above listric	Bounding, Crestal (2 minor)	In	Yes
10		Uniacke	Apr-84	Sandstone	Mic Mac	Undeveloped	OP	OP	4WD	Rollover above listric	Bounding	In	No
11		West Olympia	Nov-85	Sandstone	Mic Mac - L. Missisauga	Undeveloped	OP	OP	4WD	Rollover above listric	Bounding (Bounded by 2)	In	No
12		West Venture C-62	Mar-85	Sandstone	Mic Mac - L. Missisauga	Undeveloped	OP	OP	4WD	Rollover above listric	Bounding	In	No
13		West Venture N-91	Jul-85	Sandstone	U. Mic Mac - L. Missisauga	Undeveloped	OP	OP	4WD	Rollover above listric	Bounding	In	Yes
14													
15	<b>Commercial Fields</b>	Thebaud	Oct-72	Sandstone	Mic Mac - L. Missisauga	Developed	OP	HP, OP (Commercial)	4WD	Rollover above listric	Bounding, Crestal, En echelon, Peripher	In	Yes
16		Venture	Jun-79	Sandstone	Mic Mac - L. Missisauga	Developed	OP	HP, OP (Commercial)	4WD	Rollover above listric	Bounding, Crestal, Peripheral	In	No
17		South Venture	Jan-83	Sandstone	L. Missisauga	Developed	OP	HP	4WD	Rollover above listric	Bounding, Peripheral	In	No
18		Alma	Jul-84	Sandstone	U. Missisauga	Developed	OP	HP	4WD	Rollover above listric	Bounding, Crestal, Peripheral	Out	No
19		North Triumph	Jan-86	Sandstone	U. Missisauga - L. C	Developed	?	HP	3WD	Rollover above listric	Bounding (Bounded by 2), En echelon cr	Out	No
20		Deep Panuke	Apr-99	Fractured Lime	Abenaki Formation	Abandoned	?	HP	4WD	Carbonate	Bounding	?	No
21													
22		(Oil Fields)											
23		Panuke	Aug-86	Sandstone	U. Missisauga - L. C	Abandoned	?	HP	4WD	Drape over salt	Bounding	?	No
24		Cohasset	Apr-73	Sandstone	U. Missisauga	Abandoned	?	HP	4WD	Drape over salt	Bounding	?	No



While minor amounts of hydrocarbons are not consistent with observations from rollover anticlines drilled in the rest of the basin, most of the closures ranked as failures contained gas in their bottom reservoirs (Table 6. 2). This may be attributed to the trapping mechanisms discussed from the modelling of the Migrant Structure (Section 5.4.). In the seven producing fields offshore Nova Scotia (Section 2.4.), the presence of thick shale seals appears to be a common characteristic in all the structures (SOEP, 1997). Sealing is mainly provided by the regional Naskapi Shale in the case of the Alma and North Triumph fields. In other fields like the Thebaud, Venture, and South Venture fields, intraformational shales are believed to be responsible for the effective trapping of hydrocarbons (SOEP, 1997; Richards et al., 2008; Richards et al., 2010; Skinner, 2016). Therefore, in addition to the sealing provided by the 200 m thick Naskapi Shale in the Upper Missisauga Formation, a combination of a low net-to-gross and the presence of thick fault constrained limestone intervals with localized intraformational shales associated with the Lower Missisauga and Upper Mic Mac formation intervals have contributed to the effective hydrocarbon trapping in the Jurassic sediments.

With the reservoirs targeted during past exploration occurring in the Late Jurassic Mic Mac and Early Cretaceous Missisauga formations, they are arranged in a stacked succession of sand and shale pairs that reach greater thicknesses in the areas of Thebaud and Venture fields (SOEP 1997; OETR 2011; Figure 6.29). This is related to the progradational sequence consisting of reservoir-seal pairs that exhibit blocky and cleaning up trends (Section 3.4.3.), with some intervals reaching thicknesses of up to 50 m likely in response to a combination of deltaic sediment progradation and lobe avulsion (SOEP 1997). Based on the lithological properties, associated sedimentary structures and lithostratigraphic relationships with adjacent units, the reservoir sands in the Sable Subbasin have been classified into shelf and strand-plain, delta plain, and valley-fill depositional facies (SOEP, 1997). Hence, an interfingering of prodeltaic sands and marine (i.e pro-delta) shales gradually changed upward with an increase in the sand-shale ratio as the sediments of the Sable Delta prograded.

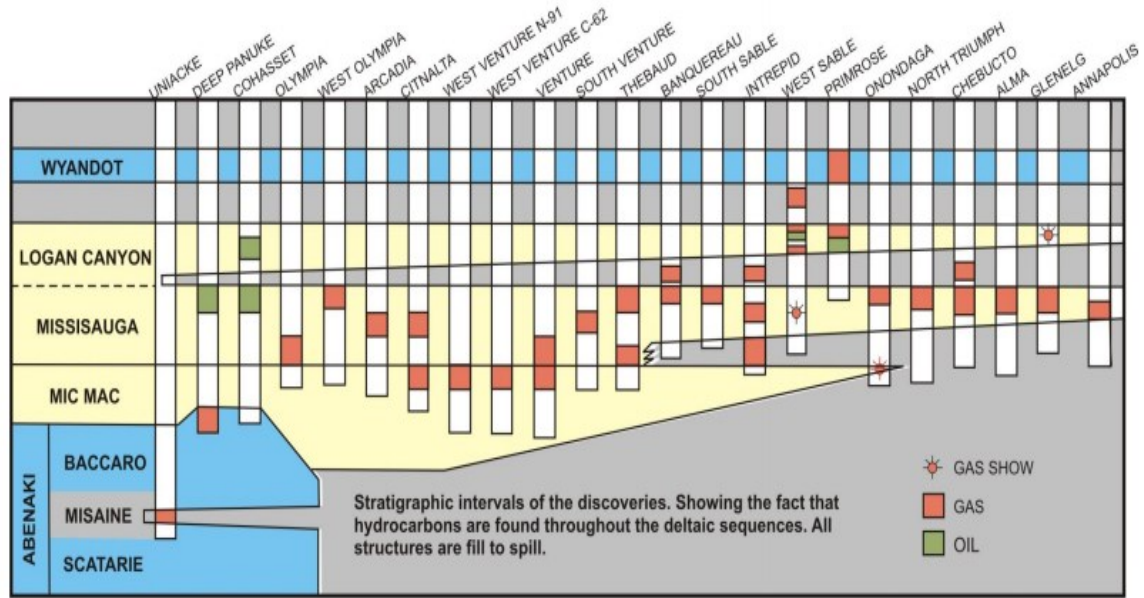


Figure 6.29: A figure of the stratigraphic distribution of discoveries in the Scotian Basin (OETR, 2011). The yellow areas comprise clastics, blues are carbonate, and grey shales. Most of the hydrocarbon discoveries on the Scotian Margin occur within Upper Jurassic and Lower Cretaceous deltaic sand reservoirs of the Missisauga and Mic Mac formations (SOEP, 1997). Shales of the Verrill Canyon Formation (the distal marine equivalents of the Mic Mac and Missisauga formations) are thought of as the main hydrocarbon source rocks (Mukhopadhyay, 2006; Silva et al., 2015; Fowler et al., 2016).

#### 6.3.3.4. Risks and Opportunities in Rollover Structures on the Scotian Shelf

To ensure the success of future exploration, the various geological complexities from the Migrant Structure can be used to match/compare previous work to provide the best estimate of prospect size. In addition to the two obvious stratigraphic positions where fault seal is most effective below the Cretaceous Naskapi Shale and in the Jurassic section, enhanced reservoir quality from chlorite rims is common in fields that occur at greater water depth east and north of Migrant. For this reason, a pattern exists regarding the success or failure cases. With an estimated 120 TCF of unrisked gas offshore Nova Scotia (OETR 2011; Table 6.5), this was established on the assumption that every structural closure with greater than 2 sq km area contains gas in every sand within the trap (OETR, 2011).

*Table 6.5: Unrisked in place hydrocarbon volumes. The PFA reported that substantial trapping in shallow water/shelf areas account for the large-scale gas/condensate volumes. In zone 3 (the area containing the Sable Subbasin), ~35 trillion cubic feet (TCF) of unrisked gas was estimated by the PFA (OETR, 2011).*

By Zone	Total Gas Volume in Surface (TCF)	Total Oil Volume in Surface (Mbbbl)	Total Oil Equivalent Volume (Billion Bble)	GOR (Scf/Sbbl)
Zone 1	14	2,470	4.4	6,000
Zone 3	35	1,130	6.3	31,000
Zone 5	27	1,650	5.5	16,000
Zone 6	26	1,090	5.0	24,000
Zone 4	16	990	3.3	16,000
Zone 2	4.2	820	1.4	5,000
Whole Basin	121	8,150	26	15,000

However, results from Migrant may challenge the estimate that is likely optimistic especially based on the analyses of old 2D seismic data. In Figure 6.30, zones 3 and 5 constitute the lowest risk parcels with proven petroleum systems elements in the PFA divisions of petroleum potential on the Scotian Margin. From a reported 35 TCF of unrisked gas in place estimated for Zone 3 (OETR, 2011), a production of ~3 TCF to date mainly from rollover anticline is 5 TCF less than the estimated 8 TCF obtained by the CNSOPB for the same unrisked volume of gas (CNSOPB, 2008). Given the disparity in the estimates reported by both groups, it is evident that these low recoveries of 8% and 22% for the PFA and CNSOPB are too small when ranking the Sable Subbasin against global prolific gas basins (Sandrea, 2006). Despite the low recoverable estimate, the production, and sales of close to 2 TCF of gas proves that the basin was of commercial significance.

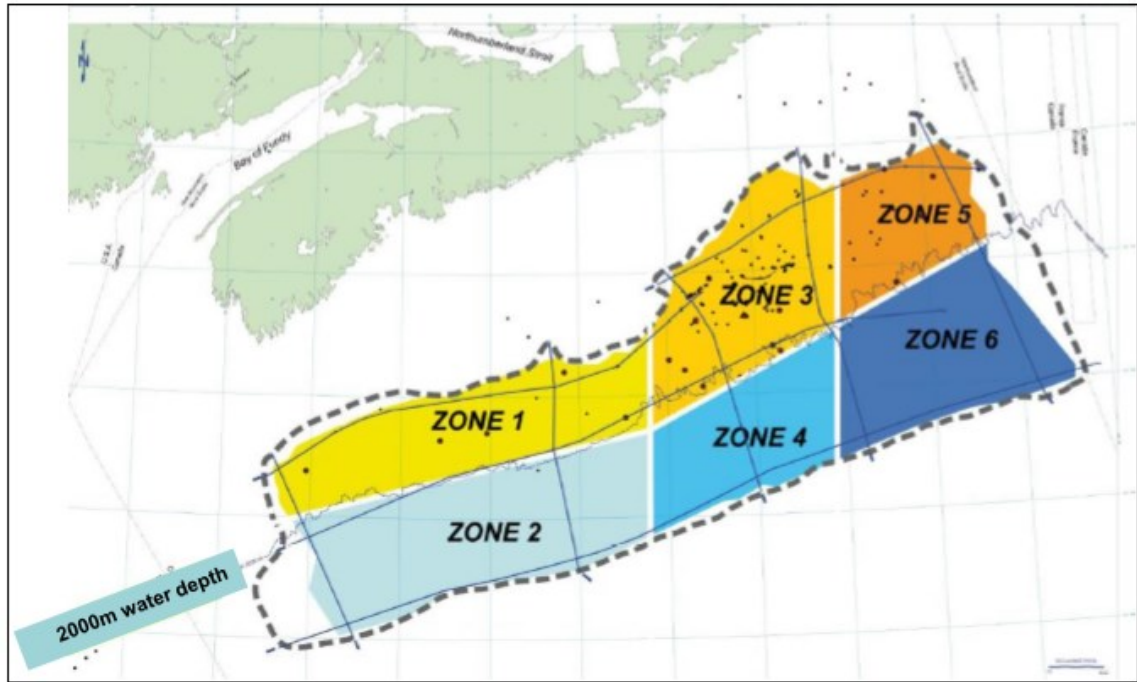


Figure 6.30: The Scotian Margin showing the division of the margin into six zones (OETR, 2011). The Migrant Structure is situated in zone 3, which comprises the most explored/drilled area containing most of the significant gas discoveries around the Sable Island. The black dot represents offshore wells, with the highest well density on the margin occurring in Zone 3.

With up to 100 similar undrilled rollover structures occurring in the proximal areas within water depths of less than 200 m, most of the reservoirs contained in these structures (faulted or non-faulted) may have a shared risk, especially in faulted four-way dip closures. Future assessment of trap integrity, may be first approached by identifying the amount of closure and investigating the extent of overpressure between the key wells from published maps of structural closures offshore Nova Scotia (e.g Figure 6.31). For example, the thick shale seals in the South Venture Field being continuous throughout the structure with no observable stratigraphic offsets on the crest of the structure (SOEP 1997), the absence of crestal faulting in the field supports the idea that the increased shale influence in such areas makes for suitable trapping. In such a structure, the accumulations contained in any given reservoir extend to the structural spill point (Richards et al., 2008). Also, with overburden stress exerting a higher effect on permeability, the preservation of primary porosity in fields in the central Sable Subbasin like Venture is linked to the presence of authigenic chlorites (Piper). Therefore, wells targeting rollover structures with continuous

shales will likely encounter less risk with regards to trapping. However, where reservoirs are isolated by thick shales, this may constitute a production risk if the connectivity is poorly understood (Skinner, 2016).

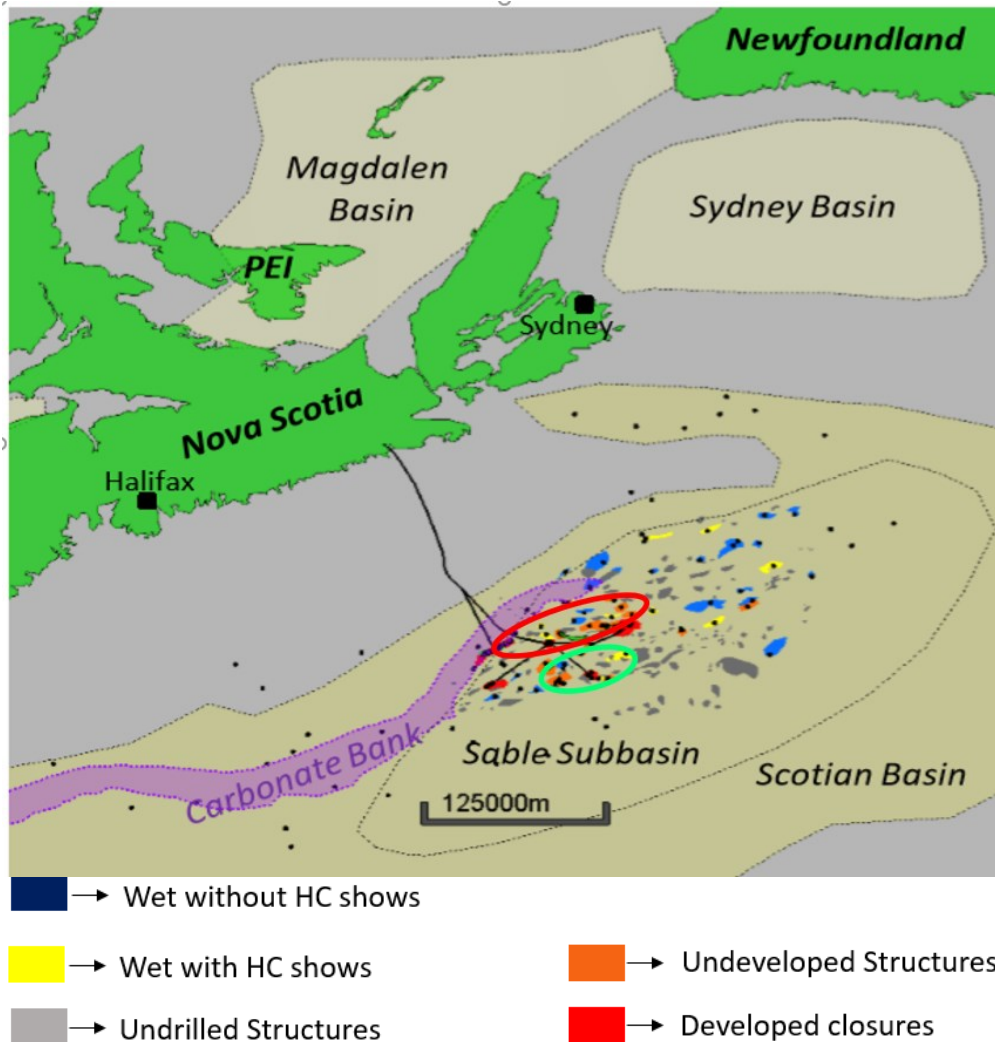


Figure 6.31: A map of the offshore sedimentary basin with the fields, closures, wells, and pipelines linking various hydrocarbon structures from the Sable Subbasin (Modified by O'Connor et al. (2018) after Williams & Keen, 1990; and NSPD, 1999). The red oval contains the structures on the proximal shelf with increased net-to-gross and associated faulting. The green oval shows structures in much distal positions where some commercial successes have been encountered.

From the table of failed rollover structures in the Sable Subbasin in Section 6.3.3.3., one common characteristic of structures targeting reservoirs in the Mic Mac Formation (e.g Acadia, Uniacke, and Migrant) is that reservoirs in these structures are characterized by the same mechanism (simple closure). Also, the closure is confined to the base of the respective structures. It appears that the occurrence of reservoirs at ~ 4000 m (or greater),

have been negatively influenced by the solubility of quartz (Bjørlykke et al., 1989; Bloch, 1991; Summa, 1995; Bloch et al., 2002; Thyberg et al., 2010), which inevitably has contributed to diagenetic trapping conditions favorable for the accumulation of gas. Besides, based on the position of the various structures in the basin, the absence of early authigenic chlorite rims poses some risk to the reservoir quality as the chlorite rims appear to limit diagenesis (Gould et al., 2010). Therefore, reservoirs deposited distally have proven to be successful commercial targets due to their good primary porosity retention capacity from the chlorites.

Generally, it may be assumed that a correlation exists between field location in the Scotia Basin and their porosity and permeability preservation (particularly primary porosity) seen in more distal fields in the basin. This is linked to the deposition of reservoirs in a low-energy offshore environment, where chlorite rims are available to act as grain coats. Alternatively, the extensive hydrostatically connected reservoirs in proximal structures along the shelf suggest that the issue of leakage associated with small extensional faults is risky especially in the presence of thin shales. As a result, the issue of lateral sealing becomes as a trap risk. Poor lateral shale continuity likely contributed to some of the wells drilled being dry holes with no commercial volumes present in their targeted reservoirs. However, despite their negative outcomes, they may give way to new plays and concepts through lessons learned from analyzing the data from such wells (Mackie, 2017).

A review of the literature highlights various success terms used in the assessment of a prospect including economic, commercial, and geologic (technical) success (Bao, 2016). The geologic success case has more to do with hydrocarbon presence. Nonetheless, unless proven moveable, hydrocarbon shows do not equate to commercial success. With the success characterization of prospects determined based on a minimum flowable amount of hydrocarbon encountered by the test well, this suggests that all 23 significant discoveries in the Sable Subbasin represent a geologic success (Rose, 1992). However, they can only be elevated to the rank of a commercial entity when they are in large accumulations (Rose, 2001). In the Sable Subbasin, the need for a favorable juxtaposition of strata combined with the thick extensive Naskapi Shales suggests that this is true for outboard (distal fields) where most of the commercial successes have been encountered. However, the success assumption based on the minimum flowable amount from accumulations in the high net-



to-gross Missisauga Formation fields and some targets in the Mic Mac Formation is unreliable given their associated sealing risk.

Before any dependency at an existing boundary growth fault may be considered, the dependency at a crestal fault (where present) must be considered (Richards et al., 2008, 2010). Therefore, based on a hierarchy established from such considerations of fault dependency, structures with crestal faults have a higher risk. This suggests that most of the crestally faulted structures containing commercial volumes of hydrocarbon in Zones 3 and 5 are constrained by sealing faults, which depend on a favorable juxtaposition of strata in the presence of a thick shale (Richards et al., 2008, 2010). Modelling results from the Migrant Structure (Chapter 5) indicate that the interplay between the fault throw and seal thickness in the rollover structures exerts a key control on their ability to trap hydrocarbons. Hence, displacement along the crestal fault in the high NTG section at Migrant was significant enough to impact the commerciality of the trap. Given the obvious hydrocarbon charge, the risk factor of each petroleum system element within the Migrant Structure would score a relatively low probability P factor rating (CCOP, 2000; Rose, 2001; Milkov, 2015; APPENDIX E.3.). Therefore, a poor/low geologic probability of success is expected for most of the key petroleum systems elements in the Migrant Structure (Figure 6.32).

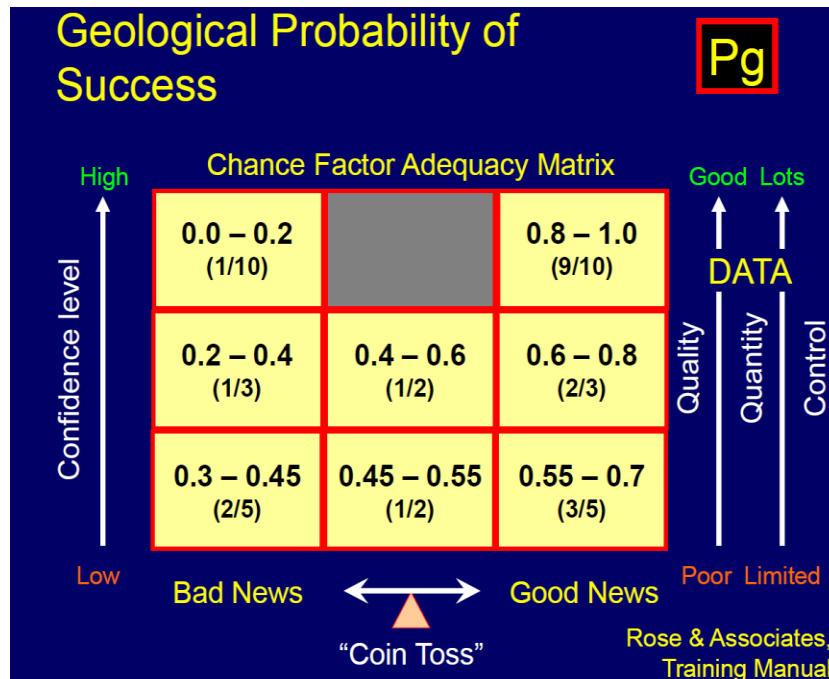
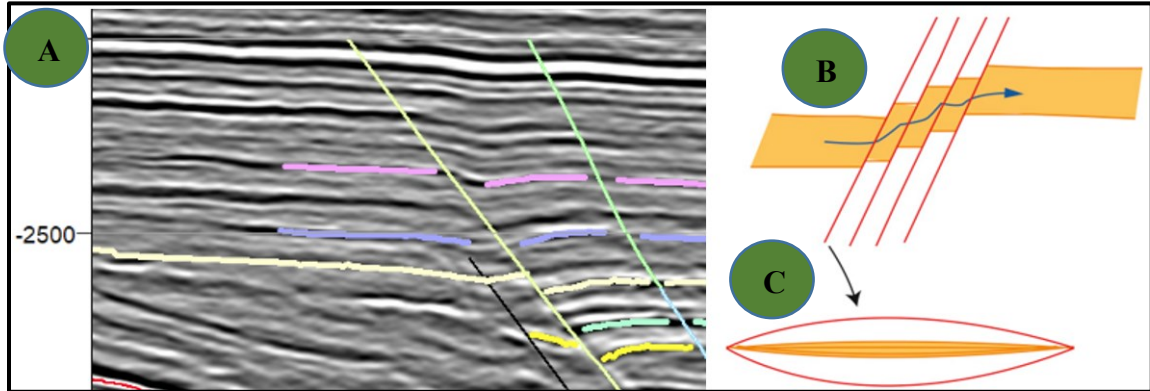


Figure 6.32: A probability matrix showing the confidence (degree of how much is known) on the Y-axis and the chance of success on the X-axis (Rose, 2001). The top right demonstrates higher confidence, and the bottom left low confidence with more unknowns.

## 6.4. Uncertainties

### 6.4.1. Seismic Uncertainties

For this study, some inaccuracies with the interpretations around the faulted area (including the boundary fault and crestal fault) around the Migrant expansion trend and intervals deeper in the section where there are interfingering siliciclastics and carbonates comprised key interpretive error. The chaotic nature of the seismic data around the base has contributed to disrupting the seismic resolution from salt influence in the image shown in (Section 6.1.1.). Considering the expanded vertical scale relative to growth faulting, some preliminary errors were encountered in determining the fault displacement from key stratigraphic marker horizons. Structural maps including features such as structural saddles, crestal faults, as well as the overall relief of the Migrant Structure were a product of interpretations that honored the distance between packages while adjusting to changes in sediment thickness on either side of a fault. Hence, despite the lack of quantification regarding this type of error, a close inspection and careful correlation of the interpreted seismic troughs and peaks between key faults was important in minimizing any source of interpretation error (Bond, 2015; Figure 6.33).



*Figure 6.33: A seismic image from the Migrant rollover (A) showing a fault zone comprising cumulatively offset. Schematic of similar cumulative offsets identified by Bond (2015)(B) and a plan view of the schematic (C).*

Furthermore, a small fault below seismic resolution as shown in Section 6.3.3.1 introduces uncertainties to the analysis. While the resolution of the seismic data (imaging) is important, some interpretations sit on the seismic line while some do not, which is bound to impose some error on the interpretations. A close observation shows a case where some of the interpretations were done on the original cube and have values where there appears

to be no data now in the present 5-gigabyte seismic volume provided to the basin and reservoir lab for this study, which has had every second line spacing removed.

#### 6.4.2. Uncertainties from Well Data

There are several wells amongst all three expansion trends, but the spacing of the Migrant and Adamant wells and the Adamant and the Thebaud wells meant that log-based reservoir correlations across wells from Thebaud to Adamant and to Migrant challenging. The high net to gross nature of the system made it useful to incorporate the sonic and density logs into the interpretation composite alongside the Gamma-Ray logs to correlate the reservoir zones reservoir quality suitable for the containment of gas. The missing sections of density and sonic logs in the Migrant N-20 well impeded the interpretation. Also, the top of overpressure at Migrant is open to debate since stratigraphic correlation was affected by the absence of critical Gamma-Ray data at Migrant (4025-4095 MD). This limits the ability to identify and link the overpressure at the Migrant Structure to a shale interval. Hence, with formation pressure reading around 4015 mRT appearing to be higher than the other formation pressures in the trend, this may be taken to be the effective top of overpressure.

Additionally, being an averaging tool, the wireline resistivity log may give low resistivities that may complicate the distribution of pay zones. This is especially regarding the averaging of low resistivities associated with the presence of conductive minerals (e.g. ilmenite, pyrite, and hematite) as well as thin beds. Also, the presence of siderite content (iron-rich carbonates) with a higher density than quartz would contribute to a lower porosity than there is, which could impact the net pay estimation. Similarly, such an effect may occur (increased net pay estimation) in the presence of kaolinite clays, which are non-radioactive and may be missed by the GR log from which the Vsh was derived.

#### 6.4.3. Uncertainties from Modelling

In this study, property modelling was possible through applying some geostatistical techniques to the petrophysical data. With the use of the stochastic Sequential Gaussian Simulator (SGS) that populates each modelled layer differently each time it is ran within the limits defined by the data set. As a result, it is likely that the permeable juxtapositions on the constructed fault plane profile will be in slightly different places each time it is run. However, the differences are probably not enough to turn a

leaking juxtaposition into a completely sealing one. This may change the level of the cross-fault leak, which will change the hydrocarbon water contact of a fault-controlled pool - and the economics. Hence, running an analysis many times to see what range of column height result is obtained (Monte Carlo analysis) forms the idea behind stochastic fault seal analysis. Given the close nature of the fault in this study to the well where the sand layers have been intersected, any differences are likely to be of no consequence to the fault seal analysis.

## CHAPTER 7

### CONCLUSIONS AND RECOMMENDATIONS

#### 7.1. Conclusions

##### 7.1.1. Stratigraphy and Sediment Deposition

The Migrant Structure is one of many northeast-trending rollover features that resulted from the interaction between gravity-driven extension, synsedimentary deposition, and the movement of a mobile substrate (Vandeville, 1990). Located in a near marginal shelf position, it is one of numerous NE trending four-way dip closures that formed above the low side of a normal listric fault in the Sable Subbasin characterized by an active petroleum system with an abundance of stacked sandstone reservoirs. This active petroleum system is demonstrated with migration of gas (with a daily gas flow rate of 10 MMscf/day) through the Migrant Structure and suggests that it was not in a fluid migration shadow. Thus, we can reject the second hypothesis that the Migrant Structure may be in a fluid migration shadow, and thus is a potential source of failure.

Similar to deposits of the Thebaud rollover structure, down-dip from Migrant the thick reservoirs in the Thebaud area are characteristic of a prograding deltaic sequence. Although, some of the Thebaud overpressured reservoirs below the thebaud shale do not exist at Migrant. With some continuity of Thebaud Shale in the Adamant Structure resulting to the increased pressure, the absence of any significant shale unit at a similar depth at Migrant suggests that the overpressure at Migrant is different and not stratigraphically tied to the shale unit. This was possible through the establishment of a consistent stratigraphic template to show the succession of key zones from the proximal to distal areas (first objective). This was then integrated to the evaluation of pressure-depth relationship between reservoir intervals to confirm if there is a stratigraphic control on the overpressure from Migrant to Thebaud (second objective) in Section 1.4.

##### 7.1.2. Pressure Connectivity and Petrophysical Log Analysis

In terms of pressure, the highly connected system above the isolated reservoir that flowed gas at Migrant is in hydrostatic continuity. The distal fields are normally pressured above the Naskapi (a regionally continuous shale unit). Overall, most of the wells drilled in the significant discoveries recorded some overpressure. While the Thebaud Shale marks

the onset of overpressure in the Thebaud rollover, and partly at Adamant, it is speculative to assume that an equivalent of the unit exists around the Migrant Structure. Given the absence of a corresponding shale unit as observed at Adamant and Thebaud, the slight overpressure around 4000 m where silica dissolution and quartz cementation occur at Migrant confirms a combination of diagenetic and stratigraphic control on the overpressure in the Migrant Expansion Trend. This addresses the second objective of this study in Chapter 1 (Section 1.4) relating to the evaluation of pressure-depth relationship and contributed to why we rejected the first hypothesis regarding top seal failure at Migrant given the hydrostatic continuity at Migrant.

After determining the key reservoir parameters at Migrant including porosity, permeability, and water saturation (third objective in Section 1.4.), a combination of  $V_{sh}$ , porosity, and water saturation were used as cut-off criteria for establishing net pay from the available reservoir interval. This study shows that net pay < net reservoir < net sand < gross reservoir. Despite the reduction in interval thickness, the net pay thickness represents parts of the reservoir capable of supporting the flow of hydrocarbons. Where water saturation was not included in the criteria, this resulted in a thicker reservoir segment that satisfies the attributes of porosity, and  $V_{sh}$ . Using  $V_{sh}$  as the lone criteria resulted in a rather optimistic estimate in terms of thickness than what was established using all three parameters ( $V_{sh}$ ,  $S_w$ , and Porosity). The low porosity of the reservoirs encountered in the Migrant Structure made very little difference to the net thickness from the value initially established using the  $V_{sh}$  term alone. Overall, log-based wireline depths of reservoir interval offered the best estimate of true net pay than that derived through casing and open hole depths in DST 2 and the bottom intervals.

### 7.1.3. Seismic Interpretation and Depth Conversion

After applying the check shot velocity survey, some reasonable thicknesses were determined for each corresponding seismic time interval relative to the fault in this study. Slight miscalculations in the velocities can have negative implications on the overall depth conversion result, and closure configuration. A satisfactory result from depth conversion of mapped seismic surfaces to produce accurate depth maps addresses the depth conversion objective in Section 1.4 and the third hypothesis in Section 1.5. This apparent 4-way dip



closure of the Migrant Structure after depth conversion suggests that the Migrant N-20 well checkshot survey was a reliable source of velocity data

From depth conversion (using a constant average velocity of 2900 m/s), a minimum marker offset of ~ 6 m and a maximum offset of 39 m was estimated in the Migrant Structure. This suggests that all reservoirs in the structure would have contained gas to their structural spill point in the presence of good quality shales with minimum thickness of 40 m. Gas trapped in thin, tight sands within closure limited to the bottom of the Migrant Structure is attributed to simple closure deep in the structure where the crestal fault appeared to have terminated or moved off the crest of the structure.

#### 7.1.4. Fault Seal Analysis

From the fault plane profile constructed in this study, the crestal fault appears to be the obvious mode of leakage through stair-stepping. In the absence of the crestal fault at Migrant, assuming there is sufficient hydrocarbon charge the shallow reservoirs will be filled up to the saddle point before spilling out of the structure. Therefore, sand on sand juxtaposition at a perceived crestal fault may impact the ability of a rollover structure to be filled up to its saddle. In the presence of thin seals (typical in the proximal shelf positions), this study shows that up to 10 m of crestal fault offset is enough to disrupt the integrity of the trap. This is especially in good quality reservoirs limited to the shallow sections of the Migrant Structure that would have made for ideal commercial targets.

To ensure adequate trapping in the Migrant Structure, optimum fault displacement relative to shale thicknesses is needed. Despite the crestal faulting of the Migrant Structure, the trap would likely have been a success in the presence of thicker shales. As a result, in the presence of thin shales, greater fault offset than the shale thickness results in the juxtaposition of sand against sand beneath the thin shale units across the crestal fault. As shown in this study, this allowed for the cross fault/ stair-stepping migration of hydrocarbons and addresses the fourth hypothesis in Chapter 1 (Section 1.5)

The results of this thesis have applications to the Scotian Margin and other passive margins with deltaic inputs e.g. Mississippi on the Gulf of Mexico (Sydow et al., 1992; Sydow & Roberts, 1994), Nile Delta (Newton et al., 2004), Niger Delta (Mitchum & Wach, 2002), Orinoco (Wood, 2000; Sydow et al., 2003) and ancient deltaic systems and producing fields e.g. McAllan Ranch (Wach et al., 2002a, 2002b; Wach et al., 2003).

Furthermore, it may positively affect the de-risking/ranking of suitable structures for CO<sub>2</sub> injection as well as those in need of constant monitoring to ensure long-term storage of CO<sub>2</sub> (Romanak & Bomse, 2020).

#### 7.1.5. New Findings and Risk Mitigation in Other Basins.

This thesis demonstrates that crestal faults are a risk factor for rollover traps and constitutes the primary mechanism of cross-fault leakage in the faulted Migrant Structure. Whereby small faults in high net-to-gross sections can have profound effects on trap-fill (or absence of), this research demonstrates the sensitivity of rollover structures to small faults in which there is a fine balance between seal thickness and fault displacement. This will have consequences in unexplored and extensively explored basins where fault seal analyses have not been utilized. In addition, they are relevant to other large deltas that have extensionally faulted rollover anticlines above listric growth-faults. This includes young deltas with mobile thick shales, where 2D seismic has been used to investigate cross-fault leakage and its influence on gas water contacts (GWC). This study highlights the importance of 3D modelling over 2D modelling for exploration purposes.

Also, results from this study suggests that pressure and fluid distribution are important scientific and commercial problems in sedimentary basins, and the lessons learnt from analyzing failed wells such as Migrant N-20 may unlock new plays/concepts. While residual hydrocarbons are conclusive evidence of an active hydrocarbon system, they are indicative of leakage in an anticlinal trap. These conclusions can be applied consistently to other faulted anticlines in the Sable Subbasin. Also, the results are applicable in understanding dynamic systems where greater influx than expulsion of a fluid may lead to overpressure. This makes them applicable in aquifer studies, and emerging carbon storage.

#### 7.2. Additional Recommendations.

For future consideration, it is advisable to observe a good sample preparation practices such as pulverization of any physical rock sample intended for XRF analyses compared to the whole rock sample used for this study. This will allow for a more consistent rock sample analysis and an overall enhancement of obtained results. Furthermore, the geochemical results from the XRF analyses maybe used to match Gamma Ray log signature or supplement for areas with missing or unreliable Gamma ray log sections in a well. In such a case, the classifications of the analysed data can be ordered

according to decreasing reservoir quality with the highest quality quartzarenite at the left grading through sublitharenite and subarkose, through litharenite and arkose to wacke and shale (Herron, 1988).

The difference in depth between drill pipe-based casing depth and wireline depth ranges from 0-5 m in the well, with much of the difference due to the thermal expansion and stretching of drillpipe in the warmer wellbore environment. The use of the same depth reference for the top and bottom of the bottom zone means that a wireline-vs-drillpipe depth adjustment was not necessary. As a result, the apparent depth of the casing shoe may have impacted the net thicknesses of the DST #2 interval and bottom zone both open holes. Rather than using the drill pipe depth from which the zone perforations in DST 5 is based on, doing the net pay summation using wireline log-based depth yielded a more accurate net thickness. Using the interval depth for the DST #2 interval in Figure 7. 1 and the estimates for the DST #2 and DST #5 zones from Table 7.1, Table 7.2, and Table 7.3, a 20% drop in water saturation and 4 m increase in net pay for DST 2 presents an increased estimate from the initial analysis done with drill pipe depth in Section 4.4.4.

From the tables below Table 7.1, Table 7.2, and Table 7.3, DST 5 results appear to be on the conservative end regarding the net pay thickness. After applying a Vsh cutoff, there is a noticeable drop in reservoir thickness of just below 1 m (Table 7.3). The low Vsh and porosity values in Table 7.2 and Table 7.3 that fails to meet cutoff when subsequent cutoff criterias are added may explain why there is no change despite the re-selected interval (now based on log signature instead of drill depth-based perf interval). Based on the distribution of porosity vs porosity cutoff in the DST #5 interval, the results make sense.

Table 7.1: Net pay thickness and attribute estimates based on wireline derived interval depths. The Vsh, effective porosity and water saturation were applied as cutoff criteria.

DST #	Depth of zone	Vsh. (v/v)	Total Porosity (v/v)	Effective Porosity (v/v)	Sw. (v/v)	Perm. index (mD)	Gross Interval (m)	Net. (m)
DST 2	4329 – 4361 m	0.067	0.085	0.080	0.395	0.378	32	7.6
DST 5	4270 – 4275 m	0.085	0.071	0.057	0.322	0.105	5	2.8
DST 8	4205 – 4212 m	0.017	0.069	0.067	0.506	0.175	7	6.8
Bottom Zone	4400 - 4430 m	0.142	0.088	0.067	0.553	0.191	30	10.4
<b>Cutoffs</b>	_____	$\leq$ <b>0.25</b>	_____	$\geq$ <b>0.05</b>	$\leq$ <b>0.70</b>	_____	_____	_____

Table 7.2: Net reservoir and attribute estimates based on wireline derived interval depths. The Vsh and effective porosity were applied as cutoff criterias.

DST #	Depth of zone	Vsh. (v/v)	Total Porosity (v/v)	Effective Porosity (v/v)	Sw. (v/v)	Perm. index (mD)	Gross Interval (m)	Net. (m)
DST 2	4329 – 4361 m	0.098	0.085	0.074	0.547	0.296	32	10.2
DST 5	4270 – 4275 m	0.085	0.071	0.057	0.322	0.105	5	2.8
DST 8	4205 – 4212 m	0.017	0.069	0.067	0.506	0.175	7	6.8
Bottom Zone	4400 - 4430 m	0.145	0.088	0.066	0.597	0.196	30	12.4
<b>Cutoffs</b>	_____	$\leq$ <b>0.25</b>	_____	$\geq$ <b>0.05</b>	_____	_____	_____	_____

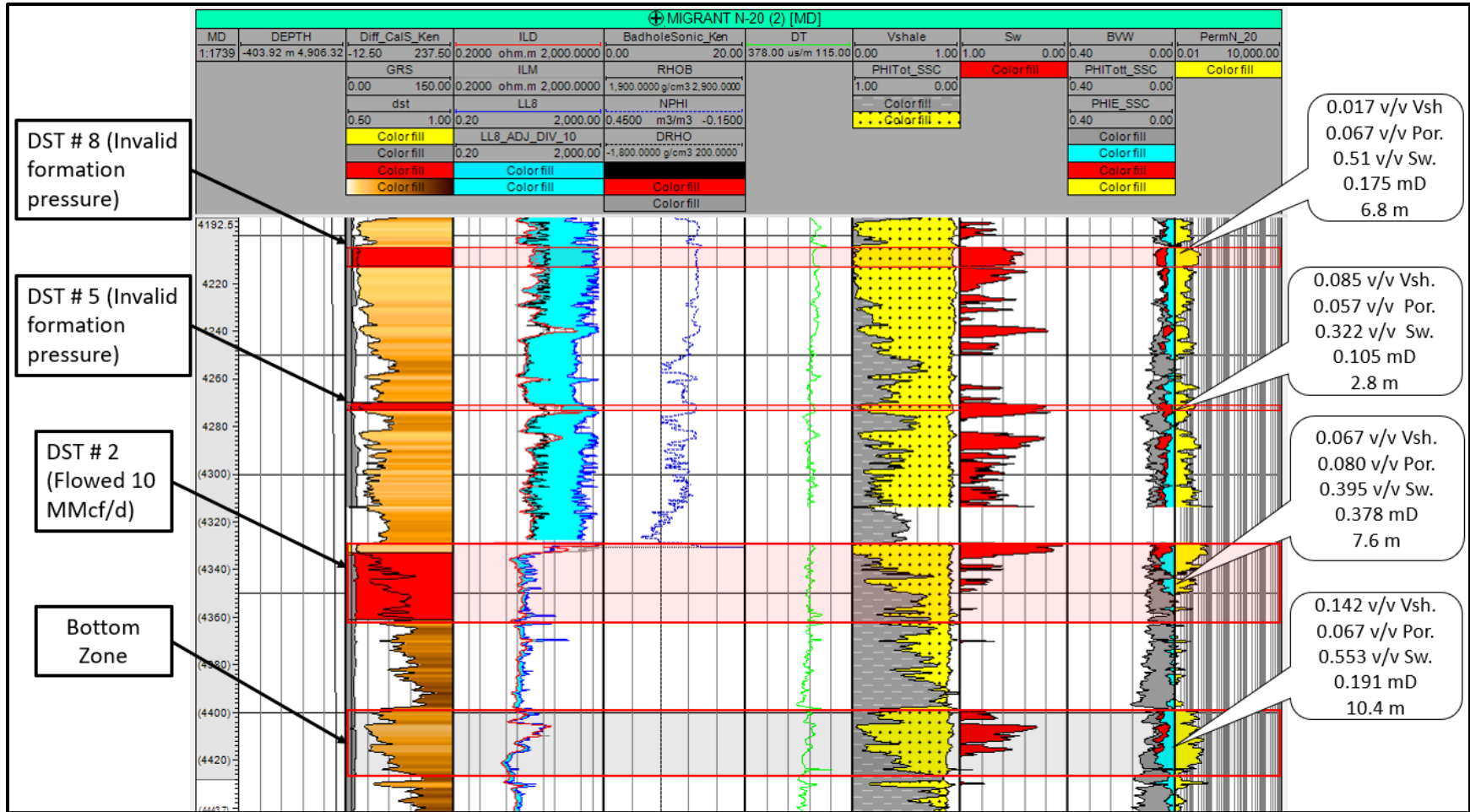


Figure 7. 1: A formation evaluation composite from the Migrant N-20 well. Note the similarity in Section 4.3.1. The DST 2 and DST 5 gross interval thicknesses are based on wireline depth and are different from the composite in section 4.3.1, which is based on drill pipe depth. This difference in depth schemes (drill pipe depth vs wireline log derived depth) is responsible for the changed summation results displayed on the right showing an increased DST #2 net pay thickness.

Table 7.3: Net clean rock thickness and attribute estimates based on wireline derived interval depths when only the Vsh has been used as the cutoff criteria.

DST #	Depth of zone	Vsh. (v/v)	Total Porosity (v/v)	Effective Porosity (v/v)	Sw. (v/v)	Perm. index (mD)	Gross Interval (m)	Net. (m)
DST 2	4329 – 4361 m	0.108	0.081	0.069	0.582	0.274	32	11
DST 5	4270 – 4275 m	0.106	0.069	0.052	0.304	0.085	5	4.2
DST 8	4205 – 4212 m	0.016	0.068	0.067	0.511	0.172	7	7
Bottom Zone	4400 - 4430 m	0.145	0.087	0.066	0.605	0.192	30	12.8
<b>Cutoffs</b>	_____	<= <b>0.25</b>	_____	_____	_____	_____	_____	_____

Comparing permeabilities of 0.105, 0.175 and 0.193 mD for DST 5, DST 8 and the Bottom Interval respectively against an average permeability of ~0.4 mD in the DST #2 interval shows better permeability in the DST #2 interval. Combined with the net pay thickness of 7.6 m for the DST #2 interval, the average permeability of 0.4 mD results to a permeability thickness product (K\*H) of 3 mD-m or 9.8 mD-ft. This revised permeability thickness product is a result of revising the top of the analysis interval to the 4329m wireline depth that the apparent drillstem test top of 4333mmRT was set to.



## REFERENCES

- Adam, J., Krezsek, C., & Grujic, D. (2006). Thin-skinned extension, salt dynamics and deformation in dynamic depositional systems at passive margins. Paper presented at the Proceedings of the 8th SEGJ International Symposium.
- Allan, U. S. (1989). Model for hydrocarbon migration and entrapment within faulted structures. *AAPG bulletin*, **73(7)**, 803-811.
- Almon, W. R., & Dawson, W. C. (2004). Seal character and variability within deep-marine depositional systems: Seal quantification and prediction. Paper presented at the AAPG Annual Meeting.
- Angela, L., Bosence, D. W., Church, K. D., Dan, W., Flint, S. S., Kevin, D., . . . Wilson, R. C. L. (2003). *The sedimentary record of sea-level change*: Cambridge University Press.
- Asquith, G., & Krygowski, D. (2004). *Basic Well Log Analysis*. **244**.
- Bain, R. C. (2015). Pitfalls in the seismic interpretation of fault shadow events—Vicksburg formation of south Texas. *Interpretation*, **3(1)**, SB17-SB22.
- Bao, C. (2016). *Verification for Chance of Geologic Success*. Master's Thesis NTNU.
- Beach, A., & Trayner, P. (1991). The geometry of normal faults in a sector of the offshore Nile Delta, Egypt. *Geological Society, London, Special Publications*, **56(1)**, 173-182.
- Beaubouef, R., Abreu, V., & Van Wagoner, J. (2003). Basin 4 of the Brazos-Trinity slope system: the terminal portion of a late Pliocene lowstand systems tract. *Shelf Margin Deltas and Linked Down Slope Petroleum Systems: Global Significance and Future Exploration Potential*, Gulf Coast Soc SEPM.
- Beaubouef, R., & Friedmann, S. (2000). High resolution seismic/sequence stratigraphic framework for the evolution of Pleistocene intra slope basins, western Gulf of Mexico: depositional models and reservoir analogs. Paper presented at the Deep-water reservoirs of the world: Gulf Coast Section SEPM 20th Annual Research Conference.
- Bhattacharya, J. P., & Willis, B. J. (2001). Lowstand deltas in the Frontier Formation, Powder River Basin, Wyoming: implications for sequence stratigraphic models. *AAPG bulletin*, **85(2)**, 261-294.
- Bjørlykke, K., Ramm, M., & Saigal, G. C. (1989). Sandstone diagenesis and porosity modification during basin evolution. *Geologische Rundschau*, **78(1)**, 243-268.
- Bloch, S. (1991). Empirical prediction of porosity and permeability in sandstones. *AAPG bulletin*, **75(7)**, 1145-1160.
- Bloch, S., Lander, R. H., & Bonnell, L. (2002). Anomalously high porosity and permeability in deeply buried sandstone reservoirs: Origin and predictability. *AAPG bulletin*, **86(2)**, 301-328.

- Bond, C. E. (2015). Uncertainty in structural interpretation: Lessons to be learnt. *Journal of Structural Geology*, **74**, 185-200.
- Boyd, R., R.W. Dalrymple and B.A. Zaitlin, 2006. Estuarine and Incised-Valley Facies Models. Vol. 84, SEPM Special Publication, USA., Pages: 171.
- Boyd, R., R. Dalrymple and B.A. Zaitlin, 1992. Classification of clastic coastal depositional environments. *Sediment. Geol.*, **80**: 139-150.
- Braga, J. C., Martin, J. M., & Wood, J. L. (2001). Submarine lobes and feeder channels of redeposited, temperate carbonate and mixed siliciclastic-carbonate platform deposits (Vera Basin, Almería, southern Spain). *Sedimentology*, **48(1)**, 99-116.
- Brown, A. (2003). Improved interpretation of wireline pressure data. *AAPG bulletin*, **87(2)**, 295-311.
- Campbell, T. & Wach, G. (2014). Seismic Stratigraphy and Attribute Analysis of the Mesozoic and Cenozoic of the Penobscot Area, Offshore Nova Scotia. The Atlantic Geoscience Society (AGS), Program with Abstracts (ed.). Colloquium and Annual General Meeting, February 2014, Wolfville, Nova Scotia
- Campbell, T.J., Richards, F.W.(B.), Silva, R.L., Wach, G., Eliuk, L., 2015. Interpretation of the Penobscot 3D Seismic Volume Using Constrained Sparse Spike Inversion, Sable sub-Basin, Offshore Nova Scotia, Marine and Petroleum Geology. doi:10.1016/j.marpetgeo.2015.08.009.
- Campbell, T. (2018). Seismic Stratigraphy and Architecture of the Jurassic Abenaki Margin, at Cohasset-Migrant, and Potential for Distal Organic-Rich Facies.
- Carruthers, D., Cartwright, J., Jackson, M. P., & Schutjens, P. (2013). Origin and timing of layer-bound radial faulting around North Sea salt stocks: New insights into the evolving stress state around rising diapirs. *Marine and Petroleum Geology*, **48**, 130-148.
- Cathles, L.M., Colling, E.L., Erendi, A., Wach, G.D. & Hoffman, M.W., Manhardt, P.D. (2003). 3D Flow Modeling in Complex Fault Networks: Illustration of New Methods with an Exploration Application in Offshore Nigeria. *American Association Petroleum Geologists Data Pages Discovery Series No. 7*, pp. 177-195.
- Catuneanu, O., Abreu, V., Bhattacharya, J., Blum, M., Dalrymple, R., Eriksson, P., . . . Gibling, M. (2009). Towards the standardization of sequence stratigraphy. *Earth-Science Reviews*, **92(1-2)**, 1-33.
- CBC. (2018). After unsuccessful drilling, no wells are being explored off Nova Scotia. Retrieved from <https://www.cbc.ca/news/canada/nova-scotia/bp-canada-hess-offshore-drilling-1.4904190>
- CCOP. (2000). The CCOP Guidelines for Risk Assessment of Petroleum Prospects. In: CCOP Technical Secretariat Bangkok.

- Cecil, C. B. (2003). The concept of autocyclic and allocyclic controls on sedimentation and stratigraphy, emphasizing the climatic variable.
- Cecil, C. B. (2013). An overview and interpretation of autocyclic and allocyclic processes and the accumulation of strata during the Pennsylvanian–Permian transition in the central Appalachian Basin, USA. *International Journal of Coal Geology*, **119**, 21-31.
- Cervený, K., Davies, R., Dudley, G., Fox, R., Kaufman, P., Knipe, R., & Krantz, B. (2004). Reducing uncertainty with fault-seal analysis. *Oilfield Review*, **16(4)**, 38-51.
- Chen, A. (2014). The practice of graphical fluid-gradient interpretations of formation tester pressure data. *AAPG bulletin*, **98(7)**, 1431-1448.
- Childs, C., Manzocchi, T., Nell, P., Walsh, J., Strand, J., Heath, A., & Lygren, T. (2002). Geological implications of a large pressure difference across a small fault in the Viking Graben. *Hydrocarbon seal quantification: Norwegian Petroleum Society Special Publication*, **11**, 187-201.
- CNSOPB (1987). Canada-Nova Scotia Offshore Petroleum Resources Accord Implementation Act, S.C. 1988, c.28 and the Canada-Nova Scotia Offshore Petroleum Resources Accord Implementation (Nova Scotia) Act, S.N.S. 1987, c.3.
- CNSOPB (2007). Canada Nova Scotia Offshore Petroleum Board CNSOPB Call For Bids NO. NS07-1. Retrieved January 2020 from <https://callforbids.cnsopb.ns.ca/2007/01/PDF/Call%20for%20Bids%20NS07-1b.pdf>
- CNSOPB (2009). Canada Nova Scotia Offshore Petroleum Board CNSOPB Call for Bids No. NS09-1. Retrieved February 2019 from [https://callforbids.cnsopb.ns.ca/2009/01/PDF/Call\\_for\\_Bids\\_NS09-1.pdf](https://callforbids.cnsopb.ns.ca/2009/01/PDF/Call_for_Bids_NS09-1.pdf)
- CNSOPB (2012). Canada Nova Scotia Offshore Petroleum Board CNSOPB Call for Bids No. NS 12-1. Retrieved June 2019 from <https://callforbids.cnsopb.ns.ca/2012/01/overview/regional-geoscience/regional-geoscience-overview.html>
- CNSOPB (2013). Canada Nova Scotia Offshore Petroleum Board CNSOPB Call for Bids No. NS 13-1. Retrieved February 2019 from [https://callforbids.cnsopb.ns.ca/2013/01/sites/default/files/inline-pdf/cfb\\_ns13-1\\_standard\\_finalapril\\_23\\_2013v2\\_.pdf](https://callforbids.cnsopb.ns.ca/2013/01/sites/default/files/inline-pdf/cfb_ns13-1_standard_finalapril_23_2013v2_.pdf)
- CNSOPB (2018). Call for Bids NS18-3 Information Package. <https://callforbids.cnsopb.ns.ca/2018/-3/> Accessed June 28, 2020.
- CNSOPB (2018). Canada Nova Scotia Offshore Petroleum Board Directory of wells Nova Scotia Offshore Area. Retrieved from <https://www.cnsopb.ns.ca/sites/default/files/resource/dow.pdf>
- CNSOPB (2008). Canada Nova Scotia Offshore Petroleum Board CNSOPB Nova Scotia Conventional Offshore Resource Estimates. Retrieved from

[https://www.cnsopb.ns.ca/sites/default/files/resource/ns\\_offshore\\_resource\\_estimates\\_-\\_2008.pdf](https://www.cnsopb.ns.ca/sites/default/files/resource/ns_offshore_resource_estimates_-_2008.pdf)

- Cobbold, P. R., & Szatmari, P. (1991). Radial gravitational gliding on passive margins. *Tectonophysics*, 188(3-4), 249-289.
- Cohen, H. A., & McClay, K. (1996). Sedimentation and shale tectonics of the northwestern Niger Delta front. *Marine and Petroleum Geology*, 13(3), 313-328.
- Collins, M.B., C.L. Amos and G. Evans, (1981). Observations of Some Sediment-Transport Processes Over Intertidal Flats, the Wash, U.K. In: *Holocene Marine Sedimentation in the North Sea Basin*, Nio, S.D., R.T.E. Shuttenhelm and T.C.E. van Weering (Eds.), Blackwell Publishing Ltd., Oxford, UK.
- Cummings, D. I., & Arnott, R. W. C. (2005). Growth-faulted shelf-margin deltas: a new (but old) play type, offshore Nova Scotia. *Bulletin of Canadian Petroleum Geology*, **53(3)**, 211-236.
- Dalrymple, R.W., B.A. Zaitlin and R. Boyd, (1992). Estuarine facies models: Conceptual basis and stratigraphic implications: Perspective. *J. Sediment. Petrol.*, **62**: 1130-1146.
- Davis G. (2010). Presentation and Tutorials. Graham's World. Retrieved in June 2018  
Retrieved from [Presentations & Tutorials \(g-davis.com\)](http://www.g-davis.com/Presentations%20&%20Tutorials)
- Dawson, W. C., & Almon, W. R. (2002). Top seal potential of Tertiary deep-water Gulf of Mexico shales.
- Dawson, W. C., & Almon, W. R. (2006). Shale facies and seal variability in deepwater depositional systems. *Search and Discovery Article*, 40199.
- Delfiner, P. (2007). Three statistical pitfalls of Phi-K transforms. *SPE Reservoir Evaluation & Engineering*, **10(06)**, 609-617.
- Deptuck, M. (2011). Proximal to distal postrift structural provinces on the western Scotian Margin, offshore Eastern Canada: Geological context and parcel prospectivity for Call for Bids NS11-1. Canada-Nova Scotia Offshore Petroleum Board Geoscience Open File Report 2011001MF, 42.
- Deptuck, M., & Kendell, K. (2017). A review of Mesozoic-Cenozoic salt tectonics along the Scotian margin, eastern Canada. In *Permo-Triassic Salt Provinces of Europe, North Africa and the Atlantic Margins* (pp. 287-312): Elsevier.
- Deptuck, M. E., Kendell, K., Brown, D. E., & Smith, B. M. (2014). Seismic stratigraphic framework and structural evolution of the eastern Scotian Slope: geological context for the NS14-1 Call for Bids area, offshore Nova Scotia. Nova Scotia, Canada, Canada–Nova Scotia Offshore Petroleum Board, Geoscience Open File Report.
- Dickens, G. R., Droxler, A. W., Bentley, S. J., Peterson, L. C., Opdyke, B. N., Beaufort, L., Harris, P. T. (2006). Sediment accumulation on the shelf edges, adjacent slopes, and basin floors of the Gulf of Papua. Paper presented at the Workshop Report.

- Dickinson, W.R. (1985). Interpreting provenance relations from detrital modes of sandstones. In: Zuffa, G. G. (ed.) *Provenance of Arenites*. Reidel Publishing Company. Dordrecht. 331–361.
- Diegel, F. A., Karlo, J., Schuster, D., Shoup, R., & Tauvers, P. (1995). Cenozoic structural evolution and tectono-stratigraphic framework of the northern Gulf Coast continental margin.
- Doust, H., & Omatsola, E. (1989). Niger delta. 238.
- Downey, M. W. (1994). *Hydrocarbon Seal Rocks: Chapter 8: Part II. Essential Elements*.
- Droxler, A. W., Haddad, G. A., Kroon, D., Gartner, S., Wei, W., & McNeill, D. (1993). 17. Late Pliocene (2.9 Ma) Partial Recovery Of Shallow Carbonate Banks On The Queensland Plateau: Signal Of Bank-Top Reentry Into The Photic Zone During A Lowering In Sea Level.
- Eliuk, L. (2016). Abenaki carbonate platform in relation to the Jurassic-Cretaceous Sable Island Delta, offshore Nova Scotia, Canada.
- Eliuk, L., & Wach, G. (2009). Carbonate and siliciclastic sequence stratigraphy—Examples from the Late Jurassic Abenaki Limestone and West Venture deltaic beds, offshore Nova Scotia, Canada. Canada: Presented at CSPG/CSEG/CWLS GeoConvention.
- Etris, E. L., Crabtree, N. J., Dewar, J., & Pickford, S. (2001). True depth conversion: more than a pretty picture. *CSEG Recorder*, **26(9)**, 11-22.
- Fensome, A., & Williams, G. L. (2001). *The Last Billion Years: A Geological History of the Maritime Provinces of Canada*. Atlantic Geoscience Society.
- Folk, R. L. (1968). *Petrology of sedimentary rocks: Hemphill's*. Austin, Texas, 170, 85.
- Fowler, M., Webb, J., Obermajer, M., Monnier, F., Mort, A., Luheshir, M., & MacDonald, A. (2016). Petroleum Systems of the Scotian Basin. Search and Discovery Article, 10871.
- Francis, J. M., Dunbar, G. B., Dickens, G. R., Sutherland, I. A., & Droxler, A. W. (2007). Siliciclastic sediment across the North Queensland margin (Australia): a Holocene perspective on reciprocal versus coeval deposition in tropical mixed siliciclastic–carbonate systems. *Journal of Sedimentary Research*, **77(7)**, 572-586.
- Gibson, R. G., & Bentham, P. A. (2003). Use of fault-seal analysis in understanding petroleum migration in a complexly faulted anticlinal trap, Columbus Basin, offshore Trinidad. *AAPG bulletin*, **87(3)**, 465-478.
- Glover, P. (2009). What is the cementation exponent? A new interpretation. *The Leading Edge*, **28(1)**, 82-85.
- Glover, P. (2012a). Fluid Testing and Pressure Logs. *Petrophysics MSc Course Notes*, 84.

- Glover, P. (2012b). The spectral Gamma-Ray log. Petrophysics MSc Course Notes, 111-120.
- Gould, K., PE-PIPER, G., & Piper, D. J. (2010). Relationship of diagenetic chlorite rims to depositional facies in Lower Cretaceous reservoir sandstones of the Scotian Basin. *Sedimentology*, **57**(2), 587-610.
- Hafid, M., Loudenk, K., & Zizi, M. (2012). The conjugate margins of Morocco and Nova Scotia. *Regional Geology and Tectonics: Phanerozoic Passive Margins, Cratonic Basins and Global Tectonic Maps*, **1**, 285.
- Hansen, D. M., Shimeld, J. W., Williamson, M. A., & Lykke-Andersen, H. (2004). Development of a major polygonal fault system in Upper Cretaceous chalk and Cenozoic mudrocks of the Sable Subbasin, Canadian Atlantic margin. *Marine and Petroleum Geology*, **21**(9), 1205-1219.
- Hantschel, T., & Kauerauf, A. I. (2009). Pore pressure, compaction and tectonics. In *Fundamentals of basin and petroleum systems modeling* (pp. 31-101): Springer.
- Herron, M. M. (1988). Geochemical classification of terrigenous sands and shales from core or log data. *Journal of Sedimentary Research*, **58**(5), 820-829.
- Hilterman, F. J. (2001). *Seismic amplitude interpretation: Society of Exploration Geophysicists and European Association of Geoscientists and Engineers.*
- Ings, S. J., & Shimeld, J. W. (2006). A new conceptual model for the structural evolution of a regional salt detachment on the northeast Scotian margin, offshore eastern Canada. *AAPG bulletin*, **90**(9), 1407-1423.
- Ingersoll, R.V., and Suczek, C.A. 1979. Petrology and provenance of Neogene sand from Nicobar and Bengal fans, DSDP sites 211 and 218. *Journal of Sedimentary Petrology*. **49**: 1217–1228.
- James, W. R., Fairchild, L. H., Nakayama, G. P., Hippler, S. J., & Vrolijk, P. J. (2004). Fault-seal analysis using a stochastic multifault approach. *AAPG bulletin*, **88**(7), 885-904.
- Jansa, L., LF, J., & JA, W. (1975). *Geology Of The Continental Margin Off Nova Scotia And Newfoundland.*
- Kaldi, J. (2019). *Integrated Approaches to Determining Net Pay: Caveats & Lessons Learned.* In: *Society of Petroleum Engineers*
- Kendell, K. L. (2012). Variations in salt expulsion style within the Sable Canopy Complex, central Scotian margin. *Canadian Journal of Earth Sciences*, **49**(12), 1504-1522.
- Keen, M. J., & Williams, G. L. (1990). *Geology of the Continental Margin of Eastern Canada.*
- Kidston, A. G., Brown, D. E., Smith, B. M., & Altheim, B. (2005). *The Upper Jurassic Abenaki Formation, Offshore Nova Scotia: A Seismic and Geologic Perspective.* Canada-Nova Scotia Offshore Petroleum Board, Halifax, Nova Scotia, 168.



- Kidston, A.G., Smith, B., Brown, D.E., Makrides, C. and Altheim, B., (2007). Nova Scotia Deep Water Offshore Post-Drill Analysis – 1982-2004. Canada-Nova Scotia Offshore Petroleum Board, Halifax, Nova Scotia, 181p. Retrieved from [http://www.cnsopb.ns.ca/sites/default/files/pdfs/Deep\\_Water\\_Post\\_Drill\\_Analysis\\_2007.pdf](http://www.cnsopb.ns.ca/sites/default/files/pdfs/Deep_Water_Post_Drill_Analysis_2007.pdf)
- Knipe, R. (1997). Juxtaposition and seal diagrams to help analyze fault seals in hydrocarbon reservoirs. AAPG bulletin, **81(2)**, 187-195.
- Knipe, R. J., Jones, G., & Fisher, Q. (1998). Faulting, fault sealing and fluid flow in hydrocarbon reservoirs: an introduction. Geological Society, London, Special Publications, **147(1)**, vii-xxi.
- Koeshidayatullah, A., Al-Ramadan, K., Collier, R., & Hughes, G. W. (2016). Variations in architecture and cyclicity in fault-bounded carbonate platforms: Early Miocene Red Sea Rift, NW Saudi Arabia. Marine and Petroleum Geology, **70**, 77-92.
- Korotev, R. (2009). Element-Oxide Conversion. Retrieved from [Element - Oxide Conversions \(wustl.edu\)](http://www.wustl.edu/Element-Oxide-Conversions).
- Lee, W. J. (2009). Modernization of the SEC Oil and Gas Reserves Reporting Requirements. Paper presented at the SPE Annual Technical Conference and Exhibition.
- Lubeseder, S., Redfern, J., & Boutib, L. (2009). Mixed siliciclastic-carbonate shelf sedimentation—Lower Devonian sequences of the SW Anti-Atlas, Morocco. Sedimentary Geology, **215(1-4)**, 13-32.
- MacLean, B., & Wade, J. (1993). Seismic markers and stratigraphic picks in the Scotian Basin wells. East Coast Basin Atlas Series. Geological Survey of Canada. 276p.
- Mallarino, G., Beaubouef, R. T., Droxler, A. W., Abreu, V., & Labeyrie, L. (2006). Sea level influence on the nature and timing of a minibasin sedimentary fill (northwestern slope of the Gulf of Mexico). AAPG bulletin, **90(7)**, 1089-1119.
- Milkov, A. V. (2015). Risk tables for less biased and more consistent estimation of probability of geological success (PoS) for segments with conventional oil and gas prospective resources. Earth-Science Reviews, **150**, 453-476.
- Mitchum Jr, R. M., Vail, P. R., & Sangree, J. B. (1977). Seismic stratigraphy and global changes of sea level: Part 6. Stratigraphic interpretation of seismic reflection patterns in depositional sequences: Section 2. Application of seismic reflection configuration to stratigraphic interpretation.
- Mitchum, R. M., & Wach, G. D. (2002). Niger Delta Pleistocene leveed-channel fans: Models for offshore reservoirs. Paper presented at the Sequence Stratigraphic Models for Exploration and Production: Evolving Methodology, Emerging Models and Applications History: Houston, GCSSEPM Foundation Bob F. Perkins Research Conference, December 8-11, 2002, Houston, Texas.
- Mobil et al. (1987). Thebaud C-74 Well History Report. Canada Nova Scotia Offshore Petroleum Board Archive.

- Mobil et al. (2000). Adamant N-97 End of Well Report. D369, Canada Nova Scotia Offshore Petroleum Board Archive. 2000005028.
- Morley, C. (2003). Mobile shale related deformation in large deltas developed on passive and active margins. Geological Society, London, Special Publications, **216(1)**, 335-357.
- Morrison, N. (2017). Seismic Inversion and Source Rock Evaluation on Jurassic Organic Rich Intervals in the Scotian Basin, Nova Scotia.
- Moss-Russell, A. C. (2009). Stratigraphic architecture of a prograding shelf-margin delta in outcrop, the Sobrarbe Formation, Ainsa Basin, Spain, The Doctoral dissertation, Colorado School of Mines.
- Move. (2016). Fault seal analysis in Move. Retrieved from [https://www.petex.com/media/2664/2016-nov\\_fault-seals.pdf](https://www.petex.com/media/2664/2016-nov_fault-seals.pdf).
- Mukhopadhyay, P. (2006). Evaluation of the petroleum systems by 1D and 2D numerical modeling and geochemical analysis in the area of most recent exploration wells on the deepwater Scotian slope, offshore Nova Scotia. Nova Scotia Department of Energy, unpublished report.
- Newton, C., Shipp, R., Mosher, D., & Wach, G. (2004). Importance of mass transport complexes in the Quaternary development of the Nile Fan, Egypt. Paper presented at the Offshore Technology Conference.
- NSPD (1999). Natural Resource Canada and Nova Scotia Petroleum Directorate.
- O'Connor, D., Silva, R. L., & Wach, G. (2018). Earliest sedimentological evidence for marine incursions in the eastern North American rift system, Central Atlantic Margin. *Lithosphere*, **10(6)**, 783-791.
- O'Connor, D., Richards, B., Angel, M., & Wach, G. (2020). Dynamic Modeling of Buoyant Fluids: Implications for Hydrocarbon Distribution and Potential Carbon Capture and Storage (CCS).
- ODP 2007: [http://www-odp.tamu.edu/publications/182\\_IR/chap\\_05/c5\\_f35.htm](http://www-odp.tamu.edu/publications/182_IR/chap_05/c5_f35.htm)
- Offshore Energy Technical Research Association. (2011). Play Fairway Analysis Atlas - Offshore Nova Scotia. Nova Scotia Department of Energy. (Also available on the OERA website: <http://www.novascotiaoffshore.com>)
- Oomkens, E. (1970). Depositional sequences and sand distribution in the postglacial Rhone delta complex.
- Osborne, M. J., & Swarbrick, R. E. (1997). Mechanisms for generating overpressure in sedimentary basins: a reevaluation. *AAPG bulletin*, 81(6), 1023-1041.
- Pe-Piper, G., & Piper, D. J. (2011). The impact of early cretaceous deformation on deposition in the passive-margin scotian basin, offshore Eastern Canada. *Tectonics of sedimentary basins: Recent advances*, 270-287.

- Porębski, S. J., & Steel, R. J. (2003). Shelf-margin deltas: their stratigraphic significance and relation to deepwater sands. *Earth-Science Reviews*, **62(3-4)**, 283-326.
- Posamentier, H. W. (2009). *Sequence stratigraphy and facies associations (Vol. 100)*: John Wiley & Sons.
- Quora. (2019). How does the Repeat Formation Test (RFT) work? What is its objective? Answer by McGinness T. Retrieved from [How does the Repeat Formation Test \(RFT\) work? What is its objective? - Quora](#)
- Reineck, H. E., & Wunderlich, F. (1968). Classification and origin of flaser and lenticular bedding. *Sedimentology*, **11(1-2)**, 99-104.
- Richards, B., Fairchild, L., Vrolijk, P., & Hippler, S. (2008). Reservoir connectivity analysis, hydrocarbon distribution, resource potential and production performance in the clastic plays of the Sable Subbasin, Scotian Shelf. Paper presented at the Central Atlantic Conjugate Margins Conference.
- Richards, F., Vrolijk, P., Gordon, J., & Miller, B. (2010). Reservoir connectivity analysis of a complex combination trap: Terra Nova Field, Jeanne d'Arc Basin, Newfoundland, Canada. *Geological Society, London, Special Publications*, **347(1)**, 333-355.
- Rider, M., & Kennedy, M. (2011). *The Geological Interpretation of Well Logs*. published by Rider-French Consulting Ltd.
- Romanak, K. D., & Bomse, D. S. (2020). Field assessment of sensor technology for environmental monitoring using a process-based soil gas method at geologic CO2 storage sites. *International Journal of Greenhouse Gas Control*, **96**, 103003.
- Rose, P. (2001). *AAPG Methods in Exploration No. 12, Chapter 5: Exploration Plays-- Risk Analysis and Economic Assessment*.
- Rose, P. R. (1992). *Chance of success and its use in petroleum exploration: Chapter 7: Part II. nature of the business*.
- Rowan, M. G., Peel, F. J., & Vendeville, B. C. (2004). Gravity-driven fold belts on passive margins.
- Rudolph, K. W., & Goulding, F. J. (2017). Benchmarking exploration predictions and performance using 20+ yr of drilling results: One company's experience. *AAPG bulletin*, **101(2)**, 161-176.
- Ruppel, S. C., Rowe, H., Milliken, K., Gao, C., & Wan, Y. (2017). Facies, rock attributes, stratigraphy, and depositional environments: Yanchang Formation, central Ordos Basin, China. *Interpretation*, **5(2)**, SF15-SF29.
- Ryan, J. G., Shervais, J. W., Li, Y., Reagan, M. K., Li, H., Heaton, D., Pearce, J. (2017). Application of a handheld X-ray fluorescence spectrometer for real-time, high-density quantitative analysis of drilled igneous rocks and sediments during IODP Expedition 352. *Chemical Geology*, **451**, 55-66.

- Sales, J. K. (1997). Seal strength vs. trap closure—a fundamental control on the distribution of oil and gas. Seals, traps, and the petroleum system.
- Sandrea, R. (2006). Global natural gas reserves—a heuristic viewpoint. Middle east economic survey, 49.
- Saffer, D., McNeill, L., Byrne, T., Araki, E., Toczko, S., Eguchi, N., Takahashi, K., and the Expedition 319 Scientists. (2010). Integrated Ocean Drilling Program Expedition Report. Proceeding Volume 319. Directory 102. Figure F1: Schematic diagram of position and components of single probe module of MDT tool. CQG = crystal quartz gauge. Retrieved from [Proc. IODP, 319, Methods](#)
- Schlische, R. W. (1993). Anatomy and evolution of the Triassic-Jurassic continental rift system, eastern North America. *Tectonics*, **12**(4), 1026-1042.
- Schlumberger. (2016). Schlumberger Oil Field Glossary [online]. Retrieved from <http://www.glossary.oilfield.slb.com>
- Schlumberger (2020). Abnormal Pressure. Oilfield Glossary. Retrieved January 2020 from [https://www.glossary.oilfield.slb.com/en/Terms/a/abnormal\\_pressure.aspx](https://www.glossary.oilfield.slb.com/en/Terms/a/abnormal_pressure.aspx)
- Schroeder F.W. (2006). Lecture 7; Well-Seismic Ties. Published by Aidan McPherson. Retrieved from [Well-Seismic Ties Lecture 7 Depth Time Synthetic Trace SLIDE 1 - ppt video online download \(slideplayer.com\)](#)
- Scruton, P.C. 1960. Delta building and the deltaic sequence. In: Shepard, F.P., Phleger, F.B., and van Andel, T.H. (eds.). *Recent sediments Northwest Gulf of Mexico*. American Association of Petroleum Geologist. pp. 82-102.
- Serck, C. S., & Braathen, A. (2019). Extensional fault and fold growth: Impact on accommodation evolution and sedimentary infill. *Basin Research*, **31**(5), 967-990.
- Sestini, G. (1989). Nile Delta: a review of depositional environments and geological history. Geological Society, London, Special Publications, **41**(1), 99-127.
- Sibuet, J.-C., Rouzo, S., & Srivastava, S. (2012). Plate tectonic reconstructions and paleogeographic maps of the central and North Atlantic oceans. *Canadian Journal of Earth Sciences*, **49**(12), 1395-1415.
- Siddiqui, N. A., Rahman, A. H. A., Sum, C. W., Yusoff, W. I. W., & Ismail, M. (2017). Shallow-marine sandstone reservoirs, depositional environments, stratigraphic characteristics and facies model: a review. *Journal of Applied Sciences*, **17**, 212-237.
- Silva, R. L., Wong, C., & Wach, G. (2015). Source rocks and petroleum systems of the Scotian Basin. *CSEG Recorder*, **40**(8), 22-27.
- Sinclair I. (2003). *Hibernia: Promise and Progress*.
- Skinner, C. (2016). Excess Pressure and Reservoir Compartmentalization in the Sable Subbasin, Offshore Nova Scotia.

- Skinner, C.H., Silva, R., Watson, N., Bill, R., Wach, G., 2016. Reservoir Connectivity, Compartmentalization and Overpressure Conditions in the Sable Subbasin (Nova Scotia, Canada) and Porcupine Basin (Ireland). AAPG Annual Convention & Exhibition 2016, 19-22 June 2016, Calgary, Alberta, Canada.
- Smalley Jr, R., Turcotte, D. L., & Solla, S. A. (1985). A renormalization group approach to the stick-slip behavior of faults. *Journal of Geophysical Research: Solid Earth*, **90(B2)**, 1894-1900.
- Smith, B., Makrides, C., Altheim, B., & Kendell, K. (2014). Resource Assessment of Undeveloped Significant Discoveries on the Scotian Shelf. Canada-Nova Scotia Offshore Petroleum Board.
- Smith, D. A. (1980). Sealing and nonsealing faults in Louisiana Gulf Coast salt basin. *AAPG bulletin*, **64(2)**, 145-172.
- SOEI, S. O. E. I. (2000). Core Analysis Report for Thebaud 5. Sable Offshore Energy Thebaud 5 End of Well Report. Canada Nova Scotia Offshore Petroleum Board Archive.
- Sable Offshore Energy Project (1997). Development Plan Application. (Also available on the OERA website:  
[https://callforbids.cnsopb.ns.ca/2012/01/sites/default/files/pdfs/sable\\_dpa\\_vol2a.pdf](https://callforbids.cnsopb.ns.ca/2012/01/sites/default/files/pdfs/sable_dpa_vol2a.pdf))
- Steele, D. R., Mulders, J., & Crisp, M. (2011). Sable Sub Basin Near Field Exploration Prospectivity. Paper presented at the Offshore Technology Conference.
- Summa, L. L. (1995). Diagenesis and reservoir quality prediction. *Reviews of Geophysics*, **33(S1)**, 87-94.
- Swarbrick, R. E., Osborne, M. J., & Yardley, G. S. (2001). AAPG Memoir 76, Chapter 1: Comparison of Overpressure Magnitude Resulting from the Main Generating Mechanisms.
- Sydow, J., Finneran, J., Bowman, A. P., Roberts, H., Rosen, N., Fillon, R., & Anderson, J. (2003). Stacked shelf-edge delta reservoirs of the Columbus Basin, Trinidad, West Indies. In *Shelf-Margin Deltas and Linked Downslope Petroleum Systems* (Vol. 23, pp. 441-465): GCSSEPM Foundation.
- Sydow, J., & Roberts, H. H. (1994). Stratigraphic framework of a late Pleistocene shelf-edge delta, northeast Gulf of Mexico. *AAPG bulletin*, **78(8)**, 1276-1312.
- Sydow, J., Roberts, H. H., Bouma, A. H., & Winn, R. (1992). Constructional subcomponents of a shelf-edge delta, northeast Gulf of Mexico.
- Tcherepanov, E. N. (2008). Cenozoic evolution of the mixed carbonate-siliciclastic depositional system in the Gulf of Papua, Papua New Guinea.
- Tcherepanov, E. N., Droxler, A. W., Lapointe, P., Dickens, G. R., Bentley, S. J., Beaufort, L., Opdyke, B. N. (2008). Neogene evolution of the mixed carbonate-siliciclastic

system in the Gulf of Papua, Papua New Guinea. *Journal of Geophysical Research: Earth Surface*, 113(F1).

- Tetco, M. (1978). Migrant N-20 Well History Report.
- Thyberg, B., Jahren, J., Winje, T., Bjørlykke, K., Faleide, J. I., & Marcussen, Ø. (2010). Quartz cementation in Late Cretaceous mudstones, northern North Sea: changes in rock properties due to dissolution of smectite and precipitation of micro-quartz crystals. *Marine and Petroleum Geology*, **27(8)**, 1752-1764.
- Vail, P. (1977). Seismic recognition of depositional facies on slopes and rises.
- Van Wagoner, J., R. Mitchum, K. Campion and V. Rahmanian, (1990). *Siliciclastic Sequence Stratigraphy in well Logs, Cores and Outcrops: Concepts for High-Resolution Correlation of time and Facies*. American Association of Petroleum Geologists, USA., ISBN: 9780891816577, Pages: 55.
- Van Wagoner, J. C. (1991). High-frequency sequence stratigraphy and facies architecture of the Segro Sandstone in the Book Cliffs of western Colorado and eastern Utah.
- Vendeville, B. (1991). Mechanisms generating normal fault curvature: a review illustrated by physical models. Geological Society, London, Special Publications, **56(1)**, 241-249.
- Vendeville, B. C. (2005). Similarities and differences between salt and shale tectonics. Paper presented at the Geophysical Research Abstracts.
- Vrolijk, P. (2005). Reservoir Connectivity Analysis-Defining Reservoir Connections & Plumbing. Paper presented at the SPE Middle East Oil and Gas Show and Conference.
- Wach, G.D., Hoffman, M.W., Colling, E.L., Ogunyomi, O., Fritzel, T., Russo, P. and Olear, S., (1997). The sedimentology, sequence stratigraphy and fluid migration history of non-marine and shallow marine reservoirs, North of Apoi and Funiwa fields, offshore Niger Delta. Proceedings of the GCSEPM Foundation 18<sup>th</sup> Annual Research Conference, Shallow Marine and Nonmarine Reservoirs, December 7-10, 1997, Houston Texas 365-376.
- Wach, G. D., Hoffman, M., Colling, E., Ogunyomi, O., Fritzel, T., Russo, P., Robison, C. (1998). The Sedimentology, Sequence Stratigraphy, and Fluid Migration History of Non-Marine and Shallow Marine Reservoirs, North Apoi-Funiwa Field, Offshore Niger Delta.
- Wach, G.D., Hoffman, M.W., Colling, E.L., Ogunyomi, O., Fritzel, T., Russo, P. and Olear, S., (1998). Sedimentology, sequence stratigraphy, and fluid migration history of non-marine and shallow marine reservoirs, North Apoi-Funiwa field, offshore Niger delta. American Association of Petroleum Geologists International Meeting, Rio de Janeiro, Brazil, November 1998.
- Wach, G. D., M. W. Hoffman, E. L. Colling, O. Ogunyomi, T. L. Fritzel, P. Russo, S.

- Olear, and C. R. Robison. (1998). The sedimentology, sequence stratigraphy, and fluid migration history of non-marine reservoirs, North Apoi-Funiwa field, offshore Niger delta. TSOP, 15<sup>th</sup> Ann. Mtg., Abstracts & Program, vol. **15**: p. 93.
- Wach, G. D., Kuhfal, D. L., Nemec, T. S., McCarty, D. K., & Hugel, M. (2002). McAllan Ranch Field--A Multi-Disciplinary Approach to Casing Failure.
- Wach, G.D., D. Kuhfal, T.S. Nemec, D.K. McCarty and M. Hugel. (2002). McAllan Ranch Field-application of a multi-disciplinary approach to the casing failure problem. Proceedings GCAGS Annual Meeting, Austin, Texas, October, 2002.
- Wach, G.D., Kuhfal D.L. and McCarty D., 2003, McAllan Ranch, S.E. Texas- Vicksburg Shelf Margin deltas, 23rd Annual GCSSEPM Foundation Bob F. Perkins Research Conference, Shelf Margin Deltas and Linked Down Slope Depositional Systems: Global Significance and Future Exploration Potential, December 8-11, 2003, Houston, Texas.
- Wach & Hirschmiller. (2012). Structural Control and Closures, Sable Island Area. Unpublished.
- Wach, G. T., Lyton, R., McCarthy, D., Korn, L., & Moate, S. (2000). Sequence Stratigraphy, Biostratigraphy, Depositional Environments, and Reservoir Compartmentalization of the Mid-Miocene Queen Bess Field, Jefferson Parish, Louisiana.
- Wade, J., Brown, D., Durling, P., MacLean, B., & Marillier, F. (2000). Depth to pre-Mesozoic and pre-Carboniferous basements (Map). Geological Survey of Canada.
- Wade, J., & MacLean, B. (1990). The geology of the southeastern margin of Canada. *Geology of the continental margin of eastern Canada*, 2, 167-238.
- Watson R.N., Fondyga T., Scott B. & Sinclair I. (2000) - Calibration of log-based permeability alternatives with core data. Lower Hibernia Formation, well B-16\_17, Hibernia Field, Newfoundland. CSEG Conference. Conference theme: Geo Canada 2000 - The Millennium Geoscience Summit.
- Watson, N. (2017). Deterministic Analysis Sequence.
- Webb, N. D., Seyler, B., & Grube, J. P. (2015). Geologic reservoir characterization of Carboniferous fluvio-tidal deposits of the Illinois Basin, USA. In *Developments in Sedimentology* (Vol. **68**, pp. 395-443). Elsevier.
- Weinheber, P. J., Boratko, E. C., Contreiras, K. D., Van-Dunem, F., Spaeth, R. L., Dussan, E. B., Gisolf, A. (2008). Best Practices for formation testing in low-permeability reservoirs. Paper presented at the SPE Annual Technical Conference and Exhibition.
- Welner R and Co. (2000). Core facies assemblage Thebaud 5. Excerpt of operators report D359, Canada Nova Scotia Offshore Petroleum Board Archive. 2000005557.



- Welsink, H., Dwyer, J., & Knight, R. (1989). Tectono-Stratigraphy of the Passive Margin Off Nova Scotia: Chapter 14: North American Margins.
- Weston, J. F., MacRae, R. A., Ascoli, P., Cooper, M. K. E., Fensome, R. A., Shaw, D., & Williams, G. L. (2012). A revised biostratigraphic and well-log sequence-stratigraphic framework for the Scotian Margin, offshore eastern Canada. This article is one of a series of papers published in this CJES Special Issue on the theme of Mesozoic–Cenozoic geology of the Scotian Basin. 2Earth Sciences Sector Contribution 20120137. Canadian Journal of Earth Sciences, **49(12)**, 1417-1462.
- Wielens, H., & Jauer, C. (2001). Overpressure, thermal maturity, temperature and log responses in basins of the Grand Banks of Newfoundland. Geological Survey of Canada, Open File Report, 3937.
- Williams, G., Bates, J., Calder, J., Fensome, R., Ferguson, L., Mann, H., Wade, J. (1997). The Last Billion Years: A Geological History of Maritime Canada.
- Williams, H., Grant, A., Oakley, G., & Vardey, D. (1998). Tectonic assemblages, Atlantic region, Canada: Geological Survey of Canada (Atlantic).
- Withjack, M. O., Schlische, R. W., & Olsen, P. E. (1998). Diachronous rifting, drifting, and inversion on the passive margin of central eastern North America: an analog for other passive margins. AAPG bulletin, **82(5)**, 817-835.
- Wood, L. J. (2000). Chronostratigraphy and tectonostratigraphy of the Columbus Basin, eastern offshore Trinidad. AAPG bulletin, **84(12)**, 1905-1928.
- Wu, S., Bally, A. W., Mohriak, W., & Talwani, M. (2000). Slope tectonics-comparisons and contrasts of structural styles of salt and shale tectonics of the northern Gulf of Mexico with shale tectonics of offshore Nigeria in Gulf of Guinea. Geophysical Monograph-American Geophysical Union, **115**, 151-172.
- Yielding, G., Bretan, P., & Freeman, B. (2010). Fault seal calibration: a brief review. Geological Society, London, Special Publications, **347(1)**, 243-255.

## APPENDIX A.

### A.1. Sediment Core Description

Sediment cores from Thebaud I-93 with inferred facies breaks (Figure A.1.1) described in this study represents rocks of the Lower Missisauga Formation. This combined with a photo collage of slabbed core from the same cored interval (3065.68-3081.27 mRT MD) from which X-ray fluorescence XRF measurements were collected for rock classifications (Figure A.1.2). These form the key building blocks of the stratigraphic and core analysis of this study done in Chapter 3.

**Box 24:** White coarse to medium to lower coarse sands with poor sorting. The presence of mud rip ups and coal fragments and Sulphur smell were characters of the bottom shaly unit in the core. Occupied 1/3 of the available core space in the box.

**Box 23:** White micaceous sand, with some burrowing and clay mud drape and fossil. The presence of parallel cross lamina with reactivation surfaces and asymmetric ripple forms. Some lamina dipping at ~ 30 degrees. This transitions to a mixed sandy and coaly/shaly interval

**Box 22:** White very fine-grained sand to medium-grained sand. There is a reactivation surface with the presence of small-scale beds. At a higher resolution, these surfaces constitute small permeability barriers. Also, there are bed set surfaces with scouring and erosional surfaces with lots of mud rip-up clast.

**Box 21:** White, medium-grain sandstone with some coarse grains. Numerous reactivation surfaces with intermittent mud drape. Also, mud rip-up clasts with coal drapes can be seen.

**Box 20:** White medium to coarse-grained massive sandstone.

**Box 19:** White medium to coarse-grained massive sandstone.

**Box 18:** The white medium to coarse channel sandstones that shares abrupt contact to a bioturbated section that is shale rich with some rip-up sand clasts and siderite nodules. There is some mix of channel sand throughout the section.

**Box 17:** Bioturbated section that is shale rich with some rip-up sand clasts and siderite nodules. Some missing sections up to 1/3 of the box. There is some mix of channel sand throughout the section.

**Box 16:** Bioturbated section that is shale rich with some rip-up sand clasts and siderite nodules. Some missing sections up to 1/3 of the box. There is some mix of channel sand throughout the section.

**Box 15:** Bioturbated section that is shale rich with some rip-up sand clasts and siderite nodules. Some missing sections up to 1/3 of the box. There is some mix of channel sand throughout the section.

**Box 14:** Bioturbated section that is shale rich with some rip up sand clasts and siderite nodules. Some missing sections up to 1/3 of the box. There are some mix of channel sand throughout the section.

**Box 13:** Bioturbated section that is shale rich with some rip-up sand clasts and siderite nodules. Some missing sections up to 1/3 of the box. There is some mix of channel sand throughout the section.

**Box 12:** Dark shale with some sand mixture. There are erosional surfaces with a bit of shell patch and bioturbation.

**Box 11:** Dark shale with some sand mixture. There are erosional surfaces with a bit of shell patch and bioturbation.

**Box 10:** Dark shale with some sand mixture. There are erosional surfaces with a bit of shell patch and bioturbation.

**Box 9:** Dark shale with some sand mixture. There are erosional surfaces with a bit of shell patch and bioturbation.

**Box 8:** Dark shale with some sand mixture. There are erosional surfaces with a bit of shell patch and bioturbation.

**Box 7:** Dark to grey color shales. Small black organic-rich laminations.

**Box 6:** White medium to coarse-grained massive sandstone although some changes in the grain size and lithology changes as if from different provenance.

**Box 5:** White medium to coarse-grained massive sandstone. Missing 1/3 of the cored section in the box.

**Box 4:** White medium to coarse-grained massive sandstone.

**Box 3:** White medium to coarse-grained massive sandstone. Some sand lithic fragments with some mud rip-up clasts.

**Box 2:** White medium to coarse-grained massive sandstone although some changes in the grain size and lithology changes as if from different provenance. Missing 1/3 of the cored section in the box.

**Box 1:** White medium to coarse-grained massive sandstone although some changes in the grain size and lithology changes as if from different provenance. Missing 1/3 of the cored section in the box.

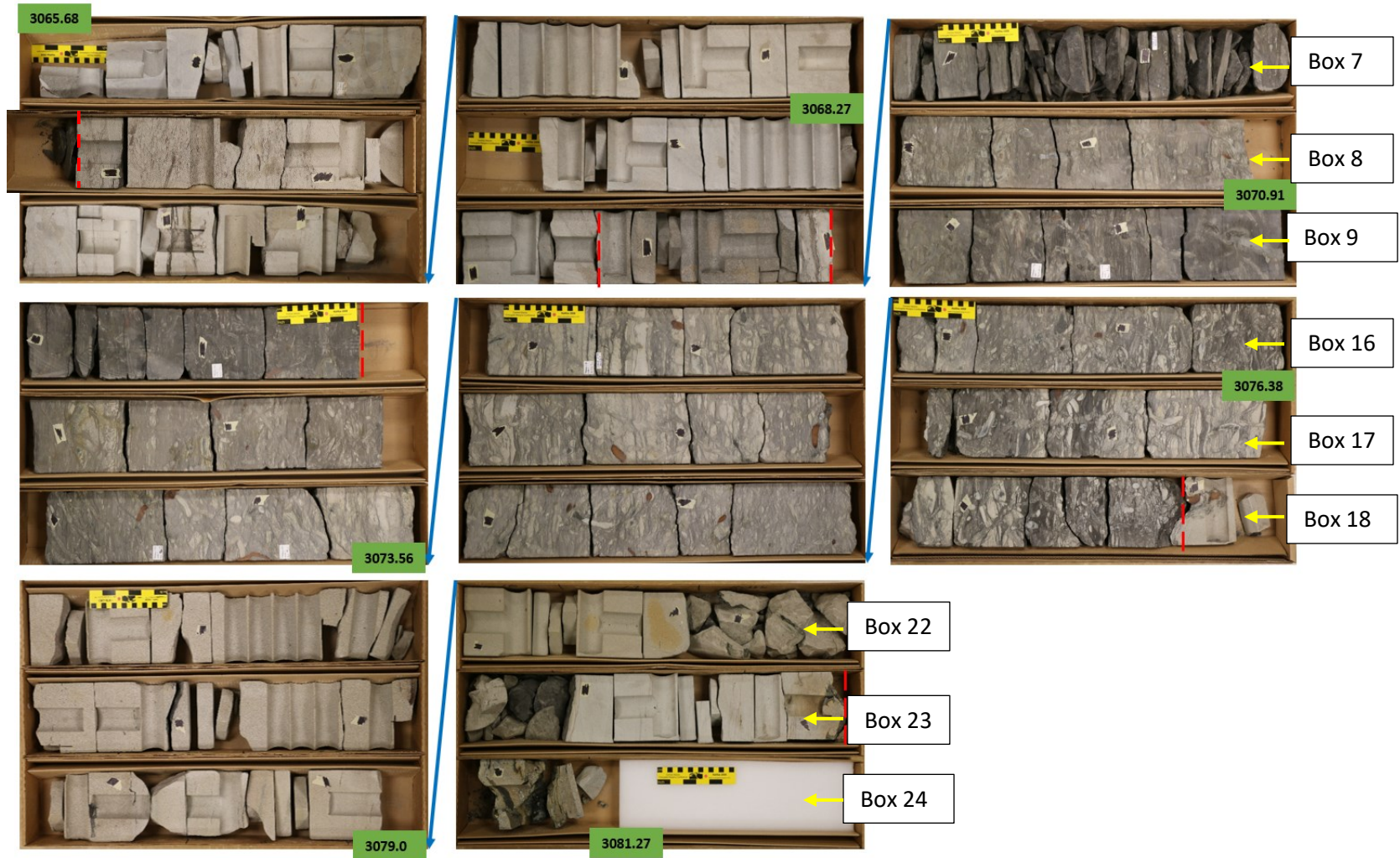


Figure A.1.1: A figure of the Lower Missisauga Formation Sedimentary Cores Described for this Study from the Thebaud I-93 Well. The dashed red lines are indicative of the facies breaks. The yellow arrows are indicative of the respective core boxes and the sequence of their arrangement. The blue arrows show the flow of the arrangement between the arranged sets of boxes.





205

Figure A.1.2: Photo compilation of slabbled core from the Thebaud I-93 well's core No. 1 (3065.68-3081.27 mRT MD). The blue arrows indicate the flow of the core description generally from right to left and top to bottom of each box. The red arrow is generally indicative of the increment in box number from left to right. Small white square tapes with black shadings indicate the point where X-ray fluorescence XRF measurements were collected for rock classifications according to Herron (1988). The colored ovals represent the sand class facies distribution from our analyses. Green represents the litharenite, red for Fe-Sands, yellow for shales, orange for subarkose, dark/navy blue for wackes, and light blue for sublitharenite.

## A.2. XRF analysis

### A.2.1. Sampling, Elemental Conversions and Resulting Tables

For comparison purposes, a combination of major, minor, and trace elements extracted from the hand-held analyzer for classification in a Sand-class plot after Herron (1988) was converted to their corresponding oxides by multiplying the result from the XRF scan with the appropriate conversion constant using the table below. Averages determined from the sandclass plots were transferred to their corresponding fields in various ternary diagrams.

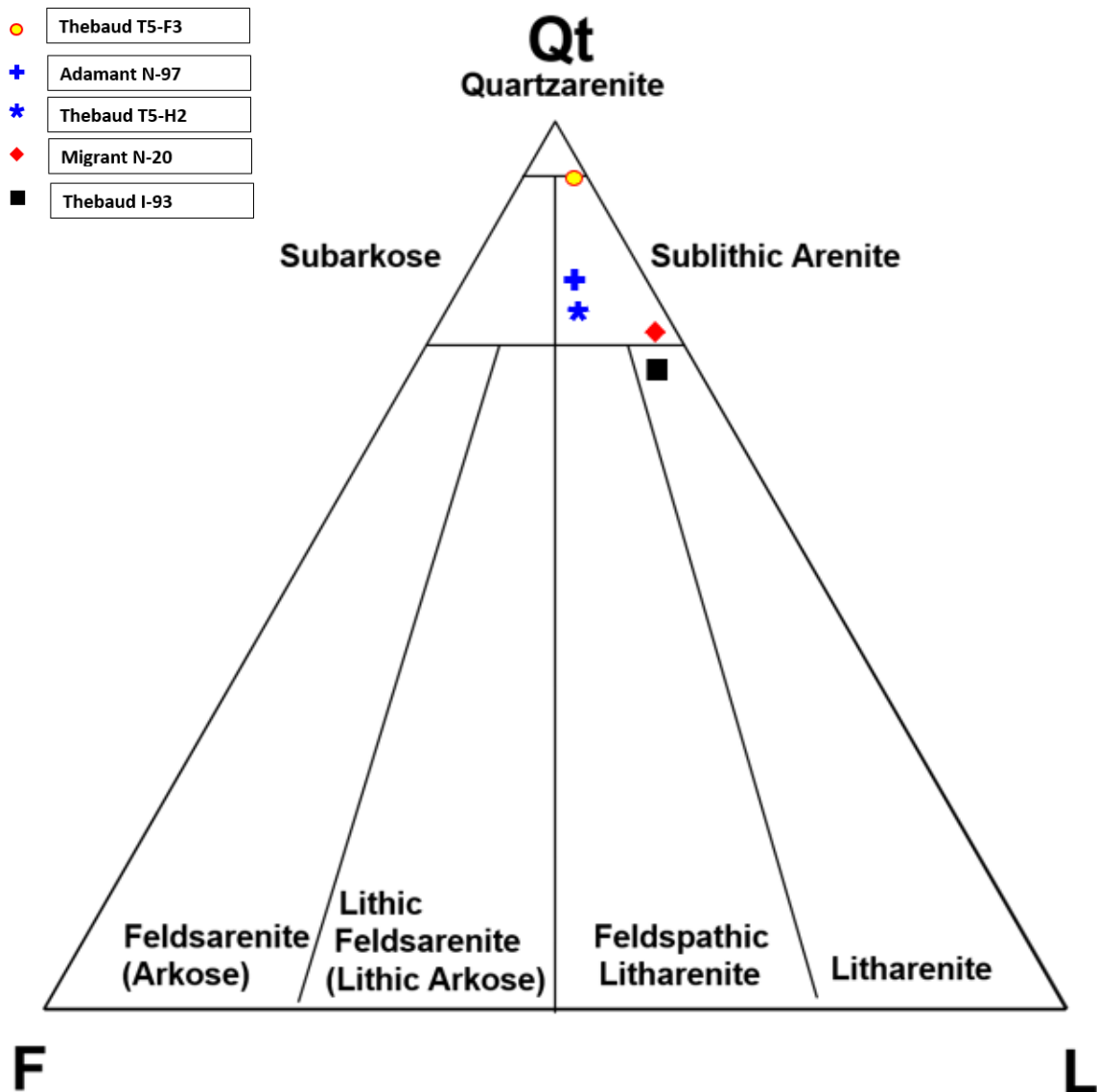


Figure A.2.1: A QtFL classification of Folk (1968). Based on the Folk classification diagram the average analysed data for the wells used in this project mainly plot in the sublithic arenite field with one plotting in the litharenite field.



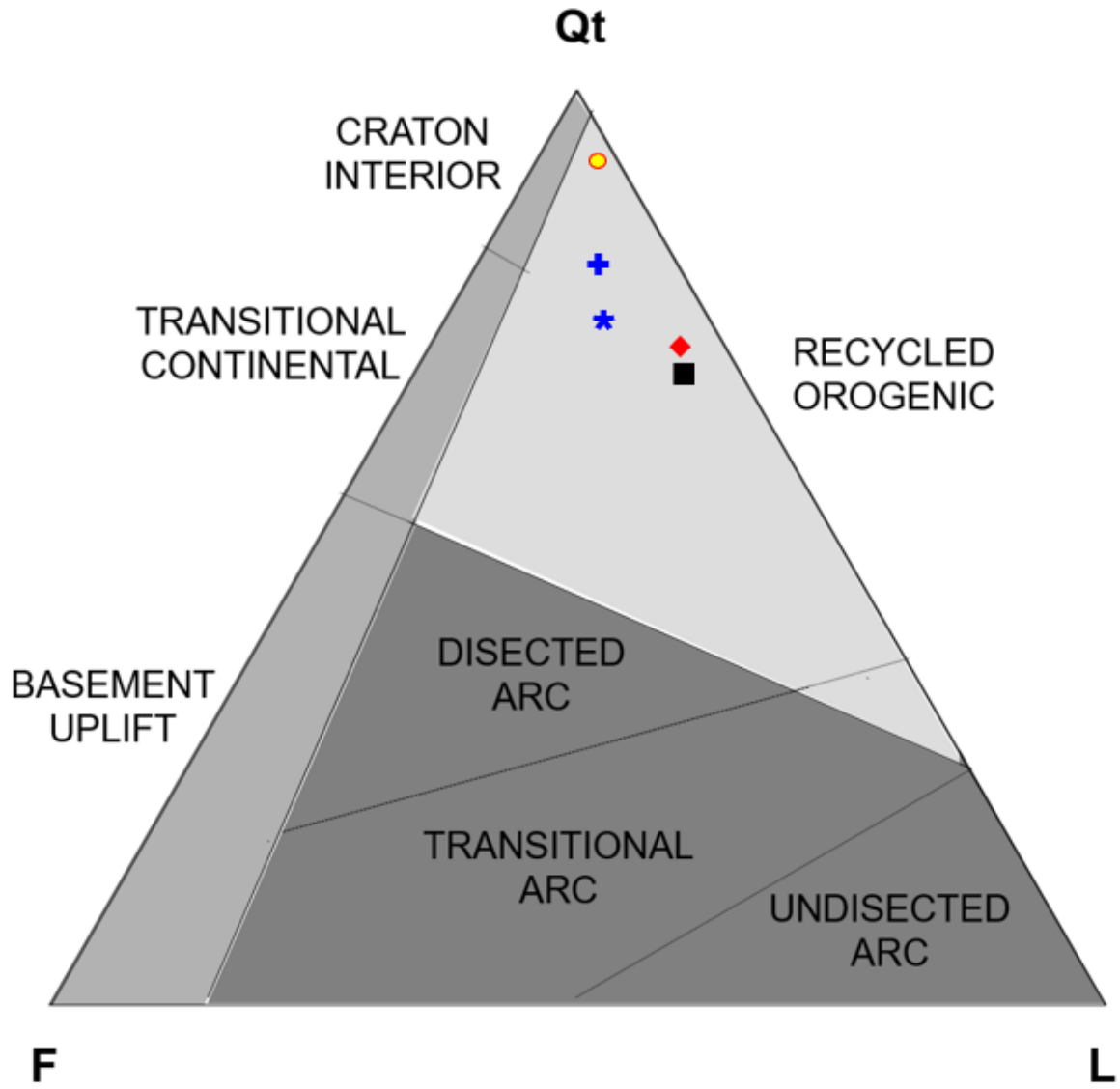


Figure A.2.2: A QtFL provenance indicator plot after Ingersoll and Suczek (1979) and Dickinson (1985). From the provenance indicator plot, all averages from the analyzed wells plot in the recycled orogen field.

Table A.2.1: Conversion of elements to oxides after Korotev (2009).

to element	element		oxide	to oxide
<b>0.4674</b>	Si	—	<b>SiO<sub>2</sub></b>	<b>2.1393</b>
<b>0.5994</b>	Ti	—	<b>TiO<sub>2</sub></b>	<b>1.6683</b>
<b>0.5293</b>	Al	—	<b>Al<sub>2</sub>O<sub>3</sub></b>	<b>1.8895</b>
<b>0.6994</b>	Fe	—	<b>Fe<sub>2</sub>O<sub>3</sub></b>	<b>1.4297</b>
<b>0.7236</b>	Fe	—	<b>Fe<sub>3</sub>O<sub>4</sub></b>	<b>1.3820</b>
<b>0.8998</b>	FeO	—	<b>Fe<sub>2</sub>O<sub>3</sub></b>	<b>1.1113</b>
<b>0.7773</b>	Fe	—	<b>FeO</b>	<b>1.2865</b>
<b>0.6030</b>	Mg	—	<b>MgO</b>	<b>1.6583</b>
<b>0.7745</b>	Mn	—	<b>MnO</b>	<b>1.2912</b>
<b>0.7147</b>	Ca	—	<b>CaO</b>	<b>1.3992</b>
<b>0.8957</b>	Ba	—	<b>BaO</b>	<b>1.1165</b>
<b>0.7419</b>	Na	—	<b>Na<sub>2</sub>O</b>	<b>1.3480</b>
<b>0.8301</b>	K	—	<b>K<sub>2</sub>O</b>	<b>1.2046</b>
<b>0.4364</b>	P	—	<b>P<sub>2</sub>O<sub>5</sub></b>	<b>2.2914</b>
<b>0.6842</b>	Cr	—	<b>Cr<sub>2</sub>O<sub>3</sub></b>	<b>1.4616</b>
<b>0.7403</b>	Zr	—	<b>ZrO<sub>2</sub></b>	<b>1.3508</b>

Table A.2.2: Calculated results from geochemical analysis of the sandstones in the Migrant N-20 cuttings samples. Overall, an average error of  $\pm 0.02$  was obtained for the oxides.

1	Al	Al2O3	Al Error	Si	SiO2	Si Error	P	P2O5	P Error	K	K2O	K Error	Ca	CaO	Ca Error	Ti	TiO2	Ti Error	Mn	MnO	Mn Error	Fe	Fe2O3	Fe Error	Mg	MgO	Mg Error
2	22840.5	43157.2	1098.5	212342.8	454264.9	4562.7	937.9	2149	202.3	11540.3	13901.5	402	10514.72	14712.2	495.7	5872.8	9797.6	193.53	858.4	1108	70.36	64167.9	91740.8	2337.8	<LOD	#####	2836.01
3	23283.8	43994.7	789.11	257712.6	551324.5	1491.4	654.1	1499	204.7	11429.7	13768.3	234.5	5688.24	7958.985	123.52	5228.3	8722.4	95.23	225	290.6	47.47	32657.3	46690.2	311.64	<LOD	#####	3752.83
4	20483.8	38704.2	761.67	258581.8	553184.1	1472.9	<LOD	#####	389	10176.6	12258.7	209.1	27815.04	38918.8	507.47	3709.3	6188.2	75.83	398.6	514.7	47.75	23414.8	33476.1	247.09	<LOD	#####	2302.64
5	27396.1	51764.9	919.59	231111.4	494416.6	1468	409.4	938.1	208.8	12270.3	14780.8	256	30846.23	43160.05	599.85	4893.3	8163.5	94.47	481.3	621.5	56.39	36132.7	51659	340.45	<LOD	#####	2570.18
6	39927	75442	1120.3	166320.8	355810.1	1270.1	431.5	988.8	188.6	19191.1	23117.6	334	14093.05	19719	459.1	6792.6	11332	151.29	332.6	429.4	54.66	40080.7	57303.4	364.59	<LOD	#####	4389.69
7	27815.6	52557.6	967.88	232628.6	497662.3	1478.7	<LOD	#####	373.4	12468	15018.9	255.5	47937.79	67074.56	726	5376.4	8969.5	101.79	465.7	601.3	54.11	30706	43900.3	304.97	<LOD	#####	2677.46
8	21438.5	40508.1	775.39	192923.8	412721.8	1297.4	<LOD	#####	433.3	10660.9	12842.1	228.2	18314.04	25625	450.91	4432.9	7395.4	138.66	443.7	572.9	51.89	32432.4	46368.6	296.39	<LOD	#####	2683.05
9	20492.2	38720.1	735.71	257421.3	550701.5	1525.1	358	820.3	196	10017.4	12066.9	213.7	6452.79	9028.744	126.87	3810.5	6357.1	84.08	180.3	232.8	48.64	33790.4	48310.1	322.25	<LOD	#####	2497.89
10	35386	66861.8	935.57	225068.9	481489.8	1429.5	703.4	1612	187.7	15454.4	18616.4	280.8	2660.32	3722.32	100.84	6285.8	10487	107.59	208.6	269.3	49.62	36746.5	52536.5	343.42	2477.4	4108.2	1639.18
11	35071.2	66267	1117.5	219418.2	469401.4	1476	839.6	1924	221.5	15112.4	18204.4	298.2	28438.48	39791.12	619.09	7035	11736	116.91	519.3	670.5	59.91	44365.1	63428.8	385.59	4955.8	8218.2	2276.63
12	35450.9	66984.4	986.4	234000.5	500597.3	1453.3	867.6	1988	204.9	19526.2	23521.2	316.1	8229.61	11514.87	148.22	7782.7	12984	112.92	253.4	327.2	50.78	34327.8	49078.4	330.66	3882.8	6438.9	1865.71
13	20375.7	38499.9	845.12	267638.6	572559.2	1581.5	378	866.1	225.3	10003.9	12050.7	219.5	32041.54	44832.52	571.56	5094.6	8499.3	90.86	510.4	659	53.61	24498.6	35025.6	264.96	<LOD	#####	4597.23
14	12805.1	24195.3	650.62	293813.3	628554.7	1473.9	<LOD	#####	342.8	7560.78	9107.72	165.3	17529.73	24527.6	367.05	1963	3274.8	55.07	176.3	227.7	37.43	14251.1	20374.8	167.89	<LOD	#####	2371.04
15	9832.3	18578.1	628.53	320539.7	685730.5	1696.6	<LOD	#####	366.7	6462.1	7784.25	136	25029.85	35021.77	411.26	1711.4	2855	56.71	85.69	110.6	37.35	5325.51	7613.88	98.79	<LOD	#####	2232.83
16	10595	20019.3	620.09	332763.8	711881.5	1477.6	<LOD	#####	356.1	5791.62	6976.59	137.4	14666.74	20521.7	314.08	1857	3098	45.57	112.6	145.3	31.52	11226.1	16049.9	135.49	<LOD	#####	2424.93
17	12550	23713.2	646.51	308952.9	660943	1584.1	426.9	978.2	230.2	8131.21	9794.86	163.2	6273.57	8777.979	106.51	3243.2	5410.6	66.38	126.9	163.9	38.25	17313.6	24753.3	204.85	5849.8	9700.8	1819.87
18	33337.2	62990.7	1062.7	266190.7	569461.7	1594.6	394.6	904.2	239.5	18462.1	22239.5	302.2	6925.97	9690.817	132.84	5803.2	9681.5	99.51	239.2	308.9	49.11	27573.3	39421.5	291.65	<LOD	#####	4608.97
19	13821.2	26115.1	652.57	293710.8	628335.5	1634.7	388.2	889.5	212.9	8028.35	9670.95	173.3	8240.33	11529.87	128.14	3551.9	5925.7	80.15	337	435.2	50.76	28168.3	40272.2	288.88	<LOD	#####	2352.76
20	15318.9	28945	662.53	275076.4	588471	1567.3	537.6	1232	201.5	9776.45	11776.7	198	7034.48	9842.644	126.03	3529.7	5888.5	79.81	362.6	468.1	52.26	33682.7	48156.1	321.43	5040.4	8358.4	1675.18
21	17242.6	32579.8	697.43	303154	648537.4	1646	540.1	1238	223.3	9988.41	12032	180.1	7195.86	10068.45	114.51	2983.8	4977.9	70.89	175.9	227.2	42.99	17812.5	25466.5	224.63	<LOD	#####	2464.53
22	25273.4	47754.1	1120.9	280618.8	600327.7	6058.8	685.2	1570	209.8	10668.8	12851.6	365.5	4331.31	6060.369	263.84	2933.1	4893.3	105.46	308.6	398.4	50.14	31979	45720.3	1513	3737.2	6197.4	1657.92
23	14297.5	27015.2	657.78	292657.5	626082.2	1604.7	619.1	1419	208.4	7454.29	8979.44	179.2	7057.37	9874.672	127.8	3708.9	6187.5	80.68	449.7	580.6	54.74	37856.4	54123.3	339.16	<LOD	#####	3274.8
24	8860.24	16741.4	627.74	295023.2	631143.1	1645.1	988.7	2266	236.4	4010.94	4831.58	132.4	29289.63	40982.05	505.71	2088.9	3484.9	61.4	491.5	634.7	53.33	26139.7	37371.9	277.7	<LOD	#####	3983.63
25	9984.62	18865.9	635.52	348426.8	745389.4	1719.1	560.1	1283	254.4	5356.6	6452.56	124	10105.58	14139.73	269.45	1992	3323.3	52.98	163.6	211.2	38.11	12142.1	17359.6	170.05	<LOD	#####	2161.74
26	34133	64494.3	998.18	280129.7	599281.4	1601.3	870.1	1994	225.8	12194.1	14689	241.3	8230.38	11515.95	139.51	6098.2	10174	98.62	471.8	609.1	54.74	32282.6	46154.5	307.92	<LOD	#####	2639.17
27	29109.5	55002.4	915.81	203311.7	434944.7	1333.5	478.9	1097	182.2	11484.2	13833.9	269.7	13973.33	19551.48	462.48	5673.1	9464.5	129.24	829.1	1070	71.99	67830.7	96977.6	499.55	3110.2	5157.7	1863.81
28	6499.6	12281	745.17	119559.7	255774	1211.5	<LOD	#####	299.5	4947.8	5960.12	194.4	130872.1	183116.2	1157.4	864.23	1441.8	160.55	755.2	975	75.18	23663.8	33832.1	302.44	<LOD	#####	7467.11
29	7060.29	13340.4	671.53	182989.3	391468.9	1360	<LOD	#####	313.7	2823.48	3401.16	153.3	109362.8	153020.4	1000.7	801.27	1336.8	126.66	381.4	492.5	56.44	14500.3	20731	216.54	<LOD	#####	4275.1
30	11625.3	21965.9	615.52	295397.4	631943.6	1614.4	463.2	1061	214.9	4988.09	6008.65	133.8	21761.26	30448.35	404.24	2198.1	3667	66.96	289.4	373.6	46.98	17951.3	25665	227.22	5333.9	8845.1	1705.22
31	10964.7	20717.7	691.77	270709.5	579128.8	5374.2	<LOD	#####	498.6	2803.07	3376.58	134.4	29393.77	41127.76	894.94	1351.2	2254.2	73.02	390.4	504.1	48.59	24376.1	34850.6	1234.2	<LOD	#####	2229.27
32	16085.1	30392.8	863.11	244593.2	523258.3	1597.4	<LOD	#####	520.6	5623.62	6774.21	166.6	47750.57	66812.6	686.96	3438.2	5735.9	151.05	602.6	778	64.21	26012.8	37190.5	293	<LOD	#####	4796.78
33	12898.8	24372.3	636.42	268252.2	573871.8	1588.9	<LOD	#####	420.5	6999.34	8431.4	163.5	17742.01	24824.62	388.94	3529.5	5888.3	104.97	298	384.8	50.53	20355.5	29102.3	248.43	<LOD	#####	2048.13
34	13898.4	26261	658.33	269362.8	576247.9	1563.4	<LOD	#####	307.3	7195.67	8667.9	171.9	16996.34	23781.28	398.97	4152.1	6926.9	100.61	330	426	52.63	25438.9	36370	274.49	2837.8	4706	1631.73
35	25108.6	47442.4	942.99	260379.7	557030.3	1600	496.2	1137	229.9	9160.57	11034.8	203.4	18589.87	26010.95	454.43	4544.5	7581.5	115.19	616.2	795.7	60.94	38280.8	54730.1	350.93	5503.3	9126.1	2131.7
36	17753.6	33545.4	716.79	273537.6	585179	1565.2	498.4	1142	210.3	6980.08	8408.2	161.2	25094.49	35112.21	461.77	3210.4	5355.9	99.54	387.5	500.3	51.8	21836.4	31219.5	252.59	<LOD	#####	2086.28

Table A.2.3: Calculated results from geochemical analysis of the sandstones in the Adamant N-97 sidewall cores. Overall, an average error of  $\pm 0.02$  was obtained for the oxides.

1	Core	Reading No	Al	Al2O3	Al Error	Si	SiO2	Si Error	P	P2O5	P Error	K	K2O	K Error	Ca	CaO	Ca Error	Ti	TiO2	Ti Error	Mn	MnO	Mn Error	Fe	Fe2O3	Fe Error	Mg	MgO	Mg Error
2	SWC	4485	21775.7	41145.3	826.73	363559.8	777763.5	1497.4	676.3	1549.7	265.88	5374.23	6473.8	82.9	4302.34	6019.834	54.66	2426.9	4048.8	51.21	174.86	225.78	29.05	8375.53	11974.5	103.91	<LOD	#VALUE!	2598.27
3	SWC	4486	9305.73	17583.2	672.03	320030.2	684640.6	1435.4	<LOD	#VALUE!	577.17	3408.91	4106.37	80.76	16498.01	23084.02	245.99	2595.67	4330.36	114.73	305.48	394.44	31.17	5822.86	8324.943	70.25	<LOD	#VALUE!	3867.82
4	SWC	4487	9346.53	17660.3	598.89	377560.4	807714.9	1450.2	681.22	1560.9	250.77	2916.65	3513.4	68.96	9367.61	13107.16	81.4	4024.89	6714.72	67.22	194.21	250.76	28.39	6762.94	9668.975	91.1	<LOD	#VALUE!	3526.78
5	SWC	4488	12615.4	23836.9	695.06	374095.9	800303.4	1458	525.82	1204.9	265.55	3881.26	4675.37	81.72	9496	13286.8	86.65	2854.81	4762.68	78.4	214.51	276.98	28.01	10370.38	14826.53	108.23	<LOD	#VALUE!	3856.17
6	SWC	4489	24901.3	47051.1	897.12	367230	785615.1	1437.2	734.36	1682.7	274.99	8055.99	9704.25	113.8	6075.1	8500.28	73.69	3843	6411.28	77.82	246.61	318.42	29.43	11795.41	16863.9	113.4	4456.79	7390.69	1938.32
7	SWC	4490	4807.25	9083.3	530.24	394402.3	843744.7	1394.6	644.96	1477.9	263.14	1653.5	1991.81	50.03	5184.53	7254.194	55.88	3929.95	6556.34	42.47	87.58	113.08	24.11	1698.79	2428.76	37.77	<LOD	#VALUE!	2009.56
8	SWC	4491	71952.6	135954	1549	254084.4	543562.7	1305.5	1209.7	2771.9	237.23	22175.2	26712.2	264.1	4168.07	6671.484	104.24	8911.37	14866.8	104.82	500.62	646.4	41.53	48463.42	69288.15	270.41	9004.82	14932.7	2462.77
9	SWC	4492	63335.6	119673	1467.6	294548.1	630126.8	1373.7	1245.5	2854	255.09	18892	22757.3	246	5142.85	7195.876	110.02	8592.85	14335.5	104.84	620.4	801.06	43.98	52689.37	75329.99	283.72	6555.62	10871.2	2326.37
10	SWC	4493	27008.6	51032.7	981.09	309312.7	661712.7	1355.9	2583.3	5919.4	296.06	3040.47	3662.55	86.9	4958.45	6937.863	76.35	17469.3	29143.9	121.68	425.82	549.82	36.52	25784.87	36864.63	181.8	<LOD	#VALUE!	2966.22
11	SWC	4494	16993.6	32109.3	708.09	347797.8	744043.7	1362.5	739.88	1695.4	245.47	4138.52	4985.26	77.42	6364.77	8905.586	66.98	3821.3	6375.07	57.64	122.03	157.57	24.39	4899.07	7004.2	72.65	<LOD	#VALUE!	2225.98
12	SWC	4495	22183.8	41916.2	828.04	373727.3	799514.9	1471.7	1031.1	2362.6	264.03	8362.23	10073.1	119.1	4548.2	6363.841	67.28	4662.59	7778.6	64.5	225.3	290.91	31.34	16515.86	23612.73	145.07	3658.37	6066.67	1770.19
13	SWC	4496	1885.52	3562.69	1085.1	12749.01	27273.96	551.07	<LOD	#VALUE!	274.87	1843.89	2221.15	214.5	442605	619293	1680.8	1022.01	1705.02	91.46	830.81	1072.7	46.76	12895.08	18436.1	143.38	<LOD	#VALUE!	13609.8
14	SWC	4497	1718.4	22142	701.64	402527.7	851127.6	1469	830.06	1902	281.76	4429.43	5335.69	89.32	8379.69	11724.86	85.2	2702.08	4507.88	49.77	232.45	300.14	29.95	14173.02	20263.17	130.55	<LOD	#VALUE!	2852.75
15	SWC	4498	34408.1	65014.2	1216.1	312641.3	668833.6	1443.4	921.06	2110.5	290.52	10877.3	13102.7	152	2762.58	3865.402	65.19	9416.25	15709.1	82.07	200.32	258.65	29.87	17284.27	24711.32	141.55	<LOD	#VALUE!	4036.75
16	SWC	4499	8531.33	16119.9	894.44	289524.6	619380	1797.7	<LOD	#VALUE!	4690.3	4531.86	6459.08	125	144356.8	201984	786.5	6227.31	10389	70.95	544.22	702.7	41.35	11273.53	16117.77	128.94	<LOD	#VALUE!	6078.83
17	SWC	4500	41607.7	78617.7	1355.3	210616.2	450571.2	1448.7	<LOD	#VALUE!	4147.1	18117	21823.8	237.4	2393	3342.286	76.35	13998.5	23353.6	157.18	486.94	628.74	46.65	40314.36	57637.44	259.17	<LOD	#VALUE!	5584.41
18	SWC	4501	13997.8	24941.1	717.37	350489.4	749802.1	1412.1	<LOD	#VALUE!	400.77	5878.22	7080.9	101.8	28589.4	40002.29	312.21	2284.84	3811.8	63.66	217.94	281.4	28.64	5327.08	7616.126	66.65	<LOD	#VALUE!	2454.2
19	SWC	4502	21647.1	40902.3	909.09	312806.3	669186.5	1422.5	510.53	1169.8	269.16	9944.99	11979.7	136.7	24367.9	34095.57	323.97	3118.4	5202.43	106.59	318.37	411.08	33.52	15493.35	22150.84	141.47	<LOD	#VALUE!	4861.95
20	SWC	4503	5779.8	10920.9	623.89	392291	839228.1	1437	848.64	1944.6	300.48	3143.65	3786.84	66.81	11035.62	15441.04	177.61	2615.57	4363.56	46.51	120.18	155.18	26.24	5211.5	7450.882	78.65	<LOD	#VALUE!	3775.68
21	SWC	4505	8069.68	15247.7	580.04	381254.1	815617	1470	480.49	1101	260.12	1415.2	1704.75	47.42	4918.38	6881.797	54.79	979.31	1633.78	39.4	89.44	115.48	24.94	2302.87	3292.413	44.45	<LOD	#VALUE!	2000.94
22	SWC	4506	3340.66	6312.18	542.81	398565.2	852650.5	1393.3	701.64	1607.7	274.9	992.6	1195.69	48.25	18470.83	25844.39	226.27	3497.35	5834.63	45.34	158.22	204.29	26.37	5164.64	7383.886	76.87	4424.29	7336.8	1742.4
23	SWC	4507	81240.5	153504	1625.9	246300.6	526910.8	1313.4	1279.9	2932.6	234.16	25757.4	31027.4	267.1	2468.39	3453.771	86.13	10107.8	16862.8	101.27	355.41	458.91	36.78	36329.2	51939.86	224.89	5488.75	9101.99	2210.42
24	SWC	4508	73386.6	138664	1558.9	255186.1	545919.7	1307.3	1180.2	2704.3	241.1	24084.5	29012.2	268.7	3197.07	4473.34	91.62	9220.52	15382.6	100.75	373.24	481.93	38.02	43920.69	62793.41	254.54	7593.74	12592.7	2402.24
25	SWC	4509	15692.8	29651.5	828.6	312702.5	668964.5	1407.5	<LOD	#VALUE!	400.89	8180.31	9854	109.2	6810.59	9529.378	73.74	4114.83	6864.77	56.18	158.57	204.75	27.2	10628.76	15195.94	108.72	<LOD	#VALUE!	3377.52
26	SWC	4510	8462.07	15989.1	627.66	396896	849079.7	1421.2	943.23	2161.3	279.15	1489.91	1794.75	51.93	9136.92	12784.38	76.81	1428.04	2382.4	41.6	96.23	124.25	24.82	3362.71	4807.666	52.01	<LOD	#VALUE!	3588.25
27	SWC	4511	5647.47	10670.9	550.77	406301.8	869201.5	1413.6	703.75	1612.6	273.45	981.51	1182.33	43.75	5513.57	7714.587	58.93	485.16	809.392	29.3	90.1	116.34	24.65	1813.9	2593.333	39.82	<LOD	#VALUE!	3528.25
28	SWC	4512	10903.3	20601.8	684.92	305673.8	653927.9	1405.5	641.72	1470.4	267.18	5479.05	6600.06	95.85	10749.6	15040.84	204.68	4224.28	7047.37	140.13	325.72	420.57	31.48	4650.36	6648.62	61.85	<LOD	#VALUE!	2524.5
29	SWC	4513	3362.18	6352.84	509.73	395354.2	845781.3	1404.1	682.53	1563.9	265.15	907.07	1092.66	37.78	3971.97	5557.58	45.54	363.42	605.294	26.62	54.15	69.918	22.4	469.44	671.1584	22.82	2601.39	4313.89	1556.74
30	SWC	4514	49580.4	94192.3	1193.6	298804.8	639233.1	1363.9	824.23	1888.6	240.56	16922	20384.2	196.3	3126.57	4274.697	70.33	5631.96	9395.8	67.96	213.36	275.49	31.55	25185.39	36007.55	177.29	3762.86	6239.95	1919.14
31	SWC	4515	12264.8	23174.4	713.57	372518.4	796928.6	1451.5	967.18	2216.2	276.16	3880.75	4674.75	80.36	7911.98	11070.44	78.83	2682.1	4474.55	74.91	136.05	175.67	26.21	8467.23	12105.6	95.51	<LOD	#VALUE!	4121.37
32	SWC	4516	15153.7	28632.8	681.72	331903.4	710041	1374.2	774.67	1775.1	244.4	5023.95	6051.85	75.87	8395.08	11746.4	68.88	1707.92	2849.32	34	114.47	147.8	26.06	3462.81	4950.779	54.64	2654.36	4401.73	1688.7
33	SWC	4517	84136.2	158975	1623.66	235579.8	503975.9	1303.4	726.26	1664.2	217.64	30206.1	36386.3	290.2	1580.35	2211.226	79.37	7249	12093.5	86.89	282.4	364.63	35.68	35699.36	51039.37	224.8	4825	8001.3	2133.94
34	SWC	4518	22656.4	42809.2	801.11	250921.4	536796.2	1271.6	387.79	888.58	207.87	2937.05	3537.97	82.67	10788.25	15094.92	216.56	996.5	1662.46	95.54	229.81	296.73	32.34	16940.17	24219.36	150.51	5556.82	9214.87	2000.22
35	SWC	4519	24280.5	45877.9	916.88	198048.7	423685.6	1215.4	1129.2	2587.4	215.63	4932.52	5941.71	109.6	4920.03	6884.106	79.87	4685.82	7817.35	63.1	180.8	233.45	33.3	45327.69	64805	247.05	<LOD	#VALUE!	4142.64
36	SWC	4520	65671.2	124086	1540.7	203329.3	434982.4	1248.1	930.74	2132.7	216.66	29420.8	35440.3	287.9	1228.84	1719.393	66.8	7521.32	12547.8	80.39	267.4	345.27	36.66	45504.66	65058.01	264.08	<LOD	#VALUE!	4912.66
37	SWC	4521	14673.1	27724.9	661.23	295331.9	631803.6	1306.9	509.54	1167.6	233.53	3818.51	4599.78	69.41	5145.89	7200.129	56.94	1315	2193.81	29.13	104.93	135.49	26.93	8595.07	12288.37	104.32	<LOD	#VALUE!	2800.13
38	SWC	4522	29528.6	55794.2	940.82	211737.1	452969.2	1235.5	918.46	2104.6	207.6	9209.45	11093.7	112.8	13117.82														



Table A.2.4: Calculated results from geochemical analysis of the sandstones in the Thebaud I-93 full diameter cores. Overall, an average error of  $\pm 0.02$  was obtained for the oxides.

1	Core	Reading No	Al	Al2O3	Al Error	Si	SiO2	Si Error	P	P2O5	P Error	K	K2O	K Error	Ca	CaO	Ca Error	Ti	TiO2	Ti Error	Mn	MnO	Mn Error	Fe	Fe2O3	Fe Error	Mg	MgO	Mg Error
2	I-93T	4534	25495.1	48173	1087.3	201800.1	431711	1271.8	<LOD	#####	344.98	12090.8	14564.6	171.7	102017.8	142743.3	692.02	3330.41	5556.12	56.71	485.65	627.07	37.53	23657.71	33823.43	179.9	<LOD	#VALUE!	5678.48
3	I-93T	4535	15157.3	28639.7	930.76	237437.8	507950.7	1381.6	<LOD	#####	364.61	7840.07	9444.15	144.7	98339.55	137596.7	687.09	586.96	979.225	31.91	1249.4	1613.2	50.35	28011.53	40048.08	199.99	5975.9	9909.83	2894.61
4	I-93T	4536	15329.5	28965.1	1191.9	143776.5	307581.1	1271.5	<LOD	#####	343.45	7832.12	9434.57	201.7	233061.6	326099.8	1149.3	985.03	1643.33	48.33	1088.4	1405.3	52.21	37694.74	53892.17	258.34	<LOD	#VALUE!	6566.71
5	I-93T	4537	19862.7	37530.6	1298.3	150787.8	322580.2	1309.6	<LOD	#####	353.55	9438.69	11369.8	199.6	261939.5	366505.7	1144	930.31	1552.04	42.8	709.33	915.89	42.49	11127.34	15908.76	128.12	<LOD	#VALUE!	5843.81
6	I-93T	4538	9453.92	17863.2	1128.5	154370.9	330245.6	1334.7	<LOD	#####	360.14	6932.92	8351.4	204.1	289249.2	404717.4	1202.5	647.57	1080.34	56.72	811.28	1047.5	43.04	12291.86	17573.67	131.01	8385.75	13906.1	4791.35
7	I-93T	4539	6818.62	12883.8	850.3	225847.7	483156	1378	<LOD	#####	380.33	4420.77	5325.26	132.2	193875.8	271271	917.85	985.78	1644.58	35.57	656.97	848.28	40.03	3223.47	4608.595	58.83	<LOD	#VALUE!	4888.1
8	I-93T	4540	6224.99	11762.1	929.65	172729	369519.1	1340.4	<LOD	#####	367.56	3890.18	4686.11	155.4	251136.3	351389.9	1080.9	488.66	815.231	45.92	903.33	1166.4	43.32	4879.95	6976.865	69.83	<LOD	#VALUE!	4772.04
9	I-93T	4541	8266.52	15619.6	866.74	228010.8	487783.4	1379.3	<LOD	#####	375.32	6160.37	7420.78	146.5	188421.2	263638.9	879.49	707.91	1181.01	37.17	596.35	770.01	38.4	3301.83	4720.626	58.47	<LOD	#VALUE!	4153.79
10	I-93T	4542	9246.41	17471.1	953.95	232619.6	497643	1426.4	<LOD	#####	398.03	7032.88	8471.81	162.1	198920.8	278329.9	922.68	826.06	1378.12	36.04	910.32	1175.4	44.17	3913.01	5594.43	64.21	<LOD	#VALUE!	5793.55
11	I-93T	4543	6592.16	12455.9	774.27	226668.5	484911.8	1350.4	<LOD	#####	372.78	5165.81	6222.73	116	162799.3	227788.8	822.22	542.81	905.57	34.16	884.83	1142.5	43.26	4086.98	5843.155	64.84	<LOD	#VALUE!	4151.23
12	I-93T	4544	23077.1	43604.1	766.48	299598.4	640930.8	1308.3	<LOD	#####	510.12	6119.97	7372.11	103.8	15350.09	21477.85	248.41	1394.77	2326.89	32.74	230.22	297.26	30.58	16829.83	24061.61	144.17	<LOD	#VALUE!	2475.84
13	I-93T	4545	24965	47174.1	1194.5	255709.2	547038.6	1415.7	<LOD	#####	381.25	9612.29	11579	197	61995.12	86659.62	646.43	1241.88	2071.83	49.43	1786.3	2306.4	63.66	69818.23	99819.12	356.33	<LOD	#VALUE!	7242.64
14	I-93T	4546	57483.2	108614	1329.4	280923.3	600979.3	1350.7	2434	5577.2	249.93	18904.6	22772.5	222.7	1063.02	1487.378	61.81	8817.62	14710.4	85.37	193.81	250.25	33.58	33963.04	48556.96	217.9	8525.56	14137.9	2253.83
15	I-93T	4547	68599.6	129614	1390.7	266916.7	571014.9	1311.7	971.46	2226	226.24	22590.6	27212.7	245.5	450.51	630.3536	63.37	9144.08	15255.1	91.16	161.09	208	32.27	32852.28	46968.9	209.39	<LOD	#VALUE!	2770.73
16	I-93T	4548	47160.5	89109.7	1264.6	282447.3	604239.6	1371.3	652.57	1495.3	245.19	17986.6	21666.6	224.5	1608.41	2250.487	71.21	8339.7	13913.1	87.99	185.12	239.03	32.84	36010.14	51483.7	222.44	3757.57	6231.18	2323.2
17	I-93T	4549	53153.5	100434	1340.5	253035.4	541318.7	1316.7	1428	3272	236.97	21814.8	26278.1	249.8	3820.91	5346.217	89.86	7768.84	12960.8	84.84	279.71	361.16	35.92	38523.98	55077.73	235.09	<LOD	#VALUE!	4717.66
18	I-93T	4550	65236.1	123264	1383.1	273692.3	585510	1326.5	863.32	1978.2	227.32	22294.2	26855.6	252.4	1250.41	1749.574	73.25	9421.06	15717.2	95.03	209.41	270.39	33.93	38338.21	54812.14	233.82	5488.13	9100.97	2044.85
19	I-93T	4551	62455.5	118010	1310.7	278692.4	596206.7	1319.5	1277.8	2927.9	225.93	21852.7	26323.8	249.2	1842.24	2577.662	78.31	9125.72	15224.4	94	218.41	282.01	34.68	38415.31	54922.37	233.28	<LOD	#VALUE!	2706.35
20	I-93T	4552	55927.5	105675	1308.9	263309.9	563298.9	1304.4	960.47	2200.8	237.55	21683	26119.4	256.1	1934.28	2706.445	78.06	7988.17	13326.7	88.85	194.67	251.36	33.88	41411.68	59206.28	244.45	4435.82	7355.92	2164.1
21	I-93T	4553	65481.3	123727	1417.8	283698.6	606916.3	1351.4	1271.5	2913.4	240.45	22717.8	27367	261.3	1118.6	1565.145	75	9286.25	15492.3	97.2	225.54	291.22	35.57	42213.07	60352.02	248.82	4689.16	7776.03	2081.85
22	I-93T	4554	50173.3	94802.4	1310.2	275574.7	589536.9	1358.8	1253	2871.1	239.17	20263.6	24409.6	248.2	1811.97	2535.308	77.83	8388.07	13993.8	92.75	215.03	277.65	35.1	42540.45	60820.08	248.24	<LOD	#VALUE!	4684.41
23	I-93T	4555	58658.9	110836	1439.3	243405.3	520716.9	1300.9	895.25	2051.4	238.45	23675.9	28519.9	253.9	4540.48	6353.04	97.38	9012.83	15036.1	90.43	223.08	288.04	33.24	35933.82	51374.58	217.66	9803.51	16257.2	2668.11
24	I-93T	4556	58876.9	111248	1337.4	269729.2	577031.7	1330.6	1224.4	2805.5	234.49	22855.5	27531.7	249.5	1404.35	1964.967	73.3	9034.65	15072.5	91.63	196.14	253.26	33.31	32252.4	46111.26	210.53	4472.92	7417.44	2128.52
25	I-93T	4557	36690.4	69326.5	1321.4	261016.3	558392.1	1787.3	<LOD	#####	5598.7	14446.2	17401.9	194.5	788.23	1102.891	56.05	7555.31	12604.5	80.01	155.23	200.43	32.15	33571.68	47997.43	215.03	5591.27	9272	3331.37
26	I-93T	4558	28192.6	53270	999.85	262647.5	561881.9	1330.8	664.3	1522.2	239.22	15175.7	18280.6	193.7	1362.55	1906.48	55.17	5637.02	9404.24	63.75	118.52	153.03	29	28726.78	41070.68	187.47	<LOD	#VALUE!	3834.87
27	I-93T	4559	26893.7	50815.6	1287.6	236439.6	505815.3	1725.6	<LOD	#####	5149.1	12288.6	14802.8	180.1	773.29	1081.987	52.18	5528.67	9223.48	69.26	142.25	183.67	33.47	32901.84	47039.76	218.24	<LOD	#VALUE!	5731.51
28	I-93T	4560	28600.9	54041.5	1040.2	265050.4	567022.4	1347.5	<LOD	#####	365.09	12642	15228.5	182.2	27340.19	38254.39	396.61	4086.35	6817.26	62.61	301.04	388.7	34.4	31990.73	45737.15	208.7	<LOD	#VALUE!	3654.75
29	I-93T	4561	24780	46821.8	1222.9	204397.7	437268	1606.4	<LOD	#####	5652.3	13172.2	15867.2	184.1	13027.06	18227.46	284.43	6722.1	11214.5	75.15	156.59	202.19	31.92	28427.44	40642.71	200.93	<LOD	#VALUE!	8155.86
30	I-93T	4562	35187.1	66486.1	1347.6	219928	470492	1498.7	<LOD	#####	3618.6	14850.8	17889.3	204.1	2079.52	2909.664	70.68	8172.09	13633.5	86.07	151.19	195.22	31.76	32701.66	46753.56	212.37	6151.42	10200.9	3717.78
31	I-93T	4563	14670.4	27719.8	1048.2	139813.1	299102.1	1280.7	<LOD	#####	570.42	12601.2	15179.4	176.4	3323.97	4650.899	60.55	4949.76	8257.68	53.9	115.66	149.34	32.3	25998.41	37169.93	196.76	<LOD	#VALUE!	5913.93
32	I-93T	4564	24882.7	47015.8	1243.3	219312.2	469174.5	1415.4	<LOD	#####	632.78	11892.7	14325.9	173	2684.28	3755.845	67.85	5119.37	8540.64	64.68	151.74	195.93	31.08	28937.95	41372.59	199.31	<LOD	#VALUE!	7633.11
33	I-93T	4565	42696.2	80674.5	1548.2	170564.1	364887.8	1302.7	599.8	1374.4	272.62	21107.4	25425.9	243.1	10743.7	15032.59	290.85	9412.2	15702.4	92.86	187.87	242.58	33.06	36165.02	51705.13	222.45	<LOD	#VALUE!	6080.11
34	I-93T	4566	56869.7	107455	1356.6	249360	533455.7	1290.7	1116.7	2558.7	240.42	22518.4	27125.6	260.6	7709.66	10787.36	121.99	7871.12	13131.4	90.71	237.45	306.6	34.86	40739.62	58245.43	239.46	4653.14	7716.3	2287.26
35	I-93T	4567	36741.4	69423	1058.9																								

Table A.2.5: Calculated results from geochemical analysis of the sandstones in the Thebaud E-74 (T5) F3 full diameter cores. Overall, an average error of  $\pm 0.02$  was obtained for the oxides.

1	Core	Reading No	Al	Al2O3	Al Error	Si	SiO2	Si Error	P	P2O5	P Error	K	K2O	K Error	Ca	Ca Error	Ti	TiO2	Ti Error	Mn	MnO	Mn Error	Fe	Fe2O3	Fe Error	Mg	MgO	Mg Error	
2	TSF	4581	23847.4	45059.7	1018.1	304336.9	651067.9	1435.5	584.96	1340.4	273.53	5965.48	7186.02	122	52269.27	73135.16	501.37	3848.73	6420.84	66.92	652.85	842.96	40.85	30950.99	44250.63	208.02	4523.27	7500.94	2454.13
3	TSF	4582	18479.1	34916.2	900.8	352882.9	754922.4	1489.8	493.39	1130.6	287.98	4521.94	5447.13	105.3	35874.5	50195.6	395.45	4681.35	7809.9	61.84	399.79	516.21	35.09	21403.68	30600.84	165.75	3696.93	6130.62	2171.42
4	TSF	4583	65938.1	124590	1538.2	216048.2	462192	1265	737.91	1690.8	248.42	20522.7	24721.6	256.8	1395.98	1953.255	70.47	9016.75	15042.6	110.74	361.5	466.77	39.09	47395.8	67761.78	266.93	3913.86	6490.35	2551.93
5	TSF	4584	25486.2	48156.1	844.52	345577.2	739293.3	1411.2	876.51	2008.4	248.99	6442.06	7760.11	103.4	11959.75	16734.08	211.25	4976.01	8301.48	58.78	205.59	265.46	29.5	11277.26	16123.1	118.26	3483.45	5776.61	1721.55
6	TSF	4585	18024.8	34057.9	776	365011.9	780870	1713.9	3883.4	8898.4	2268.6	4370.89	5265.17	92.91	22633.25	31668.44	296.66	4822.79	8045.86	70.66	300.46	387.95	33.49	13100.12	18729.24	130.02	4413.18	7318.38	1828.02
7	TSF	4586	29458.7	55662.2	935.47	322963.5	690915.9	1395.5	930.99	2133.3	246.5	7737.43	9320.51	110.1	5459.7	7639.212	69.27	4525.15	7549.31	57.91	189.64	244.86	29.66	14022.36	20047.77	131.69	<LOD	#VALUE!	4279.08
8	TSF	4587	25998.6	49124.3	867.33	367821.8	786881.3	1464.4	873.96	2002.6	260.91	6067.21	7308.56	101.1	10412.69	14569.44	198.77	5290.18	8825.61	70.11	188.81	243.79	29.67	9963.4	14244.67	112.29	5546.69	9198.08	1824.08
9	TSF	4588	44640.2	84347.6	1119.7	272307.9	582548.4	1458.8	3940.3	9028.7	2073.5	13442.8	16193.2	171.4	1290.39	1805.514	52.41	7613.13	12701	75	225.66	291.37	32.52	21550.67	30810.99	168.75	<LOD	#VALUE!	2985.58
10	TSF	4589	35230.1	66567.2	1043.2	298477.2	638532.3	1764.4	<LOD	#####	5184	9202.82	11085.7	116.6	4901.31	6857.913	65.28	5151.57	8594.36	52.11	178.04	229.89	28.88	12741.3	18216.24	122.6	<LOD	#VALUE!	4468.43
11	TSF	4590	47570.5	89884.5	1213.9	245689.2	525602.9	1438.2	<LOD	#####	3302.7	13156.3	15848.1	169.1	5601.53	7837.661	84.07	7502.1	12515.8	76.95	280.33	361.96	34.04	20166.4	28831.9	165.75	<LOD	#VALUE!	3219.43
12	TSF	4591	23410.4	44233.9	831.15	332858.3	712083.7	1406.7	642.79	1472.9	247.62	7236.09	8716.59	112.6	11338.85	15865.32	214.71	4505.47	7516.48	78.47	276.73	357.31	31.79	13498.32	19298.55	130.24	<LOD	#VALUE!	3332.27
13	TSF	4592	49588.3	93697.2	1197	290536.6	621544.9	1492.3	4304.6	9863.6	2163.4	13907.9	16030.7	171.2	1518.8	2125.105	56.96	8800.89	14682.5	84.14	225.71	291.44	31.4	20393.47	29156.54	154.43	<LOD	#VALUE!	3796.49
14	TSF	4593	24789.6	46839.9	872.03	259532.1	555216.9	1457.8	4105.7	9407.8	2103.5	6930.15	8348.06	97.38	10116.08	14154.42	202.84	5084.74	8482.87	55.55	163.73	211.41	30.34	11183.51	15989.06	124.08	<LOD	#VALUE!	4143.6
15	TSF	4594	36335.8	68656.4	1004.1	325933	697268.5	1578.8	4933.5	11305	2161.2	8086.2	9740.66	112.3	4797.48	6712.634	65.66	5409.63	9024.89	55.05	172.94	223.3	28.44	11229.36	16032.62	116.53	<LOD	#VALUE!	3912.87
16	TSF	4595	44898.5	84835.8	1150.2	284140.6	607862	1396.5	1011.5	2317.6	241.96	11748.4	14152.1	170.9	8010.71	11208.59	103	6503.14	10849.1	73.4	486.47	628.13	37.25	28889.01	41302.62	194.86	4158.14	6895.44	2024.48
17	TSF	4596	35419.8	66925.6	1060.4	224720.1	480743.7	1258.2	864.17	1980.2	228.38	12483.4	15037.5	173.6	5046.5	7061.063	73.78	5890.04	9826.35	63.37	287.26	370.91	32.49	24765.97	35407.91	173.52	<LOD	#VALUE!	3842.46
18	TSF	4597	38802	73316.3	1074.8	296608.5	634534.6	1363.8	1024.6	2347.7	243.34	11388.5	13718.6	139	7630.48	10676.57	85.83	5743.3	9581.55	70.45	176.9	228.41	30.14	13982.47	19990.74	133.48	<LOD	#VALUE!	4308.86
19	TSF	4598	54838.1	103616	1390.2	234064.1	500733.4	1300.7	862.74	1976.9	242.87	15844.6	19086.4	204	7982.79	11169.52	106.62	7667.59	12791.8	87.65	351.67	454.08	36.13	32730.05	46794.15	213.46	5077.66	8420.28	2577.75
20	TSF	4599	48008.9	90712.8	1296.7	254908	545324.7	1341.3	697.3	1597.8	246.6	13287.1	15999.2	178.1	4635.74	6486.327	82.98	7730.92	12897.5	86.54	320.11	413.33	35.4	25026.16	35779.9	185.62	<LOD	#VALUE!	4046.53
21	TSF	4600	40534.1	76589.2	1248.9	228350	488509.1	1327.1	<LOD	#####	367.94	10275.3	12377.7	144.8	6337.29	8887.136	81.98	6500.09	10844.1	68.42	235.46	304.03	31.95	18292.69	26153.06	156.04	<LOD	#VALUE!	4228.24
22	TSF	4601	51939.8	98140.2	1376	253142.4	541547.6	1350.7	864.73	1981.4	248.84	13696.1	16498.3	179.6	2256.35	3157.085	64.79	6749.16	11259.6	78.75	300.83	388.43	35.07	26058.22	37255.44	191.16	4758.06	7890.29	2708.36
23	TSF	4602	59029.4	111536	1537.7	234633	501950.3	1447.5	<LOD	#####	3604.7	14689.3	17694.7	231.6	10895.47	15244.94	322.71	7825.88	13055.9	105	859.56	1109.9	51.23	65062.14	93019.34	336.39	7334.58	12162.9	2946.15
24	TSF	4603	31072.2	58710.9	943.76	275298	588944.9	1321.3	647.06	1482.7	227.74	10271.8	12373.4	148.3	6332.19	8860	78.77	5835.44	9735.26	62.45	219.65	283.61	31.86	18899.4	27020.47	157.09	<LOD	#VALUE!	3916.69
25	TSF	4604	45161.3	85332.3	1148.5	293688.2	628287.1	1352.3	1045.5	2395.6	248.69	12267.2	14777	161.9	7123.08	9966.614	91.98	7349.45	12261.1	83.12	313.57	404.88	34.26	22141.11	31655.14	169.79	4202.32	6968.71	2008.02
26	TSF	4605	14812.5	27988.2	612.08	93560.86	200154.7	837.34	477.79	1094.8	146.3	9455.19	11389.7	134.8	4938.75	6910.299	75.02	7998.48	13343.9	74.8	224.88	290.37	30.93	19038.91	27219.93	155.9	<LOD	#VALUE!	3454.24
27	TSF	4606	22788.2	43058.3	848.42	354837.9	759104.8	1438	630.78	1445.4	261.28	6747.37	8127.88	108.6	28044.58	39239.98	317.91	4389.53	7323.05	52.59	236.73	305.67	30.35	11173.06	15974.12	118.76	<LOD	#VALUE!	2453.07
28	TSF	4607	36603	69161.4	1057.9	323280.8	691594.5	1398.3	1099.6	2519.6	260.48	10270.6	12371.9	136.9	11762.71	16458.38	229.28	5805.24	9684.88	66.19	250.85	323.9	31.97	17288.47	24717.33	148.17	7235.4	11998.5	2145.38
29	TSF	4609	43457.2	82112.4	1345.9	264485.1	565813	1390	942.66	2160	256.64	12444.1	14990.1	177.9	4066.84	5690.323	78.83	5918.82	9874.37	78.32	328.57	424.25	35.17	25104.8	35892.33	185.12	<LOD	#VALUE!	5944.85
30	TSF	4610	41485	78385.9	1135.2	290989.2	622513.1	1370.4	942.52	2159.7	251.9	11410.2	13744.7	155.3	10681.1	14945	232.69	7083.77	11817.9	86.45	293.24	378.63	33.59	20174.16	28843	162.15	<LOD	#VALUE!	3114.96
31	TSF	4611	54971.2	103868	1657.3	207507.4	443920.6	1356.1	771.27	1767.3	267.29	16716.1	20136.2	220.3	7690.63	10760.73	112.76	7718.53	12876.8	94.29	423.03	546.22	39.24	38768.17	55426.85	240.7	6042.51	10020.3	3710.12
32	TSF	4612	26300.5	49694.9	1246.7	253811.5	542979	1432.5	522.61	1197.5	267.92	7173.95	8641.74	176.1	37088.67	51894.47	575.66	2939.87	4904.59	76.07	1504	1942	64.39	93291.65	133379.1	446.15	5554.58	9211.16	3550.61
33	TSF	4614	48059.4	90808.2	1657.2	167712.8	358788.1	1313.7	<LOD	#####	570.58	12215.4	14714.6	175.5	14246	19993	289.39	4968.84	8289.52	76.23	284.59	367.46	34.44	25753.85	36820.28	188.93	<LOD	#VALUE!	6204.09
34	TSF	4615	39400.9	74448	1401.4	210547.1	450423.3	1350.1	<LOD	#####	397.51	10204.6	12292.4	158.9	14326.21	20045.23	284.42	5812.92	9697.69	71.46	318.62	411.4	36.3	30666.82	43844.35	210.6	<LOD	#VALUE!	5410.07
35	TSF																												



Core	Reading No	Al	Al2O3	Al Error	Si	SiO2	Si Error	P	P2O5	P Error	K	K2O	K Error	Ca	Ca Error	Ti	TiO2	Ti Error	Mn	MnO	Mn Error	Fe	Fe2O3	Fe Error	Mg	MgO	Mg Error		
48	T5F	4630	47806	90329.5	1391.8	256035.7	547737.2	1347.9	661.34	1515.4	254.03	12626.7	15210.1	190.5	7369.79	10311.81	109.4	6994.01	11668.1	82.54	476.59	615.37	38.66	40063.13	57278.26	236.82	<LOD	#VALUE!	5187.96
49	T5F	4631	49959.7	94398.8	1650.3	168107.3	359631.8	1278.9	389.82	893.23	252.61	14788.6	17814.3	202.8	6635.97	9285.049	104.11	6487.26	10822.7	80.28	349.91	451.8	36.33	36649.2	52397.36	228.82	<LOD	#VALUE!	6237.48
50	T5F	4632	39821.5	75242.7	1131.3	280035.7	599080.4	1359	591.16	1354.6	245.34	10748.1	12947.2	149.5	22524.27	31515.96	319.44	4552.66	7595.2	72.88	301.63	389.46	33.19	20802.85	29741.83	165.21	<LOD	#VALUE!	3220.42
51	T5F	4633	64096.6	121111	1769.8	203103.8	434500	1343.3	632.39	1449.1	265.25	18097.1	21799.8	232.7	11510.86	16106	302.01	7169.05	11960.1	108.34	454	586.2	39.71	40002.08	57190.97	243	<LOD	#VALUE!	5292.28
52	T5F	4635	42739.8	80756.8	1365.9	225553.3	482526.3	1480.1	<LOD	#####	3684.7	10873.5	13098.2	166.4	33682.35	47128.34	424.14	5904.46	9850.41	86.81	439.5	567.48	38.42	24824.56	35491.67	186.97	6207.28	10293.5	3161.27
53	T5F	4636	<LOD	#VALUE!	1328.1	7741.72	16561.86	868	507.02	1161.8	274.01	10172.5	12253.8	226.6	15195.82	21261.99	411.57	5307.99	8855.32	120.49	407.69	526.41	52.09	27303.36	39035.61	280.13	<LOD	#VALUE!	5696.53
54	T5F	4637	48116.7	90916.5	1442.1	206307.1	441352.8	1318.2	790.93	1812.3	247.22	12868.7	15501.7	183.9	8620.28	12061.5	110.96	6813.71	11367.3	97.3	390.83	504.64	37.58	31327.29	44788.63	211.51	5874.11	9741.04	3263.23
55	T5F	4638	43859.7	82872.9	1343.8	242011.2	517734.5	1363.1	546.77	1252.9	257.17	10027.5	12079.1	149.1	7572.79	10595.85	92.53	5444.6	9083.23	94.57	291.9	376.9	33.49	19780.42	28280.07	162.85	5071.58	8410.2	3057.99
56	T5F	4639	50048.2	94566	1648.8	188968.5	404260.2	1370.6	<LOD	#####	601.92	16269.8	19598.6	202.4	4540.34	6352.844	84.03	6273.26	10465.7	81.15	403.03	520.39	36.8	31147.13	44531.05	208.73	<LOD	#VALUE!	5694.44
57	T5F	4640	41348.8	78128.5	1511.8	220862.6	472491.3	1368.9	688.56	1577.8	264	10387.7	12513.1	157.6	8256.46	11552.44	99.71	5516.88	9203.81	87.87	309.54	399.68	33.72	23865.1	34119.93	176.99	<LOD	#VALUE!	8324.91
58	T5F	4641	48617.2	91862.2	1449.5	240221.9	513906.7	1332.3	920.82	2110	258.37	10563.8	12725.2	172	15998.24	22384.74	319.63	6310.18	10527.3	84.98	508.73	656.87	38.64	39421.76	56361.29	233.05	<LOD	#VALUE!	5766.4
59	T5F	4642	47665.3	90065.3	1833.8	195459.6	418146.7	1386	578.93	1326.6	268.73	11610.3	13985.7	173.2	4735.77	6626.289	84.09	5045.28	8417.04	81.64	386.53	499.09	36.07	30943.3	44239.64	205.48	<LOD	#VALUE!	10262.7
60	T5F	4643	48468.9	91582.1	1779.8	175454.4	375349.6	1314.4	<LOD	#####	365.94	13842.8	16675	208.5	3271.98	4578.154	85.35	5907.27	9855.1	99.19	499.68	645.19	39.85	44078.23	63018.65	254.32	<LOD	#VALUE!	9598.18
61	T5F	4644	37390.7	70649.7	1535.8	199280.1	426319.9	1427.4	442.5	1013.9	273.17	13823.3	16651.6	199.4	4510.98	6311.763	90.26	8253.96	13770.1	89.61	431.85	557.6	39.62	38558.86	55127.05	240.02	<LOD	#VALUE!	6363.91
62	T5F	4645	17717.7	33477.6	960.75	318423.2	681202.8	1460.3	<LOD	#####	692.2	3525.87	4247.26	103	100613.5	140778.4	612.87	3434.55	5729.86	57.55	430.63	556.03	34.83	6204.93	8871.188	75.57	<LOD	#VALUE!	3666.1
63	T5F	4646	43205.6	81637	1620.2	198863.4	425428.6	1402	1262.2	2892.2	280.16	11422.9	13760	170.9	23352.84	32675.29	371.67	5842.97	9747.83	81.09	521.03	672.75	40.21	34549.01	49394.72	224.38	<LOD	#VALUE!	7162.89
64	T5F	4647	26722.2	50491.6	1584.6	134040.6	286753.1	1346.1	<LOD	#####	592.18	11322.4	13639	166.2	5584.69	7814.098	84.16	5605.2	9351.16	65.86	286.61	370.70	34.84	27896.4	39883.48	198.22	<LOD	#VALUE!	11619.4
65	T5F	4648	46706.2	88251.3	1610.1	196124.5	419569	1362.7	<LOD	#####	381.4	13810.6	16636.2	194	3631.3	5080.915	81.1	6301.72	10513.2	75.13	372.97	481.58	35.26	33942.18	48527.13	211.33	6546.45	10856	4171.92
66	T5F	4649	44557.9	84192.1	1608.3	194769.4	416670.3	1383.4	461.95	1058.5	260.88	14643.2	17639.2	193.7	3113.46	4356.353	73.78	6765.76	11287.3	74.13	333.49	430.6	34.97	30875.78	44143.1	204.85	<LOD	#VALUE!	7268.16
67	T5F	4650	29561.2	55855.8	1553.4	105097.1	224834.3	1210.6	<LOD	#####	385.07	9828.11	11838.9	138.1	6334.5	8863.232	83.96	3386.7	5650.03	51.72	288.93	373.07	32.92	24523.27	35060.92	179.19	<LOD	#VALUE!	8292.72
68	T5F	4651	42727.4	80733.4	1616	150536.2	322042	1289	468.86	1074.3	266.5	10806.5	13017.5	165.6	14771.08	20667.7	291.96	5496.88	9170.44	71.9	288.98	373.13	34.28	26334.04	37649.78	190.99	<LOD	#VALUE!	6572.12
69	T5F	4652	32922.3	62206.6	1729.2	148627.3	317958.4	1358.2	<LOD	#####	623.62	10027.7	12079.3	165.4	10210.34	14286.31	257.98	4341.73	7243.31	63.36	454.34	586.64	37.32	37650.46	53828.86	221.99	<LOD	#VALUE!	12213.6
70	T5F	4653	36293.6	68576.7	1330.5	177066.1	378797.5	1310.8	<LOD	#####	383.5	12701.5	15300.2	170.2	15605.06	21834.6	284.61	4219.11	7038.74	56.97	230.17	297.2	32.68	21406.32	30604.62	169.57	<LOD	#VALUE!	5032.4
71	T5F	4654	46592	88035.5	1582.9	189260.7	404885.4	1335.4	392.73	899.9	247.77	14554.7	17532.6	189.3	3912.67	5474.608	76.12	5832.45	9730.28	73.79	318.75	411.57	35.65	29340.61	41948.27	202.4	<LOD	#VALUE!	7220.88
72	T5F	4655	37693.2	71221.2	1637.6	144533.5	309200.4	1329.5	<LOD	#####	608.49	15219.2	18333.1	192.6	1911.39	2674.417	63.04	6594.38	11001.4	72.31	252.37	325.86	33.09	25513.78	36477.05	186.91	<LOD	#VALUE!	7633.25
73	T5F	4656	15742.4	29745.2	899.2	307827.5	658535.4	1414.9	<LOD	#####	402.97	3680.58	4433.63	106.8	100917.4	141203.6	622	2941.83	4907.85	54.55	427.26	551.68	33.92	5510.38	7878.19	70.38	<LOD	#VALUE!	5093.37
74	T5F	4657	50523.7	95464.6	1773.5	163106.2	348933	1316.8	1462.7	3351.7	258.03	13298	16018.8	218.9	12543.41	17550.74	340.6	7170.86	11963.1	100.27	872.37	1126.4	48.67	59817.39	85520.92	312.6	8108.12	13445.7	4593.14
75	T5F	4658	55843.5	105516	1643.8	187058.7	400174.6	1310	2849.5	6529.3	260.32	11111.1	13384.4	194.5	27062.32	37865.6	447.39	6970.89	11629.5	98.96	927.92	1198.1	50.22	52545.4	75124.16	293.62	<LOD	#VALUE!	5223.15
76	T5F	4659	31780.2	60048.7	1567.8	125896.4	269330.3	1184.9	4426.7	10143	255.38	9292.73	11194	258.4	25554.05	35755.23	639.17	2680.91	4472.56	82.78	3169.8	4092.9	91.72	200318.6	286395.6	952.35	10543.7	17484.7	5357.4
77	T5F	4660	43043.7	81331.1	1487.7	204384.7	437240.2	1366	512.24	1173.7	254.99	15727.7	18945.5	202.1	3091.11	4325.081	76.51	6810.97	11362.7	77.45	298.08	384.88	35.3	32092.48	45882.62	211.36	<LOD	#VALUE!	6004.16
78	T5F	4662	66648.6	125933	1509.6	211969.3	453465.9	1251.4	514.82	1179.7	237.92	21395.5	25773	245.6	15162.61	21215.52	332.46	8490.01	14163.9	98.27	358.59	463.01	38.4	39478.48	56442.38	242.22	<LOD	#VALUE!	3568.58
79	T5F	4663	48492.9	91627.4	1208.3	260072.3	556372.6	1309.8	803.01	1840	229.59	15289.4	18417.6	201.6	21123.24	16976.83	284.96	7779.67	12978.8	85.67	461.46	595.84	39.52	33946.45	48533.24	220.48	5227.76	8669.19	2137.48
80	T5F	4664	47114.6	89023	1552.6	200343.5	428594.8	1344.8	<LOD	#####	382.09	14110.5	16997.5	193.3	4964.94	6946.944	89.7	6465.04	10785.6	76.59	349.33	451.05	35.19	33829.9	48366.61	207.87	<LOD	#VALUE!	5718.45
81	T5F	4665	43964.7	83071.4	1118.4	253486.2	542283.1	1284.7	661.87	1516.6	223.05	10150.5	12227.3	155.4	24058.12	33662.12	351.13	4857.98	8104.57	71.88	339.92	438.9	35.09	25940.58	37087.25	186.52	<LOD	#VALUE!	2927.43
82	T5F	4666	57697.2	109019	1367.1	214969.1	459883.5	1260	632.18	1448.6	226.83	18281.4	22021.8	217.5	7079.31	9905.371	99.02	7257.16	12107.1	81.69	290.45	375.03	34.99	30146.88	43100.99	202.2	<LOD	#VALUE!	3434.59
83	T5F	4667	27341.7	51662.1	1294.8	126118.1	269804.5	1119.4	512.54	1174.4	178.69	5978.22	7201.36	219.3	21226.57	29700.22	607	2129.22	3552.18	81.03	3520.5	4545.7	99.93	239428.6	342311	1169.4	11328.2	18785.5	4031.46
84	T5F	4668	55719.4	105282	1415.9	234074.8	500756.2	1298.1	647.54	1483.8	227.3	16705.6	20123.5	216.6	5576.62	7802.807	98.15	6754.51	11268.5	88.5	398.72	514.							



Table A.2.6: Calculated results from geochemical analysis of the sandstones in the Thebaud E-74 (T5) H2 full diameter cores.

1	Core	Reading No	Al	Al2O3	Al Error	Si	SiO2	Si Error	P	P2O5	P Error	K	K2O	K Error	Ca	CaO	Ca Error	Ti	TiO2	Ti Error	Mn	MnO	Mn Error	Fe	Fe2O3	Fe Error	Mg	MgO	Mg Error
2	TSH	4670	15082.6	28498.6	711.37	367253.5	785665.5	1460.3	563.79	1291.9	257.8	2139.45	2577.18	59.73	15106.56	21137.1	209.67	2489.12	4152.6	52.05	154.67	199.71	26.64	4115.15	5883.43	58.5	4377.79	7259.69	1709.98
3	TSH	4671	8020.19	15154.1	649.66	359166.9	768365.8	1464.5	<LOD	#VALUE!	481.19	1456.1	1754.02	60.35	32875.23	45999.02	338.29	1645.14	2744.59	40.55	244.59	315.81	29.73	12848.81	18369.94	125.8	3275.9	5432.42	1868.22
4	TSH	4672	14613.2	27611.7	663.36	368755.4	788878.4	1458.7	442.25	1013.4	247.51	3816.74	4597.65	71.65	5809.99	8129.338	61.59	2243.23	3742.38	55.53	124.15	160.3	26.4	2448.14	3500.106	46.76	<LOD	#VALUE!	2408.51
5	TSH	4673	18379.8	34728.7	797.68	307870.3	658627	1372.1	2919	6688.5	264.36	5075.55	6114.01	101.3	32317.61	45218.8	347.28	2674.46	4461.8	88.09	270.27	348.97	30.77	12138.45	17354.34	121.35	3706.59	6146.64	1958.32
6	TSH	4674	10496.4	19833	605.85	337453.1	721913.5	1618.5	4636.1	10623	1132.5	2905.55	3500.03	64.45	3544.1	4958.905	49.88	5927.38	9888.65	90.26	129.52	167.24	27.64	1293.32	1849.06	35.78	<LOD	#VALUE!	2212.45
7	TSH	4675	9434.86	17827.2	544.35	359924.2	769985.8	1414.1	850.14	1948	230.87	2261.18	2723.82	51.34	2158.46	3020.117	35.15	2041.3	3405.5	37.92	50.2	64.818	24.64	817.73	1169.109	30.04	<LOD	#VALUE!	2417.84
8	TSH	4676	19054.9	36004.2	718.27	406083.2	868733.8	1459.6	760.07	1741.6	259.47	3152.34	3797.31	61.85	916.99	1283.052	27.35	2327.62	3883.17	40.79	85.92	110.94	25.34	664.59	950.1643	27.76	2660.53	4411.96	1437.09
9	TSH	4677	6322.05	11945.5	442.82	239435.5	512224.4	1245.4	376.13	861.86	179.3	2180.27	2626.35	42.86	1525.96	2135.123	26.25	1472.68	2456.87	25.19	67.66	87.363	26.35	1153.41	1649.03	36.14	<LOD	#VALUE!	2948.34
10	TSH	4678	16758.3	31664.7	740.02	370658.8	792950.5	1434.5	694.19	1590.7	261.57	3816.94	4597.89	76.17	12813.24	17928.25	196.51	2120.58	3537.76	54.98	162.2	209.43	27.96	5443.59	7782.701	83.98	3917.31	6496.08	1734.57
11	TSH	4679	27785.1	52499.9	810.82	356101.9	761808.8	1417.4	790.38	1811.1	237.23	7997.59	9633.9	103	949.75	1328.89	34.72	3635.18	6064.57	51.79	80.69	104.19	26.39	6100.45	8721.813	89	<LOD	#VALUE!	3070.26
12	TSH	4681	14913.8	28179.6	681.16	385931.3	825622.9	1412.7	694.42	1591.2	259.64	3667.13	4417.42	67.82	1590.83	2225.889	34.65	3246.37	5415.92	48.68	84.02	108.49	24.5	1848.49	2642.786	39.71	2327.83	3860.24	1522.02
13	TSH	4682	11966.2	22610.1	660.39	395186.3	845422.1	1447.3	<LOD	#VALUE!	395.01	2921.25	3518.94	65.92	11191.06	15658.53	181.71	2177.23	3632.27	39.63	99.78	128.84	26.24	5004.58	7155.048	79.71	<LOD	#VALUE!	3507.24
14	TSH	4683	10076.7	19039.9	690.36	387701.3	829409.5	1447.5	496.92	1138.6	278.1	1494.53	1806.48	64.02	31079.53	43486.46	334.22	1073.28	1790.55	52.72	274.58	354.54	30.26	11962.81	17103.23	119.8	<LOD	#VALUE!	2637.61
15	TSH	4684	15490.3	29268.8	665.26	383289	819970.1	1411	517.22	1185.2	245.35	3691.01	4446.19	68.45	4635.96	6486.635	53.92	2376.7	3965.05	38.46	58.8	75.923	24.62	1702.03	2433.392	39.85	<LOD	#VALUE!	3455.57
16	TSH	4685	7279.71	13755	543.61	403980	864234.4	1454.4	630.1	1443.8	253.4	1956.94	2357.33	50.21	2515.01	3519.002	38.55	2967.79	4951.16	39.75	84.2	108.72	25.31	905.97	1295.265	31.1	<LOD	#VALUE!	2493.44
17	TSH	4686	23529.9	44459.9	755.96	336986.8	720915.9	1377.8	579.03	1326.8	230.52	7216.16	8692.59	96.78	2855.48	3995.388	48.17	6973.88	11634.5	72.17	117.6	151.85	27.17	2097.06	2998.167	44.06	2428.55	4027.26	1513.15
18	TSH	4687	10686.2	20191.6	584.55	358208.5	766315.4	1411.1	797.96	1828.4	240.85	3698.45	4455.15	66.41	4007.1	5606.734	49.07	1279.97	2135.37	27.33	45.6	58.879	23.22	1414.89	2022.868	35.42	<LOD	#VALUE!	1911.1
19	TSH	4688	33762.6	63794.4	927.97	300254.2	642333.9	1336	796.15	1824.3	226.82	10629.2	12803.9	130.1	1471.89	2059.468	45.45	3142.77	5243.08	58.22	97.31	125.65	26.93	8937.7	12778.23	105.53	<LOD	#VALUE!	3863.54
20	TSH	4689	34892.1	65928.5	1091.3	207404.6	443700.7	1193.9	<LOD	#VALUE!	559.17	12197.5	14693.1	180	722.18	1010.474	51.1	5666.35	9453.17	76.17	146.77	189.51	32.82	44772.12	64047.02	252.76	<LOD	#VALUE!	5092.63
21	TSH	4690	16888.9	31907.9	944.15	272332.7	582601.3	1402.1	<LOD	#VALUE!	391.93	5627.53	6778.92	138.8	72321.38	101192.1	632.06	2092.91	3491.6	87.05	691.97	893.47	43.18	36261.84	51433.55	230.83	<LOD	#VALUE!	5750.43
22	TSH	4691	36503	68972.3	1009.9	253256.5	541791.6	1295.5	473.48	1084.9	223.92	11380.1	13708.4	124.1	1963.68	2747.581	46.29	4259.59	7106.27	73.62	122.84	158.61	27.67	6626.39	9473.75	92.69	<LOD	#VALUE!	3086.89
23	TSH	4692	9983.76	18864.3	703.98	369810.6	791135.9	1452.2	<LOD	#VALUE!	406.9	2752.16	3315.25	82.65	35645.57	49875.28	372.64	2271.25	3789.13	49.23	308.25	398.01	31.14	15431.9	22062.99	134.85	6741.61	11179.6	2076.18
24	TSH	4693	15697.4	29680.2	669.11	364305.5	779358.8	1443.3	541.11	1239.9	244.38	4824.17	5811.2	78.99	1598.09	2236.048	36.86	3686.71	6150.54	67.94	78.72	101.64	25.66	1453.24	2077.697	37.17	<LOD	#VALUE!	3359.39
25	TSH	4694	20538.3	38807	742.98	338298.5	723721.9	1408	660.49	1513.4	245.24	6199.5	7467.92	89.93	2936.12	4108.219	57.92	3022.07	5044.72	67.39	83.07	107.26	26.04	2388.35	3433.624	46.94	<LOD	#VALUE!	2047.88
26	TSH	4695	10343.6	19544.2	634.52	268293.6	573960.6	1369.1	<LOD	#VALUE!	363.65	3634.91	4378.61	76.84	4291.11	6004.121	49.98	2316.58	3864.75	159.37	277.59	487.16	34.44	2051.51	2914.044	44.97	<LOD	#VALUE!	2592.92
27	TSH	4696	12542.4	23698.9	615.21	384304.1	822141.8	1412	821.33	1882	246.61	3200.64	3855.49	59.5	1308.62	1831.021	29.58	2342.56	3908.09	58.05	71.91	92.45	24.16	810.75	1159.129	28.78	2317.02	3842.31	1407.67
28	TSH	4697	21549.8	40718.4	982.95	284366.3	608344.8	1396.1	890.9	2041.4	262.61	6774.75	8160.86	135.4	63315.23	88590.67	549.61	2146.44	5808.91	57.73	561.26	72.87	39.01	29615.78	42341.68	202.81	4354.75	7221.48	2572.23
29	TSH	4698	18710.4	35353.4	910.85	279654.7	598265.3	1379.9	<LOD	#VALUE!	373.54	6055.9	7294.94	129.3	60082.21	84067.03	548.14	2029.08	3385.11	51.06	555.26	716.95	38.51	28848.1	41244.13	195.88	4324.71	7171.67	2464.48
30	TSH	4699	11238.5	21235.1	801.04	298674.9	638955.2	1404.8	<LOD	#VALUE!	384.09	2530.37	3048.08	103.3	71671.23	100282.4	596.17	2036.76	3397.93	57.47	592.58	765.14	39.71	31720.94	43531.43	202.32	<LOD	#VALUE!	4337.62
31	TSH	4700	12149	22955.5	779.33	322533.2	689995.2	1410.3	<LOD	#VALUE!	387.64	3163.01	3810.16	101.3	61624.98	82265.61	531.23	1578.5	6233.41	44.88	541.23	698.84	38.24	27029.68	38684.33	189.81	3809.88	6317.92	2201.56
32	TSH	4701	8322.29	15725	567.91	388198.1	830472.2	1447.9	499.88	1145.4	252.83	1890.26	2277.01	48.35	1627.49	2277.184	31.4	2291.1	3822.24	33.25	69.28	89.454	24.4	863.35	1234.321	29.87	<LOD	#VALUE!	1908.37
33	TSH	4702	9613.5	18198.7	610.5	352279.8	753632.1	1429.5	<LOD	#VALUE!	366.47	2494.24	3004.56	59.39	2675.71	3743.853	42.97	1760.46	2936.98	40.51	60.42	78.044	24.59	1757.94	2513.327	40.39	3068.96	5089.26	1757.59
34	TSH	4703	17886.1	33795.9	836.83	328804.4	703411.3	1420.3	<LOD	#VALUE!	390.27	5967.04	7187.9	114.3	39808.05	55699.42	401.65	3058.89	5103.15	54.3	339.57	438.45	31.9	17727.48	25344.98	145.85	<LOD	#VALUE!	2920.2
35	TSH	4704	41722.1	78833.9	1313.3	228539.9	488915.5	1302.3	<LOD	#VALUE!	491.21	12970.6	15624.3	189.9	44805.61	62692.01	507.13	4544.09	7580.91	76.22	528.61	682.54	41.47	42012.18	60964.81	254.45	<LOD	#VALUE!	5920.33
36	TSH	4705	46568.4	87991	1305.7	213844.8	457478.2	1276.5	<LOD	#VALUE!	341.34	16113.7	19410.5	202.9	45127.38	63142.23	493.22	5527.19	9221.01	81.25	550.97	711.41	40.44	31795.04	45457.37	214.1	5170.63	8574.46	2576.7
37	TSH	4706	19700.6	37224.3	752.12	372089.5	796011.1	1428.6	615.42	1410.2	253.88	3176.79	3826.76	63.81	6948.57	9722.439	63.16	2052.51	3424.2	34.06	89.93	116.12	25.31	3749.3	5360.374	69.72	2675.05	4436.04	1555.05
38	TSH	4707	11766	22231.8	625.94	382224.7	817693.3	1457	1194.6	2737.4	253.22	2370.83	2855.9	64.58	15832.06	22152.22	224.99	1751.12	2921.39										

Table A.2.7: Log-ratio estimates from corresponding oxide ratios from the Migrant N-20 well.

1	SiO2/Al2O3	Fe2O3/K2O		LogSiO2/Al2O3	LogFe2O3/K2O
2	10.525824	6.59935444		1.022256096	0.819501454
3	12.531606	3.39114606		1.09800674	0.530346496
4	14.292605	2.73081018		1.155111391	0.436291513
5	9.5511982	3.49500666		0.980057859	0.543448007
6	4.7163404	2.47878223		0.673605142	0.394238374
7	9.4688945	2.92300073		0.976299276	0.465828924
8	10.188634	3.61067917		1.008115959	0.5575889
9	14.22263	4.00350663		1.152979908	0.602440552
10	7.2012721	2.82205117		0.857409224	0.450564884
11	7.0834904	3.48425469		0.850247312	0.542109894
12	7.4733417	2.08655737		0.873514842	0.319430331
13	14.871691	2.90653318		1.172360351	0.463375286
14	25.97841	2.23708886		1.414612564	0.349683235
15	36.910629	0.97811426		1.567151446	-0.009610412
16	35.559709	2.30054387		1.550958204	0.361830519
17	27.872405	2.52717323		1.44517444	0.402635013
18	9.0404158	1.77259127		0.956188406	0.248608605
19	24.060255	4.16424177		1.381300231	0.619535936
20	20.330646	4.08909795		1.308151176	0.611627514
21	19.906108	2.11655639		1.298986352	0.325629843
22	12.571241	3.55755398		1.099378153	0.551151499
23	23.175197	6.02747198		1.365023437	0.7801352
24	37.699489	7.73492002		1.576335464	0.888455827
25	39.509795	2.69033677		1.596704781	0.429806647
26	9.2919994	3.14211908		0.968109174	0.497222639
27	7.9077403	7.01013652		0.898052399	0.845726476
28	20.826816	5.67641852		1.318622873	0.754074408
29	29.344576	6.09526838		1.467527832	0.784992833
30	28.769289	4.27133309		1.458929133	0.63056344
31	27.953328	10.3212679		1.446433518	1.01373305
32	17.216502	5.49001073		1.235944922	0.739573193
33	23.546085	3.45165332		1.371918714	0.538027169
34	21.943068	4.19594213		1.341297358	0.62282949
35	11.741187	4.9597615		1.069712014	0.695460793
36	17.444413	3.71298587		1.241656359	0.569723296
<b>Average</b>				<b>1.205660944</b>	<b>0.553616595</b>

Table A.2.8: Log-ratio estimates from corresponding oxide ratios from the Adamant N-97 well.

1	SiO <sub>2</sub> /Al <sub>2</sub> O <sub>3</sub>	Fe <sub>2</sub> O <sub>3</sub> /K <sub>2</sub> O	LogSiO <sub>2</sub> /Al <sub>2</sub> O <sub>3</sub>	LogFe <sub>2</sub> O <sub>3</sub> /K <sub>2</sub> O
2	18.9028697	1.849686	1.27652774	0.267098108
3	38.9372555	2.027323	1.590365337	0.306922871
4	45.7362765	2.752031	1.660260805	0.439653276
5	33.5742018	3.171203	1.526005697	0.501223992
6	16.6970672	1.737786	1.222640194	0.239996181
7	92.8896808	1.219376	1.967967471	0.086137555
8	3.99812434	2.593875	0.601856297	0.413948963
9	5.26542357	3.310148	0.721433313	0.519847357
10	12.9664517	10.06529	1.112821145	1.002826282
11	23.1722097	1.404982	1.364967449	0.147670645
12	19.0741284	2.344127	1.280444702	0.369981143
13	7.65543923	8.300248	0.883970113	0.91909109
14	38.8912166	3.797665	1.589851529	0.579516616
15	10.2875056	1.885967	1.012310086	0.27553399
16	38.4232033	2.95247	1.584593569	0.470185498
17	5.73116705	2.641041	0.758243067	0.421775064
18	30.0629134	1.075587	1.478031065	0.031645441
19	16.3606206	1.849026	1.213799774	0.266943039
20	76.8458341	1.967572	1.885620329	0.293930613
21	53.4912859	1.931317	1.728283039	0.285853661
22	135.080259	6.175439	2.130591883	0.790667842
23	3.43255524	1.673999	0.535617535	0.223755196
24	3.93699563	2.164381	0.595164933	0.335333758
25	22.5609061	1.542108	1.353356539	0.188114897
26	53.1037189	2.678745	1.725124936	0.427931439
27	81.455357	2.193414	1.910919651	0.34112067
28	31.7412323	1.007357	1.501623783	0.003183369
29	133.134378	0.614245	2.124290213	-0.211658653
30	6.78646957	1.766443	0.831643906	0.247099561
31	34.3883207	2.589571	1.536410968	0.413227749
32	24.7981485	0.81806	1.394419257	-0.087214587
33	3.17015217	1.40271	0.501080109	0.146967833
34	12.539268	6.845552	1.098272186	0.835408483
35	9.23506292	10.90679	0.965439859	1.03769679
36	3.50549655	1.835705	0.544749544	0.263802864
37	22.7883094	2.671515	1.357712108	0.426757544
38	8.11856588	2.035626	0.909479319	0.308697893
39	41.4453081	0.57348	1.617475372	-0.241482056
40	5.87712727	5.428789	0.769165095	0.734702975
41	3.7311961	5.919134	0.571848075	0.77225819
42	2.99882794	2.688525	0.476951549	0.429514076
43	9.04143689	1.620645	0.956237455	0.209687895
44	104.766313	2.628074	2.020221661	0.419637671
45	58.8605923	1.903342	1.769824628	0.279516801
46	13.1244726	1.852753	1.118081859	0.267817582
47	27.4368254	8.228973	1.438333859	0.915345654
48	9.59412011	9.828826	0.982005151	0.992501628
<b>Average</b>			<b>1.259490088</b>	<b>0.38957818</b>

Table A.2.9: Log-ratio estimates from corresponding oxide ratios from the H2 interval of the Thebaud E-74-T5 well.

	SiO2/Al2O3	Fe2O3/K2O	LogSiO2/Al2O3	LogFe2O3/K2O
1				
2	27.5685904	2.28289316	1.44041456	0.358485587
3	50.7033269	10.4730641	1.705036456	1.020073764
4	28.5704822	0.7612823	1.45591757	-0.118454268
5	18.9649262	2.8384561	1.277951156	0.453082182
6	36.3996026	0.52829889	1.561096642	-0.277120301
7	43.1917072	0.42921694	1.635400371	-0.367323146
8	24.1286941	0.25022045	1.382533817	-0.601677192
9	42.8800626	0.62787833	1.63225541	-0.202124508
10	25.0420854	1.69266936	1.398670492	0.228572133
11	14.5106589	0.90532559	1.161687134	-0.043195206
12	29.2985551	0.59826398	1.466846203	-0.223107142
13	37.3913196	2.0332977	1.572770792	0.308200969
14	43.5615945	9.50015358	1.639103768	0.977730626
15	28.015115	0.54729823	1.447392409	-0.261775953
16	62.8305094	0.54946289	1.798170581	-0.260061635
17	16.2149986	0.34491077	1.209916916	-0.462293239
18	37.9522342	0.45405136	1.579237348	-0.342895016
19	10.0688073	0.9979915	1.002978031	-0.000873156
20	6.73002622	4.35652605	0.828016756	0.639140315
21	18.258856	7.64775694	1.261473563	0.883534077
22	7.85520119	0.69109043	0.895157313	-0.160465119
23	41.9382257	6.65499572	1.622610053	0.82314778
24	26.2762145	0.35753355	1.419562798	-0.446683202
25	18.6492509	0.4572391	1.270661393	-0.339856635
26	29.3673175	0.6698569	1.467864279	-0.174017966
27	34.6911348	0.30064376	1.540218507	-0.521947813
28	14.9402852	5.18838219	1.174358887	0.71503196
29	16.9224386	5.65380178	1.228462948	0.752340578
30	30.0895387	14.8786688	1.478415529	1.172564077
31	30.0578999	10.1424388	1.477958634	1.006142398
32	52.8123319	0.54208502	1.722735344	-0.265932593
33	41.4112731	0.8365037	1.617118582	-0.077532133
34	20.8135348	3.52606337	1.318345843	0.547290113
35	6.20183915	3.84431131	0.792520498	0.584818549
36	5.19914975	2.34189112	0.715932327	0.369566699
37	21.3841768	1.40076004	1.330092536	0.146363743
38	36.7803789	3.33306266	1.565616198	0.522843478
39	35.7423311	0.55705953	1.553182874	-0.254098388
40	30.9080524	0.49971933	1.49007164	-0.301273851
41	12.8672211	1.93969486	1.109484764	0.287733416
42	41.3541435	0.4356741	1.616519031	-0.360838262
43	9.82532115	1.56233552	0.992346755	0.193774306
44	30.7622124	0.96219306	1.488017567	-0.016737782
45	60.1554135	1.15834855	1.779274716	0.063839258
46	43.0822594	2.16855798	1.634298471	0.336171038
47	19.2667829	0.41464202	1.284809203	-0.382326687
48	22.256019	0.36832371	1.347447484	-0.43377032
49	6.65102384	2.14947989	0.822888504	0.332333385
50	36.7493028	0.7181516	1.565249104	-0.14378387
51	24.102531	1.19402176	1.382062649	0.07701224
52	23.5443474	0.55072609	1.371886657	-0.259064353
53	21.557368	3.35205586	1.333595736	0.525311247
54	47.8331434	1.90340478	1.679728922	0.279531156
55	35.5434171	0.47549466	1.550759178	-0.322854352
56	40.8566509	3.12926759	1.611262764	0.495442702
57	18.6338472	1.03385811	1.27030253	0.014460938
58	11.5962663	0.92485769	1.06431818	-0.033925088
59	10.3279659	1.80320831	1.014014796	0.256045899
<b>Average</b>			<b>1.380276262</b>	<b>0.115768542</b>



Table A.2.10: Log-ratio estimates from corresponding oxide ratios from the F3 interval of the Thebaud E-74-T5 well.

	SiO <sub>2</sub> /Al <sub>2</sub> O <sub>3</sub>	Fe <sub>2</sub> O <sub>3</sub> /K <sub>2</sub> O	LogSiO <sub>2</sub> /Al <sub>2</sub> O <sub>3</sub>	LogFe <sub>2</sub> O <sub>3</sub> /K <sub>2</sub> O
1	14.44899411	6.15788	1.159837614	0.789431209
2	21.62096508	5.617793	1.334875075	0.749565712
3	3.709703591	2.740992	0.56933921	0.437907843
4	15.35201756	2.077691	1.186165459	0.317580886
5	22.92770857	3.557193	1.360360653	0.551107455
6	12.41265545	2.150931	1.0938647	0.332626438
7	16.01815576	1.949039	1.204612512	0.289820597
8	6.906516684	1.902707	0.839259065	0.279371805
9	9.592298451	1.643217	0.981922683	0.215694872
10	5.847534324	1.819264	0.76697278	0.259895677
11	16.09813986	2.214001	1.206775696	0.345177818
12	6.633550119	1.818797	0.821746015	0.259784311
13	11.85349142	1.915303	1.07384629	0.282237554
14	10.15591087	1.64821	1.006718881	0.217012585
15	7.165163559	2.91847	0.855226108	0.465155254
16	7.183254311	2.35464	0.856321242	0.371924514
17	8.654756145	1.457198	0.937254836	0.163518666
18	4.832564458	2.451701	0.684177655	0.389467447
19	6.011555038	2.236361	0.778986828	0.349541955
20	6.378299627	2.112924	0.804704917	0.324883854
21	5.518103824	2.258142	0.741789868	0.353751155
22	4.500339523	5.256909	0.65324528	0.720730484
23	10.03126401	2.183753	1.001355661	0.33920352
24	7.362827166	2.142184	0.867044606	0.33085671
25	7.151402518	2.389868	0.854391223	0.378373879
26	17.62968819	1.965349	1.246244631	0.293439663
27	9.999722728	1.997854	0.999987958	0.300563649
28	6.890714374	2.394396	0.838264248	0.37919603
29	7.941645761	2.098485	0.899910511	0.321905785
30	4.273888494	2.752604	0.630823187	0.439743698
31	10.92626279	15.43428	1.038471642	1.188486487
32	3.951052165	2.502294	0.596712764	0.398338305
33	6.050176356	3.566785	0.781768034	0.552276944
34	18.07972124	14.84174	1.25719173	1.171484874
35	4.393737197	3.020599	0.642834077	0.480093104
36	11.85292562	5.700259	1.073825559	0.755894617
37	12.70497095	2.16531	1.103973676	0.335520102
38	7.193541239	3.241397	0.856942738	0.510732208
39	4.533133159	2.81248	0.656398476	0.449089413
40	7.100228059	3.356225	0.851272298	0.525851015
41	4.090315171	2.825521	0.611756773	0.45109854
42	12.49803061	28.37437	1.096841584	1.452926208
43	4.224994521	2.724337	0.62582615	0.435260872
44	4.97256511	2.832757	0.696580478	0.452209283
45	6.813500418	3.128109	0.833370287	0.495281882
46	4.311404884	2.626935	0.634618809	0.419449319
47	6.063769914	3.765792	0.782742714	0.575856385
48	3.809706367	2.941301	0.580891504	0.468539495
49	7.961969364	2.297162	0.901020502	0.361191581
50	3.587631302	2.623463	0.554807805	0.418874926
51	5.975053181	2.709664	0.776341775	0.432915457
52	4.854482898	2.889275	0.686142975	0.460788859
53	6.247330563	2.341244	0.795694486	0.369446629
54	4.2749002	2.27216	0.63092598	0.356438947

	SiO2/Al2O3	Fe2O3/K2O	LogSiO2/Al2O3	LogFe2O3/K2O
57	5.594323701	4.429125	0.747747592	0.646317898
58	4.642798725	3.163203	0.666779856	0.500127115
59	4.09850517	3.779234	0.612625487	0.577403829
60	6.034278992	3.310657	0.780625386	0.519914196
61	20.34804414	2.088684	1.308522671	0.319872649
62	5.211222322	3.589735	0.716939601	0.555062431
63	5.679224611	2.924221	0.754289045	0.466010192
64	4.754252876	2.916962	0.677082278	0.464930816
65	4.949041447	2.50255	0.694521091	0.398382816
66	4.0252599	2.961491	0.604793927	0.471510429
67	3.988957362	2.892252	0.600859394	0.461236099
68	5.111326352	4.456283	0.708533611	0.648972745
69	5.523702913	2.00027	0.742230312	0.301088717
70	4.599113636	2.392588	0.66267414	0.378867939
71	4.341408141	1.989687	0.637630616	0.298784755
72	22.13921087	1.776918	1.345162137	0.249667346
73	3.655105565	5.33879	0.562899925	0.727442863
74	3.792539733	5.612817	0.578930139	0.749180877
75	4.48520081	25.58469	0.651781892	1.407980102
76	5.376048229	2.421816	0.730463156	0.384141226
77	3.600864627	2.189978	0.556406795	0.340439838
78	6.072121241	2.635149	0.783340434	0.420805127
79	4.814427627	2.845516	0.682544663	0.454160985
80	6.527917257	3.033162	0.814774641	0.481895589
81	4.218386095	1.957198	0.625146327	0.291634742
82	5.22248404	47.53419	0.717877121	1.677006119
83	4.756343161	2.669794	0.677273181	0.426477831
84	14.13819231	8.496692	1.150393885	0.929249853

<b>Average</b>	<b>0.830089301</b>	<b>0.490984654</b>
----------------	--------------------	--------------------



## APPENDIX B.

### B.1. Wireline Logs

Wireline logs are a continuous recording of geophysical rock characteristics of a rock formation measured as a function of borehole depth (Asquith & Krygowski, 2004; Rider & Kennedy, 2011). After a well has been drilled, rock characteristics are recorded by various tools in a wireline-conveyed assembly called a logging tool, which is conveyed across a drilled interval. The data is displayed and analyzed on a log composite for a complete evaluation of the formation. Key wireline logs used in this study include the Gamma-Ray, density, resistivity, sonic and lithology logs (which are acquired and used during the drilling process).

#### B.1.1. Gamma-Ray Log

The Gamma-Ray tool is a passive device that responds to and measures the naturally occurring radioactivity of the formation in API (American Petroleum Institute) units versus depth (Asquith & Krygowski, 2004). All rock units contain some number of radioactive elements including Uranium, Thorium, and Potassium (radioactive isotopes). The Gamma-Ray log reading is a composite of these three elements. The conventional deterministic analysis sequence used in petroleum exploration begins with using the Gamma-Ray log to determine clean versus shale units with depth. From the Gamma-Ray signatures across various lithologies, gross, simplified reservoirs/non-reservoir units can be established. Once the clean vs shale units have been established, the Gamma-Ray logs are used for picking formation tops, correlating well logs, and calculating shale volume  $V_{sh}$ , (normalization of the Gamma- Ray log). Rocks rich in sheet silicates such as clays and mudrocks have a higher potassium and thorium content giving an increased Gamma-Ray response (Asquith & Krygowski, 2004; Rider & Kennedy, 2011).

Gamma-Ray logs are usually scaled increasing from left to right going from 0-150 API units. With increasing clay content, there is an increase in the Gamma-Ray response measured in gamma API Units, measured in counts per second in earlier times (Schlumberger, 2017). Lithologies with a low clay or shale content (i.e. sandstones and carbonates) have low concentrations of radioactive elements (K, Th, U), and therefore exhibit a low Gamma-Ray response. Sandstone reservoirs exhibit a low “clean” Gamma-

Ray response whereas their carbonate clean counterparts are characterized by an even lower gamma response.

### B.1.2. Density Log

The density log is a continuous measurement of the bulk density of a rock formation. It includes the combined density measurement of the rock matrix and fluids enclosed in the pore spaces of the rock in the near-wellbore areas (Rider & Kennedy, 2011). The density tool is an active device that targets a formation with a beam of Gamma-Rays (typically cesium-137) then measures the (typically reduced) amounts of the Gamma-Rays arriving at a detector on the other end of the tool (Asquith & Krygowski, 2004; Rider & Kennedy, 2011). The presence of low-density fluids such as gas, oil, or water in the pore spaces contained in the higher density rock matrices reduces the overall density measurements, which aids in identifying reservoir zones.

Based on the Canadian oilfield standard, bulk density is measured in kilograms per cubic meter ( $\text{Kg}/\text{m}^3$ ). Furthermore, the density track on a log composite is typically scaled such that density increases from left to right across the track going from 1.65-2.65  $\text{g}/\text{cm}^3$ , or 1650-2650  $\text{Kg}/\text{m}^3$  especially when the lithologies are mainly higher porosity sandstones and shales. Scaling of 1.9-2.9  $\text{g}/\text{cm}^3$  or 1900-2900  $\text{Kg}/\text{m}^3$  can be applied to deeper intervals to ensure that the density curve is centered in the middle of the track in deeper, lower porosity sandstones or when it is known that the zone of interest are carbonate-based. Clean sandstones exhibit a moderate bulk density value with an increase in bulk density resulting from compaction and diagenesis, usually with a depth of burial. Thus, cemented sandstones will have a higher density. The density of shales increases with depth in normally pressured sedimentary rocks. This relationship is largely due to the loss of water from shales through compaction, which squeezes the water out. However, a reversal of this trend is common in overpressured (pressure great than a hydrostatic column at that depth) sediments. This is attributed to the low escape potential of water contained in the clay matrix that makes up the shales (Skinner, 2016).

### B.1.3. Resistivity Log

The resistivity of a rock formation is measured by beaming electrical current into the formation and the resistance of the rock to the flow of electric current is measured

(Davis 2010; Rider & Kennedy, 2011). An indirect approach involves the use of an induction tool, which induces an alternating current in a reservoir through a coil to create a fluctuating magnetic field around the tool (Davis 2010; Rider & Kennedy, 2011). This magnetic field in turn induces a current in the formation. The higher the porosity of a given rock, the higher its water holding capacity, and the lower its resistivity. Similarly, the higher the salinity of water in the formation, the higher the electrical conductivity, and the lower the resistivity of a rock formation (Davis 2010; Rider & Kennedy, 2011).

Resistivity log measurements are useful for determining the types of fluid contained in a reservoir rock. According to Rider & Kennedy (2011), resistivity is an intrinsic property of matter that quantifies its ability to conduct electricity. To determine the resistivity of the underlying fluids in a formation, the resistivity log measures the electrical conductivity of formation fluids and the rock matrices and provides both conductivity and resistivity values based on electrical current in parallel flow. Given that hydrocarbons are typically non-conductive, they exhibit a high resistivity reading which cannot be measured directly. The resistivity measurement of a rock formation is a function of the conductive (non-resistive) portions of the rock matrix, shale content, and the formation water in the formation. Thus, low resistivity (high conductivity) formation water contained in the pore spaces of the rock dominates the overall resistivity value. Generally, the resistive behavior of formation water is dependent on the temperature of the formation and salinity content (Asquith & Krygowski, 2004; Rider & Kennedy, 2011) (See Below in Section 4.10.).

With salinity directly impacting the formation  $R_w$ , resistivity data acquired for shallow, intermediate, and deeper radii of investigation, provide information on the properties of a reservoir as well as the interaction between the reservoir fluid, and the drilling mud filtrate. Three main categories of drilling mud include water-based mud (both fresh and saltwater), synthetic-based mud, and oil-based mud with each having some influence on the recorded resistivities (Davis 2010; Rider & Kennedy, 2011). The unit of resistivity being  $\text{ohm}/\text{m}^2$ , the scaled resistivity log ranging from 0.2- 2000  $\text{ohm}/\text{m}^2$  which increases from left to right going across the track has been applied in this study.

#### B.1.4. Sonic Log

The sonic tool measures the time taken for sound to travel through a layer of rock from a transmitter to multiple receivers. Like the density tool, the sonic tool is an active

device. Transmitting acoustic waves through a rock formation recording the travel time in microseconds per foot or microseconds per meter. Given that sound travels faster in solids, a faster travel time is indicative of a low porosity rock. Conversely, the slower the travel time the more pore spaces in the rock. The fluids contained in the pore space also have different sound velocities but influence the resulting overall velocity to a lesser extent. The interval transit time or slowness of a rock is a function of the rock matrix, the degree of pore spaces in the rock, and fluid contained in the pore spaces. Slower velocities are expected for rock layers with greater interval transit time confirming an inverse relationship between interval transit time and velocity (Rider & Kennedy, 2011). Faster velocities are more common in carbonates than siliciclastic lithologies because of their (usually) considerably lower porosities and higher matrix velocities. Typically, shales exhibit lower velocities with higher interval transit time due to the presence of increased amounts of slow velocity-water bound to their pore spaces.

The sonic log is scaled such that the interval transit time decreases (gets faster) from left to right going from 378-114 us/m (Glover, 2012). This is the equivalent of a 0.45 to -0.15 (left to right across the track) porosity scaling assuming a clastic matrix value of 180 us/m and a fluid value of 620 us/m (assumed to be water only for simplicity of calculation). Conventionally, porosity on the sonic log track is displayed increasing from right to left with velocity increasing from left to right across the same track. Continuous sonic logs were used in this study to calculate a total and effective porosity for intervals where the density log coverage was missing or rendered invalid due to hole wash out or hole rugosity.

#### B.1.5. Lithology

In the absence of core data, continuous lithology logs used in this study were provided by Canadian Stratigraphic Services Ltd (CanStrat). These lithology logs were generated from petrographic analyses of well cuttings. Cuttings are rock particles liberated from the rock face underneath the drill bit during bit rotation. During drilling, drilling mud pumped down the drill pipe is circulated back up-hole through the annulus. The drilling mud acts to reduce friction and wearing away of the drilling bit. Also, the mud transports cuttings from drilled intervals up the borehole to the surface. At the surface, the mud and rock cuttings are separated by a shale shaker before being cleaned and analyzed. During

cuttings analyses, the geologist at the well site, using microscopic examination, determines the rock types and abundance, grain size, grain shape (i.e. roundness and angularity), degree of grain sorting, presence of accessory rocks, and their porosity. Also, they analyze for hydrocarbon staining, fluorescence, mineralogy, and fossil types (if any) from the cuttings (Skinner, 2016). The same examination process is followed by CanStrat geologists at a later time, using wireline logs to guide them, and the results then compiled in a graphical composite log and also is compiled into a .LAS digital file by CanStrat at a later time. This data is imported into the Petrel™ log composite for each well used in this study to guide interpretation and well correlation

## B.2. Calculations Involving Wireline Logs

### B.2.1. Lithology and Shale Volume (Vsh) Prediction from Wireline Gamma-Ray Log

Vsh is the measure of shaliness of a rock interval (Glover, 2012). It is an index based on the Gamma-Ray value at each depth in comparison to sand and shale baseline values. As the first step of the petrophysical workflow, mathematical computation of shale volume (Vsh) was done for all the project wells using the Gamma-Ray logs (run in combination with either the sonic or density log). While gamma-ray minimum and maximum values can be picked by looking at the gamma-ray curve displayed on the log composite, a cross plot of the gamma-ray and density data for every depth measured in the well (Figure B.2.1) allowed for a more rigorous selection of sand and shale endpoints.

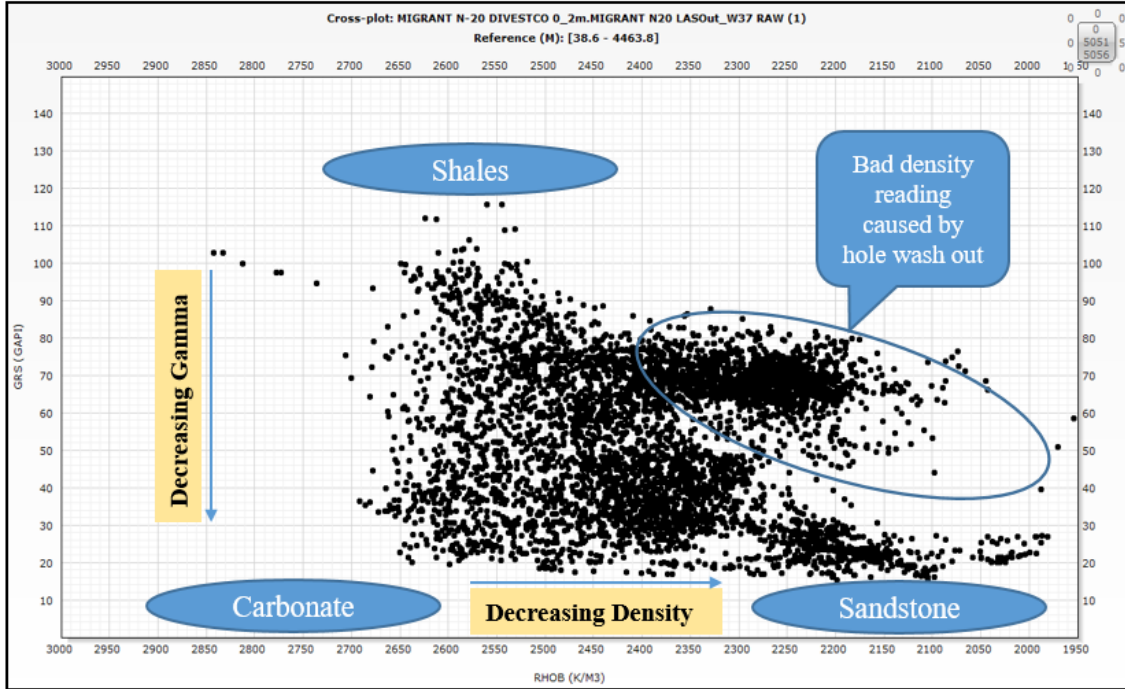


Figure B.2.1: A cross plot of Density against Gamma-Ray curves made in Techlog™. The clean sand Gamma-Ray value on the cross plot makes up  $V_{Sh} = 0.0$ . Calcareous sandstone or limestone intervals will frequently have even lower values of GR than the reservoir clean sand value. Hence, it is important to ensure that the  $GR_{min}$  values are selected using the cross plot, which allows the two lithologies to be differentiated. Wrong selection of the  $GR_{min}$  to a limestone value will lead to even the cleanest, porous sand having a computed  $V_{sh}$  value above zero.

The  $V_{sh}$  index is scaled on a log composite like the source gamma-ray log. This can be considered as stretching the gamma-ray curve from zero to one such that the lowest values (representative of sandstones or carbonate lithologies) occupy the left side of the track with and the highest values (representative of shales) on the right. The  $V_{sh}$  log is mathematically computed using the following expression:

$$V_{sh} = \frac{GR_{log} - GR_{min}}{GR_{max} - GR_{min}} \quad \dots\dots\dots (1)$$

Where  $GR_{log}$  is the gamma-ray reading

$GR_{max}$  is the maximum gamma-ray reading associated with shales

$GR_{min}$  is the minimum gamma-ray reading associated with sand reservoirs.



### B.2.2. Porosity Estimation

Porosity is a measure of the volume of pore spaces in a reservoir rock volume. It is obtained through a linear computation involving either the density or sonic log (Glover, 2012). Like the Vsh estimation, the porosity calculation can be considered as the assignment of a fractional value going from 0.0 (a theoretical value where the observed log density matches the matrix density) to 1.0 (when there is only formation water in the investigated volume). Typically, the neutron and density logs are scaled to maintain their porosity curves in the middle of the track. The scale of the neutron log ranges from 0.60v/v on the left to 0.00 v/v on the right, whereas the density scale ranges from 1.65 on the left to 2.65 g/cc on the right (equivalent to 1650-2650 Kg/m<sup>3</sup>). This is assuming a sandstone matrix density and using the density of freshwater as the fluid density. Frequently, the density curve will be redisplayed as density porosity, so that the same porosity units are used in the track for both neutron and density porosity.

For this study, porosities in the Adamant and two Thebaud wells were calculated using the density log through the following mathematical relationship:

$$\Phi_T = \frac{\rho_{ma} - \rho_b}{\rho_{ma} - \rho_{fl}} \quad \dots\dots\dots (2)$$

Where:  $\Phi_T$  = Total porosity from density log

$\rho_{ma}$  = Density of matrix (quartz matrix usually, 2.65 g/cm<sup>3</sup> or 2650 Kg/m<sup>3</sup>)

$\rho_b$  = Bulk density of formation (measured by the density tool)

$\rho_{fl}$  = Formation fluid density (usually 1.025 g/cm<sup>3</sup> or 1025 Kg/m<sup>3</sup> based on the density of seawater)

Porosity estimation in the Migrant N-20 well was completed using the sonic log through the Wylie equation below.

$$\Phi_T = \frac{\Delta t - \Delta t_{ma}}{\Delta t_f - \Delta t_{ma}} \quad \dots\dots\dots (3)$$

Where:  $\Phi_T$  = Total porosity from sonic log

$\Delta t$  = Sonic reading of formation (measured by the sonic tool)

$\Delta t_f$  = Sonic formation fluid reading (usually 620 us/m)

$\Delta t_{ma}$  = Sonic of matrix (quartz matrix usually 182 us/m)

Given that the sonic tool also responds to the presence of bound water in shales, a calculated sonic total porosity may be corrected to show only the porosity capable of containing movable fluids. This involves reducing the total porosity to effective porosity by applying a shale correction. In the presence of increased shale, the volume of the shale and the Dt will act to reduce total porosity in pores of all sizes since the water is fully bound to the pore walls/throat. The shale correction removes the shale pores and shale porosity since they are so small that fluids cannot be put in and taken out. Formation tops (Figure B.2.2) or bit run intervals (Figure B.2.3) can be used to divide the well into zones with varying shale porosity factors (slowness) applied to the calculated total porosity for the various intervals (Glover, 2012). The effective porosity from density and sonic logs can be computed using equation 4 and equation 5 respectively.

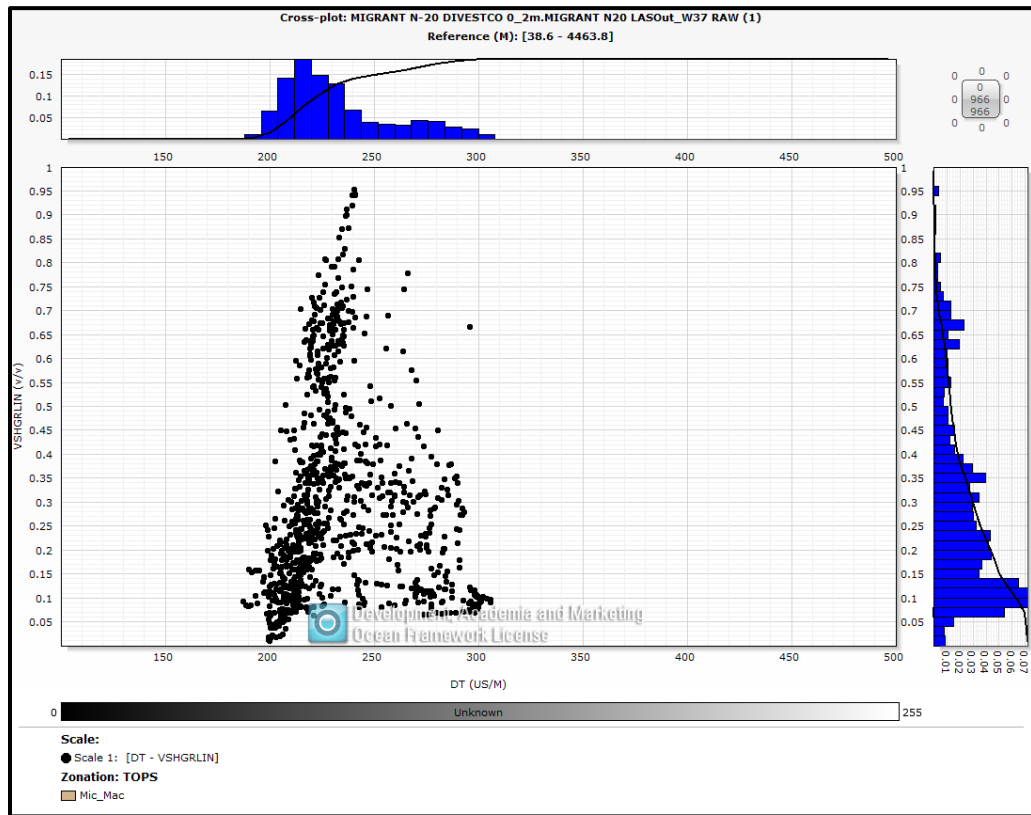


Figure B.2.2: A cross plot of sonic and shale volume logs used for determining the slowness (shale velocity) to be used for porosity correction. Given that the Dt value of the shales doesn't stay the same from the top to bottom of the well, adjustments were made to target the actual zone comprising the analyzed intervals in the well. In this case, the data points for the Mic Mac zone comprised selection and were preferred to that of the bit run selection in Figure B.2.3. From the plot, a Dt value of 220-225 us/m (225 us/m) is favored.

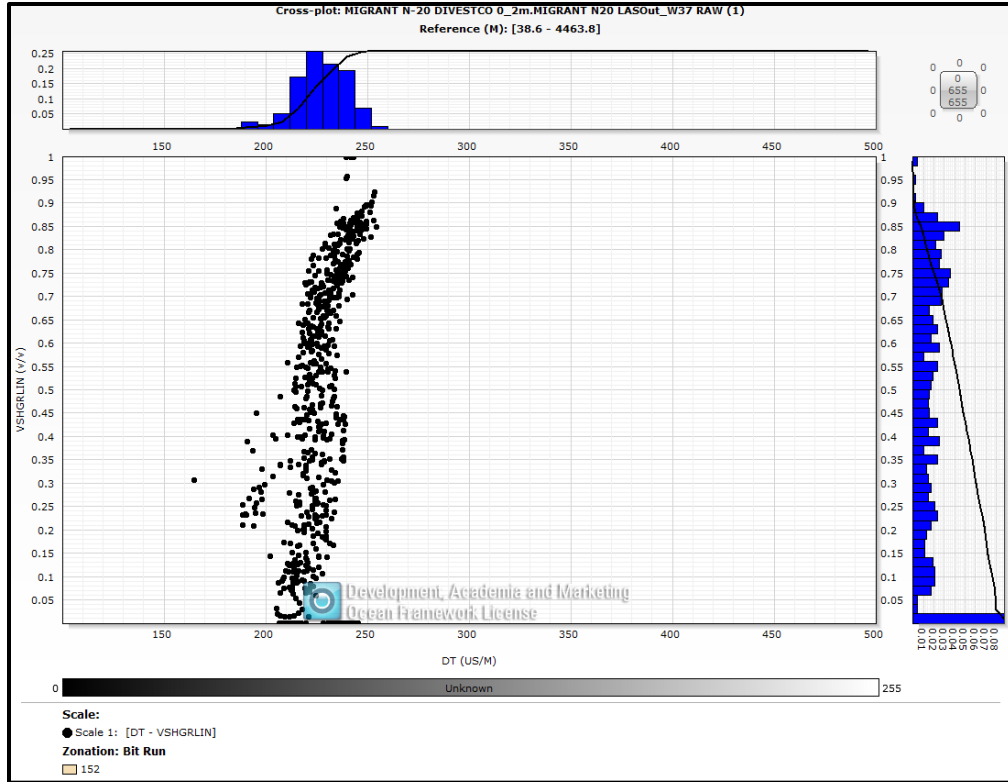


Figure B.2.3: A cross plot of sonic and shale volume logs used for determining the slowness (shale velocity) to be used for porosity correction. In this case, the data points for the 152 mm bit run interval comprising the zones of interest are displayed. Using the bit run intervals is a good enough way of dividing up the sections of the well to reset the Dt value for shale in the different intervals. From the plot, a Dt value of 225 us/m was used in the analysis.

$$\Phi_E = \left( \frac{\rho_{ma} - \rho_b}{\rho_{ma} - \rho_{fl}} \right) - Vsh \left( \frac{\rho_{ma} - \rho_{sh}}{\rho_{ma} - \rho_{fl}} \right) \dots\dots\dots (4)$$

Where:  $\Phi_E$  = Effective porosity from density log

Vsh = Volume of shale

$\rho_{sh}$  = Shale density of formation (sorted by intervals)

$$\Phi_E = \left( \frac{\Delta t - \Delta t_{ma}}{\Delta t_f - \Delta t_{ma}} \right) - Vsh \left( \frac{\Delta t_{sh} - \Delta t_{ma}}{\Delta t_f - \Delta t_{ma}} \right) \dots\dots\dots (5)$$

Where:  $\Phi_E$  = Effective porosity from sonic log

Vsh = Volume of shale

$\Delta t_{sh}$  = Shale slowness from sonic log (sorted by intervals)

### B.2.3. Water and Hydrocarbon Saturation Estimation

There are different ways of making use of  $R_w$ . One of the ways within a petrophysical package is to take the salinity, convert it, and take the  $R_w$  equivalent to that salinity at the lab indicated temperature (surface) and convert to a much lower  $R_w$  and temperature of the zone of interest. While this may be useful, the Pickett plot solution for  $R_w$  is deemed to be more useful since all inputs come from formation logs in the interval of interest. Where there may be limited formation data, and  $R_w$  derived from surface sample salinity from a nearby well converted to surface  $R_w$ , then converted to formation  $R_w$  is useful if you have a hydrocarbon-bearing zone with the absence of any associated water communication. This would introduce inaccuracies if there is no continuity between that nearby wet zone and a presumed zone of hydrocarbon presence to be analyzed.

A porous rock under reservoir conditions hosts either 100 % of a certain fluid type (either oil, gas, or water) or a combination of fluid types in their pore spaces (Davis, 2010). As a result, it is possible to estimate the proportions of other fluids contained in the reservoir rock if the water saturation  $S_w$  is known. This is possible if the formation water resistivity ( $R_w$ ) is known as well as the effective porosity, and assumptions are made of the other inputs present in the Archie equation. The formation water resistivity ( $R_w$ ) of an interval at any depth is dependent on the temperature and the salinity at that depth. During logging, the well temperature is recorded at the bottom of the well.

A linear scaled temperature log going from the highest recorded temperature at total depth and an arbitrary minimum temperature at the surface is used to assign temperatures at intermediate depths. This is used in terms of calculated  $R_w$  values at different depths in the well. To calculate water and hydrocarbon saturations contained in a reservoir, this requires a known or assumed wet zone – having an assigned  $R_w$  appropriate for that salinity and temperature. Thus, at any given temperature, a salinity of a formation can be converted to a corresponding  $R_w$  using a chart (later discussed) or an online calculator such as in Figure B.2.4.

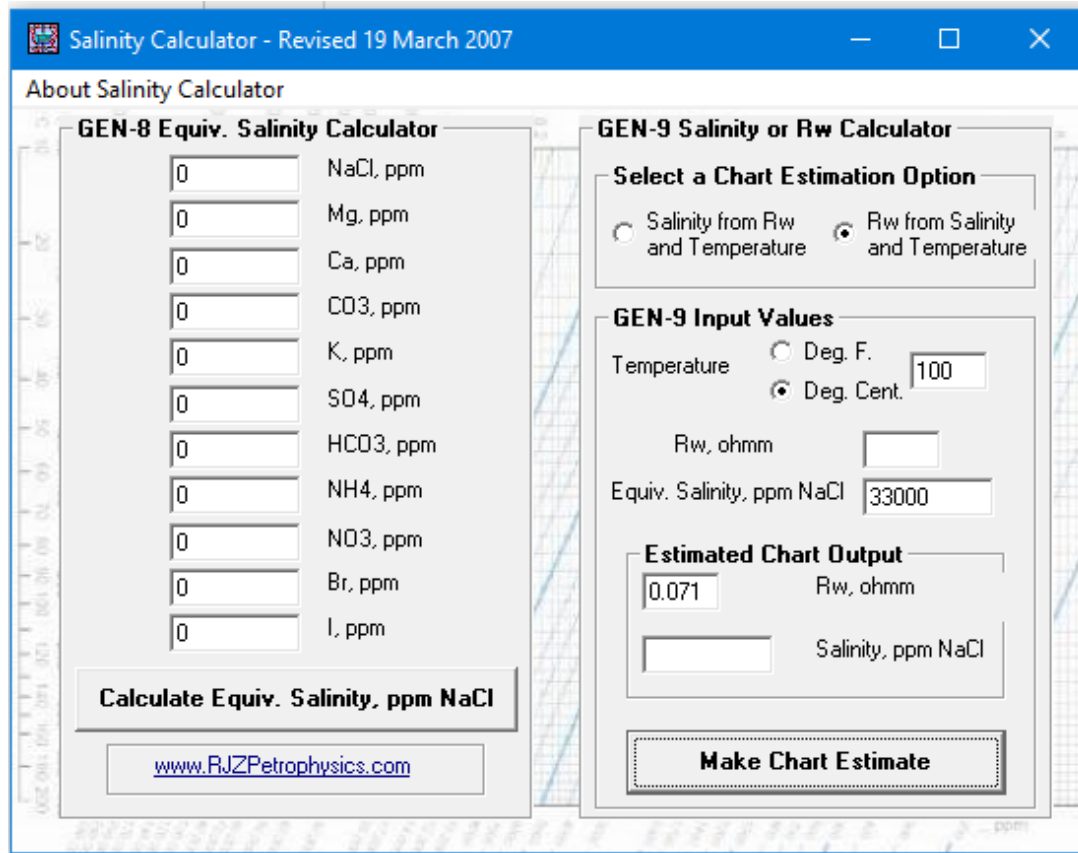


Figure B.2.4: A temperature, salinity, and  $R_w$  conversion calculator online version. Formulas have been incorporated in these calculators for carrying out the conversion of a formation  $R_w$  or salinity at one temperature to the  $R_w$  or salinity at a different temperature.

Alternatively, a Pickett plot (Figure B.2.5), which is a graphical representation of Archie's solution that plots input values of resistivity and porosity on a logarithmic scale, can be used for estimating the  $R_w$  under reservoir conditions for the zone in question. The formation deep resistivity measurement is plotted on the x-axis and either total or effective porosity on the y-axis both on logarithmic scaling.

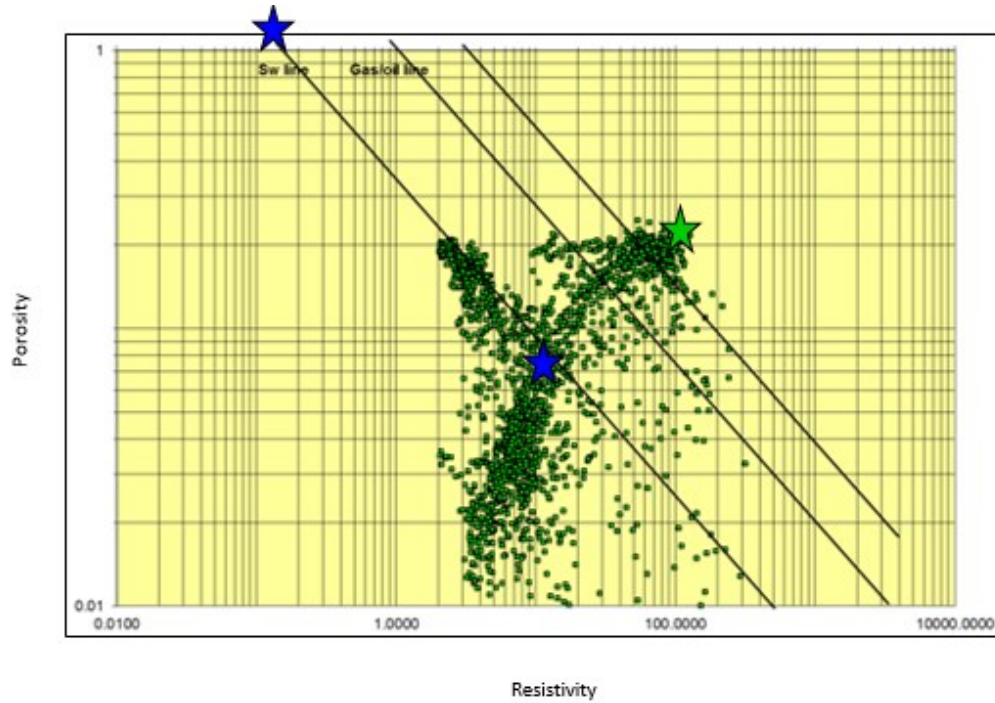


Figure B.2.5: A Pickett plot of resistivity presented on a logarithmic scale on the x-axis against porosity on a double-decade logarithmic scale on the y-axis (Watson, 2017). The blue stars represent values from the wet zone that are positioned almost perpendicular to the trend in the hydrocarbon (oil or gas) zone. In this example, the  $R_w$  (apparent) is  $\sim$  to 0.15 ohms, the slope  $m$  of the 100% water saturation line = 2.0. For a porosity of 0.20v/v, the wet reservoir has a resistivity of 2 ohms, while for an equivalent porosity at the top of the hydrocarbon column, the resistivity is 100 ohms.

This is done in the absence of any known water salinity and temperature data for formations in a zone of interest. A Pickett plot is useful for working out key input parameters that are then fed into Archie's equation as follows:

$$S_w = [(a / \Phi^m) * (R_w / R_t)]^{(1/n)} \dots \dots \dots (6)$$

Where:  $S_w$  = Water Saturation

$a$  = tortuosity exponent (normally a constant of 1)

$\Phi$  = Porosity

$R_w$  = Formation water resistivity (at the temperature of the formation in question)

$R_t$  = True resistivity of formation (from the deepest borehole resistivity log reading)

$m$  = cementation exponent (normally around 2)

$n$  = Saturation exponent (normally around 2)



Additionally, hydrocarbon saturation can be calculated using the following:

$$S_h = 1 - S_w \dots \dots \dots (7)$$

Where:  $S_h$  = Hydrocarbon Saturation

When the  $S_w$  curve is multiplied by the porosity curve, the result is a bulk volume of water curve (BVW). This provides a convenient way of displaying the apparent partitioning of fluids in the effective pore spaces. As a result,  $S_w$  can be re-displayed as a bulk volume of water BVW curve with a remaining partition of the area under the  $\Phi_{ie}$  curve representing a bulk volume of hydrocarbon BVH (where hydrocarbons are present) and bound water. Numerically, the BVH is the result of subtracting the BVW from the porosity value used in the analysis.

#### B.2.4. Permeability Estimation

Permeability values (or approximations that are not closely calibrated to core data are sometimes called permeability indices) are commonly computed using a combination of calculated porosity and water saturation (assumed to be irreducible) using a few generic formulas (e.g Berg equation, Timur equation, Morris and Biggs equation). Alternatively, permeability can be computed based on using core-based porosity-permeability relationships where the input core porosity is replaced by the assumed-equivalent log porosity. Given the unavailability of core data at Migrant and sparse sampling of sidewall cores in the Adamant well, plugs cut from full diameter cores from the F3 and H2 overpressured sands in the E-74 (T5) well and from the top core #1 at Thebaud I-93 were combined to derive a generic porosity/permeability relationship. Data from the cores were used to generate a cross plot of core porosity (scaled linearly on the x-axis) against permeability (scaled logarithmically on the y-axis) with a resulting linear relationship.

## APPENDIX C.

### C.1. Pressure Relations from Flow Test – Migrant N-20

A Drill Stem Test (DST) measures the productive capacity of a well. The test is useful for differentiating fluids contained in a formation as well as determining their rates of fluid recovery, which is a function of the reservoir permeability and the reservoir pressures (Figure C.1.1; Rigzone 2020). During testing, a measurement device is connected to the bottom of the drill string, which is lowered to the bottom of the well before being isolated and activated at a set datum. After it is activated, the instrument measures the flow of hydrocarbons (oil or gas) for an extended period (usually an hour) with successive shut-in periods in between. Due to the extended flow test period, little DST analysis is currently done. The amount of recovered flow during the test period, and formation shut-in pressures obtained during each shut-in period are extrapolated on a horner plot to determine whether the apparent formation pressure observed during successive shut-in periods indicates the formation pressure is being reduced because of the volumes of fluid produced. This indicates a limited volume reservoir and therefore is likely of little economic interest or worth completion.

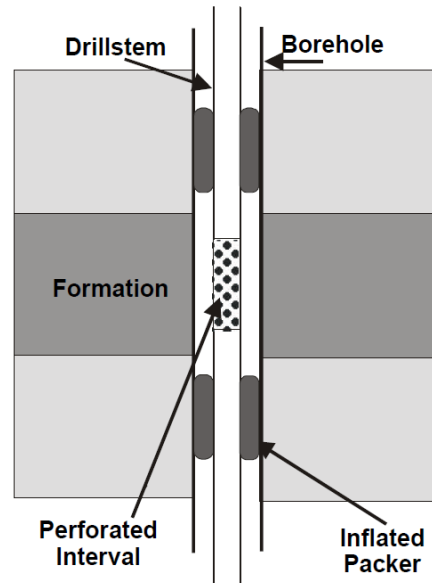


*Figure C.1.1: A diagram of a Drill Stem Test application in a borehole (Glover, 2012a). A perforated anchor in the tool at the bottom of the assembly allows fluids to enter an empty pipe. The expansion of rubber packers against the sides of the hole provides support for sealing of pressures as a series of valves open and close to control the flow of the hydrocarbons into the empty drill stem. This data is read by a pressure-measuring device in the tool.*

At Migrant, three DST tests were reviewed with two tight tests and one successful test. Out of DST #2, DST #5, and DST #8, the deepest of the three - DST #2 - was the only test that successfully flowed gas. It tested gas at a maximum rate of 10 million standard cubic feet a day (mmscf/d) to the surface. DST analysis report suggests a decrease in formation shut-in pressure in the Migrant N-20 well between the initial and final shut-in periods (Figure C.1.2). The decreasing formation pressure at the end of successive shut-in pressures is indicative of a depleting reservoir, which is not evident when viewing the data through the BASIN database. Based on Figure C.1.2, a rapid increase in pressure to a value above the initial indicated reservoir pressure partway through shut-in # 4 is likely from mechanical issues due to packer failure, which results in the tool experiencing a rapid, but momentary, return to hydrostatic pressure.

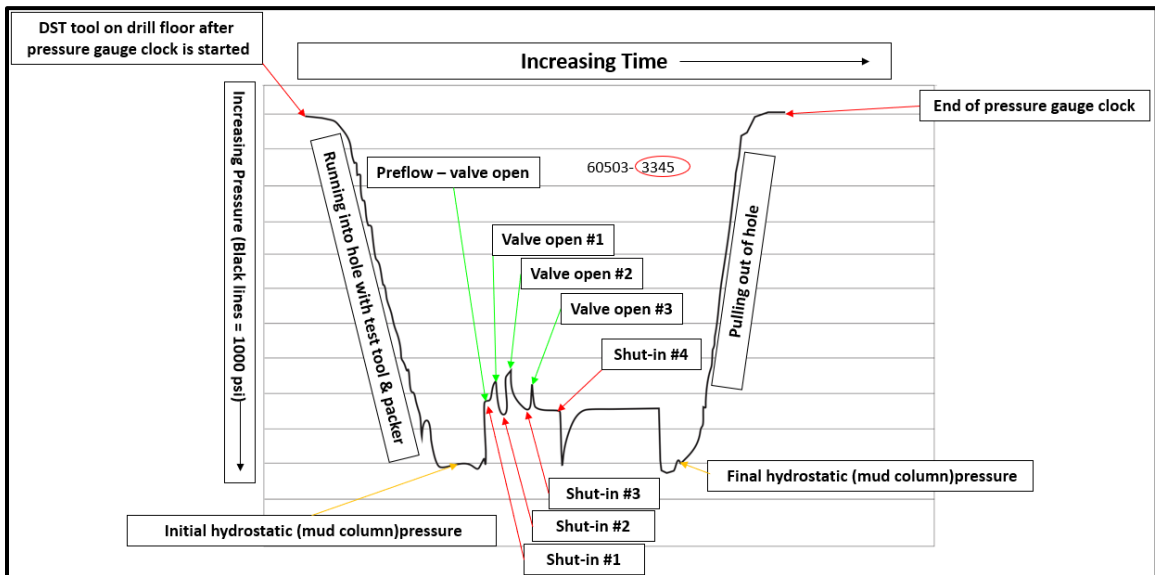


Figure C.1.2: A DST pressure response from test #2 done in the Migrant Structure (Tetco, 1978). The horizontal scale represents the test time with each horizontal line in the DST chart indicating an additional 1000 psi of pressure. The Pressure is highest at the end of the first shut-in 8790 psi (60605 kPa in the online BASIN database). As a result, the formation pressure must be equal to or higher than the pressure recorded in the final shut-in.

DST #5 (Figure C.1.3), displays a hint of incomplete pressure build-up at the end of the second final shut-in (non-stabilized pressure-in other words the chart line of pressure versus time is not horizontal), results in an invalid final shut-in pressure of 6,221 psi (42,893 kPa). A lack of stabilization in formation pressure at the end of the first shut-in indicates the presence of a tight reservoir despite the extended shut-in period. At the time

of recording the final hydrostatic pressure, there seemed to have been some problems disengaging the packer from the formation, given the extreme pressure surges. Similarly, in DST #8 (Figure C.1.4), there is a hint of incomplete pressure build-up at the end of the second final shut-in, resulting in an invalid final shut-in pressure of 5,748 psi (39,631 kPa) from data in the well report.

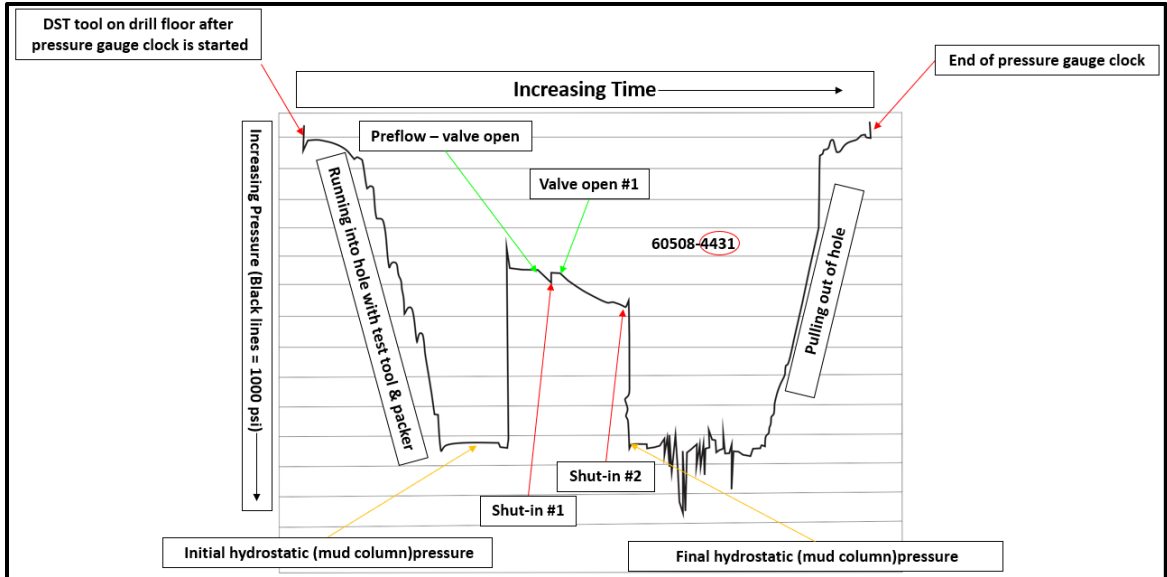


Figure C.1.3: A figure of traditional pressure analysis based on a DST chart of DST test #5 done in the Migrant Structure (Tetco, 1978). Like test #8, there is continuing build-up of pressure at the end of the second (final) shut-in. As a result, the final shut-in pressure of 5,748 psi (39,631 kPa in BASIN) is an invalid formation pressure.

Results for test intervals #5 and #8 indicate that they are low permeability zones. Neither plot gave the actual reservoir pressure since at the end of each shut-in for these two DSTs the apparent reservoir pressure was continuing to increase slowly in response to the presence of a low permeability rock. Following a brief interruption to the running in during DST #8, the pre-flow was followed by a reduction in pressure after the first shut-in to around 6000 psi. Since the tool and downhole pressure gauge experience the full weight of the mud column at the time the packer was released, the increase in pressure above the hydrostatic threshold is attained as the tool is cycled and eventually stabilized.

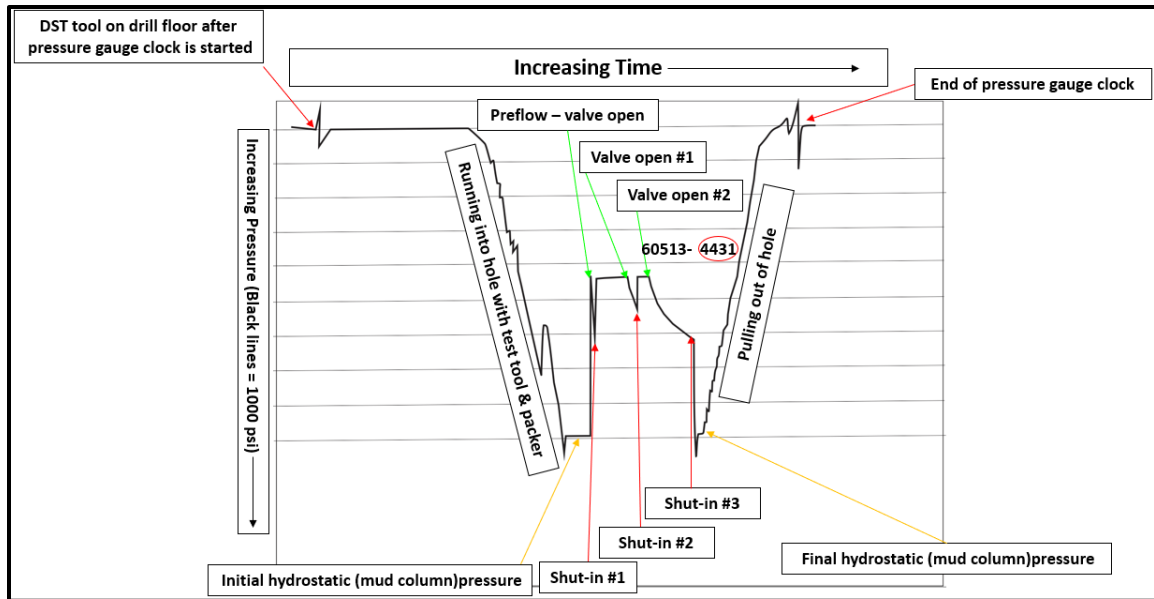


Figure C.1.4: A DST chart from test #8 done in the Migrant Structure (Tetco, 1978). There is a continuing build-up of pressure at the end of the second (final) shut-in of the test. As a result, the final shut-in pressure of 6221 psi (42893 kPa in BASIN) is an invalid formation pressure.

## C.2. Horner Plot Relations from Flow Test – Migrant N-20

A Horner plot is an extrapolation used for calculating the theoretical virgin reservoir pressure. The Horner plot of the DST test interval #2 (Figure C.2.1) gives increasing pressure as a function of increasing time and points to the theoretical virgin reservoir pressure at an infinite time (right axis of the plot in this case). Typically, the observed increase in pressure never reaches the right-hand side of the Horner plot since it is impractical to continue the test long enough on the shut-in to get to infinite time. As a result, the way the reservoir shut-in pressure responds during a DST can be used to estimate the volume of a reservoir or at least confirm that there has been no drop in extrapolated virgin formation pressure as a result of the fluid volumes withdrawn during the test.

The point of intersection between a line through the pressure measurements vs time during the initial shut-in extended to the right side of the graph would be in theory, represent the actual reservoir pressure  $P^*$ . For an infinite reservoir size, identical  $P^*$  values for each of the shut-in periods are expected. Hence, a series of lesser  $P^*$  values on the Horner plot for successive shut-in periods is normal for a reservoir with limited volume in accordance with the ideal gas law which establishes the relationship between pressure, volume, and temperature ( $pV=nRT$ ). From the exhibited pressure behavior, the operators

concluded that the tested reservoir (despite testing high-flow rate gas) could not produce economically viable amounts of gas. This was likely a contributing factor to the decision to plug and abandon the well.

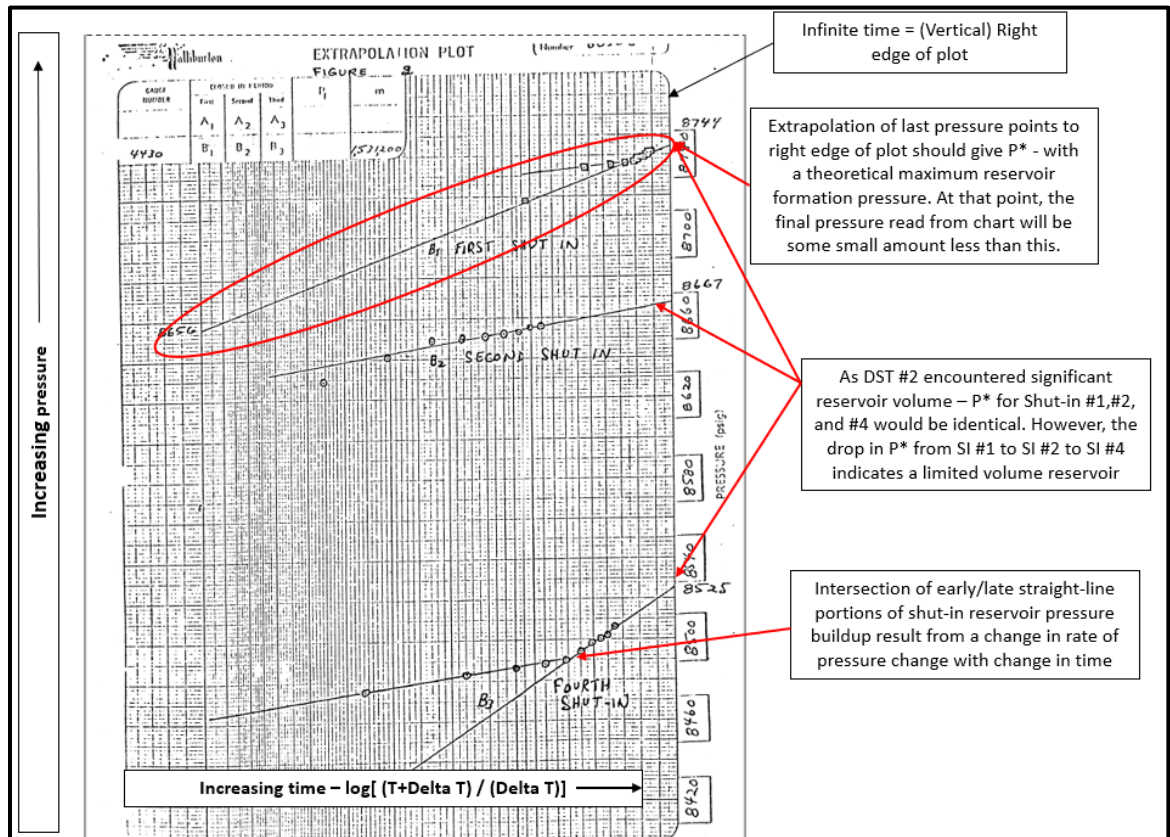


Figure C.2.1: A Horner plot of the Migrant N-20 DSTs based on the log of time + change in time/ change in time and pressure at each of those times (Tetco, 1978). The right axis of the Horner plot represents projection to infinite time. Hence, the pressure increases as it is extrapolated in time. The result associated with formation pressure is the value of  $P^*$  (theoretical pressure) – a value of 8744 psi for the first shut-in. The plot indicates a decline in pressure by 77 psi (531 kPa) between the first and second shut-in, and 142 psi (979 kPa) between the second and fourth suggesting a depletion in pressure with time, corresponding to a depleting reservoir. A bend such as that seen for the fourth shut-in period indicates that a reservoir boundary (possibly a fault) was encountered in the reservoir some distance from the wellbore. The third shut in was not considered since it was not a successful test (Watson, pers comm. Oct. 2019). Therefore, the second and fourth shut-in were very vital to the text.

### C.3. Pressure Relations from Flow Test – Adamant N-97

Designed to be conveyed down the borehole on a wireline string (Figure C.3.1), the RFT tool measures pressure at specific depths. Positioned at the right depth, a pad is fixed against the wellbore wall with the formation sample probe on the opposite wall of the



borehole. To engage in testing, a valve is opened to the formation, which tests the pressure and flow of formation fluids (a function of permeability) over a short time, repeated for numerous test intervals in the borehole.

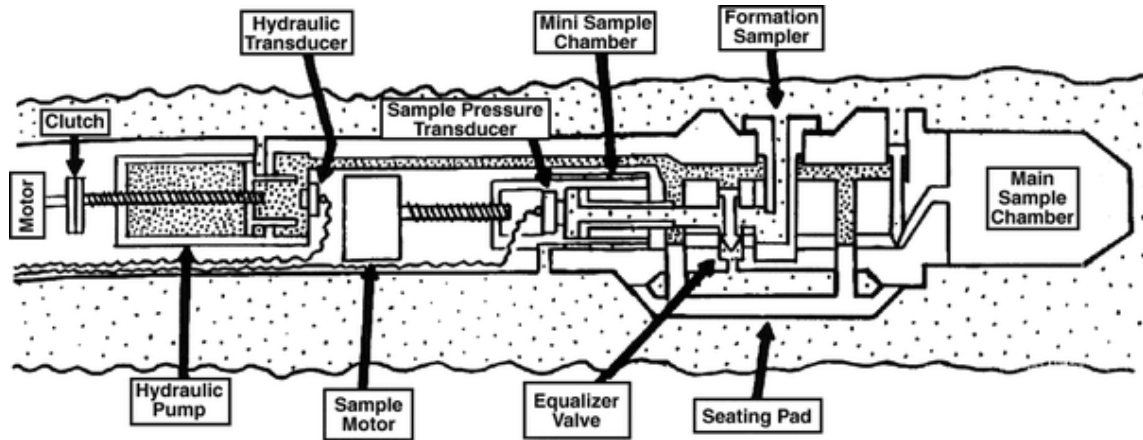
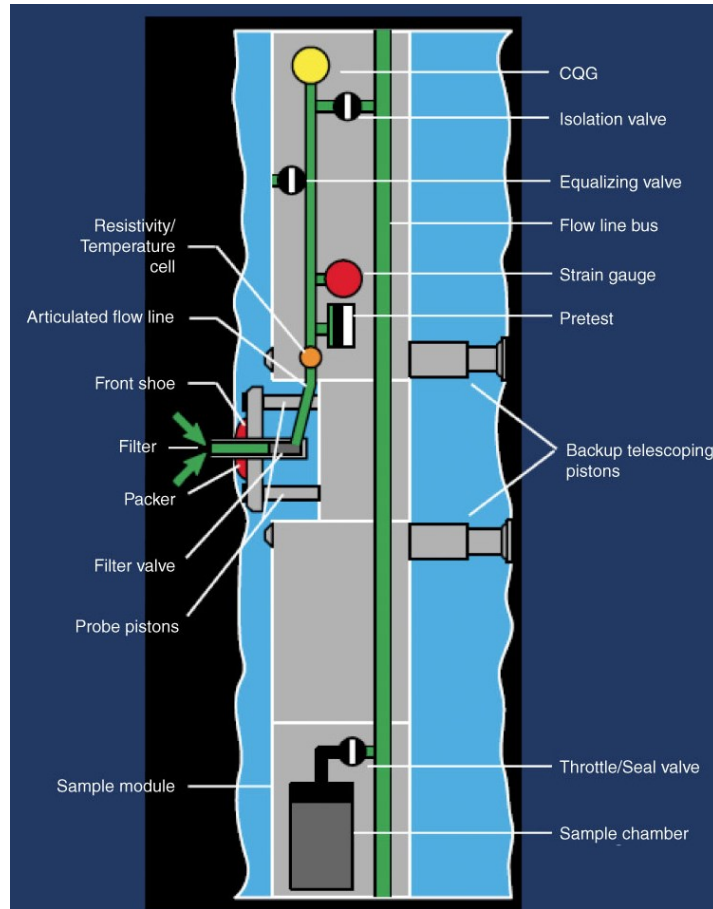


Figure C.3.1: A figure of the RFT tool showing the key components involved in the positioning and testing with the tool (Quora, 2019).

On the other hand, the MDT tool uses a combination of pad/probe or packer and fluid sampler to determine the pressure and characteristics of fluids (Figure C.3.2). Similar to the Repeat Formation Test tool RFT, the Modular Dynamic tester MDT reading returns to the pressure of the mud column as the pad is pulled away from the wellbore wall seen in their hydraulic spikes. The MDT tests are planned around the withdrawal of small pre-set volumes of reservoir and drilling fluid through the wireline-conveyed tools. Real-time readings in the logging unit at the surface allow monitoring of pressure changes in the tool as the test sequence proceeds. Unlike the strain gauges used in the RFT tool, the quartz gauges in the MDT makes it more resistant to downhole temperature and pressure effects, which may introduce error to measurements. For its application, the tool is extended against the borehole walls, which provides a pathway for the transfer of reservoir fluids into the flowline. To guarantee that the permeability and pressure readings are accurate, good hydraulic sealing must be made during a preset.



*Figure C.3.2: A figure of the MDT tool showing the key components involved in the positioning and testing with the tool (IODP, 2010). A quartz gauge is employed in the MDT tool for better measurement accuracy.*

The pre-flow is associated with a piston volume of 20 cm<sup>3</sup> withdrawal (smaller amounts are also possible) that goes immediately to pressure build-up. The shut-in period can either be terminated automatically by program when the apparent formation pressure has ceased to change (horizontal line on a time-based plot of pressure) or can be overridden by the logging engineer for shorter or longer shut-in times, similar to a slow build (Brown, 2003).

When the probe and pad of the MDT tool are pushed against the wellbore wall, the tool starts reading the initial hydrostatic pressure as soon as the test sequence commences. Once the pad containing the MDT probe has been pushed against the formation wall, the hydraulic activation pressure causes a short-term spike in apparent pressure above the ongoing hydrostatic pressure of the mud column. This is like the characteristic increase in pressure to slightly above hydrostatic in the DST tool. Then, a piston is pulled from the

middle of the packer in the MDT tool with a standard volume of 20 cm<sup>3</sup> withdrawn from the formation. This opens the flow line for the inflow of fluid, from the near-wellbore area to replace the 20 cm<sup>3</sup> of withdrawn volume. The next hydraulic spike represents the cycling of the hydraulics to move the piston in the middle of the packer back through a 20-cc volume of movement.

In Figure C.3.3, after the piston movement, the pressure drops to ~15,000kPa from just under 55,000 kPa. After an initial slow build in pressure, it becomes constant - an indication that a good formation pressure has been arrived at. Additionally, it indicates a reservoir of low permeability. By contrast, the drop in pressure to about 34,750 kPa in Figure C.3.4 from an initial hydrostatic pressure of ~ 49,000 kPa after the 20 cm<sup>3</sup> piston withdrawal is done, suggests the presence of a good quality reservoir.

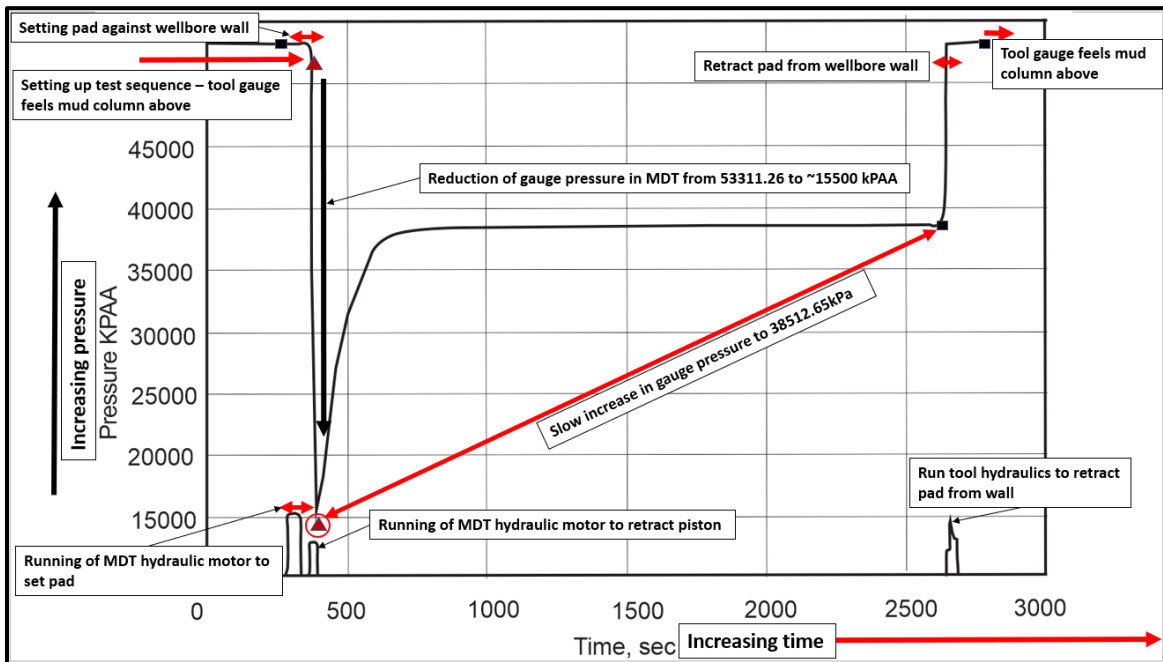


Figure C.3.3: An MDT chart from the Adamant N-97 well test depth at 4222 m showing the various acquired measurements during testing (Mobil et al., 2000). The black boxes indicate certain specified periods with the box before the end (before the final hydrostatic pressure) being the apparent formation pressure because of the movement/withdrawal of the volume withdrawal and subsequent pressure build up. Given the extreme drawdown of pressure during the 20cc withdrawal, and the character of the increase in pressure afterward - this test would be considered to represent the formation doing a "slow build" towards the formation reservoir pressure but not reaching it at the time the tool experiences the resumption of mud column pressure again.

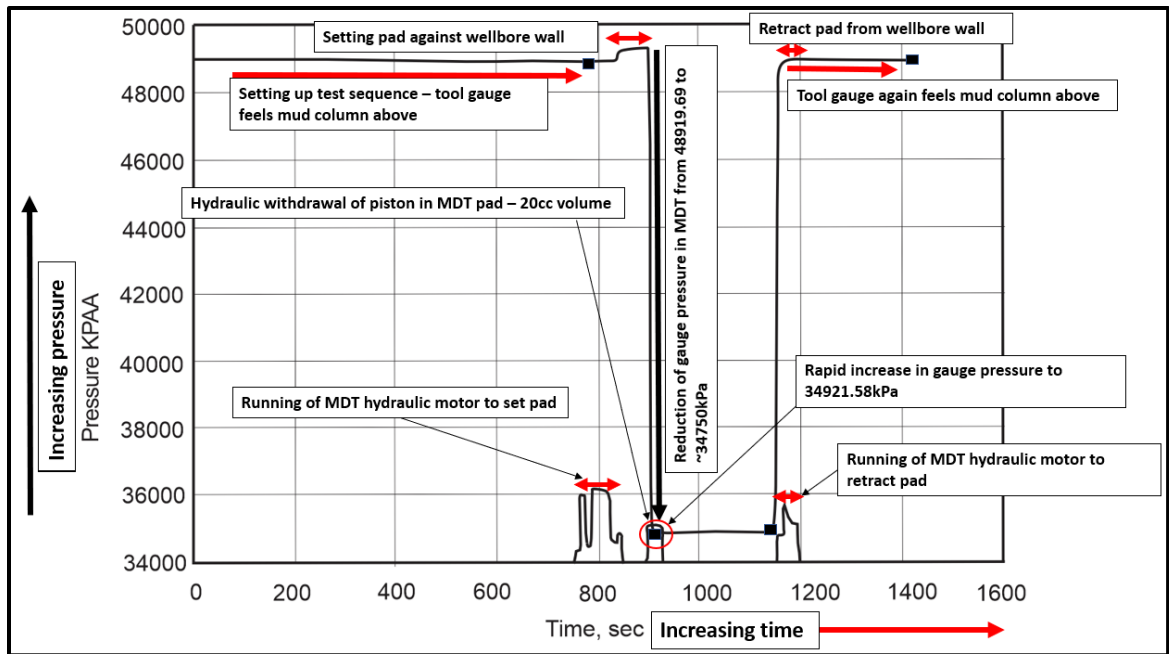


Figure C.3.4: An MDT chart from the Adamant N-97 well test depth 3634 m showing the various measured components during testing (Mobil et al., 2000). From the pressure progression in this chart, after the 20 cc had been withdrawn and the piston withdrawal stops, it drives back to formation pressure almost immediately. Based on these characteristics, the test would be considered valid and the apparent formation pressure at the end of the build-up period would be considered a good representation of the formation pressure in the reservoir.

Figure C.3.5 is characterized by a large pressure drawdown of  $\sim 54000$  kPa and no subsequent build-up of pressure. This likely suggests that the test probe was placed across a zone having no permeability. Also, Figure C.3.6 shows the hydraulic response from setting the packer followed by the  $20 \text{ cm}^3$  of volume withdrawn, which resulted in a drawdown of  $\sim 60000$  kPa from an initial hydrostatic pressure of  $64700$  kPa. Since apparent formation pressure is still increasing at the time the probe and pad are retracted, this test would be deemed a “slow build” given the longer time taken before stabilizing. With the apparent final reservoir pressure expected to take much longer, the test may be terminated in a typical manner of saving rig time (Brown, 2003).

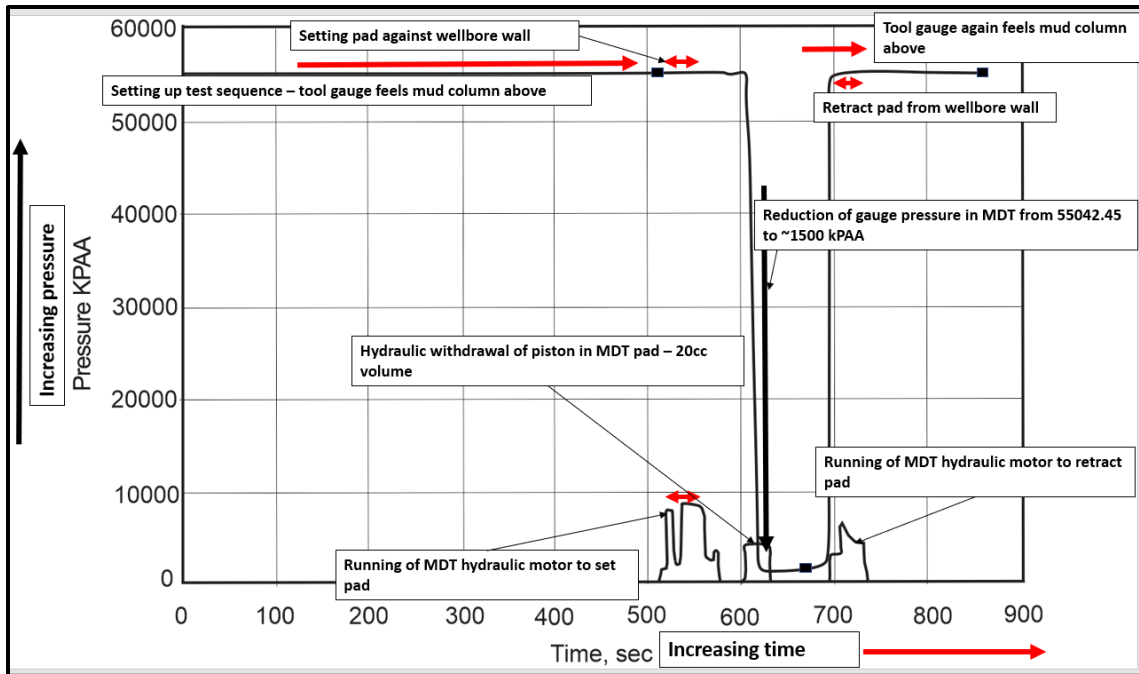


Figure C.3.5: An MDT chart from the Adamant N-97 well test depth 4120 m showing the various measurements during testing (Mobil et al., 2000). Due to the extreme pressure drawdown seen by the gauge during the 20cc withdrawal of fluids, and lack of any pressure buildup after that (the equivalent of a shut-in) - this test can be characterized as a tight test - and the apparent shut-in pressures are not representative of formation reservoirs.

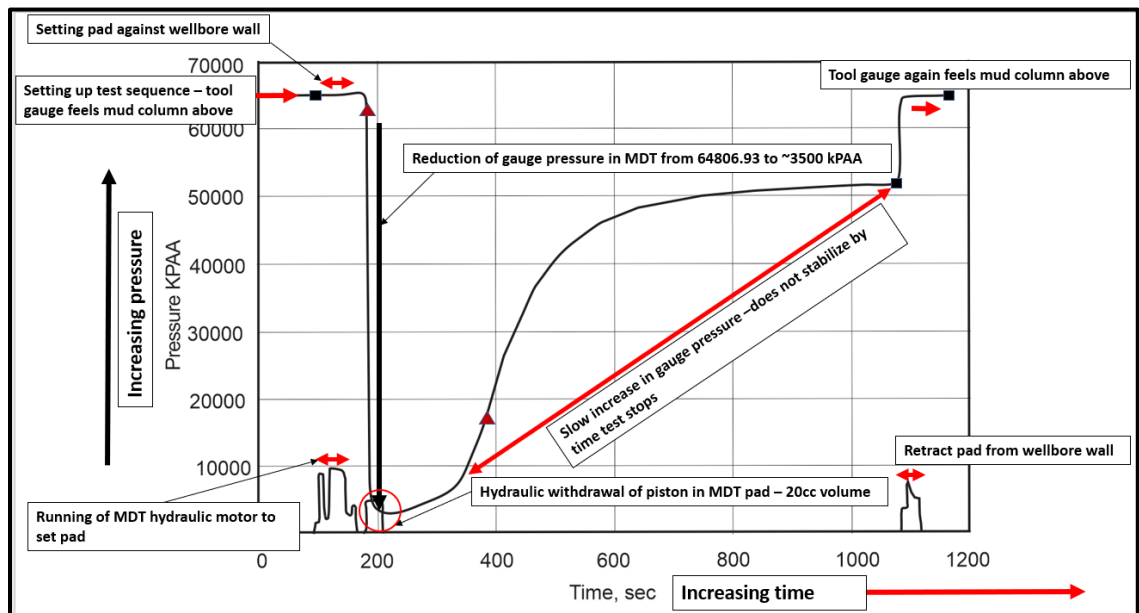


Figure C.3.6: An MDT chart from the Adamant N-97 well test depth 3978 m showing the various measured components during testing (Mobil et al., 2000). From the chart, the running of the tool into the hole associated with the DST has been removed. From the test chart, it took a few seconds to become stabilized at about 38,600 kPaa.

During testing, a “slow build” may occur when the formation pressure does not return to the initial state during the shut-in period. Similarly, a “dry test” formation pressure tests can be identified based on apparent formation pressures during the shut-in period being so low that the test may be considered a failure that it is terminated. A slow build in pressure indicates some very low permeability in the zone tested, commonly resulting in a value lesser than the true formation pressure (Brown, 2003). An opposite, yet the similar response is termed supercharging and may result from the hydrostatic column more than balancing reservoir pressure when a zone is drilled through (Chen, 2014). In doing this, reservoir fluids pushed out of a zone by the drilling mud acts to further pressurize the system giving invalid results that may be higher than the actual formation pressure (Weinheber et al., 2008). Both slow build and supercharging responses are a result of testing done in a low permeability interval with limited pore volume (Watson, pers comm. Oct. 2019).



## APPENDIX D.

A check shot survey is borehole data that measure the one-way time of sound waves from the surface to various depths in a borehole. It measures the travel time from the surface to a known depth (Schlumberger, 2016) represented in Figure D.1 and Figure D.2. The data is used to produce a time-depth pair, which is typically used to calibrate the relationship between the depths in a well and the time component of seismic data.

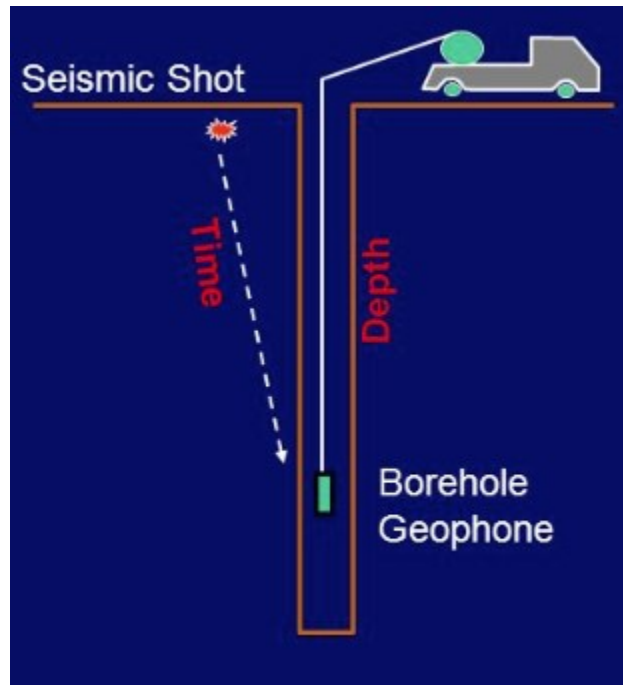


*Figure D.1: A schematic of a borehole checkshot data (Schroeder, 2006).*

It is a measure of the average speed of travel for a signal approaching the receiver from the source typically measured at a regular spacing interval between the various receivers. The resulting average velocity is used for calibrating the time data to the right depth. For velocity data acquired from a sonic log, a localized velocity of the rock is taken, which is consistent with the interval velocity. Taking an average of the various interval velocities results in a similar velocity domain derived when check shot data is used (average velocity). The velocity-depth relationship extracted from a checkshot survey in the Migrant N-20 well report was used to ensure accurate well-to-seismic ties and depth conversion of seismic two-way time models built in Petrel™. These were used to generate depth maps that depict the true structure of the subsurface (Etris et al., 2001).

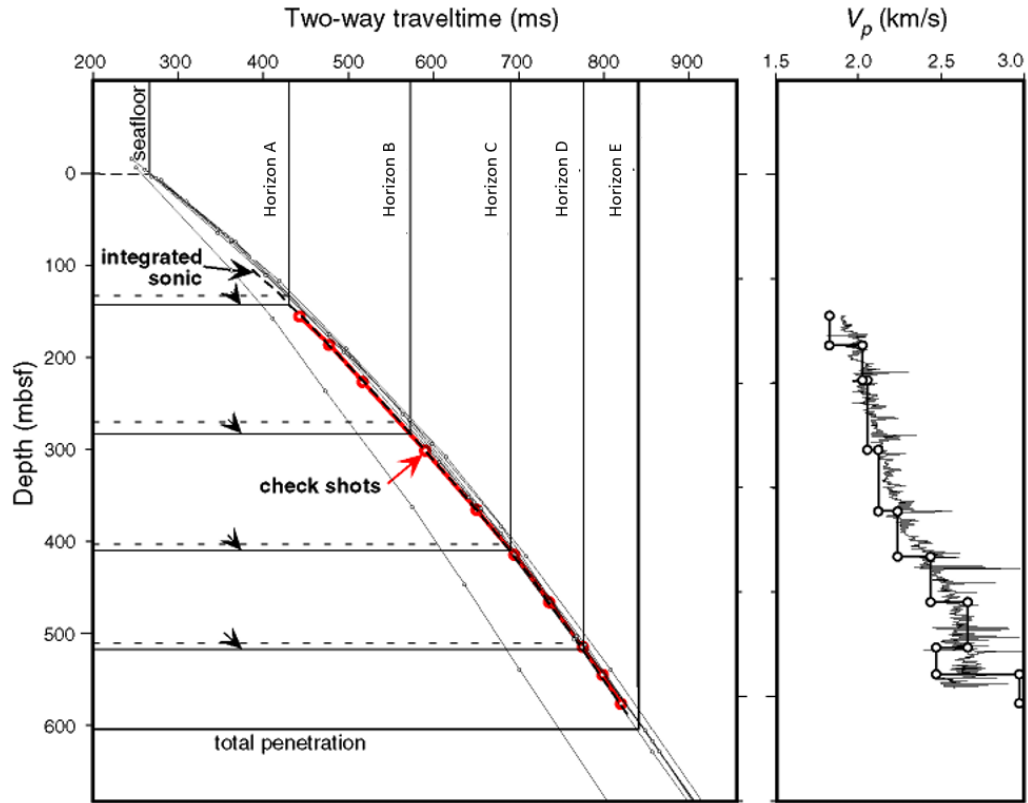


Figure D.2: An example of a typical time-depth velocity relationship extracted from a well's checkshot survey (ODP, 2007). Notice the change in gradient with depth. [http://www-odp.tamu.edu/publications/182\\_IR/chap\\_05/c5\\_f35.htm](http://www-odp.tamu.edu/publications/182_IR/chap_05/c5_f35.htm)

Based on the spreadsheet associated with the N-20 checkshots below (Table D.1), the subsea depth, TWT, average velocity to sea level, and interval velocity between checkshot points can be used to determine the depth of seismic markers interpreted in this study. From the depth and time in the table, an average velocity to sea level for each point as well as an interval velocity between points has been estimated in the table. For this study, the interval velocity was used to convert the horizon picks on either side of the crestal fault in the Migrant Structure from time to depth.

Table D.1: Checkshot values from the Migrant N-20 well.

1	MD	OWT	Average velocity	Interval velocity	Sonic time	Sonic Int. Vel	Drift	Well
2	25.9	0		1121.43	0		0	MIGRANT N-20
3	151.5	112	1121.43	2875.47	57.78	2173.72	-54.22	MIGRANT N-20
4	303.9	165	1684.85	2362.79	133.06	2024.51	-31.94	MIGRANT N-20
5	456.3	229.5	1875.38	2041.62	218.73	1778.94	-10.77	MIGRANT N-20
6	608.61	304.1	1916.16	2340.98	304.58	1773.93	0.48	MIGRANT N-20
7	761.01	369.2	1991.07	2140.43	380.82	1998.94	11.62	MIGRANT N-20
8	913.41	440.4	2015.22	2486.17	452.82	2116.66	12.42	MIGRANT N-20
9	1065.81	501.7	2072.76	2673.7	514.24	2481.37	12.54	MIGRANT N-20
10	1218.21	558.7	2134.07	2680.74	576.34	2454.22	17.64	MIGRANT N-20
11	1523.01	672.4	2226.51	2875.47	695.1	2566.42	22.7	MIGRANT N-20
12	1827.81	778.4	2314.88	3569.11	797.7	2970.77	19.3	MIGRANT N-20
13	2132.62	863.8	2438.88	3398.04	891.46	3251.14	27.66	MIGRANT N-20
14	2437.42	953.5	2529.11	3526.62	979.75	3452.27	26.25	MIGRANT N-20
15	2742.12	1039.9	2611.99	2790.93	1058.5	3869.27	18.6	MIGRANT N-20
16	3046.61	1149	2628.98	6295.49	1134.94	3983.31	-14.06	MIGRANT N-20
17	3351.34	1197.4	2777.19	4232.17	1212.26	3940.45	14.86	MIGRANT N-20
18	3656.11	1269.4	2859.71	4616.39	1284.03	4245.77	14.63	MIGRANT N-20
19	3960.83	1335.4	2946.53	4379.31	1353.62	4378.55	18.22	MIGRANT N-20
20	4265.71	1405	3017.51	5263.01	1419.95	4595.34	14.95	MIGRANT N-20
21	4450	1440	3072.09		1461.27	4457.22	21.27	MIGRANT N-20

APPENDIX E.

E.1. Core Reservoir Estimate Tables

Table E.1.1: A summary table of core data estimates for the I-93 Sand in the Thebaud Field.

CORE LABORATORIES - CANADA, LTD.												
WELL	MOBIL et al THEBAUD I-93										PAGE	10
FORMATION	MISSISSAUGA #2 SAND											
SUMMARY INTERVAL	3065.68-3358.29										FILE	7801-85-12
TOTAL	292.61											
METRES ANALYZED	7.22											
METRES NOT ANALYZED:	TOTAL	285.39	DENSE	8.00	LOST	3.00	*NA	0.00	DRILLED	274.02	RUBBLE	0.37
SUMMARY OF ANALYZED CORE:		METRES	FRACTION OF ANALYZED CORE	WEIGHTED AVERAGE POROSITY	POROSITY METRES	WEIGHTED AV. HORIZONTAL PERMEABILITY	PERMEABILITY METRES	WEIGHTED AVERAGE RESID. OIL	WEIGHTED AVERAGE TOT. WATER			
	TOTAL	7.220	1.000	0.123	0.887	242.566	1751.325	0.011	0.741			
	BY PERM RANGES											
	LESS THAN 0.01 mD	0.330	0.046	0.029	0.010	0.005	0.002	0.000	0.790			
	0.01 0.09 mD	2.070	0.287	0.049	0.101	0.043	0.088	0.000	0.644			
	0.10 0.49 mD	1.240	0.172	0.082	0.101	0.237	0.294	0.000	0.489			
	0.50 0.99 mD	0.210	0.029	0.086	0.018	0.500	0.105	0.000	0.492			
	1.0 9.99 mD	0.220	0.030	0.091	0.020	3.720	0.818	0.000	0.653			
	GREATER THAN 9.99 mD	3.150	0.436	0.202	0.637	555.561	1750.018	0.016	0.805			
		*NOT ANALYZED BY REQUEST										
THESE ANALYSES, OPINIONS OR INTERPRETATIONS ARE BASED ON OBSERVATIONS AND MATERIALS SUPPLIED BY THE CLIENT TO WHOM; AND FOR WHOSE EXCLUSIVE AND CONFIDENTIAL USE; THIS REPORT IS MADE. THE INTERPRETATIONS OR OPINIONS EXPRESSED REPRESENT THE BEST JUDGMENT OF CORE LABORATORIES - CANADA LTD. (ALL ERRORS AND OMISSIONS EXCEPTED); BUT CORE LABORATORIES - CANADA LTD. AND ITS OFFICERS AND EMPLOYEES, ASSUME NO RESPONSIBILITY AND MAKE NO WARRANTY OR REPRESENTATIONS, AS TO THE PRODUCTIVITY, PROPER OPERATIONS, OR PROFITABILITY OF ANY OIL, GAS OR OTHER MINERAL WELL OR SAND IN CONNECTION WITH WHICH SUCH REPORT IS USED OR RELIED UPON.												

247

Table E.1.2: A cumulative of interval porosity and permeability estimates for the I-93 sand interval.

1	Sample	Depth	Interval	Max K	Por. Frac	Por.Product	K. Product	
2	1	3065.68-65.90	0.22	0.11	0.074	0.01628	0.0242	
3	2	3065.90-66.11	0.21	0.28	0.077	0.01617	0.0588	
4	3	3066.11-66.37	0.26	0.04	0.059	0.01534	0.0104	
5	1	3066.39-66.70	0.31	0.01	0.058	0.01798	0.0031	
6	4	3066.70-66.98	0.28	0.06	0.059	0.01652	0.0168	
7	2	3066.98-67.31	0.33	0	0.029	0.00957	0	
8	5	3067.31-67.58	0.27	0.03	0.026	0.00702	0.0081	
9	3	3067.58-67.88	0.3	0.16	0.084	0.0252	0.048	
10	6	3067.88-68.15	0.27	0.3	0.082	0.02214	0.081	
11	7	3068.15-68.39	0.24	0.34	0.089	0.02136	0.0816	
12	8	3068.39-68.60	0.21	0.5	0.086	0.01806	0.105	
13	4	3068.60-68.90	0.3	0.03	0.033	0.0099	0.009	
14	9	3068.90-69.06	0.16	0.06	0.035	0.0056	0.0096	
15	10	3069.06-69.28	0.22	27.8	0.13	0.0286	6.116	
16	11	3069.28-69.54	0.26	449	0.179	0.04654	116.74	
17	12	3077.52-77.81	0.29	413	0.209	0.06061	119.77	
18	13	3077.81-78.12	0.31	60.2	0.214	0.06634	18.662	
19	14	3078.12-78.32	0.2	1160	0.232	0.0464	232	
20	5	3078.32-70.65	0.33	1240	0.23	0.0759	409.2	
21	15	3078.65-78.90	0.25	876	0.228	0.057	219	
22	16	3078.90-79.18	0.28	363	0.196	0.05488	101.64	
23	6	3079.18-79.49	0.31	472	0.204	0.06324	146.32	
24	17	3079.49-79.71	0.22	535	0.201	0.04422	117.7	
25	18	3079.71-79.94	0.23	394	0.197	0.04531	90.62	
26	19	3079.94-80.19	0.25	689	0.203	0.05075	172.25	
27	20	3080.56-80.82	0.26	0.04	0.058	0.01508	0.0104	
28	21	3080.82-81.05	0.23	0.09	0.057	0.01311	0.0207	
29	22	3081.05-81.27	0.22	3.72	0.091	0.02002	0.8184	
30	<b>Summation:</b>		<b>7.22</b>		<b>Sum Por-Interval:</b>	<b>0.88914</b>	<b>Sum K-interval:</b>	<b>1751.3231</b>
						<b>Cumm Por-Interval: 0.12315</b>	<b>Cumm K-Interval: 242.566</b>	

Table E.1.3: A summary table of core data estimates for the H2 Sand in the Thebaud Field.

ZONE AND CUTOFF DATA		CHARACTERISTICS REMAINING AFTER CUTOFFS			
<b>ZONE:</b>		<b>ZONE:</b>		<b>PERMEABILITY:</b>	
Identification -----	H2 SAND	Number of Samples -----	101	Flow Capacity -----	3930.90 mD-m
Top Depth -----	4922.00 m	Thickness Represented -	26.90 m	Arithmetic Average ----	146. mD
Bottom Depth -----	4948.90 m			Geometric Average -----	27.6 mD
Number of Samples -----	101	<b>POROSITY:</b>		Harmonic Average -----	0.99 mD
		Storage Capacity -----	4.218 $\phi$ -m	Minimum -----	0.04 mD
<b>DATA TYPE:</b>		Arithmetic Average ----	0.157 frac	Maximum -----	953. mD
Porosity -----	(HELIUM)	Minimum -----	0.039 frac	Median -----	45.5 mD
Permeability -----	(MAXIMUM) Kair	Maximum -----	0.257 frac	Standard Dev. (Geom) --	K-10 $\pm$ 1.012 mD
		Median -----	0.165 frac		
<b>CUTOFFS:</b>		Standard Deviation ----	$\pm$ 0.044 frac	<b>HETEROGENEITY (Permeability):</b>	
Porosity (Minimum) -----	0.000 frac			Dykstra-Parsons Var. --	0.900
Porosity (Maximum) -----	100.000 frac	<b>GRAIN DENSITY:</b>		Lorenz Coefficient ----	0.626
Permeability (Minimum) ---	0.0000 mD	Arithmetic Average ----	2658. kg/m3		
Permeability (Maximum) ---	100000. mD	Minimum -----	2620. kg/m3	<b>AVERAGE SATURATIONS (Pore Volume):</b>	
Water Saturation (Maximum)	1.000 frac	Maximum -----	2760. kg/m3		
Oil Saturation (Minimum) -	0.000 frac	Median -----	2650. kg/m3	Water -----	0.107 frac
Grain Density (Minimum) --	2000. kg/m3	Standard Deviation ----	$\pm$ 30. kg/m3		
Grain Density (Maximum) --	3000. kg/m3				
Lithology Excluded -----	NONE				



Table E.1.4: A cumulative of interval porosity and permeability estimates for the H2 sand interval.

1	Sample	Number	Depth	Interval	Max K	Por. Frac	Por.Product	K. Product
2	SP	36	4922.00- 22.22	0.22	474	0.257	0.05654	104.28
3	AST	37	4922.22- 22.30	0.08	911	0.242	0.01936	72.88
4	SP	37	4922.30- 22.51	0.21	911	0.242	0.05082	191.31
5	SP	38	4922.51- 22.62	0.11	669	0.227	0.02497	73.59
6	AST	38	4922.62- 22.99	0.37	669	0.227	0.08399	247.53
7	AST	39	4922.99- 23.04	0.05	511	0.203	0.01015	25.55
8	SP	39	4923.04- 23.09	0.05	511	0.203	0.01015	25.55
9	AST	40	4923.09- 23.18	0.09	820	0.224	0.02016	73.8
10	SP	40	4923.18- 23.35	0.17	820	0.224	0.03808	139.4
11	SP	41	4923.35- 23.60	0.25	91.5	0.163	0.04075	22.875
12	SP	42	4923.60- 24.04	0.44	0.17	0.054	0.02376	0.0748
13	SP	43	4924.04- 24.27	0.23	132	0.185	0.04255	30.36
14	AST	44	4924.27- 24.41	0.14	18.2	0.144	0.02016	2.548
15	SP	44	4924.41- 24.55	0.14	18.2	0.144	0.02016	2.548
16	SP	45	4924.55- 24.91	0.36	32.8	0.152	0.05472	11.808
17	SP	46	4924.91- 25.34	0.43	18.6	0.147	0.06321	7.998
18	SP	47	4925.34- 25.55	0.21	65.7	0.197	0.04137	13.797
19	SP	48	4925.55- 25.74	0.19	1.75	0.123	0.02337	0.3325
20	SP	49	4925.74- 26.04	0.3	2.16	0.126	0.0378	0.648
21	SP	50	4926.04- 26.40	0.36	41.3	0.157	0.05652	14.868
22	SP	51	4926.40- 26.60	0.2	55.6	0.185	0.037	11.12
23	SP	52	4926.60- 26.93	0.33	100	0.164	0.05412	33
24	SP	53	4926.93- 27.29	0.36	251	0.167	0.06012	90.36
25	SP	54	4927.29- 27.64	0.35	34.1	0.151	0.05285	11.935
26	SP	55	4927.64- 28.09	0.45	44.9	0.17	0.0765	20.205
27	SP	56	4928.09- 28.29	0.2	50.2	0.146	0.0292	10.04
28	SP	57	4928.29- 28.46	0.17	36.9	0.168	0.02856	6.273
29	AST	59	4929.06- 29.35	0.29	144	0.17	0.0493	41.76
30	SP	60	4929.35- 29.64	0.29	36	0.154	0.04466	10.44
31	SP	61	4929.64- 29.87	0.23	37.1	0.129	0.02967	8.533
32	SP	62	4929.87- 30.10	0.23	67.3	0.157	0.03611	15.479
33	SP	63	4930.10- 30.50	0.4	5.67	0.138	0.0552	2.268
34	SP	64	4930.50- 30.81	0.31	4.34	0.124	0.03844	1.3454
35	SP	65	4930.81- 30.98	0.17	6.28	0.105	0.01785	1.0676
36	SP	66	4930.98- 31.37	0.39	1.89	0.13	0.0507	0.7371
37	SP	67	4931.37- 31.81	0.44	45.5	0.151	0.06644	20.02
38	SP	68	4931.81- 31.94	0.13	9.53	0.141	0.01833	1.2389
39	SP	69	4931.94- 32.14	0.2	2.48	0.123	0.0246	0.496
40	SP	70	4932.14- 32.65	0.51	19.6	0.142	0.07242	9.996
41	SP	71	4932.65- 32.92	0.27	6.97	0.148	0.03996	1.8819
42	SP	72	4932.92- 33.16	0.24	53.2	0.165	0.0396	12.768
43	SP	73	4933.16- 33.60	0.44	9.67	0.131	0.05764	4.2548
44	SP	74	4933.60- 33.94	0.34	42.3	0.145	0.0493	14.382
45	SP	75	4933.94- 34.27	0.33	4.01	0.115	0.03795	1.3233

	Sample	Number	Depth	Interval	Max K	Por. Frac	Por.Product	K. Product
46	SP	76	4934.27- 34.57	0.3	6.15	0.139	0.0417	1.845
47	SP	77	4934.57- 34.77	0.2	16.3	0.149	0.0298	3.26
48	SP	78	4934.77- 35.06	0.29	19.5	0.144	0.04176	5.655
49	SP	79	4935.06- 35.24	0.18	15.2	0.131	0.02358	2.736
50	SP	80	4935.24- 35.58	0.34	24.2	0.14	0.0476	8.228
51	SP	81	4935.58- 35.82	0.24	5.5	0.135	0.0324	1.32
52	SP	82	4935.82- 36.19	0.37	1.8	0.107	0.03959	0.666
53	SP	83	4936.19- 36.46	0.27	1.84	0.134	0.03618	0.4968
54	SP	84	4936.46- 36.65	0.19	0.21	0.101	0.01919	0.0399
55	SP	85	4936.65- 37.11	0.46	0.04	0.039	0.01794	0.0184
56	SP	86	4937.11- 37.51	0.4	0.05	0.072	0.0288	0.02
57	SP	87	4937.51- 37.75	0.24	0.99	0.084	0.02016	0.2376
58	SP	88	4937.75- 38.04	0.29	1.27	0.124	0.03596	0.3683
59	SP	89	4938.04- 38.28	0.24	27.9	0.166	0.03984	6.696
60	SP	90	4938.28- 38.57	0.29	449	0.222	0.06438	130.21
61	SP	91	4938.57- 38.93	0.36	99.8	0.186	0.06696	35.928
62	SP	92	4938.93- 39.18	0.25	93.9	0.185	0.04625	23.475
63	AST	93	4939.18- 39.52	0.34	2.37	0.108	0.03672	0.8058
64	SP	93	4939.52- 39.59	0.07	2.37	0.108	0.00756	0.1659
65	AST	93	4939.59- 39.67	0.08	2.37	0.108	0.00864	0.1896
66	SP	94	4939.67- 39.93	0.26	4.51	0.108	0.02808	1.1726
67	SP	95	4939.93- 40.25	0.32	13.8	0.126	0.04032	4.416
68	SP	96	4940.25- 40.40	0.15	110	0.172	0.0258	16.5
69	AST	96	4940.40- 40.65	0.25	110	0.172	0.043	27.5
70	AST	97	4940.65- 40.75	0.1	141	0.189	0.0189	14.1
71	SP	97	4940.75- 40.85	0.1	141	0.189	0.0189	14.1
72	SP	98	4940.85- 40.98	0.13	168	0.188	0.02444	21.84
73	AST	98	4940.98- 41.31	0.33	168	0.188	0.06204	55.44
74	AST	99	4941.31- 41.37	0.06	529	0.221	0.01326	31.74
75	SP	99	4941.37- 41.43	0.06	529	0.221	0.01326	31.74
76	SP	100	4941.43- 41.80	0.37	225	0.195	0.07215	83.25
77	SP	101	4941.80- 42.22	0.42	177	0.177	0.07434	74.34
78	SP	102	4942.22- 42.51	0.29	0.31	0.051	0.01479	0.0899
79	SP	103	4942.51- 42.86	0.35	0.41	0.086	0.0301	0.1435
80	SP	104	4942.86- 43.10	0.24	54.2	0.166	0.03984	13.008
81	SP	105	4943.10- 43.40	0.3	499	0.21	0.063	149.7
82	SP	106	4943.40- 43.70	0.3	630	0.229	0.0687	189
83	SP	107	4943.70- 43.98	0.28	81.6	0.165	0.0462	22.848
84	SP	108	4943.98- 44.20	0.22	630	0.224	0.04928	138.6
85	SP	109	4944.20- 44.70	0.5	953	0.228	0.114	476.5
86	SP	110	4944.70- 44.87	0.17	163	0.168	0.02856	27.71
87	SP	111	4944.87- 45.24	0.37	243	0.201	0.07437	89.91
88	SP	112	4945.24- 45.73	0.49	795	0.214	0.10486	389.55
89	SP	113	4945.73- 45.83	0.1	655	0.203	0.0203	65.5
90	AST	113	4945.83- 45.94	0.11	655	0.203	0.02233	72.05

	Sample	Number	Depth	Interval	Max K	Por. Frac	Por.Product	K. Product
91	SP	114	4945.94- 46.39	0.45	148	0.171	0.07695	66.6
92	SP	115	4946.39- 46.66	0.27	10.3	0.123	0.03321	2.781
93	SP	116	4946.66- 46.90	0.24	15.1	0.162	0.03888	3.624
94	SP	117	4946.90- 47.38	0.48	124	0.201	0.09648	59.52
95	SP	118	4947.38- 47.64	0.26	121	0.195	0.0507	31.46
96	SP	119	4947.64- 47.83	0.19	2.04	0.19	0.0361	0.3876
97	SP	120	4947.83- 48.22	0.39	125	0.191	0.07449	48.75
98	SP	121	4948.22- 48.40	0.18	23.5	0.167	0.03006	4.23
99	SP	122	4948.40- 48.90	0.5	28.2	0.153	0.0765	14.1
100			Summation:	26.3		Sum Por-Interval:	4.11431	Sum Per-Interval: 3857.23
							Cum Por-Interval: 0.1564	Cum Per-Interval: 146.66

Table E.1.5: A summary table of core data estimates for the F3 Sand in the Thebaud Field.

ZONE AND CUTOFF DATA		CHARACTERISTICS REMAINING AFTER CUTOFFS			
<b>ZONE:</b>		<b>ZONE:</b>		<b>PERMEABILITY:</b>	
Identification -----	F3 SAND	Number of Samples -----	39	Flow Capacity -----	8.02 mD-m
Top Depth -----	4621.00 m	Thickness Represented -	18.21 m	Arithmetic Average ----	0.44 mD
Bottom Depth -----	4639.50 m			Geometric Average ----	0.09 mD
Number of Samples -----	39	<b>POROSITY:</b>		Harmonic Average -----	0.01 mD
<b>DATA TYPE:</b>		Storage Capacity -----	1.416 $\phi$ -m	Minimum -----	0.00 mD
Porosity -----	(HELIUM)	Arithmetic Average ----	0.078 frac	Maximum -----	4.05 mD
Permeability -----	(MAXIMUM) Kair	Minimum -----	0.049 frac	Median -----	0.11 mD
		Maximum -----	0.121 frac	Standard Dev. (Geom) --	$K \cdot 10^{\pm 0.718}$ mD
<b>CUTOFFS:</b>		Median -----	0.079 frac	<b>HETEROGENEITY (Permeability):</b>	
Porosity (Minimum) -----	0.000 frac	Standard Deviation ----	$\pm 0.016$ frac	Dykstra-Parsons Var. --	0.461
Porosity (Maximum) -----	1.000 frac	<b>GRAIN DENSITY:</b>		Lorenz Coefficient ----	0.738
Permeability (Minimum) ---	0.0000 mD	Arithmetic Average ----	2701. kg/m3	<b>AVERAGE SATURATIONS (Pore Volume):</b>	
Permeability (Maximum) ---	100000. mD	Minimum -----	2670. kg/m3	Water -----	0.501 frac
Water Saturation (Maximum)	1.000 frac	Maximum -----	2740. kg/m3		
Oil Saturation (Minimum) -	0.000 frac	Median -----	2700. kg/m3		
Grain Density (Minimum) --	2000. kg/m3	Standard Deviation ----	$\pm 18.$ kg/m3		
Grain Density (Maximum) --	3000. kg/m3				
Lithology Excluded. -----	NONE				

Table E.1.6: A cumulative of interval porosity and permeability estimates for the F3 sand interval.

1	Sample	Number	Depth	Interval	Max K	Por. Frac	Por.Product	K. Product
2	AST	1	4621.00- 21.26	0.26	0.11	0.067	0.01716	0.0286
3	SP	1	4621.26- 21.41	0.15	0.11	0.067	0.01117	0.0165
4	AST	2	4621.41- 21.51	0.1	0.16	0.079	0.0076	0.016
5	SP	2	4621.51- 21.57	0.06	0.16	0.079	0.00426	0.0096
6	AST	3	4621.57- 21.85	0.28	0.16	0.09	0.02128	0.0448
7	SP	3	4621.85- 22.01	0.16	0.16	0.09	0.01168	0.0256
8	SP	4	4622.01- 22.32	0.31	0.11	0.087	0.02449	0.0341
9	SP	5	4622.32- 22.60	0.28	0.07	0.121	0.02156	0.0196
10	AST	5	4622.60- 22.68	0.08	0.07	0.121	0.00648	0.0056
11	SP	6	4622.68- 22.83	0.15	0.1	0.091	0.0135	0.015
12	SP	7	4622.83- 23.13	0.3	0.11	0.112	0.0201	0.033
13	SP	8	4623.13- 23.47	0.34	0.2	0.065	0.02822	0.068
14	SP	9	4623.47- 23.89	0.42	0.17	0.068	0.03318	0.0714
15	SP	10	4623.89- 24.31	0.42	0.11	0.093	0.03444	0.0462
16	AST	10	4624.31- 24.43	0.12	0.11	0.093	0.01116	0.0132
17	SP	11	4624.43- 24.59	0.16	0.07	0.075	0.012	0.0112
18	SP	12	4624.59- 24.90	0.31	0.4	0.082	0.02542	0.124
19	SP	13	4624.90- 25.18	0.28	0.11	0.059	0.01652	0.0308
20	SP	14	4625.18- 25.43	0.25	0.07	0.062	0.0155	0.0175
21	SP	15	4625.43- 25.67	0.24	0.16	0.057	0.01368	0.0384
22	SP	16	4625.67- 26.06	0.39	0.11	0.049	0.01911	0.0429
23	SP	17	4626.06- 26.51	0.45	0.1	0.093	0.04185	0.045
24	SP	18	4626.51- 26.88	0.37	0.04	0.087	0.03219	0.0148
25	SP	19	4626.88- 27.13	0.25	0.07	0.064	0.016	0.0175
26	SP	20	4627.13- 27.43	0.3	0.05	0.09	0.027	0.015
27	SP	21	4627.43- 27.87	0.44	0.25	0.076	0.03344	0.11
28	SP	22	4627.87- 28.40	0.53	0.04	0.066	0.03498	0.0212
29	SP	23	4628.40- 29.47	1.07	0	0.078	0.08346	0
30	SP	24	4529.47- 30.20	0.73	0.01	0.076	0.05548	0.0073
31	SP	25	4630.20- 31.29	1.09	0.24	0.071	0.07739	0.2616
32	SP	26	4631.29- 32.28	0.99	0.76	0.076	0.07524	0.7524
33	SP	27	4632.28- 33.20	0.92	0.31	0.073	0.06716	0.2852
34	SP	28	4633.20- 34.14	0.94	0.66	0.079	0.07426	0.6204
35	SP	29	4634.14- 35.16	1.02	0.11	0.077	0.07854	0.1122
36	SP	30	4635.16- 35.70	0.54	0.1	0.081	0.04374	0.054
37	SP	31	4635.70- 36.32	0.62	0.001	0.09	0.0558	0.00062
38	SP	32	4636.32- 37.40	1.08	0.001	0.067	0.07236	0.00108
39	SP	33	4637.40- 38.32	0.92	0.001	0.083	0.07636	0.00092
40	SP	34	4638.32- 39.21	0.89	0.74	0.079	0.07031	0.6586
41	SP	35	4639.21- 39.80	0.59	0.66	0.082	0.04838	0.3894
42			<b>Summation:</b>	<b>18.8</b>		<b>Sum Por-Interval:</b>	<b>1.43298</b>	<b>Sum Per-Interval: 4.07922</b>

**Cum Por-Interval: 0.07622**      **Cum Per-Interval: 0.21698**

## E.2. Well Log Reservoir Estimate Tables

Table E.2.1: Summation table of intervals that meet contribution criteria when only Vsh, is applied to the open hole DST 2 interval. Cells flagged in red are a summation of zones that do not meet the criteria and do not contribute to the total estimate at the bottom.

1	DST 2	Increments	MD	Vsh	Phie_Sc	Sw	Phit_Sc	Perm
2			4333	0	0.09	0.27	0.08	0.61
3		0.2	4333.2	0	0.09	0.39	0.09	0.68
4		0.2	4333.4	0	0.09	0.44	0.09	0.67
5		0.2	4333.6	0.03	0.09	0.51	0.09	0.52
6		0.2	4333.8	0.09	0.08	0.6	0.09	0.35
7		0.2	4334	0.13	0.07	0.68	0.09	0.23
8		0.2	4334.2	0.15	0.07	0.7	0.09	0.19
9		0.2	4334.4	0.13	0.07	0.66	0.09	0.22
10		0.2	4334.6	0.11	0.07	0.69	0.09	0.21
11		0.2	4334.8	0.11	0.07	0.76	0.09	0.19
12		0.2	4335	0.14	0.07	0.81	0.09	0.19
13		0.2	4335.2	0.19	0.07	0.84	0.1	0.2
14		0.2	4335.4	0.24	0.07	0.94	0.1	0.17
15		1	4336.4	0.24	0.06	1	0.09	0.1
16		0.2	4336.6	0.21	0.06	1	0.09	0.1
17		0.2	4336.8	0.18	0.05	1	0.08	0.09
18		0.2	4337	0.19	0.05	1	0.07	0.05
19		0.2	4337.2	0.23	0.04	1	0.07	0.04
20		0.6	4337.8	0.22	0.06	0.98	0.09	0.09
21		0.2	4338	0.15	0.07	0.79	0.09	0.18
22		0.2	4338.2	0.1	0.08	0.68	0.1	0.33
23		0.2	4338.4	0.08	0.09	0.6	0.1	0.57
24		0.2	4338.6	0.12	0.09	0.61	0.11	0.56
25		0.2	4338.8	0.19	0.09	0.62	0.12	0.53
26		0.2	4339	0.25	0.08	0.67	0.12	0.41
27		0.8	4339.8	0.16	0.08	0.63	0.11	0.36
28		0.2	4340	0.1	0.08	0.6	0.1	0.4
29		0.2	4340.2	0.08	0.08	0.62	0.09	0.3
30		0.2	4340.4	0.16	0.06	0.85	0.08	0.11
31		3.6	4344	0.22	0.06	0.84	0.09	0.09
32		0.2	4344.2	0.11	0.07	0.7	0.08	0.15
33		0.2	4344.4	0.1	0.06	0.78	0.07	0.1
34		0.2	4344.6	0.11	0.05	0.96	0.06	0.06
35		0.2	4344.8	0.12	0.05	0.93	0.07	0.06
36		0.2	4345	0.11	0.06	0.79	0.08	0.1
37		0.2	4345.2	0.11	0.06	0.73	0.08	0.13
38		0.2	4345.4	0.12	0.06	0.74	0.08	0.13
39		0.2	4345.6	0.13	0.06	0.78	0.08	0.13
40		0.2	4345.8	0.15	0.06	0.82	0.08	0.13
41		0.2	4346	0.17	0.07	0.78	0.09	0.16
42		0.2	4346.2	0.2	0.07	0.75	0.1	0.18
43		12.4	4358.6	0.25	0.01	1	0.04	0.01
44		0.2	4358.8	0.22	0	1	0.03	0
45		0.2	4359	0.23	0	1	0.02	0
46		0.2	4359.2	0.25	0	1	0.02	0
47		1.8						
48		7.8		0.14622	0.063556	0.76756	0.083556	0.224



Table E.2.2: Summation table of intervals that meet contribution criteria when the Vsh and Effective porosity are applied to the open hole DST 2 interval. Cells flagged in red are a summation of zones that do not meet the criteria and do not contribute to the total estimate at the bottom.

1	DST 2	Increments	MD	Vsh	Phie_Sc	Sw	Phit_Sc	Perm
2			4333	0	0.09	0.27	0.08	0.61
3		0.2	4333.2	0	0.09	0.39	0.09	0.68
4		0.2	4333.4	0	0.09	0.44	0.09	0.67
5		0.2	4333.6	0.03	0.09	0.51	0.09	0.52
6		0.2	4333.8	0.09	0.08	0.6	0.09	0.35
7		0.2	4334	0.13	0.07	0.68	0.09	0.23
8		0.2	4334.2	0.15	0.07	0.7	0.09	0.19
9		0.2	4334.4	0.13	0.07	0.66	0.09	0.22
10		0.2	4334.6	0.11	0.07	0.69	0.09	0.21
11		0.2	4334.8	0.11	0.07	0.76	0.09	0.19
12		0.2	4335	0.14	0.07	0.81	0.09	0.19
13		0.2	4335.2	0.19	0.07	0.84	0.1	0.2
14		0.2	4335.4	0.24	0.07	0.94	0.1	0.17
15		1	4336.4	0.24	0.06	1	0.09	0.1
16		0.2	4336.6	0.21	0.06	1	0.09	0.1
17		0.2	4336.8	0.18	0.05	1	0.08	0.09
18		0.2	4337	0.19	0.05	1	0.07	0.05
19		0.8	4337.8	0.22	0.06	0.98	0.09	0.09
20		0.2	4338	0.15	0.07	0.79	0.09	0.18
21		0.2	4338.2	0.1	0.08	0.68	0.1	0.33
22		0.2	4338.4	0.08	0.09	0.6	0.1	0.57
23		0.2	4338.6	0.12	0.09	0.61	0.11	0.56
24		0.2	4338.8	0.19	0.09	0.62	0.12	0.53
25		0.2	4339	0.25	0.08	0.67	0.12	0.41
26		0.8	4339.8	0.16	0.08	0.63	0.11	0.36
27		0.2	4340	0.1	0.08	0.6	0.1	0.4
28		0.2	4340.2	0.08	0.08	0.62	0.09	0.3
29		0.2	4340.4	0.16	0.06	0.85	0.08	0.11
30		3.6	4344	0.22	0.06	0.84	0.09	0.09
31		0.2	4344.2	0.11	0.07	0.7	0.08	0.15
32		0.2	4344.4	0.1	0.06	0.78	0.07	0.1
33		0.2	4344.6	0.11	0.05	0.96	0.06	0.06
34		0.2	4344.8	0.12	0.05	0.93	0.07	0.06
35		0.2	4345	0.11	0.06	0.79	0.08	0.1
36		0.2	4345.2	0.11	0.06	0.73	0.08	0.13
37		0.2	4345.4	0.12	0.06	0.74	0.08	0.13
38		0.2	4345.6	0.13	0.06	0.78	0.08	0.13
39		0.2	4345.8	0.15	0.06	0.82	0.08	0.13
40		0.2	4346	0.17	0.07	0.78	0.09	0.16
41		0.2	4346.2	0.2	0.07	0.75	0.1	0.18
42		14.8						
43		7		0.135	0.07025	0.7385	0.0895	0.2508



Table E.2.3: Summation table of intervals that meet contribution criteria when the Vsh, Effective porosity, and Water Saturation parameters (which incorporates flowable amounts of hydrocarbons) are applied to the open hole DST 2 interval. Cells flagged in red are a summation of zones that do not meet the criteria and do not contribute to the total estimate at the bottom.

1	DST 2	Increments	MD	Vsh	Phie_Sc	Sw	Phit_Sc	Perm
2			4333	0	0.09	0.27	0.08	0.61
3		0.2	4333.2	0	0.09	0.39	0.09	0.68
4		0.2	4333.4	0	0.09	0.44	0.09	0.67
5		0.2	4333.6	0.03	0.09	0.51	0.09	0.52
6		0.2	4333.8	0.09	0.08	0.6	0.09	0.35
7		0.2	4334	0.13	0.07	0.68	0.09	0.23
8		0.2	4334.2	0.15	0.07	0.7	0.09	0.19
9		0.2	4334.4	0.13	0.07	0.66	0.09	0.22
10		0.2	4334.6	0.11	0.07	0.69	0.09	0.21
11		3.6	4338.2	0.1	0.08	0.68	0.1	0.33
12		0.2	4338.4	0.08	0.09	0.6	0.1	0.57
13		0.2	4338.6	0.12	0.09	0.61	0.11	0.56
14		0.2	4338.8	0.19	0.09	0.62	0.12	0.53
15		0.2	4339	0.25	0.08	0.67	0.12	0.41
16		0.8	4339.8	0.16	0.08	0.63	0.11	0.36
17		0.2	4340	0.1	0.08	0.6	0.1	0.4
18		0.2	4340.2	0.08	0.08	0.62	0.09	0.3
19		4	4344.2	0.11	0.07	0.7	0.08	0.15
20		1	4345.2	0.11	0.06	0.73	0.08	0.13
21		0.2	4345.4	0.12	0.06	0.74	0.08	0.13
22		0.8	4346.2	0.2	0.07	0.75	0.1	0.18
23		14.8						
24		3		0.108	0.0785714	0.61381	0.094762	0.3681

Table E.2.4: Summation table of intervals that meet cutoff criteria when only Vsh, is applied to the casing depth derived DST 5 interval. Cells flagged in red are a summation of zones that do not meet the criteria and do not contribute to the total estimate at the bottom.

1	DST 5	Increments	MD	Vsh	Phie_Sc	Sw	Phit_Sc	Perm
2		0.2	4270.2	0.22	0.05	0.68	0.09	0.08
3		0.2	4270.4	0.15	0.06	0.58	0.08	0.11
4		0.2	4270.6	0.11	0.06	0.56	0.07	0.09
5		0.2	4270.8	0.08	0.05	0.4	0.07	0.09
6		0.2	4271	0.07	0.06	0.27	0.07	0.11
7		0.2	4271.2	0.06	0.06	0.22	0.07	0.13
8		0.2	4271.4	0.05	0.06	0.2	0.07	0.14
9		0.2	4271.6	0.05	0.06	0.21	0.07	0.13
10		0.2	4271.8	0.05	0.06	0.22	0.07	0.12
11		0.2	4272	0.05	0.06	0.22	0.07	0.12
12		0.2	4272.2	0.05	0.06	0.23	0.07	0.12
13		0.2	4272.4	0.05	0.06	0.23	0.07	0.11
14		0.2	4272.6	0.07	0.06	0.24	0.07	0.1
15		0.2	4272.8	0.1	0.05	0.27	0.07	0.07
16		0.2	4273	0.12	0.05	0.3	0.06	0.06
17								
18		<b>2.8</b>		<b>0.08533</b>	<b>0.0573333</b>	<b>0.322</b>	<b>0.0713333</b>	<b>0.10533</b>

Table E.2.5: Summation table of intervals that meet cutoff criteria when the Vsh and Effective porosity are applied to the casing depth derived DST 5 interval. Cells flagged in red are a summation of zones that do not meet the criteria and do not contribute to the total estimate at the bottom.

1	DST 5	Increments	MD	Vsh	Phie_Sc	Sw	Phit_Sc	Perm
2		0.2	4270.2	0.22	0.05	0.68	0.09	0.08
3		0.2	4270.4	0.15	0.06	0.58	0.08	0.11
4		0.2	4270.6	0.11	0.06	0.56	0.07	0.09
5		0.2	4270.8	0.08	0.05	0.4	0.07	0.09
6		0.2	4271	0.07	0.06	0.27	0.07	0.11
7		0.2	4271.2	0.06	0.06	0.22	0.07	0.13
8		0.2	4271.4	0.05	0.06	0.2	0.07	0.14
9		0.2	4271.6	0.05	0.06	0.21	0.07	0.13
10		0.2	4271.8	0.05	0.06	0.22	0.07	0.12
11		0.2	4272	0.05	0.06	0.22	0.07	0.12
12		0.2	4272.2	0.05	0.06	0.23	0.07	0.12
13		0.2	4272.4	0.05	0.06	0.23	0.07	0.11
14		0.2	4272.6	0.07	0.06	0.24	0.07	0.1
15		0.2	4272.8	0.1	0.05	0.27	0.07	0.07
16		0.2	4273	0.12	0.05	0.3	0.06	0.06
17								
18		<b>2.8</b>		<b>0.08533</b>	<b>0.057333</b>	<b>0.322</b>	<b>0.071333</b>	<b>0.10533</b>

Table E.2.6: Summation table of intervals that meet cutoff criteria when the Vsh, Effective porosity, and Water Saturation parameters (which incorporates flowable amounts of hydrocarbons) are applied to the casing depth derived DST 5 interval. Cells flagged in red are a summation of zones that do not meet the criteria and do not contribute to the total estimate at the bottom.

1	DST 5	Increments	MD	Vsh	Phie_Sc	Sw	Phit_Sc	Perm
2		0.2	4270.2	0.22	0.05	0.68	0.09	0.08
3		0.2	4270.4	0.15	0.06	0.58	0.08	0.11
4		0.2	4270.6	0.11	0.06	0.56	0.07	0.09
5		0.2	4270.8	0.08	0.05	0.4	0.07	0.09
6		0.2	4271	0.07	0.06	0.27	0.07	0.11
7		0.2	4271.2	0.06	0.06	0.22	0.07	0.13
8		0.2	4271.4	0.05	0.06	0.2	0.07	0.14
9		0.2	4271.6	0.05	0.06	0.21	0.07	0.13
10		0.2	4271.8	0.05	0.06	0.22	0.07	0.12
11		0.2	4272	0.05	0.06	0.22	0.07	0.12
12		0.2	4272.2	0.05	0.06	0.23	0.07	0.12
13		0.2	4272.4	0.05	0.06	0.23	0.07	0.11
14		0.2	4272.6	0.07	0.06	0.24	0.07	0.1
15		0.2	4272.8	0.1	0.05	0.27	0.07	0.07
16		0.2	4273	0.12	0.05	0.3	0.06	0.06
17								
18		<b>2.8</b>		<b>0.08533</b>	<b>0.0573333</b>	<b>0.322</b>	<b>0.071333</b>	<b>0.10533</b>

Table E.2.7: Summation table of intervals that meet cutoff criteria when only Vsh, is applied to the casing depth derived DST 8 interval.

1	DST 8	Increments	MD	Vsh	Phie_Sc	Sw	Phit_Sc	Perm
2			4205	0	0.04	0.67	0.04	0.05
3		0.2	4205.2	0	0.05	0.6	0.05	0.07
4		0.2	4205.4	0.01	0.05	0.59	0.05	0.08
5		0.2	4205.6	0.02	0.05	0.58	0.06	0.08
6		0.2	4205.8	0.03	0.05	0.6	0.06	0.08
7		0.2	4206	0.04	0.06	0.58	0.06	0.09
8		0.2	4206.2	0.05	0.06	0.56	0.07	0.11
9		0.2	4206.4	0.06	0.06	0.54	0.07	0.12
10		0.2	4206.6	0.05	0.06	0.5	0.07	0.14
11		0.2	4206.8	0.02	0.07	0.46	0.07	0.17
12		0.2	4207	0	0.07	0.43	0.07	0.2
13		0.2	4207.2	0	0.07	0.42	0.07	0.21
14		0.2	4207.4	0.01	0.07	0.42	0.07	0.21
15		0.2	4207.6	0.02	0.07	0.41	0.08	0.24
16		0.2	4207.8	0.03	0.08	0.41	0.08	0.27
17		0.2	4208	0.03	0.08	0.42	0.08	0.28
18		0.2	4208.2	0.03	0.08	0.45	0.08	0.26
19		0.2	4208.4	0.03	0.07	0.51	0.08	0.2
20		0.2	4208.6	0.03	0.07	0.54	0.07	0.18
21		0.2	4208.8	0.02	0.07	0.54	0.07	0.18
22		0.2	4209	0.02	0.07	0.52	0.07	0.18
23		0.2	4209.2	0.01	0.07	0.51	0.07	0.19
24		0.2	4209.4	0	0.07	0.51	0.07	0.19
25		0.2	4209.6	0	0.07	0.5	0.07	0.2
26		0.2	4209.8	0	0.07	0.5	0.07	0.2
27		0.2	4210	0	0.07	0.51	0.07	0.19
28		0.2	4210.2	0	0.07	0.52	0.07	0.19
29		0.2	4210.4	0	0.07	0.54	0.07	0.18
30		0.2	4210.6	0.01	0.07	0.54	0.07	0.18
31		0.2	4210.8	0.01	0.07	0.53	0.07	0.18
32		0.2	4211	0.02	0.07	0.51	0.07	0.19
33		0.2	4211.2	0.02	0.07	0.49	0.07	0.18
34		0.2	4211.4	0.01	0.07	0.49	0.07	0.18
35		0.2	4211.6	0	0.07	0.49	0.07	0.18
36		0.2	4211.8	0	0.07	0.49	0.07	0.18
37		0.2	4212	0.01	0.07	0.51	0.07	0.17
38								
39		<b>7</b>		<b>0.01639</b>	<b>0.0666667</b>	<b>0.51083</b>	<b>0.068611</b>	<b>0.17167</b>

Table E.2.8: Summation table of intervals that meet cutoff criteria when the Vsh and Effective porosity are applied to the casing depth derived DST 8 interval. Cells flagged in red are a summation of zones that do not meet the criteria and do not contribute to the total estimate at the bottom.

1	DST 8	Increments	MD	Vsh	Phie_Sc	Sw	Phit_Sc	Perm
2		0.2	4205.2	0	0.05	0.6	0.05	0.07
3		0.2	4205.4	0.01	0.05	0.59	0.05	0.08
4		0.2	4205.6	0.02	0.05	0.58	0.06	0.08
5		0.2	4205.8	0.03	0.05	0.6	0.06	0.08
6		0.2	4206	0.04	0.06	0.58	0.06	0.09
7		0.2	4206.2	0.05	0.06	0.56	0.07	0.11
8		0.2	4206.4	0.06	0.06	0.54	0.07	0.12
9		0.2	4206.6	0.05	0.06	0.5	0.07	0.14
10		0.2	4206.8	0.02	0.07	0.46	0.07	0.17
11		0.2	4207	0	0.07	0.43	0.07	0.2
12		0.2	4207.2	0	0.07	0.42	0.07	0.21
13		0.2	4207.4	0.01	0.07	0.42	0.07	0.21
14		0.2	4207.6	0.02	0.07	0.41	0.08	0.24
15		0.2	4207.8	0.03	0.08	0.41	0.08	0.27
16		0.2	4208	0.03	0.08	0.42	0.08	0.28
17		0.2	4208.2	0.03	0.08	0.45	0.08	0.26
18		0.2	4208.4	0.03	0.07	0.51	0.08	0.2
19		0.2	4208.6	0.03	0.07	0.54	0.07	0.18
20		0.2	4208.8	0.02	0.07	0.54	0.07	0.18
21		0.2	4209	0.02	0.07	0.52	0.07	0.18
22		0.2	4209.2	0.01	0.07	0.51	0.07	0.19
23		0.2	4209.4	0	0.07	0.51	0.07	0.19
24		0.2	4209.6	0	0.07	0.5	0.07	0.2
25		0.2	4209.8	0	0.07	0.5	0.07	0.2
26		0.2	4210	0	0.07	0.51	0.07	0.19
27		0.2	4210.2	0	0.07	0.52	0.07	0.19
28		0.2	4210.4	0	0.07	0.54	0.07	0.18
29		0.2	4210.6	0.01	0.07	0.54	0.07	0.18
30		0.2	4210.8	0.01	0.07	0.53	0.07	0.18
31		0.2	4211	0.02	0.07	0.51	0.07	0.19
32		0.2	4211.2	0.02	0.07	0.49	0.07	0.18
33		0.2	4211.4	0.01	0.07	0.49	0.07	0.18
34		0.2	4211.6	0	0.07	0.49	0.07	0.18
35		0.2	4211.8	0	0.07	0.49	0.07	0.18
36		0.2	4212	0.01	0.07	0.51	0.07	0.17
37								
38		6.8		0.016857	0.06742857	0.506286	0.0694286	0.175143

Table E.2.9: Summation table of intervals that meet cutoff criteria when the Vsh, Effective porosity, and Water Saturation parameters (which incorporates flowable amounts of hydrocarbons) are applied to the casing depth derived DST 8 interval. Cells flagged in red are a summation of zones that do not meet the criteria and do not contribute to the total estimate at the bottom.

1	DST 8	Increments	MD	Vsh	Phie_Sc	Sw	Phit_Sc	Perm
2		0.2	4205.2	0	0.05	0.6	0.05	0.07
3		0.2	4205.4	0.01	0.05	0.59	0.05	0.08
4		0.2	4205.6	0.02	0.05	0.58	0.06	0.08
5		0.2	4205.8	0.03	0.05	0.6	0.06	0.08
6		0.2	4206	0.04	0.06	0.58	0.06	0.09
7		0.2	4206.2	0.05	0.06	0.56	0.07	0.11
8		0.2	4206.4	0.06	0.06	0.54	0.07	0.12
9		0.2	4206.6	0.05	0.06	0.5	0.07	0.14
10		0.2	4206.8	0.02	0.07	0.46	0.07	0.17
11		0.2	4207	0	0.07	0.43	0.07	0.2
12		0.2	4207.2	0	0.07	0.42	0.07	0.21
13		0.2	4207.4	0.01	0.07	0.42	0.07	0.21
14		0.2	4207.6	0.02	0.07	0.41	0.08	0.24
15		0.2	4207.8	0.03	0.08	0.41	0.08	0.27
16		0.2	4208	0.03	0.08	0.42	0.08	0.28
17		0.2	4208.2	0.03	0.08	0.45	0.08	0.26
18		0.2	4208.4	0.03	0.07	0.51	0.08	0.2
19		0.2	4208.6	0.03	0.07	0.54	0.07	0.18
20		0.2	4208.8	0.02	0.07	0.54	0.07	0.18
21		0.2	4209	0.02	0.07	0.52	0.07	0.18
22		0.2	4209.2	0.01	0.07	0.51	0.07	0.19
23		0.2	4209.4	0	0.07	0.51	0.07	0.19
24		0.2	4209.6	0	0.07	0.5	0.07	0.2
25		0.2	4209.8	0	0.07	0.5	0.07	0.2
26		0.2	4210	0	0.07	0.51	0.07	0.19
27		0.2	4210.2	0	0.07	0.52	0.07	0.19
28		0.2	4210.4	0	0.07	0.54	0.07	0.18
29		0.2	4210.6	0.01	0.07	0.54	0.07	0.18
30		0.2	4210.8	0.01	0.07	0.53	0.07	0.18
31		0.2	4211	0.02	0.07	0.51	0.07	0.19
32		0.2	4211.2	0.02	0.07	0.49	0.07	0.18
33		0.2	4211.4	0.01	0.07	0.49	0.07	0.18
34		0.2	4211.6	0	0.07	0.49	0.07	0.18
35		0.2	4211.8	0	0.07	0.49	0.07	0.18
36		0.2	4212	0.01	0.07	0.51	0.07	0.17
37								
38		6.8		0.016857	0.06742857	0.506286	0.0694286	0.175143



Table E.2.10: Summation table of intervals that meet contribution criteria when only Vsh, is applied to the Bottom Sand open hole Interval below DST 2. Cells flagged in red are a summation of zones that do not meet criteria and do not contribute to the total estimate at the bottom.

1	Base Sand	Increments	MD	Vsh	Phie_Sc	Sw	Phit_Sc	Perm
2			4400	0.18	0.08	0.67	0.1	0.26
3		0.2	4400.2	0.14	0.07	0.68	0.09	0.19
4		0.2	4400.4	0.14	0.06	0.74	0.08	0.12
5		0.2	4400.6	0.17	0.05	0.84	0.08	0.07
6		0.2	4400.8	0.21	0.05	0.79	0.08	0.07
7		0.2	4401	0.25	0.05	0.71	0.09	0.08
8		0.6	4401.6	0.25	0.06	0.69	0.1	0.14
9		0.2	4401.8	0.24	0.07	0.7	0.1	0.15
10		0.2	4402	0.24	0.07	0.7	0.1	0.16
11		0.2	4402.2	0.23	0.07	0.67	0.1	0.19
12		0.2	4402.4	0.23	0.07	0.65	0.11	0.21
13		0.2	4402.6	0.24	0.07	0.69	0.11	0.22
14		2.2	4404.8	0.23	0.04	1	0.07	0.03
15		0.2	4405	0.1	0.04	0.74	0.06	0.05
16		0.2	4405.2	0.05	0.05	0.53	0.06	0.07
17		0.2	4405.4	0.04	0.05	0.42	0.06	0.08
18		0.2	4405.6	0.04	0.06	0.35	0.06	0.09
19		0.2	4405.8	0.03	0.06	0.3	0.07	0.12
20		0.2	4406	0.03	0.07	0.29	0.07	0.17
21		0.2	4406.2	0.04	0.07	0.29	0.08	0.21
22		0.2	4406.4	0.04	0.08	0.29	0.08	0.27
23		0.2	4406.6	0.05	0.08	0.3	0.09	0.3
24		0.2	4406.8	0.06	0.07	0.33	0.08	0.24
25		0.2	4407	0.07	0.07	0.35	0.08	0.18
26		0.2	4407.2	0.08	0.06	0.38	0.08	0.14
27		0.2	4407.4	0.09	0.06	0.4	0.07	0.13
28		0.2	4407.6	0.09	0.06	0.42	0.07	0.12
29		0.2	4407.8	0.09	0.06	0.42	0.08	0.12
30		0.2	4408	0.11	0.06	0.45	0.08	0.12
31		0.2	4408.2	0.13	0.06	0.51	0.08	0.11
32		0.2	4408.4	0.15	0.05	0.6	0.08	0.08
33		0.2	4408.6	0.13	0.05	0.63	0.07	0.07
34		0.2	4408.8	0.09	0.05	0.63	0.07	0.07
35		0.2	4409	0.08	0.05	0.66	0.06	0.06
36		0.2	4409.2	0.11	0.05	0.69	0.06	0.06
37		0.2	4409.4	0.13	0.05	0.64	0.07	0.06
38		0.2	4409.6	0.14	0.05	0.5	0.07	0.07
39		0.2	4409.8	0.15	0.06	0.45	0.08	0.09
40		0.2	4410	0.18	0.06	0.51	0.08	0.09
41		0.2	4410.2	0.23	0.06	0.59	0.09	0.09
42		0.2	4410.4	0.23	0.06	0.62	0.09	0.11

	Base Sand	Increments	MD	Vsh	Phie_Sc	Sw	Phit_Sc	Perm
44		0.2	4410.8	0.21	0.07	0.58	0.1	0.22
45		0.2	4411	0.2	0.08	0.55	0.11	0.31
46		0.2	4411.2	0.2	0.08	0.53	0.11	0.38
47		0.2	4411.4	0.19	0.08	0.54	0.11	0.41
48		0.2	4411.6	0.2	0.08	0.56	0.11	0.38
49		0.2	4411.8	0.21	0.08	0.6	0.11	0.35
50		0.2	4412	0.25	0.08	0.66	0.11	0.27
51		1.6	4413.6	0.16	0.07	0.78	0.09	0.17
52		0.2	4413.8	0.11	0.06	0.78	0.08	0.14
53		0.2	4414	0.1	0.06	0.78	0.08	0.12
54		0.2	4414.2	0.13	0.06	0.78	0.08	0.1
55		0.2	4414.4	0.14	0.06	0.77	0.08	0.09
56		0.2	4414.6	0.14	0.06	0.74	0.08	0.09
57		0.2	4414.8	0.13	0.06	0.69	0.08	0.12
58		0.2	4415	0.13	0.07	0.61	0.09	0.19
59		0.2	4415.2	0.13	0.08	0.54	0.1	0.31
60		0.2	4415.4	0.14	0.08	0.52	0.11	0.41
61		0.2	4415.6	0.11	0.08	0.52	0.1	0.41
62		0.2	4415.8	0.09	0.08	0.59	0.09	0.27
63		0.2	4416	0.09	0.08	0.58	0.09	0.34
64		0.2	4416.2	0.12	0.08	0.63	0.1	0.35
65		0.2	4416.4	0.16	0.08	0.68	0.1	0.35
66		0.2	4416.6	0.22	0.08	0.75	0.11	0.32
67		12.8	4429.4	0.24	0.08	0.95	0.12	0.41
68		0.2	4429.6	0.18	0.09	0.81	0.12	0.67
69		0.2	4429.8	0.16	0.09	0.78	0.11	0.57
70		0.2	4430	0.15	0.05	1	0.07	0.06
71								
72		12.8		0.14522	0.065652	0.60493	0.0872464	0.19159

Table E.2.11: Summation table of intervals that meet contribution criteria when the Vsh and Effective porosity are applied to the Bottom Sand open hole Interval below DST 2. Cells flagged in red are a summation of zones that do not meet the criteria and do not contribute to the total estimate at the bottom.

1	Bottom Sand	Increments	MD	Vsh	Phie_Sc	Sw	Phit_Sc	Perm
2			4400	0.18	0.08	0.67	0.1	0.26
3		0.2	4400.2	0.14	0.07	0.68	0.09	0.19
4		0.2	4400.4	0.14	0.06	0.74	0.08	0.12
5		0.2	4400.6	0.17	0.05	0.84	0.08	0.07
6		0.2	4400.8	0.21	0.05	0.79	0.08	0.07
7		0.2	4401	0.25	0.05	0.71	0.09	0.08
8		0.6	4401.6	0.25	0.06	0.69	0.1	0.14
9		0.2	4401.8	0.24	0.07	0.7	0.1	0.15
10		0.2	4402	0.24	0.07	0.7	0.1	0.16
11		0.2	4402.2	0.23	0.07	0.67	0.1	0.19
12		0.2	4402.4	0.23	0.07	0.65	0.11	0.21
13		0.2	4402.6	0.24	0.07	0.69	0.11	0.22
14		2.6	4405.2	0.05	0.05	0.53	0.06	0.07
15		0.2	4405.4	0.04	0.05	0.42	0.06	0.08
16		0.2	4405.6	0.04	0.06	0.35	0.06	0.09
17		0.2	4405.8	0.03	0.06	0.3	0.07	0.12
18		0.2	4406	0.03	0.07	0.29	0.07	0.17
19		0.2	4406.2	0.04	0.07	0.29	0.08	0.21
20		0.2	4406.4	0.04	0.08	0.29	0.08	0.27
21		0.2	4406.6	0.05	0.08	0.3	0.09	0.3
22		0.2	4406.8	0.06	0.07	0.33	0.08	0.24
23		0.2	4407	0.07	0.07	0.35	0.08	0.18
24		0.2	4407.2	0.08	0.06	0.38	0.08	0.14
25		0.2	4407.4	0.09	0.06	0.4	0.07	0.13
26		0.2	4407.6	0.09	0.06	0.42	0.07	0.12
27		0.2	4407.8	0.09	0.06	0.42	0.08	0.12
28		0.2	4408	0.11	0.06	0.45	0.08	0.12
29		0.2	4408.2	0.13	0.06	0.51	0.08	0.11
30		0.2	4408.4	0.15	0.05	0.6	0.08	0.08
31		0.2	4408.6	0.13	0.05	0.63	0.07	0.07
32		0.2	4408.8	0.09	0.05	0.63	0.07	0.07
33		0.2	4409	0.08	0.05	0.66	0.06	0.06
34		0.2	4409.2	0.11	0.05	0.69	0.06	0.06
35		0.2	4409.4	0.13	0.05	0.64	0.07	0.06
36		0.2	4409.6	0.14	0.05	0.5	0.07	0.07
37		0.2	4409.8	0.15	0.06	0.45	0.08	0.09
38		0.2	4410	0.18	0.06	0.51	0.08	0.09
39		0.2	4410.2	0.23	0.06	0.59	0.09	0.09
40		0.2	4410.4	0.23	0.06	0.62	0.09	0.11
41		0.2	4410.6	0.22	0.07	0.62	0.1	0.15
42		0.2	4410.8	0.21	0.07	0.58	0.1	0.22

	Bottom Sand	Increments	MD	Vsh	Phie_Sc	Sw	Phit_Sc	Perm
43		0.2	4411	0.2	0.08	0.55	0.11	0.31
44		0.2	4411.2	0.2	0.08	0.53	0.11	0.38
45		0.2	4411.4	0.19	0.08	0.54	0.11	0.41
46		0.2	4411.6	0.2	0.08	0.56	0.11	0.38
47		0.2	4411.8	0.21	0.08	0.6	0.11	0.35
48		0.2	4412	0.25	0.08	0.66	0.11	0.27
49		1.6	4413.6	0.16	0.07	0.78	0.09	0.17
50		0.2	4413.8	0.11	0.06	0.78	0.08	0.14
51		0.2	4414	0.1	0.06	0.78	0.08	0.12
52		0.2	4414.2	0.13	0.06	0.78	0.08	0.1
53		0.2	4414.4	0.14	0.06	0.77	0.08	0.09
54		0.2	4414.6	0.14	0.06	0.74	0.08	0.09
55		0.2	4414.8	0.13	0.06	0.69	0.08	0.12
56		0.2	4415	0.13	0.07	0.61	0.09	0.19
57		0.2	4415.2	0.13	0.08	0.54	0.1	0.31
58		0.2	4415.4	0.14	0.08	0.52	0.11	0.41
59		0.2	4415.6	0.11	0.08	0.52	0.1	0.41
60		0.2	4415.8	0.09	0.08	0.59	0.09	0.27
61		0.2	4416	0.09	0.08	0.58	0.09	0.34
62		0.2	4416.2	0.12	0.08	0.63	0.1	0.35
63		0.2	4416.4	0.16	0.08	0.68	0.1	0.35
64		12.8	4416.6	0.22	0.08	0.75	0.11	0.32
65		0.2	4429.4	0.24	0.08	0.95	0.12	0.41
66		0.2	4429.6	0.18	0.09	0.81	0.12	0.67
67		0.2	4429.8	0.16	0.09	0.78	0.11	0.57
68		0.2	4430	0.15	0.05	1	0.07	0.06
69								
70		12.4		0.14463	0.0664179	0.59701	0.08791	0.19612

Table E.2.12: Summation table of intervals that meet contribution criteria when the Vsh, Effective porosity and Water Saturation parameters (which incorporates flowable amounts of hydrocarbons) are applied in the Bottom Sand open hole Interval Below DST 2. Cells flagged in red are a summation of zones that do not meet the criteria and do not contribute to the total estimate at the bottom.

1	Bottom Sand	Increments	MD	Vsh	Phie_Sc	Sw	Phit_Sc	Perm
2		0.2	4400	0.18	0.08	0.67	0.1	0.26
3		0.2	4400.2	0.14	0.07	0.68	0.09	0.19
4		0.2	4400.4	0.14	0.06	0.74	0.08	0.12
5		0.6	4401	0.25	0.05	0.71	0.09	0.08
6		0.4	4401.6	0.25	0.06	0.69	0.1	0.14
7		0.2	4401.8	0.24	0.07	0.7	0.1	0.15
8		0.2	4402	0.24	0.07	0.7	0.1	0.16
9		0.2	4402.2	0.23	0.07	0.67	0.1	0.19
10		0.2	4402.4	0.23	0.07	0.65	0.11	0.21
11		0.2	4402.6	0.24	0.07	0.69	0.11	0.22
12		2.6	4405.2	0.05	0.05	0.53	0.06	0.07
13		0.2	4405.4	0.04	0.05	0.42	0.06	0.08
14		0.2	4405.6	0.04	0.06	0.35	0.06	0.09
15		0.2	4405.8	0.03	0.06	0.3	0.07	0.12
16		0.2	4406	0.03	0.07	0.29	0.07	0.17
17		0.2	4406.2	0.04	0.07	0.29	0.08	0.21
18		0.2	4406.4	0.04	0.08	0.29	0.08	0.27
19		0.2	4406.6	0.05	0.08	0.3	0.09	0.3
20		0.2	4406.8	0.06	0.07	0.33	0.08	0.24
21		0.2	4407	0.07	0.07	0.35	0.08	0.18
22		0.2	4407.2	0.08	0.06	0.38	0.08	0.14
23		0.2	4407.4	0.09	0.06	0.4	0.07	0.13
24		0.2	4407.6	0.09	0.06	0.42	0.07	0.12
25		0.2	4407.8	0.09	0.06	0.42	0.08	0.12
26		0.2	4408	0.11	0.06	0.45	0.08	0.12
27		0.2	4408.2	0.13	0.06	0.51	0.08	0.11
28		0.2	4408.4	0.15	0.05	0.6	0.08	0.08
29		0.2	4408.6	0.13	0.05	0.63	0.07	0.07
30		0.2	4408.8	0.09	0.05	0.63	0.07	0.07
31		0.2	4409	0.08	0.05	0.66	0.06	0.06
32		0.2	4409.2	0.11	0.05	0.69	0.06	0.06
33		0.2	4409.4	0.13	0.05	0.64	0.07	0.06
34		0.2	4409.6	0.14	0.05	0.5	0.07	0.07
35		0.2	4409.8	0.15	0.06	0.45	0.08	0.09
36		0.2	4410	0.18	0.06	0.51	0.08	0.09
37		0.2	4410.2	0.23	0.06	0.59	0.09	0.09
38		0.2	4410.4	0.23	0.06	0.62	0.09	0.11
39		0.2	4410.6	0.22	0.07	0.62	0.1	0.15
40		0.2	4410.8	0.21	0.07	0.58	0.1	0.22
41		0.2	4411	0.2	0.08	0.55	0.11	0.31
42		0.2	4411.2	0.2	0.08	0.53	0.11	0.38

	Bottom Sand	Increments	MD	Vsh	Phie_Sc	Sw	Phit_Sc	Perm
43		0.2	4411.4	0.19	0.08	0.54	0.11	0.41
44		0.2	4411.6	0.2	0.08	0.56	0.11	0.38
45		0.2	4411.8	0.21	0.08	0.6	0.11	0.35
46		0.2	4412	0.25	0.08	0.66	0.11	0.27
47		2.6	4414.6	0.14	0.06	0.74	0.08	0.09
48		0.2	4414.8	0.13	0.06	0.69	0.08	0.12
49		0.2	4415	0.13	0.07	0.61	0.09	0.19
50		0.2	4415.2	0.13	0.08	0.54	0.1	0.31
51		0.2	4415.4	0.14	0.08	0.52	0.11	0.41
52		0.2	4415.6	0.11	0.08	0.52	0.1	0.41
53		0.2	4415.8	0.09	0.08	0.59	0.09	0.27
54		0.2	4416	0.09	0.08	0.58	0.09	0.34
55		0.2	4416.2	0.12	0.08	0.63	0.1	0.35
56		0.2	4416.4	0.16	0.08	0.68	0.1	0.35
57		0.2	4416.6	0.22	0.08	0.75	0.11	0.32
58		13.4						
59		10.4		0.14179	0.06660714	0.5525	0.0875	0.19054

Table E.2.13: Summation table of intervals that meet cutoff criteria when only Vsh, is applied to the wireline derived DST 5 interval. Cells flagged in red are a summation of zones that do not meet the criteria and do not contribute to the total estimate at the bottom.

1	DST 5	Increments	MD	Vsh	Phie_Sc	Sw	Phit_Sc	Perm
2		0.2	4270.2	0.22	0.05	0.68	0.09	0.08
3		0.2	4270.4	0.15	0.06	0.58	0.08	0.11
4		0.2	4270.6	0.11	0.06	0.56	0.07	0.09
5		0.2	4270.8	0.08	0.05	0.4	0.07	0.09
6		0.2	4271	0.07	0.06	0.27	0.07	0.11
7		0.2	4271.2	0.06	0.06	0.22	0.07	0.13
8		0.2	4271.4	0.05	0.06	0.2	0.07	0.14
9		0.2	4271.6	0.05	0.06	0.21	0.07	0.13
10		0.2	4271.8	0.05	0.06	0.22	0.07	0.12
11		0.2	4272	0.05	0.06	0.22	0.07	0.12
12		0.2	4272.2	0.05	0.06	0.23	0.07	0.12
13		0.2	4272.4	0.05	0.06	0.23	0.07	0.11
14		0.2	4272.6	0.07	0.06	0.24	0.07	0.1
15		0.2	4272.8	0.1	0.05	0.27	0.07	0.07
16		0.2	4273	0.12	0.05	0.3	0.06	0.06
17		0.2	4273.2	0.14	0.04	0.31	0.06	0.05
18		0.2	4273.4	0.15	0.04	0.33	0.06	0.04
19		0.2	4273.6	0.15	0.04	0.34	0.06	0.04
20		0.2	4273.8	0.14	0.04	0.28	0.06	0.04
21		0.2	4274	0.14	0.04	0.24	0.06	0.04
22		0.2	4274.2	0.15	0.04	0.16	0.07	0.05
23		0.2	4274.4	0.19	0.04	0.2	0.07	0.04
24		0.6						
25								
26		4.2		0.106364	0.0518182	0.3041	0.0686364	0.085455



Table E.2.14: Summation table of intervals that meet cutoff criteria when the Vsh and Effective porosity are applied to the wireline derived DST 5 interval. Cells flagged in red are a summation of zones that do not meet the criteria and do not contribute to the total estimate at the bottom.

1	DST 5	Increments	MD	Vsh	Phie_Sc	Sw	Phit_Sc	Perm
2		0.2	4270.2	0.22	0.05	0.68	0.09	0.08
3		0.2	4270.4	0.15	0.06	0.58	0.08	0.11
4		0.2	4270.6	0.11	0.06	0.56	0.07	0.09
5		0.2	4270.8	0.08	0.05	0.4	0.07	0.09
6		0.2	4271	0.07	0.06	0.27	0.07	0.11
7		0.2	4271.2	0.06	0.06	0.22	0.07	0.13
8		0.2	4271.4	0.05	0.06	0.2	0.07	0.14
9		0.2	4271.6	0.05	0.06	0.21	0.07	0.13
10		0.2	4271.8	0.05	0.06	0.22	0.07	0.12
11		0.2	4272	0.05	0.06	0.22	0.07	0.12
12		0.2	4272.2	0.05	0.06	0.23	0.07	0.12
13		0.2	4272.4	0.05	0.06	0.23	0.07	0.11
14		0.2	4272.6	0.07	0.06	0.24	0.07	0.1
15		0.2	4272.8	0.1	0.05	0.27	0.07	0.07
16		0.2	4273	0.12	0.05	0.3	0.06	0.06
17		2						
18								
19		2.8		0.08533	0.0573333	0.322	0.0713333	0.105333

Table E.2.15: Summation table of intervals that meet cutoff criteria when the Vsh, Effective porosity, and Water Saturation parameters (which incorporates flowable amounts of hydrocarbons) are applied to the wireline derived DST 5 interval. Cells flagged in red are a summation of zones that do not meet the criteria and do not contribute to the total estimate at the bottom.

1	DST 5	Increments	MD	Vsh	Phie_Sc	Sw	Phit_Sc	Perm
2		0.2	4270.2	0.22	0.05	0.68	0.09	0.08
3		0.2	4270.4	0.15	0.06	0.58	0.08	0.11
4		0.2	4270.6	0.11	0.06	0.56	0.07	0.09
5		0.2	4270.8	0.08	0.05	0.4	0.07	0.09
6		0.2	4271	0.07	0.06	0.27	0.07	0.11
7		0.2	4271.2	0.06	0.06	0.22	0.07	0.13
8		0.2	4271.4	0.05	0.06	0.2	0.07	0.14
9		0.2	4271.6	0.05	0.06	0.21	0.07	0.13
10		0.2	4271.8	0.05	0.06	0.22	0.07	0.12
11		0.2	4272	0.05	0.06	0.22	0.07	0.12
12		0.2	4272.2	0.05	0.06	0.23	0.07	0.12
13		0.2	4272.4	0.05	0.06	0.23	0.07	0.11
14		0.2	4272.6	0.07	0.06	0.24	0.07	0.1
15		0.2	4272.8	0.1	0.05	0.27	0.07	0.07
16		0.2	4273	0.12	0.05	0.3	0.06	0.06
17		2						
18								
19		2.8		0.08533	0.0573333	0.322	0.0713333	0.105333

Table E.2.16: Summation table of intervals that meet cutoff criteria when only Vsh is applied to the open hole DST 2 interval. Cells flagged in red are a summation of zones that do not meet the criteria and do not contribute to the total estimate at the bottom.

1	DST 2	Increments	MD	Vsh	Phie_Sc	Sw	Phit_Sc	Perm
2		0.2	4329	0.25	0.05	0.62	0.09	0.08
3		0.2	4329.2	0.13	0.06	0.1	0.08	0.12
4		0.2	4329.4	0.06	0.07	0.06	0.08	0.16
5		0.2	4329.6	0.02	0.08	0.05	0.08	0.28
6		0.2	4329.8	0.01	0.08	0.05	0.08	0.32
7		0.2	4330	0	0.1	0.05	0.08	0.71
8		0.2	4330.2	0	0.09	0.09	0.07	0.47
9		0.2	4330.4	0	0.08	0.2	0.07	0.41
10		0.2	4330.6	0	0.08	0.29	0.07	0.4
11		0.2	4330.8	0	0.08	0.24	0.07	0.36
12		0.2	4331	0	0.08	0.18	0.07	0.3
13		0.2	4331.2	0	0.07	0.16	0.06	0.24
14		0.2	4331.4	0	0.08	0.15	0.06	0.28
15		0.2	4331.6	0	0.08	0.13	0.07	0.36
16		0.2	4331.8	0	0.09	0.13	0.07	0.48
17		0.2	4332	0	0.09	0.13	0.08	0.53
18		0.2	4332.2	0	0.09	0.14	0.08	0.5
19		0.2	4332.4	0	0.09	0.14	0.08	0.55
20		0.2	4332.6	0	0.09	0.17	0.08	0.6
21		0.2	4332.8	0	0.09	0.22	0.08	0.6
22		0.2	4333	0	0.09	0.27	0.08	0.61
23		0.2	4333.2	0	0.09	0.39	0.09	0.68
24		0.2	4333.4	0	0.09	0.44	0.09	0.67
25		0.2	4333.6	0.03	0.09	0.51	0.09	0.52
26		0.2	4333.8	0.09	0.08	0.6	0.09	0.35
27		0.2	4334	0.13	0.07	0.68	0.09	0.23
28		0.2	4334.2	0.15	0.07	0.7	0.09	0.19
29		0.2	4334.4	0.13	0.07	0.66	0.09	0.22
30		0.2	4334.6	0.11	0.07	0.69	0.09	0.21
31		0.2	4334.8	0.11	0.07	0.76	0.09	0.19
32		0.2	4335	0.14	0.07	0.81	0.09	0.19
33		0.2	4335.2	0.19	0.07	0.84	0.1	0.2
34		0.2	4335.4	0.24	0.07	0.94	0.1	0.17
35		1	4336.4	0.24	0.06	1	0.09	0.1
36		0.2	4336.6	0.21	0.06	1	0.09	0.1
37		0.2	4336.8	0.18	0.05	1	0.08	0.09
38		0.2	4337	0.19	0.05	1	0.07	0.05
39		0.2	4337.2	0.23	0.04	1	0.07	0.04
40		0.6	4337.8	0.22	0.06	0.98	0.09	0.09
41		0.2	4338	0.15	0.07	0.79	0.09	0.18
42		0.2	4338.2	0.1	0.08	0.68	0.1	0.33
43		0.2	4338.4	0.08	0.09	0.6	0.1	0.57
44		0.2	4338.6	0.12	0.09	0.61	0.11	0.56
45		0.2	4338.8	0.19	0.09	0.62	0.12	0.53
46		0.2	4339	0.25	0.08	0.67	0.12	0.41
47		0.8	4339.8	0.16	0.08	0.63	0.11	0.36

	DST 2	Increments	MD	Vsh	Phie_Sc	Sw	Phit_Sc	Perm
49		0.2	4340.2	0.08	0.08	0.62	0.09	0.3
50		0.2	4340.4	0.16	0.06	0.85	0.08	0.11
51		4.4	4344	0.22	0.06	0.84	0.09	0.09
52		0.2	4344.2	0.11	0.07	0.7	0.08	0.15
53		0.2	4344.4	0.1	0.06	0.78	0.07	0.1
54		0.2	4344.6	0.11	0.05	0.96	0.06	0.06
55		0.2	4344.8	0.12	0.05	0.93	0.07	0.06
56		0.2	4345	0.11	0.06	0.79	0.08	0.1
57		0.2	4345.2	0.11	0.06	0.73	0.08	0.13
58		0.2	4345.4	0.12	0.06	0.74	0.08	0.13
59		0.2	4345.6	0.13	0.06	0.78	0.08	0.13
60		0.2	4345.8	0.15	0.06	0.82	0.08	0.13
61		0.2	4346	0.17	0.07	0.78	0.09	0.16
62		0.2	4346.2	0.2	0.07	0.75	0.1	0.18
63		12.4	4358.6	0.25	0.01	1	0.04	0.01
64		0.2	4358.8	0.22	0	1	0.03	0
65		0.2	4359	0.23	0	1	0.02	0
66		0.2	4359.2	0.25	0	1	0.02	0
67		1.8						
68								
69		11		0.1085	0.0689231	0.58215	0.080923	0.27431

Table E.2.17: Summation table of intervals meeting cutoff when the Vsh and Effective porosity are applied in the open hole DST 2 interval. Cells flagged in red are a summation of zones that do not meet criteria and do not contribute to the total estimate.

1	DST 2	Increments	MD	Vsh	Phie_Sc	Sw	Phit_Sc	Perm
2		0.2	4329	0.25	0.05	0.62	0.09	0.08
3		0.2	4329.2	0.13	0.06	0.1	0.08	0.12
4		0.2	4329.4	0.06	0.07	0.06	0.08	0.16
5		0.2	4329.6	0.02	0.08	0.05	0.08	0.28
6		0.2	4329.8	0.01	0.08	0.05	0.08	0.32
7		0.2	4330	0	0.1	0.05	0.08	0.71
8		0.2	4330.2	0	0.09	0.09	0.07	0.47
9		0.2	4330.4	0	0.08	0.2	0.07	0.41
10		0.2	4330.6	0	0.08	0.29	0.07	0.4
11		0.2	4330.8	0	0.08	0.24	0.07	0.36
12		0.2	4331	0	0.08	0.18	0.07	0.3
13		0.2	4331.2	0	0.07	0.16	0.06	0.24
14		0.2	4331.4	0	0.08	0.15	0.06	0.28
15		0.2	4331.6	0	0.08	0.13	0.07	0.36
16		0.2	4331.8	0	0.09	0.13	0.07	0.48
17		0.2	4332	0	0.09	0.13	0.08	0.53
18		0.2	4332.2	0	0.09	0.14	0.08	0.5
19		0.2	4332.4	0	0.09	0.14	0.08	0.55
20		0.2	4332.6	0	0.09	0.17	0.08	0.6
21		0.2	4332.8	0	0.09	0.22	0.08	0.6
22		0.2	4333	0	0.09	0.27	0.08	0.61
23		0.2	4333.2	0	0.09	0.39	0.09	0.68
24		0.2	4333.4	0	0.09	0.44	0.09	0.67
25		0.2	4333.6	0.03	0.09	0.51	0.09	0.52
26		0.2	4333.8	0.09	0.08	0.6	0.09	0.35
27		0.2	4334	0.13	0.07	0.68	0.09	0.23
28		0.2	4334.2	0.15	0.07	0.7	0.09	0.19
29		0.2	4334.4	0.13	0.07	0.66	0.09	0.22
30		0.2	4334.6	0.11	0.07	0.69	0.09	0.21
31		0.2	4334.8	0.11	0.07	0.76	0.09	0.19
32		0.2	4335	0.14	0.07	0.81	0.09	0.19
33		0.2	4335.2	0.19	0.07	0.84	0.1	0.2
34		0.2	4335.4	0.24	0.07	0.94	0.1	0.17
35		1	4336.4	0.24	0.06	1	0.09	0.1
36		0.2	4336.6	0.21	0.06	1	0.09	0.1
37		0.2	4336.8	0.18	0.05	1	0.08	0.09
38		0.2	4337	0.19	0.05	1	0.07	0.05
39		0.8	4337.8	0.22	0.06	0.98	0.09	0.09
40		0.2	4338	0.15	0.07	0.79	0.09	0.18
41		0.2	4338.2	0.1	0.08	0.68	0.1	0.33
42		0.2	4338.4	0.08	0.09	0.6	0.1	0.57
43		0.2	4338.6	0.12	0.09	0.61	0.11	0.56
44		0.2	4338.8	0.19	0.09	0.62	0.12	0.53
45		0.2	4339	0.25	0.08	0.67	0.12	0.41
46		0.8	4339.8	0.16	0.08	0.63	0.11	0.36
47		0.2	4340	0.1	0.08	0.6	0.1	0.4

	DST 2	Increments	MD	Vsh	Phie_Sc	Sw	Phit_Sc	Perm
48		0.2	4340.2	0.08	0.08	0.62	0.09	0.3
49		0.2	4340.4	0.16	0.06	0.85	0.08	0.11
50		4.4	4344	0.22	0.06	0.84	0.09	0.09
51		0.2	4344.2	0.11	0.07	0.7	0.08	0.15
52		0.2	4344.4	0.1	0.06	0.78	0.07	0.1
53		0.2	4344.6	0.11	0.05	0.96	0.06	0.06
54		0.2	4344.8	0.12	0.05	0.93	0.07	0.06
55		0.2	4345	0.11	0.06	0.79	0.08	0.1
56		0.2	4345.2	0.11	0.06	0.73	0.08	0.13
57		0.2	4345.4	0.12	0.06	0.74	0.08	0.13
58		0.2	4345.6	0.13	0.06	0.78	0.08	0.13
59		0.2	4345.8	0.15	0.06	0.82	0.08	0.13
60		0.2	4346	0.17	0.07	0.78	0.09	0.16
61		0.2	4346.2	0.2	0.07	0.75	0.1	0.18
62		14.8						
63								
64		10.2		0.0978	0.073833	0.55	0.084667	0.29633

Table E.2.18: Summation table of intervals that meet contribution criteria when the Vsh, Effective porosity, and Water Saturation parameters (which incorporates flowable amounts of hydrocarbons) are applied to the DST 2 interval. Cells flagged in red are a summation of zones that do not meet the criteria and do not contribute to the total estimate at the bottom.

1	DST 2	Increments	MD	Vsh	Phie_Sc	Sw	Phit_Sc	Perm
2		0.2	4329	0.25	0.05	0.62	0.09	0.08
3		0.2	4329.2	0.13	0.06	0.1	0.08	0.12
4		0.2	4329.4	0.06	0.07	0.06	0.08	0.16
5		0.2	4329.6	0.02	0.08	0.05	0.08	0.28
6		0.2	4329.8	0.01	0.08	0.05	0.08	0.32
7		0.2	4330	0	0.1	0.05	0.08	0.71
8		0.2	4330.2	0	0.09	0.09	0.07	0.47
9		0.2	4330.4	0	0.08	0.2	0.07	0.41
10		0.2	4330.6	0	0.08	0.29	0.07	0.4
11		0.2	4330.8	0	0.08	0.24	0.07	0.36
12		0.2	4331	0	0.08	0.18	0.07	0.3
13		0.2	4331.2	0	0.07	0.16	0.06	0.24
14		0.2	4331.4	0	0.08	0.15	0.06	0.28
15		0.2	4331.6	0	0.08	0.13	0.07	0.36
16		0.2	4331.8	0	0.09	0.13	0.07	0.48
17		0.2	4332	0	0.09	0.13	0.08	0.53
18		0.2	4332.2	0	0.09	0.14	0.08	0.5
19		0.2	4332.4	0	0.09	0.14	0.08	0.55
20		0.2	4332.6	0	0.09	0.17	0.08	0.6
21		0.2	4332.8	0	0.09	0.22	0.08	0.6
22		0.2	4333	0	0.09	0.27	0.08	0.61
23		0.2	4333.2	0	0.09	0.39	0.09	0.68
24		0.2	4333.4	0	0.09	0.44	0.09	0.67
25		0.2	4333.6	0.03	0.09	0.51	0.09	0.52
26		0.2	4333.8	0.09	0.08	0.6	0.09	0.35
27		0.2	4334	0.13	0.07	0.68	0.09	0.23
28		0.2	4334.2	0.15	0.07	0.7	0.09	0.19
29		0.2	4334.4	0.13	0.07	0.66	0.09	0.22
30		0.2	4334.6	0.11	0.07	0.69	0.09	0.21
31		3.8	4338.2	0.1	0.08	0.68	0.1	0.33
32		0.2	4338.4	0.08	0.09	0.6	0.1	0.57
33		0.2	4338.6	0.12	0.09	0.61	0.11	0.56
34		0.2	4338.8	0.19	0.09	0.62	0.12	0.53
35		0.2	4339	0.25	0.08	0.67	0.12	0.41
36		0.2	4339.8	0.16	0.08	0.63	0.11	0.36
37		0.2	4340	0.1	0.08	0.6	0.1	0.4
38		0.2	4340.2	0.08	0.08	0.62	0.09	0.3
39		4	4344.2	0.11	0.07	0.7	0.08	0.15
40		1	4345.2	0.11	0.06	0.73	0.08	0.13
41		0.2	4345.4	0.12	0.06	0.74	0.08	0.13
42		0.8	4346.2	0.2	0.07	0.75	0.1	0.18
43		14.8						
44								
45		7.6		0.06659	0.0797561	0.39488	0.085122	0.37756



### E.3. Risking

For risk assessment, the tables provided in this section are applicable in establishing a set of qualitative sensitivities for each petroleum systems element or applicable reservoir parameters.

Table E.3.1: Relative probability scale for the probability of structural closure (Milkov, 2015).

Structure (closure, geometry, container)			Data (existence and reliability)				
			3D seismic	2D seismic Number of lines per structure (with obligatory availability of in-line and cross lines)			
				Dense (7 lines and more)	Sparse (3-6 lines)	Very sparse (2 lines) (Lead)	
Models (existence and reliability)	Seismic mapping and correlation	High-relief structure ( $\geq 3$ times higher than seismic accuracy) AND low structural complexity (4-way)	Easy to interpret, reliable correlation based on nearby (<50 km) wells	1.00	0.90	0.80	0.60
			Uncertain correlation (horizons are interrupted laterally) or based on remote (> 50 km) wells	0.95	0.85	0.75	0.55
			Difficult to interpret, unreliable correlation (horizons are interrupted by thrust faults, diapirs, etc.) or model developed using analogues without wells in the basin	0.85	0.75	0.70	0.45
		Medium-relief structure (1-3 times higher than seismic accuracy) OR high-relief structure with high structural complexity (3-way, stratigraphic)	Easy to interpret, reliable correlation based on nearby (<50 km) wells	0.80	0.70	0.60	0.35
			Uncertain correlation (horizons are interrupted laterally) or based on remote (> 50 km) wells	0.75	0.65	0.50	0.25
			Difficult to interpret, unreliable correlation (horizons are interrupted by thrust faults, diapirs, etc.) or model developed using analogues without wells in the basin	0.70	0.55	0.45	0.20
		Low-relief structure (lower than seismic accuracy) OR high uncertainty of depth conversion (subsalt, below lava flows) OR areas with rapidly changing lateral velocities in the overburden	Easy to interpret, reliable correlation based on nearby (<50 km) wells	0.55	0.45	0.35	0.15
			Uncertain correlation (horizons are interrupted laterally) or based on remote (> 50 km) wells	0.50	0.40	0.25	0.10
			Difficult to interpret, unreliable correlation (horizons are interrupted by thrust faults, diapirs, etc.) or model developed using analogues without wells in the basin	0.40	0.30	0.20	0.05
		Low-relief structure (lower than seismic accuracy) AND EITHER high uncertainty of depth conversion (subsalt, below lava flows) OR areas with rapidly changing lateral velocities in the overburden		0.35	0.25	0.15	0.05

Table E.3.2: Probability scheme for the probability of effective migration (CCOP, 2000).

Timing Migration	The trap is formed before onset of hydrocarbon migration	Time of trap formation and time of migration are overlapping	The trap is formed when the source rock is supposed to be "overcooked"
Local migration	0.9 - 1.0	0.4 - 0.8	0.1 - 0.4
Lateral migration without barriers	0.8 - 0.9	0.4 - 0.7	0.1 - 0.3
Lateral migration with barriers	0.5 - 0.8	0.2 - 0.5	0.1 - 0.3
Vertical migration without barriers	0.7 - 0.9	0.3 - 0.6	0.1 - 0.3
Vertical migration with barriers	0.4 - 0.6	0.2 - 0.4	0.1 - 0.2
Long-distance "fill-spill" migration	0.4 - 0.6	0.2 - 0.4	0.1 - 0.2
The trap is in the "shadow" of migration	0.2 - 0.4	0.1 - 0.3	0.1

Table E.3. 3: Probability scheme for the probability of effective trapping/ retention (CCOP, 2000).

Geological processes after accumulation		Data control	Positive unambiguous data (seismic, wells, etc.)	Data control and interpretation is poor to fair	Negative unambiguous data (seismic, wells, etc.)
No late activity	No tectonic activity after accumulation		0.9 - 1.0	0.8 - 1.0	0.7 - 1.0
	Shallow traps, possible biodegradation		0.8 - 0.9	0.4 - 0.7	0.1 - 0.3
Erosion	Trap in connection to generating source		0.7 - 0.9	0.3 - 0.6	0.1 - 0.3
	Trap not connected to generating source		0.5 - 0.8	0.2 - 0.5	0.1 - 0.2
Uplift and tilting	Form, volume, top-point not changed		0.7 - 0.9	0.4 - 0.7	0.2 - 0.4
	Form, volume, top-point changed		0.5 - 0.6	0.3 - 0.4	0.1 - 0.2
Reactivated faults	Compression and/or transpression		0.5 - 0.7	0.4 - 0.5	0.3 - 0.4
	Tension		0.4 - 0.6	0.3 - 0.4	0.1 - 0.3

Table E.3.4: Probability schemes for the probability of effective reservoir facies (CCOP, 2000).

Depositional environment		Data reliability			
		Direct data, proximal deposits	Direct data, more distal deposits	Limited data, discontinuous deposits	Indirect data, seismic sequence analysis
Marine	Shallow marine, "blanket"	0.9 - 1.0	0.7 - 0.8	0.6 - 0.7	0.4 - 0.6
	Coastal, deltaic, tidal	0.8 - 1.0	0.7 - 0.8	0.6 - 0.7	0.4 - 0.6
	Submarine fan	0.7 - 0.8	0.5 - 0.6	0.3 - 0.5	0.1 - 0.3
	Carbonates	0.8 - 1.0	0.6 - 0.8	0.5 - 0.7	0.3 - 0.5
Continental	Lacustrine deltaic	0.7 - 0.9	0.5 - 0.7	0.4 - 0.6	0.3 - 0.5
	Alluvial fan, braided stream, meand. chan.	0.7 - 0.9	0.5 - 0.7	0.4 - 0.6	0.3 - 0.5
	Eolian	0.8 - 1.0	0.6 - 0.8	0.4 - 0.6	0.4 - 0.6
Others	Fractured basement	0.4 - 0.6	0.3 - 0.5	0.2 - 0.4	0.1 - 0.3
	Fractured, porous lava	0.4 - 0.6	0.3 - 0.5	0.2 - 0.4	0.1 - 0.3

Table E.3.5: General relative probability scale for the probability (CCOP, 2000).

P	General scale	Analogue or theoretical models	Proven geological models	P
1.0	Condition is <b>virtually to absolutely certain</b> . Data quality and control is excellent.	Only possible model applicable for the concerned area. Unfavourable models are impossible.	Identical geological factor to those found in fields and discoveries in immediate vicinity. Conditions are verified by unambiguous well and seismic control.	1.0
0.9		The model is very likely to absolutely certain. Unfavourable models are not impossible.		0.9
0.8	Condition is <b>most probable</b> . Data control and quality is <b>good</b> . Most likely interpretation.	The model is very likely. Only minor chance that unfavourable models can be applied.	Similar geological factor successfully tested by wells in the trend. Lateral continuity is probable as indicated by convincing well and seismic control.	0.8
0.7		The model is likely to very likely. Unfavourable models can be applied.		0.7
0.6	Condition is <b>probable</b> or data control and quality is <b>fair</b> . Favourable interpretation.	The model is mor likely than all otherunfavourable models.	Similar geological factor is known to exist within the trend. Lateral continuity is probable as indicated by limited well and seismic data.	0.6
0.5		Likely model, however, unfavourable are also likely.		0.5
0.4	Condition is <b>possible</b> or data control and quality is <b>poor to fair</b> . Less favourable interpretation possible.	Unfavourable models are more likely than applied model.	Similar geological factor may exist within the trend. Valid concepts, but unconvincing data only hints at possible presence of the feature.	0.4
0.3		The model is questionable. and unfavourable models are likely to very likely.		0.3
0.2	Condition is <b>virtually to absolutely impossible</b> . Data control and quality is <b>excellent</b> .	The model is unlikely and very questionable. Unfavourable models are very likely.	The geological factor is not known to exist within the trend. Conditions are verified by unambiguous well and seismic control.	0.2
0.0		The model is unlikely and highly questionable. Unfavourable models are very likely to certain.		0.0

SIGNATURE PAGE

DEPARTMENT OF EARTH SCIENCES

The undersigned hereby certify that they have read and recommend to the Faculty of Graduate Studies for acceptance a thesis titled “**An Integrated Lithostratigraphic, Formation and Structural Evaluation of the Migrant Structure, Sable Subbasin, Offshore Nova Scotia**” by Kenneth Martyns-Yellowe in partial fulfilment of the requirements for the degree of Master of Science.

Dated: March 23, 2021

Supervisors: \_\_\_\_\_  
Professor Grant Wach

External Examiner: \_\_\_\_\_  
Dr. Janice Allen

Readers: \_\_\_\_\_  
Dr. Owen Sherwood

\_\_\_\_\_  
Mr. Neil Watson

\_\_\_\_\_  
Mr. Bill Richards

Departmental Representative: \_\_\_\_\_  
Dr. Yana Fedortchouk

DALHOUSIE UNIVERSITY